CORROSION OF FUSION WELDED MAGNESIUM-ALUMINUM ALLOY, AZ31: EFFECTS OF MICROSTRUCTURE AND COMPOSITION IN ISOLATED WELD ZONES

A Dissertation

Presented to
the Faculty of the School of Engineering and Applied Science
University of Virginia

In partial Fulfilment
of the requirements for the degree
Doctor of Philosophy in Materials Science and Engineering

by

Leslie Gail Bland
October 2016

APPROVAL SHEET

The dissertation
is submitted in partial fulfillment of the requirements
for the degree of
Doctor of Philosophy (Materials Science and Engineering)

Leslie G. Bland
(Author)

The dissertation has been read and approved by the examining committee:

Dr. John R. Scully
(Dissertation Advisor)

Dr. Sean R. Agnew
(Committee Chairmen)

Dr. James M. Fitz-Gerald
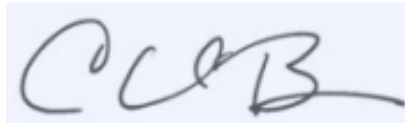(Committee Member)

Dr. Elizabeth J. Opila
(Committee Member)

Dr. David L. Green
(Committee Member)

Dr. Nick Birbilis
(Committee Member)

Accepted for the School of Engineering and Applied Science:

Craig H. Benson, Dean, School of Engineering and Applied Science
October 2016

Executive Summary

The corrosion behavior of tungsten inert gas (TIG) welded magnesium alloy AZ31B was explored using a variety of approaches. The main goals were to elucidate the microstructural and compositional factors that control corrosion and provide insight for corrosion mitigation strategies. In the initial work, the corrosion resistance of the as-received commercially pure Mg rod, AZ31B-H24 wrought base plate and AZ31B-H24 TIG welds were investigated by DC electrochemical methods as well as a 24 h open circuit potential (OCP) measurement complimented by electrochemical impedance spectroscopy (EIS) in 0.6 M NaCl solution. This approach provided a reliable indication of corrosion rate corroborated using four independent methods (1) mass loss, (2) EIS, (3) hydrogen gas collection and (4) Inductively Coupled Plasma Optical Emission Spectroscopy (ICP-OES) chemical analysis of exposure solutions. Analysis and comparison of corrosion rates of the wrought base and the isolated weld zones using these four parallel measurements enabled an unparalleled and reliable estimation of weld zone corrosion rate and provided a clear analysis of weld corrosion as a function of heat affected zone (HAZ), base and liquated base metal weld zones.

Weld structure and composition were characterized with optical microscopy and SEM. Significant changes to the alloy microstructure and corrosion behavior were observed after welding. The differences in corrosion rate can be attributed to microstructure attributes in the weld fusion zone (FZ) and HAZ. These include constituent particles which grow by Ostwald ripening within the α-Mg matrix during processing, eutectic solidification structures as well as recrystallization to form various grain sizes seen throughout the various weld zones. This dissertation is focused on first identifying and isolating the microstructural variables within the weld and then assessing how these factors in isolation affect the corrosion rate. These include mainly grain size, intermetallic particle (IMP) formation and distribution, solute segregation and crystallographic orientation. Specifically, the FZ was characterized by a randomized texture, large grain size and Al-Zn rich solidification boundaries. The HAZs were characterized by a basal texture, large recrystallized grains and larger, more widely spaced IMPs (in comparison to the wrought base). Further mechanistic understanding of corrosion as a function of weld zone was investigated by attempting to isolation and examine the effect of specific microstructural details on the corrosion rate.

The galvanic interactions between zones were also investigated using multichannel multi-electrode arrays (MMAs) comprised of sectioned weld zones in conjunction with in-situ time lapse video, scanning electron microscope (SEM) surface analysis and mixed potential theory analysis. The controlling region in weld corrosion was determined from time lapse videos by examining the dominate location of the hydrogen evolution reaction (HER) and darkening within the various weld zones which is considered characteristic of cathodic activation in Mg alloys. The variation in the anodic dissolution rates between weld zones and subsequent cathodic activation caused polarity reversal between electrochemically connected zones. The galvanic coupling between electrochemically connected weld zones was investigated diagnostically in three different environments, specifically 0.6 M NaCl, 0.6 M NaCl saturated with $Mg(OH)_2$ and tris(hydroxymethyl)aminomethane (TRIS). The resulting corrosion morphology in each of these environments were compared and contrasted.

The first microstructural characteristics identified were IMP distribution and grain size. Due to the different electrochemical potentials between the Mg matrix and any impurities or IMPs which may form during processing, micro-galvanic corrosion occurs. The IMPs function as active cathodic sites. Moreover, "activated" zones in the Mg matrix around the IMPs contribute to the corrosion behaviour. This was rigorously assessed through the use of furnace heat treatments, model alloys, electron microscopy and electrochemical methods. The relationship between particle size, particle spacing, and the resultant corrosion behaviour was explained. Additionally, model samples were developed to study IMP effects in isolation from other metallurgical effects (particularly grain size and residual stresses), with particles simulated by Al electrodes embedded in a Mg matrix. Arrays of model Mg-Al electrodes were constructed using high purity Al as a surrogate for Al-rich IMPs and flush mounted in commercial purity Mg. The area fraction, size and spacing of these electrodes each altered the corrosion rate and cathodic reaction kinetics over a 24 and 48 hour immersion period at the open circuit potential. The grain size was ruled out as a governing factor controlling the corrosion rate. However, small, close spaced Al-rich IMPs or synthesized electrodes raised the overall corrosion rates on Mg. The decrease in the corrosion rate with increasing particle spacing could help explain the decrease in the corrosion rate in the HAZ (in comparison to the baseplate) due to the larger particle spacings determined to exist in these weld zones.

Another metallurgical characteristic to evaluate was the effect of crystallographic orientation on corrosion rate due to the variation in crystallographic texture in the FZ versus the HAZ and baseplate. The electrochemical dissolution of Mg indicates strong crystallographic dependence based on film thickness in chloride-containing, environments. For non-chloride containing, neutral pH environments which dissolve air-formed MgO and support very little film growth, such as TRIS and Ethylenediaminetetraacetic (EDTA), there was initially limited crystallographic orientation dependence on the corrosion rate which correlated with surface energy. The origins of the corrosion rate trend were investigated utilizing EIS. EIS constant phase elements were exploited to determine oxide thicknesses. In 0.6 M NaCl, the corrosion rate varied with the film thickness. The fastest corrosion rate occurred on the basal plane and the slowest corrosion rate occurred on low index, prismatic and pyramidal planes. This variation in the corrosion kinetics with crystallographic orientation in 0.6 M NaCl was directly proportional to MgO film thickness. In particular, the variation in the MgO and $Mg(OH)_2$ thickness for faces with various crystallographic orientations may strongly alter the corrosion kinetics. The fastest corrosion rate was observed on the basal plane which correlates to the faster corrosion rate observed in the basal oriented HAZ and base material of the TIG weld.

The variation in the corrosion rate due to solidification structures formed during melting and resolidification of the FZ was also identified and characterized. Due to the high temperatures seen during welding and the differing solubility of the Mg and its alloying elements, solute-rich solidification boundaries can form in the FZ. To evaluate the corrosion of these regions with solidification structures and high solute content, the corrosion morphology was evaluated after exposure in 0.6 M NaCl. The corrosion rates for several die-cast Mg-Al alloys (AM50, AM50 and AZ91) were determined utilizing the four parallel methods used previously as these alloys enabled systematic evaluation of the effects of increased Al content and solidification boundaries on corrosion rate, as these alloys were deemed to be structurally similar to the FZ. The variation in the cathodic kinetics for the die-cast alloys were determined over 3, 24 and 48 hour immersion periods, at the OCP, in three electrolytes, unbuffered 0.6 M NaCl, 0,1 M TRIS, and 0.6 M NaCl buffered with TRIS. It was observed that the corrosion rate decreased with increasing Al content in spite of an increase in the phase fraction of IMPs. Variation in the cathodic activation with time for each of these environments is observed with lower levels of cathodic activation

occurring in 0.1 M TRIS. The lower corrosion rate observed on the alloys containing large solute segregation correlates to the lower corrosion rate observed in the resolidified FZ.

An additional study mapped the actively corroding sites in the weld and base material. The nature of the galvanic couples within the material (between weld zones and at localized IMP sites) was investigated using scanning kelvin prove force microscopy (SKPFM) and scanning electrochemical microscopy (SECM) to map the potential differences due to various microstructural features across the weld. Variations in the activity on the solidification boundaries in the FZ as well as the IMPs in the HAZ can be mapped using these in-situ techniques to better define how the microstructure alters the corrosion rate for a heterogeneous metal system.

The outcome of this research provided a fundamental understanding of the Mg weld microstructure property paradigm to (a) understand metallurgical factors which control corrosion, (b) provide insight regarding attributes to maximize or minimize in weld microstructures for a combination of intrinsic and galvanic corrosion resistance. Examples of this are provided in the future work section.

Bibliography

The publications that resulted/will result from this dissertation are listed below:

1. L.G. Bland, A.D. King, N. Birbilis, and J.R. Scully, "Assessing the Corrosion of Commercially Pure Magnesium and Commercial AZ31B by Electrochemical Impedance, Mass-loss, Hydrogen Collection and ICP-OES Solution Analysis," Corrosion Journal 71, 2 [Special Issue] (2015): p. 128-145.

2. L.G. Bland, J.M. Fitz-Gerald, and J.R. Scully, "Metallurgical and Electrochemical Characterization of the Corrosion of AZ31B-H24 Tungsten Inert Gas Weld: Isolated Weld Zones," Corrosion Journal 72, 9 (2016): p. 1116-1132.

3. L.G. Bland, B.C.R. Troconis, R.J. Santucci Jr., J.M. Fitz-Gerald, and J.R. Scully, "Metallurgical and Electrochemical Characterization of the Corrosion of Mg-Al-Zn Alloy AZ31B-H24 Tungsten Inert Gas Weld: Galvanic Corrosion Between Weld Zones " Corrosion Journal in press (DOI: 10.5006/2078), (2016).

4. L.G. Bland, J.J. Bhattacharyya, S.R. Agnew, J.M. Fitz-Gerald, and J.R. Scully, "Effect of Al-Mn and Al-Mn-Fe Intermetallic Particle Size and Distribution on the Corrosion of Mg-3Al-1Zn alloy: AZ31," Acta Mater In Review, (2016).

5. L.G. Bland, N. Birbilis, and J.R. Scully, "Exploring the Effects of Intermetallic Particle Size and Spacing on the Corrosion of Mg-Al Alloys Using Model Electrodes," J Electrochem Soc In Press, (2016).

6. L.G. Bland, K. Gusieva and J.R. Scully (2016), "Effect of Crystallographic Orientation on the Corrosion of Commercially Pure Mg," E. Acta. In Review.

7. L.G. Bland, L.C. Scully, and J.R. Scully (2016), "Assessing the Corrosion of High Al Composition and Multi-phase Mg-Al Alloys by Electrochemical Impedance, Mass-Loss, Hydrogen Collection, and ICP-OES Solution Analysis: Effect of Al Composition on the Corrosion of Mg-Al Alloys" In Progress.

8. L.G. Bland, R.F. Schaller and J.R. Scully (2016), "Utilization of a Partially Non-aqueous Electrolyte for the Spatial Mapping of Mg Corrosion using a Model Mg-Al Electrode," TMS Supplemental Proceedings. In Review.

9. L.G. Bland, R.F. Schaller, M.F. Hurley, J.M. Fitz-Gerald and J.R. Scully (2016), "Spatial Mapping of the Localized Corrosion Behavior of Magnesium Alloy AZ31 Tungsten Inert Gas Welds," In Progress.

Table of Contents

List of Tables

List of Figures

1 Introduction

1.1 Background

1.1.1 Cellular Materials

Magnesium (Mg) alloys are potential alternative materials for the construction of lightweight cellular truss structures[1-5]. This class of materials is attractive due to their mechanical, acoustic and thermal properties in combination with their low density, high specific strength and high thermal conductivity[1,2,6]. These properties can be combined with novel sandwich configurations to make potentially low cost, lightweight structures. However, corrosion is a challenge in the case of Mg, as corrosion mitigation in mildly aggressive and pH neutral conditions is difficult[1]. An additional challenge for the fabrication of these structures is joining strategy. The focus of this thesis is on welding as a joining strategy and its implications towards corrosion.

Characterization and optimization of different processing parameters for Mg-Al alloys, such as AZ31 were previously researched[7-10]. The addition of Al in these Mg-Al alloys helps to improve the weldability of the material by refining the grain structure[11]. Aluminum, as an alloying element, also decreases the overall corrosion rates for current commercial alloys[5]. For this reason, these alloys are of particular interest for industrial applications. Joining of Mg structures using conventional welding methods may present additional corrosion issues including Mg evaporation which can lead to alloying element enrichment and subsequent multi-phase formation and solidification induced dendritic segregation, both of which can increase the corrosion rates[12]. Given the application, Mg evaporation is a prevalent issue during weld processing given the low melting temperature, high vapor pressure, and oxide formation characteristics of Mg[7,8,10]. Due to the high thermal conductivity of Mg, large regions of material become heated. These regions cool at different rates; therefore, different regions of the weld recrystallize different amounts. This leads to a large variation in grain sizes seen throughout the material.

Currently, sandwich panels can be constructed in a multitude of geometries from honeycomb closed cell structures to open cell configurations[4]. To reduce the cost of these sandwich structures, alternative open cell configurations have recently been researched, as well as alternative connection methods[4]. Due to the extensive cost of Mg extraction (due to its high

reactivity), this material is often very expensive despite its abundance[15,16]. Research of different connection methods for these open cell designs will be important to decrease the overall cost of the Mg sandwich structures due to Mg's high price by decreasing the total amount of material necessary. Also, by allowing for an open cell design, heat is more readily dissipated[11] than in a traditional closed cell design[4] which is of particular importance for Mg due to its high thermal conductivity[17]. Furthermore, major improvements in joining technologies will help to expand the use of sandwich panels in diverse industries such as ground transportation, aerospace and shipbuilding[18].

1.1.2 Joining Strategy and Welding Types

The wider implementation of Mg in automotive, naval and aerospace applications requires better understanding of the processing of these materials, particularly the use of reliable joining methods such as welding. Many different types of welding, including laser and tungsten inert gas (TIG) welding have been proposed as feasible methods for joining various Mg alloys in order to fabricate low-cost welded structures[6,7,9,19-24].

The application of laser welding for Mg alloys has been suggested as an applicable welding strategy[7,19,20]. Laser welding of Mg alloys typically involves either a neodymium-doped yttrium aluminum garnet (Nd:YAG) or CO_2 laser where the material is shielded with either argon (0.0093 atm) or nitrogen (0.781 atm) gas. Laser beam welding is typically used due to its advantages such as high travel speeds, minimal amount of total heat added during welding which results in a small or minimized heat affected zone, and flexibility in design[11]. Typically, the sample is covered by an inert shielding gas which helps to protect the sample from oxygen and water vapor, both of which may cause the sample to oxidize during processing (Figure 1.1)[1,11].

Using a laser welding system gives the researcher flexibility in the design of the system as well as control over many of the operating parameters for optimization and testing of the weld characteristics. Despite these advantages, the higher heat input can also lead to detrimental mechanical defects, such as high porosity throughout the weld, as well as larger segregation of the alloying elements[11] to the weld zone. The issues with laser welding, such as the unstable weld pool, a large tendency for keyhole formation, porous oxide formation, diffusion of alloying elements and cracking have been thoroughly documented by other research groups [6,7,24,45,46]. It has been shown that use of proper welding parameters and shielding gas can alleviate some of these problems[11,24,47].

Another type of welding which is commonly used for the welding of Mg is arc welding, particularly inert gas tungsten arc welding (TIG), and inert gas metal arc welding (MIG). Arc welding methods, such as those stated, have been largely used to date for most welding of Mg alloys particularly for the removal and repair of casting defects[7,11]. A schematic for this welding process is shown in Figure 1.2.

During the TIG welding process, an arc is generated between the non-consumable tungsten electrode and the welded metal. Similar to the laser welding process, the electrode and welded metal are shielded with an inert gas, typically argon. Feasibility and characterization studies have been done on multiple studies using TIG welding and have found that this joining strategy can be used to make sound joints[48,49]. TIG welding has been researched on multiple commercial Mg alloys, particularly on Mg-Al alloys[26,50,51], and the mechanical and microstructural properties of this type of welding are well established for a variety of processing parameters. Similar with other welding techniques on Mg alloys, there remain issues with cracking and porosity in TIG welds[26,39,52] as well as intermetallic particle (IMP) formation.

Mg material properties dictate the types of welding which are feasible for Mg as well as which are best for its final corrosion properties (Table 1. 1). The inherent characteristics of this family of materials, such as the low absorptivity of laser beams, strong tendency to oxidize, high thermal conductivity, high coefficient of thermal expansion, low melting and boiling temperatures, wide solidification temperature range and a tendency to form low melting-point constituents make these alloy classes hard to process, meaning that more reliable understanding of the welding of these alloys is important. The specific heat of Mg is approximately 1 $J \cdot g^{-1} K^{-1}$, but due to lower density of Mg, its heat capacity is lower than aluminum or steel. Also, the relatively high coefficient of thermal expansion, approximately 25×10^{-6} K^{-1} and high thermal conductivity of 51 $W \cdot m^{-1} K^{-1}$ make this family of materials more susceptible to first heating and then distortion during welding, making lower power processes particularly important. For this reason, high power density welding methods, such as laser welding can be particularly detrimental to the mechanical and corrosion properties of Mg over TIG welding. Also, welds made through TIG welding are shown to have less porosity and less tendency to weld cracking than other processes[47,53]. Due to this, TIG welding has been offered as an alternative to other welding methods. This method allows for the joining of thick metal sections as well as thin sheets depending on the processing parameters. This variability in the material thickness and size

is extremely important to various industrial applications where different part sizes are frequently required[1]. However, the weld zones present in a TIG weld are much larger than in a laser weld. For the purposes of this dissertation, this was beneficial for isolating the corrosion properties of the weld with some spatial variation. To address corrosion, the zones of a weld are considered separately and the microstructure and composition of each zone is addressed.

1.1.3 Welding Metallurgy and Resultant Microstructures

The weld can be separated into several distinct metallurgical zones, mainly the Fusion Zone (FZ), Heat Affected Zones (HAZ) and wrought baseplate as labeled in Figure 1.3 where HAZ1 and HAZ2 are specified as two separate regions which have been affected during weld but heating produces slightly different microstructures. Typically, 2-3 HAZs are delineated within a weld based on the scale and precision of the experiments. For this work, 2 have been identified which are compositionally the same but have variations in grain size and IMP distribution.

The FZ denotes a region of direct interaction with the weld tool or heat source such that complete melting and solidification has occurred. The HAZ represents a region where sufficient heat input via the FZ is being conducted away in the material, resulting in significant grain growth, reduced hardness over the base material due to grain growth and recrystallization during processing, and a local variation in chemistry. These zones each have their own distinct characteristics which must be identified and are dependent on the type of processing used. These changes include local variations in recrystallization and grain growth, secondary phase formation and IMPs, and crystallographic orientation[29].

The top plate of the configuration shown, close to the heat source, experiences the highest temperature and the grains in this region experience some grain growth. Similar grain growth is also observed in the surrounding HAZ. The FZ contains fine, equiaxed grains solidified as in a casting in a hot mold (the HAZ). In the HAZ, the grains next to the FZ experience recrystallization and grain growth due to the high temperature experienced during welding. Further away from this zone, the grains were more or less same in size as that of the base metal.

Solidification boundaries are formed throughout the material[39]. The formation of these precipitates is due to the rapid non-equilibrium cooling within the weld zone where dendritic growth in front of the liquid/solid interface occurs in the molten FZ[44]. Along with this rejection of solute to the FZ, evaporation of the Mg can occur due to its low boiling temperature[7]. This

4

further enriches the FZ in the solute elements and leads to formation of Al-Zn interdendritic regions as shown by the pseudo-binary phase diagram (Figure 1.4(b)).

Also, solidification structures are formed in the fusion zone. The formation of these structures occurs as the temperature falls in the liquid in advance of the interface. The liquid then becomes unstable and crystalline fingers form in the liquid from the central interface[44]. This process is also complicated by dendritic growth within an alloy given solute elements that are more soluble in the liquid state than in the solid state. Upon solidification such solute is rejected from the solid which can lead to solute segregation of the solute elements upon solidification. When this occurs, the liquid becomes progressively richer in the solute element as the material solidifies. The solute concentrations in the solid rise in those regions which solidify last, such as the center of the dendritic branch, and is frequently referred to as coring[44]. In the case of Mg-Al, the last liquid to form is at the eutectic composition. The microstructure of this region depends on the temperature gradient (G) and the growth rate (R) of the interface. With arc welding, there is less undercooling, leading to a more planar or cellular microstructure as opposed to a dendritic microstructure. During solidification, the specific solidification microstructural geometry can be planar, cellular or dendritic depending on the temperature gradient within the weld and the material starting composition[25]. With increased constitutional supercooling, the solidification mode changes from planar to cellular to columnar dendritic and finally to equiaxed dendritic. Figure 1.5 shows how the temperature gradient and growth rate affect the resultant microstructure. It is unclear whether this shape impacts corrosion propagation.

1.1.4 Corrosion of Magnesium

Although Mg is of interest due to its light weight, this material system is extremely active due to its low electrochemical potential relative to other material systems according to the following reactions.

$$2H_2O + 2e^- \rightarrow H_2 + 2OH^- \hspace{4cm} \text{Equation 1.1}$$

$$Mg \rightarrow Mg^{2+} + 2e^- \hspace{5cm} \text{Equation 1.2}$$

From the Pourbaix diagram (Figure 1.6), it can be seen that Mg corrodes in a wide range of potentials and pH environments. Similarly, the protective film, compromising of a mixture of MgO and $Mg(OH)_2$ which can form on Mg only forms at high pH values and has shown to be only semi-protective and frequently porous[60]. This film has been characterized in multiple studies[61-63] and has been shown to form relatively thickly (~500 nm) on the sample surface over

5

short exposure times, up to about 3 or 4 hours. However, upon longer exposure, this passive film will begin to breakdown as the electrolyte can permeate through the porous film and react with the underlying surface layer[62]. The presence and intermittent breakdown of this film can complicate the accurate calculation of the long term corrosion rate of the Mg.

1.1.5 Corrosion of Mg-Al-Zn Alloy: AZ31B

There has been a large focus on measuring the corrosion performance of, not only commercially pure Mg, but also commercial Mg alloys; in particular AZ31, AZ91 and AM60[57-67]. Much focus has been given to Mg-Al alloys due to their improved mechanical properties that arise without adversely influencing the corrosion rate relative to Mg[61,68]. Similarly, in order to improve the weldability and the corrosion properties of Mg, alloying elements are typically added which will enhance these features.

For Mg alloy, AZ31, the main constituent elements must be understood. It is generally accepted that the addition of Al to Mg alloys increases the corrosion resistance when alloying remains in solid solution (Figure 1. 8) [5,87-89]. Aluminum is traditionally added to Mg due to the fact that it is relatively cheap, soluble, and improves the strength of Mg[90]. The relative concentration of the Al in solution can alter the corrosion rate. Additionally, at low Zn content, there is no increase in the corrosion rate. It is only when Zn is above a few wt% that it will detrimentally affect the corrosion rate as has been reported [92,93]. At these higher concentrations, the Zn can precipitate along the grain boundaries and form a local cathodic site for corrosion and therefore an increased cathodic corrosion rate[93,94].

An additional effect on the corrosion rate can be due to the addition of Mn[92,95,96]. As an alloying element added in isolation, Mn has little effect on the corrosion rate up to concentrations of approximately 5wt%[92]. However, the deliberate addition of Mn sequesters detrimental impurity Fe into an Al-Mn-Fe intermetallic. An ideal Fe/Mn ratio of 0.032 is necessary in order to completely mitigate the detrimental corrosion effects from Fe impurities in Mg, whereas greater ratios will sharply increase the corrosion rates [57,86,92,95]. A summary of the effect of these alloying additions on the electrochemical potential of Mg can be seen in Figure 1.7 and Table 1. 2.

There have been multiple studies on the corrosion rate of welded Mg alloys[10,22,2312,24,33,45,46]. In general, particularly for Al-containing alloys, it is found that the corrosion rate in the FZ and HAZs decrease after welding[19,21,69]. The FZ typically has the lowest

corrosion rate, and corrosion has been shown to initiate in this zone after the HAZ[70]. However, there is little understanding of the controlling microstructural factors on corrosion rate and this effect is therefore the focus of this dissertation.

1.2 Possible Impact of Isolated Metallurgical Factors on the Weld Corrosion for Mg-Al-Zn Alloys

1.2.1 General Overview on Critical Factors of Weld Corrosion of Mg Alloys

Due to the significant heating and cooling of the material during welding, there are large differences in the metallurgy as a function of weld zone. The differences in microstructure will have a large impact on the final corrosion rate due to variations in the grain size, IMP formation, solidification boundaries and crystallographic orientation.

1.2.2 Effects of Weld Induced Grain Size on Corrosion

The impact of grain size measured throughout different weld zones and for different processing procedures has been studied[62,71-74]. Typically, the corrosion resistance of the weld zone, in comparison to the base metal, is not closely related to the relative difference in grain size[70]. Many of these studies have been on the corrosion resistance of friction stir weld (FSW) samples which have found that the finer-grained surface of the stir zone exhibited improved corrosion resistance[70,75]. Friction Stir Welded AZ31B samples in various temper designations were found to have an improved corrosion resistance in the stir zone over the base material, where the finer grain structure within the weld zone may have had an impact on this improvement[70,75]. Other literature states that there is a correlation between the measured i_{corr} and grain size where they hypothesized that the differences in corrosion resistance between the base metal and weld zones may be attributed to the formation of a more protective surface film on the finer-grained surface within the stir zone[75]. However, this is little evidence to support this.

1.2.3 Effects of Weld Induced Intermetallic Particles on Corrosion

Due to the high processing temperatures during welding combined with the low solubility of most alloying elements in Mg, the presence of IMPs are expected upon cooling. It has been reported that these IMPs appear in weld structures after processing for a multitude of processes (i.e., TIG, laser welding, FSW)[84-87]. The presence of these phases will therefore affect the subsequent corrosion properties of the weld. During welding, Al_8Mn_5 and Al_3Mg_2 phases are commonly present within the alloy, both of which can alter the corrosion rate[12,88-90]. It has been

argued that the Al-Mn IMP formed during processing will have a greater impact on the overall corrosion resistance of the material after weld processing than grain size[91]. There particles are typically cathodic to the α-Mg matrix which can increase micro-galvanic corrosion at the IMP/α-Mg interface (Table 1. 3). The effect of the particle size, spacing and area fraction of these IMPs have not been studied for Mg alloys.

1.2.4 Effects of Weld Induced Solidification Structure Compositional Changes and Solute Enrichment on Corrosion

Solute partitioning during welding is a common phenomenon which will affect the weldability of the structure as well as its resultant microstructural, compositional and corrosion properties. As the alloy solidifies, extensive solute redistribution can occur at the solid-liquid interface due to coring as solute is rejected during solidification of the Mg rich α-phase, leading to solute segregation of the solute elements into the remaining liquid solution upon solidification [80]. Solute segregation of the Al and Zn to the weld zone has been reported along with the second phases which form during processing[83]. In particular, there has been little study on the effect of this solute segregation of the corrosion rates in a TIG welded samples. This solute segregation leads to micro-galvanic corrosion between the solidification boundary and the α-Mg. This is affected by the composition of both the solidification boundary and the solid solution α-Mg.

1.2.5 Effects of Weld Induced Crystal Orientation on Corrosion

The texture in the FZ after fusion welding is significantly different than the texture in either the HAZ or the base material[29]. The original base material typically has a basal (0001) texture[76,77]. However, this texture changes after fusion welding due to the melting and resolidification of the FZ[78]. This leaves the FZ with a highly randomized texture while the HAZ and the wrought base retain the strong basal {0 0 0 1} texture albeit recrystallized. This research program explains the crystallographic dependence on corrosion rate for the Mg system. The schematic shown in Figure 1.9 illustrates the variation in crystallographic orientation with weld zone.

1.3 Critical Unresolved Issues in Current Research

Identification of the structure property paradigm, from a mechanistic, metallurgical, and corrosion point of view needs to be a research focus so that ultimately the beneficial properties of cellular metal structures can be enabled in light-weight Mg structures and preserved in harsh marine environments. However, to understand how to optimize the processing parameters for

corrosion resistance, the critical metallurgical factors that control Mg weld corrosion must be understood. To advance the ability to develop joining technologies which optimize fabrication of cellular metal structures fabricated from welded Mg alloys, the following critical questions must be addressed in the case of welded structures subjected to aqueous corrosion:

- How can the instantaneous corrosion rate of commercially pure Mg and AZ31 be determined reliably across various weld microstructures?

- What are the corrosion mechanisms and modes of attack of commercial Mg alloy sheet as a function of differing marine environmental scenarios such as variations in the pH and chloride content?

- What is the overall galvanic behavior of the weld, considering it a composite constructed of a combination of each of the weld zones?

- How do metallurgical variables, such as grain size, IMP size/spacing and area fraction, Al solute enrichment and crystallographic orientation control the corrosion rate of commercial Mg alloys and welds?

- How does cathodic activation alter the corrosion of commercial Mg alloys and how does this affect the corrosion in each weld zone?

1.4 Research Overview

There is a need to understand (a) the metallurgical factors that control the intrinsic corrosion of each weld zone, (b) the galvanic coupling of the weld zones and (c) the effect of anodically induced activation on each of these aspects. This understanding is necessary to guide follow-on selection of corrosion mitigation strategies and best practices for welds. To advance the ability to develop joining technologies which optimize fabrication of cellular metal structures fabricated from welded Mg alloys, the previous critical questions must be addressed in the case of TIG welded structures.

A key related objective of this dissertation is to develop methods to enable determining the instantaneous corrosion rate of Mg as well as the critical metallurgical variables controlling Mg corrosion and their effect on corrosion within a welded specimen, particularly for commercially pure Mg as well as the Mg-Al alloy, AZ31B. The work will strive to better understand how these variables, mainly grain size, orientation, IMPs and solute enrichment, are detrimental to the intrinsic corrosion rate of each weld zone as well as the overall effect of each

9

zone together on the global corrosion of the weld in order to better understand what processing parameters would be best implemented.

1.5 Thesis Organization

The research outline for this dissertation consists of several tasks, strategically developed to isolate and determine the corrosion properties of each of the specified weld metallurgical attributes that will be researched in isolation to the maximum extent possible.

The first task of this research program was to investigate how to accurately determine the instantaneous corrosion rate of commercially pure Mg and AZ31B-H24. The methods for this portion of the research program were initially performed on commercially pure Mg using a combination of H_2 collection, EIS and gravimetric mass loss. ICP-OES solution analysis has been added to further enhance this analysis and the method has been refined for AZ31B-H24 plate. This same procedure has also been used to analyze the corrosion rate of the TIG welded material. This method can be applied to small regions of the weld zones to determine the corrosion rate of each isolated weld zones. For this research program, certain attributes of the welds will also then be isolated to the maximum extent possible in model materials in order to determine their isolated effect on the corrosion of Mg. The concepts learned in these studies will be applied to the corrosion of a weld.

The second task was to characterize the metallurgy of the as-received AZ31B as well as the TIG welded materials. Optical microscopy as well as SEM and EDS compositional analysis were performed on both the as-received and the TIG welded materials and the TIG welded materials before and after corrosion to determine which metallurgical features, within each weld zone, may be important for weld corrosion. These metallurgical characteristics (i.e., grain size, IMP formation, solute clustering and crystallographic orientation) were studied in isolation using model systems.

The third task was to evaluate the effect of IMPs and grain size on the corrosion rate. Due to the different electrochemical potentials between the Mg matrix and any impurities or IMPs which may form during processing, micro-galvanic corrosion can occur. This task involved looking at the impact of Al-Mn and Al-Mn-Fe IMP size and population density on the corrosion of AZ31B-H24. A strategic metallurgical and electrochemical characterization of IMP size/spacing as well as grain size and its corresponding corrosion rate was undertaken. This task

included differing heat treatments to achieve different grain sizes and particle sizes/spacings on AZ31B. The corrosion rate was determined using the four corroborated methods used previously and correlated with IMP size/spacing as well as grain size. To further isolate the effect of Al-rich IMPs on the corrosion rate, a study was also performed of model alloys, developed as an array of Al electrodes embedded in the Mg matrix, to determine the impact of various IMP size, spacing and area fraction on the corrosion rate and cathodic kinetics.

The fourth task was to evaluate the effect of crystallographic orientation on the corrosion rate. During processing, each of the weld zones has a distinct texture which varies from the as received alloy. The different corrosion rates of each zone depend on the composite corrosion rates which correspond to the ensemble of grains of particular orientations. Better understanding of factors controlling texture effects helps to better understand how the corrosion initiates and propagates according to these specified crystallographic orientations[93,94]. This task included determining how the crystallographic texture of the material changes with different heat treatments using EBSD. This involved using the differently grain sized materials from the previous task and determining how their texture changed with heat treatment. Additionally, the crystallographic texture of the FZ may be different than these materials; therefore, additional studies were performed to determine the texture of the FZ and how this affects the corrosion behavior. Corrosion was evaluated on samples which were heat treated to achieve large grains so that the preferential corrosion was measured using a 3D optical method such as white light interferometry as well as evaluation of the crystallographic orientation in specified weld regions.

The fifth task was to evaluate the effect of solidification eutectic structure on the corrosion rate, by comparing the corrosion rate of an AZ31 sheet to several die-cast alloys used to model alloys with higher alloying content possible in the FZ where Mg evaporation may have occurred. These alloys each contain solidification boundaries with varying amounts of Al, Mn and Zn. The corrosion rate of these alloys was compared using the four proven methods. The corrosion morphology was then evaluation after exposure in 0.6 M NaCl. The impact of composition and these solidification boundaries on the corrosion rate and cathodic kinetics was evaluated. This allowed for insight into the FZ as seen in a weld.

An additional, sixth task, was to spatially map the active corrosion of Mg using scanning electrochemical microscopy (SECM) and Scanning Kelvin Probe Force Microscopy (SKPFM). This allowed for real-time evaluation of active corrosion within an AZ31B material.

References

1.   M.M. Avedesian and H. Baker, "Magnesium and Magnesium Alloys," ASM International (1999).
2.   G. Song and A. Atrens, "Understanding Magnesium Corrosion—A Framework for Improved Alloy Performance," Adv Eng Mater 5, 12 (2003): p. 837-858.
3.   H.N.G. Wadley, "Cellular metals manufacturing," Adv Eng Mater 4, 10 (2002): p. 726-733.
4.   H.N.G. Wadley, "Multifunctional periodic cellular metals," Philos T Roy Soc A 364, 1838 (2006): p. 31-68.
5.   I.J. Polmear, "Light Alloys: From Traditional Alloys to Nanocrystals 4th Edition," Elsevier (2006).
6.   G. Padmanaban and V. Balasubramanian, "Effects of laser beam welding parameters on mechanical properties and microstructure of AZ31B magnesium alloy," T Nonferr Metal Soc 21, 9 (2011): p. 1917-1924.
7.   X. Cao, M. Jahazi, J.P. Immarigeon, and W. Wallace, "A review of laser welding techniques for magnesium alloys," J Mater Process Tech 171, 2 (2006): p. 188-204.
8.   J.H. Zhu, L. Li, and Z. Liu, "CO_2 and diode laser welding of AZ31 magnesium alloy," Appl Surf Sci 247, 1-4 (2005): p. 300-306.
9.   L. Liming, W. Jifeng, and S. Gang, "Hybrid laser–TIG welding, laser beam welding and gas tungsten arc welding of AZ31B magnesium alloy," Materials Science and Engineering: A 381, 1–2 (2004): p. 129-133.
10.   G. Song, L.M. Liu, M.S. Chi, and J.F. Wang, "Investigations on laser-TIG hybrid welding of magnesium alloys," Mater Sci Forum 488-489, (2005): p. 371-375.
11.   F. Czerwinski, "Magnesium Alloys-Design, Processing and Properties," (2011).
12.   A.D. Südholz, N.T. Kirkland, R.G. Buchheit, and N. Birbilis, "Electrochemical Properties of Intermetallic Phases and Common Impurity Elements in Magnesium Alloys," Electrochemical and Solid-State Letters 14, 2 (2011): p. C5-C7.
13.   N.N. Aung and W. Zhou, "Effect of grain size and twins on corrosion behaviour of AZ31B magnesium alloy," Corros Sci 52, 2 (2010): p. 589-594.
14.   A. Pardo, M.C. Merino, A.E. Coy, F. Viejo, R. Arrabal, and S. Feliú Jr, "Influence of microstructure and composition on the corrosion behaviour of Mg/Al alloys in chloride media," Electrochim Acta 53, 27 (2008): p. 7890-7902.
15.   F.H. Froes, D. Eliezer, and E. Aghion, "The Science, Technology, and Applications of Magnesium," JOM: Light Metals (1998): p. 30-34.
16.   S. Das, "Magnesium for Automotive Applications: Primary Production Cost Assesment," Jom-Us: p. 22-26.
17.   A.A. Lou, "Recent magnesium alloy development for elevated temperature applicatiosn," Int Mater Rev 49, 1 (2004): p. 13-30.
18.   J.C. Williams and E.A. Starke Jr, "Progress in structural materials for aerospace systems," Acta Mater 51, 19 (2003): p. 5775-5799.
19.   H. Haferkamp, F.W. Bach, I. Burmester, K. Kreutzburg, and M. Niemeyer. *Nd:YAG laser beam welding of magnesium constructions*. in *Third International Magnesium Conference*. 1996. Manchester, UK.

20.   G.K. K.H. Leong, P.G. Sanders, and J.S. Keske, *Laser beam welding of AZ31B-H24 magnesium alloy*, in *ICALEO 98: Laser Materials Processing Conference*. 1998: Orlando, FL. p. 28-36.

21.   L. Liu and R. Xu, "Investigation of the corrosion behaviour of laser-TIG hybrid welded Mg alloys," Corros Sci 52, 9 (2010): p. 3078-3085.

22.   P. Liu, Y. Li, H. Geng, and J. Wang, "Microstructure characteristics in TIG welded joint of Mg/Al dissimilar materials," Mater Lett 61, 6 (2007): p. 1288-1291.

23.   Y. Quan, Z. Chen, X. Gong, and Z. Yu, "CO_2 laser beam welding of dissimilar magnesium-based alloys," Materials Science and Engineering: A 496, 1–2 (2008): p. 45-51.

24.   L.D. Scintilla, L. Tricarico, M. Brandizzi, and A.A. Satriano, "Nd:YAG laser weldability and mechanical properties of AZ31 magnesium alloy butt joints," J Mater Process Tech 210, 15 (2010): p. 2206-2214.

25.   Escobar, Thermal desorption spectroscopy study of experimental Ti/S containing steels, 2012.

26.   Z.D. Zhang, L.M. Liu, Y. Shen, and L. Wang, "Mechanical properties and microstructures of a magnesium alloy gas tungsten arc welded with a cadmium chloride flux," Mater Charact 59, 1 (2008): p. 40-46.

27.   S.M. Chowdhury, D.L. Chen, S.D. Bhole, E. Powidajko, D.C. Weckman, and Y. Zhou, "Microstructure and Mechanical Properties of Fiber-Laser-Welded and Diode-Laser-Welded AZ31 Magnesium Alloy," Metall Mater Trans A 42A, 7 (2011): p. 1974-1989.

28.   S. Kou. *Welding Metallurgy, Second Edition*. 2002; Available from: http://www.123library.org/book_details/?id=25724.

29.   R.S. Coelho, A. Kostka, H. Pinto, S. Riekehr, M. Koçak, and A.R. Pyzalla, "Microstructure and mechanical properties of magnesium alloy AZ31B laser beam welds," Materials Science and Engineering: A 485, 1–2 (2008): p. 20-30.

30.   G. Padmanaban and V. Balasubramanian, "Metallurgical characterization of pulsed current gas tungsten arc, friction stir and laser beam welded AZ31B magnesium alloy joints," Mater Chem Phys 125, 3 (2011): p. 686-697.

31.   C.-M. Lin, H.-L. Tsai, C.-L. Lee, D.-S. Chou, and J.-C. Huang, "Evolution of microstructures and properties of magnesium alloy weldments produced with CO2 laser process," Materials Science and Engineering: A 548, 0 (2012): p. 12-18.

32.   M.B. Kannan, W. Dietzel, C. Blawert, S. Riekehr, and M. Koçak, "Stress corrosion cracking behavior of Nd:YAG laser butt welded AZ31 Mg sheet," Materials Science and Engineering: A 444, 1–2 (2007): p. 220-226.

33.   D. Min, J. Shen, S.Q. Lai, J. Chen, N. Xu, and H. Liu, "Effects of heat input on the low power Nd:YAG pulse laser conduction weldability of magnesium alloy AZ61," Opt Laser Eng 49, 1 (2011): p. 89-96.

34.   M. Wahba, M. Mizutani, Y. Kawahito, and S. Katayama, "Laser welding of die-cast AZ91D magnesium alloy," Mater Design 33, (2012): p. 569-576.

35.   L. Commin, M. Dumont, R. Rotinat, F. Pierron, J.E. Masse, and L. Barrallier, "Texture evolution in Nd:YAG-laser welds of AZ31 magnesium alloy hot rolled sheets and its influence on mechanical properties," Mat Sci Eng a-Struct 528, 4-5 (2011): p. 2049-2055.

36.   J. Shen, G. You, S. Long, and F. Pan, "Abnormal macropore formation during double-sided gas tungsten arc welding of magnesium AZ91D alloy," Mater Charact 59, 8 (2008): p. 1059-1065.

37. L. Liu and C. Dong, "Gas tungsten-arc filler welding of AZ31 magnesium alloy," Mater Lett 60, 17–18 (2006): p. 2194-2197.

38. D. Min, J. Shen, S. Lai, and J. Chen, "Effect of heat input on the microstructure and mechanical properties of tungsten inert gas arc butt-welded AZ61 magnesium alloy plates," Mater Charact 60, 12 (2009): p. 1583-1590.

39. T. Zhu, Z.W. Chen, and W. Gao, "Microstructure formation in partially melted zone during gas tungsten arc welding of AZ91 Mg cast alloy," Mater Charact 59, 11 (2008): p. 1550-1558.

40. D.Q. Sun, D.X. Sun, S.Q. Yin, and J.B. Li, "Microstructures and Mechanical Properties of Tungsten Inert Gas Welded Magnesium Alloy AZ91D Joints," Isij Int 46, 8 (2006): p. 1200-1204.

41. L. Liu and Z. Wu, "Microstructure and interfacial reactions of soldering magnesium alloy AZ31B," Mater Charact 61, 1 (2010): p. 13-18.

42. L. Ma, D.Y. He, X.Y. Li, and J.M. Jiang, "High-frequency induction soldering of magnesium alloy AZ31B using a Zn−Al filler metal," Mater Lett 64, 5 (2010): p. 596-598.

43. Y.J. Jin and T.I. Khan, "Effect of bonding time on microstructure and mechanical properties of transient liquid phase bonded magnesium AZ31 alloy," Materials & Design 38, 0 (2012): p. 32-37.

44. R.E. Reed-Hill and R. Abbaschian, Physical metallurgy principles (Boston: PWS-Kent Pub., 1992.

45. G. Padmanaban and V. Balasubramanian, "Optimization of laser beam welding process parameters to attain maximum tensile strength in AZ31B magnesium alloy," Optics & Laser Technology 42, 8 (2010): p. 1253-1260.

46. L.K. Pan, C.C. Wang, Y.C. Hsiao, and K.C. Ho, "Optimization of Nd:YAG laser welding onto magnesium alloy via Taguchi analysis," Optics & Laser Technology 37, 1 (2005): p. 33-42.

47. X. Cao and M. Jahazi, "Effect of welding speed on butt joint quality of Ti–6Al–4V alloy welded using a high-power Nd:YAG laser," Opt Laser Eng 47, 11 (2009): p. 1231-1241.

48. P. Carlone and G.S. Palazzo, "Characterization of TIG and FSW weldings in cast ZE41A magnesium alloy," J Mater Process Tech 215, 0 (2015): p. 87-94.

49. J. Shen, D.j. Zhai, K. Liu, and Z.-m. Cao, "Effects of welding current on properties of A-TIG welded AZ31 magnesium alloy joints with TiO2 coating," T Nonferr Metal Soc 24, 8 (2014): p. 2507-2515.

50. A. Munitz, C. Cotler, A. Stern, and G. Kohn, "Mechanical properties and microstructure of gas tungsten arc welded magnesium AZ91D plates," Materials Science and Engineering: A 302, 1 (2001): p. 68-73.

51. T. Zhu, Z.W. Chen, and W. Gao, "Incipient melting in partially melted zone during arc welding of AZ91D magnesium alloy," Materials Science and Engineering: A 416, 1–2 (2006): p. 246-252.

52. C.J. Huang, C.M. Cheng, and C.P. Chou, "The Influence of Aluminum Content of AZ61 and AZ80 Magnesium Alloys on Hot Cracking," Materials & Manufacturing Processes 26, 9 (2011): p. 1179-1187.

53. L. Liu, G. Song, G. Liang, and J. Wang, "Pore formation during hybrid laser-tungsten inert gas arc welding of magnesium alloy AZ31B—mechanism and remedy," Materials Science and Engineering: A 390, 1–2 (2005): p. 76-80.

54. H. Zhao, D.R. White, and T. DebRoy, "Current issues and problems in laser welding of automotive aluminium alloys," Int Mater Rev 44, 6 (1999): p. 238-266.

55. A. Weisheit, R. Galun, and B. Mordike, "CO {sub 2} laser beam welding of magnesium-based alloys," Weld J 77, 4 (1998).

56. D. Montiel, L. Liu, L. Xiao, Y. Zhou, and N. Provatas, "Microstructure analysis of AZ31 magnesium alloy welds using phase-field models," Acta Mater 60, 16 (2012): p. 5925-5932.

57. G. Song and A. Atrens, "Corrosion mechanisms of magnesium alloys," Adv Eng Mater 1, 1 (1999): p. 11-33.

58. P. Volovitch, M. Serdechnova, and K. Ogle, "Aqueous Corrosion of Mg-Al Binary Alloys: Roles of Al and Mg," Corrosion 68, 6 (2012): p. 557-570.

59. A.D. Südholz, K. Gusieva, X.B. Chen, B.C. Muddle, M.A. Gibson, and N. Birbilis, "Electrochemical behaviour and corrosion of Mg-Y alloys," Corros Sci 53, 6 (2011): p. 2277-2282.

60. G. Song and D. St. John, "The effect of zirconium grain refinement on the corrosion behaviour of magnesium-rare earth alloy MEZ," Journal of Light Metals 2, 1 (2002): p. 1-16.

61. A.D. Südholz, N. Birbilis, C.J. Bettles, and M.A. Gibson, "Corrosion behaviour of Mg-alloy AZ91E with atypical alloying additions," J Alloy Compd 471, 1–2 (2009): p. 109-115.

62. K.D. Ralston, G. Williams, and N. Birbilis, "Effect of pH on the Grain Size Dependence of Magnesium Corrosion," Corrosion 68, 6 (2012): p. 507-517.

63. G. Williams, K. Gusieva, and N. Birbilis, "Localized Corrosion of Binary Mg-Nd Alloys in Chloride-Containing Electrolyte Using a Scanning Vibrating Electrode Technique," Corrosion 68, 6 (2012): p. 489-498.

64. D.B. Huang, J.Y. Hu, G.L. Song, and X.P. Guo, "Self-corrosion, galvanic corrosion and inhibition of GW103 and AZ91D Mg alloys in ethylene glycol solution," Corros Eng Sci Techn 48, 2 (2013): p. 155-160.

65. M.C. Turhan, D. Ruckle, M.S. Killian, H. Jha, and S. Virtanen, "Corrosion Behavior of Polypyrrole/AZ91D in Simulated Body Fluid Solutions and its Functionalization with Albumin Monolayers," Corrosion 68, 6 (2012): p. 536-547.

66. G. Baril, C. Blanc, M. Keddam, and N. Pebere, "Local electrochemical impedance spectroscopy applied to the corrosion behavior of an AZ91 magnesium alloy," J Electrochem Soc 150, 10 (2003): p. B488-B493.

67. G. Baril, C. Blanc, and N. Pebere, "AC impedance spectroscopy in characterizing time-dependent corrosion of AZ91 and AM50 magnesium alloys - Characterization with respect to their microstructures," J Electrochem Soc 148, 12 (2001): p. B489-B496.

68. G. Ballerini, U. Bardi, R. Bignucolo, and G. Ceraolo, "About some corrosion mechanisms of AZ91D magnesium alloy," Corros Sci 47, 9 (2005): p. 2173-2184.

69. R.C. Zeng, J. Chen, W. Dietzel, R. Zettler, J.F. dos Santos, M.L. Nascimento, and K.U. Kainer, "Corrosion of friction stir welded magnesium alloy AM50," Corros Sci 51, 8 (2009): p. 1738-1746.

70. J.R. Kish, G. Williams, J.R. McDermid, J.M. Thuss, and C.F. Glover, "Effect of Grain Size on the Corrosion Resistance of Friction Stir Welded Mg Alloy AZ31B Joints," J Electrochem Soc 161, 9 (2014): p. C405-C411.

71.   N. Birbilis, K.D. Ralston, S. Virtanen, H.L. Fraser, and C.H.J. Davies, "Grain character influences on corrosion of ECAPed pure magnesium," Corrosion Engineering, Science & Technology 45, 3 (2010): p. 224-230.

72.   J. Liao, M. Hotta, and N. Yamamoto, "Corrosion behavior of fine-grained AZ31B magnesium alloy," Corros Sci 61, 0 (2012): p. 208-214.

73.   K.D. Ralston and N. Birbilis, "Effect of Grain Size on Corrosion: A Review," Corros Sci 66, 7 (2010).

74.   R. Ambat, N.N. Aung, and W. Zhou, "Evaluation of microstructural effects on corrosion behaviour of AZ91D magnesium alloy," Corros Sci 42, 8 (2000): p. 1433-1455.

75.   Y.H. Jang, S.S. Kim, C.D. Yim, C.G. Lee, and S.J. Kim, "Corrosion behaviour of friction stir welded AZ31B Mg in 3·5%NaCl solution," Corrosion Engineering, Science & Technology 42, 2 (2007): p. 119-122.

76.   X.Y. Lou, M. Li, R.K. Boger, S.R. Agnew, and R.H. Wagoner, "Hardening evolution of AZ31B Mg sheet," International Journal of Plasticity 23, 1 (2007): p. 44-86.

77.   A. Styczynski, C. Hartig, J. Bohlen, and D. Letzig, "Cold rolling textures in AZ31 wrought magnesium alloy," Scripta Mater 50, 7 (2004): p. 943-947.

78.   V.A. Karkhin, V.V. Plochikhine, A.S. Ilyin, and H.W. Bergmann, "Inverse Modelling of Fusion Welding Processes," Weld World 46, 11-12 (2002): p. 2-13.

79.   R. Xin, B. Li, L. Li, and Q. Liu, "Influence of texture on corrosion rate of AZ31 Mg alloy in 3.5 wt.% NaCl," Materials & Design 32, (2011): p. 4548-4552.

80.   S. Lampman and A.S.M. International. *Weld integrity and performance a source book adapted from ASM international handbooks, conference proceedings, and technical books*. 1997.

81.   T.H. Gao, R.S. Liu, L.L. Zhou, Z.A. Tian, and Q. Xie, "Formation Properties of Cluster Structures during the Rapid Solidification of Liquid Ca7Mg3 Alloy," Acta Phys-Chim Sin 25, 10 (2009): p. 2093-2100.

82.   D. Orlov, K.D. Ralston, N. Birbilis, and Y. Estrin, "Enhanced corrosion resistance of Mg alloy ZK60 after processing by integrated extrusion and equal channel angular pressing," Acta Mater 59, 15 (2011): p. 6176-6186.

83.   S. Niknejad, L. Liu, M.Y. Lee, S. Esmaeili, and N.Y. Zhou, "Resistance spot welding of AZ series magnesium alloys: Effects of aluminum content on microstructure and mechanical properties," Materials Science and Engineering: A 618, 0 (2014): p. 323-334.

84.   A. Kostka, R.S. Coelho, J. dos Santos, and A.R. Pyzalla, "Microstructure of friction stir welding of aluminium alloy to magnesium alloy," Scripta Mater 60, 11 (2009): p. 953-956.

85.   J. Yan, Z. Xu, Z. Li, L. Li, and S. Yang, "Microstructure characteristics and performance of dissimilar welds between magnesium alloy and aluminum formed by friction stirring," Scripta Mater 53, 5 (2005): p. 585-589.

86.   Y.S. Sato, S.H.C. Park, M. Michiuchi, and H. Kokawa, "Constitutional liquation during dissimilar friction stir welding of Al and Mg alloys," Scripta Mater 50, 9 (2004): p. 1233-1236.

87.   L. Liu, X. Liu, and S. Liu, "Microstructure of laser-TIG hybrid welds of dissimilar Mg alloy and Al alloy with Ce as interlayer," Scripta Materialia 55, 4 (2006): p. 383-386.

88.   R.M. Wang, A. Eliezer, and E. Gutman, "Microstructures and dislocations in the stressed AZ91D magnesium alloys," Materials Science and Engineering: A 344, 1–2 (2003): p. 279-287.

89. O. Lunder, J.E. Lein, T.K. Aune, and K. Nisancioglu, "The Role of Mg17Al12 Phase in the Corrosion of Mg Alloy AZ91," Corros Sci 45, 9 (1989).

90. O. Lunder, T.K. Aune, and K. Nisancioglu, "Effect of Mn Additions on the Corrosion Behavior of Mould-Cast Magnesium ASTM AZ91," Corrosion 43, 5 (1987): p. 291-295.

91. G.L. Song and Z. Xu, "Effect of microstructure evolution on corrosion of different crystal surfaces of AZ31 Mg alloy in a chloride containing solution," Corros Sci 54, 0 (2012): p. 97-105.

92. D. Dietrich, D. Nickel, M. Krause, T. Lampke, M.P. Coleman, and V. Randle, "Formation of intermetallic phases in diffusion-welded joints of aluminium and magnesium alloys," J Mater Sci 46, 2 (2011): p. 357-364.

93. R.S. Lillard, G.F. Wang, and M.I. Baskes, "The Role of Metallic Bonding in the Crystallographic Pitting of Magnesium," J Electrochem Soc 153, 9 (2006): p. B358-B364.

94. G.L. Song and Z. Xu, "Crystal orientation and electrochemical corrosion of polycrystalline Mg," Corros Sci 63, 0 (2012): p. 100-112.

95. M. Jönsson, D. Thierry, and N. LeBozec, "The influence of microstructure on the corrosion behaviour of AZ91D studied by scanning Kelvin probe force microscopy and scanning Kelvin probe," Corros Sci 48, 5 (2006): p. 1193-1208.

96. S.M. Chowdhury, D.L. Chen, S.D. Bhole, E. Powidajko, D.C. Weckman, and Y. Zhou, "Microstructure and Mechanical Properties of Fiber-Laser-Welded and Diode-Laser-Welded AZ31 Magnesium Alloy," Metall and Mat Trans A 42, 7 (2011): p. 1974-1989.

97. V.B. G. Padmanaban, and J.K. Sarin Sundar, "Influences of Welding Processes on Microstructure, Hardness, and Tensile Properties of AZ31B Magnesium Alloy," J Mater Eng Perform 19, 2 (2010): p. 155-165.

98. K. Gusieva, C.H.J. Davies, J.R. Scully, and N. Birbilis, "Corrosion of magnesium alloys: the role of alloying," Int Mater Rev (2014): p. 169-194.

Table 1. 1. Properties of pure Mg, Al and Fe at their melting points[7,19,54-56]

Properties	Magnesium	Aluminum	Iron
Ionization energy (eV)	7.6	6	7.8
Specific heat ($J \cdot g^{-1} K^{-1}$)	1.36	1.08	0.795
Specifc heat of fusion (J/kg)	3.7×10^5	4.0×10^5	2.7×10^5
Melting point (°C)	650	660	1536
Boiling point (°C)	1090	2520	2860
Viscosity ($kg \cdot m^{-1} s^{-1}$)	0.00125	0.0013	0.0055
Surface tension (Nm^{-1})	0.559	0.914	1.872
Coefficient of thermal expansion (1/K)	26×10^{-6}	24×10^{-6}	10×10^{-6}
Thermal conductivity ($W \cdot m^{-1} K^{-1}$)	78	94.03	38
Thermal diffusivity (m^2 s^{-1})	3.7×10^{-5}	3.6×10^{-5}	6.8×10^{-5}
Density (kg m^{-3})	1590	2385	7015
Vapor Pressure (Pa)	360	10^{-6}	2.3

Table 1. 2. Electrochemical potentials of typical alloying elements to Mg alloys

Alloying Element	Reaction	Effect on E_{corr} compared to Mg	Standard Oxidation-Reduction Potential E^o (V_{NHE})
Ca	$Ca^{2+} + 2e^- \rightleftharpoons Ca$	Decrease	-2.868
La	$La^{3+} + 3e^- \rightleftharpoons La$	Increase	-2.379
Y	$Y^{3+} + 3e^- \rightleftharpoons Y$	Increase	-2.372
Mg	$Mg^{2+} + 2e^- \rightleftharpoons Mg$	--	-2.372
Ce	$Ce^{3+} + 3e^- \rightleftharpoons Ce$	Increase	-2.336
Nd	$Nd^{3+} + 3e^- \rightleftharpoons Nd$	Increase	-2.323
Gd	$Gd^{3+} + 3e^- \rightleftharpoons Gd$	Increase	-2.279
Nd	$Nd^{2+} + 2e^- \rightleftharpoons Nd$	Increase	-2.1
Al	$Al^{3+} + 3e^- \rightleftharpoons Al$	Increase	-1.676
Zr	$Zr^{4+} + 4e^- \rightleftharpoons Zr$	Decrease	-1.45
Mn	$Mn^{2+} + 2e^- \rightleftharpoons Mn$	Increase	-1.185
Zn	$Zn^{2+} + 2e^- \rightleftharpoons Zn$	Increase	-0.7618
Cr	$Cr^{3+} + 3e^- \rightleftharpoons Cr$	Increase	-0.74
Bi	$Bi^{3+} + 3e^- \rightleftharpoons Bi$	Increase	+0.308
Ag	$Ag^+ + e^- \rightleftharpoons Ag$	Increase	+0.7996
Au	$Au^+ + e^- \rightleftharpoons Au$	Increase	+1.83

Table 1. 3. Summary of IMP Corrosion Potentials typically seen in Mg

Alloy system	Intermetallic	[Cl⁻]	Corrosion Potential (V_{SCE})	Reference
Mg-Ca	Mg_2Ca	0.01 M	-1.75	
Commercially pure Mg	--	0.01 M	-1.62	This Work
Commercially pure Mg	--	0.6 M	-1.70	This Work
Commercially pure Mg	--	5.0 M	-1.72	This Work
AZ31B	--	0.01 M	-1.55	This Work
AZ31B	--	0.6 M	-1.59	This Work
AZ31B	--	5.0 M	-1.62	This Work
Mg-Y	$Mg_{24}Y$	0.01 M	-1.60	[12]
Mg-La	$Mg_{12}La$	0.01 M	-1.60	[12]
Mg-Nd	Mg_3Nd	0.01 M	-1.55	[12]
Mg-Si	Mg_2Si	0.01 M	-1.54	[12]
Mg-Ce	$Mg_{12}Ce$	0.01 M	-1.50	[12]
Mg-Al	$Mg_{17}Al_{12}$	0.1 M	-1.35	[12]
Mg-Al	$Mg_{17}Al_{12}$	0.01 M	-1.142	[95]
Mg-Al	$Mg_{17}Al_{12}$	0.1 M	-1.172	[95]
Mg-Al	$Mg_{17}Al_{12}$	0.85 M	-1.222	[95]
Mg-Al	$Mg_{17}Al_{12}$	1.0 M	-1.202	[95]
Al-Mg	Mg_2Al_3	0.1 M	-1.01	[12]
Al-Mg	Al_8Mn_5	0.1 M	-0.662	[95]
Al-Mg	Al_8Mn_5	0.1 M	-0.732	[95]
Al-Mg	Al_8Mn_5	0.85 M	-1.212	[95]
Al-Mg	Al_8Mn_5	1.0 M	-0.772	[95]
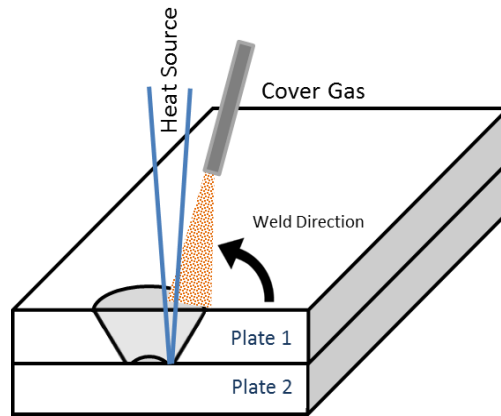
Figure 1.1. Schematic of Laser Welding Process. All samples were welded through a 45° countersunk hole in order to have full penetration through both plates.
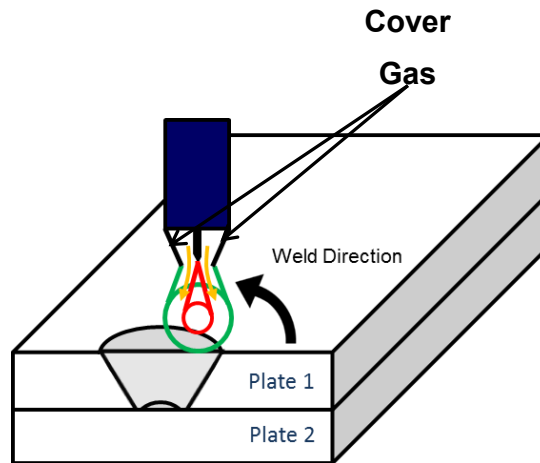
Figure 1.2. Schematic of TIG welding process. All samples were welded through a 45° countersunk hole in order to have full penetration through both plates.
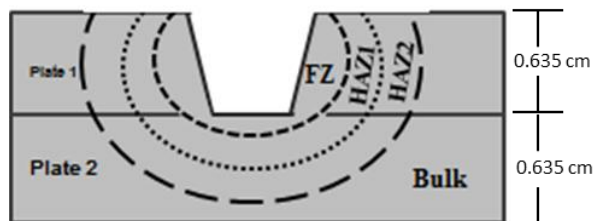
Figure 1.3 Schematic of weld zones, specifying the FZ and HAZs. Far enough away from the weld zone, the sample will become unaffected base material. All samples were welded through a 45° countersunk hole in order to have full penetration through both plates.
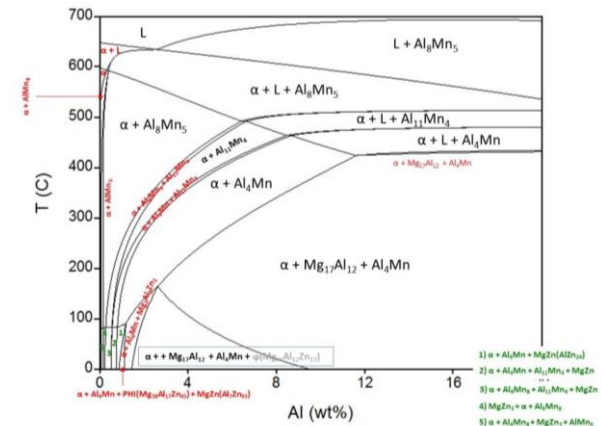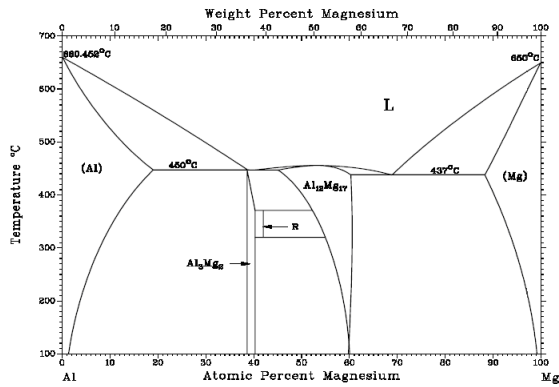
Figure 1.4. (a) binary equilibrium phase diagram of the Al-Mg system, (b) Pseudo-binary equilibrium phase diagram of the Mg-Al-Zn material system
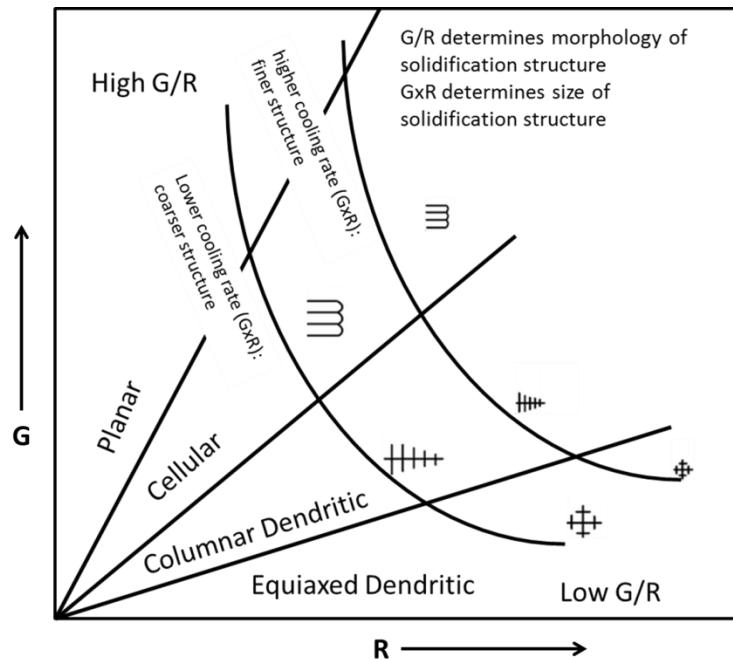
Figure 1.5 Effect of temperature gradient (G) in the weld zone and growth rate (R) of the solid/liquid interface on the formation of various solidification microstructures[26,27] as dependent on the rate of solidification. It can be seen that both G and R dominate the solidification microstructure. The ratio of G/R determines the mode of solidification while the product GR governs the size of the solidification structure[28]. During growth of the solid in the weld pool, the shape of the solid-liquid interface controls the development of microstructural features.
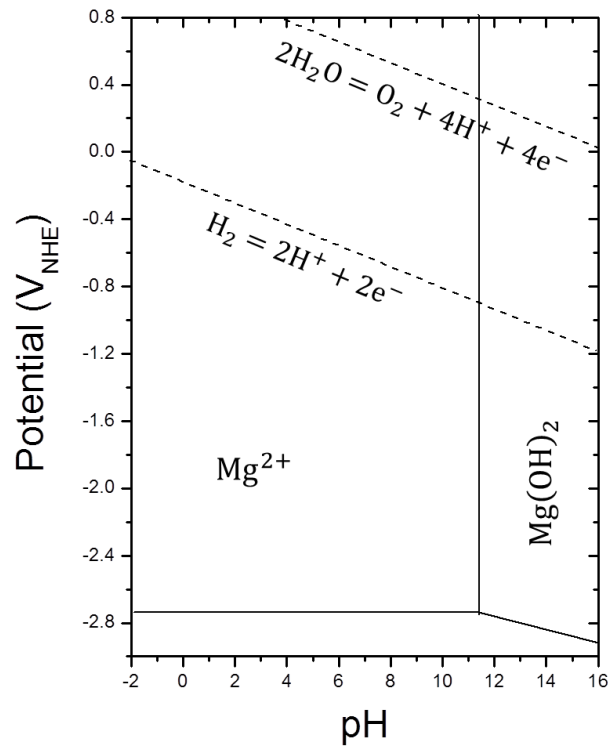
Figure 1.6. Stability domains of the magnesium compounds in aqueous solutions with hydrogen.
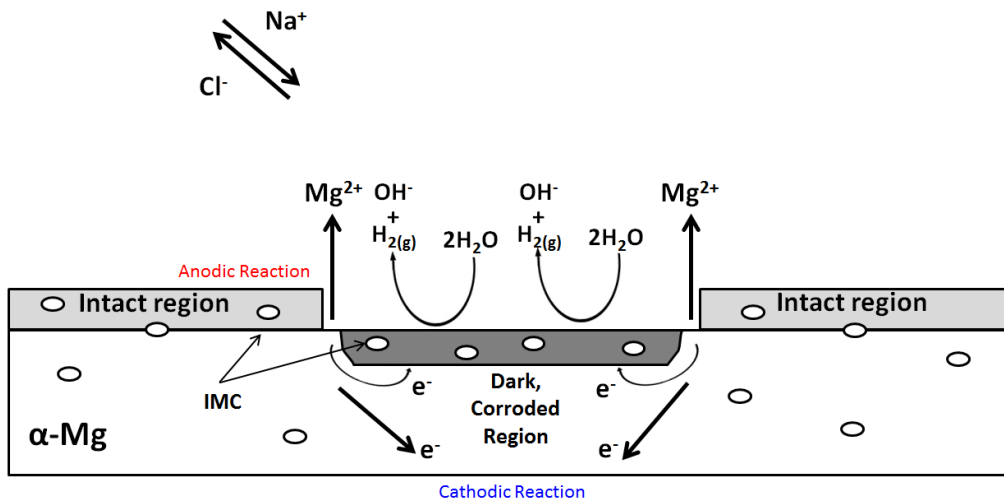
Figure 1.7. Shematic of the corrosion process on Mg. The cathodic, hydrogen evolution reaction, occurs at the sample surface while the anodic reaction of Mg^{2+} dissolution also occurs. IMP's within the sample can act as active cathodic reaction sites and increase the anodic reaction.
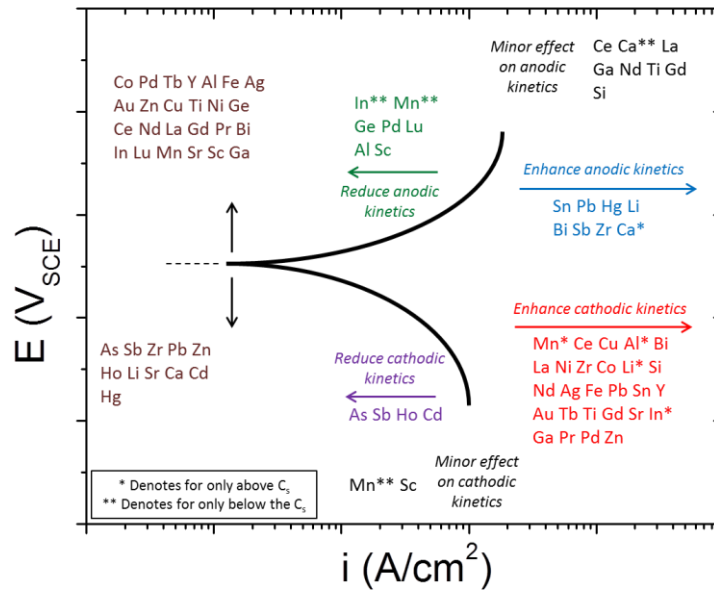
Figure 1.8. Schematic representation of the electrochemical impact of alloying elements studied (data extracted from the papers cited in Section 4). Plot depicts the ability of alloying additions to modify anodic or cathodic kinetics (or both), leading to changes in the resultant corrosion rate i_{corr}, along with changes in corrosion potential E_{corr}.[98]
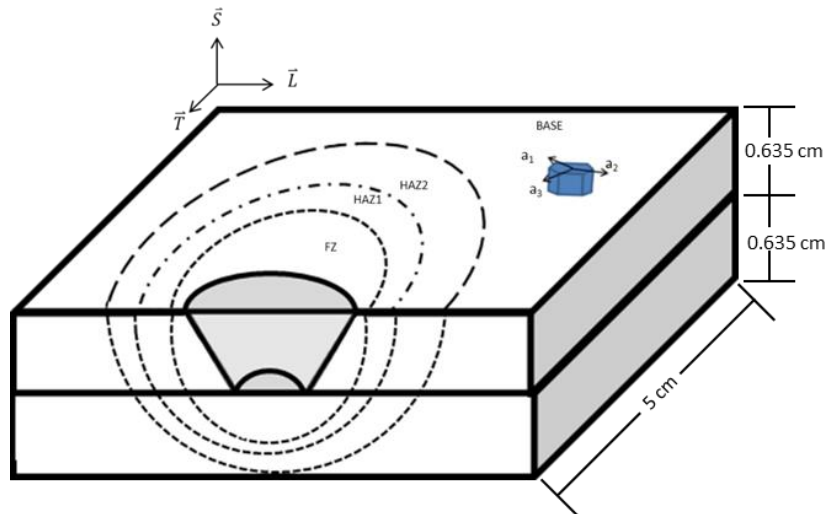
Figure 1.9. Texture evolution within an Mg-Al fusion weld for isolated weld zones in comparison to the original basal distribution in the base material

2 Assessing the Corrosion of Commercially Pure Magnesium and Commercial AZ31B by Electrochemical Impedance, Mass-loss, Hydrogen Collection and ICP-OES Solution Analysis

The corrosion of commercially pure Mg and AZ31B-H24 with simultaneous measurement of electrochemical impedance (EIS) and hydrogen gas evolved over a 24 hr immersion period was studied in solutions of three chloride concentrations. The corrosion rate was determined from the Stern-Geary approach and the integral electrochemical-based mass loss was compared to the gravimetric mass loss and Inductively Coupled Plasma Optical Emission Spectrometry (ICP-OES) solution analysis of the total Mg concentration released. The use of ICP-OES to support the other assessment methods has not been previously reported. Assuming Mg dissolves as Mg^{2+}, there was agreement using these four unique measures of magnesium corrosion. The integration of the polarization resistance (R_P) over time, as evaluated from EIS at the low frequency limit incorporating full consideration of the pseudo-inductive impedance behavior of Mg, provided excellent correlation to the cumulative mass loss, ICP-OES solution analysis and volume of hydrogen collected for commercially pure Mg and reported for the first time for AZ31. The choice of Tafel slope to utilize in the Stern-Geary approach, as well as subsequent comparison of results to corrosion rate data in the literature, are discussed.

Representative author contributions:
L.G. Bland: experiments, data analysis and data fitting.
A.D. King: analysis
N. Birbilis: analysis, interpretation
J.R. Scully: Adviser, analysis and interpretation

2.1 <u>Introduction</u>

One of the key barriers in the wider application of Mg is the need for further understanding and improvement of Mg alloy corrosion. A clearer understanding of Mg corrosion, and its measurement, will enable the development of corrosion resistant Mg alloys, protective systems, and permit evaluation and implementation of Mg alloys for industrial applications[1-10].

There has been a large focus on measuring the corrosion performance of, not only commercially pure Mg, but also commercial Mg alloys; in particular AZ31 [UNSM11311] and AM60 [UNS M10600][11-21]. Much focus has been given to Mg-Al alloys due to their improved mechanical properties that arise without adversely influencing the corrosion rate relative to Mg[15,22]. However, while interest in other Mg-alloys is large, the formation of intermetallic phases in Mg alloy systems, be it due to solidification or aged structures, nominally affects the overall corrosion rate by promoting local cathodic sites [22,23]. Much of the focus of previous works has been on the effect of different alloying elements in order to characterize the overall effect of different alloying additions on corrosion[15,24,25]. While composition and microstructure details are not a focus of this work, understanding the corrosion rate and assessing a means for ready assessment of global and local corrosion rates of both commercially pure Mg and its alloys is critical to establish a baseline analysis for more complicated alloy systems. Further, whilst other works have purported to take a similar approach, it is seen herein that key factors in the unified assessment of corrosion have not been previously elucidated entirely, justifying the consolidated study herein.

There are several methods for the determination of both the instantaneous and long-term corrosion rates for Mg. In particular, the instantaneous corrosion rate can be determined by Tafel extrapolation from polarization curves, the H_2 evolution rate, electrochemical impedance spectroscopy (EIS) derived polarization resistance, R_P[26] and spectrochemical approaches[27,28]. Furthermore, the long-term cumulative corrosion can be determined by mass loss, measurement of the H_2 evolved over the entire testing period, solution analysis for Mg cations and integration of i_{corr} vs. time data determined by the temporal evolution of R_P over time. The later method is complicated by both the fact that R_P and Tafel slopes calculated as a function of time are often difficult to assess. Moreover, both parameters typically change over exposure time. Additionally, R_P can be determined by EIS with minimal perturbation to the corroding system while Tafel

extrapolation is 'destructive' to an electrode surface unless extracted from near the corrosion potential which in and of itself introduces errors. Therefore short-term and long-term corrosion assessment methods are often difficult to directly compare. Nonetheless, there are many advantages and disadvantages to using each of these techniques. DC polarization curves can provide information on both the anodic and cathodic reaction rates for a given system, which is mechanistically important. The Tafel extrapolation assessment of the instantaneous corrosion rate necessitates a wide range of E-i data which must be iR corrected and may not follow a Tafel law. Furthermore, Tafel extrapolation may be complicated by the formation of surface films upon the sample which alters the active surface area, as well as activation of the cathodic reaction[26]. In the Mg system, non-Tafel behavior can be seen owing to coverage dependence of reaction rates and significant errors due to substantial iR voltages[29]. For EIS determination of long-term corrosion rates, the difference between the measured R_P and the charge transfer resistance (R_t) must be considered and proper interpretation is required to accurately measure the corrosion rate of the system[26]. The use of R_t can lead to underestimation of the corrosion rate by a factor between 2 to $\geq$10 when disregarding the characteristic inductive loop often seen in Mg systems[29]. However, fitting of EIS data with inductive behavior can be challenging and requires use of a relevant equivalent circuit that is able to faithfully capture the pseudo-inductive electrochemical impedance response of the system.

For the dissolution of Mg under open circuit conditions, $i_{anode}=i_{cathode}$ where the cathodic and anodic reactions are defined using the divalent Mg^{2+} ion as seen in Equations 2.1 and 2.2, respectively[30]. Under the condition that $i_a=i_c$ at open circuit, the primary cathodic reaction is a measure of the rate of anodic dissolution.

$$2H_2O + 2e^- \rightarrow H_2 + 2OH^- \hspace{4cm} \text{Equation 2.1}$$
$$Mg \rightarrow Mg^{2+} + 2e^- \hspace{5cm} \text{Equation 2.2}$$
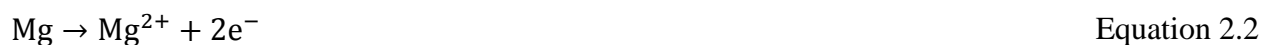
There has existed debate on intermediates and whether some Mg^+ is oxidized to Mg^{2+} in solution, some distance from the electrode whereupon the second de-electronization event rate is not inventoried by electrochemical instrumentation; however, it has been largely concluded that Mg dissolves at the electrode surface even if by several steps to form the divalent Mg^{2+} ion[1,27,28,30,31]. A similar lack of inventory by electrochemical instrumentation can occur during polarization when some of the ionized Mg contributes to forming an $Mg(OH)_2$ surface film[32]. This lack of inventory can even occur with Mg^{2+}, and is a basis for the negative difference effect

(NDE). Some have reported that the assumption of Mg^+ oxidation at the surface led to an inability of electrochemical methods to measure i_{corr} in previous electrochemical analysis and produced an underestimation of the Mg corrosion assessed by mass loss or hydrogen collection. These notions are elaborated below from the electrochemical perspective[33]. However in regards to the collection of H_2 from a dissolving electrode, a salient and often overlooked point is that the electrolyte should be pre-saturated to alleviate the error from the solubility of hydrogen in the electrolyte as well as in solid Mg[34].

In the context of correlating electrochemically determined corrosion rates using EIS to physically determined corrosion rates, another possible source of discrepancy includes the interpretation of EIS data. EIS analysis and interpretation is the focus of this chapter. Previously, King et. al. described the correlation between gravimetric mass loss, H_2 collection and EIS-estimated R_P techniques[29] for commercially pure Mg, which highlighted several key issues. The impedance response for Mg under open circuit conditions and conditions dominated by an anodic reaction was shown to include a physically justified inductive component that is evident with decreasing frequency and which should not be ignored. The natural corrosion process occurs at the low frequency limit, at ~zero AC frequency[26]. Traditionally, an inductance at AC frequencies approaching such a limit can be physically explained by a surface coverage consisting of an adsorbed intermediate that enables a faster reaction rate. This concept is common in electrochemical kinetics. The use of R_t at intermediate frequencies represents a situation where the AC frequency is high enough and the AC voltage excitation changes so rapidly that the surface coverage is nearly frozen and cannot adjust with the fast potential changes. Thus $R_t > R_P$ compared to a changing coverage adjusting for potential which enables a faster reaction rate. The use of R_P at the zero frequency limit, instead of R_t, was shown by King to yield good agreement with H_2 gas evolution and gravimetric mass loss[29]. The inductive behavior was also shown to be enhanced at anodic potentials but was suppressed at cathodic potentials where the dominant electrochemical reaction characterized by EIS becomes HER (hydrogen evolution reaction). This indicates that the nature of the inductive loop is dependent on the extent of dissolution (or potential), however further details are needed in future work, on the basis that it has been demonstrated that anodic dissolution of Mg can lead to other changes in the surface such as those responsible for cathodic activation[1,35]. Indeed, the effects anodic and cathodic processes on both the AC and DC components of current are difficult to decouple

during anodic polarization. It is conceivable that enhanced dissolution occurs as a result of enhanced cathodic activity (in response to anodic activity). None-the-less, an equivalent circuit which accounts for the inductive behavior of Mg and which includes the minimum number of capacitive time-constants to faithfully represent the electrochemical response of Mg. The corrosion rate of a freely corroding metal was determined through an evaluation of the polarization resistance, R_P using the well-known Stern-Geary relationship[26,36]:

$$i_{corr} = \frac{B}{R_P} = \frac{\beta_a \beta_c}{2.303 R_P (\beta_a + \beta_c)}$$
Equation 2.3

where β_a and β_c are the anodic and cathodic Tafel slopes, respectively, and $B = (1/2.303) \times (\beta_a.\beta_c/(\beta_a + \beta_c))$. It should be noted that this is a simplified expression that introduces some error due to the potential dependent coverage effects which can also alter the value of B, usually assumed in Equation 2.3. However, for the Stern-Geary equation, there is a stronger dependence of i_{corr} on the value of R_P than on B[39]. The more general expression, incorporating coverage effects (of the native oxide) on Tafel slopes, can be seen in Equation 2.4.

$$\frac{1}{R_P} = \frac{\partial I_{app}}{\partial E} = 2.303 I_{corr} \left[\left(\frac{1}{\beta_{a\theta(a)corr}} + \frac{1}{\beta_{c\theta(c)corr}} \right) + \left(\frac{1}{\theta_a} \frac{\partial \theta_a}{\partial E} - \frac{1}{\theta_c} \frac{\partial \theta_c}{\partial E} \right) \right]$$
Equation 2.4

where θ_a and θ_c are the coverage of the anodic and cathodic intermediates, respectively and $\beta_{a\theta(a)corr}$ and $\beta_{a\theta(c)corr}$ are the Tafel slopes at the coverage present at E_{corr}. R_P is equal to R_t when the strong dependency of coverage on the conditions such as applied potential are absent. When a coverage is present, R_t obtained at intermediate frequency may be obtained for a frozen coverage with respect to frequency and time and the second term on the right of Equation 2.4 is zero[26]. Such situations may also exist in the case of Mg dissolution in solutions where an intermediate is not formed such as when the surface does not dissolve uniformly. Instead, in the dissolution of Mg, the surface of the electrode contains highly local anodic sites which grow with time and later function as strong active cathodes[1]. As these cathode regions grow with time, the anodic site coverage across the electrode changes[1]. This change in anodic and cathodic activity on the electrode surface has been previously visualized and also analyzed in several previous works[28,30,31,37,38].

The anodic charge consumed can then be estimated by integrating the EIS-estimated corrosion rate over the time of exposure, with knowledge of appropriate Tafel slopes via

Equation 2.5, assuming the magnitude of the second term on the right of Equation 2.4 is negligible:

$$Q_a^{EIS} = \int i_{corr} \cdot A \cdot dt = \int \frac{\beta_a \beta_c A}{2.303 R_p (\beta_a + \beta_c)} dt$$

Equation 2.5

To calculate the EIS-estimated corrosion rate using Equation 2.5, appropriate Tafel slopes must be assumed. The experimental Tafel slopes quoted in the literature for Mg and AZ31 are difficult to determine, the reasons for which are several. Tafel slopes can vary with chloride concentration and also time of exposure. A collection of Tafel slopes derived from $\partial E_{app}/\partial i_{app}$ data have been extracted from potentiodynamic polarization[39], online spectrometry[27] and other methods. A summary is given in Table 2.1. In order to accurately determine the Tafel slope with potentiodynamic polarization, at least one of the branches of the polarization curve should exhibit Tafel behavior over at least one decade of current[40,41]. Additionally, the error due to ohmic drop through the test solution should be minimal, the apparent current density must be the true anodic or cathodic current density, dissolution should be weakly dependent on coverage or the coverage should not be a strong function of applied potential, the active area should not be changing with time or potential and the anodic corrosion reaction mechanism should not change over the ΔE range explored. In addition, the Tafel extrapolation should be extracted from E-log(i) data at least 50 mV away from E_{corr} in order to assure that the Tafel slope is being analyzed over a linear E-log(i) region [40,41]. Quoted β_a values can be approximated as ≤ 150 mV/dec while the β_c values can be approximated as ≥ 200 mV for commercially pure Mg[27,30,42-45]. In the literature for AZ31, the β_a and β_c values are quoted from 20 mV/dec to 300 mV/dec[45-47]. For many of these measured Tafel slopes, the testing conditions are extremely varied and, due to the rapid corrosion rates normally observed for the Mg system, the Tafel characteristics can change dramatically between a short and long-term test. Along with the testing duration, there is a large variation in the electrolyte used for each of the cited tests in the literature. Many tests are conducted in 0.6 M NaCl, but several use a buffer to control the pH of their solution while others do not. This may alter the Tafel behavior by slowing down the reaction kinetics and also modifying the catalytic nature of Mg surfaces. Along with these considerations, there are several different techniques cited for the evaluation of Tafel slopes in literature, namely the use of traditional Tafel extrapolation, fitting software and the Levenberg-Marquart method. The

Levenberg-Marquart method is a curve fitting method for least-squares regression fitting [48]. This method has been utilized to yield a Tafel slope approximation similar to that estimated through Tafel slope extrapolation[39,43,44]. However, there is no evidence on whether these calculations accurately reflect the true Tafel behavior of Mg[1].

The accurate determination of a long-term corrosion rate of Mg from electrochemical methods is strongly dependent on the analysis of R_p or the polarization resistance. In much of the prior research utilizing EIS determined corrosion rate, the analysis rested on utilizing a charge transfer resistance, R_t, at intermediate frequencies in place of R_p and subsequently omitting the significant inductive loop in the Mg Nyquist plot for many solutions and many Mg alloys which results in a substantial underestimation of the corrosion rate[43,45]. Furthermore, on the basis of EIS determined R_t (where R_P is much less than R_t), underestimating the corrosion rate as determined from other methods (mass loss or hydrogen collection), authors have previously used this as a means for rationalizing the existence of Mg^+ [43,44]. It has been agrued that use of Mg^+ in the calculation of corrosion rate by H_2 generation is justified because H_2 generated from the assumed Mg^+ reaction on the metal surface as well as the proposed Mg^+/Mg^{2+} reaction in solution are both collected. Consequently $Q_{\Delta m} \cong Q_{H_2}$[33]. However, this is also the case when Mg^{2+} is assumed and hydrogen gas collected is assumed to come from the Mg surface. Moreover, Q_{EIS} using R_t has been reported to underestimate the corrosion rate where it can be approximated that $Q_{\Delta m} \cong Q_{H_2} \cong \frac{1}{2} Q_{EIS}$. In this case, one assumption has been that Mg^+ reacts in solution, instead of at the electrode surface; therefore, the measured Q_{EIS} analysis does not account for the second electron which is transferred in solution away from the elctrode surface [33]. Alternatively, in order to fully determine the corrosion rate, the full electrochemical response, including the inductive behavior at lower frequencies, must be fully utilized[20,21,38,49-54]. In this case, Q_{EIS} should agree with $Q_{\Delta m}$ for z=2+. While many papers acknowledge the existance of this inductive loop, most do not attempt to explain this electrochemical response. It is acknowledged that the measured difference between R_t and R_p may be dependent on the testing environment and alloy, where R_t can be larger than R_P by a factor of 4 or more depending on the environment. Similarly, B can differ by a factor of 2 to 3 for different testing conditions. In order to accurately determine R_P, an

---

[1] *The E-log(i) data is fit to an electrochemical charge transfer expression where i_{corr}, β_a and β_c must all be fit simultaneously to the assumed expression. Such fits are complicated and in theory possible but in practice confounded by most of the same effects as discussed above.*

equivalent electrical circuit model must be used which represents this response. The equivalent circuit used in this study (Figure 2.1) was seen to be capable of accurately describing the electrochemical response of Mg at the zero frequency limit[29]. However, this approach was first developed for commercially pure Mg and has not been confirmed for Mg alloys.

The objective of this work is to further explore an approach to EIS where the inductive loop is considered in determination of polarization resistance, R_p. To show that the proposed approach is robust, the EIS measurement and subsequent analysis method is extended to a commercial Mg-Al alloy, AZ31B[29]. In addition, Inductively Coupled Plasma Optical Emission Spectrometry (ICP-OES) was employed independently to assess the metal dissolved. A previous study by Swiatowska et al. studied the dissolution of Mg using this technique[27] and confirmed that Mg dissolves with z=2+ [27]. However, there is no combined study of Mg alloys i_{corr} by H_2, EIS, ICP–OES and gravimetric mass loss which accounts for the inductive behavior following the approach of King.

2.2 Experimental Procedures
2.2.1 Materials

Commercially pure magnesium rod (99.9%) supplied by Alfa Aesar was used in this study along with AZ31B-H24 sheet supplied by Magnesium Elektron. The chemical composition of these materials is given in Table 2.2. Each of the bare electrodes were prepared by alternating grinding with silicon-carbide paper and rinsing with ethanol to a final grit of 1200 prior to testing. A nickel ribbon was attached to the back of the un-mounted sample before testing in a vertical flat cell.

2.2.2 Corrosion Determination

A full immersion, electrochemical testing regimen was designed to simultaneously measure electrochemical impedance, mass loss, and the volume of H_2 gas evolved on the test electrode. The sample was immersed in ambient exposed solution for 24 hours with open circuit measurements followed by intermittent EIS measurements at frequencies from 10 kHz to as low as 10 mHz. Some runs were terminated at slightly higher frequencies and fit to frequencies necessary to obtain Z"=0. EIS scans were analyzed and fit using the software program ZView to an equivalent circuit, seen in Figure 2.1. Figure 2.1(a) shows the circuit that was used for 0.01 and 0.6 M NaCl. Figure 2.1(b) shows the circuit that was used for 5.0 M NaCl. The use of an

additional resistor and capacitor couple is required for these higher concentrations in order to fully capture the electrochemical response of the system. Each of the respective EIS experiments were fit to a low frequency limit of at least 0.001 Hz.

The experimental setup consisted of a vertical flat cell with a 1 cm^2 sample window attached to a vertically mounted, inverted, volumetric burette. The inverted burette was placed above the sample window in order to collect the H$_2$ gas evolved from the sample surface. A piece of Pt mesh was used as a counter electrode and a saturated calomel electrode (SCE) was used as the reference electrode. Prior to testing, the electrolyte was pre-saturated with H$_2$ in order to reduce error in measuring the volume of the H$_2$ generated on the sample surface since H$_2$ gas is extremely soluble in most aqueous environments[55]. Tests were performed in quiescent 0.01, 0.6 and 5.0 M NaCl with established pH values of 5.3, 5.2 and 5.1 respectively. Following testing, samples were cleaned with ASTM G1 standard chromic acid solution (200 g/L CrO$_3$) and dried in a dry box for a least 24 hrs[56]. Negligible mass loss from the bulk Mg or Mg-alloys resulted from this cleaning procedure.

All solutions were retained and analyzed using Inductively Coupled Plasma Optical Emission Spectrometry (ICP-OES). A Thermo Scientific^{TM} iCAP 7200 ICP-OES was used for analysis. Samples were prepared by mixing 1 M HCl into the solution after electrochemical testing and prepared using a 10 part dilution. All samples were shaken before solution analysis to ensure that no corrosion product was left on the bottom of the container. This acidified the solution and dissolved the salt and corrosion products in order to be more accurately measured during analysis. Before analyzing, standards containing known amounts of Mg as well as each of the alloying elements were used to calibrate the instrument.

In this work, the emission intensity of Mg (2025 Hz), Mg (2790 Hz), Mg (2795 Hz), Mg (2852 Hz), Zn (2062 Hz), Zn (2138 Hz)), Al (2269 Hz), Al(3082 Hz), Al (3961 Hz), Zr (3391 Hz) and Zr (3438 Hz) were recorded and used for the calculation of charge consumed using solution analysis.

Electrochemical experiments were performed using either a Solatron 1287A potentiostat and 1255B FRA or Gamry Reference 600 potentiostat, both of which are set up to be EIS capable. EIS scans were acquired from 100 kHz to 0.005 Hz with 6 points per decade and an AC amplitude of $\pm$20 mV before fitting.

Anodic potentiodynamic scans were conducted after a 10 minute OCP a typical anodic scan started at -0.05 V vs OCP to +0.5 V vs OCP and scanned at a rate of 1.0 mV per second. This fast scan rate was used in an attempt to freeze in the absorbed coverages. IR correction was made via the linear fit method. The electrolyte resistance, R_Ω, was determined to be 142 Ω, 11.3 Ω and 6.7 Ω (1 cm^2 test area) for 0.1, 1.0, and 5.0 M NaCl, respectively. The E-log(i) data was acquired to show a general trend in behavior but was conducted over insufficient E-I range for Tafel extrapolation to obtain i_{corr}.

The mass loss of Mg (Δm), as measured gravimetrically with ± 0.1 mg resolution, can be converted to consumed anodic charge (Q_a) via Faraday's law[40]:

$$Q_a^{\Delta m} = znF = \frac{z\Delta mF}{a}$$
Equation 2.6

Where z is equivalent electrons per mole of Mg oxidized, +2, n is the number of moles of Mg, F is Faraday's constant and a is the molar mass of Mg. For this analysis, a z of 2 was assumed for commercially pure Mg. For alloys, the alloy composition was considered to determine the equivalent weight for the alloy. The equivalent weight was determined as the weighted average of a/z for the major alloying elements in a given alloy[40]. The recommended procedure, as specified by ASTM G106[57], is to sum the fractional number of equivalents (f_i) of all alloying elements to determine the total number of equivalents in the alloy, N_{eq}. This is:

$$N_{eq} = \sum \left(\frac{f_i}{a_i/z_i}\right) = \sum \left(\frac{f_i z_i}{a_i}\right)$$
Equation 2.7

The equivalent weight (grams/equivalent) is then the reciprocal of the total number of equivalents (EW= N_{eq}^{-1}). For this analysis, the equivalent weight for AZ31B was determined to be 12.13 g/eq. This was determined assuming congruent Mg^{2+}, Al^{3+}, and Zn^{2+} oxidation where z=2+, z=3+, and z=2+, respectively.

Under freely corroding conditions, measured at open circuit, all of the H_2 gas evolved on the surface of the Mg electrode is assumed to be produced by a coupled cathodic reaction assumed to be generated on Mg by Equation 2.1. The volume of H_2 gas evolved can be converted to a corresponding cathodic charge (Q_c) via a combination of the Ideal Gas Law and Faraday's Law, which, during OCP corrosion, equals the anodic charge (Q_a) per unit area of Mg corroding[40]. Thus:

$$Q_c^{H2} = Q_a^{H2} = znF = \frac{zPVF}{RT}$$
<div align="right">Equation 2.8</div>

Where P is the pressure inside the burette (assumed to be approximately 1 atm at sea level), V is the volume of H_2 gas collected, R is the ideal gas constant, T is the temperature and z as well as n are defined above.

2.3 <u>Results</u>

For both commercially pure Mg and AZ31, the anodic E-log(i) characteristics in quiescent 0.01, 0.6, and 5.0 M NaCl indicate high dissolution currents for relatively low anodic overpotentials characteristic of Mg (Figure 2.2). For commercially pure Mg in all three electrolytes an E_{corr} can be measured as equal to or less than -1.53 V vs. SCE (Figure 2.2 (a)). For AZ31, E_{corr} can be measured as equal to or less than -1.57 V vs. SCE (Figure 2.2 (b)). These potentials are representative of typical E_{corr} measurements for Mg and AZ31 as seen in current literature[58-63]. By increasing the [Cl-], there is an increase in the anodic dissolution rate. This is also consistent with a decrease in the measured E_{corr} (via activation of the anodic reaction).

The iR correction here has been implemented for the EIS determined electrolyte resistance (R_Ω). From the iR corrected anodic potentiodynamic scans for both commercially pure Mg and AZ31, there is a low apparent anodic Tafel slope that is representative of a non-polarizable system (Figure 2.2). The true Tafel slope value is hard to determine from such data and these E-log(i) are 'over corrected' (given the realized current densities rapidly extend to very high values and that the R_Ω is likely not a single fixed value during the scan) and therefore cannot be assumed to make a completely accurate determination of the corrosion rate. These rapidly acquired anodic characteristics make it difficult to calculate accurate long-term corrosion rates using either Tafel extrapolation or linear polarization resistance based techniques. For this reason, experimentally derived Tafel slopes from Figure 2.2 have not been solely used in the analysis for this study, instead, Tafel slopes augmented from a wide survey of the current literature are reported (and also discussed further below). Both AZ31 and commercially pure Mg exhibit two capacitive time constants and an inductive loop, as seen in Figure 2.3. This has been previously seen in independent literature for both commercially pure Mg and AZ31[38,43,45,51,53,54,64,65]. The inductive loop has a positive imaginary component (Z") and decreasing real component (Z') with decreasing frequency. This inductive behavior is also

readily observed in the Bode magnitude plot (Figure 2.3) by the decreasing impedance magnitude at low frequencies (f < 0.1 Hz) as previously seen explained for commercially pure Mg.

2.3.1 EIS for commercially pure Mg

EIS of commercially pure Mg as a function of time and chloride concentration

For the [Cl⁻] range studied, the EIS spectra of pure Mg at open circuit has two capacitive loops and an inductive loop [20,21,38,49-54]. As per fitting to the equivalent circuits in Figure 2.1, the determination of the various equivalent electrical circuit elements are provided in Table 2.3. These fitting results are reported for when the sample had been immersed in 0.01, 0.6, and 5.0 M NaCl for 3, 12 and 24 hrs. The note is made here that in the environments studied, the equivalent circuits required the use of two (0.01 and 0.6 M NaCl) or three (5.0 M NaCl) capacitive loops at high or moderate frequencies in combination with an inductive loop at low frequencies. The capacitive elements were able to be faithfully represented by conventional capacitors, as opposed to constant phase elements, and experimental data and showed a good fit where the error % was estimated at approximately 20% for each run. The charge consumed over the 24 hour period was calculated using three different Tafel assumptions[29,39,44], found in Table 2.4. Over the 24 hr period, the low frequency |Z| steadily increases and the breakpoint frequency shifts toward lower frequencies (Figure 2.3); which is concomitant with a decrease in the rate of H_2 collection (Figure 2.4). Similarly, there is also an increase in the H_2 evolved with chloride content. It is important to note the difference in H_2 rate with time for different [Cl⁻] (Figure 2.4). As the concentration of Cl⁻ is increased, the slope decreases with time. The calculation of R_P has been calculated using the following equations derived from the respective equivalent circuit.

$$\frac{1}{R_p} = \frac{1}{R_1 + R_2} + \frac{1}{R_3}$$

Equation 2.9

$$\frac{1}{R_p} = \frac{1}{R_1 + R_2 + R_4} + \frac{1}{R_3}$$

Equation 2.10

The rate of H_2 evolved over time decreased which was consistent with an increase in the measured R_P. There is a decrease in the measured R_P with chloride content as shown in Figure 2.5 indicating that as [Cl⁻] increases, the corrosion rate also increases. For commercially pure Mg, the measured R_p generally varies within a finite window for the duration of the test, and the

range of the window being largely detminered by the [Cl$^-$]. In the most dilute [Cl$^-$], there is a subtle increase in R_p with the test duration, concomitant with slightly reduced rates of corrosion as time proceeds (Figure 2.5). This may be indicative of the evolution of a partially protective surface film, consisting of MgO/Mg(OH)$_2$ as has been reported in literature[1,63,66,67] and also indicative of changes in the local surface environment (such as elevation of pH towards the Mg^{+2}/Mg(OH)$_2$ equilibrium). This effect is overwhelmed with higher [Cl$^-$], with little change in R_p with time, albeit that corrosion rates are inherently high at high [Cl$^-$]. What is not observed given the present experimental configuration and timescale of testing (or more accurately, the interval between tests and anodic charge accumulated) is any activation effects that may lead to enhanced corrosion (as a result of breakdown during early immersion) prior to any surface alkalization. It merits comment that a decrease in R_p was initially observed (following ~30 mins immersion) in the case of 0.6M NaCl, however time specific effects require dedicated study and not the focus of this paper which is aiming to contrast the veracity of corrosion results from various methods over a period of accumulated corrosion.

Corroborating mass loss, H$_2$ collection and ICP-OES of commercially pure Mg

The polarization resistance of pure Mg, and subsequently the corrosion current density according to Equation 2.3 was calculated from the periodic measurement of EIS throughout exposure in quiescent 0.01, 0.6, and 5.0 M NaCl (Figure 2.5). A decrease in the corrosion rate (i_{corr}) in 0.01, 0.6 and 5.0 M NaCl occurs with increasing exposure time. The decrease in corrosion rate with time is rationalized on the basis of alkalization of the near surface electrolyte[29].

Integration of the corrosion current density over the 24 hr immersion time using Equation 2.5, conversion of the mass loss using Faraday's Law using Equation 2.6, calculation of the H$_2$ collected over 24 hrs using the ideal gas law and Faraday's Law, and measurement of the magnesium dissolved in solution using ICP-OES and Faraday's Law resulted in anodic charge estimations that were similar in value for each environment (Table 2.4-2.5, Figure 2.6). The addition of ICP-OES solution analysis has been used in previous research[27] for online instantaneous measurement using a flow cell, but has yet to be corroborated with a range of other techniques. The addition and comparison of ICP-OES to Mass loss, H$_2$ collection and EIS gives a good comparison for the corrosion rate of Mg. i_{corr} and Q_{EIS} were repeated at several estimated Tafel slopes and it was determined that the corrosion rate could still accurately be determined

using EIS derived R_P under different B assumptions. Figure 2.7 shows this analysis over the 24 hour period for each of the chloride concentrations, showing that the R_P fitting and subsequent electrochemical characteristics of the material are accurate throughout the full span of the immersion.

2.3.2 EIS for AZ31B

EIS of AZ31B as a function of time and chloride concentration

The same method was used to analyze AZ31B as was used to analyze commercially pure Mg: H_2 collection, gravimetric mass loss, EIS analysis, and ICP-OES solution analysis.

From the EIS spectra for AZ31B measured at open circuit, there can be seen two capacitive loops and an inductive loop. This is particularly clear at lower [Cl⁻] where the loops are more distinct. The determination of the equivalent electrical circuit elements are presented in Table 2.6 following sample immersion in 0.01, 0.6, and 5.0 M NaCl for 3, 12 and 24 hrs. The same equivalent circuits for commercially pure Mg were also determined to be applicable to AZ31B. The charge consumed over the 24 hour period was calculated using three different Tafel assumptions[29,39,44], and found in Table 2.7. For short immersion times, the low frequency |Z| is high in comparison to the |Z| following 24 hr exposure. In terms of the |Z| evolution, for longer immersion times, the low frequency |Z| initially decreases, before increasing upon further immersion where, after this point, the breakpoint frequency shifts toward lower frequencies (Figure 2.8), seen for all [Cl⁻]. For AZ31B, it is similarly observed that the measured R_p is initially high, correlating to a slower corrosion rate. In the early stages of immersion, this slow corrosion rate may correlate to the presence of a partially protective surface film[1,63,66,67]. Overtime, the sample surface becomes actived and the corrosion rate increases, correlating with a decrease in the measured R_p. Near the end of the 24 hour immersion, the measured R_p slightly elevates, tending to stabilize, as shown in Figure 2.9 for AZ31B, which may correlate to the local alkalization after longer immersion times and perhaps even Al accumulation.

To accurately fit the EIS data, in the case of the 0.01 M NaCl, some of the elements in the equivalent circuit were required to be held constant. In particular, R_3 and L, which are used to model the inductive loop, were manually adjusted and then fixed during automated iterations in order to converge to an accurate fit on the inductive loop (Table 2.6). This was not required at

[Cl⁻] ≥ 0.01 M NaCl. Herein, the determined R_P values follow approximately the same trend as that seen in higher concentrations over the 24 hr period as shown in Figure 2.11.

Corroborating mass loss, H_2 collection and ICP-OES of AZ31B

The polarization resistance of AZ31B, and subsequently the corrosion rate (i_{corr}) according to Equation 2.1, was calculated from the periodic measurement of EIS throughout exposure in quiescent 0.01, 0.6, and 5.0 M NaCl (Figure 2.9). The measured i_{corr} in 0.01 and 0.6 M NaCl generally increases during the full 24 hr immersion time. There is a large increase around the 3 hour point correlating with a decrease in the calculated R_p. There is an observed increase in the corrosion rate (i_{corr}) in 0.01, 0.6 and 5.M NaCl that occurs with increasing exposure time after the breakdown of the passive film has occurred. This trend can be rationalized as a tradeoff between the alkalization of the near surface electrolyte[29] and the development and breakdown of anodes and cathodes upon the sample surface. Similarly, this trend can also be observed in the H_2 collection with time in Figure 2.10. Also in the measured H_2 data, this can be correlated with the difference in the measured low frequency |Z| seen in the EIS data. Over short immersion times the H_2 evolved increases after about 3 hours and then, at longer immersion times the H_2 evolved begins to stabilize.

The quantification of Mg dissolved into solution following immersion was determined using ICP-OES. The wavelengths used herein were selected from those with high enough signal and significantly away from the wavelengths of typical alloying elements and impurities (such as Al, Zn and Fe). The alloying elements were thus included in the analysis and AZ31B was assumed to be dissolving congruently. This assumption was corroborated by detecting cations of all alloying elements in solution above the baseline level; however, this is not the focus of this study in particular.

Integration of i_{corr} over the 24 hr immersion using Equation 2.5, along with the conversion of the mass loss, H_2 collected, and Mg dissolved in solution via ICP-OES all resulted in anodic charge estimations that are similar in value for each environment (Table 2.7-2.8, Figure 2.11). This corroborating outcome is similar to that from commercially pure Mg, indicating that the comparison of unique methods provides not only good comparison for the corrosion rate of AZ31B, but validates the electrochemical approach as a standalone method. Figure 2.12 reveals the EIS analysis over the 24 hour period for each of the [Cl⁻] concentrations studied, indicating

the inductive loop, R_P fitting and subsequent electrochemical characteristics of the material are accurate throughout the full span of the immersion.

2.4 <u>Discussion</u>

2.4.1 Corrosion rate of AZ31B contrasted to commercially pure Mg.

It is generally accepted that the addition of Al to Mg alloys increases in the corrosion resistance when the alloying element remains in solid solution[68-71]. There is evidence that Al additions up to 4 wt. % reduce the corrosion rate, synonymous with the corrosion rate of AZ31 representing the benchmark for commercial Mg alloys. However, for Mg alloys with higher Al content such as AZ80 and AZ91 (with 8 and 9 wt% Al respectively) the free corrosion rate is increased[65] due to the presence of β phase ($Mg_{17}Al_{12}$)[72,73]. The β phase, along with the majority of Mg-based intermetallics (with the exception of Mg_2Ca) are more noble than Mg in isolation, and are therefore polarised cathodically when in the Mg matrix, increasing the free corrosion rate due to accelerated cathodic kinetics[1,73,74]. The deliberate addition of Mn to the AZ family of alloys is also beneficial from the corrosion perspective, on the basis that the presence of both Al and Mn will sequester any detrimental impurity Fe into an Al-Mn-Fe intermetallic[75,76]. Additionally, at low Zn content, there is no increase in the free corrosion rate. It is only when Zn is above a few wt% that it will detrimentally affect the free corrosion rate[77].

If the alloying elements are therefore in solid solution, AZ31 should have a lower corrosion rate than commercially pure Mg. This is elaborated here, not to rank the alloys per se, but to highlight that the methods employed herein, when applied effectively, can permit such a discrimination in alloy corrosion rates readily. It was indicated that AZ31 used in this study, by all four analysis techniques, presents a lower corrosion rate than commercially pure Mg. To provide a wider content, this is also correlated with previous research that has analysed the corrosion behaviour of commercially pure Mg and Mg-Al alloys using mass loss and H_2 evolution[45,69] with a summary of corrosion rates for both Mg and AZ31 given in Table 2.9. In addition to the literature data in Figure 2.9, the data from tests herein has been added in order to provide the comparison between the rates determined herein with those in the literature determined via other / complementary methods. For the data presented in Table 2.9 from this study, congruent dissolution was assumed in order to normalise the units from the various

studies. However, it is appreciated that for any Mg alloy (even commercially pure Mg or solid solution alloys such as AZ31B), that corrosion will not be ideally uniform[1,17,63].

2.4.2 Selection of Tafel slope and complicating factors

There is a range of reported Tafel slopes that have been used to determine corrosion rate[27,29,30,39,43-45] of Mg and its alloys[45-47,78]. From determination of B, there is not a straight forward linear change in the evaluated i_{corr} except under simplifying assumptions of Equation 2.3 compared to Equation 2.4[29]. During the evolution of the free corrosion of Mg and Mg alloys, anodic and cathodic areas undoubtedly differ based on physical inspection[17,63]. Such changes in the surface condition (i.e. the ratio of active and inactive sites and perhaps even cathodic activation[1,73,74] should occur during an EIS experiment. The evolution of the corroding Mg surface is also likely to lead to discrete surface filming associated with $Mg(OH)_2$ formation[79,80]. Due to these known characteristics of the Mg system, β_a is difficult to determine using typical DC polarization methods. However, a relatively wide range of β_a values would subsequently lead to a rather minimal scatter in calculated i_{corr} values (Table 2.4, 2.7) on the basis that Mg is weakly polarizable and that anodic Tafel slopes are limited to a reasonably confined range. As such, a range of assumed values for β_a may be used for the interpretation of Mg corrosion rates while still maintaining some accuracy.

For a definitive determination of corrosion rates for the Mg system, the Tafel slope should be determined recalling that at least one of the branches of the polarization curve should exhibit Tafel behavior over at least one decade of current density and the influence of iR related effects should be minimal[40,41]. The appropriateness of these Tafel assumptions can also be related to the mechanistic properties of the system. More specifically, a mechanistically well-grounded anodic Tafel slope is typically a multiple or fraction of 2.303RT/F where 2.3RT/$(\alpha+\nu)$F provides one example where α may be related to a symmetry factor and ν may be an integer related to reaction steps and/or the rate determining step[81]. Clearly further understanding of this subject and use of Equation 2.4 is necessary to evaluate Mg corrosion. In the meantime, for the Tafel slope extracted from E-logi data to be deemed appropriate, typically the criterion that $\eta/\beta > 1$ should be satisfied. However, for both commercially pure Mg and AZ31, this is difficult, especially after iR correction. This is due to the polarization scans on Mg

not yielding a linear Tafel region due to the aforementioned coverage effects, catalysis of HER and changing active areas with time and potential as well as films.

The plot in Figure 2.13 shows the calculated error between the true anodic or cathodic current density as a function of overpotential with respect to E_{corr} as estimated by the Tafel approximation when compared to a full activation controlled Butler-Volmer relationship accounting for both the anodic and cathodic reactions, assuming various assumed values of β_a and β_c in accordance with King[29], Shi[39], Cao[44], and Turhan [42]. Figure 2.13 shows that the Tafel approximation, when reasonable values for β_a and β_c are assumed, does not provide a reliable estimation of applied current density within an overpotential of 100 mV from OCP (more generally $\eta/\beta<1$) and as a result, it may be difficult to deduce and extract a valid Tafel slope from polarization data obtained within 100 mV from OCP. Therefore, low values of Tafel slope taken from E-logi data taken near E_{corr} should be treated with caution. Amongst other concerns, this also points towards the difficulty and errors likely during Tafel extrapolation to determine i_{corr}.

2.4.3 Selection of R_p versus R_t and physical justification of inductance

The Mg corrosion process will involve both a surface film, active sites for both anodic and cathodic reactions, susceptibility to cathodic activation and perhaps adsorbed intermediates. The unique contribution from each of these processes no doubt depends on both the Mg alloy and the environment. Mg was additionally tested in a range of environments in this work. A well-defined inductive loop was seen in both this study (not shown) and the literature [38,39,44,82-84] when HP Mg and AZ31B were tested in $MgCl_2$ solution; also reported in NaCl + $MgCl_2$ mixtures[84]. A range of other environments, including Na_2SO_4 and $MgSO_4$, also reveal an inductive loop. According to Guadrrama-Munoz et al., when Mg does not fulfill the chemical composition specified for a sacrificial Mg anode as given by ASTM B843-13, an inductive loop will appear in the subsequent Nyquist plot [83,85]. EIS testing with a cathodic bias and certain environments, including TRIS[2] and Ethylene glycol, do not exhibit this loop over the frequency range reported as summarized in Table 2.10. Consequently, the analysis of the corrosion rate of Mg can be challenging and therefore the choice between the use of R_P or R_t in Equation 2.3 and 2.5 is critically important. Through the use of R_t at intermediate frequencies, the proposed rate

---

[2] *tris(hydroxymethyl)aminomethane*

determining coverage term is frozen and therefore cannot fluctuate with the AC signal. Subsequently the AC current density cannot fluctuate with coverage and R_t overestimates R_P. In order to fully capture this characteristic response of Mg, the inductive loop must be analyzed in the determination of corrosion rate when it appears in the data and R_P must be calculated by considering low frequency EIS data even if Z" is positive by extrapolation to the zero frequency limit. An $R_P < R_t$ by itself produces a higher (and more realistic) i_{corr} which is then in agreement with mass loss and H_2 gas collection, as shown previously by King et al.[29] and validated herein over a wider range of conditions. This last point merits specific attention, since recent criticisms of EIS for Mg have suggested that EIS determined corrosion rates are significant underestimations of the actual rate determined by mass loss and are very similar to corrosion rates determined from a simple three component (Randle's type) equivalent circuit to determine R_t[86]. It is however noted that in that work[86], there was no concurrent validation via ICP-OES (as herein), and the values of B used were below any ever reported (included the authors own), whilst finally the inductive loop is an irrefutable feature of the data (documented by many[38,39,44,50,82-84,87-89]) and it cannot be summarily ignored. As such, a method for treating EIS data for Mg, based on analyses of R_p and more typically reported Tafel slope values, is included in the present paper.

2.5 <u>Conclusion</u>

1. The accurate instantaneous and long-term capable determination of corrosion rate was accomplished via the combined study of mass loss, H_2 evolution, EIS, and ICP-OES solution analysis in unbuffered NaCl solution. The ability to employ one of the adopted methods alone can hereby be utilized to provide a valid corrosion rate measurement on the basis of the close correlations observed here.

2. The corrosion rate of commercially pure Mg as well as AZ31B was seen to be different, and dependent on composition and microstructure; with a consistent trend seen that commercially pure Mg has a higher corrosion rate than AZ31B in unbuffered NaCl solution.

3. EIS determined i_{corr} values derived from R_t are systematically shown to be lower than those evaluated through the measurement of R_P. Underestimation of i_{corr} is due to (a) the use of an equivalent circuit without the inclusion and/or consideration of an inductor, (b)

tests which do not terminate at sufficiently low frequency or provide reasonable fitting of data to the zero frequency limit and (c) the use of too low a value of the Tafel slope.

4. In order to accurately determine the corrosion rate of Mg alloys, an appropriate Tafel slope must be used as deemed appropriate by typical Tafel slope methods and/or mechanistic analysis of reaction mechanisms.

References

1. G. Williams, N. Birbilis, and H.N. McMurray, "The source of hydrogen evolved from a magnesium anode," Electrochemistry Communications 36, 0 (2013): p. 1-5.
2. A.D. King, B. Kannan, and J.R. Scully, "Environmental Degradation of a Mg-Rich Primer in Selected Field and Laboratory Environments – Part I. Without a Topcoat," Corrosion (2013).
3. A.D. King, B. Kannan, and J.R. Scully, "Environmental Degradation of a Mg-Rich Primer in Selected Field and Laboratory Environments – Part II. Primer and Topcoat," Corrosion (2013).
4. A.D. King and J.R. Scully. *Blistering Phenomena in Early Generation Mg-Rich Primer Coatings on AA2024-T351 and the Effects of CO_2*. in *NACE DoD 2011 Conference Proceedings*. 2011. Palm Springs, CA.
5. A.D. King and J.R. Scully, "Sacrificial Anode-Based Galvanic and Barrier Corrosion Protection of 2024-T351 by a Mg-Rich Primer and Development of Test Methods for Remaining Life Assessment," Corrosion 67, 5 (2011): p. 05500401-05500422.
6. B. Maier and G.S. Frankel, "Behavior of Magnesium-Rich Primers on AA2024-T3," Corrosion 67, 5 (2011): p. 055001.
7. G.P. Bierwagen, D.E. Tallman, M. Nanna, D. Battocchi, A. Stamness, and V.J. Gelling, "New developments in Cr-free primers for aerospace alloys.," Abstracts of Papers of the American Chemical Society 228, (2004): p. U360-U360.
8. M.E. Nanna and G.P. Bierwagen, "Mg-rich coatings: A new paradigm for Cr-free corrosion protection of al aerospace alloys," Jct Research 1, 2 (2004): p. 69-80.
9. A. Simoes, D. Battocchi, D. Tallman, and G. Bierwagen, "Assessment of the corrosion protection of aluminium substrates by a Mg-rich primer: EIS, SVET and SECM study," Prog Org Coat 63, 3 (2008): p. 260-266.
10. H. Xu, D. Battocchi, D.E. Tallman, and G.P. Bierwagen, "Use of Magnesium Alloys as Pigments in Magnesium-Rich Primers for Protecting Aluminum Alloys," Corrosion 65, 5 (2009): p. 318-325.
11. G. Song and A. Atrens, "Corrosion mechanisms of magnesium alloys," Adv Eng Mater 1, 1 (1999): p. 11-33.
12. P. Volovitch, M. Serdechnova, and K. Ogle, "Aqueous Corrosion of Mg-Al Binary Alloys: Roles of Al and Mg," Corrosion 68, 6 (2012): p. 557-570.
13. A.D. Südholz, K. Gusieva, X.B. Chen, B.C. Muddle, M.A. Gibson, and N. Birbilis, "Electrochemical behaviour and corrosion of Mg-Y alloys," Corros Sci 53, 6 (2011): p. 2277-2282.
14. G. Song and D. St. John, "The effect of zirconium grain refinement on the corrosion behaviour of magnesium-rare earth alloy MEZ," Journal of Light Metals 2, 1 (2002): p. 1-16.
15. A.D. Südholz, N. Birbilis, C.J. Bettles, and M.A. Gibson, "Corrosion behaviour of Mg-alloy AZ91E with atypical alloying additions," J Alloy Compd 471, 1–2 (2009): p. 109-115.
16. K.D. Ralston, G. Williams, and N. Birbilis, "Effect of pH on the Grain Size Dependence of Magnesium Corrosion," Corrosion 68, 6 (2012): p. 507-517.

17. G. Williams, K. Gusieva, and N. Birbilis, "Localized Corrosion of Binary Mg-Nd Alloys in Chloride-Containing Electrolyte Using a Scanning Vibrating Electrode Technique," Corrosion 68, 6 (2012): p. 489-498.

18. D.B. Huang, J.Y. Hu, G.L. Song, and X.P. Guo, "Self-corrosion, galvanic corrosion and inhibition of GW103 and AZ91D Mg alloys in ethylene glycol solution," Corros Eng Sci Techn 48, 2 (2013): p. 155-160.

19. M.C. Turhan, D. Ruckle, M.S. Killian, H. Jha, and S. Virtanen, "Corrosion Behavior of Polypyrrole/AZ91D in Simulated Body Fluid Solutions and its Functionalization with Albumin Monolayers," Corrosion 68, 6 (2012): p. 536-547.

20. G. Baril, C. Blanc, M. Keddam, and N. Pebere, "Local electrochemical impedance spectroscopy applied to the corrosion behavior of an AZ91 magnesium alloy," J Electrochem Soc 150, 10 (2003): p. B488-B493.

21. G. Baril, C. Blanc, and N. Pebere, "AC impedance spectroscopy in characterizing time-dependent corrosion of AZ91 and AM50 magnesium alloys - Characterization with respect to their microstructures," J Electrochem Soc 148, 12 (2001): p. B489-B496.

22. G. Ballerini, U. Bardi, R. Bignucolo, and G. Ceraolo, "About some corrosion mechanisms of AZ91D magnesium alloy," Corros Sci 47, 9 (2005): p. 2173-2184.

23. S. Mathieu, C. Rapin, J. Hazan, and P. Steinmetz, "Corrosion behaviour of high pressure die-cast and semi-solid cast AZ91D alloys," Corros Sci 44, 12 (2002): p. 2737-2756.

24. J. Zhang, J. Wang, X. Qiu, D. Zhang, Z. Tian, X. Niu, D. Tang, and J. Meng, "Effect of Nd on the microstructure, mechanical properties and corrosion behavior of die-cast Mg–4Al-based alloy," J Alloy Compd 464, 1–2 (2008): p. 556-564.

25. W. Liu, F. Cao, L. Chang, Z. Zhang, and J. Zhang, "Effect of rare earth element Ce and La on corrosion behavior of AM60 magnesium alloy," Corros Sci 51, 6 (2009): p. 1334-1343.

26. J.R. Scully, Corrosion Journal 56, (2000): p. 199-218.

27. J. Światowska, P. Volovitch, and K. Ogle, "The anodic dissolution of Mg in NaCl and Na2SO4 electrolytes by atomic emission spectroelectrochemistry," Corros Sci 52, 2010 (2010): p. 2372-2378.

28. S. Lebouil, A. Duboin, F. Monti, P. Tabeling, P. Volovitch, and K. Ogle, "A novel approach to on-line measurement of gas evolution kinetics: Application to the negative difference effect of Mg in chloride solution," Electrochim Acta 124 (2013).

29. A.D. King, N. Birbilis, and J.R. Scully, "Accurate Electrochemical Measurement of Magnesium Corrosion Rates; a Combined Impedance, Mass-Loss and Hydrogen Collection Study," Electrochim Acta 121, 1 (2014): p. 394-406.

30. G.S. Frankel, A. Samaniego, and N. Birbilis, "Evolution of hydrogen at dissolving magnesium surfaces," Corrosion Science 70, (2013): p. 104-111.

31. R.M. Souto, A. Kiss, J. Izquierdo, L. Nagy, I. Bitter, and G. Nagy, "Spatially-resolved imaging of concentration distributions on corroding magnesium-based materials exposed to aqueous environments by SECM," Electrochemistry Communications 26, (2013): p. 25-28.

32. L. Rossrucker, K.J.J. Mayrhofer, G.S. Frankel, and N. Birbilis, "Investigating the Real Time Dissolution of Mg Using Online Analysis by ICP-MS," J Electrochem Soc 161, 3 (2014): p. C115-C119.

33. A. Atrens, G. Song, F. Cao, Z. Shi, and P.K. Bowen, "Advances in Mg corrosion and research suggestions," Journal of Magnesium and Alloys 1, 3 (2013): p. 177-200.

34. Z.D. Popovic and G.R. Piercy, "Measurement of the Solubility of Hydrogen in Solid Magnesium," Metallurgical Transactions 6A, (1975).

35. N. Birbilis, A.D. King, S. Thomas, G.S. Frankel, and J.R. Scully, "Evidence for enhanced catalytic activity of magnesium arising from anodic dissolution," Electrochim Acta 132, 0 (2014): p. 277-283.

36. M. Stern and A.I. Geary, J Electrochem Soc 104: p. 56-63.

37. T.R. Thomaz, C.R. Weber, T. Pelegrini Jr, L.F.P. Dick, and G. Knörnschild, "The negative difference effect of magnesium and of the AZ91 alloy in chloride and stannate-containing solutions," Corros Sci 52, 7 (2010): p. 2235-2243.

38. G. Song, A. Atrens, D. St John, X. Wu, and J. Nairn, "The anodic dissolution of magnesium in chloride and sulphate solutions," Corros Sci 39, 10-11 (1997): p. 1981-2004.

39. Z. Shi, F. Cao, G.L. Song, M. Liu, and A. Atrens, "Corrosion behaviour in salt spray and in 3.5% NaCl solution saturated with Mg(OH)2 of as-cast and solution heat-treated binary Mg–RE alloys: RE=Ce, La, Nd, Y, Gd," Corros Sci 76, 0 (2013): p. 98-118.

40. D.A. Jones, "Principles and Prevention of Corrosion," Prentice Hall Upper Saddle River. NJ. 2nd Ed (1996).

41. R.G. Kelly, J.R. Scully, D.W. Shoesmith, and R.G. Buchheit, "Electrochemical Techniques in Corrosion Science and Engineering," (2002).

42. M.C. Turhan, Q. Li, H. Jha, R.F. Singer, and S. Virtanen, "Corrosion behaviour of multiwall carbon nanotube/magnesium composites in 3.5% NaCl," Electrochim Acta 56, 20 (2011): p. 7141-7148.

43. Z. Qiao, Z. Shi, N. Hort, N.I. Zainal Abidin, and A. Atrens, "Corrosion behaviour of a nominally high purity Mg ingot produced by permanent mould direct chill casting," Corros Sci 61, 0 (2012): p. 185-207.

44. F. Cao, Z. Shi, J. Hofstetter, P.J. Uggowitzer, G. Song, M. Liu, and A. Atrens, "Corrosion of ultra-high-purity Mg in 3.5% NaCl solution saturated with Mg(OH)2," Corros Sci 75, (2013): p. 78-99.

45. A. Pardo, S.F. Jr., M.C. Merino, R. Arrabal, and E. Matykina, "Electrochemical Estimation of the Corrosion Rate of Magnesium/Aluminium Alloys," International Journal of Corrosion 2010, (2010).

46. T.S. Lim, H.S. Ryu, and S.-H. Hong, "Electrochemical corrosion properties of CeO2-containing coatings on AZ31 magnesium alloys prepared by plasma electrolytic oxidation," Corros Sci 62, 0 (2012): p. 104-111.

47. L. Li, Q. Qu, Z.Fang, L. Wang, Y. He, R. Yuan, and Z. Ding, "Enhanced Corrosion Resistance of AZ31B Magnesium Alloy by Cooperation of Rare Earth Cerium and Stannate Conversion Coating," International Journal of Electrochemical Science 7, (2012): p. 12690-12705.

48. D.W. Marquardt, "An Algorithm for Least-Squares Estimation of Nonlinear Parameters," Journal of the Society for Industrial and Applied Mathematics 11, 2 (1963): p. 431-441.

49. G. Baril, G. Galicia, C. Deslouis, N. Pebere, B. Tribollet, and V. Vivier, "An impedance investigation of the mechanism of pure magnesium corrosion in sodium sulfate solutions," J Electrochem Soc 154, 2 (2007): p. C108-C113.

50. G. Baril and N. Pebere, "The corrosion of pure magnesium in aerated and deaerated sodium sulphate solutions," Corros Sci 43, 3 (2001): p. 471-484.

51. I. Nakatsugawa, R. Martin, and E.J. Knystautas, "Improving Corrosion Resistance of AZ91D Magnesium Alloy by Nitrogen Ion Implantation," Corrosion 52, 12 (1996): p. 921-926.

52. Y.C. Xin, C.L. Liu, W.J. Zhang, J. Jiang, T.Y. Guoyi, X.B. Tian, and P.K. Chua, "Electrochemical behavior Al2O3/Al coated surgical AZ91 magnesium alloy in simulated body fluids," J Electrochem Soc 155, 5 (2008): p. C178-C182.

53. A.M. Fekry and M.A. Ameer, "Electrochemistry and impedance studies on titanium and magnesium alloys in Ringer's solution," International Journal of Electrochemical Science 6, 5 (2011): p. 1342-1354.

54. S. Feliu, C. Maffiotte, A. Samaniego, J.C. Galvan, and V. Barranco, "Effect of the chemistry and structure of the native oxide surface film on the corrosion properties of commercial AZ31 and AZ61 alloys," Appl Surf Sci 257, 20 (2011): p. 8558-8568.

55. J.L. Bullister, N.L. Guinasso, and D.R. Schink, "Dissolved hydrogen, carbon monoxide, and methane at the CEPEX site," Journal of Geophysical Research: Oceans 87, C3 (1982): p. 2022-2034.

56. ASTM-G1, "Standard Practice for Preparing, Cleaning, and Evaluating Corrosion Test Specimens," ASTM International G1, (2011).

57. ASTM-G106, "Standard Practice for Verification of Algorithm and Equipment for Electrochemical Impedance Measurements," ASTM International (2010).

58. N. Birbilis, M.A. Easton, A.D. Sudholz, S.M. Zhu, and M.A. Gibson, "On the corrosion of binary magnesium-rare earth alloys," Corros Sci 51, 3 (2009): p. 683-689.

59. G. Song and A. Atrens, "Understanding Magnesium Corrosion—A Framework for Improved Alloy Performance," Adv Eng Mater 5, 12 (2003): p. 837-858.

60. M. Liu, P. Schmutz, P.J. Uggowitzer, G. Song, and A. Atrens, "The influence of yttrium (Y) on the corrosion of Mg–Y binary alloys," Corros Sci 52, 11 (2010): p. 3687-3701.

61. F. Zucchi, V. Grassi, A. Frignani, C. Monticelli, and G. Trabanelli, "Electrochemical behavior of a magnesium alloy containing rare earth elements," J Appl Electrochem 36, (2006): p. 195-204.

62. T. Cain, L. Bland, N. Birbilis, and J. Scully, "A compilation of corrosion potentials for magnesium alloys," Corrosion 70, 10 (2014): p. 1043-1051.

63. G. Williams, H. ap Llwyd Dafydd, and R. Grace, "The localised corrosion of Mg alloy AZ31 in chloride containing electrolyte studied by a scanning vibrating electrode technique," Electrochim Acta 109, 0 (2013): p. 489-501.

64. Y. Xina, C. Liua, W. Zhanga, J. Jianga, G. Tangb, X. Tianc, and P.K. Chua, "Electrochemical Behavior Al2O3∕Al Coated Surgical AZ91 Magnesium Alloy in Simulated Body Fluids," J Electrochem Soc 155, 5 (2008): p. C178-C182.

65. A. Pardo, M.C. Merinoa, A.E. Coya, F. Viejob, R. Arrabalb, and S.F. Jr., "Influence of microstructure and composition on the corrosion behaviour of Mg/Al alloys in chloride media," Electochimica Acta 53, 27 (2008): p. 7890-7902.

66. M. Taheri, R.C. Phillips, J.R. Kish, and G.A. Botton, "Analysis of the surface film formed on Mg by exposure to water using a FIB cross-section and STEM–EDS," Corros Sci 59, 0 (2012): p. 222-228.

67. R.C. Phillips and J.R. Kish, "Nature of Surface Film on Matrix Phase of Mg Alloy AZ80 Formed in Water," Corrosion 69, 8 (2013): p. 813-820.

68. E. Ghali, W. Dietzel, and K.U. Kainer, "General and localized corrosion of magnesium alloys: A critical review," J Mater Eng Perform 13, 1 (2004): p. 7-23.

69. G.L. Makar and J. Kruger, "Corrosion Studies of Rapidly Solidified Magnesium Alloys," J Electrochem Soc 137, 2 (1990): p. 414-421.
70. I.J. Polmear, "Light Alloys: From Traditional Alloys to Nanocrystals 4th Edition," Elsevier (2006).
71. P. Hoyer, G.L. Angrisani, C. Klose, F.W. Bach, and T. Hassel, "Influence of aluminium on the corrosion behaviour of binary magnesium–aluminium alloys in saline solutions," Materials and Corrosion 65, 1 (2014): p. 23-30.
72. O. Lunder, J.E. Lein, T.K. Aune, and K. Nisancioglu, "The Role of Mg17Al12 Phase in the Corrosion of Mg Alloy AZ91," Corros Sci 45, 9 (1989).
73. A.D. Südholz, N.T. Kirkland, R.G. Buchheit, and N. Birbilis, "Electrochemical Properties of Intermetallic Phases and Common Impurity Elements in Magnesium Alloys," Electrochemical and Solid-State Letters 14, 2 (2011): p. C5-C7.
74. C. Blawert, D. Fechner, D. Höche, V. Heitmann, W. Dietzel, K.U. Kainer, P. Živanović, C. Scharf, A. Ditze, J. Gröbner, and R. Schmid-Fetzer, "Magnesium secondary alloys: Alloy design for magnesium alloys with improved tolerance limits against impurities," Corros Sci 52, 7 (2010): p. 2452-2468.
75. J.A. Boyer: p. 38.
76. J.D. Hanawalt, C.E. Nelson, and J.A. Peloubet, Transactions of AIME 147, (1942): p. 273-299.
77. N. Kirkland, M. Staiger, D. Nisbet, C.J. Davies, and N. Birbilis, "Performance-driven design of Biocompatible Mg alloys," Jom-Us 63, 6 (2011): p. 28-34.
78. D. Song, A.B. Ma, J.H. Jiang, P.H. Lin, D.H. Yang, and J.F. Fan, "Corrosion behaviour of bulk ultra-fine grained AZ91D magnesium alloy fabricated by equal-channel angular pressing," Corros Sci 53, 1 (2011): p. 362-373.
79. Y. Zhu, G. Wu, Y.H. Zhang, and Q. Zhao, "Growth and characterization of Mg(OH)2 film on magnesium alloy AZ31," Appl Surf Sci 257, 14 (2011): p. 6129-6137.
80. L. Wang, B.-P. Zhang, and T. Shinohara, "Corrosion behavior of AZ91 magnesium alloy in dilute NaCl solutions," Mater Design 31, 2 (2010): p. 857-863.
81. E. Gileadi, Electrode Kinetics for Chemists, Chemical Engineers, and Materials Scientists (New York: Wiley-VCH, 1993.
82. N. Pebere, C. Riera, and F. Dabosi, "Investigation of Magnesium Corrosion In Aerated Sodium Sulfate Solution By Electrochemical Impedance Spectroscopy," Electochimica Acta 35, 2 (1990): p. 555-561.
83. F. Guadarrama-Muñoz, J. Mendoza-Flores, R. Duran-Romero, and J. Genesca, "Electrochemical study on magnesium anodes in NaCl and CaSO4–Mg(OH)2 aqueous solutions," Electrochim Acta 51, 8–9 (2006): p. 1820-1830.
84. B. Borresen, G.M. Haarberg, and R. Tunold, "Kinetics and Mechanism of the Magnesium Electrode Reaction in Molten MgCI2-NaCI Binary Mixtures," J Electrochem Soc 144, 5 (1997): p. 1646-1651.
85. ASTM-B843, "Standard Specification for Magnesium Alloy Anodes for Cathodic Protection," ASM International (2013).
86. Z. Shi, F. Cao, G.-L. Song, and A. Atrens, "Low apparent valence of Mg during corrosion," Corros Sci 88, 0 (2014): p. 434-443.
87. G. Baril and N. Pébère, "The corrosion of pure magnesium in aerated and deaerated sodium sulphate solutions," Corros Sci 43, 3 (2001): p. 471-484.

88. G. Galicia, N. Pébère, B. Tribollet, and V. Vivier, "Local and global electrochemical impedances applied to the corrosion behaviour of an AZ91 magnesium alloy," Corros Sci 51, 8 (2009): p. 1789-1794.

89. G. Song and D. St John, "Corrosion behaviour of magnesium in ethylene glycol," Corros Sci 46, 6 (2004): p. 1381-1399.

90. J. Liao, M. Hotta, and N. Yamamoto, "Corrosion behavior of fine-grained AZ31B magnesium alloy," Corros Sci 61, 0 (2012): p. 208-214.

91. R.E. McNulty and J.D. Hanawalt, "Some Corrosion Characteristics of High Purity Magnesium Alloys," Transactions of the Electrochemical Society 81, (1942): p. 423-433.

92. M. Liu, P.J. Uggowitzer, A.V. Nagasekhar, P. Schmutz, M. Easton, G.-L. Song, and A. Atrens, "Calculated phase diagrams and the corrosion of die-cast Mg–Al alloys," Corros Sci 51, 3 (2009): p. 602-619.

93. M.-C. Zhao, P. Schmutz, S. Brunner, M. Liu, G.l. Song, and A. Atrens, "An exploratory study of the corrosion of Mg alloys during interrupted salt spray testing," Corros Sci 51, 6 (2009): p. 1277-1292.

94. Z. Shi and A. Atrens, "An innovative specimen configuration for the study of Mg corrosion," Corros Sci 53, 1 (2011): p. 226-246.

95. S. Budruk Abhijeet, R. Balasubramaniam, and M. Gupta, "Corrosion behaviour of Mg–Cu and Mg–Mo composites in 3.5% NaCl," Corros Sci 50, 9 (2008): p. 2423-2428.

96. A. Pardo, M.C. Merino, A.E. Coy, R. Arrabal, F. Viejo, and E. Matykina, "Corrosion behaviour of magnesium/aluminium alloys in 3.5 wt.% NaCl," Corros Sci 50, 3 (2008): p. 823-834.

97. D. Song, A. Ma, J. Jiang, P. Lin, D. Yang, and J. Fan, "Corrosion behavior of equal-channel-angular-pressed pure magnesium in NaCl aqueous solution," Corros Sci 52, 2 (2010): p. 481-490.

98. N.N. Aung and W. Zhou, "Effect of grain size and twins on corrosion behaviour of AZ31B magnesium alloy," Corros Sci 52, 2 (2010): p. 589-594.

99. Z. Pu, G.L. Song, S. Yang, J.C. Outeiro, O.W. Dillon Jr, D.A. Puleo, and I.S. Jawahir, "Grain refined and basal textured surface produced by burnishing for improved corrosion performance of AZ31B Mg alloy," Corros Sci 57, 0 (2012): p. 192-201.

100. G. Song, A. Atrens, D. Stjohn, J. Nairn, and Y. Li, "The electrochemical corrosion of pure magnesium in 1 N NaCl," Corros Sci 39, 5 (1997): p. 855-875.

101. G. Song, A. Atrens, X. Wu, and B. Zhang, "Corrosion behaviour of AZ21, AZ501 and AZ91 in sodium chloride," Corros Sci 40, 10 (1998): p. 1769-1791.

102. M.C. Zhao, M. Liu, G.L. Song, and A. Atrens, "Influence of Microstructure on Corrosion of As-cast ZE41," Adv Eng Mater 10, 1-2 (2008): p. 104-111.

103. ASTMG97, "Standard Test Method for Laboratory Evaluation of Magnesium Sacrifical Anode Test Specimens for Underground Applications," ASM International (2013).

Table 2. 1. A selection of Tafel slope determination methods reported in the literature.

Alloy	Tafel determination method	Immersion time	E_{corr} (mV$_{SCE}$)	β_a (mV/dec)	β_c (mV/dec)	B (mV)	[Cl⁻]	pH	Ref
CP Mg	Tafel extrapolation	0 hours	-1.627	31.0	186.0	11.5	0.6	--	[42]
CP Mg	Tafel extrapolation	1800 sec	-1.550	150.0	315.0	44.1	0.1	5.4	[29]
CP Mg	Tafel extrapolation	1800 sec	-1.550	90.0	315.0	30.4	1.0	5.2	[29]
CP Mg	Tafel extrapolation	1800 sec	-1.550	30.0	315.0	11.9	5.0	5.1	[29]
CP Mg	Tafel extrapolation	1000 sec	-1.650	--	530.0	--	0.03	--	[27]
CP Mg	as reported	--	-1.650	--	300.0	--	0.1	--	[30]
CP Mg	Tafel extrapolation	--	-1.650	--	260.0	--	0.1	--	[30]
CP Mg	Tafel extrapolation	6 hours	-1.531	58.0	246.0	20.4	0.6	--	[42]
CP Mg	average-Levenberg Marquardt Method	3 days	-1.578	64.5	362.5	23.8	0.6	--	[43]
CP Mg	average-Tafel extrapolation	3 days	-1.578	--	362.5	--	0.6	--	[43]
CP Mg	average-Levenberg Marquardt Method	5 days	-1.587	54.5	334.5	20.3	0.6	--	[43]
CP Mg	average-Tafel extrapolation	5 days	-1.587	--	330.0	--	0.6	--	[43]
CP Mg	average-Levenberg Marquardt Method	7 days	-1.588	50.0	304.67	18.8	0.6	--	[43]
CP Mg	average-Tafel extrapolation	7 days	-1.588	--	305.33	--	0.6	--	[43]
CP Mg	experimental-Tafel extrapolation	7 days	-1.631	--	161.00	--	0.6	--	[39]
CP Mg	experimental-Levenberg Marquardt Method	7 days	-1.631	180.0	160.00	36.8	0.6	--	[39]
CP Mg	experimental-Levenberg Marquardt Method	14 days	-1.549	82.0	260.0	27.1	0.6	--	[44]
CP Mg	experimental-Levenberg Marquardt Method	14 days	-1.299	31.5	183.0	11.7	0.6	--	[44]
CP Mg	experimental-Levenberg Marquardt Method	14 days	-1.620	25.1	303.0	10.1	0.6	--	[44]
CP Mg	experimental-Levenberg Marquardt Method	14 days	-1.396	90.0	160.0	25.0	0.6	--	[44]
AZ91	experimental-Tafel extrapolation	300s	--	80.1	175.0	23.9	0.6	--	[78]
AZ31	experimental-Tafel extrapolation	1800 sec	--	146.0	390	13.4	0.6	--	[47]
AZ31	experimental-Tafel extrapolation	48 hrs	-1.550	27.0	168.0	10.1	0.6	--	[46]
AZ31	experimental-Tafel extrapolation	28 days	--	--	50.0	--	0.6	--	[45]
AZ31	monovalent and divalent ions are proportional	28 days	--	--	50.0	--	0.6	--	[45]
AZ31	EIS and gravimetric measurements	28 days	--	--	32.0	--	0.6	--	[45]

Table 2.2. Compositions of 99.9% Mg Rod (Alfa Aesar) and, AZ31B-H24 ([UNS M11311] Magnesium Elektron). All compositions reported in wt. %, with the actual compositions provided by QUANT (Quality Analysis and Testing Corporation).

	UNS #	Al	Mn	Zn	Si	Cu	Ni	Fe	Mg
Mg Rod	--	0.01	0.01	0.01	0.021	0.005	0.001	0.006	Bal.
AZ31B-H24	M11311	3.02	0.33	0.99	0.025	0.005	0.002	0.005	Bal.

Table 2.3. Typical fitting results of electrochemical impedance measurements made on commercially pure Mg, in 0.1, 1.0, and 5.0 M NaCl solution at open circuit after 3, 12, and 24 hrs of immersion, as per the equivalent circuits seen in Figure 2.1. All runs were performed with a vertical flat cell with a 1 cm^2 sample window.

	0.01 M NaCl			0.6 M NaCl			5 M NaCl		
	3 hrs	12 hrs	24 hrs	3 hrs	12 hrs	24 hrs	3 hrs	12 hrs	24 hrs
R_s (Ω)	80.5	95.1	117	80.7	92.5	102	4.40	6.00	6.40
C_1 (μF)	163	104	73.5	162	114	89.8	11.4	13.8	12.4
R_1 (Ω)	145	585	1170	142	397	820	18.9	33.1	30.7
C_2 (μF)	5040	8300	2300	3580	9510	4690	79.0	80.7	79.5
R_2 (Ω)	21.4	136	253	22.5	77.2	165	13.2	22.7	27.7
L (L)	5950	1.99×10^4	3.30×10^4	3610	9870	2.62×10^4	1616	22.7	27.6
R_3 (Ω)	600	600	600	100	100	100	5.00	5.00	5.00
R_p (Ω)	130	327	422	62.2	82.6	90.8	12.9	10.9	27.7
C_4 (μF)	--	--	--	--	--	--	1.00×10^4	2.00×10^4	1.50×10^4
R_4 (Ω)	--	--	--	--	--	--	5.00	10.5	6.30

Table 2.4. Anodic charge consumed on commercially pure Mg as calculated by integration of i_{corr} derived from EIS-estimated polarization resistance for three different Tafel approximations after exposure in 0.01, 0.6, and 5.0 M NaCl at open circuit for 24 hrs.

		Tafel Assumptions		
		0.01 M NaCl	0.6 M NaCl	5 M NaCl
B_{king}[29]	β_c	315.0 mV/dec	315.0 mV/dec	315.0 mV/dec
	β_a	150.0 mV/dec	112.5 mV/dec	30 mV/dec
	B	44.2 mV	36.0 mV	11.9 mV
	ΣQ_{EIS}	17.0 ± 8.6 C/cm^2	97.5 ± 18.3 C/cm^2	228.9 ± 47.8 C/cm^2
B_{Shi}	β_c	--	160.0 mV/dec	--
	β_a	--	180.0 mV/dec	--
	B	--	36.8 mV	--
	ΣQ_{EIS}	--	99.6 ± 17.6 C/cm^2	--
B_{Cao}	B	--	31.1 mV	--
	ΣQ_{EIS}	--	84.1 ± 12.2 C/cm^2	--

Table 2.5. Anodic charge consumed by commercially pure Mg as calculated by mass loss, hydrogen accumulation, and ICP-OES after exposure in 0.01, 0.6, and 5.0 M NaCl at open circuit for 24 hrs.

	99.9% Pure Mg		
	0.01 M NaCl	0.6 M NaCl	5 M NaCl
Δm	1.1 ± 0.3 mg	6.7 ± 1.0 mg	14.0 ± 2.4 mg
$\Sigma Q_{\Delta m}$	12.67 ± 5.5 C/cm^2	104.9 ± 20.6 C/cm^2	221.1 ± 39.8 C/cm^2
ΔV_{H2}	1.25 ± 0.6 cm^3	5.71 ± 1.4 cm^3	17.0 ± 2.5 cm^3
ΣQ_{H2}	21.42 ± 9.7 C/cm^2	97.93 ± 23.6 C/cm^2	239.9 ± 42.3 C/cm^2
ΣQ_{ICP}	20.8 ± 10.0 C/cm^2	71.55 ± 14.3 C/cm^2	214.9 ± 50.0 C/cm^2

Table 2.6. Typical fitting results of electrochemical impedance measurements made on AZ31B, in 0.1, 1.0, and 5.0 M NaCl solution at open circuit after 3, 12, and 24 hrs of immersion as per the equivalent circuits seen in Figure 2.1. All runs were performed with a vertical flat cell with a 1 cm^2 sample window.

	0.01 M NaCl			0.6 M NaCl			5 M NaCl		
	3 hrs	12 hrs	24 hrs	3 hrs	12 hrs	24 hrs	3 hrs	12 hrs	24 hrs
R_s (Ω)	923	694	890	31.9	31.4	31.3	5.2	10.6	3.8
C_1 (μF)	1.59	7.54	1.50	19.0	21.1	23.7	9.1	9.82	8.2
R_1 (Ω)	4430	1605	5267	693	443	607	84.7	29.4	31.6
C_2 (μF)	202	184	109	40.3	69.7	48.0	11.1	11.3	22.2
R_2 (Ω)	2715	574	675	310	184	301	2500	382	567
L (L)	3.0×10^3	1.00×10^8	1.36×10^4	310	227	301	200	200	200
R_3 (Ω)	5000	6000	5000	1160	687	1150	400	400	500
R_p (Ω)	2940	1590	2710	471	174	324	215	121	159
C_4 (μF)	--	--	--	--	--	--	1.70	2.20	2.80
R_4 (Ω)	--	--	--	--	--	--	20	40	3.8

Table 2.7. Anodic charge consumed on AZ31B as calculated by integration of i_{corr} derived from EIS-estimated polarization resistance for three different Tafel approximations after exposure in 0.01, 0.6, and 5.0 M NaCl at open circuit for 24 hrs.

		Tafel Assumptions		
		0.01 M NaCl	0.6 M NaCl	5 M NaCl
B_{king}	β_c	315 mV/dec	315 mV/dec	315 mV/dec
	β_a	150 mV/dec	112.5 mV/dec	300. mV/dec
	B	44.2 mV	36.0 mV	11.9 mV
	ΣQ_{EIS}	7.99 ± 0.5 C/cm^2	15.9 ± 5.3 C/cm^2	40.1 ± 11.3 C/cm^2
B_{Shi}	β_c	--	160 mV/dec	--
	β_a	--	180 mV/dec	--
	B	--	36.8 mV	--
	ΣQ_{EIS}	--	13.1 ± 4.5 C/cm^2	--
B_{Cao}	B	--	31.1 mV	--
	ΣQ_{EIS}	--	11.1 ± 3.2 C/cm^2	--

Table 2.8. Anodic charge consumed by AZ31B as calculated by mass loss, hydrogen accumulation, and ICP-OES after exposure in 0.01, 0.6, and 5.0 M NaCl at open circuit for 24 hrs.

	Tafel Assumptions		
	0.01 M NaCl	0.6 M NaCl	5 M NaCl
Δm	0.4 ± 0.4 mg	1.1 ± 0.4 mg	3.3 ± 0.4 mg
$\Sigma Q_{\Delta m}$	10.6 ± 6.4 C/cm^2	16.9 ± 5.7 C/cm^2	52.2 ± 6.7 C/cm^2
ΔV_{H2}	0.7 ± 0.3 cm^3	1.0 ± 0.3 cm^3	3.1 ± 0.4 cm^3
ΣQ_{H2}	13.32 ± 4.9 C/cm^2	16.6 ± 4.6 C/cm^2	54.1 ± 6.1 C/cm^2
Q_{ICP}	10.2 ± 5.1 C/cm^2	21.2 ± 8.0 C/cm^2	51.7 ± 10.0 C/cm^2

Table 2.9. Summary of corrosion rates for commercially pure Mg and AZ31 as well as experimentally determined corrosion rates.

Alloy, condition	Composition (wt.%)	[Cl⁻]	Method	Corrosion rate (mm y^{-1})	Ref
CP Mg	0.01Al, 0.01Mn, 0.01 Zn, 0.021Si, 0.005Cu, 0.001 Ni, 0.006 Fe	0.01 M	Mass loss	18.9	This study
CP Mg	0.01Al, 0.01Mn, 0.01 Zn, 0.021Si, 0.005Cu, 0.001 Ni, 0.006 Fe	0.01 M	H$_2$ evolution	24.2	This study
AZ31B-H24	3.02Al, 0.33Mn, 0.99 Zn, 0.025Si, 0.005Cu, 0.002 Ni, 0.005 Fe	0.01 M	Mass loss	6.9	This study
AZ31B-H24	3.02Al, 0.33Mn, 0.99 Zn, 0.025Si, 0.005Cu, 0.002 Ni, 0.005 Fe	0.01 M	H$_2$ evolution	13.6	This study
HP Mg, 5 h at 420 °C	0.0040Fe	0.1 M	Mass loss	6.0	[13]
AZ31B, GS = 11 μm	3.19Al, 1.05Zn, 0.39Mn, 0.003Fe, 0.01Cu	0.1 M	Mass loss	0.63	[90]
AZ31B, GS = 2.3 μm	3.19Al, 1.05Zn, 0.39Mn, 0.003Fe, 0.01Cu	0.1 M	Mass loss	0.63	[90]
AZ31B, GS = 1.4 μm	3.19Al, 1.05Zn, 0.39Mn, 0.003Fe, 0.01Cu	0.1 M	Mass loss	0.56	[90]
HP Mg	0.006 Fe	0.5 M	H$_2$ evolution	36.5	[91]
Cast HP Mg	0.0045Fe, 0.0008Mn	0.5 M	H$_2$ evolution	0.9	[92]
Cast HP Mg	0.0045Fe, 0.0008Mn	0.5 M	H$_2$ evolution	1.8	[92]
HP Mg, 1 d 550 °C	0.0045Fe, 0.0008Mn	0.5 M	H$_2$ evolution	8.2	[92]
HP Mg, 2 d 550 °C	0.0045Fe, 0.0008Mn	0.5 M	H$_2$ evolution	10.0	[92]
AZ31	2.69Al, 0.83Zn, 0.0021Fe, 0.62Mn	0.5 M	H$_2$ evolution	2.3	[93]
CP Mg	0.007Al, 0.0045Fe, 0.008Mn	0.5 M	H$_2$ evolution	2.7	[93]
Cast HP Mg	0.1Al, 0.002Fe, 0.017Mn, 0.003Zn, 0.01Si	0.6 M	Mass loss	0.38 ± 0.24	[94]
Cast HP Mg	0.100Al, 0.0020Fe, 0.017Mn, 0.003Zn	0.6 M	Mass loss	0.67 ± 0.02	[43]
Cast HP Mg	0.008Al, 0.0032Fe, 0.034Mn, 0.006Zn	0.6 M	Mass loss	8.10 ± 5.00	[43]
CP Mg	0.00016Fe, 0.00013Mn	0.6 M	Mass loss	0.25 ± 0.07	[44]
CP Mg	--	0.6 M	Mass loss	15 ± 0.1	[95]
CP Mg	0.004Fe, 0.03Mn	0.6 M	EIS	91.0	[65]
CP Mg	0.006Al, 0.014Zn, 0.03Mn, 0.004Fe	0.6 M	Mass loss	624.0	[96]
CP Mg	--	0.6 M	Mass loss	18.0	[97]
AZ31	3.1Al, 0.73Zn, 0.25Mn, 0.005Fe	0.6 M	Mass loss	11.6	[96]
AZ31B	2.95Al, 1.07Zn, 0.38Mn, 0.0035Fe	0.6 M	Mass loss	216	[98]
AZ31B, 3 h at 300 °C	2.95Al, 1.07Zn, 0.38Mn, 0.0035Fe	0.6 M	Mass loss	181	[98]
CP Mg	0.01Al, 0.01Mn, 0.01 Zn, 0.021Si, 0.005Cu, 0.001 Ni, 0.006 Fe	0.6 M	Mass loss	115.45	This study
CP Mg	0.01Al, 0.01Mn, 0.01 Zn, 0.021Si, 0.005Cu, 0.001 Ni, 0.006 Fe	0.6 M	H$_2$ evolution	110.56	This study
AZ31B-H24	3.02Al, 0.33Mn, 0.99 Zn, 0.025Si, 0.005Cu, 0.002 Ni, 0.005 Fe	0.6 M	Mass loss	18.95	This study
AZ31B-H24	3.02Al, 0.33Mn, 0.99 Zn, 0.025Si, 0.005Cu, 0.002 Ni, 0.005 Fe	0.6 M	H$_2$ evolution	19.35	This study
AZ31B	--	0.9 M	H$_2$ evolution	5.6	[99]
AZ31B	--	0.9 M	H$_2$ evolution	3.6	[99]
AZ31B	--	0.9 M	H$_2$ evolution	3.4	[99]
Cast HP Mg	0.0017Fe, 0.0012Mn	1.0 M	Mass loss	1.1	[100]
Cast LP Mg	0.0240Fe, 0.0010Mn	1.0 M	Mass loss	50.0	[100,101]

Cast HP Mg	0.0045Fe, 0.0086Mn	1.0 M	Mass loss	0.92	[102]
CP Mg	0.01Al, 0.01Mn, 0.01 Zn, 0.021Si, 0.005Cu, 0.001 Ni, 0.006 Fe	5.0 M	Mass loss	241.24	This study
CP Mg	0.01Al, 0.01Mn, 0.01 Zn, 0.021Si, 0.005Cu, 0.001 Ni, 0.006 Fe	5.0 M	H_2 evolution	329.18	This study
AZ31B-H24	3.02Al, 0.33Mn, 0.99 Zn, 0.025Si, 0.005Cu, 0.002 Ni, 0.005 Fe	5.0 M	Mass loss	56.86	This study
AZ31B-H24	3.02Al, 0.33Mn, 0.99 Zn, 0.025Si, 0.005Cu, 0.002 Ni, 0.005 Fe	5.0 M	H_2 evolution	60.02	This study

Table 2.10. Electrolytes which have resulted in a reported inductive loop in EIS data for commercially pure Mg and Mg-Al alloys.

Alloy	Solution	Anodic, OCP, Cathodic	Minimum Frequency	Inductance Loop at Low Frequency	Ref
CP Mg	1 M Na_2SO_4	Anodic	10 mHz	Yes	[38]
CP Mg	1 M Na_2SO_4	OCP	10 mHz	Yes	[38]
CP Mg	0.5 M Na_2SO_4	Cathodic	10 mHz	No	[38]
CP Mg g	0.5 M Na_2SO_4	Anodic	15 mHz	Yes	[82]
CP Mg	0.5 M Na_2SO_4	Cathodic	15 mHz	No	[82]
AZ91	0.1 M Na_2SO_4	OCP	35 mHz	Yes	[87]
AZ91	1 mM Na_2SO_4	OCP	10 mHz	Yes	[88]
CP Mg	1 M Na_2SO_4	OCP	5 mHz	Yes	This study
AZ31B	1 M Na_2SO_4	OCP	5 mHz	Yes	This study
CP Mg	ASTM G97[3]	OCP	10 mHz	Yes	[83]
CP Mg	Molten $MgCl_2$ and NaCl	OCP	1 mHz	Yes	[84]
CP Mg	1 M $MgCl_2$	OCP	5 mHz	Yes	This study
AZ31B	1 M $MgCl_2$	OCP	5 mHz	Yes	This study
CP Mg	0.6 M NaCl and saturated $Mg(OH)_2$	OCP	10 mHz	Yes	[44]
CP Mg	0.6 M NaCl and saturated $Mg(OH)_2$	OCP	10 mHz	Yes	[44]
CP Mg	0.6 M NaCl and saturated $Mg(OH)_2$	OCP	10 mHz	Yes	[39]
CP Mg	Saturated $Mg(OH)_2$	OCP	5 mHz	Yes	This study
AZ31B	Saturated $Mg(OH)_2$	OCP	5 mHz	Yes	This study
CP Mg	1 M $MgSO_4$	OCP	5 mHz	Yes	This study
AZ31 B	1 M $MgSO_4$	OCP	5 mHz	Yes	This study
CP Mg	0.6 M TRIS	OCP	5 mHz	No	This study
AZ31B	0.6 M TRIS	OCP	5 mHz	No	This study
CP Mg	Ethylene glycol	OCP	1 mHz	No	[89]

---

[3] *ASTM G97 solution is prepped as follows: 5 g of reagent grade $CaSO_4 \cdot 5H_2O$, 0.1 g of reagent grade $Mg(OH)_2$ to 1000 mL or reagent grade water103.   ASTMG97, "Standard Test Method for Laboratory Evaluation of Magnesium Sacrifical Anode Test Specimens for Underground Applications," ASM International (2013).*
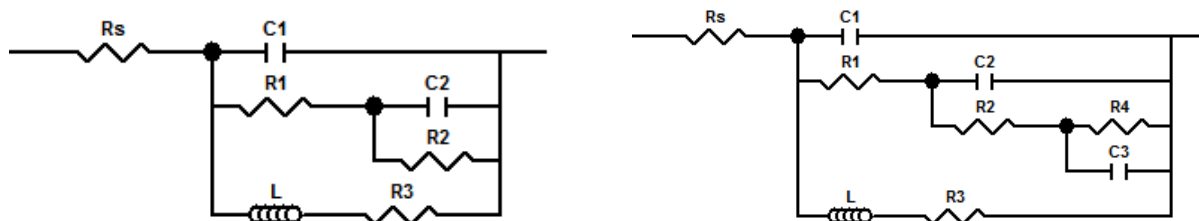
Figure 2.1. Equivalent circuit diagram used to model pseudo-inductive electrochemical impedance response on corroding Mg in (a) 0.01 and 0.6 M NaCl solution and (b) 5.0 M NaCl
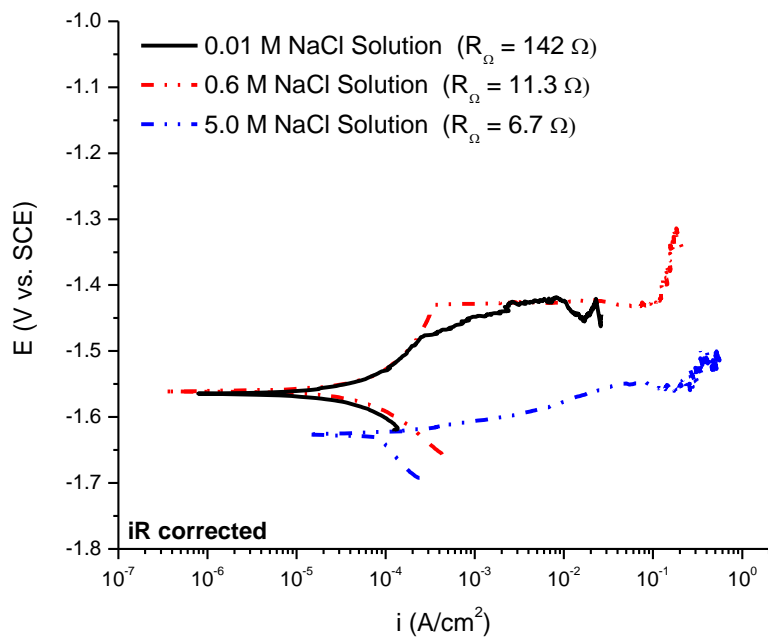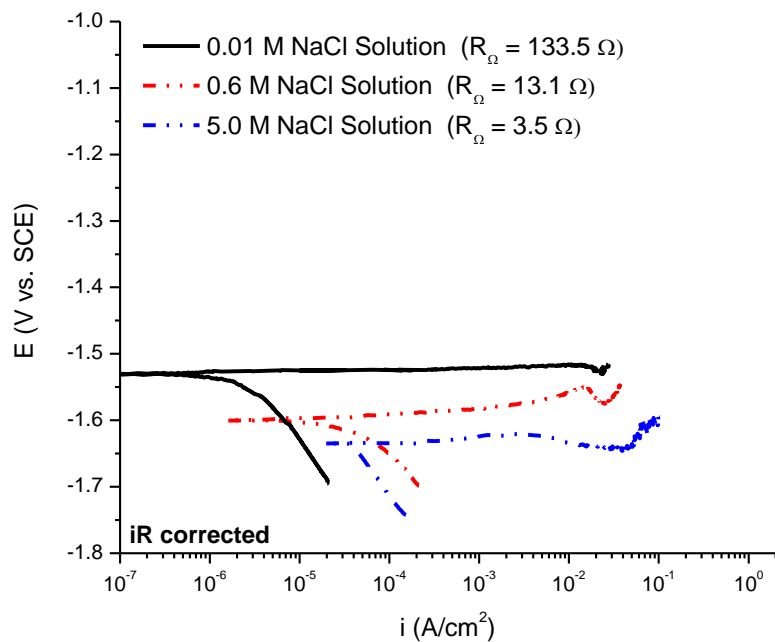
Figure 2.2. iR corrected E vs. log(i) polarization behavior of commercially pure Mg (top) and AZ31B (bottom) in 0.01, 0.6 and 5.0 M NaCl.
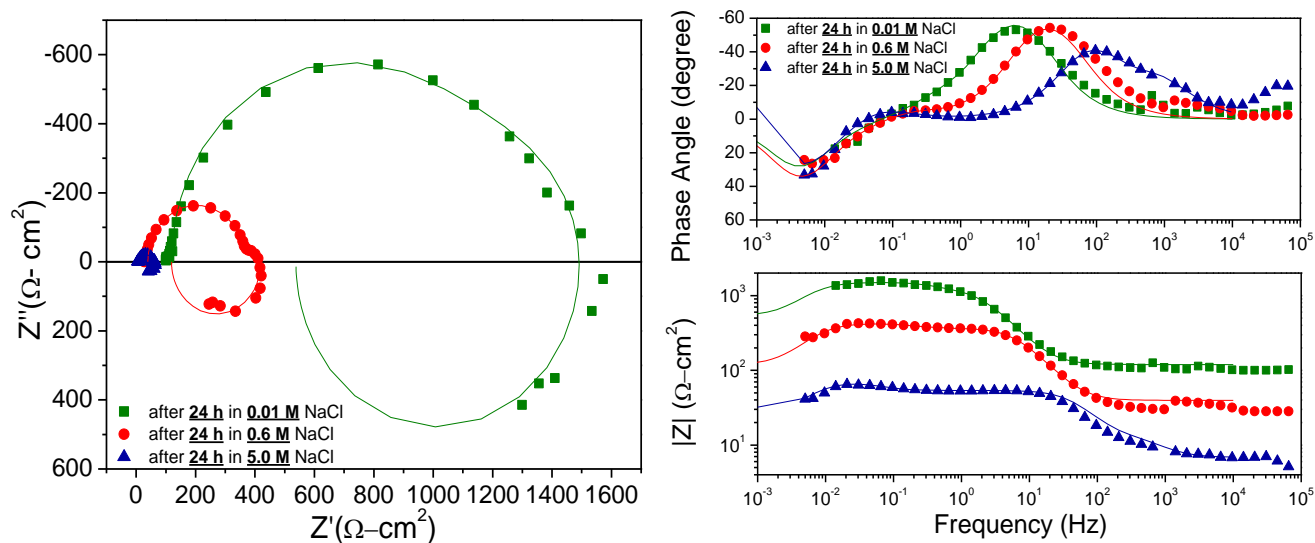
Figure 2.3. (left) Nyquist plots and (right) Bode magnitude and phase plots for commercially pure Mg. Data shown along with respective fits following 24 hrs in 0.01, 0.6, and 5.0 M NaCl at open circuit.
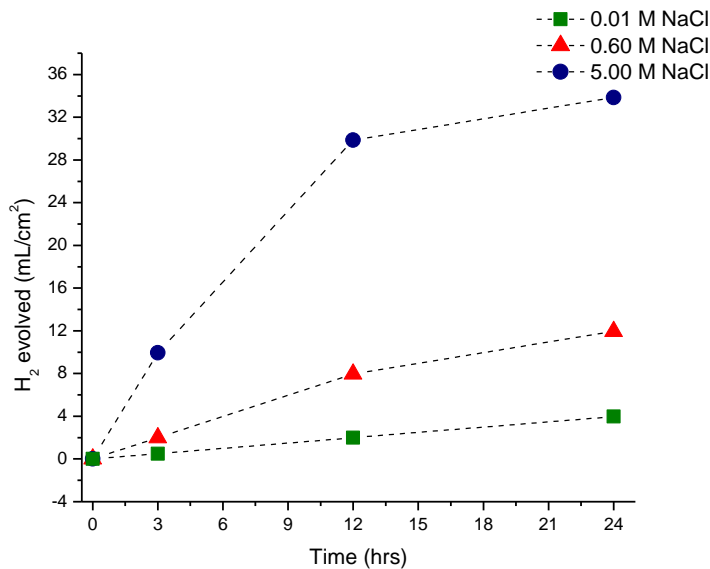
Figure 2.4. A typical dataset showing the H_2 evolved upon commercially pure Mg at 0,3,12, and 24 hrs in 0.01, 0.6,and 5.0 M NaCl at open circuit.
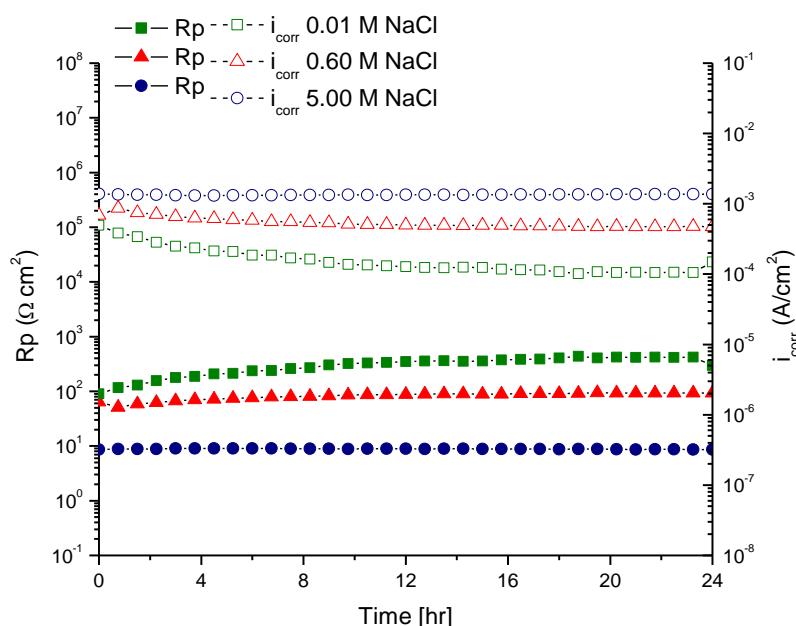
Figure 2.5. Typical EIS-estimated polarization resistance and corresponding corrosion current density vs. time of exposure in 0.01 M NaCl, 0.6 M NaCl and 5.0 M NaCl on commercially pure Mg.
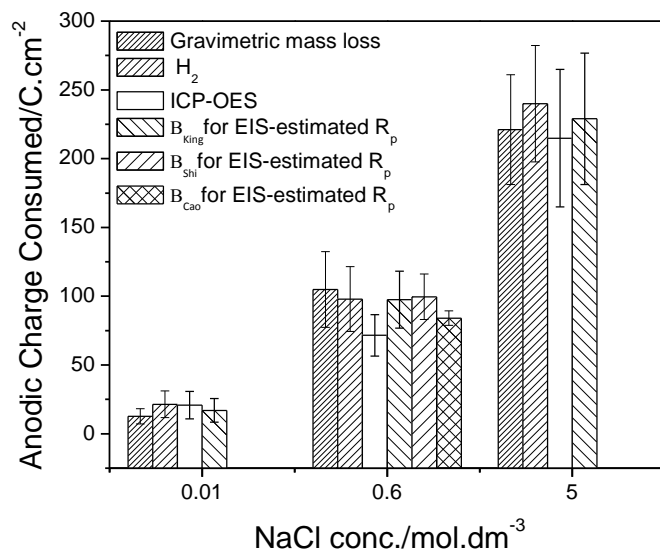
Figure 2.6. Anodic charge consumed by commercially pure Mg in 0.01, 0.6, and 5.0 M NaCl at open circuit after 24 hrs immersion as estimated by gravimetric mass loss, H_2 collection, ICP-OES, and EIS-estimated R_P where B_{King}=44.2 mV in 0.01 M NaCl, B_{King}=36.0 mV in 0.6 M NaCl is used, B_{King}=11.9 mV in 5.0 M NaCl [29], B_{Shi}=36.8 mV is used [39], and B_{Cao}=31.1 mV is used[44].
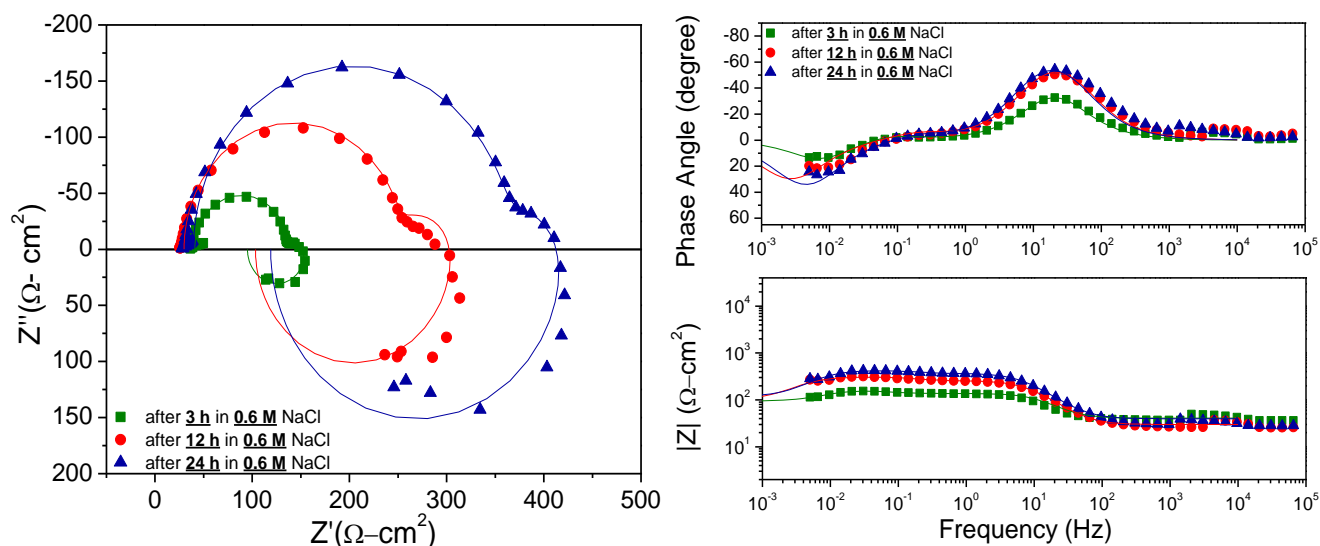
Figure 2.7. EIS measurements (a, b, c) and regression fits (d, e, f) of commercially pure Mg, after 3, 12, and 24 hrs of immersion at open circuit in 0.6 M NaCl.
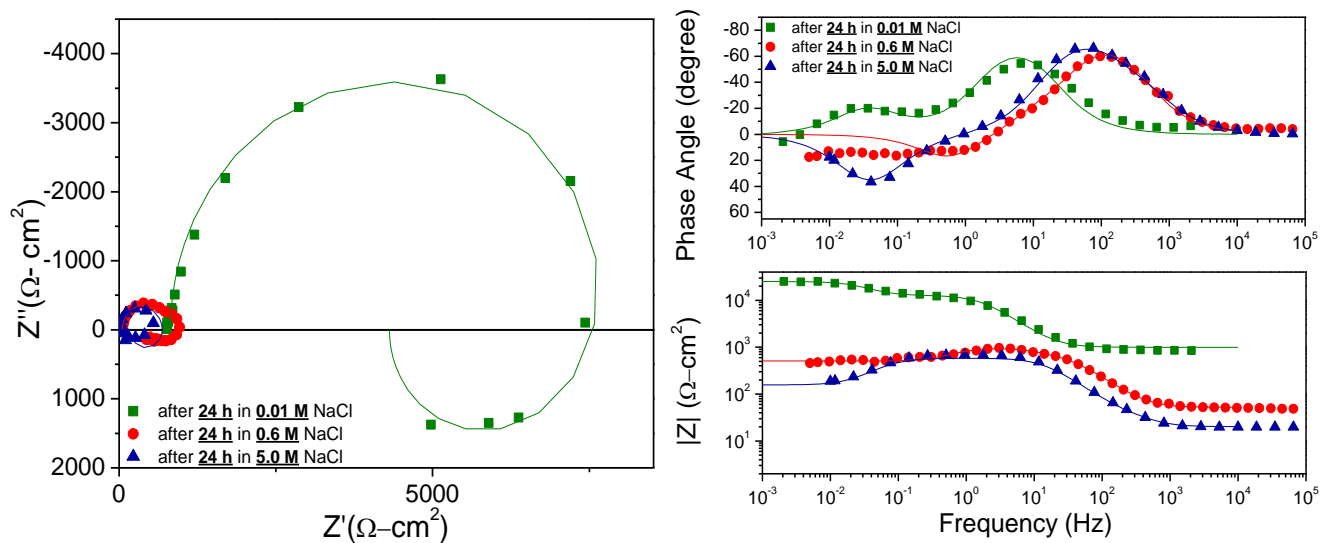
Figure 2.8. (left) Nyquist plots and (right) Bode magnitude and phase plot for AZ31B. Data shown along with respective fits following 24 hrs in 0.01, 0.6, and 5.0 M NaCl at open circuit.
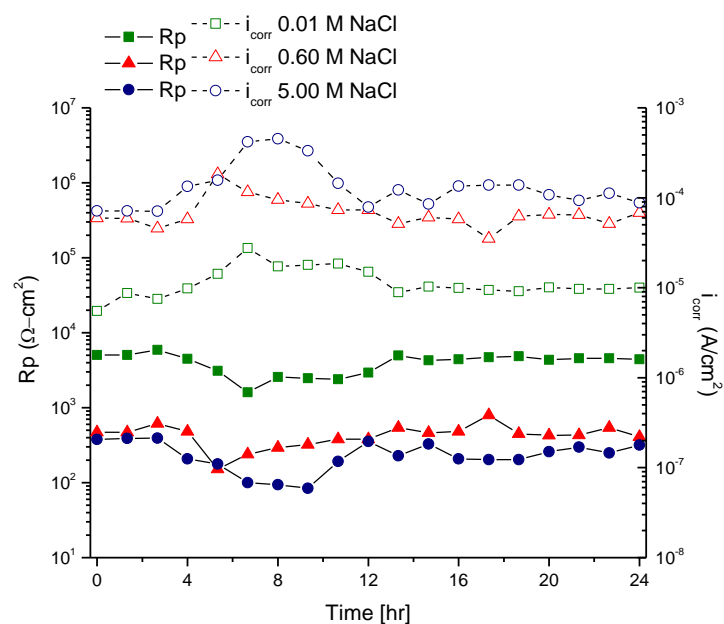
Figure 2.9. Typical EIS-estimated polarization resistance and corresponding corrosion current density vs. time of exposure in 0.01 M NaCl, 0.6 M NaCl, and 5.0 M NaCl on AZ31B.
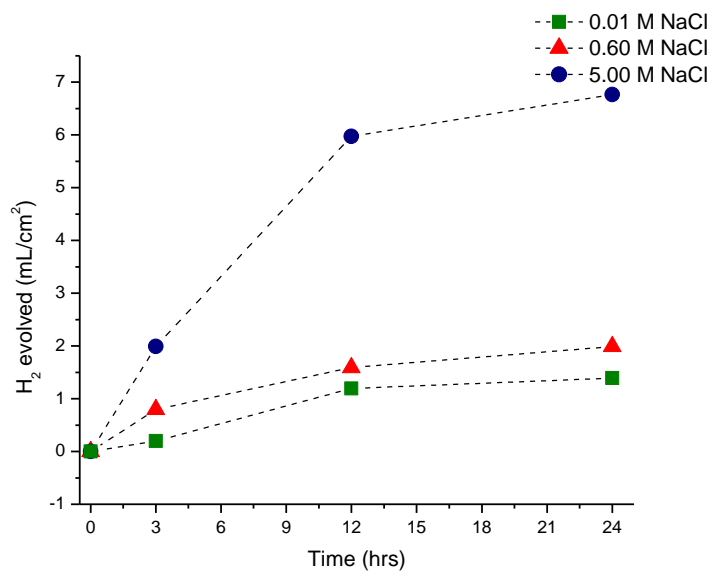
Figure 2.10. A typical dataset showing the H_2 evolved upon AZ31B at 0,3,12, and 24 hrs in 0.01, 0.6,and 5.0 M NaCl at open circuit.
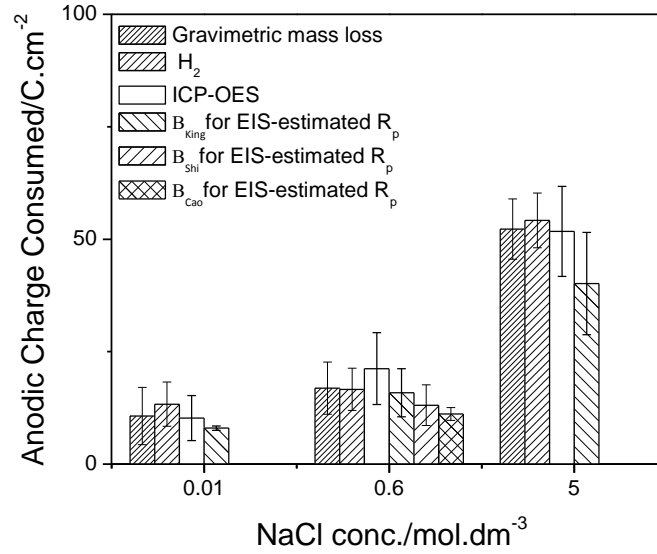
Figure 2.11. Anodic charge consumed by AZ31B in 0.01, 0.6, and 5.0 M NaCl at open circuit after 24 hrs immersion as estimated by gravimetric mass loss, H_2 collection, ICP-OES, and EIS-estimated R_P where B_{King}=44.2 mV in 0.01 M NaCl, B_{King}=36.0 mV in 0.6 M NaCl is used, B_{King}=11.9 mV in 5.0 M NaCl [29], B_{Shi}=36.8 mV is used [39], and B_{Cao}=31.1 mV is used[44].
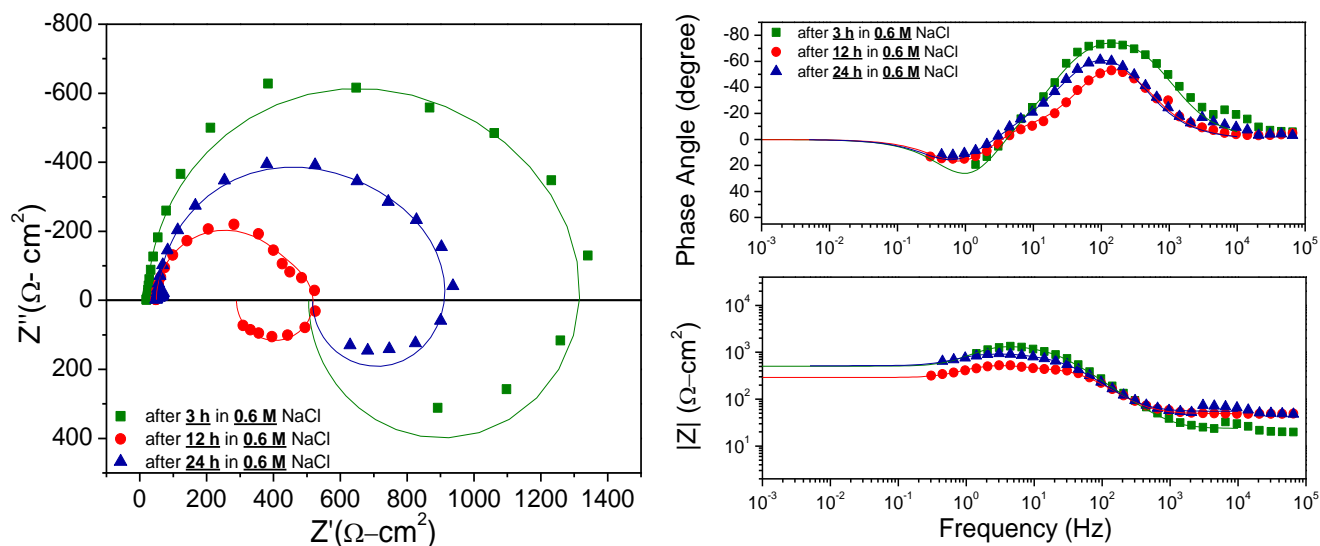
Figure 2.12. (left) Nyquist plots and (right) Bode magnitude and phase plot for AZ31B after 3, 12, and 24 hrs of immersion at open circuit in 0.6 M NaCl.
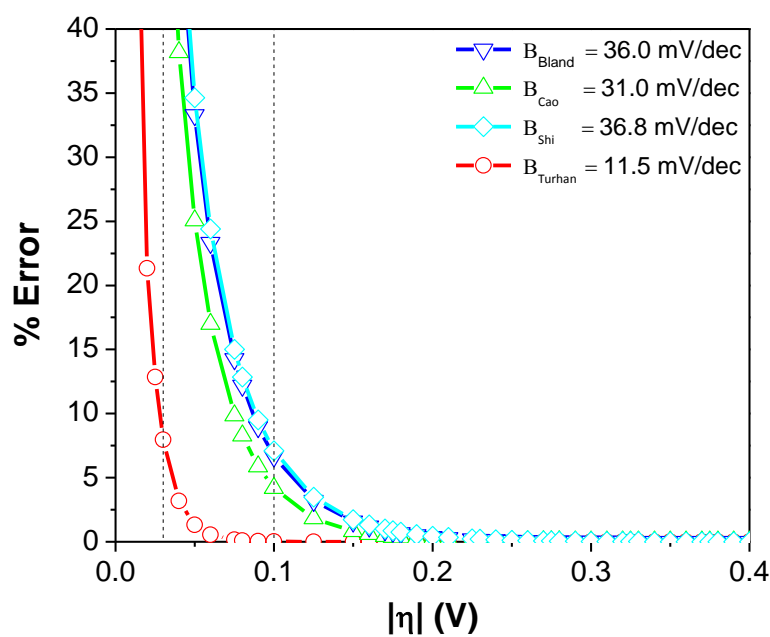
Figure 2.13. Percent error between the measured current density and the actual anodic or cathodic current density as a function of overpotential for different Tafel Law assumptions compared to a simple charge transfer controlled description of anodic and cathodic kinetics. In this plot of Tafel assumptions in 0.6 M NaCl, $B_{Bland\ 0.6M}$ = 36.0 mV for 1 M NaCl, B_{Shi} = 36.8 mV, B_{Cao} = 31.0 mV, and B_{Turhan} = 11.5 mV where B is given in the text. Note that this is not the error in $\partial E/\partial log i$ used to obtain Tafel slope which is likely much greater.

3 Metallurgical and Electrochemical Characterization of the Corrosion of AZ31B-H24 Tungsten Inert Gas Weld: Isolated Weld Zones

The corrosion behavior of a magnesium (Mg) alloy, AZ31B-H24 joined by tungsten inert gas (TIG) welding was investigated. The corrosion rates and morphology were characterized for each weld zone in isolation and the microstructural and compositional factors which control corrosion were identified. Initially, the corrosion resistance of various isolated weld regions were determined utilizing electrochemical impedance spectroscopy (EIS). Major microstructural changes included grain growth and crystallographic orientation within the weld regions. In addition, solute solidification microstructures, composition in the α-Mg phase and the area fraction of secondary phases changed significantly due to the formation of Al and Zn solidification structures within the weld fusion zone. Variations in corrosion rate by weld zone were rationalized in the context of microstructure attributes and anodically induced cathodic activation. The polarization resistance, R_P, over time, was evaluated by electrical impedance spectroscopy (EIS), at the low frequency limit, incorporating full consideration of the pseudo-inductive impedance behavior of Mg. Integrated, EIS based corrosion rates showed a strong correlation to cumulative mass loss, Inductively Coupled Plasma Optical Emission Spectrometry (ICP-OES) solution analysis for Mg^{2+} concentration and hydrogen gas were collected for each isolated weld zone. The wrought base plate exhibited a greater corrosion rate than the isolated weld zones. However, the fusion zone possessed the fastest corrosion rate of the designated weld zones and the distinct heat affected zones had the slowest corrosion rates. The metallurgical factors accounting for these distinct corrosion rates are discussed herein.

A manuscript based on this chapter has been published in Corrosion Journal as a Full Research Paper, "Metallurgical and Electrochemical Characterization of the Corrosion of AZ31B-H24 Tungsten Inert Gas Weld: Isolated Weld Zones."

Respective author contributions:
L. G. Bland: Manuscript co-author, experiments, metallurgical and electrochemical characterization
J. M. Fitz-Gerald: metallurgical characterization interpretation, analysis
J.R. Scully: Adviser, analysis and interpretation

3.1 <u>Introduction</u>

The corrosion of magnesium (Mg) alloy welds is of great interest.[1] During processing, a multitude of different microstructures are created across Mg welds which are dependent on (1) composition, (2) weld speed, (3) weld energies and (4) inert environment.[2,3] The starting composition of the material relative to phase equilibrium as well as the interaction between the cooling rate and phase transformation behavior control the resulting weld microstructure.[4-8] The weld can be separated into two encompassing zones: the fusion zone (FZ) and the heat affected zones (HAZs) as labeled on the schematic shown in Figure 3. 1. Both composition and metallurgy impact microstructure and subsequent corrosion. Depending on the metallurgical factors, the liquated base metal, which forms the FZ, undergoes solidification in a non-equilibrium regime. Within this regime, the weld microstructure at the interface may form by planar, cellular, or dendritic growth[9] where both the temperature gradient and growth rate are important for determining the final microstructure.[10] These aspects are discussed herein.

3.1.1 Composition and Metallurgy of Mg-Al-Zn Alloy AZ31B on Weld Microstructure

The resulting mechanical and corrosion properties of a Mg weld are dependent on the chemical composition of the starting material as well as the final microstructure after processing.[11-14] For Mg, the applicability of an alloy to welded structures can be dependent on specific alloying elements in the starting material. AZ31B (3 wt. % aluminum (Al), 1 wt. % zinc (Zn) and 0.33 wt. % manganese (Mn)) contains Al, which has been shown to improve the weldability of Mg when added, up to 10 wt %, and refines the grain size, while Zn is added (around 1 wt. %) to decrease hot shortness (the tendency of an alloy to separate along grain boundaries when stressed or deformed near their melting point) and decrease the susceptibility to weld cracking.[12] These alloying elements also impact the corrosion resistance of AZ31B. The addition of Al up to 4 wt. % increases the corrosion resistance[15-19] while Zn when above a few wt. % reduces the corrosion resistance.[20-22] The addition of Mn in isolation has little effect on the corrosion rate up to concentrations of 5 wt. % but does increase the corrosion resistance by sequestering detrimental impurity Fe into an Al-Mn-Fe intermetallic particle (IMP).[20] The compositions of these IMPs will affect the extent of attack in the material. For instance, the cathodic activity of Al_8Mn_5 is much greater than either $Mg_{12}Al_{17}$ or Al_3Mg_2.[23-25]

3.1.2 Welding Metallurgy and Resultant Microstructures in Mg Alloys

During tungsten inert gas (TIG) welding, the FZ is completely melted and resolidified[3]. This zone contains fine equiaxed grains with intergranular precipitates[26] which form due to the rapid solidification within the weld zone.[27] Additionally, the texture in the FZ is significantly different than the texture in either the HAZ or the base material, both of which retain the typical basal texture seen in AZ31.[7] As the material cools, the solute elements are more soluble in the liquid state than in the solid state; therefore, regions that solidify last will be enriched in solute. Along with this redistribution of solute to solidification boundaries, evaporation of the Mg can occur due to its low boiling temperature (1090°C).[3] Additionally, intermetallic particles (IMP) [28-31] form during heating which have their own electrochemical potentials and function as active cathodes during corrosion.[29]

Depending on the material system and processing parameters, a number of HAZs are identified in a typical weld[32,33] exhibiting a variation in grain growth, a reduced hardness and a local variation in chemistry.[7] Since one of the main strengthening mechanisms in AZ31B-H24 alloys is work hardening; processes such as cross-slip, dislocation climb and recrystallization contribute to softening and a decrease in the microhardness.[3,34,35] The high temperature gradients found in TIG welding, particularly radially from the arc, will lead to more of a planar grain structure.[5,36,37]

Significant changes in the weld microstructure and composition can lead to large variations in the intrinsic corrosion rate of the welds, particularly considering isolated weld zones.[10,22,23,12,24,33,45,46] Weld microstructures are evaluated and correlated to corrosion morphologies in different chloride environments.[11,13,16] In general, particularly for Al containing alloys, it is found that the corrosion rate in the full weld zone decreases after welding.[8,11,38] The corrosion was hypothesized to be controlled by differences in grain size and twinning after welding,[39] differences in the crystallographic orientation after processing,[7,40-42] solute segregation[7] and the presence of IMPs throughout the weld zone.[43]

The objectives of the work herein is to determine the corrosion rate of each of the selected weld zones in isolation with statistical certainty and to investigate which metallurgical factors may impact the corrosion rate of each zone. The need for this initial goal is justified by the historical uncertainty in accurate determination of corrosion rates in Mg alloys.[44-46] Moreover, the combined effect of these variables on the corrosion of Mg in electrical connection

or when galvanically coupled is of great importance and more pertinent to actual welds. Therefore, this will be discussed in detail in future work.

3.2 Experimental Procedures

3.2.1 Materials

The wrought AZ31B-H24 sheet was provided by Magnesium Elektron. All compositions reported in wt. %, with the actual compositions provided by QUANT (Quality Analysis and Testing Corporation) by Inductively Coupled Plasma optical Emission Spectroscopy (ICP-OES) analysis as given in Table 3. 1.

3.2.2 Metallurgical Characterization of Welds

All samples were fabricated by TIG welding a sandwich structure as shown in (Figure 3. 1). The top plate was drilled and countersunk 45° to approximately 0.635 cm in diameter and welded to the bottom plate along the periphery of the countersunk hole. The Miller Syncrowave 200 TIG welder was operated at 125 amps under argon gas at 48.3 kPa with a flow rate of 18.5 L/min, and air cooled. This process enabled the fabrication of large metallurgical weld zones for easy study in isolation. All samples were prepared on material freshly ground through 240 grit to remove any oxides formed before processing. Irradiated regions were investigated and compared to the baseline starting materials. All samples were examined in cross-section, polished through colloidal silica and etched with a Picric acid etch (3 g picric acid, 30 ml acetic acid, 100 ml ethanol and 15 ml distilled water) to determine the grain size and microstructure.

Wrought base plate and welds were analyzed with optical microscopy as well as scanning electron microscopy (SEM) using a FEI Quanta 650 microscope. Compositional analysis was performed using energy dispersive spectroscopy (EDS) methods.[47] Images were recorded at a working distance of 10 mm while operating at an accelerating voltage of 5 kV. Microhardness was determined using a Vickers microhardness tester.[48] Samples were indented for 15 seconds using a 0.01 kg weight. The grain size was determined using the linear intercept method at both 5x and 20x magnification.[49] The composition of the IMPs, solidification boundaries, FZ, HAZ and wrought material were determined using rigorous EDS compositional analysis with ZAF corrections on the Aztec[TM] software tool (where Z is the atomic number correction, A is the absorption correction and F is the fluorescence correction).[47] The distribution and area fraction of the Al-Mn-Fe IMPs as well as Al-Zn solidification structures were determined using the

ImageJ[TM] software package.[50] Additionally, the grain size was determined using the linear intercept method[49] for each zone. At least three measurements were analyzed for both grain size and composition and an average was reported.

3.2.3 Characterization of the Corrosion Behavior of Isolated Weld Zones

The corrosion behavior of isolated TIG weld zones was monitored with simultaneous measurement of electrochemical impedance spectroscopy (EIS) and hydrogen gas over a 24 hr immersion period in 0.6 M NaCl. The corrosion rate of the isolated weld zones was accomplished using electroplaters tape with a 1.23 mm^2 area hole to expose each zone along the *SL* surface. AZ31B-H24 grains were typically equiaxed and there was little dependence on plate orientation with corrosion rate. The corrosion rate was determined through the use of four parallel methods, gravimetric mass loss, H_2 collection, EIS-estimated polarization resistance, R_P, techniques (acquired at frequencies from 10 kHz to as low as 1 mHz) and ICP-OES[44,45] solution analysis. EIS scans were analyzed and fit using the software program ZView[51] to an equivalent circuit, seen in Figure 3. 2[44,45,52] and were fit to a low frequency limit of at least 1 mHz. The inclusion of the full inductive behavior enabled for a more accurate determination of the corrosion rate of Mg alloys by the inclusion of the full polarization resistance, R_p, at low frequencies.[44,45] All values reported here are averages of at least three runs and based on the values obtained from EIS analysis performed at the open circuit potential (OCP). Furthermore, to determine the corrosion rate with time, all samples were exposed for different immersion times to evaluate the effect of immersion time on the measured corrosion rate. Samples were immersed for 3, 24, or 48 hours at OCP in 0.6 M NaCl followed by a cathodic potentiodynamic polarization scan ranging from 0.5 mV above OCP to -2.3 V below OCP in a downward sweep at a rate of 1 mV/second. This range in immersion time allowed for analysis of the anodically induced cathodic activation with increased immersion time for each isolated weld zone as well as for the wrought base plate. All values reported here are averages of at least three runs and based on the values obtained from cathodic polarization scans.

The corrosion rate of a freely corroding metal was determined through an evaluation of R_P using the well-known Stern-Geary relationship:[53,54]

$$i_{corr} = \frac{B}{R_P} = \frac{\beta_a \beta_c}{2.303 R_P (\beta_a + \beta_c)}$$

Equation 3.1

where β_a and β_c are the anodic and cathodic Tafel slopes, respectively, and B = (1/2.303) × ($\beta_a.\beta_c/(\beta_a + \beta_c)$). It should be noted that this is a simplified expression that introduces some error due to the potential dependent film and coverage effects which can also alter the value of B, usually assumed in Equation 3.1. However, for the Stern-Geary equation, there is a stronger dependence of i_{corr} on the value of R_P than on B.[39] The anodic charge density can then be estimated by integrating the EIS-estimated corrosion rate over the time of exposure, with knowledge of appropriate Tafel slopes estimated from literature[45,55,56] via Equation 3.2.

$$Q_a^{EIS} = \int i_{corr(\theta)}dt = \int \frac{\beta_a\beta_c}{2.303R_P(t)(\beta_a + \beta_c)}dt \qquad \text{Equation 3.2}$$

The accurate determination of a long-term corrosion rate of Mg from electrochemical methods was strongly dependent on the analysis of R_p[44] and weakly dependent on B. Several values of B were considered reflecting the typical range shown in literature.[45,55,56]

The experimental setup consisted of a vertical flat cell with an inverted burette was placed above the sample window and upward facing weld zone in order to collect the H_2 gas evolved from the sample surface.[45] A Pt mesh was used as a counter electrode and a saturated calomel electrode (SCE) was used as the reference electrode. Prior to testing, the electrolyte was pre-saturated with H_2 to reduce error in measuring the volume of the H_2 generated on the sample surface since H_2 gas was extremely soluble in most aqueous environments.[57] Following testing, samples were cleaned with ASTM G1-03 standard chromic acid solution (200 g/L CrO_3) and dried in a dry box for a least 24 hrs.[58] The chromic acid cleaning solution was retained for ICP-OES solution analysis to account for any corrosion products re-dissolved from the oxide[59] and a 10 part dilution was performed to make sure that elements would not saturate the ICP-OES detector. Negligible additional mass loss resulted from this cleaning procedure.

All solutions were retained and analyzed using a Thermo Scientific[TM] iCAP 7200 Inductively Coupled Plasma Optical Emission Spectrometry (ICP-OES). Samples were prepared by mixing 5 M HCl into the solution after electrochemical testing. This acidified the solution and dissolved the salt and corrosion products in order to analyze all Mg electro-dissolved. All samples were sonicated before solution analysis to ensure that no corrosion product was left on the bottom of the container. Before analyzing, standards containing known amounts of Mg as well as each of the alloying elements were used to calibrate the instrument. The following wavelengths were used and recorded for the calculation of the charge consumed for solution

analysis: Mg (279.553 nm), Mg (280.270 nm), Al (226.910 nm), Al (308.215 nm), Al (396.152 nm), Fe (238.204 nm), Fe (239.562 nm), Mn (257.610 nm), Mn (259.373 nm), Zn (206.200 nm), and Zn (213.856 nm) following from previous work[60,61] where the detection limits for each of these elements in listed in Table 3. 2.

To compare the corrosion rate using the four parallel methods, Faraday's law was used to convert mass loss, H_2 gas evolved and solute dissolved into anodic charge consumed with time. This was compared with the R_p estimated corrosion rate calculated by the EIS equivalent circuit. In order to calculate the mass loss of Mg (Δm), as measured gravimetrically with ± 0.1 mg resolution, the consumed anodic charge density (Q_a) was calculated using Equation 3.3:

$$Q_a^{\Delta m} = \frac{znF}{A} = \frac{z\Delta mF}{A(E.W.)}$$

Equation 3.3

Where z was equivalent electrons per mole of Mg oxidized, +2, n was the number of moles of Mg, F was Faraday's constant and a was the molar mass of Mg and A was the area of the exposed electrode. The equivalent weight (E.W.) of AZ31, N_{eq}, was determined using the procedure recommended in ASTM G106.[62] The EW was determined as the weighted average of a/z for the major alloying elements in a given alloy.[63] This is given by the following expression:

$$N_{eq} = \sum \left(\frac{f_i}{a_i/z_i} \right) = \sum \left(\frac{f_i z_i}{a_i} \right)$$

Equation 3.4

Where f_i, a_i, and z_i are mass fraction, atomic weight and electrons exchanged, respectfully. The E.W. (grams/equivalent) was then the reciprocal of the total number of equivalents (E.W.= N_{eq}^{-1}). The EW for AZ31B was determined to be 12.13 g/eq and was determined assuming congruent oxidation of Mg^{2+}, Al^{3+}, Mn^{2+} and Zn^{2+} where z=2+, z=3+, z=2+ and z=2+, respectively where each element was detected by ICP-OES above the instrument detection limit (Table 3. 3). When the NaCl solution became alkaline (approximately pH 10-11), Al^{3+} dissolution may become thermodynamically favored.

Under freely corroding conditions, measured at open circuit, all of the H_2 gas evolved on the surface of the Mg electrode was assumed to be produced by a coupled cathodic reaction assumed to be generated on Mg. The volume of H_2 gas evolved can be converted to a corresponding cathodic charge (Q_c) via a combination of the Ideal Gas Law and Faraday's Law, which, during OCP corrosion, equals the anodic charge density (Q_a) per unit area of Mg corroding.[63] Thus:

73

$$Q_c^{H2} = Q_a^{H2} = \frac{znF}{A} = \frac{zPVF}{ART}$$

where P was the pressure inside the burette (assumed to be approximately 1 atm at sea level), V was the volume of H_2 gas collected, R was the ideal gas constant, T was the temperature and z as well as n are defined above.

The corrosion morphology was determined for each isolated weld zone to determine how the corrosion initiated and progressed over 24 hrs. Secondary Electron SEM micrographs were taken of each of the weld regions before immersion in 0.6 M NaCl and after immersion in 0.6 M NaCl for 3 hrs at OCP. All samples were cleaned with CrO_3 to remove any corrosion products and examine the corrosion morphology. Before the initial corrosion, the sample was marked using a Vickers hardness tester to enable examination of the corrosion morphology at each stage in precise locations.

The progression of the corrosion morphology was studied with time using a Dinolite optical microscope. The software package, ImageJ[TM], was used to calculate the area-fraction of the sample surface which was corroded with time.[50] At least three replicates were taken and analyzed. The average is reported herein.

3.3 <u>Results</u>

3.3.1 Wrought Metallurgical Characterization

The microstructure for the wrought plate AZ31B alloy is shown in Figure 3. 3. The grain size is approximately 6 ± 2.0 μm and the typical IMP particle size was 0.28 ± 0.18 μm. The material was heavily twined along with Al-Mn and Al-Mn-Fe IMPs distributed homogenously throughout the α-Mg matrix (Figure 3. 3 (a)). The composition of these IMPs was consistent (Figure 3. 4) with $(Fe,Mn)Al_6$ and Al_4Mn, two common IMPs cited for Al-Mn containing Mg alloys[43,64] (Table 3. 1). Electron Backscatter Diffraction (EBSD) showed that the AZ31B-H24 material possesses a predominant basal texture as was expected from literature (Figure 3. 3 (c-d)).[40]

3.3.2 Weld Metallurgical Characterization

The microstructure and crystallographic texture was investigated across the weld zone of the TIG weld (Figure 3. 5). Within the weld, a single FZ and two HAZs were identified. Each of

these zones has a difference texture, composition, boundary type, grain size and intermetallic particle characteristics.

EBSD revealed that the FZ had a randomized texture due to the melting and rapid solidification during processing (Figure 3. 5(a)). The FZ occurred directly at the center of the weld and showed a large amount of grain growth with grains approximately 28.4 ± 5.0 μm and microhardness was as low as 40HV (Figure 3. 6). The composition of the α-matrix in this weld zone is shown in Table 3. 1 where the matrix was depleted in Al and Zn. Instead, the Al and Zn were partitioned to the solidification structures which decorate the solidification boundaries formed during the melting and solidification of the weld under non-equilibrium processing (Figure 3. 7) along with a population of Al-Mn-Fe particles (Figure 3. 7 (c)) measuring 0.74 ±0.12 μm. The composition of these particles and solidification structures is shown in Table 3. 1. The variation of the distribution of Al-Mn-Fe particles and Al-Zn solidification structures with respect to the weld zones are shown in Figure 3. 8.

The HAZ1 and HAZ2 retain the basal texture as seen in the original, wrought plate material (Figure 3. 5(b-c)) and the compositions of these zones are approximately the same (Table 3. 1). Large grains are observed in the high temperature HAZ1 measuring approximately 19.3 ± 2.8 μm. In comparison, HAZ2 has the smallest grains of the weld regions (15.4 ± 1.4 μm) and exhibits little grain growth after recrystallization. The microhardness was determined to be approximately 50 HV and 55 HV for HAZ1 and HAZ2, respectively (Figure 3. 6). The solidification structures of the FZ are not observed in the HAZs which only partially melted during processing (Figure 3. 7). However, the Al-Mn-Fe particles were distributed throughout the HAZs (Figure 3. 7). These particles typically measure approximately 1.22 ±0.80 μm in HAZ1 and 1.52 ± 0.41 μm in HAZ2.

3.3.3 Resultant Corrosion Morphology of AZ31B-H24 TIG Weld

Compositional contrast shows Al-Mn-Fe IMPs and Al-Zn solidification structures in the FZ before corrosion (Figure 3. 8(a)) and a highly randomized texture (Figure 3. 9(b)). Corrosion initiation was seen to occur almost immediately after immersion at OCP. After a 3 hr immersion in 0.6 M NaCl, these solidification structures were no longer present and many of these IMPs were also altered by corrosion (Figure 3. 9(c)) with little variation in the corrosion with crystallographic orientation. High magnification SEM images recorded at the same location before and after corrosion illustrated the corrosion morphology in the FZ (Figure 3. 10). Figure

3. 10(a-b) (using the circled particle for reference) shows approximately the same location before and after corrosion. A schematic of this corrosion process was proposed in Figure 3. 10(c) where the solidification boundaries and IMPs have all been altered by the corrosion process, as well as the α-matrix, where a filiform morphology was observed.

Figure 3. 11 shows the before and after corrosion morphology of the HAZs. It was observed that the corrosion mechanisms in both of these zones are the same and only one example has been displayed for simplification. Figure 3. 11 (a) shows Al-Mn-Fe IMPs distributed along the *SL* plane. The EBSD of this zone, taken in the same location (Figure 3. 11 (b)) shows a mostly basal texture without any crystallographic orientation preference in the filiform morphology. Figure 3. 11 (c) reveals that filiform corrosion[65] propagates homogeneously along the weld surface along the *SL* surface in the *L* direction and there is no discernable preference for any crystallographic orientations. A higher magnification SEM image (Figure 3. 11(c)) shows that the grain boundaries in the zone have preferentially corroded, along with deeper filiform corrosion propagation in the α-Mg. Further, in Figure 3. 12(a-b) the resultant corrosion morphology of the HAZ is shown at a higher magnification where the same grain is identified in each image as reference as well as an Al-Mn-Fe particle[66] (circled in orange). This attack occurred along the particles in the α-Mg. A schematic of this corrosion process was proposed in Figure 3. 12(c). Corrosion propagation along the grain boundaries and at Al-Mn-Fe particles within the HAZ was observed.

3.3.4 Corrosion Electrochemistry of Isolated Weld Zones

Open Circuit Potential

The open circuit potential as a function of time and weld zone over a 24 hr immersion period was shown in Figure 3. 13. The OCP was determined for both the wrought base plate material and the isolated weld zones with time. When the sample was first immersed, the OCP of the wrought plate was -1.58 V_{SCE}. The FZ had the highest potential at -1.56 V_{SCE} while HAZ1 and HAZ2 had potentials of -1.57 V_{SCE} and -1.57 V_{SCE}, respectively. For each of these zones, the OCP increased slightly after 3 hrs to -1.57 V_{SCE} for the wrought plate material, -1.54 V_{SCE} for the FZ, -1.55 V_{SCE} for HAZ1 and -1.55 V_{SCE} for HAZ2. After 12 hrs and 24 hrs, the OCP decreased again to about the same OCP that was seen at 0 hrs. After 24 hrs, the OCP for the wrought plate material was -1.58 V_{SCE} while the isolated weld zones indicate potentials of -1.57 V_{SCE}, -1.56 V_{SCE}, and -1.56 V_{SCE} for the FZ, HAZ1 and HAZ2, respectively. The numbers for each of the

weld zones are similar, but it is shown that each of the weld zones are slightly ennobled over the wrought base plate.

Cathodic Activation in Isolated Weld Zones

It has been shown in literature, that as the material corrodes, the sample surface becomes dark[67] and this dark region typically contains enriched impurity or alloying elements[68] (such as Al and Zn)[66,69-71] as well as Al replating.[70] It has similarly been shown that the exchange current density for the HER, the dominant cathodic reaction on Mg, increases with time due to enhanced cathodic activity on the sample surface.[72-74] Figure 3. 14 shows the percent surface area for each isolated weld zone which has corroded with time. This surface area has been corrected for the percent of the whole weld which each isolated weld zone represents and has been determined at 3, 12 and 24 hrs of immersion using selected SEM images. It was shown that the wrought base plate has a larger amount of this corroded region formed than the TIG welded sample. It was observed that the FZ has the higher percent area corroded compared to the HAZs.

The OCP can similarly be plotted as a function of the isolated weld zone and time (Figure 3. 15 (a)). At 3 hrs, the highest OCP was observed for each weld zone (potentially due to the buildup and breakdown of the oxide film on the sample surface), as shown previously, with the FZ having the most noble OCP. After 24 hrs, the OCP is lower than that measured after 3 hrs and the HAZs became the most noble of the isolated weld zones. This was further expanded with a longer immersion of 48 hours. After 48 hrs, the OCP measures -1.57 V_{SCE} for the FZ, -1.57 V_{SCE} for HAZ1, -1.57 V_{SCE} for HAZ2 and -1.57 V_{SCE} for the wrought base plate.

The cathodic corrosion current density (i_c) at -1.8 V_{SCE} is shown as a function of time in each of the isolated weld zones after 3, 24 and 48 hrs in 0.6 M NaCl. The i_c increased with time for all weld regions (Figure 3. 15 (a)) and i_c increased the most for the wrought base plate and the least for the HAZ2 with time. The large increase in i_c for the base material is consistent with anodic induced cathodic activation. The increase in i_c with time was strong evidence for increased cathodic activity due to cathodic activation in the weld triggered by a high anodic reaction rate.

EIS of AZ31B-H24 TIG Weld as a Function of Time

Figure 3. 16 contains the Bode magnitude and Bode phase plots of each of the isolated weld zones, measured at open circuit and fit using the equivalent circuit model shown in Figure 3. 2. For each of the isolated weld zones, this equivalent circuit provided a reasonable fit over the

full frequency response. The highest R_p was found for all isolated zones after 3 hrs. This correlates with a lower corrosion rate at this immersion time. This trend can be rationalized as a tradeoff between the alkalization of the near surface electrolyte[45] and the early stages of the development and growth of anodes and enhanced cathodes on the sample surface leading to advanced cathodic activity during longer immersion times.

Figure 3. 17 shows the Nyquist plot for each of the isolated weld regions for comparison, taken after 24 hrs of immersion at OCP. From the EIS spectra for an AZ31B weld measured at OCP, two capacitive loops and an inductive loop are observed for each of the isolated weld zones. The base material has the smallest measured frequency dependent impedances and therefore the highest corrosion rate whereas the isolated weld regions were determined to have slower corrosion rates. The polarization resistance of AZ31B, and subsequently, the corrosion rate (i_{corr}) according to Equation 3.1, were calculated from the periodic measurement of EIS throughout exposure in quiescent 0.6 M NaCl (Figure 3. 18). The measured i_{corr} in 0.6 M NaCl generally remained the same during the full 24 hr immersion time. Over short immersion times the H_2 evolved increased sharply after about 3 hours and then, at longer immersion times the H_2 evolved began to stabilize Figure 3. 19. The estimation of corrosion rate determined from the H_2 evolved over 24 hrs was correlated with the difference in the measured low frequency |Z| seen in the EIS experiments to rank the weld zones as follows $i_{corr(HAZ2)} < i_{corr(HAZ1)} < i_{corr(FZ)} < i_{corr(base)}$ (Table 3. 3,Figure 3. 20).

Corroborating Mass Loss, H_2 Collection and ICP-OES of AZ31B-H24 TIG Weld

The quantification of Mg dissolved into solution following immersion was determined using ICP-OES. The wavelengths used herein were selected from those with high enough signal and significantly away from the wavelengths of typical alloying elements and impurities (such as Al, Zn, Mn and Fe). The alloying elements were thus included in the analysis and AZ31B was assumed to dissolve congruently. This assumption was corroborated by detecting cations of all alloying elements in solution above the baseline level; however, this was not the focus of this study in particular.

Using the Stern-Geary relationship as well as Faraday's law, the overall corrosion rate of the isolated weld zones was determined and compared. These were calculated and compared (Figure 3. 20, Table 3. 3) as a function of anodic charge consumed over time. This trend was shown in the calculation of the anodic charge over the 24 hr period. Charge was reported as derived from

mass loss, H_2 generation, EIS, and ICP-OES. From the four parallel methods, it was determined that the wrought base plate had the highest corrosion rate compared to the isolated weld zones. Three different Tafel assumptions were explored[55,44,45] and little variation was observed in the calculated corrosion rate. Within the isolated weld zones, the FZ had a slightly higher corrosion rate than either of the HAZs.

3.4 <u>Discussion</u>

3.4.1 Corrosion of AZ31B Weld Versus Wrought Plate

The corrosion rate of the AZ31B wrought plate material as well as the isolated weld zones were studied and compared. It was shown that, after welding, the corrosion rate for each of the isolated weld zones was lower than the wrought plate material. This agreed with the previous work which shows that wrought plate has a higher corrosion rate in the weld region.[8,75]

3.4.2 Corrosion Rates of Isolated Weld Regions

The corrosion rates for each zone, determined using four corroborating methods (EIS, gravimetric mass loss, H_2 evolution and ICP-OES solution analysis) (Figure 3. 20) were found to been in good agreement. There was also a distinct ranking within each of the weld zones after a 24 hr immersion time as follows $i_{corr(HAZ2)} < i_{corr(HAZ1)} < i_{corr(FZ)} < i_{corr(base)}$. The use of three different Tafel slope assumptions revealed little variation in the corrosion rate or ranking. The corrosion rate is non-uniform across the weld and this aspect is discussed below.

3.4.3 Resultant Corrosion Morphology in Isolated FZ, HAZ and Wrought Base Plate

In the FZ, the corrosion propagated along Al-Zn solidification boundaries within the weld and initiated at cathodic Al-Mn-Fe IMPs (Figure 3. 9-3. 10). The solidification boundaries were rich in Al and Zn and cathodic to the α-Mg matrix as both Al and Zn increase the cathodic reaction rate in Mg alloys.[76] This boundary acted as a local cathode and dissolution of the anodic Mg α-matrix (which has been depleted in Al and Zn (Table 3. 1) occurred along this solidification boundary as well as at Al-Mn-Fe IMPs contained in the FZ. The galvanic couple formed between the Mg matrix and the solidification structure caused the Mg directly adjacent to this solidification structure to corrode along with the α-matrix (Figure 3. 10(c)).

In the HAZs, filiform corrosion was seen which expands with time with initiation occurring almost immediately (Figures 3. 12-3. 13). The filiform corrosion is well reported in the AZ31 material[65,66,77] and other Mg alloys[15,71,78-80] and has been cited to be driven by the HER on

the cathodic sites (such as IMPs).[78] Prior to corrosion, it was observed that the Al-Mn-Fe particles were distributed throughout the material. The filiform growth did not appear to be isolated to one grain, but rather propagated through several grains. It also appeared that the filiform mechanism grew along the *SL* surface in the *L* direction of the material (Figure 3. 11). This corrosion propagated away from the IMPs and the grain boundaries. From Figure 3. 12, the filiform propagated until full grains were removed from the sample surface. The corrosion initiated either proximate to cathodic IMPs[64,66,81] or grain boundaries.

The difference in the corrosion mechanisms in the FZ versus the HAZs was postulated to be due to the difference in composition between the Al-Zn rich solidification structure of the FZ and the Al-Mn-Fe particles. It is speculated that the Al-Zn solidification structures largely controlled the corrosion mechanisms in the FZ while the Al-Mn-Fe IMPs in the HAZs had a larger impact on the corrosion of these isolated weld zones.[29,64] The Al-Mn-Fe particles act as active cathode sites in the α-Mg matrix.[64,66] Those particles which remain on the sample surface after CrO_3 cleaning are assumed to have been catholically active. Since Al was present in both the solidification structures and the IMPs, it can be assumed this contribution of the corrosion rate cannot be isolated by comparing these two metallurgical characteristics; however, the effect of Mn and Zn on the corrosion can be compared. It is well known that Mn is capable of incorporating sparingly soluble metals into an IMP[82] in this case for the Al-Mn-Fe particles. In recent work, it has been suggested that a higher population of Al-Mn precipitates are left behind an advancing anode and act as the source for cathodic activity on an AZ31 surface[70,73] Examining the impact from Zn on the corrosion rate, Zn containing phases acted as local cathodes in Mg and have been reported to increase the corrosion rates above 1 wt%.[16,83] Also, Zn-containing IMPs are reported to promote increased cathodic reactions.[16,22,76,83] From this, it can be assumed that both the Al-Mn-Fe IMPs and the Zn rich solidification structures in the FZ function as local cathodes and promote corrosion.

3.4.4 Corroborating Microstructural Features with Corrosion Results

It was seen that, in each of the weld regions, there were variations in the grain size, crystallographic orientation, composition, solute segregation to solidification boundaries and secondary phases. Each of these metallurgical features had an impact on the intrinsic corrosion resistance of the weld, both in the isolated weld zones, and as a composite material.

Effect of Grain Size on the Corrosion Rate of AZ31B-H24 TIG Weld

A large variation in the grain size was determined across the weld (Figure 3. 6) and grain size has been shown to have an impact on the corrosion rate in several studies. Within the weld, processing causes the grain size to vary from 5 μm to 30 μm. In low [Cl⁻] environments, the corrosion rate decreases as the grain size decreases.[84,85] However, in more aggressive environments, such as 0.6 M NaCl, the opposite trend was seen.[86,87] Also, there has been little experimental evidence to explain why these trends are seen. From this work, it was shown that the FZ has large directionally solidified grains with solidification boundaries and the highest corrosion rate. Similarly, it was shown that the HAZs, which have a larger grain size than the wrought base plate have a lower corrosion rate. Trends in corrosion rate versus grain size were not enough to explain corrosion rate as a function of weld zone. In the literature, as the grain size increases, the material was slightly ennobled and the corrosion rate decreased with increasing grain size in 0.6 M NaCl.[88] Considering the grain size of the wrought base plate versus the HAZs, it can be seen that the corrosion rates observed herein follow this grain size trend; however, this trend was not applicable to the FZ. Metallurgical aspects, such as the solute segregation in the FZ and IMP size and spacing would have a much larger impact on the corrosion rate of Mg-Al alloy AZ31 and more work needs to be done to characterize these metallurgical characteristics in isolation.

Effect of Crystallographic Orientation on the Corrosion Rate of AZ31B-H24 TIG Weld

It was also seen that there was a large variation in the crystallographic orientation with weld zones. In the FZ, there was a highly randomized orientation while the HAZs and base material retain a basal orientation (Figure 3. 3 (c), Figure 3. 5). However, there is also a large variation in the IMP size and distribution. These metallurgical factors may have a larger impact on the corrosion rate than the crystallographic orientation. The IMPs in the HAZs are clustered in the *L* direction along the *SL* surface and the filiform corrosion propagates along this direction. It is noted in previous literature that the Al_8Mn_5 particles precipitate faster along the $(0\,0\,0\,1)$ crystallographic plane (which is the prominent crystallographic plane seen in the *SL* surface (Figure 3. 5) and these IMPs will have an impact the corrosion rate,[89] However, it also noted that the galvanic corrosion due to IMPs can suppresses the original crystallographic orientation effect on the corrosion behavior of AZ31 sheet Mg alloy.[89] The surface energy for Mg (0001), $(10\bar{1}0)$ and $(11\bar{2}0)$ surfaces are 1.808, 1.868 and 2.156 eV/nm², respectively, as calculated with

empirical electron theory[90,91] but little to no impact of the corrosion dependence on surface energy was seen in this study. It is noted that the randomized texture in the FZ will lead to a higher statistical probability of having these faster corroding planes being exposed to the marine environment and lead to faster propagation within that region which is consistent with the faster corrosion rate in the FZ over the HAZ. However, the effects from the solidification boundaries and IMPs in the weld zone will likely have a larger impact on the corrosion rate.

Effect of Composition on the Corrosion Rate of AZ31B-H24 TIG Weld

After welding, there was variation in the composition of the α-Mg matrix for each weld zone (Table 3. 1). The FZ α-Mg matrix is depleted in Al and Zn due to redistribution of the alloying elements during melting and resolidification where in a fusion weld the regions that solidify last have a higher concentration of these alloying elements. In the HAZs, there was a slight decrease in the Al and Zn content although the Mn was approximately the same as the baseplate.

Effect of Solute Segregation on the Corrosion Rate of AZ31B-H24 TIG Weld

Segregation was driven by the rapid non-equilibrium solidification during processing where coring occurs as solute was rejected during solidification, leading to a heterogeneous solute distribution.[92] Alloying elements or impurities are typically more soluble in the liquid state than in the solid state which leads to solute partitioning during cooling[92]. Due to this, as the liquid becomes progressively richer in the solute as the material freezes, the solute concentrations increase in the regions which solidify last. This leads to interdendritic regions of the material which are rich in these solute elements, particularly Al and Zn. Solute segregation within Mg-Al-Zn alloys has been documented[93-95] and will have an impact on the intrinsic corrosion rate of the weld. In particular, Al, Mn and Zn have all been found to segregate within both AZ31 and AM50.[93] Extensive solute segregation of the Al and Zn occurs during welding (Figure 3. 7), leading to areas with substantially different composition. This is a particular concern for Mg alloys which are extremely susceptible to micro-galvanic corrosion.[15] These regions with higher solute content or segregation will produce materials which are more susceptible to micro-galvanic corrosion as seen in the AZ31B fusion weld (Figure 3. 9-3. 12).

Effect of Intermetallic Particles on the Corrosion Rate of AZ31B-H24 TIG Weld

IMPs will also have a large impact on the corrosion rate. There have been numerous studies on the influence of different IMPs in the corrosion rate of Mg-Al alloys.[25,29,30] There was

a wide range of electrochemical potentials and measured current densities for each of these IMPs and their composition will alter their corrosion response.[29] From the electrochemical studies, most of these IMPs have a more noble E_{corr} than either high purity Mg or typical Mg-Al alloys.[29,30,96] Reports show that these IMPs are cathodes when coupled with the α-Mg phase.[96] The extent of this cathodic activity will be dependent on the composition and other attributes of these IMPs (Table 3. 1). Al-Mn-Fe particles will be highly cathodic in comparison to the α-Mg matrix, although they do negate much of the detrimental effects of Fe galvanic effects due to the sequestering ability of these particles.[70,97] The Al_8Mn_5 phase which was observed here and in other studies[70] has been shown to be a strong cathode in the α-Mg matrix. Little work has been done on the galvanic effects of Al-Zn phases in the Mg matrix and presents a viable route for future electrochemical study. However, Mg_xZn_x phases are reported to be responsible for an overall increase in the corrosion rate of Mg-Zn alloys due to increased cathodic reactions at these particles.[16,22,76,83] This will cause the alloy to suffer from local corrosion around this particle. The fact reduction of water at this particle leads to an increase in the local pH at this location and an increase in the corrosion product which was cleaned away during the CrO_3 cleaning procedure. This agrees with the corrosion morphology seen in this study (Figure 3. 11-3. 12).

A secondary explanation to the effect of IMPs on the corrosion rate for Mg-Al alloys is dealloying. These IMPs function as strong local cathodes near a pH of 7. Al can be lost due to cathodic corrosion at these IMPs due to a local alkaline pH shift at these IMPs (Figure 3. 12).[98] During this dealloying process, the Al-Mn particle (Al_8Mn_5 in most cases) can transform to Mn-O oxide (such as Mn_3O_4).[70] This transformation or dealloying process has been noted in other literature.[70,99] Al can then replate on the sample surface. The replated alloying elements can then function as cathodes and enhance the cathodic activity on the sample surface.[70]

3.4.5 Cathodic Kinetics of AZ31B wrought plate and weld material

There is a slight difference in the composition of the α-Mg matrix in each isolated weld zone (Table 3. 1). These variations in composition can lead to differences in the electropotential between the weld zones, as measured in Figure 3. 13. From Figure 3. 13, a variation in the OCP was shown for each isolated weld zone. Initially, within the weld zones, the FZ had the highest potential. This was most likely due to the larger amount of Al and Zn within the FZ due to solute segregation (Figure 3. 7) and the slight increase in the area fraction of Al-Mn-Fe particles (Figure 3. 8). However, after longer immersion times, the FZ has an increased negative potential

83

and is anodic to the other isolated weld zones. After this time, the solidification boundaries have corroded, leaving the exposed surface less-rich in these alloying elements and higher in Mg which will decrease the measured OCP. The HAZs likewise become more cathodic with time (Figure 3. 13). This was likely due to the enrichment of alloying elements on the sample surface, and the corrosion of Mg adjacent to cathodic particles.

Examining the difference in the corrosion rate with time (Figure 3. 15), it can be seen that cathodic activation may occur in the wrought base plate and isolated weld zones as evident from the increase in the cathodic kinetics with time noted in Figure 3. 15(b). Similarly, the dark regions which expand over the sample surface (Figure 3. 14) correlate to the rate of anodic Mg dissolution reaction. Within the dark region, it has been hypothesized that metals other than Mg which typically remain as impurities, are not dissolved during the dissolution of Mg and are collected on the partially protective surface film[59,66,71,100] or dealloying.[70]

In response to this enrichment or replating, the cathodic reaction rate increases Figure 3. 15(b). Cathodic activation has been cited to frequently occur in both commercially pure Mg and Mg alloys such as AZ31[74] and has been determined using a variety of approaches.[101,68] Over time, Fe will enrich to the sample surface in commercially pure Mg and it can be assumed that this also occurs in a Mg-Al alloy. Also, cathodic activation can cause the enrichment of Al-Mn phases on the sample surface[73,100] as well as Zn.[66,102] This enrichment[101] or dealloying[70] and subsequent replating will enoble the sample surface and will increase the cathodic reaction rate over time.

3.5 Conclusions

1. The AZ31B TIG weld can be segregated into three individual and metallurgically distinct regions. Each of which have a different grain size, crystallographic orientation, solute segregation and IMPs. Each of these metallurgical characteristics has an impact on the corrosion rate.

2. The corrosion morphology of individual zones in chloride environments is dependent on the microstructural features in the isolated weld zone. In the FZ, the Al-Zn solidification structures are cathodic to the α-Mg matrix and act as initiation sites for corrosion propagation in addition to Al-Mn-Fe particles. In the HAZs, filiform corrosion

propagation is the dominant corrosion phenomenon observed and occurs in the primary α-Mg matrix.

3. The corrosion rate of the TIG welded material was lower than the wrought plate.

4. Anodically induced cathodic activation is observed in each of the isolated weld zones with time.

5. The work herein provides a straightforward approach for the accurate instantaneous and long-term capable determination of corrosion rate via the combined study of mass loss, H_2 evolution, EIS, and ICP-OES solution analysis. Each of these four techniques provided similar results.

References

1. T.B. Abbott, "Magnesium: Industrial and Research Developments Over the Last 15 Years," Corrosion 71, 2 (2015): p. 120-127.
2. W. Danzer, "Welding of magnesium and magnesium alloys," Materialwiss Werkst 36, 6 (2005): p. 264-269.
3. X. Cao, M. Jahazi, J.P. Immarigeon, and W. Wallace, "A review of laser welding techniques for magnesium alloys," J Mater Process Tech 171, 2 (2006): p. 188-204.
4. P. Carlone and G.S. Palazzo, "Characterization of TIG and FSW weldings in cast ZE41A magnesium alloy," J Mater Process Tech 215, 0 (2015): p. 87-94.
5. D. Min, J. Shen, S. Lai, and J. Chen, "Effect of heat input on the microstructure and mechanical properties of tungsten inert gas arc butt-welded AZ61 magnesium alloy plates," Mater Charact 60, 12 (2009): p. 1583-1590.
6. L. Liming, W. Jifeng, and S. Gang, "Hybrid laser–TIG welding, laser beam welding and gas tungsten arc welding of AZ31B magnesium alloy," Materials Science and Engineering: A 381, 1–2 (2004): p. 129-133.
7. R.S. Coelho, A. Kostka, H. Pinto, S. Riekehr, M. Koçak, and A.R. Pyzalla, "Microstructure and mechanical properties of magnesium alloy AZ31B laser beam welds," Materials Science and Engineering: A 485, 1–2 (2008): p. 20-30.
8. L. Liu and R. Xu, "Investigation of the corrosion behaviour of laser-TIG hybrid welded Mg alloys," Corros Sci 52, 9 (2010): p. 3078-3085.
9. S.A. David, S.S. Babu, and J.M. Vitek, "Welding: Solidification and microstructure," Jom-Us 55, 6 (2003): p. 14-20.
10. R. Trivedi, S.A. David, M.A. Eshelman, J.M. Vitek, S.S. Babu, T. Hong, and T. DebRoy, "In situ observations of weld pool solidification using transparent metal-analog systems," Journal of Applied Physics 93, 8 (2003): p. 4885-4895.
11. R.C. Zeng, J. Chen, W. Dietzel, R. Zettler, J.F. dos Santos, M.L. Nascimento, and K.U. Kainer, "Corrosion of friction stir welded magnesium alloy AM50," Corros Sci 51, 8 (2009): p. 1738-1746.
12. M.M. Avedesian and H. Baker, "Magnesium and Magnesium Alloys," ASM International (1999).
13. G. Song, L.M. Liu, M.S. Chi, and J.F. Wang, "Investigations on laser-TIG hybrid welding of magnesium alloys," Mater Sci Forum 488-489, (2005): p. 371-375.
14. M.B. Kannan, W. Dietzel, C. Blawert, S. Riekehr, and M. Koçak, "Stress corrosion cracking behavior of Nd:YAG laser butt welded AZ31 Mg sheet," Materials Science and Engineering: A 444, 1–2 (2007): p. 220-226.
15. E. Ghali, W. Dietzel, and K.U. Kainer, "General and localized corrosion of magnesium alloys: A critical review," J Mater Eng Perform 13, 1 (2004): p. 7-23.
16. G.L. Makar and J. Kruger, "Corrosion Studies of Rapidly Solidified Magnesium Alloys," J Electrochem Soc 137, 2 (1990): p. 414-421.
17. I.J. Polmear, "Light Alloys: From Traditional Alloys to Nanocrystals 4th Edition," Elsevier (2006).
18. P. Hoyer, G.L. Angrisani, C. Klose, F.W. Bach, and T. Hassel, "Influence of aluminium on the corrosion behaviour of binary magnesium–aluminium alloys in saline solutions," Materials and Corrosion 65, 1 (2014): p. 23-30.
19. T. Cain, L. Bland, N. Birbilis, and J. Scully, "A compilation of corrosion potentials for magnesium alloys," Corrosion 70, 10 (2014): p. 1043-1051.

20. J.D. Hanawalt, C.E. Nelson, and J.A. Peloubet, "Corrosion studies of magnesium and its alloys," Transactions of AIME 147, (1942): p. 273-299.
21. N. Kirkland, M. Staiger, D. Nisbet, C.J. Davies, and N. Birbilis, "Performance-driven design of Biocompatible Mg alloys," JOM 63, 6 (2011): p. 28-34.
22. Y. Song, E.-H. Han, D. Shan, C.D. Yim, and B.S. You, "The effect of Zn concentration on the corrosion behavior of Mg–xZn alloys," Corros Sci 65, (2012): p. 322-330.
23. O. Lunder, J.H. Nordlien, and K. Nisangliou, "Corrosion resistance of cast Mg-Al alloys," Corros Rev 15, 3-4 (1997): p. 439-469.
24. S. Mathieu, C. Rapin, J. Steinmetz, and P. Steinmetz, "A corrosion study of the main constituent phases of AZ91 magnesium alloys," Corros Sci 45, 12 (2003): p. 2741-2755.
25. S. Pawar, X. Zhou, G.E. Thompson, G. Scamans, and Z. Fan, "The Role of Intermetallics on the Corrosion Initiation of Twin Roll Cast AZ31 Mg Alloy," J Electrochem Soc 162, 9 (2015): p. C442-C448.
26. T. Zhu, Z.W. Chen, and W. Gao, "Microstructure formation in partially melted zone during gas tungsten arc welding of AZ91 Mg cast alloy," Mater Charact 59, 11 (2008): p. 1550-1558.
27. R.E. Reed-Hill and R. Abbaschian, Physical metallurgy principles (Boston: PWS-Kent Pub., 1992.
28. R.M. Wang, A. Eliezer, and E. Gutman, "Microstructures and dislocations in the stressed AZ91D magnesium alloys," Materials Science and Engineering: A 344, 1–2 (2003): p. 279-287.
29. A.D. Südholz, N.T. Kirkland, R.G. Buchheit, and N. Birbilis, "Electrochemical Properties of Intermetallic Phases and Common Impurity Elements in Magnesium Alloys," Electrochemical and Solid-State Letters 14, 2 (2011): p. C5-C7.
30. O. Lunder, J.E. Lein, T.K. Aune, and K. Nisancioglu, "The Role of Mg17Al12 Phase in the Corrosion of Mg Alloy AZ91," Corros Sci 45, 9 (1989).
31. O. Lunder, T.K. Aune, and K. Nisancioglu, "Effect of Mn Additions on the Corrosion Behavior of Mould-Cast Magnesium ASTM AZ91," Corrosion 43, 5 (1987): p. 291-295.
32. Z.D. Zhang, L.M. Liu, Y. Shen, and L. Wang, "Mechanical properties and microstructures of a magnesium alloy gas tungsten arc welded with a cadmium chloride flux," Mater Charact 59, 1 (2008): p. 40-46.
33. A. Munitz, C. Cotler, A. Stern, and G. Kohn, "Mechanical properties and microstructure of gas tungsten arc welded magnesium AZ91D plates," Materials Science and Engineering: A 302, 1 (2001): p. 68-73.
34. S.M. Chowdhury, D.L. Chen, S.D. Bhole, E. Powidajko, D.C. Weckman, and Y. Zhou, "Microstructure and Mechanical Properties of Fiber-Laser-Welded and Diode-Laser-Welded AZ31 Magnesium Alloy," Metall and Mat Trans A 42, 7 (2011): p. 1974-1989.
35. G.K. K.H. Leong, P.G. Sanders, and J.S. Keske, Laser beam welding of AZ31B-H24 magnesium alloy, in ICALEO 98: Laser Materials Processing Conference. 1998: Orlando, FL. p. 28-36.
36. P. Liu, Y. Li, H. Geng, and J. Wang, "Microstructure characteristics in TIG welded joint of Mg/Al dissimilar materials," Mater Lett 61, 6 (2007): p. 1288-1291.
37. L. Wang, J. Shen, and N. Xu, "Effects of TiO2 coating on the microstructures and mechanical properties of tungsten inert gas welded AZ31 magnesium alloy joints," Materials Science and Engineering: A 528, 24 (2011): p. 7276-7284.

38. H. Haferkamp, F.W. Bach, I. Burmester, K. Kreutzburg, and M. Niemeyer. *Nd:YAG laser beam welding of magnesium constructions*. in *Third International Magnesium Conference*. 1996. Manchester, UK.

39. J.R. Kish, G. Williams, J.R. McDermid, J.M. Thuss, and C.F. Glover, "Effect of Grain Size on the Corrosion Resistance of Friction Stir Welded Mg Alloy AZ31B Joints," J Electrochem Soc 161, 9 (2014): p. C405-C411.

40. L. Commin, M. Dumont, R. Rotinat, F. Pierron, J.E. Masse, and L. Barrallier, "Texture evolution in Nd:YAG-laser welds of AZ31 magnesium alloy hot rolled sheets and its influence on mechanical properties," Mat Sci Eng a-Struct 528, 4-5 (2011): p. 2049-2055.

41. B.S. Naik, D.L. Chen, X. Cao, and P. Wanjara, "Texture Development in a Friction Stir Lap-Welded AZ31B Magnesium Alloy," Metall and Mat Trans A 45, 10 (2014): p. 4333-4349.

42. R. Xin, B. Li, L. Li, and Q. Liu, "Influence of texture on corrosion rate of AZ31 Mg alloy in 3.5 wt.% NaCl," Materials & Design 32, (2011): p. 4548-4552.

43. M. Zamin, "The Role of Mn in the Corrosion Behavior of Al-Mn Alloys," Corrosion 37, 11 (1981): p. 627-632.

44. L.G. Bland, A.D. King, N. Birbilis, and J.R. Scully, "Assessing the Corrosion of Commercially Pure Magnesium and Commercial AZ31B by Electrochemical Impedance, Mass-loss, Hydrogen Collection and ICP-OES Solution Analysis," Corrosion Journal 71, 2 [Special Issue] (2014): p. 128-145.

45. A.D. King, N. Birbilis, and J.R. Scully, "Accurate Electrochemical Measurement of Magnesium Corrosion Rates; a Combined Impedance, Mass-Loss and Hydrogen Collection Study," Electrochim Acta 121, 1 (2014): p. 394-406.

46. Viacheslav Shkirskiy, Dr. Andrew D. King, Oumaïma Gharbi, Dr. Polina Volovitch, Prof. John R. Scully, Prof. Kevin Ogle, and P.N. Birbilis, "Revisiting the Electrochemical Impedance Spectroscopy of Magnesium with Online Inductively Coupled Plasma Atomic Emission Spectroscopy," ChemPhysChem 16, 3 (2014): p. 536-539.

47. "AZtecEnergy: EDS Software," Oxford Instruments (2015).

48. ASTM-E384, "Standard Test Method for Knoop and Vickers Hardness of Materials," ASTM International (2012).

49. ASTM-E112, "Standard Test Methods for Determining Average Grain Size," ASTM International (2013).

50. C.A. Schneider, W.S. Rasband, and K.W. Eliceiri, "NIH Image to ImageJ: 25 years of image analysis," Nature Methods 9, (2012): p. 671-675.

51. S. Associates, *ZView*.

52. M. Curioni, F. Scenini, T. Monetta, and F. Bellucci, "Correlation between electrochemical impedance measurements and corrosion rate of magnesium investigated by real-time hydrogen measurement and optical imaging," Electrochim Acta 166, (2015): p. 372-384.

53. J.R. Scully, Corrosion Journal 56, (2000): p. 199-218.

54. M. Stern and A.I. Geary, J Electrochem Soc 104: p. 56-63.

55. Z. Shi, F. Cao, G.L. Song, M. Liu, and A. Atrens, "Corrosion behaviour in salt spray and in 3.5% NaCl solution saturated with Mg(OH)2 of as-cast and solution heat-treated binary Mg–RE alloys: RE=Ce, La, Nd, Y, Gd," Corros Sci 76, 0 (2013): p. 98-118.

56. F. Cao, Z. Shi, J. Hofstetter, P.J. Uggowitzer, G. Song, M. Liu, and A. Atrens, "Corrosion of ultra-high-purity Mg in 3.5% NaCl solution saturated with Mg(OH)2," Corros Sci 75, (2013): p. 78-99.

57. J.L. Bullister, N.L. Guinasso, and D.R. Schink, "Dissolved hydrogen, carbon monoxide, and methane at the CEPEX site," Journal of Geophysical Research: Oceans 87, C3 (1982): p. 2022-2034.

58. ASTM-G1, "Standard Practice for Preparing, Cleaning, and Evaluating Corrosion Test Specimens," ASTM International G1, (2011).

59. M. Taheri, J.R. Kish, N. Birbilis, M. Danaie, E.A. McNally, and J.R. McDermid, "Towards a Physical Description for the Origin of Enhanced Catalytic Activity of Corroding Magnesium Surfaces," Electrochim Acta 116, (2014): p. 396-403.

60. S. Lebouil, A. Duboin, F. Monti, P. Tabeling, P. Volovitch, and K. Ogle, "A novel approach to on-line measurement of gas evolution kinetics: Application to the negative difference effect of Mg in chloride solution," Electrochimica Acta 0 (2013).

61. J. Światowska, P. Volovitch, and K. Ogle, "The anodic dissolution of Mg in NaCl and Na2SO4 electrolytes by atomic emission spectroelectrochemistry," Corros Sci 52, 2010 (2010): p. 2372-2378.

62. ASTM-G106, "Standard Practice for Verification of Algorithm and Equipment for Electrochemical Impedance Measurements," ASTM International (2010).

63. D.A. Jones, "Principles and Prevention of Corrosion," Prentice Hall Upper Saddle River. NJ. 2nd Ed (1996).

64. R.M. Asmussen, W.J. Binns, R. Partovi-Nia, P. Jakupi, and D.W. Shoesmith, "The stability of aluminum-manganese intermetallic phases under the microgalvanic coupling conditions anticipated in magnesium alloys," Materials and Corrosion 67, 1 (2016): p. 39-50.

65. A. Samaniego, I. Llorente, and S. Feliu Jr, "Combined effect of composition and surface condition on corrosion behaviour of magnesium alloys AZ31 and AZ61," Corros Sci 68, (2013): p. 66-71.

66. Z.P. Cano, M. Danaie, J.R. Kish, J.R. McDermid, G.A. Botton, and G. Williams, "Physical Characterization of Cathodically-Activated Corrosion Filaments on Magnesium Alloy AZ31B," Corrosion 71, 2 (2015): p. 146-159.

67. G. Williams and H.N. McMurray, "Localized Corrosion of Magnesium in Chloride-Containing Electrolyte Studied by a Scanning Vibrating ElectrodeTechnique," J Electrochem Soc 155, 7 (2008): p. C340-C349.

68. N. Birbilis, T. Cain, J.S. Laird, X. Xia, J.R. Scully, and A.E. Hughes, "Nuclear Microprobe Analysis for Determination of Element Enrichment Following Magnesium Dissolution," J Electrochem Soc 4, 10 (2015): p. C34-C37.

69. A. Wingersky, A. Handler, J. Fisher, A. Weiss, and K. Sieradzki, "Dealloying of Magnesium Alloys," Meeting Abstracts MA2015-02, 13 (2015): p. 661.

70. M. Danaie, R.M. Asmussen, P. Jakupi, D.W. Shoesmith, and G.A. Botton, "The cathodic behaviour of Al–Mn precipitates during atmospheric and saline aqueous corrosion of a sand-cast AM50 alloy," Corros Sci 83, (2014): p. 299-309.

71. Z.P. Cano, J.R. McDermid, and J.R. Kish, "Cathodic Activity of Corrosion Filaments Formed on Mg Alloy AM30," J Electrochem Soc 162, 14 (2015): p. C732-C740.

72. G.S. Frankel, A. Samaniego, and N. Birbilis, "Evolution of hydrogen at dissolving magnesium surfaces," Corros Sci 70, (2013): p. 104-111.

73. G. Williams, H. ap Llwyd Dafydd, and R. Grace, "The localised corrosion of Mg alloy AZ31 in chloride containing electrolyte studied by a scanning vibrating electrode technique," Electrochim Acta 109, 0 (2013): p. 489-501.

74. N. Birbilis, A.D. King, S. Thomas, G.S. Frankel, and J.R. Scully, "Evidence for enhanced catalytic activity of magnesium arising from anodic dissolution," Electrochim Acta 132, 0 (2014): p. 277-283.

75. G. Ben-Hamu, D. Eliezer, C.E. Cross, and T. Böllinghaus, "The relation between microstructure and corrosion behavior of GTA welded AZ31B magnesium sheet," Materials Science and Engineering: A 452–453, 0 (2007): p. 210-218.

76. K. Gusieva, C.H.J. Davies, J.R. Scully, and N. Birbilis, "Corrosion of magnesium alloys: the role of alloying," Int Mater Rev (2014): p. 169-194.

77. L. Wang, T. Shinohara, and B.-P. Zhang, "Influence of chloride, sulfate and bicarbonate anions on the corrosion behavior of AZ31 magnesium alloy," J Alloy Compd 496, 1–2 (2010): p. 500-507.

78. O. Lunder, J.E. Lein, S.M. Hesjevik, T.K. Aune, and K. Nişancioğlu, "Corrosion morphologies on magnesium alloy AZ 91," Materials and Corrosion 45, 6 (1994): p. 331-340.

79. M.P. Brady, G. Rother, L.M. Anovitz, K.C. Littrell, K.A. Unocic, H.H. Elsentriecy, G.-L. Song, J.K. Thomson, N.C. Gallego, and B. Davis, "Film Breakdown and Nano-Porous Mg(OH)2 Formation from Corrosion of Magnesium Alloys in Salt Solutions," J Electrochem Soc 162, 4 (2015): p. C140-C149.

80. R.C. Zeng, J. Zhang, W.J. Huang, W. Dietzel, K.U. Kainer, C. Blawert, and W. Ke, "Review of studies on corrosion of magnesium alloys," T Nonferr Metal Soc 16, (2006): p. s763-s771.

81. M. Ascencio, M. Pekguleryuz, and S. Omanovic, "An investigation of the corrosion mechanisms of WE43 Mg alloy in a modified simulated body fluid solution: The influence of immersion time," Corros Sci 87, (2014): p. 489-503.

82. G.T. Parthiban, N. Palaniswamy, V. Sivan, "Effect of manganese addition on anode characteristics of electrolytic magnesium," Anti-Corrosion Methods and Materials 56, 2 (2009): p. 79-83.

83. N.T. Kirkland, M.P. Staiger, D. Nisbet, C.H.J. Davies, and N. Birbilis, "Performance-driven design of Biocompatible Mg alloys," Jom-Us 63, 6 (2011): p. 28-34.

84. N. Birbilis, K.D. Ralston, S. Virtanen, H.L. Fraser, and C.H.J. Davies, "Grain character influences on corrosion of ECAPed pure magnesium," Corrosion Engineering, Science & Technology 45, 3 (2010): p. 224-230.

85. K.D. Ralston and N. Birbilis, "Effect of Grain Size on Corrosion: A Review," Corros Sci 66, 7 (2010).

86. K.V. Kutniy, I.I. Papirov, M.A. Tikhonovsky, A.I. Pikalov, S.V. Sivtzov, L.A. Pirozhenko, V.S. Shokurov, and V.A. Shkuropatenko, "Influence of grain size on mechanical and corrosion properties of magnesium alloy for medical implants," Materialwiss Werkst 40, 4 (2009): p. 242-246.

87. K.D. Ralston, G. Williams, and N. Birbilis, "Effect of pH on the Grain Size Dependence of Magnesium Corrosion," Corrosion 68, 6 (2012): p. 507-517.

88. N.N. Aung and W. Zhou, "Effect of grain size and twins on corrosion behaviour of AZ31B magnesium alloy," Corros Sci 52, 2 (2010): p. 589-594.

89.   G.L. Song and Z. Xu, "Effect of microstructure evolution on corrosion of different crystal surfaces of AZ31 Mg alloy in a chloride containing solution," Corros Sci 54, 0 (2012): p. 97-105.

90.   B.Q. Fu, W. Liu, and Z.L. Li, "Calculation of the surface energy of hcp-metals with the empirical electron theory," Appl Surf Sci 255, 23 (2009): p. 9348-9357.

91.   R.S. Lillard, G.F. Wang, and M.I. Baskes, "The Role of Metallic Bonding in the Crystallographic Pitting of Magnesium," J Electrochem Soc 153, 9 (2006): p. B358-B364.

92.   S. Kou. *Welding Metallurgy, Second Edition*. 2002; Available from: http://www.123library.org/book_details/?id=25724.

93.   D. Mirković and R. Schmid-Fetzer, "Directional Solidification of Mg-Al Alloys and Microsegregation Study of Mg Alloys AZ31 and AM50: Part I. Methodology," Metall and Mat Trans A 40, 4 (2009): p. 958-973.

94.   D. Mirković and R. Schmid-Fetzer, "Directional Solidification of Mg-Al Alloys and Microsegregation Study of Mg Alloys AZ31 and AM50: Part II. Comparison between AZ31 and AM50," Metall and Mat Trans A 40, 4 (2009): p. 974-981.

95.   S. Feliu Jr, A. Samaniego, V. Barranco, A.A. El-Hadad, I. Llorente, and P. Adeva, "The effect of low temperature heat treatment on surface chemistry and corrosion resistance of commercial magnesium alloys AZ31 and AZ61 in 0.6 M NaCl solution," Corros Sci 80, 0 (2014): p. 461-472.

96.   M. Jönsson, D. Thierry, and N. LeBozec, "The influence of microstructure on the corrosion behaviour of AZ91D studied by scanning Kelvin probe force microscopy and scanning Kelvin probe," Corros Sci 48, 5 (2006): p. 1193-1208.

97.   S. Pawar, X. Zhou, T. Hashimoto, G.E. Thompson, G. Scamans, and Z. Fan, "Investigation of the microstructure and the influence of iron on the formation of Al8Mn5 particles in twin roll cast AZ31 magnesium alloy," J Alloy Compd 628, (2015): p. 195-198.

98.   M. Mokaddem, P. Volovitch, F. Rechou, R. Oltra, and K. Ogle, "The anodic and cathodic dissolution of Al and Al-Cu-Mg alloy," Electochimica Acta 55, (2010): p. 3779-3786.

99.   C. Xu, R. Wang, Y. Zhang, and Y. Ding, "A general corrosion route to nanostructured metal oxides," Nanoscale 2, 6 (2010): p. 906-909.

100.   G. Williams, N. Birbilis, and H.N. McMurray, "The source of hydrogen evolved from a magnesium anode," Electrochemistry Communications 36, 0 (2013): p. 1-5.

101.   T. Cain, S.B. Madden, N. Birbilis, and J.R. Scully, "Evidence of the Enrichment of Transition Metal Elements on Corroding Magnesium Surfaces Using Rutherford Backscattering Spectrometry," J Electrochem Soc 162, 6 (2015): p. C228-C237.

102.   R.C. Phillips and J.R. Kish, "Nature of Surface Film on Matrix Phase of Mg Alloy AZ80 Formed in Water," Corrosion 69, 8 (2013): p. 813-820.

Table 3. 1. AZ31B-H24 ([UNS M11311] Magnesium Elektron). All compositions reported in wt. %, with the actual compositions provided by QUANT (Quality Analysis and Testing Corporation). Compositions of α-matrix for isolated weld zones, IMPs and solidification boundaries due to welding found by SEM EDS analysis.

	UNS #	Al	Mn	Zn	Si	Cu	Ni	Fe	Mg
AZ31B-H24	M11311	3.02	0.330	0.990	0.025	0.005	0.002	0.005	Bal.
HAZ2 α-matrix	---	2.6	0.330	0.990	---	---	---	---	Bal.
HAZ1 α-matrix	---	2.2	0.330	0.8	---	---	---	---	Bal.
FZ α-matrix	---	1.8	0.5	0.5	---	---	---	---	Bal.
Al-Mn-Fe particles	---	75.1	12.4	---	---	---	---	12.5	---
Al-Mn particles	---	67	33	---	---	---	---	---	---
Al-Zn Solidification Structure	---	52.1	--	47.9	---	---	---	--	---

Table 3. 2. Approximate elemental detection limits for the ICP-OES used in this investigation in ppm (mg/L)

	Al	Mn	Zn	Cu	Ni	Fe	Mg
ppm	0.030	0.005	0.0005	0.010	0.005	0.005	0.005

Table 3. 3: Anodic charge consumed on AZ31B wrought plate and TIG weld as calculated by integration of i_{corr} derived from EIS-estimated R_P where B_{King}=36.0 mV, B_{Shi}=36.8 mV[55], and B_{Cao}=31.1 in 0.6 M NaCl were used[44,45] after exposure in 0.6 M NaCl at open circuit for 24 hrs as per the equivalent circuit.

		Wrought Plate	FZ	HAZ 1	HAZ 2
B_{king}[45]	β_c	315 mV/dec	315 mV/dec	315 mV/dec	315 mV/dec
	β_a	113 mV/dec	113 mV/dec	113 mV/dec	113 mV/dec
	B	36.0 mV	36.0 mV	36.0 mV	36.0 mV
	ΣQ_{EIS}^{SG}	15.9 ± 5.3 C/cm^2	6.1 ± 2.3 C/cm^2	5.9 ± 1.3 C/cm^2	5.3 ± 3.7 C/cm^2
B_{Shi}	β_c	160.0 mV/dec	160.0 mV/dec	160.0 mV/dec	160.0 mV/dec
	β_a	180.0 mV/dec	180.0 mV/dec	180.0 mV/dec	180.0 mV/dec
	B	36.8 mV	36.8 mV	36.8 mV	36.8 mV
	ΣQ_{EIS}^{SG}	13.1 ± 4.5 C/cm^2	6.3 ± 2.3 C/cm^2	6.0 ± 1.3 C/cm^2	5.4 ± 3.8 C/cm^2
B_{Cao}	β_c	--	--	--	--
	β_a	--	--	--	--
	B	31.1 mV	31.1 mV	31.1 mV	31.1 mV
	ΣQ_{EIS}^{SG}	11.1 ± 3.2 C/cm^2	5.2 ± 1.8 C/cm^2	5.0 ± 1.1 C/cm^2	4.6 ± 3.2 C/cm^2
	Δm	1.1 ± 0.4 mg	0.7 ± 0.3 mg	0.5 ± 0.1 mg	0.3 ± 0.1 mg
	$\Sigma Q_{\Delta m}$	16.9 ± 5.7 C/cm^2	9.3 ± 2.8 C/cm^2	7.9 ± 1.5 C/cm^2	5.3 ± 3.3 C/cm^2
	ΔV_{H2}	1.0 ± 0.3 cm^3	0.4 ± 0.1 cm^3	0.5 ± 0.1 cm^3	0.5 ± 0.1 cm^3
	ΣQ_{H2}	16.6 ± 4.6 C/cm^2	7.4 ± 3.2 C/cm^2	5.9 ± 1.6 C/cm^2	4.2 ± 2.8 C/cm^2
	Q_{ICP}	21.2 ± 8.0 C/cm^2	7.5 ± 1.0 C/cm^2	4.7 ± 0.8 C/cm^2	4.4 ± 0.3 C/cm^2
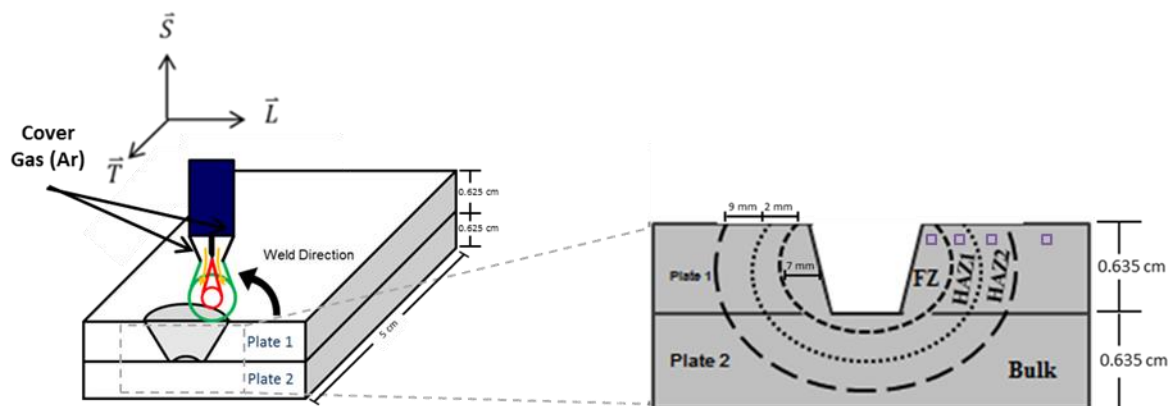
Figure 3. 1. Schematic of TIG welding process and a schematic of weld zones, specifying the FZ and HAZs. Far enough away from the weld zone, the sample will become unaffected base material. All samples were welded through a 45° countersunk hole in order to have full penetration through both plates. The area of the isolated weld zone test locations is marked.
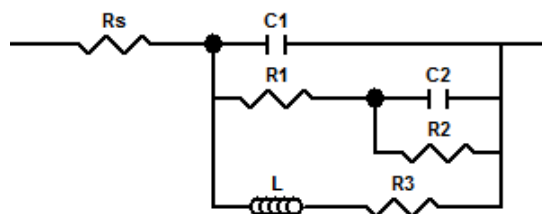
Figure 3. 2. Equivalent circuit diagram used to model pseudo-inductive electrochemical impedance response on corroding Mg in 0.6 M NaCl solution.
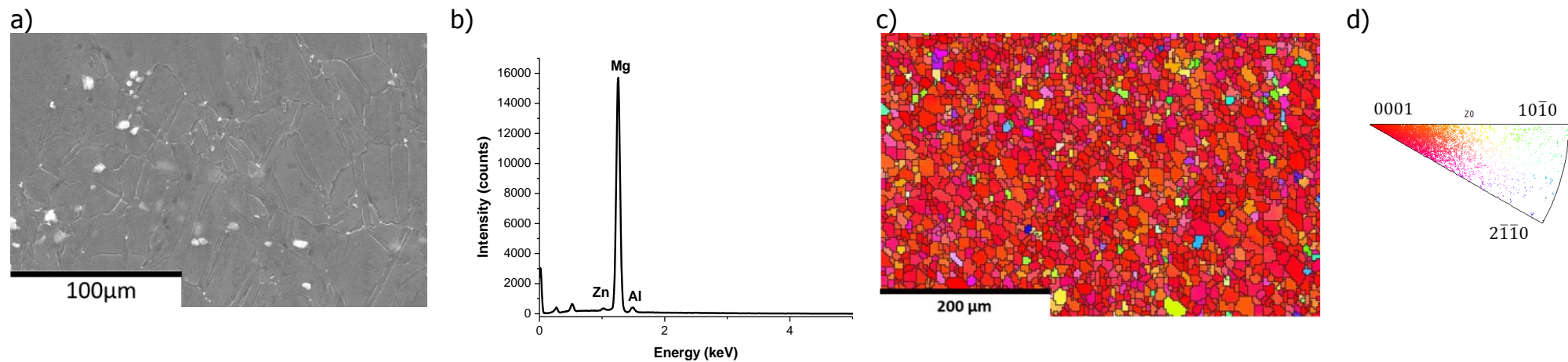
Figure 3. 3. AZ31B-H24 wrought plate a) secondary electron image showing Al-Mn-Fe particles throughout as received material, b) EDS spectrum of composition of wrought plate material, c)typical EBSD spectrum and d) inverse pole figure showing the basal texture throughout the as received material. All images taken along the SL surface.

a)
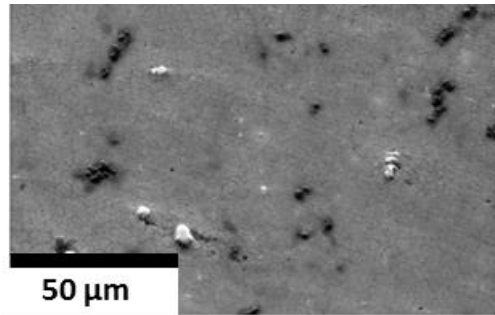
b)
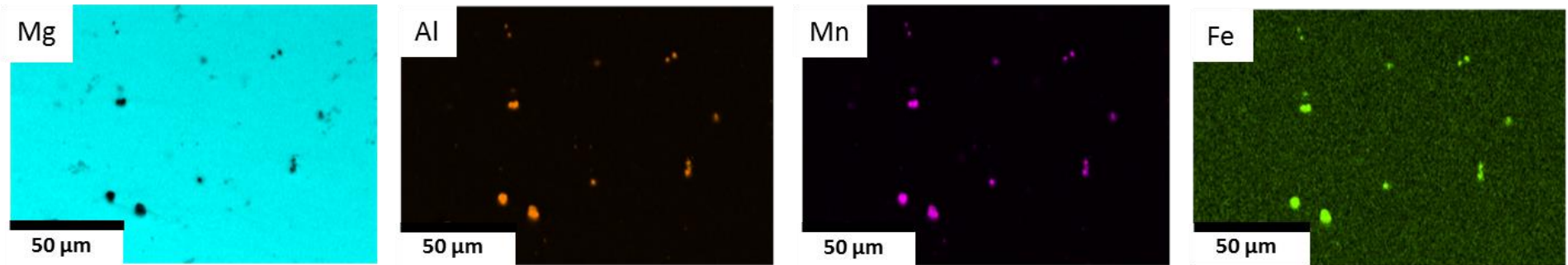
Figure 3. 4. (a) Secondary SEM image of AZ31B-H24 wrought plate (b) EDS analysis of particles within AZ31B base material. All images taken along the SL surface.
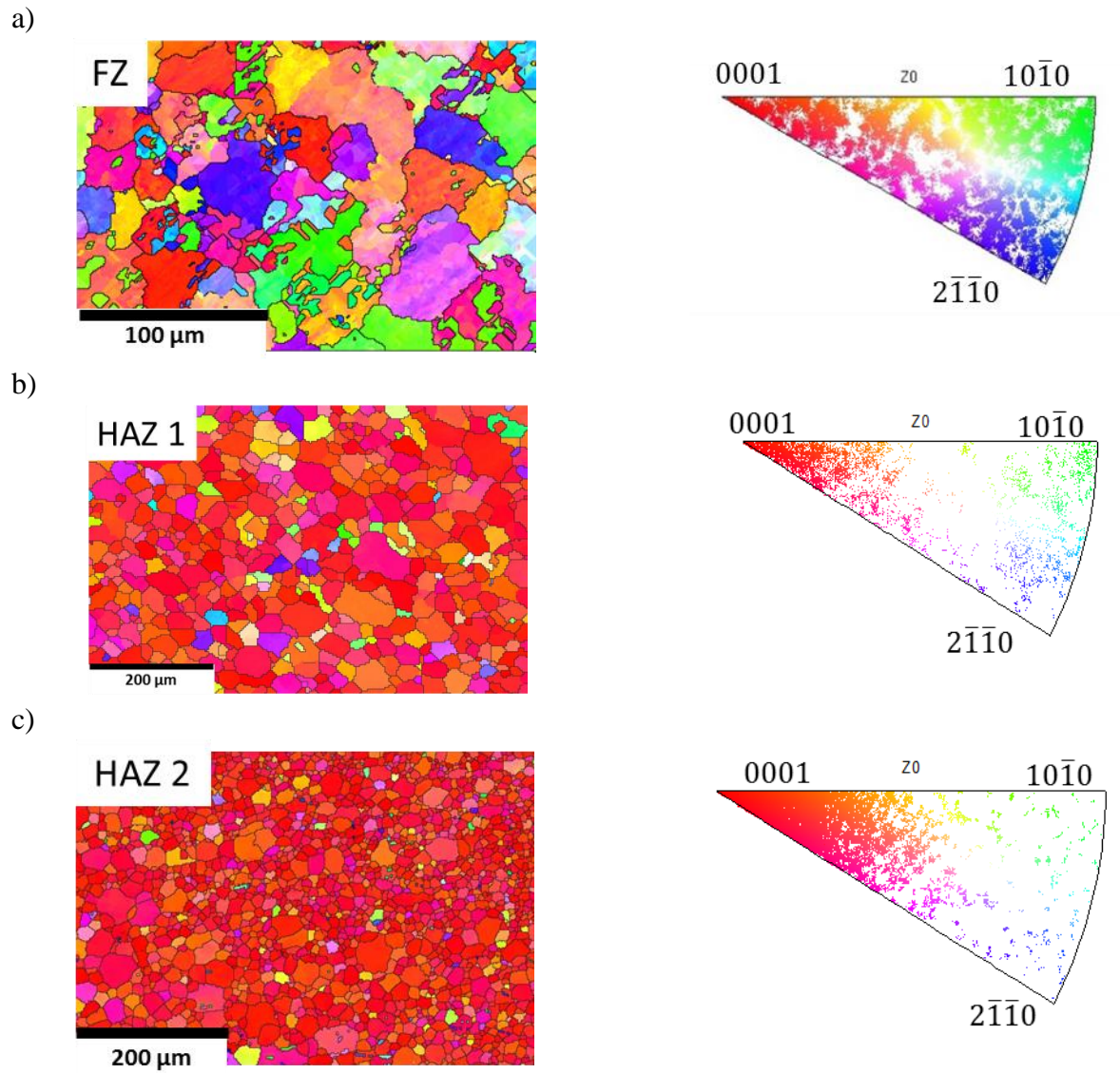
Figure 3. 5. Typical EBSD spectrums and inverse pole figures for AZ31B TIG weld (a) FZ, (b) HAZ 1 and (c) HAZ 2. All images taken along the SL surface.
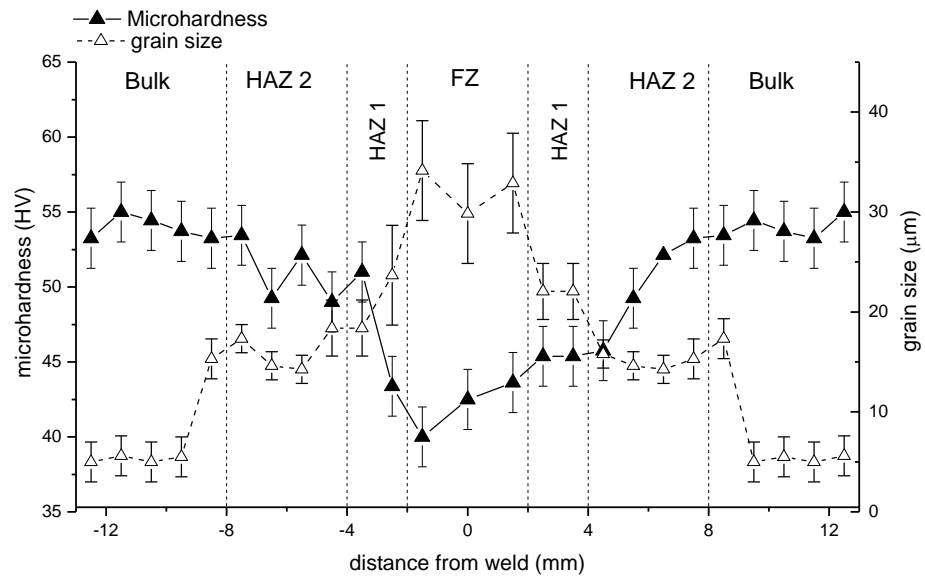
Figure 3. 6. Typical grain size and microhardness distribution of AZ31B TIG weld taken along the SL surface.
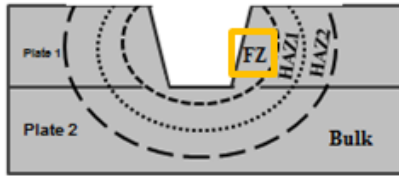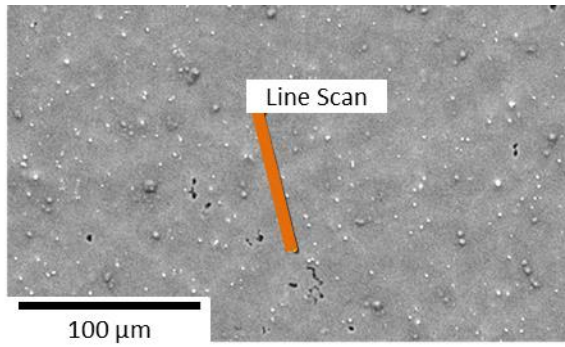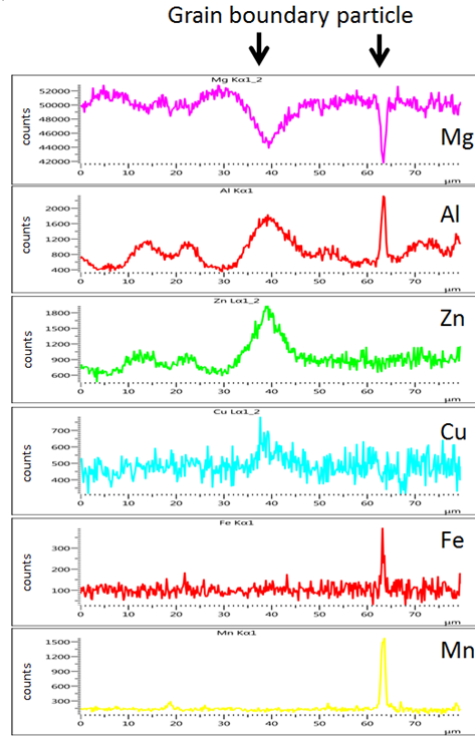
Figure 3. 7. EDS line scan of the FZ where (a) schematic of the location within the weld where the EDS line scan was taken (b) a high magnification back scattered SEM micrograph of the region and the marked line scan and (c) EDS line scan.
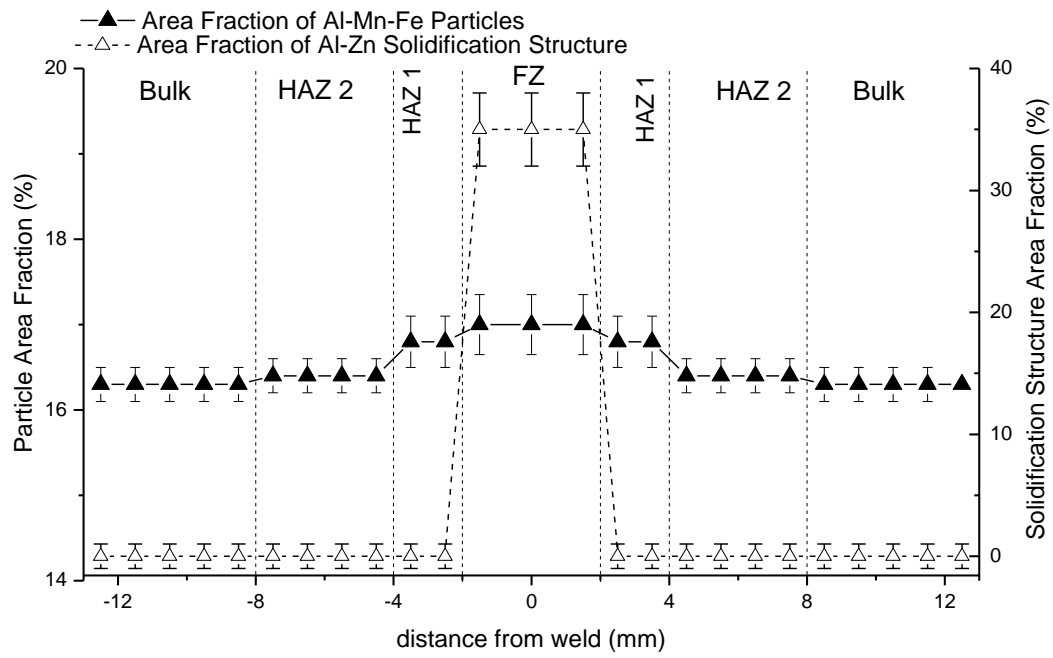
Figure 3. 8. Typical distribution of Al-Mn-Fe and Al-Zn solidification structures in all weld zones.
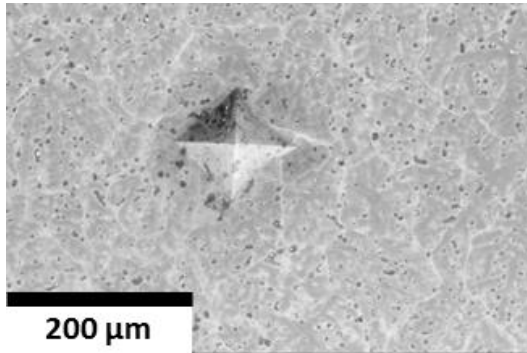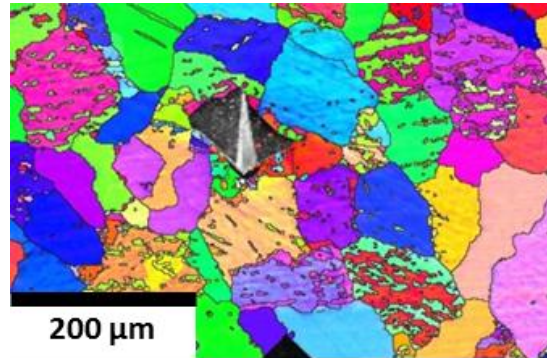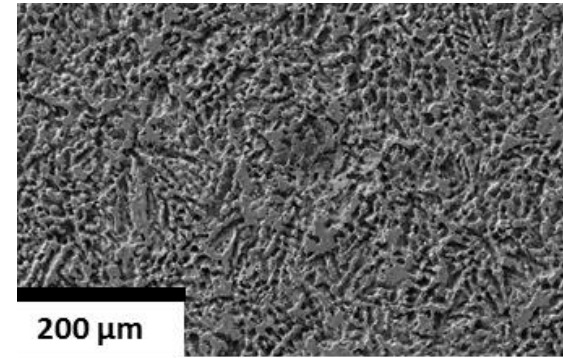
Figure 3. 9. (a) Electron micrograph of AZ31B TIG isolated FZ before corrosion, (b) corresponding EBSD of the marked location and (c) corrosion morphology after 3 hr immersion at OCP in 0.6 M NaCl and cleaned with CrO_3 to remove any oxides

a)

b)

c)

IMP (cathode)

Al-Mn-Zn rich solidification boundary (cathode)

Mg matrix (anode)

Dissolution of anodic Mg matrix along solidification structure and IMP

Resulting corrosion morphology
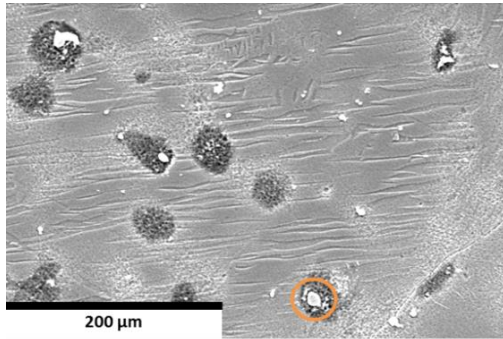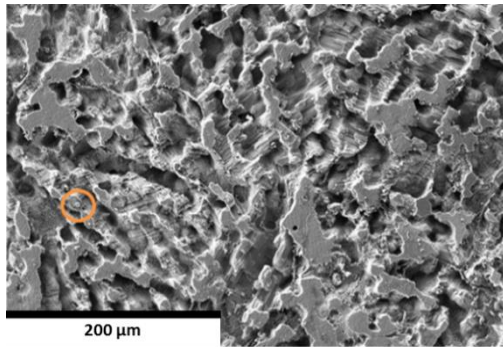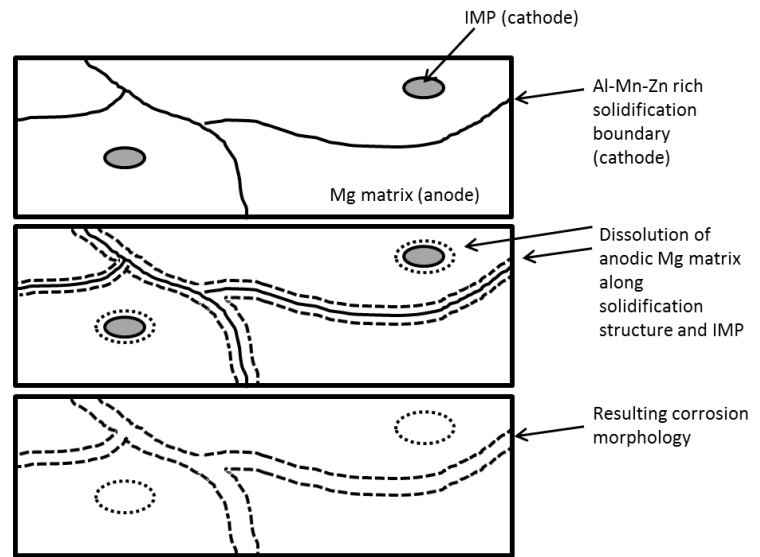
Figure 3. 10. (a) Before corrosion secondary electron image of the AZ31B isolated FZ, (b) corrosion morphology after immersion in 0.6 M NaCl for 3 hr OCP secondary electron image of the AZ31B FZ and cleaned with CrO_3 to remove any oxides and (c) schematic showing the resultant corrosion morphology in the FZ.
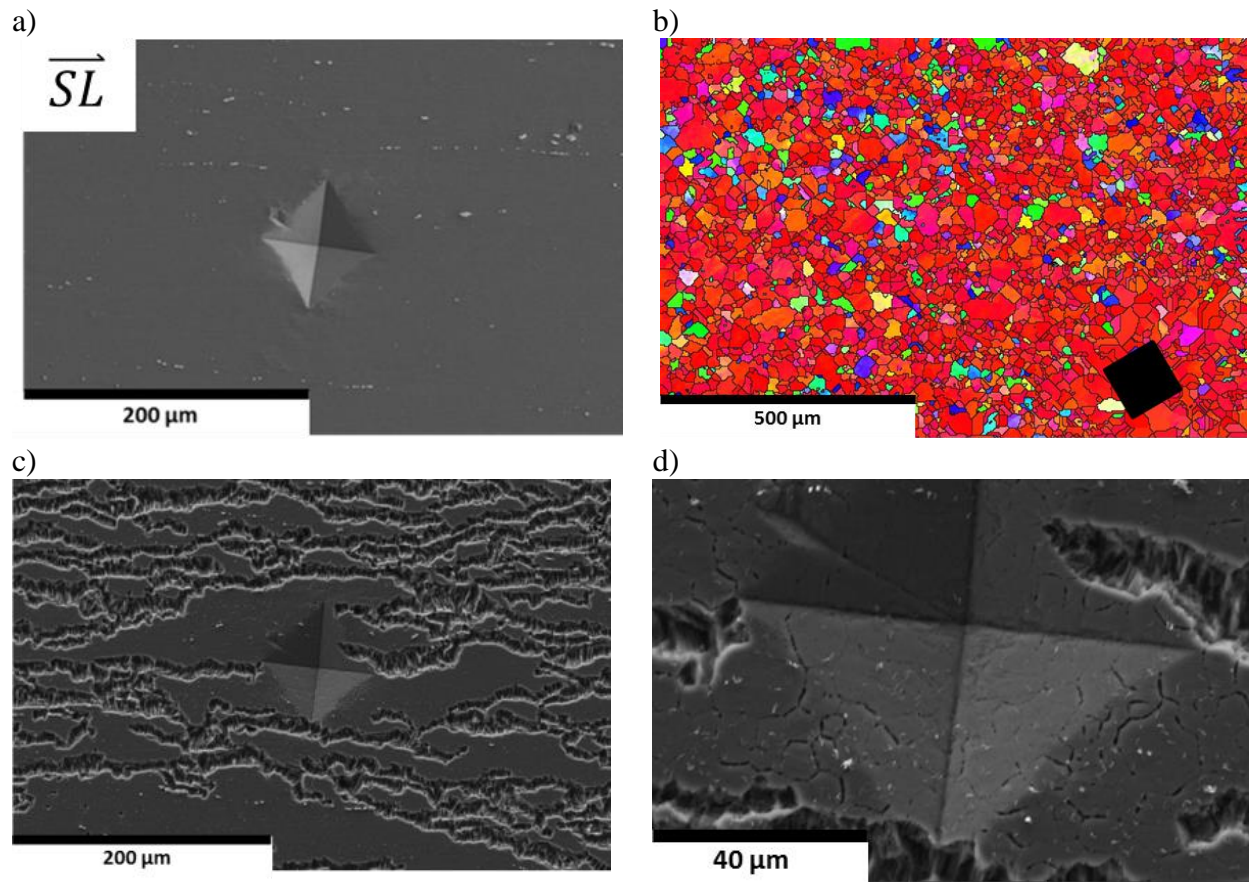
Figure 3. 11. (a) Before corrosion secondary electron image of the AZ31B isolated HAZ, (b) corresponding EBSD map with the Vickers hardness mark location shown in black, (c) resultant corrosion morphology of AZ31B-H24 TIG weld HAZ after corrosion and cleaned with CrO_3 to remove any oxides and (d) high magnification secondary electron micrograph of AZ31B-H24 FZ after 3 hr immersion at OCP in 0.6 M NaCl. All images taken along the SL surface.

a)

b)

c)

IMP (cathode)

Grain boundary (cathode)

Mg matrix (anode)

Dissolution of anodic Mg matrix propagating away from cathodic grain boundary and IMP

Some IMP remain while others have corroded

Propagation throughout grain

25 µm
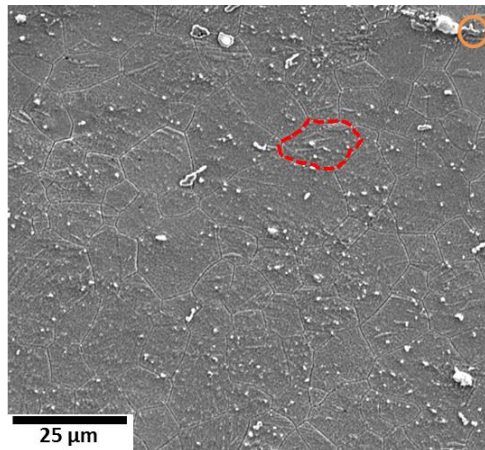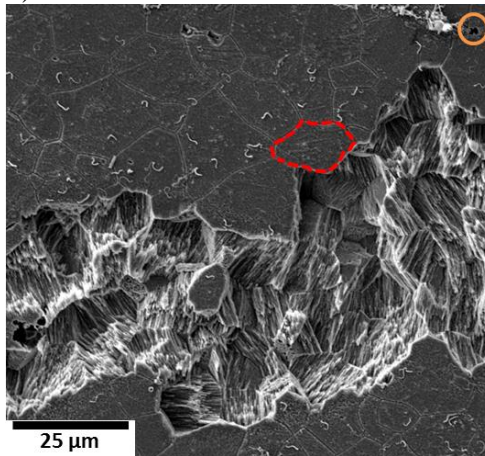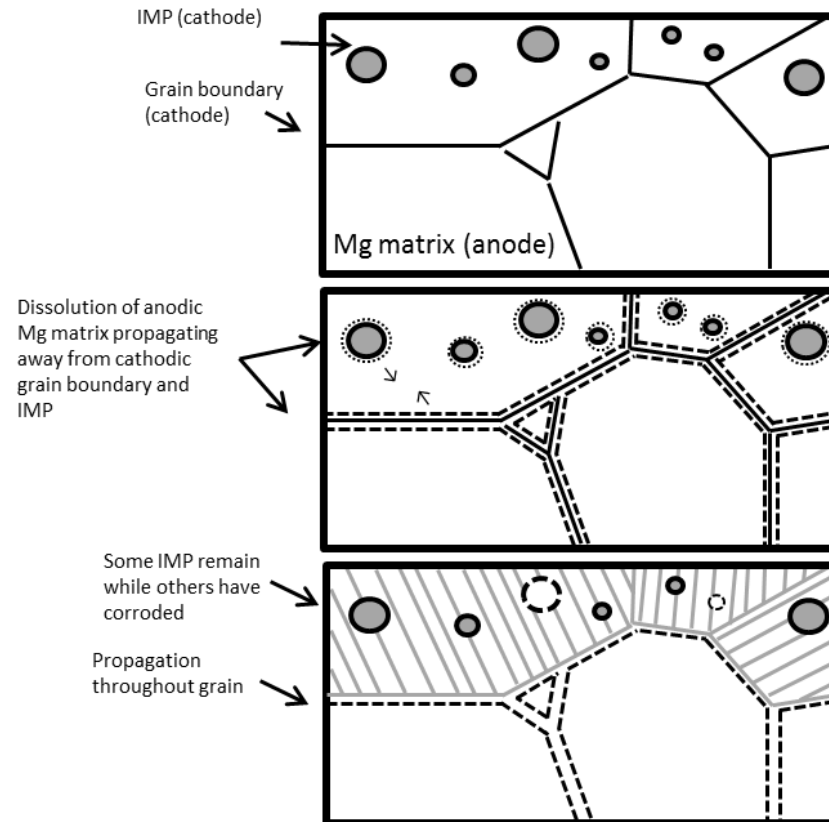
Figure 3. 12. (a) Secondary electron image of isolated HAZ before corrosion and (b) secondary electron image of resultant corrosion morphology in the same location after 3 hr immersion in 0.6 M NaCl at open circuit where the same grain was outlined in each image, showing that filiform corrosion propagation along the grain edge (red) as well as the corrosion initiation at an IMP (orange). (c) schematic of these two types of corrosion propagation occurring simultaneously showing corrosion initiation at particle edges.
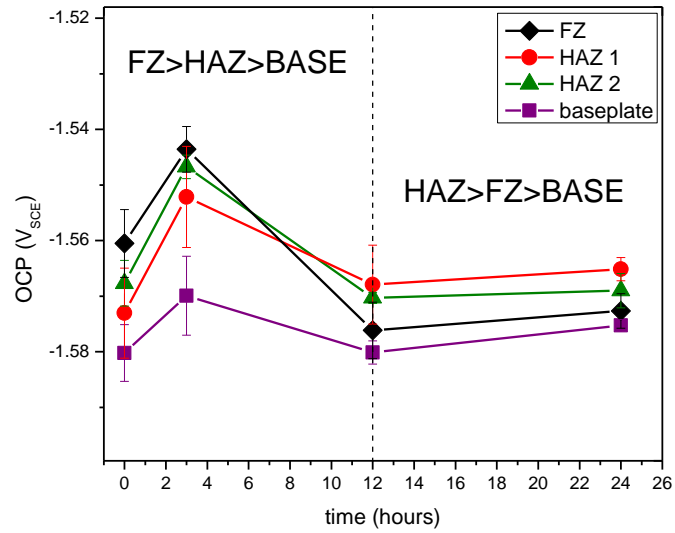
Figure 3. 13. Measured OCP for wrought plate AZ31B-H24, full TIG weld and isolated weld zones in 0.6 M NaCl measured at 0, 3, 12 and 24 hrs.
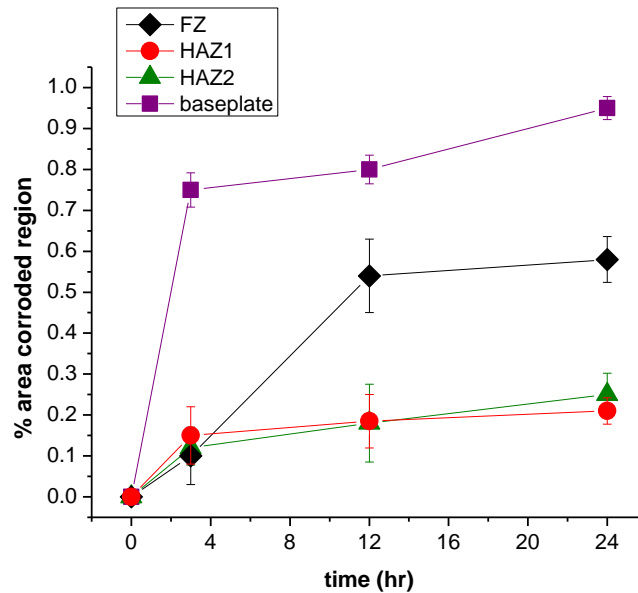
Figure 3. 14. Percent of surface area corroded with time as determined from SEM images and ImageJ where the FZ and HAZ 1 were each determined to be approximately 20% of the surface area and the HAZ2 and wrought plate were determined to each of 30% of the surface area of a full weld region. Standard deviation of three runs shown.

a)
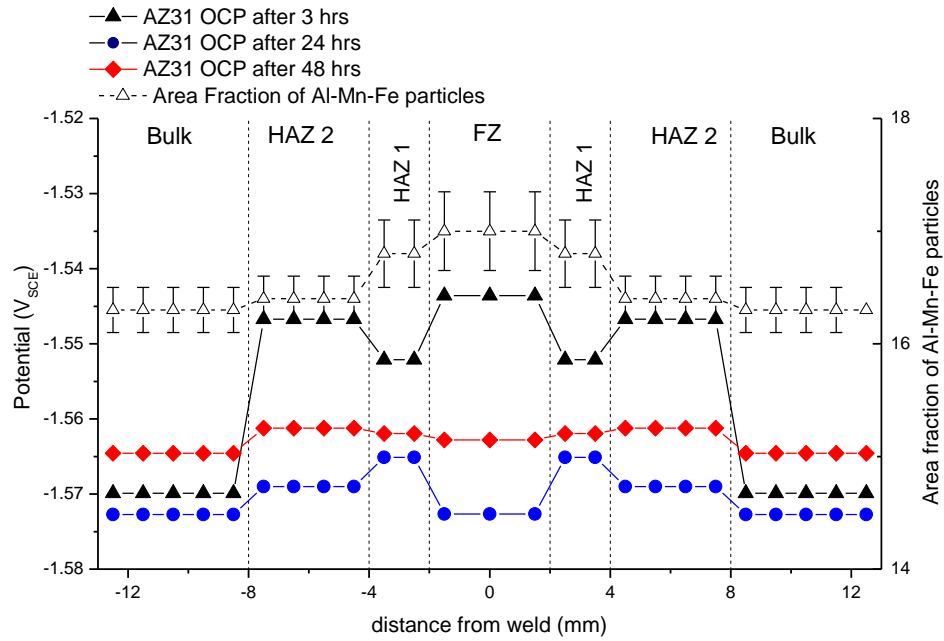
b)
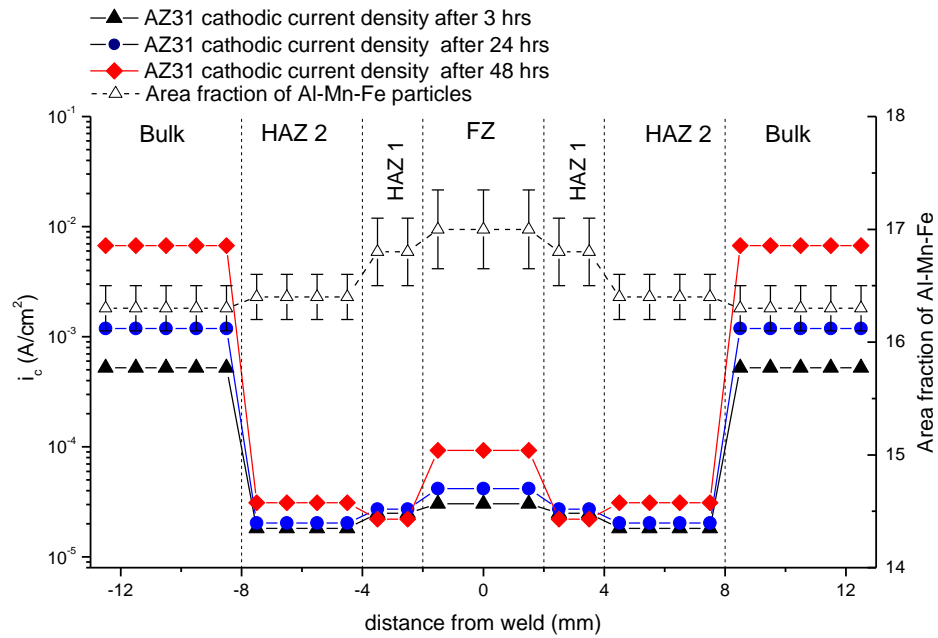
Figure 3. 15. (a) Evolution of the OCP with time between all zones. (b) evolution of the cathodic current density with time estimated at -1.8 V_{SCE} between all zones at 3, 24 and 48 hrs.
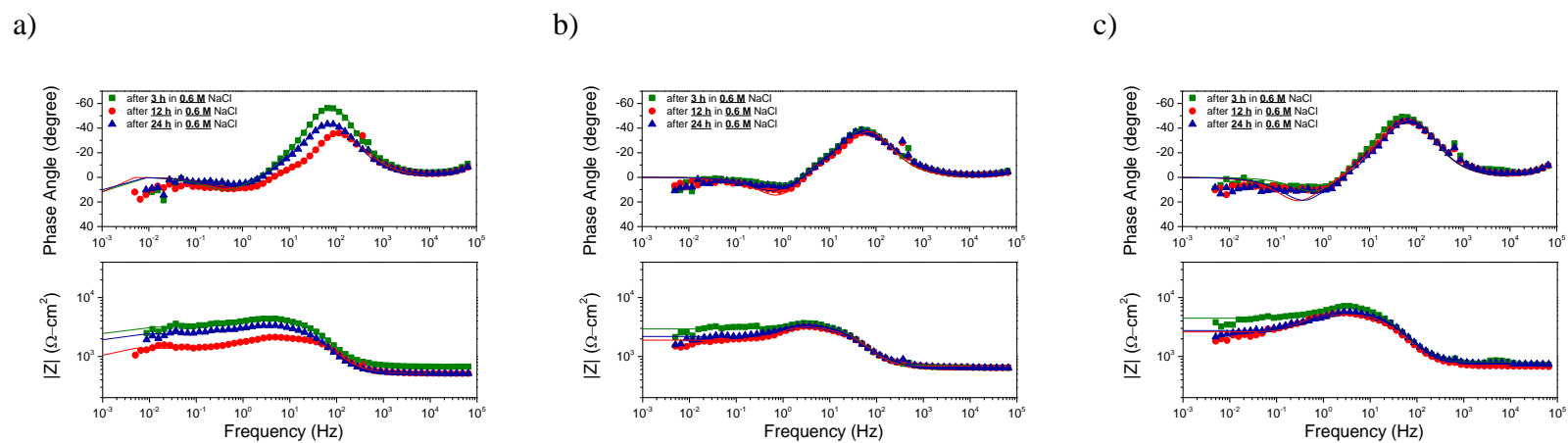
Figure 3. 16. Bode magnitude and Bode phase plot for the isolated (a) FZ, (b) HAZ1, and (c) HAZ2 weld zones. Data shown along with respective fits following 3, 12 and 24 hrs immersion in 0.6 M NaCl at open circuit.
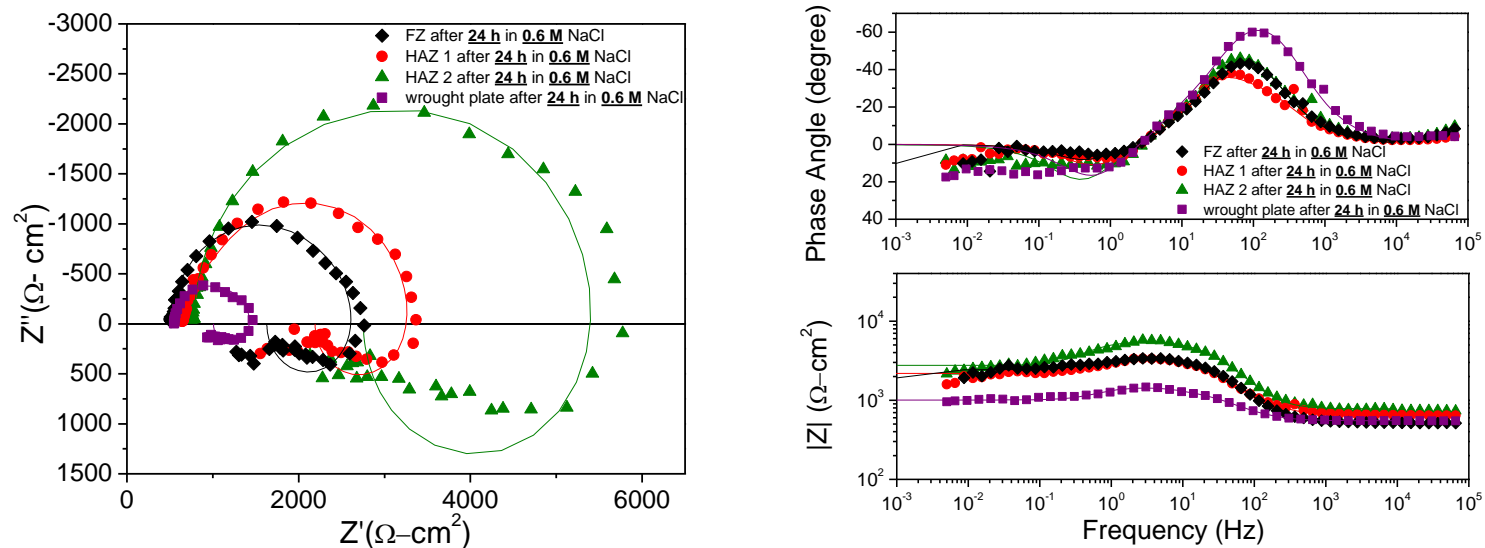
Figure 3. 17. (left) Nyquist plots and (right) Bode magnitude and phase plot for AZ31B-H24 isolated FZ, HAZ1, and HAZ2 weld zones. Data shown along with respective fits following 24 hrs immersion in 0.6 M NaCl at open circuit.
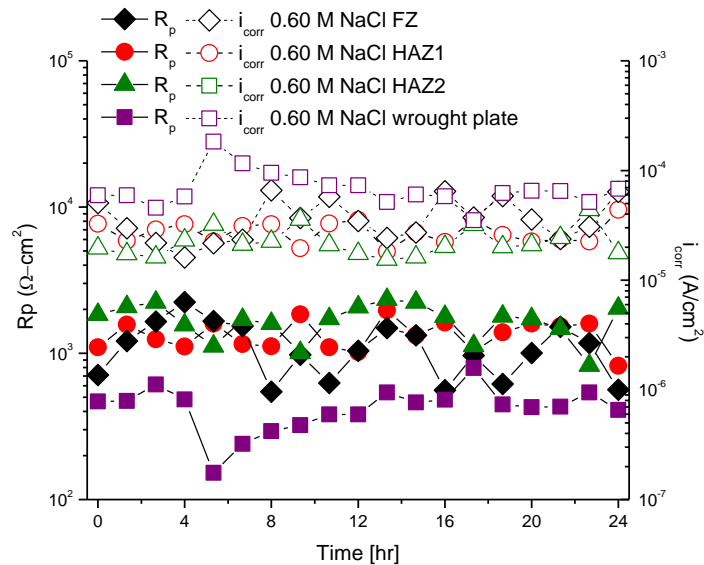
Figure 3. 18. Typical EIS-estimated polarization resistance and corresponding corrosion current density vs. time of exposure in 0.6 M NaCl on AZ31B-H24 as received and isolated FZ, HAZ1, and HAZ2 weld zones.
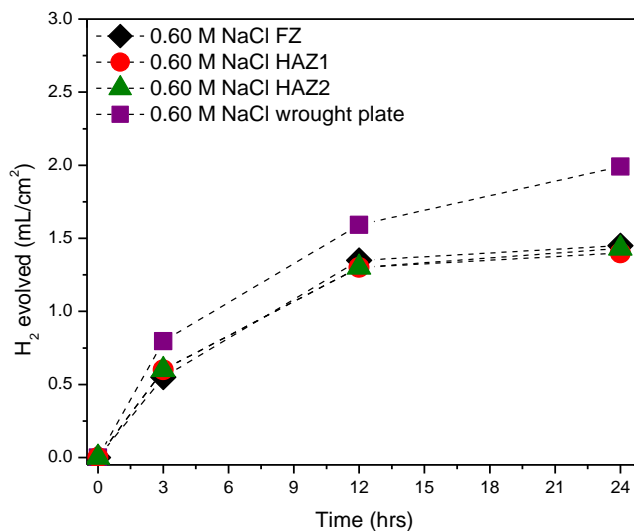
Figure 3. 19. A typical dataset showing the H_2 evolved upon AZ31B-H24 wrought plate and isolated TIG weld zones at 0,3,12, and 24 hrs in 0.6 NaCl at open circuit.
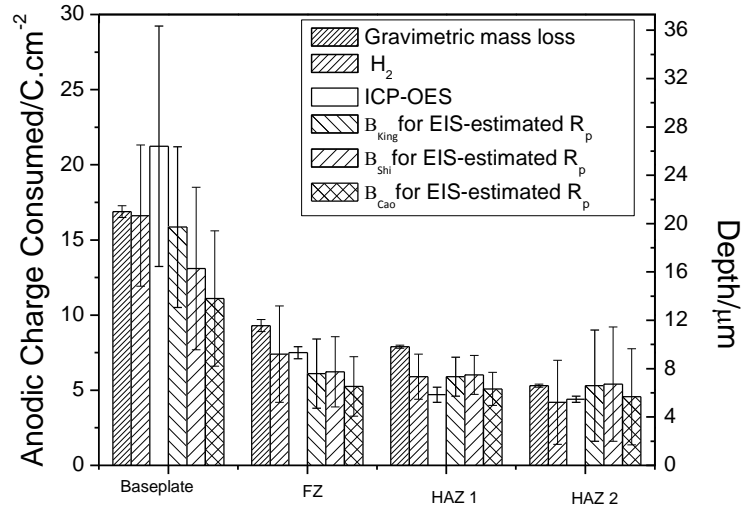
Figure 3. 20. Anodic charge consumed by wrought plate AZ31B-H24 and isolated weld zones in 0.6 M NaCl at open circuit after 24 hrs immersion as estimated by gravimetric mass loss, H_2 collection, ICP-OES, and EIS-estimated R_P where B_{King}=36.0 mV, B_{Shi}=36.8 mV[55], and B_{Cao}=31.1 in 0.6 M NaCl was used[44,45].

4 Metallurgical and Electrochemical Characterization of the Corrosion of a Mg-Al-Zn Alloy AZ31B-H24 Tungsten Inert Gas Weld: Galvanic Corrosion Between Weld Zones

Several techniques were used to investigate magnesium alloy, AZ31B-H24, joined by tungsten inert gas (TIG) welding, primarily utilizing multichannel multi-electrode arrays (MMAs) in conjunction with in-situ time lapse video, scanning electron microscope (SEM) and Raman surface analysis and mixed potential theory. Time lapse optical videos examined the dominant location of the hydrogen evolution reaction (HER) and darkening within the various weld zones which is considered characteristic of anodic zones and cathodic activation in Mg alloys. The galvanic coupling between electrochemically connected weld zones was investigated in 0.6 M NaCl, 0.6 M NaCl saturated with $Mg(OH)_2$ and tris(hydroxymethyl)aminomethane (TRIS). Anodically induced cathodic activation was also investigated after 3, 24 and 48 hour immersion times in 0.6 M NaCl and 0.1 M TRIS. The main goal was to characterize and explain the galvanic corrosion between weld zones with time. Both the heat affected zones (HAZ) and wrought base plate corrode initially relative to the fusion zone (FZ) in chloride environments. The variation in the galvanically coupled anodic dissolution rates between various weld zones and subsequent cathodic activation also caused polarity reversal between electrochemically connected zones and was an important factor in weld corrosion. The variation in the extent of this phenomenon can be explained by the presence of $Mg(OH)_2$ films. In welds the switching of anodes and cathodes is an important effect during galvanic corrosion compared to fixed galvanic couple rankings based on initial electrochemical properties. It was observed that cathodic activation and polarity reversal occurred to a far greater extent in the chloride environments than in TRIS.

Representative author contributions:

Leslie G. Bland: experiments, metallurgical and electrochemical characterization
B.C. Rincon Troconis: setup of the multichannel multi-electrode array and analysis
R.J. Santucci: Raman Spectroscopy and analysis
J.M. Fitz-Gerald: metallurgical characterization interpretation, analysis
J.R. Scully: Adviser, analysis and interpretation

4.1 Introduction

Mg-Al alloys are of interest for aerospace and automotive industries.[1,2] In particular, the effect of fusion welding on the intrinsic corrosion properties of magnesium (Mg) is a concern for the application of Mg structures should this joining strategy become of interest. However, the metallurgy of these fusion welded structures must first be understood at the multiple length scales that affect corrosion properties.

4.1.1 Galvanic Corrosion in Mg Alloys

The corrosion behavior of Mg and its alloys is complex as a result of the micro-galvanic cells which are formed in the material due to small differences in electrochemical potential between the α-Mg matrix and secondary phases.[3-5] The variation in this galvanic coupling is highly dependent on the alloying elements added into solution above or below their solubility limits[4] and the intermetallic particles (IMPs)[6] in the material. The addition of fusion welding techniques, such as Tungsten Inert Gas (TIG) welding, can further complicate this issue by forming various weld zones in the material, each of which can have individual electrochemical potentials due to differences in grain size, crystallographic texture, solidification structures and intermetallic particles (IMPs) as described in previous work.[7]

4.1.2 Galvanic Corrosion in Welds

In a fusion weld, different zones are formed during welding (Figure 4. 1). The fusion zone (FZ) is completely melted and resolidified.[8] This zone contains fine equiaxed grains as well as secondary phases which consist of intermetallic particles (IMPs) [9,10] and solidification structures and is typically characterized by a randomized texture.[11] Also several heat affected zones (HAZs) are formed. These are compositionally similar to the starting wrought base and retain the basal texture seen in AZ31 wrought base[11] but have variations in grain size and particle distribution due to non-uniform heating and cooling temperature variations across the weld.

These small variations in the metallurgy can cause dramatic changes in the electrochemical potentials of the individual weld zones and lead to the development of micro-galvanic cells which accelerate the corrosion rate of the overall weld. Therefore, when these regions are tested in electrical contact, the corrosion rate is expected to be higher than if the weld regions are tested in isolation.[7] The resulting galvanic corrosion rate is studied herein.

Galvanic corrosion rates between the wrought base and the full weld zone have been studied[12,13] but much of this literature focuses on comparing the corrosion rate of these

weldments in salt fog or atmospheric tests and does not investigate the corrosion rate of these welds in full immersion testing using electrochemical and other diagnostics.[12] While there is a significant quantity of literature on Mg,[14-21] most focus on the isolated weld zones using techniques such as microcapillary techniques,[22] solid state welding,[17,18,23,24] or small area test measurements.[7] However, once coupled, a pertinent focus is the galvanic couple potential relationships and polarity, with respect to anode or cathode, of each zone over time with respect to each other.

4.1.3 Anodically Induced Cathodic Activation

In current work as well as the study herein, the phenomenon of anodically induced cathodic activation has been cited to occur in the Mg system and plays a role in open circuit corrosion and contributes to explaining the negative difference effect (NDE).[25-27] Several potential explanations have been proposed including, transition metal enhancement[26] on the sample surface, formation of a semi-protective surface film[27,28] and Al replating.[29] This enrichment[26] or replating[29] will increase the cathodic reaction rate over time and ennoble the sample surface. It has been proposed that increased anodic activity on the sample surface can occur with time as a result of enhanced cathodic processes.[30,31] The result of this with time is an increase in the HER on the sample surface[27] at strong cathodes.[30] The increase in cathodic kinetics will also affect the interactions and galvanic relationships between weld zones and the resulting polarity of each zone. This important aspect has never been considered in weld zone corrosion.

4.1.4 Polarity Reversal Brought About by Galvanic Coupling Between Weld Zones

Galvanic couples between electrochemically connected weld zones can cause polarity reversal due to rapid changes in surface chemistry on the respective anodes and cathodes on the exposed weld. For instance, elements may be replating[29] or enriched.[32] Many material systems undergo a polarity reversal during galvanic corrosion. In particular, the polarity reversals between steel and Zn[33,34] and steel and Al[35] have been studied. Polarity reversal is typically due to a change in the surface condition of the coupled metals.[36] This polarity reversal is also highly dependent on the environmental conditions such as dissolved ions, pH and time of immersion. In the steel-Zn couple, passivation of the zinc surface and a sufficient amount of dissolved oxygen leads to this polarity reversal.[16,17] In addition, in the steel-Al couple, polarity reversal occurs in environments where Al alloys are used as sacrificial anodes for steel. It is well known that the

corrosion potential depends on the level of passivity on the alloy[37] and this passive film growth can alter the polarity between steel and Al when coupled.

For Mg, this alteration of the surface condition can occur due to the rapid formation and breakdown of the semi-protective and porous film.[38-41] Similarly, it has been hypothesized that Mg and its alloys suffer from enhanced cathodic activity due to the enrichment of transition metals.[26,32] In this work and previous work by the authors[7], cathodic activation has been shown to occur in the different weld zones, which causes initially anodic weld regions to change polarity and become cathodic weld regions with increased immersion time.

Multichannel multi-electrode arrays (MMAs) are ideal for online real-time monitoring of localized corrosion rate.[42,43] The MMA enables the measurement of the electrochemical current of each addressed electrode within the array, separately and simultaneously. The use of this technique enables investigation of a simplified geometric weld scenario in order to define the corrosion current through a specific spatial distribution. Work on MMAs in galvanic scenarios has been used previously[42,44] and have been successful at determining the corrosion rate related with localized phenomenon such as crevice corrosion.[42,45] In particular, MMAs have been used to observe the corrosion rate in systems which show non-uniform corrosion characteristics and in systems in which polarity reversal is observed when connected electrochemically, such as the polarity reversal seen in Zn-Steel galvanic couples.[46]

4.1.5 Objective

The objective of the work herein is to understand the galvanically controlled corrosion in fusion welded AZ31B-H24. The already published work is related to understanding how to determine the corrosion rate of the wrought base[41] form of these alloys and the isolated weld zones[7] but, further understanding regarding the galvanic coupling effects within the weld is also of interest. Both whole welds and weld array electrodes were investigated. In addition to the electrode configuration, various corrosion environments are investigated. Better understanding into the variables that have an impact on the galvanic corrosion in Mg welds will enable industrial application where this joining strategy is of interest.

4.2 <u>Experimental Procedures</u>

4.2.1 Materials

AZ31B-H24 sheet was provided by Magnesium Elektron. All compositions are reported in wt. %, with the actual compositions provided by QUANT (Quality Analysis and Testing Corporation) via Inductively Coupled Plasma optical Emission Spectroscopy (ICP-OES) analysis as given in Table 4.1.

4.2.2   Weld Metallurgical Characterization

All samples were fabricated by TIG welding a sandwich structure as shown in (Figure 4.1). The top plate was drilled and countersunk at 45° to approximately 0.635 cm in diameter and welded to the bottom plate along the periphery of the countersunk hole. The Miller Syncrowave 200 TIG welder was operated at 125 A under argon gas at 48.3 kPa with a flow rate of 18.5 L/min, and air cooled. This process created large metallurgical weld zones for easy study both in isolation and in the MMA. All samples were prepared on material freshly ground through 240 grit to remove any oxides formed before processing. Irradiated regions were investigated and compared to the baseline starting materials. All samples were examined along the *SL* surface, polished through colloidal silica and etched with a picric acid etch (3g picric acid, 30 mL acetic acid, 100 mL ethanol and 15 mL distilled water) to determine the grain size and microstructure.

Samples were analyzed with optical microscopy as well as scanning electron microscopy (SEM) using a FEI Quanta 650 microscope. Compositional analysis was performed using energy dispersive spectroscopy (EDS) methods.[47] Images were recorded at a working distance of 10 mm while operating at an accelerating voltage of 5 kV. Electron Backscatter Diffraction (EBSD) was performed while operating at an accelerating voltage of 20 kV.The composition of the IMPs, solidification boundaries, FZ, HAZs and wrought material were determined using rigorous EDS compositional analysis with ZAF corrections (where Z is the atomic number correction, A is the absorption correction and F is the fluorescence correction) on the Aztec software tool.[47] The distribution and area fraction of the Al-Mn-Fe IMPs as well as Al-Zn solidification boundaries were determined using the ImageJ[TM] software package.[48] At least three measurements were analyzed for both grain size and composition and an averaged were reported. Standard error from these runs has been reported where appropriate.

4.2.3 Galvanic Corrosion Determination of AZ31 TIG Welds

Samples were immersed for 3, 24, or 48 hours at open circuit potential (OCP) with the weld zones electrochemically connected in aerated 0.6 M NaCl before isolating each zone using electroplaters tape with a 1.23 mm^2 hole. This range in immersion time allowed for time-based development of the cathodic activation of each zone as a function of immersion time of the galvanically connected weld zones. The cathodic behavior of the weld zones was determined by a cathodic potentiodynamic polarization scan ranging from 50 mV above OCP to -2.3 V below OCP in a downward sweep at a rate of 1 mV/second. A Pt mesh was used as a counter electrode and a saturated calomel electrode (SCE) was used as the reference electrode.

The corrosion morphology was observed near the interface between the weld zones to determine how the corrosion morphology varied between weld zones when electrochemically connected in the solution. SEM micrographs of each of the weld regions were taken before and after immersion in 0.6 M NaCl, 0.6 M NaCl saturated with $Mg(OH)_2$ and tris(hydroxymethyl)aminomethane (TRIS) for 3 hours at OCP. The starting pH's of these environments were 5.3, 10.2 and 7.0 respectively. The pH after immersion for 24 hours of both NaCl mixtures was approximately 11. The TRIS solution functions as a buffer and retains the same pH over the full immersion period. The conductivity of the 0.6 M NaCl is 7.6×10^{-2} (ohm-cm)$^{-1}$ while the conductivity of 0.1 M TRIS is 1.97×10^{-4} (ohm-cm)$^{-1}$. Following testing, samples were cleaned following the ASTM G1-03 standard by using chromic acid solution (200 g/L CrO_3) to remove any corrosion product [49]. It should be noted that, after immersion in the chloride environments, SEM analysis (not included) showed a large amount of $Mg(OH)_2$ corrosion product similar to that observed in other works.[30,50,51] Raman spectroscopy and EIS were used to detect surface films. Before the initial corrosion, the sample was marked using a Vickers hardness tester to enable examination of the corrosion morphology in precise locations. The progression of the corrosion morphology was studied with time using a Dinolite optical microscope with time-lapse video and SEM imaging. The software package, ImageJ[TM], was used to calculate the area-fraction of the sample surface which was corroded with time.[48] The area-fraction was determined at 3, 12 and 24 hours of immersion using selected SEM images in the isolated case and time-lapsed optical videos for the galvanically connected case. The standard error is reported.

The galvanic currents of coupled weld zones were determined using a zero resistance ammeter (ZRA) in a flat cell.[52,53] The samples were coupled with one isolated weld zone as the working electrode (WE) and another isolated weld zone as the counter electrode (CE). The FZ was always assigned as the CE for each galvanic couple and the individual HAZ or base was always designated as the WE. Therefore, a positive current indicates that the HAZ was the anode. The cathode to anode ratio was kept at 1:1 with each of the weld zones isolated using electroplaters tape with a 1.23 mm^2 hole. All galvanic couples were tested at least three times and the reproducible trends are reported herein.

MMAs were also used to determine the current from the galvanically connected weld zones. The weld was sectioned into 12 sections where each electrode had a surface area of 3 mm^2 (Figure 4. 2). The individual weld zones were mounted in epoxy resin and separated using a 0.13 mm shim to fully electrically isolate individual weld zone sections while still keeping the spatial resolution on the same scale as the actual weld. In a realistic weld, the weld zones have different sizes; therefore, this was taken into account on the design of the MMA by controlling the number of channels used. Large weld zones were assigned more channels, while smaller weld zones were assigned fewer channels according to their approximate size in the weld. The approximate area fractions of the actual weld were determined by ImageJ^{TM}.[48] The measured areas for each weld zone were used to calculate the surface area fraction, giving values of 33, 33, 16.5 and 16.5 % for the wrought base, HAZ2, HAZ1 and FZ, respectively. Therefore, 4, 4, 2 and 2 equal surface area electrodes and ZRA channels were used for the weld sections, respectively. A Scribner model MMA910B was used to provide a graphical interface and data acquisition of each microelectrode current. The MMA910B is capable of galvanically coupling and measuring up to 100 working electrode current channels and contains an individual ZRA on each current channel with a measurable current range of 3.3 nA to 100 μA per channel. Neither a counter electrode nor a reference electrode was used in this study as only localized galvanic currents were obtained. Samples were immersed in 0.6 M NaCl, 0.6 M NaCl saturated with Mg(OH)$_2$ as well as TRIS to examine how the corrosion changed with the environment used. Each MMA environment was tested at least three times and a typical run is shown herein.

4.2.4 Oxide Characterization

Raman spectroscopy was performed utilizing a Renishaw InVia Raman Microscope for AZ31 samples after immersion in 0.6 M NaCl and 0.1 M TRIS environments for 24 hours at

OCP. Samples were kept in solution until approximately 30 seconds before Raman spectroscopy was performed on the sample surface to alleviate any issues with air-formed oxide growth. All samples were analyzed utilizing a 514 nm wavelength laser operating at 100 mV under a 50x objective lens with 3000 l/mm grating. Raman analysis was performed on approximately three spots on the sample surface and a typical Raman spectrum is reported.

4.3 <u>Results</u>

4.3.1 Corrosion Morphology Between Electrically Connected Weld Zones

The corrosion rate of the isolated weld zones and the wrought base were reported elsewhere.[7,41] However, when intact welds are exposed in industrial service in the presence of an electrolyte, each zone of the weld is connected (i.e., electrically and ionically).

Concerning the intact weld, SEM and EBSD were taken along the edge of the FZ and HAZ in the same location before and after corroding the sample for 3 hours at OCP in 0.6 M NaCl as shown in Figure 4. 3. From the metallurgy of the individual weld zones as summarized in Figure 4. 3, the FZ had a strongly randomized texture commensurate with grains solidified from the melt (Figure 4. 3(b)). Also, a variation in compositional contrast Figure 4. 3(a) revealed Al-Zn rich solidification boundaries formed during non-equilibrium processing in the FZ, as reported previously.[7,54] The α-Mg matrix in this zone was depleted of Al and Zn alloying elements as determined by EDS (Table 4. 1). From the corrosion morphology, it was observed that the corrosion propagated in or along the solidification boundaries in the FZ and in proximity to the Al-Mn-Fe IMPs.[7] The HAZs have their own distinct metallurgical features including a persistent basal texture ((Figure 4. 3(b)) originating from the baseplate texture combined with grain growth and an α-Mg matrix composition which was similar to the wrought base (Table 4. 1). Many Al-Mn and Al-Mn-Fe particles were detected throughout this zone and their compositions are listed in Table 4. 1. Concerning the corrosion morphology, the HAZ corroded predominantly by the filiform corrosion morphology (Figure 4. 3(c)) along the *SL* surface in the *L* direction.

In 0.6 M NaCl solution saturated with $Mg(OH)_2$, the corrosion morphology in the FZ (Figure 4. 4 (a-b)) was similar to that seen in only 0.6 M NaCl with corrosion propagating at the solidification boundaries and proximate to IMPs. In the HAZ1 and HAZ2, (Figure 4. 4(c-f)) the filiform morphology was dominantly observed. The filiform filaments grew along the *SL*

118

surface of the material. Much of the filiform corrosion initiated near the Al-Mn-Fe IMPs throughout the material and many of these particles remained on the samples surface even after corrosion (circled in orange).

The AZ31B TIG weld was also immersed in a non-chloride environment, TRIS (chemistry in methods). The FZ (Figure 4. 5(a-b)) was rather more uniformly corroded than in the chloride containing environments. However, this corrosion morphology propagated further than in the case of the chloride environments (Figure 4. 3(c) and 4. 4(b)). In the HAZs (Figure 4. 5 (c-f)), the corrosion was much more extensive than in the chloride containing environments (Figures 4. 3(c), 4. 4(d), and 4. 4(f)). In both of these weld zones, the Vickers microhardness indentation were mostly eliminated presumably due to surface recession. However, there is a different pattern or morphology with slight *L* directionality along the *SL* surface. Also, none of the Al-Mn-Fe particles that were originally on the sample surface were detected after corrosion.

4.2.3 Evolution of Darkened, Cathodically Activated Regions in AZ31B TIG Weld

It has been shown in the literature, that as the material corrodes, the surface becomes dark[55] and this region typically contains enriched transition elements[32,56] or replated Al and Al^{3+} deposits.[29] Scanning vibrating electrode technique (SVET) measurements show enhanced cathodic reactions at the edge of these regions where anodic reactions are enhanced.[17,28,55] Dark regions are typical of the anodic Mg dissolution morphology that develops in chloride containing solutions.[55] The values found for 0.6 M NaCl are statistically similar in the 0.6 M NaCl saturated with $Mg(OH)_2$. Figure 4. 6(a) contains the percent of dark surface area for each weld zone in isolation and Figure 4. 6(b) contains the percent surface area for each weld when galvanically connected. The wrought base material has the greatest percentage of this corroded region formed compared to any TIG weld zones, both in the case of isolated weld zones[7] and for the galvanically connected weld. The FZ has the next highest percent area corroded, compared to the HAZs, for both the isolated and the galvanically connected welds after 24 hours. The percent area corroded in the galvanic case is slightly higher for each zone when galvanically connected (Figure 4. 6(b)) compared to the percent area corroded in isolation (Figure 4. 6 (a)). This corresponds to the higher corrosion rates observed when the weld zones are electrochemically connected in contrast to the situation when the weld zones are corroded in isolation.[7]

4.3.3 Binary Galvanic Corrosion Between Electrochemically Connected Weld Zones

The apparent galvanic corrosion density of the isolated weld zones in electrochemical connection to other weld zones was measured over a 24 hour period. In 0.6 M NaCl, the FZ was electrically connected to the HAZ1 (Figure 4. 7). The galvanic potential of the FZ and HAZ1 immediately after immersion was -1.52 V_{SCE} but decreased, after 3 hours, to -1.60 V_{SCE} (Figure 4. 7(a)). Initially, the HAZ1 was the anode and the FZ was the cathode in the galvanic couple between the FZ and HAZ1. However, after 3 hours, the polarity between the zones switched and the FZ became the anode (Figure 4. 7(b)). Connecting FZ to the HAZ2 had similar results. The galvanic potential of the FZ and HAZ2 zones were approximately -1.54 V_{SCE} when initially immersed but decreased to -1.59 V_{SCE} after 3 hours. The HAZ2 was initially the anode but switched polarity after 3 hours and the FZ became the anode. In the galvanic couple containing the FZ and the wrought base, the galvanic potential was approximately -1.57 V_{SCE} initially but increased to -1.53 V_{SCE} after longer immersion times. The FZ was the anode initially but the wrought base became the anode after 3 hours.

In 0.6 M NaCl saturated with $Mg(OH)_2$, the galvanic potential and current were also measured (Figure 4. 8). The galvanic potential between the FZ and the HAZ1 was -1.55 V_{SCE} immediately after immersion and then -1.58 V_{SCE} after 24 hours (Figure 4. 8 (a)). The HAZ1 initially was the anode but, after 3 hours, the polarity reversed and the FZ became the anode (Figure 4. 8(b)). The galvanic couple potential of the FZ and HAZ2 couple was initially -1.44 V_{SCE} and then decreased to -1.54 V_{SCE}. The HAZ2 initially functioned as the anode but, after 3 hours, the polarity reversed and the FZ became the anode. The galvanic couple potential for the FZ and the wrought base was -1.55 V_{SCE} at hour 0 and -1.51 V_{SCE} at 24 hours. Initially, the FZ was the anode but, after 3 hours, the polarity reversed and the wrought base became the anode.

The samples were next immersed in the non-chloride containing environment, TRIS (Figure 4. 9). No polarity reversal was seen in this environment. The galvanic couple potential of the FZ and HAZ1 was initially -1.59 V_{SCE} and was -1.39 V_{SCE} after 24 hours (Figure 4. 9(a)). In the FZ to HAZ1 galvanic couple, the HAZ1 was the anode the full 24 hours (Figure 4. 9(b)). When FZ was immersed in connection with HAZ2, the galvanic couple potential was measured to be -1.68 V_{SCE} immediately after immersion and -1.42 V_{SCE} at 24 hours. In the FZ to HAZ2 galvanic couple, the HAZ2 was the anode the full 24 hours. The galvanic couple potential for the FZ and wrought base couple was initially -1.68 V_{SCE} and then -1.42 V_{SCE} after the 24 hour

immersion time. In the FZ to wrought base galvanic couple, the wrought base was the anode for the entire 24 hours. Hence, polarity switching was not observed generally in TRIS.

4.3.4 Multi-electrode Array of Sectioned Weld Zones

The MMA was tested in the same three environments. In 0.6 M NaCl (Figure 4. 10), there was a variation in the current measured with time. Different zones also underwent anodically induced cathodic activation, which was demonstrated by a polarity reversal in the measured current (Figure 4. 10). The currents switched from initially positive and anodic to negative in a consistent sequence. When the sectioned weld zone initially activated, there was an abrupt increase in the measured positive current, which remained high for a similar time seen in binary galvanic couple experiments. Then, the activated weld section became slightly less anodic, but remained positive for an additional period of time until the polarity was reversed (the current became negative). The HER was observed to occur dominantly on these anoidcally activated weld regions during this polarity reversal. The time interval of this cathodic activation was not the same for each weld region. Eventually each anodic weld zone section deactivated and then became a strong cathode. Examining at the current, the strongest anode, after deactivation, became a strong cathode. The wrought base and HAZ2 were the most likely to undergo anodically induced cathodic activation.

Concerning the MMA as exposed in 0.6 M NaCl saturated with $Mg(OH)_2$ a similar trend was shown (Figure 4. 11). Each zone activated with time and after anodic activation the channel suffered a polarity shift and became a strong cathode eventually. This cathodic current then slightly decreased. After some period of time, all anodically induced cathodically activated weld zones became strong canthodes.

A different trend was shown in the MMA exposed in TRIS (Figure 4. 12). Immediately after immersion, one of the wrought base zones started as an anode. Examining this same channel (green) at the end of the 24 hour test, it had become a cathode. Similarly, the FZ (grey) started as a strong cathode but ended as an anode. However, the changes were not as significant. While some polarity reversal was observed on various channels, there was much less than previously seen in the chloride environments and less anodically induced cathodic activation was observed (Figure 4. 10-4. 12).

4.3.5 Analysis of the Oxide Surface Film on AZ31B TIG Weld

A variation in the oxide formation may alter the corrosion response, including the polarity reversal and resultant anodically induced cathodic activation. The pH for the chloride containing environments before exposure was typically around 6.5 before becoming more alkaline with the generation of OH^-, ~11. However, the pH of TRIS was 7 after exposure, which does not allow for Mg to as readily passivate. This is confirmed through the use of Raman spectroscopy (Figure 4. 13). All scans were taken with the same instrumental parameters so they can be comared fairly. Fitting of the Raman shift to the characteristic $Mg(OH)_2$ peaks showed a strong presence of the $Mg(OH)_2$ film in the chloride containing 0.6 M NaCl solution. However, these peaks had less intensity in the TRIS solution which suggested that only a small amount of $Mg(OH)_2$ was formed. This variation in the oxide thickness with exposure environment may lead to a variation in the corrosion response.

4.3.6 Evolution of Cathodic Kinetics and OCP of AZ31B TIG Weld and Polarity Reversal

From the variation in the OCP with time (Figure 4. 14), the trend of the OCP differed depending on whether the weld zones were isolated or galvanically connected. When the weld zone OCPs were measured in isolation in 0.6 M NaCl (Figure 4. 14(a)), the highest OCP was observed for each weld zone after 3 hours, with the FZ having the most noble OCP. This is consistent with large Al-Mn or Al-Mn-Fe particles and Al-Zn solidification structures. A polarity reversal was observed between the weld zones around 12 hours coupled when measured in isolation with the OCP in order FZ>HAZ>Wrought base from 0 to 12 hours and HAZ>FZ>Wrought base from 12 to 24 hours. However, when the weld zones were galvanically connected and then disconnected to access OCP (Figure 4. 14(b)), the OCP increased over the 24 hour period for each weld zone and the highest OCP was measured at 24 hours. The polarity reversal for the galvanically connected weld zones occurred after only 3 hours where the OCP trend was FZ>HAZ>Wrought base from 0 to 3 hours but HAZ>FZ>Wrought base from 3 to 24 hours. These numbers were statistically similar to those achieved when $Mg(OH)_2$ was added to solution and have been excluded for redundancy.

However, the electrochemical behavior in the non-chloride, TRIS environment differed from the chloride environments (Figure 4. 15(a-b)). For both the isolated and galvanically connected weld zones, the measured OCP increased over the full 24 hour immersion. The largest increase from when the sample was first immersed up to 3 hours with only a small increase

between 3 hours and 24 hours. Only slight polarity reversal (Figure 4. 12) and little cathodic activation (Figure 4. 15) was seen during the 24 hour immersion and the magnitude of the OCP in order was FZ>HAZ1>HAZ2>Wrought base.

The OCP as a function of time and weld zone over a 24 hour immersion period in a chloride environment is shown in Figure 4. 16(a) for each weld zone after being galvanically connected for 3, 24 and 48 hours and at that point disconnected to measure OCP and assess cathodic kinetics. When the sample was first immersed, the FZ had the highest potential of each of the weld zones and OCP increased up to 3 hours of immersion for each weld zone. After 3 hours, the HAZs had more negative OCPs than the FZ. After 12 hours and continuing on to 48 hours, the OCP continued to increase for each galvanically connected weld zone. The net current as a function of weld zone was assessed for specified times to examine the current trends with time (determined by the MMA) (Figure 4. 16(b)) and different weld regions were cathodic at various times. Each weld zone activated at different times. To futher understand how the current changed at different locations with time, selected exposure times were selected and the cathodic current density (i_c) at -1.8 V_{SCE} was plotted as a function of weld zone for specified times (Figure 4. 16(c)). i_c increases with time for all weld regions (Figure 4. 16(c)), except for the HAZs where there was a slight decrease or no change after 24 hours. The increase was the greatest for the wrought base and the least for the HAZ2 over time. The large increase in i_c for the base material was consistent with anodically induced cathodic activation.[25,28] The net current as a function of weld zone for specified times is shown for the 0.6 M NaCl saturated with $Mg(OH)_2$ as well (Figure 4. 17). It was clear that different weld regions were cathodic at various times. The trend in the cathodic activation for the chloride containing environment saturated with $Mg(OH)_2$ was the same as the trend shown in 0.6 M NaCl and the variation in the OCP and i_c with time is excluded for brevity.

The OCP as a function of time and weld zone over a 24 hour immersion period in a non-chloride environment was shown (Figure 4. 18(a)) for each weld zone after being galvanically connected for 3, 24 and 48 hours and at that point disconnected to assess cathodic kinetics. It was observed that the OCP slightly ennobles for each weld zone with time and that the FZ was the most cathodic at each time step. Figure 4. 18(b) illustrates that different weld regions were cathodes at various times. It was also shown that, unlike in the chloride environments, multiple channels were cathodic at the same time. The variation in the net current was smaller than in the

123

chloride environments. The i_c at -1.8 V_{SCE} was plotted as a function of time in each of the isolated weld zones after 3, 24 and 48 hours in 0.6 M NaCl. In Figure 4. 18(c), there was a slight increase in the i_c with time; however, this increase was much smaller than observed in the chloride environments (Figure 4. 16). The FZ had the lowest i_c while the wrought base had the highest after each exposure time.

4.4 <u>Discussion</u>

4.4.1   Resultant Corrosion Morphology in FZ and HAZ

From the resultant corrosion morphology characterized through SEM imaging, several corrosion morphologies were seen in a weld. These corrosion morphologies were dependent on the weld zone and exposure environment. In the chloride environments, specifically 0.6 M NaCl and 0.6 M NaCl saturated with $Mg(OH)_2$ (Figure 4. 3-4. 4), the corrosion propagated along the Al-Zn solidification boundaries and proximate to Al-Mn-Fe particles within the FZ. These solidification boundaries were rich in the alloying elements and cathodic to the α-Mg (which has been depleted in Al and Zn (Table 4. 1)).[4] The galvanic couple formed between the α-Mg and the solidification structure caused the Mg directly adjacent to this solidification structure to corrode along with the α-Mg (Figure 4. 3(c),4. 4(b)). Similarly, the cathodic Al-Mn-Fe particles were affected during corrosion (Figure 4. 3(c),4. 4(b)). In the HAZ, the dominant corrosion morphology was filiform growth (Figure 4. 3(c), 4. 4(d) and 4. 4(f)). Al-Mn-Fe particles were distributed throughout the material. Filiform corrosion propagated in the proximity of these Al-Mn-Fe particles as has been reported in the AZ31 material[54,57,58] and other Mg alloys[59-63] (Figure 4. 3(c), 4. 4(d) and 4. 4(f)). This corrosion attack did not appear to be isolated to one grain, but rather propagated through several grains.

In TRIS (Figure 4. 5), the corrosion morphology was drastically different than the corrosion morphology seen in 0.6 M NaCl. In the FZ, the Al-Zn solidification boundaries and Al-Mn-Fe particles preferentially corroded due to a similar galvanic mechanism as in the chloride environment (Figure 4. 5(a-b)). The directionality of the corrosion propagation was slightly evident along the *SL* surface in the HAZs; however, the morphology uniformly covered the surface (Figure 4. 5(c-f)). The Al-Mn-Fe particles were not detected on the sample surface. In a TRIS environment, only a thin $Mg(OH)_2$ film was formed during corrosion as determined from

the weak $Mg(OH)_2$ Raman peaks (Figure 4. 13). Due to the thin $Mg(OH)_2$ film, the corrosion rate was higher with more uniform corrosion on all zones and phases.

4.4.2 Galvanic Corrosion Between Electrochemically Connected Weld Zones

There are small differences in the OCP between each of the weld zones (Figure 4. 14-4. 15). This will create a galvanic couple between the weld regions and increase the corrosion rate. These differences in the measured OCP are at first due to the microstructural and metallurgical features such as grain size, crystallographic orientation, solidification structures and IMPs. The electrochemically connected weld zones then interact with one another when immersed in the same solution for an extended period of time. Polarity reversals then start which tend to dominate the galvanic behavior instead of the initial microstructure. Due to this, cathodic activation is a key factor as it controls the polarity and galvanic couple relation (i.e. anode or cathode). These have all been factors in Mg corrosion and are the subject of ongoing studies.

4.4.3 Cathodic Kinetics of AZ31B TIG weld with time and film formation

The anodically induced cathodic kinetics as a result of AZ31B TIG welding varied depending on environment. In chloride environments, such as 0.6 M NaCl, cathodic activation occurred in all weld zones and lead to polarity reversal during galvanic coupling (Figure 4. 7-4. 8). This cathodic activation was monitored using a MMA to examine initial anodes and subsequently revealed which areas of the weld cathodically activated with time (Figure 4. 10-4. 12). In the chloride environments, individual weld sections functioned as anodes based on their starting OCP relative to the galvanic couple potential. However, these initial anode zones eventually were cathodically activated and then became strong cathodes. Most of the individual weld sections that became a strong anode subsequently became a strong cathode and the polarity was reversed during galvanic corrosion (Figure 4. 10-4. 11). Therefore, copious HER was seen to occur on those weld sections which became cathodically activated. In the TRIS environment, a large cathodic activation process was not observed (Figure 4. 12 and 4. 15). The HER occurred more uniformly across all of the weld sections. However, i_c increased somewhat when anode zones were interrogated (Figure 4. 18).

Considering the increase in i_c with time (Figure 4. 16(c)) in 0.6 M NaCl, it was clear that cathodic activation may occur in the base material as well as in the weld zones as determined by an increase in the cathodic kinetics and OCP with time. The variation in the i_c with time in TRIS

(Figure 4. 18(c)) was much smaller than in the chloride environments. This supports the observation that there is less cathodic activation in the non-chloride, TRIS environment.

The dark regions which expanded over the sample surface (Figure 4. 6) correlated to the anodic Mg dissolution reaction and show a similar correlation with corrosion rate and were observed in the chloride environments. The regions of the weld with the highest area fraction of dark region had the highest corrosion rates as determined previously.[7] Within the dark region, it has been hypothesized that metals other than Mg which typically remain as impurities within the sample, are not dissolved during the dissolution of Mg and are collected on the partially protective surface film[27,28,30,54,63] or replated.[64,65] Cathodic activation has been cited to frequently occur in both commercially pure Mg and Mg alloys such as AZ31[25] and has been determined using a variety of approaches.[26,32] It was typically stated that, over time in a commercially pure Mg sample, alloying elements or impurities will enrich to the sample surface while, in a Mg-Al alloy, cathodic activation can cause the enrichment of Al-Mn phases on the sample surface in the partially protective surface film.[27,28,30,54,63] This enrichment[26-28,30,54,63] or replating[64,65] will enoble the sample surface and will increase the cathodic reaction rate over time. In response to this enrichment or replating at the sample surface, the i_c will increase as well as cause the polarity reversal in weld zones. This process is an important factor in weld corrosion where the initial microstructure is important to the establishment of initial anodes and cathodes but the ability to undergo anodically induced cathodic activation plays a role in weld corrosion, even in 24 hours.

The variation in the film formation with environment may alter the corrosion rate and weld corrosion behavior. Samples with an $Mg(OH)_2$ film have a greater difference in OCP within each weld zone and a greater cathodic reaction rate. This finding is particularly evident in environments that allow a large amount of $Mg(OH)_2$ formation. Samples immersed in chloride-containing environments develop a thick $Mg(OH)_2$ layer while, in TRIS, only a thin film may be developed as shown through Raman spectroscopy (Figure 4. 13). It was observed that the polarity reversals and cathodic activation in TRIS were less extreme, which may be due to the variation of this film formation.

4.5 Conclusions

1. The corrosion of an AZ31B-H24 TIG weld varied with time and was dependent on the galvanic corrosion effects between electrochemically connected weld zones. All chloride

environments functioned similarly due to excess $Mg(OH)_2$ formation either as preloaded by $Mg(OH)_2$ additions or due to Mg^{2+} release with time. TRIS was dissimilar due to suppression of the thick surface film and buffered pH.

2. The cathodic activation of individual weld sections was dependent on environment where NaCl and NaCl saturated with $Mg(OH)_2$ showed large amounts of Anodically induced cathodic activation. However, in a non-chloride environment, TRIS, less of this anodically induced cathodic activation process was observed. From this study it was demonstrated that propensity for cathodic activation of each weld zone dominates the galvanic corrosion behavior over the long term compared to the metallurgy of each weld zone which was the dominant factor only at early times.

3. The OCP and cathodic kinetics, as a function of time, of a galvanically connected weld zone increased more with time than the OCP or cathodic kinetics of a single weld zone in isolation.

4. The FZ is initially the net cathode in galvanic couples. The HAZ and base are initially the net anode in galvanic couples.

References

1. C.H. Caceres, "Economical and Environmental Factors in Light Alloys Automotive Applications," Metall and Mat Trans A 38, 7 (2007): p. 1649-1662.
2. M. Hakamada, T. Furuta, Y. Chino, Y. Chen, H. Kusuda, and M. Mabuchi, "Life cycle inventory study on magnesium alloy substitution in vehicles," Energy 32, 8 (2007): p. 1352-1360.
3. T. Cain, L. Bland, N. Birbilis, and J. Scully, "A compilation of corrosion potentials for magnesium alloys," Corrosion 70, 10 (2014): p. 1043-1051.
4. K. Gusieva, C.H.J. Davies, J.R. Scully, and N. Birbilis, "Corrosion of magnesium alloys: the role of alloying," Int Mater Rev (2014): p. 169-194.
5. F. Gharavi, K.A. Matori, R. Yunus, and N.K. Othman, "Corrosion Behavior of Friction Stir Welded Lap Joints of AA6061-T6 Aluminum Alloy," Materials Research 17, 3 (2014): p. 672-681.
6. A.D. Südholz, N.T. Kirkland, R.G. Buchheit, and N. Birbilis, "Electrochemical Properties of Intermetallic Phases and Common Impurity Elements in Magnesium Alloys," Electrochemical and Solid-State Letters 14, 2 (2011): p. C5-C7.
7. L.G. Bland, J.M. Fitz-Gerald, and J.R. Scully, "Metallurgical and Electrochemical Characterization of the Corrosion of AZ31B-H24 Tungsten Inert Gas Weld: Isolated Weld Zones," Corrosion Journal In Press, (2015).
8. X. Cao, M. Jahazi, J.P. Immarigeon, and W. Wallace, "A review of laser welding techniques for magnesium alloys," J Mater Process Tech 171, 2 (2006): p. 188-204.
9. T. Zhu, Z.W. Chen, and W. Gao, "Microstructure formation in partially melted zone during gas tungsten arc welding of AZ91 Mg cast alloy," Mater Charact 59, 11 (2008): p. 1550-1558.
10. R.E. Reed-Hill and R. Abbaschian, Physical metallurgy principles (Boston: PWS-Kent Pub., 1992.
11. R.S. Coelho, A. Kostka, H. Pinto, S. Riekehr, M. Koçak, and A.R. Pyzalla, "Microstructure and mechanical properties of magnesium alloy AZ31B laser beam welds," Materials Science and Engineering: A 485, 1–2 (2008): p. 20-30.
12. A. Dhanapal, S.R. Boopathy, V. Balasubramanian, K. Chidambaram, and A.R.T. Zaman, "Experimental Investigation of the Corrosion Behavior of Friction Stir Welded AZ61A Magnesium Alloy Welds under Salt Spray Corrosion Test and Galvanic Corrosion Test Using Response Surface Methodology," International Journal of Metals 2013, (2013).
13. C.E. Cross, P. Xu, D. Eliezer, and G. Ben-Hamu, "Galvanic Weld Metal-Base Metal Corrosion in AZ31 Magnesium Weldments," Advanced Materials Research 95, (2010): p. 39-42.
14. M.M. Avedesian and H. Baker, "Magnesium and Magnesium Alloys," ASM International (1999).
15. L. Wang, J. Shen, and N. Xu, "Effects of TiO2 coating on the microstructures and mechanical properties of tungsten inert gas welded AZ31 magnesium alloy joints," Materials Science and Engineering: A 528, 24 (2011): p. 7276-7284.
16. M.B. Kannan, W. Dietzel, C. Blawert, S. Riekehr, and M. Koçak, "Stress corrosion cracking behavior of Nd:YAG laser butt welded AZ31 Mg sheet," Materials Science and Engineering: A 444, 1–2 (2007): p. 220-226.

17. J.R. Kish, G. Williams, J.R. McDermid, J.M. Thuss, and C.F. Glover, "Effect of Grain Size on the Corrosion Resistance of Friction Stir Welded Mg Alloy AZ31B Joints," J Electrochem Soc 161, 9 (2014): p. C405-C411.

18. N. Afrin, D.L. Chen, X. Cao, and M. Jahazi, "Microstructure and tensile properties of friction stir welded AZ31B magnesium alloy," Materials Science and Engineering: A 472, 1–2 (2008): p. 179-186.

19. L. Liming, W. Jifeng, and S. Gang, "Hybrid laser–TIG welding, laser beam welding and gas tungsten arc welding of AZ31B magnesium alloy," Materials Science and Engineering: A 381, 1–2 (2004): p. 129-133.

20. L. Liu and C. Dong, "Gas tungsten-arc filler welding of AZ31 magnesium alloy," Mater Lett 60, 17–18 (2006): p. 2194-2197.

21. T. Zhu, Z.W. Chen, and W. Gao, "Incipient melting in partially melted zone during arc welding of AZ91D magnesium alloy," Materials Science and Engineering: A 416, 1–2 (2006): p. 246-252.

22. Y. Savguira, T.H. North, and S.J. Thorpe, "Microcapillary polarization measurements of friction stir spot welds made in AZ31B magnesium alloy," Materials and Corrosion 65, 11 (2014): p. 1055-1061.

23. N. Afrin, D.L. Chen, X. Cao, and M. Jahazi, "Strain hardening behavior of a friction stir welded magnesium alloy," Scripta Mater 57, 11 (2007): p. 1004-1007.

24. R.P. Dobriyal, B.K. Dhindaw, S. Muthukumaran, and S.K. Mukherjee, "Microstructure and properties of friction stir butt-welded AE42 magnesium alloy," Materials Science and Engineering: A 477, 1–2 (2008): p. 243-249.

25. N. Birbilis, A.D. King, S. Thomas, G.S. Frankel, and J.R. Scully, "Evidence for enhanced catalytic activity of magnesium arising from anodic dissolution," Electrochim Acta 132, 0 (2014): p. 277-283.

26. T. Cain, S.B. Madden, N. Birbilis, and J.R. Scully, "Evidence of the Enrichment of Transition Metal Elements on Corroding Magnesium Surfaces Using Rutherford Backscattering Spectrometry," J Electrochem Soc 162, 6 (2015): p. C228-C237.

27. G. Williams, N. Birbilis, and H.N. McMurray, "The source of hydrogen evolved from a magnesium anode," Electrochemistry Communications 36, 0 (2013): p. 1-5.

28. G. Williams, H. ap Llwyd Dafydd, and R. Grace, "The localised corrosion of Mg alloy AZ31 in chloride containing electrolyte studied by a scanning vibrating electrode technique," Electrochim Acta 109, 0 (2013): p. 489-501.

29. A. Wingersky, A. Handler, J. Fisher, A. Weiss, and K. Sieradzki, "Dealloying of Magnesium Alloys," Meeting Abstracts MA2015-02, 13 (2015): p. 661.

30. M. Taheri, J.R. Kish, N. Birbilis, M. Danaie, E.A. McNally, and J.R. McDermid, "Towards a Physical Description for the Origin of Enhanced Catalytic Activity of Corroding Magnesium Surfaces," Electrochim Acta 116, (2014): p. 396-403.

31. G.S. Frankel, A. Samaniego, and N. Birbilis, "Evolution of hydrogen at dissolving magnesium surfaces," Corros Sci 70, (2013): p. 104-111.

32. N. Birbilis, T. Cain, J.S. Laird, X. Xia, J.R. Scully, and A.E. Hughes, "Nuclear Microprobe Analysis for Determination of Element Enrichment Following Magnesium Dissolution," J Electrochem Soc 4, 10 (2015): p. C34-C37.

33. P. Gilbert, "An investigation into the corrosion of zinc and zinc-coated steel in hot waters," Sheet Metal Industries 10, (1948): p. 2003-2012.

34. G. Schikorr, "The cathodic behavior of zinc versus iron in hot tap water," Transactions of the Electrochemical Society 76, 1 (1939): p. 247-258.

35. D. Gabe and A.E. Hassan, "Potential reversals for aluminium alloy-mild steel galvanic couples in simulated natural waters," British Corrosion Journal 21, 3 (1986): p. 185-190.

36. X.G. Zhang, *Uhlig's Corrosion Handbook*, R.W. Revie, Editor. 2011.

37. Z. Szklarska-Smialowska, "Pitting corrosion of aluminum," Corros Sci 41, 9 (1999): p. 1743-1767.

38. Y. Zhu, G. Wu, Y.H. Zhang, and Q. Zhao, "Growth and characterization of $Mg(OH)_2$ film on magnesium alloy AZ31," Appl Surf Sci 257, 14 (2011): p. 6129-6137.

39. M. Taheri, R.C. Phillips, J.R. Kish, and G.A. Botton, "Analysis of the surface film formed on Mg by exposure to water using a FIB cross-section and STEM–EDS," Corros Sci 59, 0 (2012): p. 222-228.

40. S.H. Salleh, S. Thomas, J.A. Yuwono, K. Venkatesan, and N. Birbilis, "Enhanced hydrogen evolution on Mg $(OH)_2$ covered Mg surfaces," Electrochim Acta 161, (2015): p. 144-152.

41. L.G. Bland, A.D. King, N. Birbilis, and J.R. Scully, "Assessing the Corrosion of Commercially Pure Magnesium and Commercial AZ31B by Electrochemical Impedance, Mass-loss, Hydrogen Collection and ICP-OES Solution Analysis," Corrosion Journal 71, 2 [Special Issue] (2015): p. 128-145.

42. N.D. Budiansky, F. Bocher, H. Cong, M.F. Hurley, and J.R. Scully, "Use of Coupled Multi-Electrode Arrays to Advance the Understanding of Selected Corrosion Phenomena," Corrosion 63, 6 (2007): p. 537-554.

43. L. Yang and K.T. Chiang, "A Review of Coupled Multielectrode Array Sensors for Corrosion Monitoring and a Study on the Behaviors of the Anodic and Cathodic Electrodes," Journal of ASTM International 6, 3 (2009).

44. A.D. King, J.S. Lee, and J.R. Scully, "Galvanic Couple Current and Potential Distribution between a Mg Electrode and 2024-T351 under Droplets Analyzed by Microelectrode Arrays," J Electrochem Soc 162, 1 (2015).

45. F. Bocher and J.R. Scully, "Stifling of Crevice Corrosion and Repassivation: Cathode Area Versus Controlled Potential Decreases Assessed with a Coupled Multi-Electrode Array," Corrosion 71, 9 (2015): p. 1049-1063.

46. D.-L. Zhang, W. Wang, and Y. Li, "An electrode array study of electrochemical inhomogeneity of zinc in zinc/steel couple during galvanic corrosion," Corros Sci 52, 4 (2010): p. 1277-1284.

47. "AZtecEnergy: EDS Software," Oxford Instruments (2015).

48. C.A. Schneider, W.S. Rasband, and K.W. Eliceiri, "NIH Image to ImageJ: 25 years of image analysis," Nature Methods 9, (2012): p. 671-675.

49. ASTM-G1, "Standard Practice for Preparing, Cleaning, and Evaluating Corrosion Test Specimens," ASTM International G1, (2011).

50. R.C. Phillips and J.R. Kish, "Nature of Surface Film on Matrix Phase of Mg Alloy AZ80 Formed in Water," Corrosion 69, 8 (2013): p. 813-820.

51. M. Taheri and J.R. Kish, "Nature of Surface Film Formed on Mg Exposed to 1 M NaOH," J Electrochem Soc 160, 1 (2013): p. C36-C41.

52. R. Baboian, "Electrochemical Techniques for Predicting Galvanic Corrosion," ASTM STP 576 (1976): p. 5-19.

53. ASTM-81, "Standard Guide for Conducting and Evaluating Galvanic Corrosion Tests in Electrolytes," ASTM International G71, (2014).

54. Z.P. Cano, M. Danaie, J.R. Kish, J.R. McDermid, G.A. Botton, and G. Williams, "Physical Characterization of Cathodically-Activated Corrosion Filaments on Magnesium Alloy AZ31B," Corrosion 71, 2 (2015): p. 146-159.

55. G. Williams and H.N. McMurray, "Localized Corrosion of Magnesium in Chloride-Containing Electrolyte Studied by a Scanning Vibrating ElectrodeTechnique," J Electrochem Soc 155, 7 (2008): p. C340-C349.

56. D. Höche, C. Blawert, S.V. Lamaka, N. Scharnagl, C. Mendis, and M.L. Zheludkevich, "The effect of iron re-deposition on the corrosion of impurity-containing magnesium.," Physical Chemistry Chemical Physics 18, 2 (2015): p. 1279-1297.

57. A. Samaniego, I. Llorente, and S. Feliu Jr, "Combined effect of composition and surface condition on corrosion behaviour of magnesium alloys AZ31 and AZ61," Corros Sci 68, (2013): p. 66-71.

58. L. Wang, T. Shinohara, and B.-P. Zhang, "Influence of chloride, sulfate and bicarbonate anions on the corrosion behavior of AZ31 magnesium alloy," J Alloy Compd 496, 1–2 (2010): p. 500-507.

59. O. Lunder, J.E. Lein, S.M. Hesjevik, T.K. Aune, and K. Nişancioğlu, "Corrosion morphologies on magnesium alloy AZ 91," Materials and Corrosion 45, 6 (1994): p. 331-340.

60. M.P. Brady, G. Rother, L.M. Anovitz, K.C. Littrell, K.A. Unocic, H.H. Elsentriecy, G.-L. Song, J.K. Thomson, N.C. Gallego, and B. Davis, "Film Breakdown and Nano-Porous Mg(OH)2 Formation from Corrosion of Magnesium Alloys in Salt Solutions," J Electrochem Soc 162, 4 (2015): p. C140-C149.

61. R.C. Zeng, J. Zhang, W.J. Huang, W. Dietzel, K.U. Kainer, C. Blawert, and W. Ke, "Review of studies on corrosion of magnesium alloys," T Nonferr Metal Soc 16, (2006): p. s763-s771.

62. E. Ghali, W. Dietzel, and K.U. Kainer, "General and localized corrosion of magnesium alloys: A critical review," J Mater Eng Perform 13, 1 (2004): p. 7-23.

63. Z.P. Cano, J.R. McDermid, and J.R. Kish, "Cathodic Activity of Corrosion Filaments Formed on Mg Alloy AM30," J Electrochem Soc 162, 14 (2015): p. C732-C740.

64. M. Danaie, R.M. Asmussen, P. Jakupi, D.W. Shoesmith, and G.A. Botton, "The cathodic behaviour of Al–Mn precipitates during atmospheric and saline aqueous corrosion of a sand-cast AM50 alloy," Corros Sci 83, (2014): p. 299-309.

65. C. Xu, R. Wang, Y. Zhang, and Y. Ding, "A general corrosion route to nanostructured metal oxides," Nanoscale 2, 6 (2010): p. 906-909.

Table 4. 1. AZ31B-H24 ([UNS M11311] Magnesium Elektron). All compositions reported in wt. %, with the actual compositions provided by QUANT (Quality Analysis and Testing Corporation).

	UNS #	Al	Mn	Zn	Si	Cu	Ni	Fe	Mg
AZ31B-H24	M11311	3.02	0.330	0.990	0.025	0.005	0.002	0.005	Bal.
HAZ2 α-matrix	---	2.6	0.330	0.990	---	---	---	---	Bal.
HAZ1 α-matrix	---	2.2	0.330	0.8	---	---	---	---	Bal.
FZ α-matrix	---	1.8	0.5	0.5	---	---	---	---	Bal.
Al-Mn-Fe particles	---	75.1	12.4	---	---	---	---	12.5	---
Al-Mn particles	---	67	33	---	---	---	---	---	---
Al-Zn solidification boundaries	---	52.1	--	47.9	---	---	---	--	---

Figure 4. 1. Schematic of the TIG welding process and schematic of weld zones, specifying the FZ and HAZs. Far enough away from the weld zone, the sample consists of unaffected base material. All samples were welded through a 45° countersunk hole in order to have full penetration through both plates.
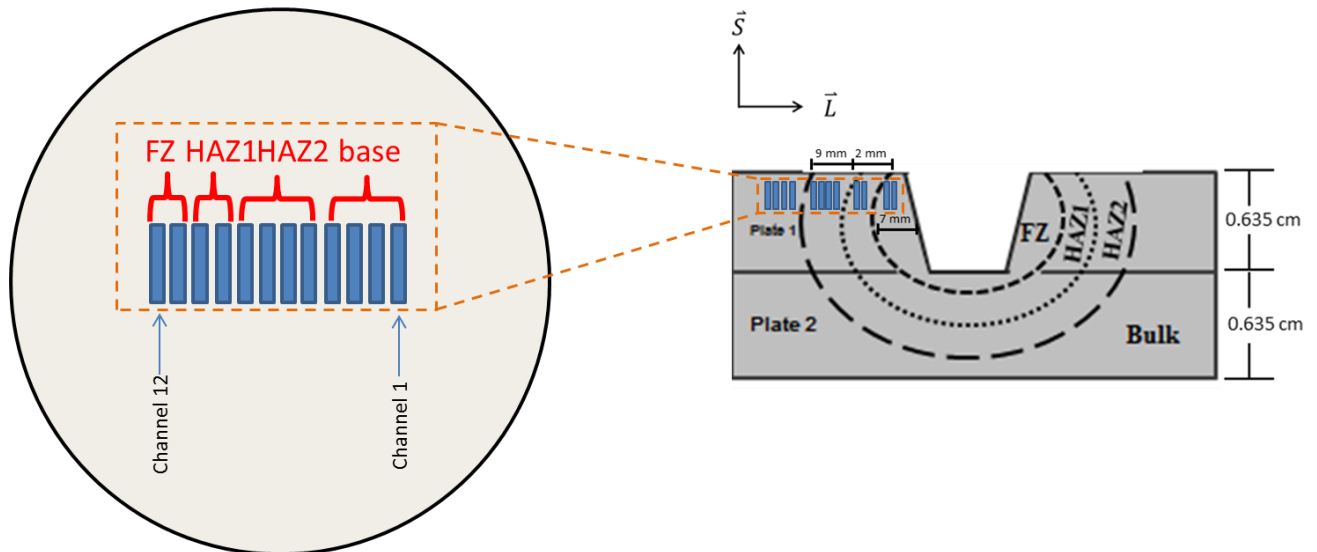
Figure 4. 2. Dimensions of the weld zones and locations of the sections for the MMA taken from a divided weld and schematic of the multi-electrode array used to determine the current across the weld zones. The weld was divided into 12 equal sized sections, each having a surface area of 3 mm^2. The number of sections was picked to represent the approximate surface area of each weld zone shown. The extracted sections were located in the MMA specimen as shown.
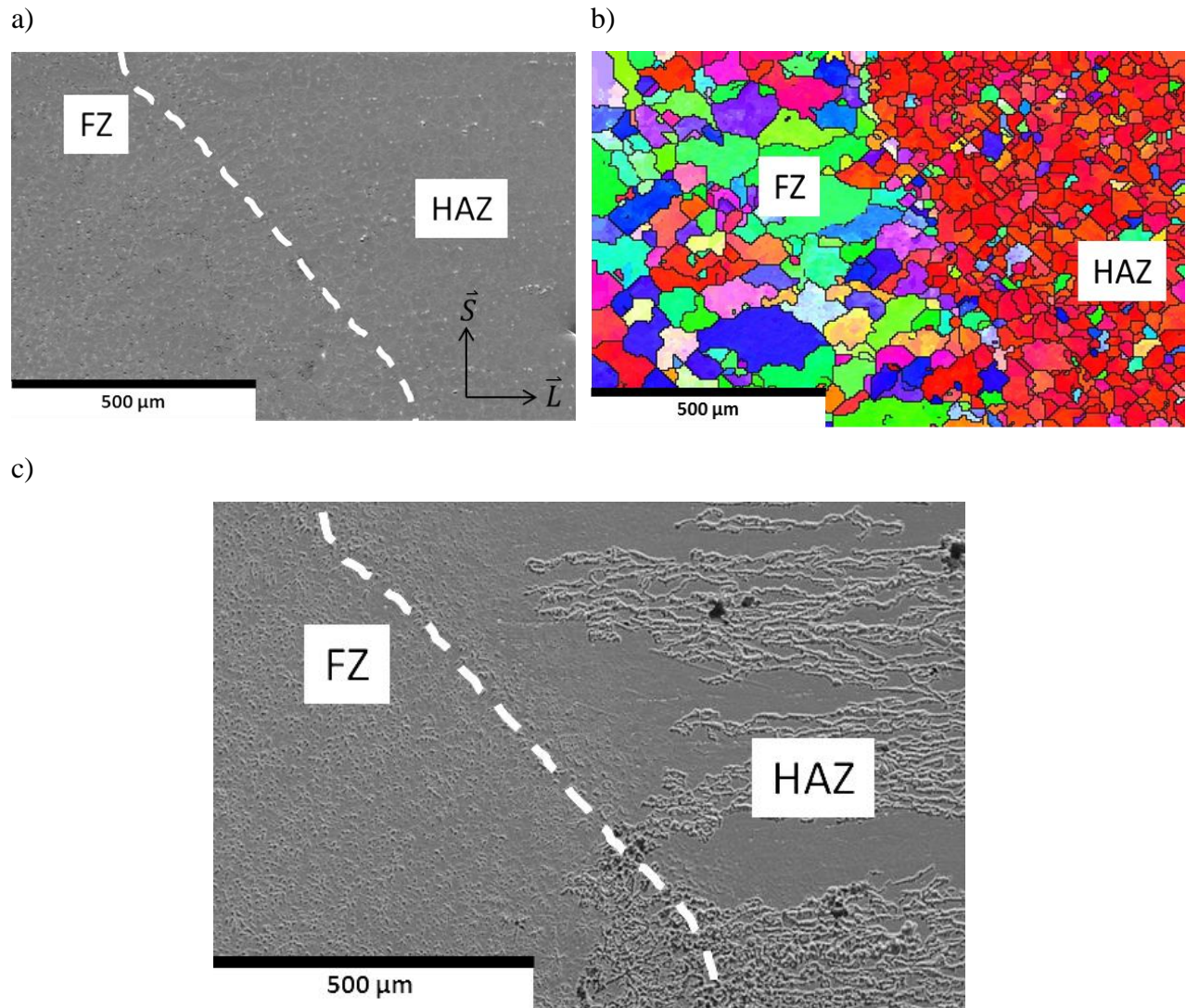
Figure 4. 3. a) Secondary electron micrograph of AZ31B-H24 TIG weld along the edge of the FZ before corrosion with b) EBSD map taken along the edge of the FZ showing the variation in crystallographic orientation along the weld regions and c) secondary electron micrograph of AZ31B-H24 TIG weld after 3 hour immersion at OCP in 0.6 M NaCl showing the difference in corrosion morphology in each of the various weld regions.
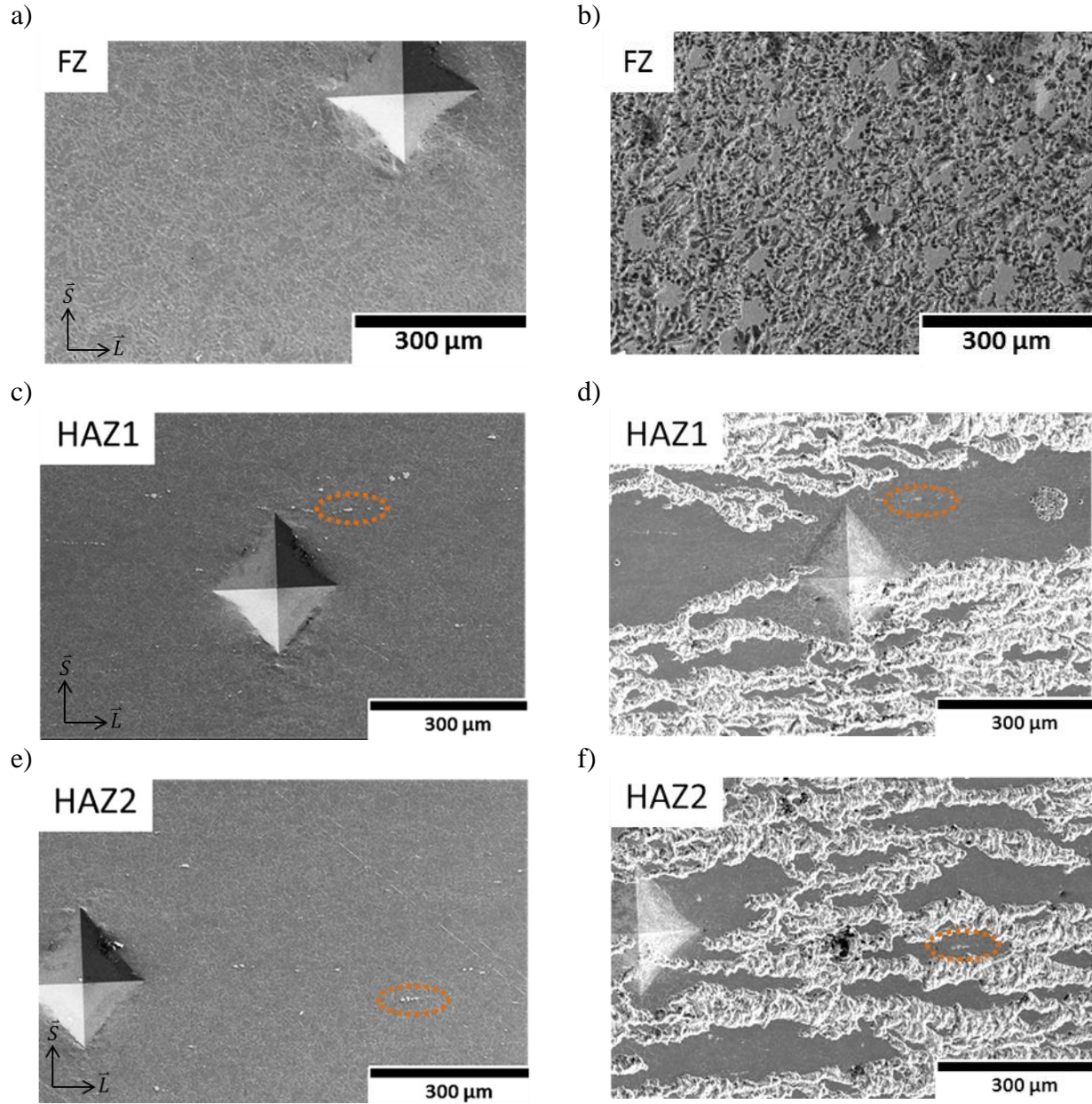
Figure 4. 4. Secondary electron micrographs of (a) AZ31B FZ specimen before exposure, (b) AZ31B FZ specimen after exposure and cleaned with CrO_3 to remove any oxides, (c) AZ31B HAZ1 specimen before exposure, (d) AZ31B HAZ1 specimen after exposure and cleaned with CrO_3 to remove any oxides, (e) AZ31B HAZ2 specimen before corrosion, (f) resultant corrosion morphology of AZ31B HAZ2 and cleaned with CrO_3 to remove any oxides after 3 hour immersion at OCP in 0.6 M NaCl + $Mg(OH)_2$.

135
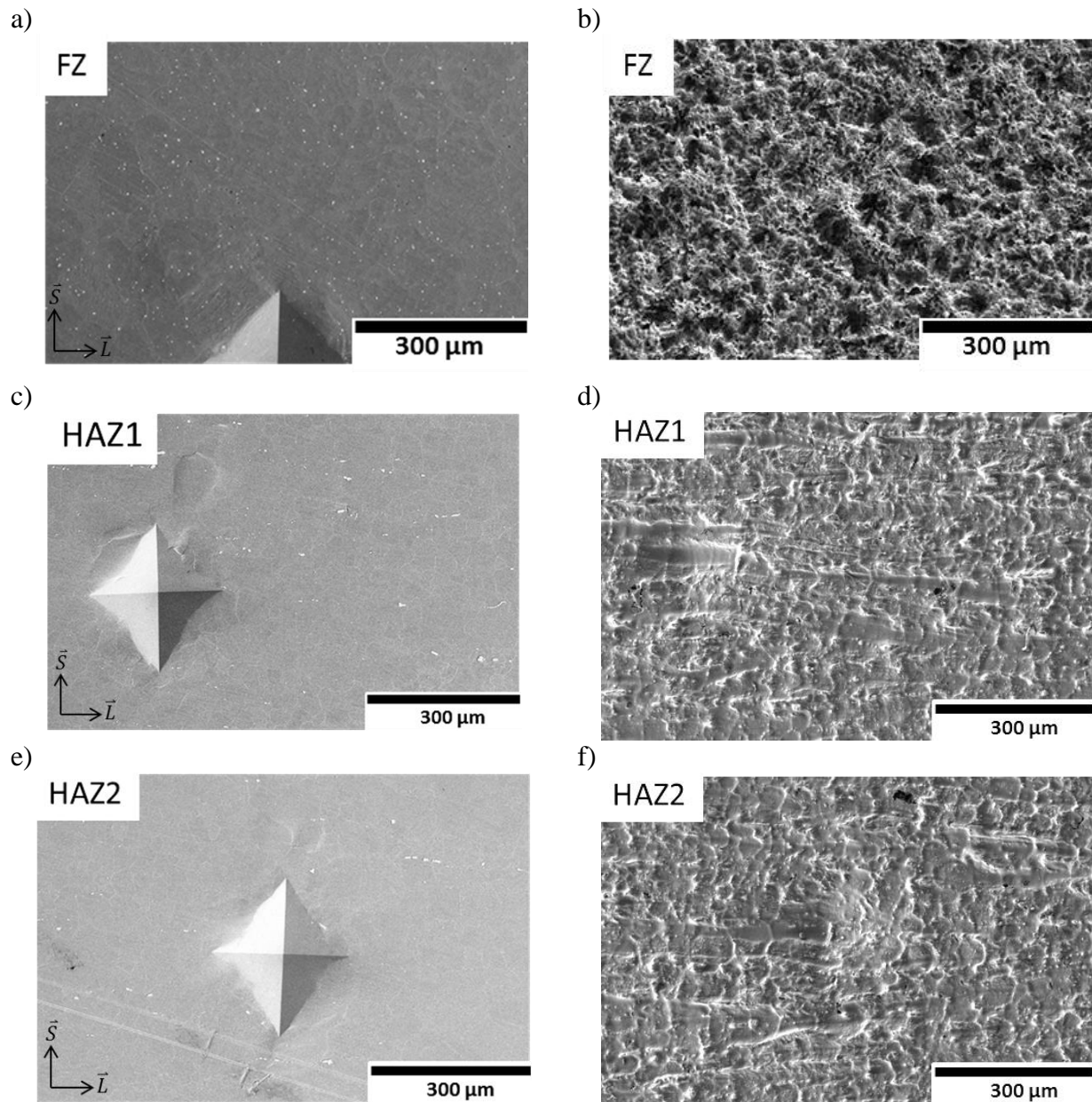
Figure 4. 5. Secondary electron micrographs of (a) AZ31B FZ specimen before exposure, (b) AZ31B FZ specimen after exposure and cleaned with CrO_3 to remove any oxides, (c) AZ31B HAZ1 specimen before exposure, (d) AZ31B HAZ1 specimen after exposure and cleaned with CrO_3 to remove any oxides, (e) AZ31B HAZ2 specimen before corrosion, (f) resultant corrosion morphology of AZ31B HAZ2 cleaned with CrO_3 to remove any oxides after 3 hour immersion at OCP in 0.1 M TRIS.
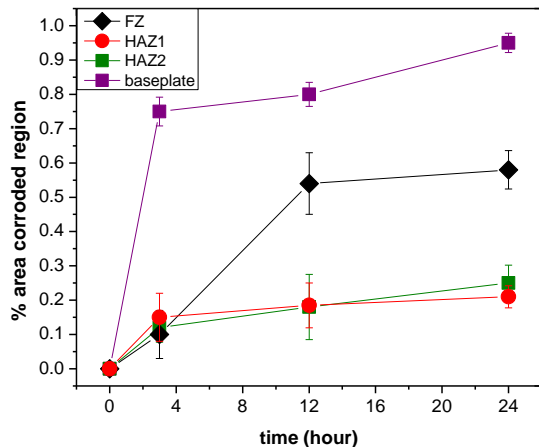
a)   b)
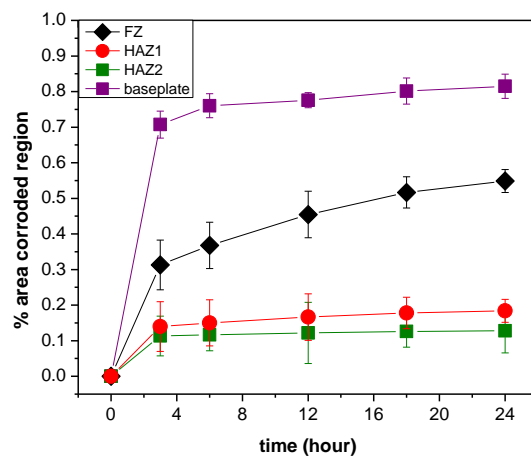
Figure 4. 6. Percent of cathodically activated black surface area corroded with time for (a) isolated weld zones and (b) galvanically coupled weld zones in 0.6 M NaCl. The values are statistically equivalent to those observed in 0.6 M NaCl + Mg(OH)$_2$.
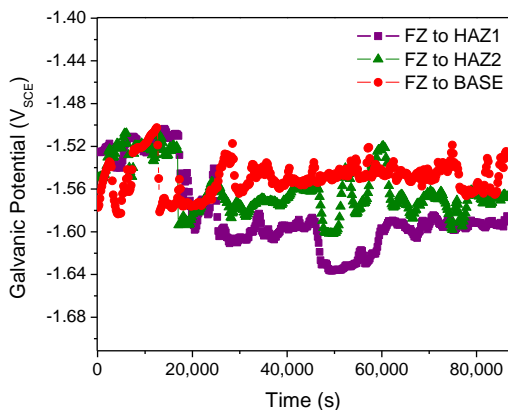
a)   b)
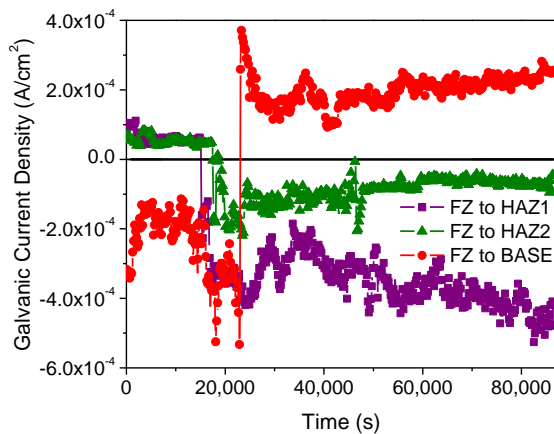
Figure 4. 7. (a) Galvanic potential and (b) galvanic current between the FZ and other weld zones and base material over 24 hours in 0.6 M NaCl where the FZ is the CE and the HAZ or BASE is the WE. Each weld zone had an exposed area of 1.23 mm^2.

a)
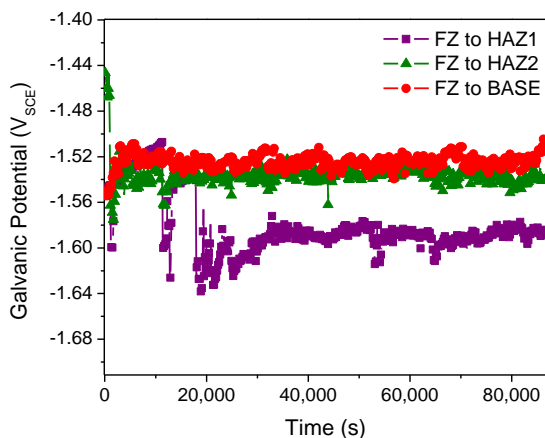
b)
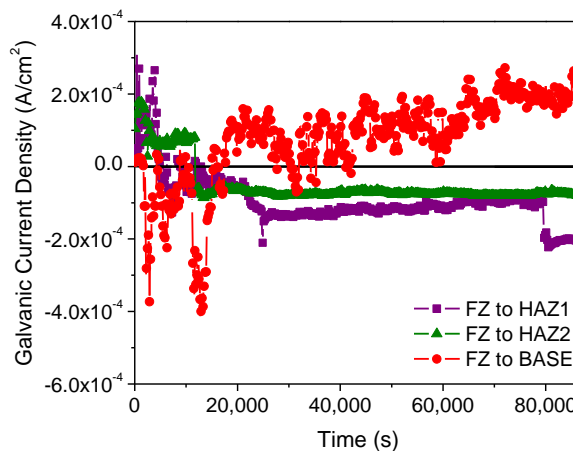
Figure 4. 8. (a) Galvanic potential and (b) galvanic current between the FZ and other weld zones and base material over 24 hours in 0.6 M NaCl saturated with $Mg(OH)_2$ where the FZ is the CE and the HAZ or BASE is the WE. Each weld zone had an exposed area of 1.23 mm^2.

a)
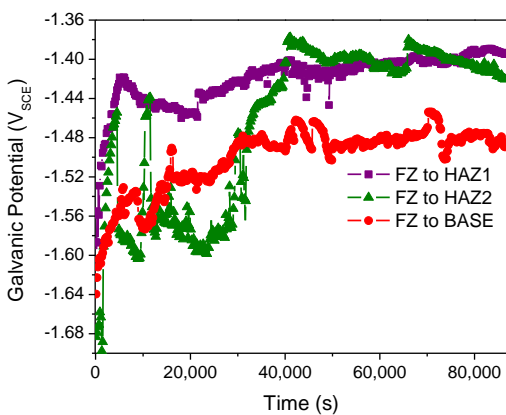
b)
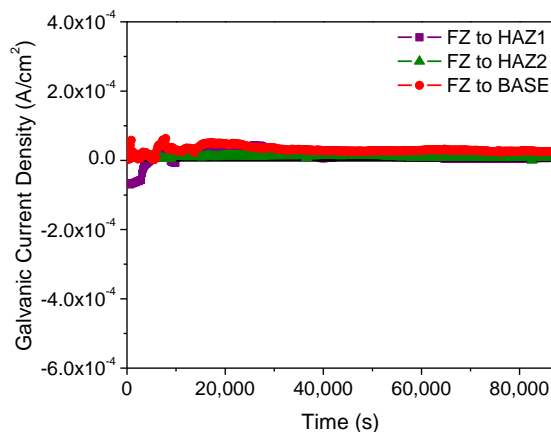
Figure 4. 9. (a) Galvanic potential and (b) galvanic current between the FZ and other weld zones and base material over 24 hours in 0.1 M TRIS where the FZ is the CE and the HAZ or BASE is the WE. Each weld zone had an exposed area of 1.23 mm^2.

138
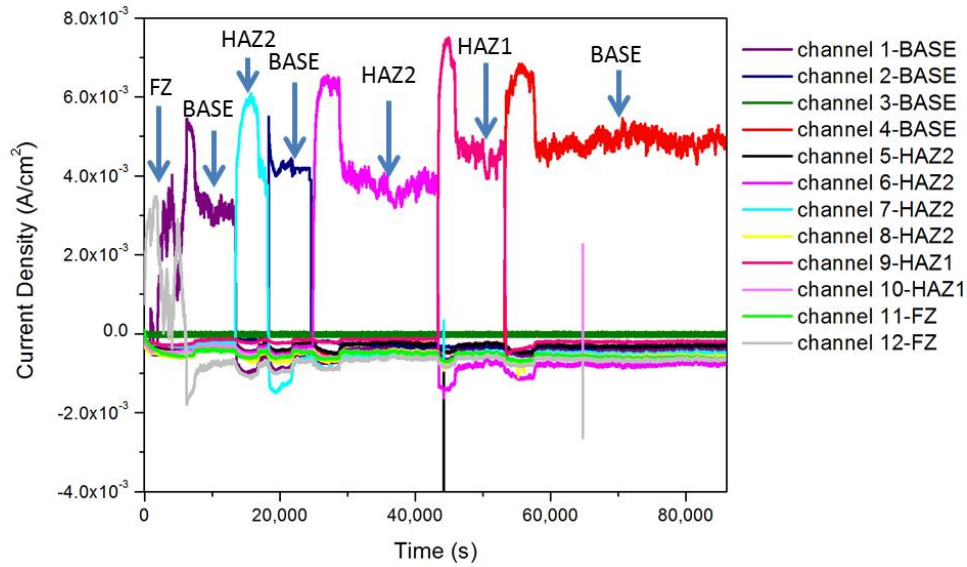
Figure 4. 10. Current distribution across the weld showing anodic activation in different sections of the weld with time in 0.6 M NaCl. Each channel has a surface area of 3 mm^2.
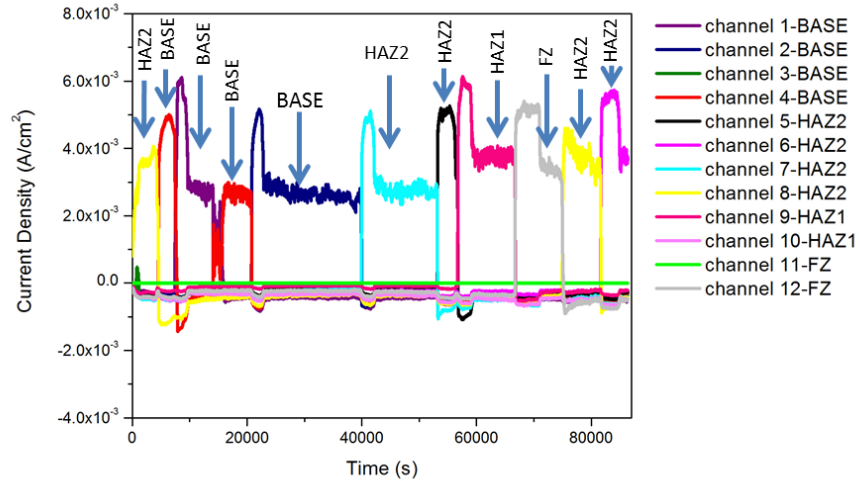
Figure 4. 11. Current distribution across the weld showing anodic activation in different sections of the weld with time in 0.6 M NaCl saturated with $Mg(OH)_2$. Each channel has a surface area of 3 mm^2.
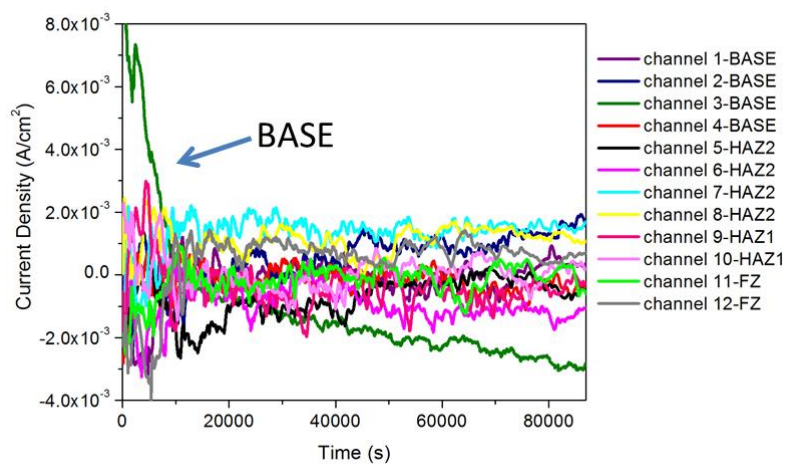
Figure 4. 12. Current distribution across the weld showing anodic activation in different sections of the weld with time in 0.1 M TRIS. Each channel has a surface area of 3 mm^2.

a)
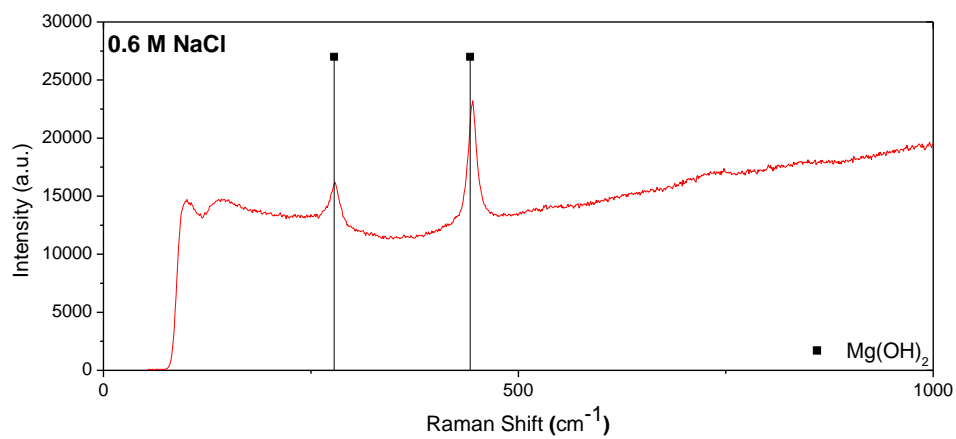
b)
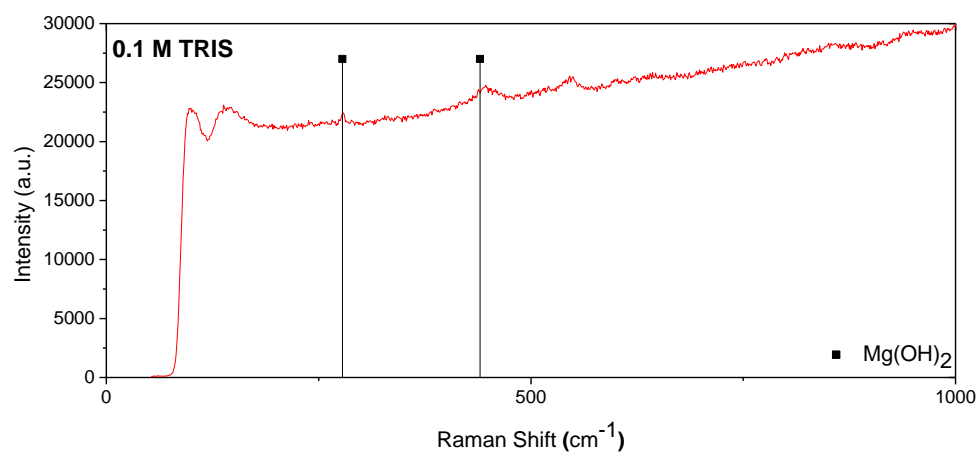
Figure 4. 13. Raman spectrum of oxide growth on Mg after 24 hours at OCP in a) 0.6 M NaCl and b) 0.1 M TRIS.
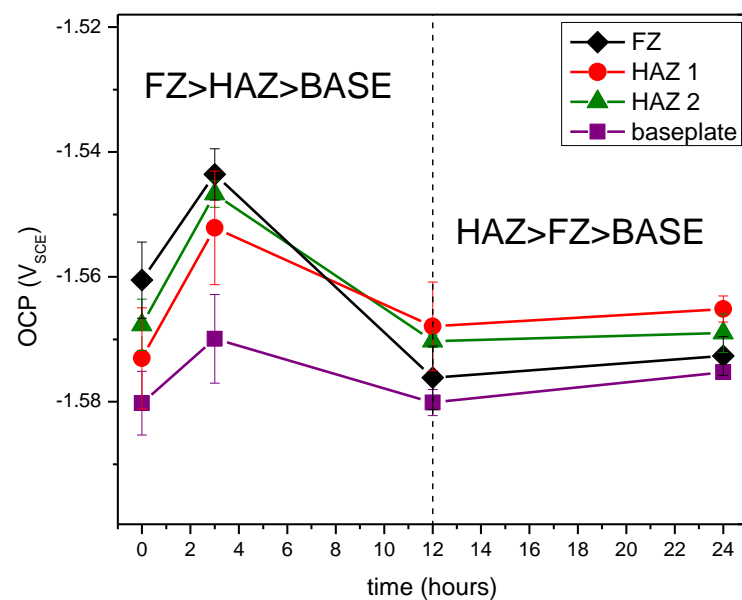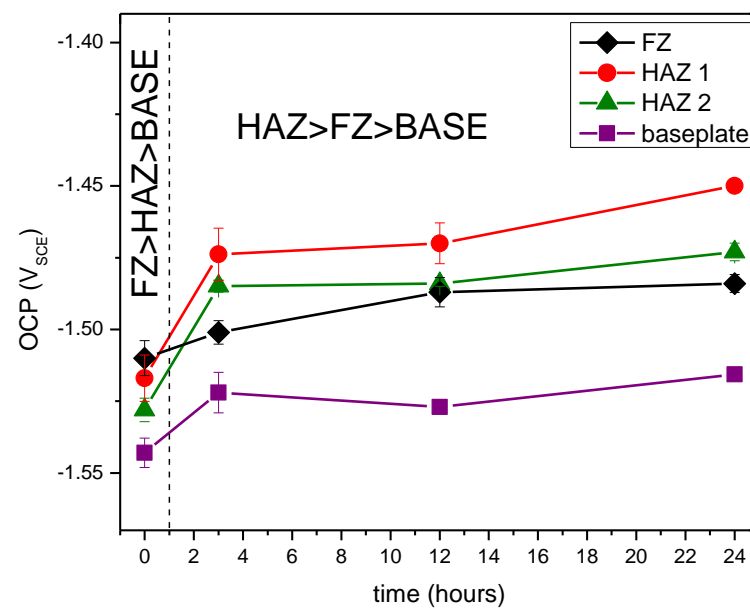
Figure 4. 14. Measured OCP for wrought plate AZ31B-H24, (a) isolated weld zones and (b) galvanically coupled TIG weld in 0.6 M NaCl uncoupled measured at 0, 3, 12 and 24 hours. Error bars determined from 3 replicates using standard error.

a)
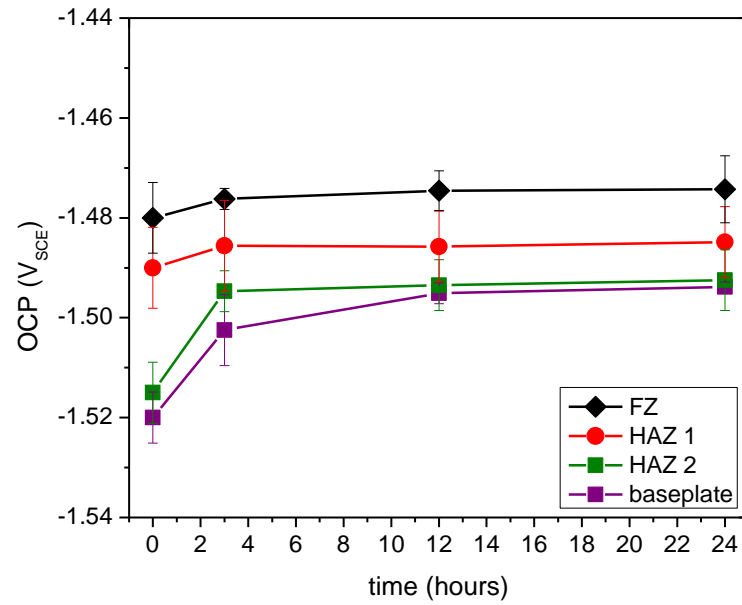
b)
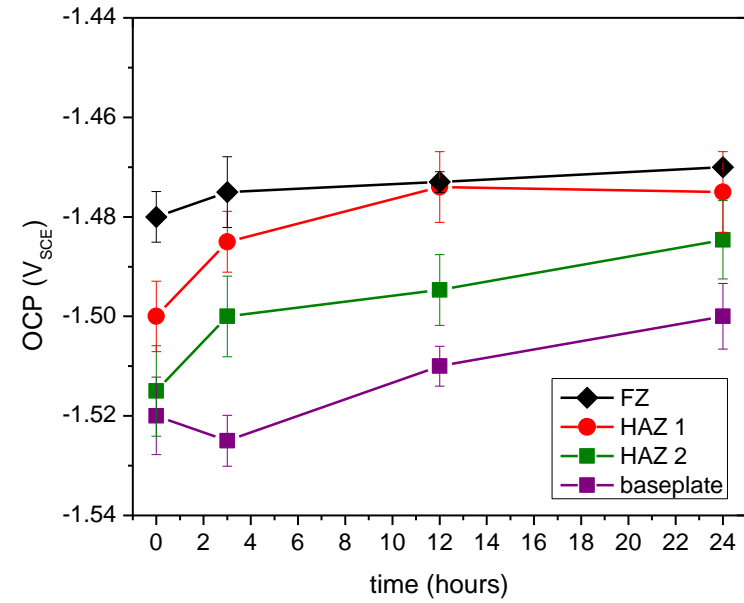
Figure 4. 15. Measured OCP for wrought plate AZ31B-H24, (a) isolated weld zones and (b) galvanically coupled TIG weld in 0.1 M TRIS uncoupled measured at 0, 3, 12 and 24 hours. Error bars determined from 3 replicates using standard error.

a)
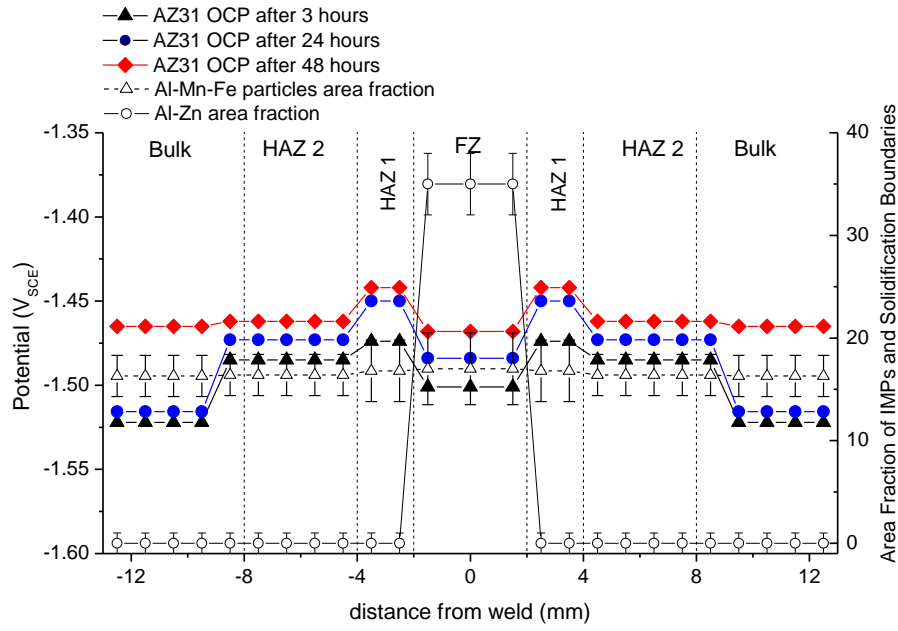
b)
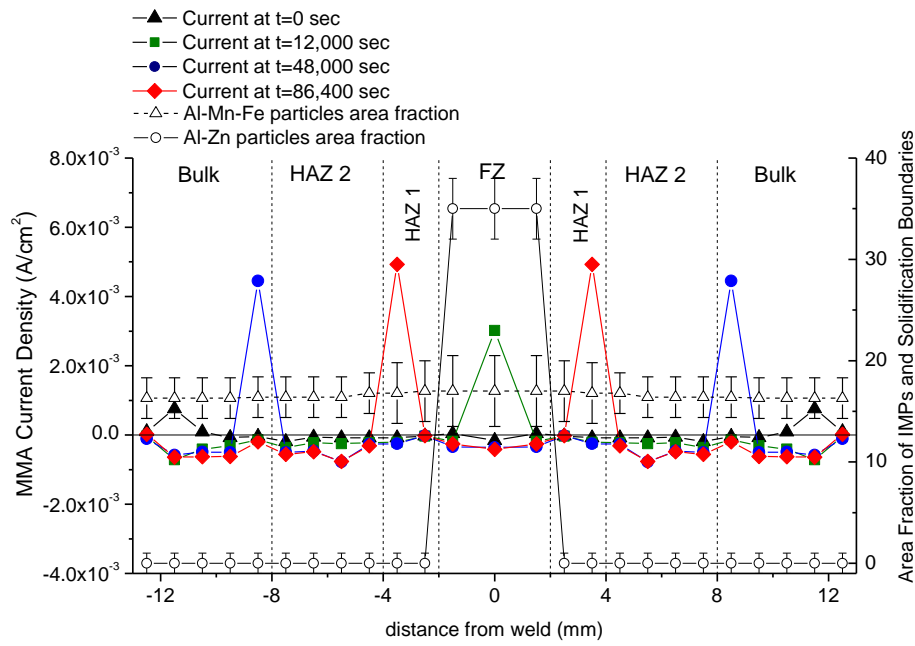
c)
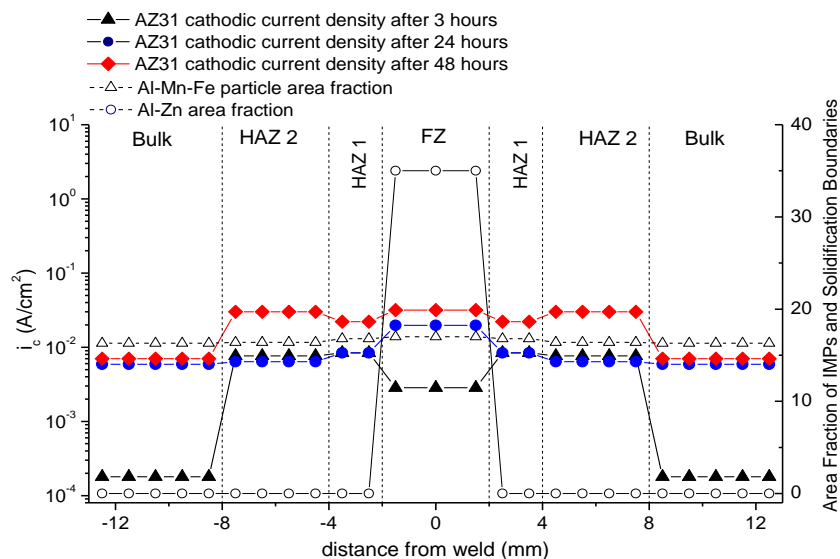
Figure 4. 16. (a) Evolution of the OCP with time between all zones where samples were galvanically connected, (b) development of current with time taken at 0, 12000, 48000 and 86400 sec showing the polarity reversal observed in different electrochemically connected channels on the MMA where each channel has a surface area of 3 mm^2 and (c) evolution of the cathodic corrosion current density with time between all zones estimated at -1.8 V$_{SCE}$ for 3, 24 and 48 hour before taking uncoupled measurements of individual zone in 0.6 M NaCl. Error bars determined from 3 replicates using standard error.
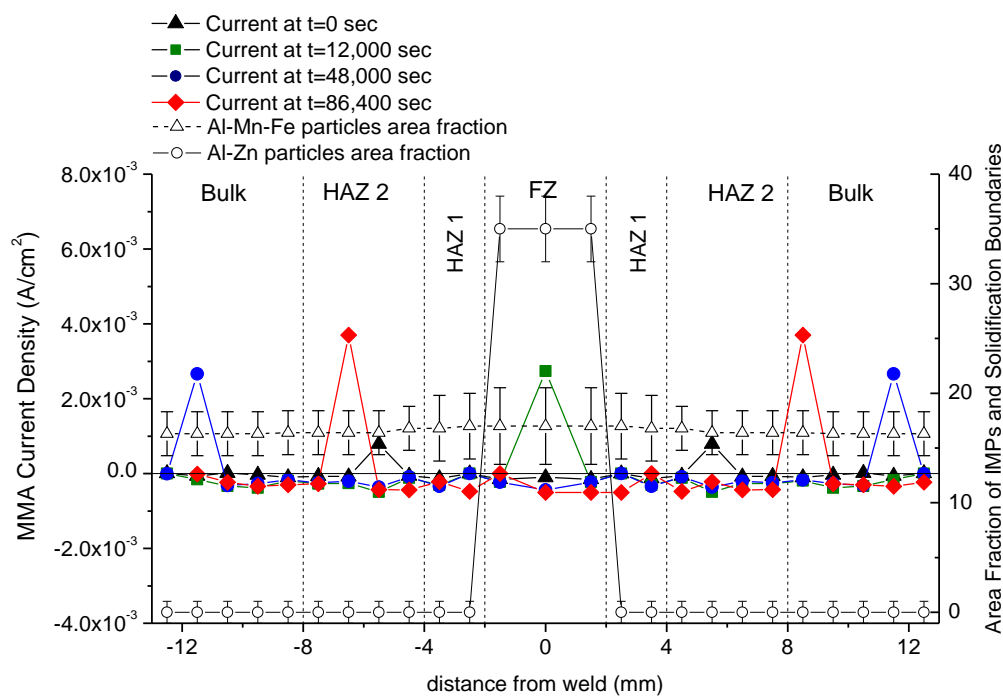
Figure 4. 17. Development of current with time taken at 0, 12000, 48000 and 86400 sec showing the polarity reversal observed in different electrochemically connected channels on the MMA in 0.6M NaCl saturated with $Mg(OH)_2$. Each channel has a surface area of 3 mm^2. Error bars determined from 3 replicates using standard error.

a)
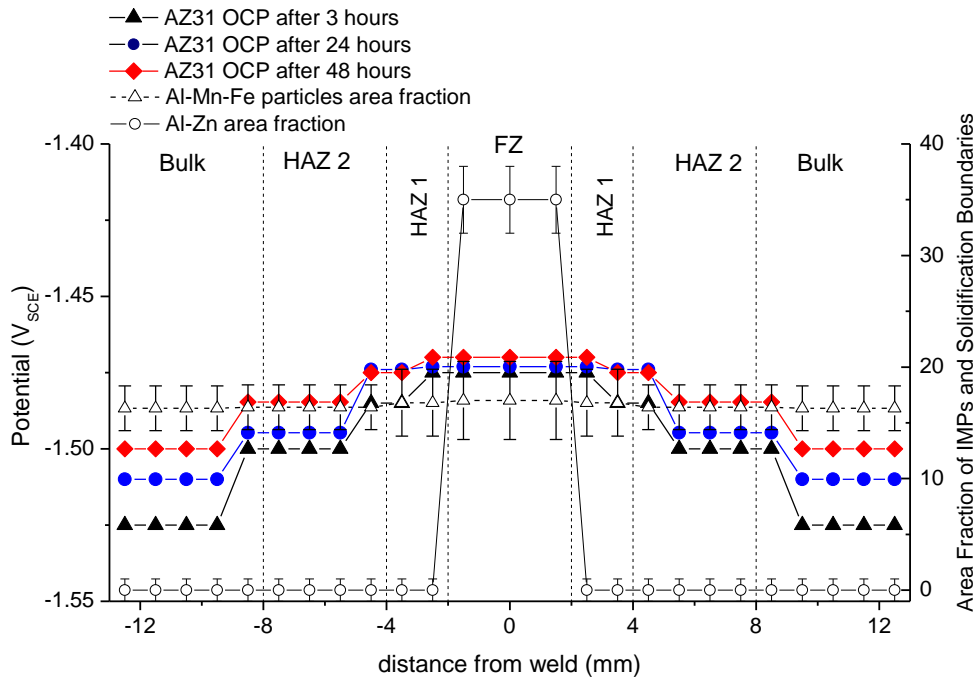
b)
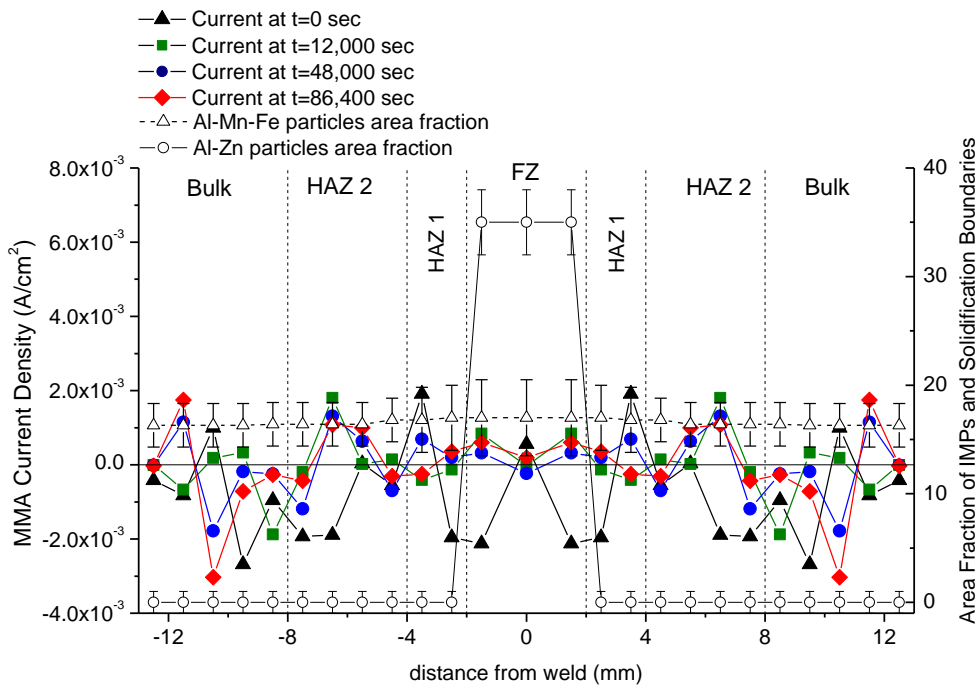
c)
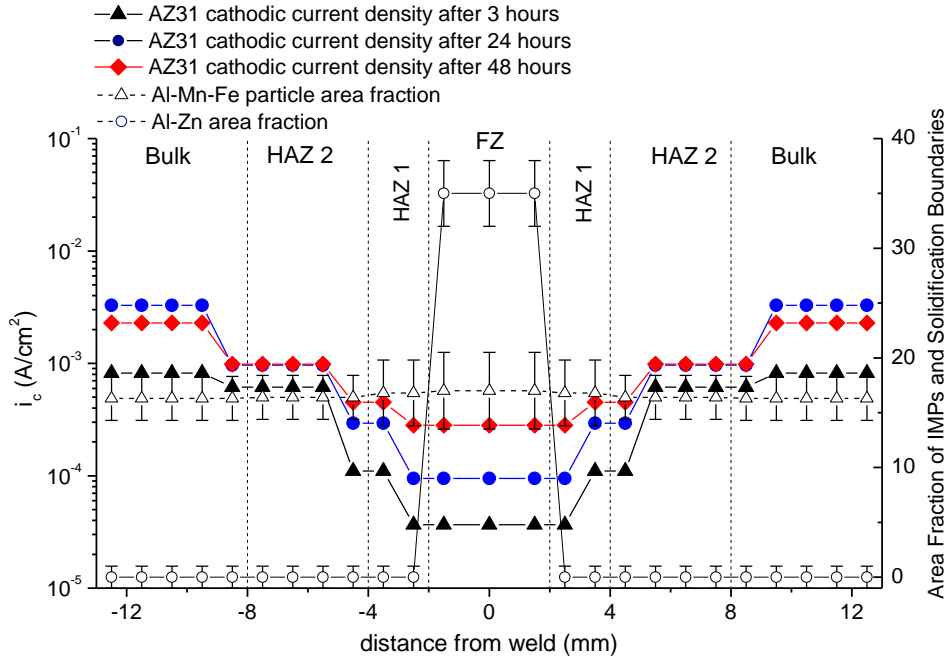
Figure 4. 18. (a) Evolution of the OCP with time between all zones where samples were galvanically connected (b) development of current with time taken at 0, 12000, 48000 and 86400 sec showing the polarity reversal observed in different electrochemically connected channels on the MMA where each channel has a surface area of 3 mm^2 and (c) evolution of the cathodic corrosion current density with time between all zones estimated at -1.8 V_{SCE} for 3, 24 and 48 hour before taking uncoupled measurements of individual zone in 01 M TRIS. Error bars determined from 3 replicates using standard error.

5 Effect of Al-Mn and Al-Mn-Fe Intermetallic Particle Size and Distribution on the Corrosion of Mg-3Al-1Zn alloy: AZ31

The effect of intermetallic particle (IMP) size and localized number density on the corrosion behavior was rigorously assessed through the use of furnace heat treatments, electron microscopy, and electrochemical methods. Particle size and spacing increased with both heat treat time and temperature, indicating particle coarsening, while the area fraction remained relatively constant. The electrochemical corrosion testing was performed in unbuffered 0.6 M NaCl and buffered tris(hydroxymethyl)aminomethane (TRIS) at the open circuit potential. Particle size and spacing impacted the corrosion behaviour. The integration of polarization resistance, R_P, over time, was evaluated by electrical impedance spectroscopy (EIS) at the low frequency limit, incorporating full consideration of the pseudo-inductive impedance behavior of Mg. The intermetallic particles function as the initial active cathodic sites. Moreover, "activated" zones in the Mg matrix around the IMPs contribute to the corrosion behaviour. Small, closely spaced IMPs increased the corrosion rate and this behaviour is explained. The changing grain size was ruled out as a governing factor controlling the corrosion rate in this study.

A manuscript based on this chapter has been submitted to Materialia as a Full Research Paper, "Effect of Al-Mn and Al-Mn-Fe Intermetallic Particle Size and Distribution on the Corrosion of Mg-3Al-1Zn alloy: AZ31."

Representative author contributions:

L.G. Bland: experiments, metallurgical and electrochemical characterization
J.J. Bhattacharyya: heat treatment of AZ31B alloys, metallurgical characterization
S.R. Agnew: analysis and interpretation
J.M. Fitz-Gerald: analysis and interpretation
J.R. Scully: Adviser, analysis and interpretation

5.1 <u>Introduction</u>

Mg alloy AZ31B [UNSM11311] is a wrought magnesium alloy known for its good balance of mechanical and corrosion properties. Currently, the aerospace and automotive industries are exploring the possibility of expanding its use [1] beyond sacrificial anodes and lithographic plate [2,3].

5.1.1 Corrosion Properties of Mg-Al Alloys

The corrosion resistance of Mg alloys is increased when certain alloying elements remain in solid solution [4]. However, if the concentration of alloying elements exceeds the solid solubility limit, intermetallic particles (IMPs) form [4-7], which can alter the electrochemical properties of the alloy depending on the IMP composition and electrochemical properties [8,9]. Annealing at high temperatures, the IMPs can undergo coarsening due to Ostwald ripening (cited to occur as low as 350 °C in AZ31[10]), which can further affect the alloy corrosion properties by altering the IMPs size and spacing while maintaining a relatively constant area fraction [10-12].

From the electrochemical studies, it has been shown that most of IMPs are more noble than either high purity Mg or typical Mg-Al alloys [13-15]. However, the extent of attack in the material will be largely dependent on the electrochemical characteristics of the IMP [13]. IMPs containing Al typically passivate spontaneously, indicating that they display some electrochemical stability and passivity, at least in low [Cl⁻] environments with passive current densities on the order of 10 $\mu A/cm^2$ However, in solutions which induce pitting, such as those containing [Cl⁻], the potential drops with saturated $Mg(OH)_2$ at pH 11, where Al is thermodynamically eligible for corrosion at the OCP of AZ31B [16]. This can lead to the release of Al as AlO_2^- and possible re-deposition or precipitation at a less alkaline site [17]. For Mn, compounds such as Al_8Mn_5, Al_6Mn or Al_4Mn are formed, and the addition of Mn helps to reduce corrosion rate via the incorporation of low solubility metals, such as Fe and other transition elements [16,18,19], within the Al–Mn IMPs. As the Zn content increases above 3 wt %, the corrosion rate increases dramatically [13,20]. Also, $MgZn_2$ IMPs have a similar OCP to the α-Mg matrix but the cathodic kinetics are enhanced in Cl⁻ environments due to the greater cathodic efficiency of Zn with respect to Mg [13] (Table 5. 1).

Although a significant body of research has been performed to identify the IMPs in these alloys and their electrochemistry in isolation, the effect of particle size and spacing on the

corrosion rate of Mg alloys is not yet established. Much of the current literature to date is on the effect of specific particle composition on the effective corrosion rate considering circumstantial evidence or IMPs in isolation [4,14,17,20,21]. However, the effect of a decrease in the corrosion rate with an increase in the particle size has been shown in the α-iron/cementite system where cementite coalescence into large particles during anneals and leads to a lower corrosion rate [22,23]. Conversely, in an austenitic steel, the corrosion rate increases as iron carbide particles sizes decrease [22] and, in copper, smaller intermetallic particles result in a higher corrosion rate under atmospheric conditions [24].

5.1.2 Effect of Heat Treatment on Mg-Al Alloys

To date, much Mg-Al literature on heat treatment deals with cast microstructures, in AM and AZ alloys (AM50, AM60, AZ31 and AZ91). For higher Al containing alloys, a body of research has been performed to establish the amount and distribution of the β-phase ($Mg_{17}Al_{12}$) and heat treatments (T3, solution treatment, and T6, peak aging treatment) [25-28]. However, for low Al content alloys, such as AZ31, little to no β-phase forms and it has no impact on the corrosion and mechanical properties of this alloy. Previous work on the heat treatment of AZ31B showed that short heat treatment times (5 min) increased the corrosion resistance [25]. However, longer heat treatments (up to 60 min) decreased the corrosion resistance due to increased enrichment of alloying elements to the oxide surface and increased cathodic activity due to this enrichment [25]. Overall, heat treatments have led to a decrease in the cathodic kinetics for AZ31 [25]. In this study, the effect of heat treatment on the corrosion rate was evaluated at the mid-plane to alleviate the additional issue of enrichment during heat treatment [25]. Processing routes which show a large increase in the area fraction of particles typically show an increase in the corrosion rate [22]. Similarly, processing routes to homogenize the IMPs in the near-surface region, such as laser surface modification, have been shown to enhance the corrosion behavior [29].

5.1.3 Variation in Corrosion Kinetics and Corrosion Rate Due to Grain Size

A complication of systematic investigations concerning the effect of IMP size and spacing on corrosion rate is that the grain size increases concurrent with particle coarsening. Current literature considered the impact of grain size as well as processing route for different Mg alloys [30-36]. In particular, there has been a focus on Equal Channel Angular Processing (ECAP) as well as Surface Mechanical Attrition Treatment (SMAT) which are used to form ultra-small grained samples, the corrosion behavior has been reported [31,33,34]. Smaller grain sizes generally

151

improve the corrosion response and many ideas have been proposed for this mechanism such as an improved oxide film at the grain boundaries function as a better barrier for corrosion [31,33,34]. However, little evidence has been presented to confirm that either mechanism has validity in the context of Mg corrosion. In terms of the effects of different processing routes, findings have been confounded if one considers the corrosion response due to the presence of twins within the starting material [37]. Generally, annealing heat treatments reduce the amount of deformation twins present in the microstructure[30]. On the other hand, the as-deformed material can contain a significant volume fraction of deformation twins and residual stresses, depending on the imposed strain path, which would potentially alter their corrosion response. Specifically, "filiform-like" corrosion has been shown to propagate at twin boundaries [37]. The conflict in literature on this issue suggests the need for more work in this area to clarify the grain size effect on Mg as well as its alloys without deformation twins.

5.1.4 Objective

The objective of the present study is to determine the effect of selected metallurgical characteristics (i.e. the combined Al-Mn and Al-Mn-Fe IMP size, spacing, as well as due consideration of grain size) on the corrosion rate of the Mg alloy AZ31B. In terms of weld corrosion, the particle distribution in an AZ31 tungsten inert gas (TIG) weld varied by weld zone. In particular, the high temperatures seen during welding cause Ostwald ripening of IMPs which increase the particle size as well as the particle spacing. Studying the effect of particle distribution through various heat treatments will allow for better systematic understanding on how this distribution alters the corrosion rate within the weld zone.

5.2 Experimental Procedures

5.2.1 Materials

The material investigated was part of a larger study focused on the effect of shear rolling on the microstructure and properties of Mg alloys [10,38]. AZ31B sheet with a thickness of 1.52 mm was obtained from Magnesium Elektron North American and shear rolled at Oak Ridge National Laboratory, with both rolls and the metal held at 200 °C. The details of the processing are described elsewhere [39]. The composition of the material is reported in wt. %, as provided by Quality Analysis and Testing Corporation (QUANT) as 3.02% Al, 0.3% Mn, 0.99% Zn, 0.025% Si, 0.005% Cu, 0.002% Ni, 0.005% Fe and Mg Bal.

5.2.2 Heat Treatment and Metallurgy on AZ31B for Variation in Grain Size and   Particle Distribution

Samples were heat treated at temperatures ranging from 300 to 450 °C for durations ranging from 240 sec (4 min) to 604,800 sec (7 days) in order to produce samples varying in particle size, particle spacing and grain size. The short duration anneals (240 sec) were performed in a KNO_3 salt bath. For all other annealing durations, an air furnace was used. At the completion of the heating cycle the samples were quenched in room temperature water after annealing [10].

Samples were analyzed using optical microscopy and scanning electron microscopy (SEM). The SEM was performed on a FEI Quanta 650 Schottky emitter equipped with energy dispersive spectroscopy (EDS) and electron backscatter diffraction (EBSD). Semi-quantitative compositional analysis was performed using EDS with full consideration of ZAF corrections where Z is the atomic cumber correction, A is the absorption correction and F is the fluorescence correction. Micrographs were taken at a working distance of 10 mm and an accelerating voltage of 5 kV. Texture variation with heat treatment was determined through X-ray diffraction (XRD) [10] and EBSD obtained at a working distance of 15 mm and an accelerating voltage of 20 kV. Although qualitatively the textures were found to be quite similar, there were some quantitative differences due to the volume averaging effects in XRD measurement, as described elsewhere [40]. All samples were polished through colloidal silica and etched with a Picric acid etch (3 g picric acid, 30 mL acetic acid, 100 mL ethanol and 15 mL distilled water) to determine the grain size and microstructure.

The grain size was determined from optical micrographs using the lineal intercept method following the ASTM Standard E113-96 [41]. The particle size and spacing of Al-Mn and Al-Mn-Fe particles were determined separately using the lineal intercept tool in the FEI Quanta 650 microscope software based on the SEM–back-scattered electron (BSE) images, which heighten the compositional contrast relative to secondary electron imaging. To obtain the area fraction, multiple (6–8) BSE images were analyzed using the analysis software, ImageJ[TM][42]. The 2D area fraction is important for electrochemical studies discussing the exposure of a single planar sample surface.

The corrosion morphology was assessed to determine how the corrosion attack initiated and progressed. SEM micrographs were recorded before and after immersion in 0.6 M NaCl for

3 hours at OCP. All samples were cleaned with chromic acid (CrO_3) [43] to remove any corrosion products and to examine the corrosion morphology. Before the initial corrosion, fiduciary marks were made using a Vickers microhardness tester, to enable examination of the corrosion morphology at each stage in precise locations.

5.2.3 Corrosion Determination

The corrosion behavior of heat-treated AZ31 was monitored non-destructively with electrochemical impedance spectroscopy (EIS) for a 24 hour immersion period in 0.6 M NaCl (pH ~5.3). The experimental setup consisted of a vertical flat cell with a 1 cm^2 sample window attached to a vertically mounted, inverted, volumetric burette. EIS scans were analyzed and fit using the software program ZView [44] to an equivalent circuit, seen in Figure 5. 1, and were fit to a low frequency limit of at least 1 mHz. Scans were run at least three times and an average is reported. The inclusion of the full inductive behavior enables a more accurate determination of the corrosion rate of Mg alloys by the inclusion of the full polarization resistance, R_p, obtained from Figure 5. 1 at the low frequency limit by circuit fitting, as discussed elsewhere [45,46].

To determine the effect of the particle distribution on the anodic kinetics, samples were immersed for 24 hours at OCP in unbuffered 0.6 M NaCl (pH ~5.3) and also buffered tris(hydroxymethyl)aminomethane (TRIS) (pH~7) followed by an anodic potentiodynamic polarization scan ranging from 0.5 V below OCP to 1.5 V above OCP in an upward sweep of 1 mV/sec. A cathodic potentiodynamic polarization scan ranging from 50 mV above OCP to -2.3 V below OCP in a downward sweep at a rate of 1 mV/second were also performed to analyze the cathodic kinetics. The cathodic current density, i_c, was determined at -1.8 V_{SCE} with the standard error reported.

The corrosion rate of a freely corroding metal was determined through an evaluation of R_P using the well-known Stern-Geary relationship [47,48]:

$$i_{corr} = \frac{B}{R_P} = \frac{\beta_a\beta_c}{2.303R_P(\beta_a + \beta_c)}$$

Equation 5.1

where β_a and β_c are the anodic and cathodic Tafel slopes, respectively and B = (1/2.303) $\times$ ($\beta_a.\beta_c/(\beta_a + \beta_c)$). Several Tafel assumptions have been used which are typical of those quoted in Mg literature in order to determine a range of Mg corrosion rates (B_{King}=36.0 mV [46], B_{Shi}=36.8 mV [49], and B_{Cao}=31.1 mV [50]) due to the non-polarizable and changing nature of Mg which makes IR-correction difficult.

154

The anodic charge density can then be estimated by integrating the EIS-estimated corrosion rate:

$$Q_a^{EIS} = \int i_{corr(\theta)}dt = \int \frac{\beta_a\beta_c}{2.303R_P(t)(\beta_a + \beta_c)}dt \qquad \text{Equation 5.2}$$

The corrosion rate determined through EIS was tested by measuring the corrosion rate through three other techniques: gravimetric mass loss, hydrogen evolution and inductively coupled optical emission spectroscopy (ICP-OES), and it has been shown that these methods are comparable for the Mg system [45,46]. For brevity, only mass loss and EIS analysis is shown in this study. The mass loss of Mg (Δm), as measured gravimetrically with ± 0.1 mg resolution, can be converted to consumed anodic charge (Q_a) via Faraday's law [51]:

$$Q_a^{\Delta m} = znF = \frac{z\Delta mF}{a} \qquad \text{Equation 5.3}$$

where z is equivalent electrons per mole of Mg oxidized, n is the number of moles of Mg, F is Faraday's constant and a is the molar mass of Mg. To determine the total number of equivalents in the alloy, N_{eq}. This is:

$$N_{eq} = \sum\left(\frac{f_i}{a_i/z_i}\right) = \sum\left(\frac{f_iz_i}{a_i}\right) \qquad \text{Equation 5.4}$$

The equivalent weight (grams/equivalent) is then the reciprocal of the total number of equivalents (EW= N_{eq}^{-1}). The equivalent weight of AZ31 was considered and determined as the weighted average of a/z for the major alloying elements in a given alloy [50] as specified by ASTM G106 [52]. The EW for AZ31B was determined to be 12.13 g/eq assuming congruent Mg^{2+}, Al^{3+}, Mn^{2+} and Zn^{2+} dissolution.

Also, the corrosion penetration depth can be calculated from Faraday's law:

$$x = \frac{Q(E.W.)}{F\rho} \qquad \text{Equation 5.5}$$

Where F is Faraday's constant (C/eq), and ρ is the density of Mg.

5.3 Results

5.3.1 Metallurgical Characterization of Heat Treated Samples

The microstructure of AZ31B samples heat treated to produce variations in the grain size, particle sizes and spacings are show in Figure 5. 2(a-i). In the as-received material (Figure 5.

2(a)) the grain size was 10.4 μm with few deformation twins[4]. The relatively small grain size and twin density was evidence of dynamic recrystallization during hot rolling of the sheet [10]. Regarding the microstructure of the heat treated samples, the short duration (up to 300 min for 300°C and 1080 min for 400°C) heat treatments have approximately uniform grain size distribution with no abnormally large grains (Figure 5. 2(b-e)). However, a distribution of larger and smaller grains were observed (Figure 5. 2(g)) for the short duration heat treatments in 450°C showing some abnormal grain growth behavior, described previously [10]. For longer duration heat treatments (Figure 5. 2(f), 5. 2(h) and 5. 2(i)), significant grain growth was observed with the grain size ranging from 21 μm to 28 μm.

The texture is shown in Figure 5. 3(a-d) for various heat treatment conditions. The texture of the wrought plate is shown in Figure 5. 3(a), revealing a basal texture [10,53]. The basal texture is largely retained so there is no texture effect. The basal texture is shown to remain and increase in intensity with annealing duration for all the temperatures investigated (Figure 5. 3(b-d)). Also, a $\{0001\} < 11\bar{2}0 >$ texture component, present in the initial microstructure, persists and becomes stronger after prolonged annealing at high temperatures. This slight change in texture is not the focus of this work and has been discussed previously [10,40].

Al-Mn and Al-Mn-Fe IMPs were distributed homogenously throughout the α-Mg matrix, with compositions similar to $(Fe,Mn)Al_6$ and Al_4Mn [21,54]. The Al-Mn particles were measured to be approximately 0.17 μm in size with a 13 μm spacing in the non-heat treated sample, as determined from their center-to-center spacing on EDS maps (Figure 5. 4(a-b)). Meanwhile, the Al-Mn-Fe particles were observed to be larger (5 μm) and spaced at greater distances (50 μm) (Figure 5. 4(c-d)) in the non-heat treated condition. The particle size, spacing and grain size increased with increasing heat treatment duration and temperature [11,12] (Figure 5. 4(a-e)). However, it was also observed that the area and volume fraction remained approximately the same for each heat treatment time and temperature (Figure 5. 4(f)) [10]. (There appears to be a slight increase in volume fraction during annealing at 450°C, which will be considered in subsequent comparative analyses.) The composition of the α-Mg matrix remained approximately the same after each heat treatment as small particles dissolved in favor of larger particles with equivalent volume fraction [12]. The variation in the Al-Mn and Al-Mn-Fe particle size and

---

[4] The presence of deformation twins within the as-received material suggests a large dissolation density.

spacing is shown in Figure 5. 4(a-d). The Al-Mn particles increased in size to approximately 0.4-0.6 μm for long duration heat treatments (Figure 5. 4(a-b)) with variation in the particle spacing from 13 μm to 25 μm. The Al-Mn-Fe particles increased in size from 5 μm to 11 μm with spacings on the order of 50 μm to 100 μm for long duration heat treatments (Figure 5. 4(c-d)). At 450 °C it is possible that the Al_4Mn phase (present at 300 °C) may undergo a phase transformation to Al_8Mn_5 (present above 375 °C) [55].

5.3.2 Corrosion Morphology of AZ31B

The corrosion morphology of a sample heat treated at 300°C for 4 min is shown in Figure 5. 5. The compositional contrast of the SEM (backscatter) micrographs shows several Al-Mn IMPs of varying sizes in the material before corrosion which are also shown in topographical contrast (Figure 5. 5(a)). From the corrosion morphology (Figure 5. 5(b)), what has been termed "filiform-like[5]" corrosion is dominant on the sample surface.

5.3.3 Variation in Corrosion Rate with Particle Size and Spacing

Figure 5. 6 contains a typical Bode magnitude and Bode phase plot from each heat treatment condition (referred to by the IMP size and spacing) with various particle sizes and spacings, acquired at OCP and fit using the equivalent circuit model shown in Figure 5. 1(a). The equivalent circuit was able to provide a reasonable fit over the full frequency range to obtain R_p (Figure 5. 6). The heat treatment condition with the largest particle size and greatest particle spacing had the highest R_p while the sample with the smallest particle size and spacing had the lowest R_p for essentially the same area fraction of Al-rich IMPs. Samples with larger particle sizes and spacings had a lower corrosion rate, based on Equation 5.1. The anodic charge consumed (C/cm^2) calculated for both EIS and from gravimetric mass loss, as determined through Faraday's law (Equation 5.3) assuming congruent dissolution, were shown result in similar values (Figure 5. 7, Table 5. 2). It was found that the as-received material had a higher corrosion rate and anodic dissolution charge compared to all samples heat treated to obtain larger particle sizes and spacings (Figure 5. 7, Table 5. 2). Variation in the assumed Tafel slope, with three different Tafel assumptions is shown to have little impact on the integral determined corrosion rate (Figure 5. 7, Table 5. 2). R_p has a larger impact on the determination of corrosion rate (Equation 5.1) in comparison to B [45,46]. It is also noted that the as-received material may

---

[5] Filiform has been used to describe regions of deep attack and darkening of bare Mg surfaces.

have a higher corrosion rate due to the high dislocation density in the material [56]. However, even when the as-received material is excluded from this analysis there is an observable trend of a decrease in the corrosion rate with an increase in particle size and spacing (Figure 5. 7).

The corrosion rate can be equivalently plotted as $1/R_p$ for variations in the IMP size (Figure 5. 8(a)) and IMP spacing (Figure 5. 8(b)). Again, it was observed that increasing particle size and spacing resulted in a decrease in the corrosion rate[6]. After 24 hours (Figure 5. 8), the as-received material had the highest $1/R_p$ while samples with a larger particle size and spacing had a much lower $1/R_p$ value as a function of both particle size and particle spacing. The 300 °C heat treatments, which had the smallest variation in the particle size and spacing over the time of heat treatment, had the smallest influence on corrosion rate in comparison to 450 °C heat treatment which had the largest influence on the corrosion rate as well as the largest variation of particle size and spacing (Figure 5. 8). It was observed, through both the analysis of the anodic charge consumed over 24 hours and $1/R_p$ that samples with the smallest particle sizes and spacings had the highest corrosion rate (Figures 5. 8(a-b)).

5.3.4   Variation in E-log(i) Corrosion Kinetics with Particle Size and Spacing

Effect of Particle Size and Spacing on the Corrosion of AZ31B

The anodic kinetics for heat treated AZ31B as a function of applied potential were investigated after 24 hours at OCP (Figure 5. 9(a)). There was little variation in the anodic kinetics with variations in the particle size or spacing for the same area fraction. This agreed with previous work which showed that the kinetics of anodically driven Mg-Al alloys, where corrosion is forced in the α-Mg matrix, did not vary with particle size given the same Al composition in the α-Mg matrix [20].

Cathodic polarization curves as a function of particle size and spacing for AZ31B in 0.6 M NaCl after 24 hrs at OCP (Figure 5. 9(b)) showed that there was a variation in the cathodic kinetics with IMP size and spacing. Similar cathodic polarization curves were used to determine the cathodic reaction rate with time, as determined at -1.8 V_{SCE} after 24 hours (Figure 5. 10) in 0.6 M NaCl. The smallest particle size (Figure 5. 10(a)) and spacing (Figure 5. 10(b)) had the

---

[6] This trend is similarly observed if the as-received material is excluded due to its high dislocation density which may alter the corrosion rate.

highest rate of the hydrogen evolution reaction for the IMP particles[7]. The samples heat treated at 400 °C and 450 °C had the highest corrosion rate as a function of IMP size and spacing (Figure 5. 10). The difference with heat treatment is consistent with Figure 5. 8.

Cathodic polarization curves were also used to determine the cathodic reaction rate with time, as determined at -1.8 V_{SCE} after 3 and 24 hours (Figure 5. 11) in the non-chloride containing buffered 0.1 M TRIS solution. In TRIS, there was only a slight decrease in the cathodic kinetics with increasing particle size (Figure 5. 11(a)) and spacing (Figure 5. 11(b)) for both Al-Mn type IMPs and Al-Mn-Fe type IMPS. However, the cathodic reaction rate for all immersion times, as a function of the particle size and spacing were the same, although there was a slight difference in the cathodic kinetics with heat treatment temperature.

Effect of Grain Size on the Corrosion of AZ31B

Considering the debate on the effect of grain size on the corrosion rate of Mg and its alloys [30-36], it is worth making a note of the trend observed in the present study, since heat treatment of AZ31B lead to a change in grain size as well as IMP size and distribution. The corrosion rate (as indicated by the EIS determined i_{corr} at OCP after 24 hours in 0.6 M NaCl) was plotted as a function of grain size (Figure 5. 12). If one excludes the as-received material from the assessment, because it is not yet fully recrystallized and contains a high dislocation density, no measurable variation in corrosion rate with grain size is observed. This suggests corrosion rate more strongly correlates to particle size[8].

5.4 <u>Discussion</u>

5.4.1 Corrosion Morphology

Corrosion in Mg typically initiates at Al-Mn-Fe particles as well as Al-Mn particles [54,57-59]. The high cathodic reaction rates that are typically observed around a particle (evidenced by higher rates of the H_2 evolution at these sites) can lead to higher overall corrosion rates [60-63].

Slight variation in the crystallographic orientation can occur upon heat treatment. The as-received material typically has a strong basal {0001} orientation with a slight preference for the {0001}⟨10$\bar{1}$0⟩ in-plane orientation [40]. Recrystallization of rolled AZ31B produces grains with

---

[7] For the methods reported, Al-Mn-Fe and Al-Mn spacing were reported together, even though they are not completely independent

[8] Future work on the effect of particle size and spacing using model alloys, which negate the effect of grain size, may give further insight into the effect of IMPs on corrosion rate for Mg alloys.

both $\{0001\}\langle 10\bar{1}0\rangle$ and $\{0001\}\langle 11\bar{2}0\rangle$ orientations, though the larger grains possess more of the $\{0001\}\langle 11\bar{2}0\rangle$ texture component. That said, the orientation variations with heat treatment are subtle enough to discount any effect in corrosion due to crystallographic orientation.

5.3.5 Aluminum Enrichment and Anodically Induced Cathodic Activation

Anodically induced cathodic activation has been cited to occur in Mg alloys, especially during anodic polarization, due to enrichment of impurity or alloying elements to the sample surface with exposure to various environments [59,62,64,65]. The elements enrich the surface due to preferential dissolution at anodic polarization of the Mg and have been observed in cross-section using various techniques [17,59,62,64]. The dissolution of Mg has been observed, optically to develop as dark, corroded regions [57,58] where the percent area of these dark regions has shown good agreement with the corrosion rate [66-68]. In particular, Al-Mn and Al-Mn-Fe IMPs have been observed to function as strong cathodes on the sample surface and enrich within the material oxide layer [17,57,62,69,70]. The pH changes with exposure time could also contribute to the enrichment or replating of constituents of these particles on the sample surface. The starting pH of 0.6 M NaCl was measured to be approximately 5.3 with the pH changing to approximately 11. This increased alkalinity of the exposure environment, particularly at the sample surface, can lead to the dissolution Al on the sample surface as well as the redeposition of Al away from the IMP interface [17,70]. At high enough pH, Al will dissolve according to the following half-cell reaction [16]:

$$Al + 2H_2O \rightarrow AlO_2^- + 4H^+ + 3e^- \hspace{2cm} \text{Equation 5.6}$$

While at low pH the dominant reaction is the formation of Al oxide in the solid state:

$$Al + 3H_2O \rightarrow Al_2O_3(s) + 6H^+ + 6e^- \hspace{2cm} \text{Equation 5.7}$$

The Nernst potential for equation 5.6 at pH=11 is -2.50 V_{SCE} (assuming an AlO_2^- concentration of 10^{-6} M), which is much lower in comparison to the OCP of pure Mg (-1.63 V_{SCE}). However, Equation 5.6 would function as the dominant reaction when the solution pH is ~7 while Equation 5.7 would be the dominant reaction for a pH≥11.The corrosion and redeposition of AlO_2^- onto the sample surface thermodynamically possible [16].

This dissolution, and subsequent redeposition of AlO_2^-, can lead to the enrichment of Al on the sample surface and also increase the cathodic kinetics and OCP with time. The diffusion of the AlO_2^- away from the particle will create a concentration gradient around the particle. This

160

Al deposition away from the particle could influence the corrosion rate. However, in the buffered TRIS environment, the starting pH was approximately 7 and the end pH was approximately the same. Therefore, the buffer solution keeps the Al from dissolving by Equation 5.6 [16]. Additionally, the presence of less Mg(OH)$_2$ leads to less of a variation in the pH with time [68]. Therefore, less cathodic activation is seen with time in TRIS (Figure 5. 11) due to less Al enrichment or replating as has been reported elsewhere [68].

The concentration gradient, C(r), of the AlO$_2^-$ released in 0.6 M NaCl solution from the IMP can be plotted assuming a one-dimensional radial diffusion from a spherical electrode according to:

$$\frac{C(r)}{C_{IMP}} = \frac{d}{r}\left[erfc\left(\frac{r-d}{2\sqrt{Dt}}\right)\right]$$

Equation 5.8

Where C$_{IMP}$ is concentration of Al from its center in solution over the IMP (taken to be 1 M), d is the radius of the particle, r is the radial distance away from the particle, D is the diffusion coefficient of AlO$_2^-$ in H$_2$O 1.0×10^{-9} m^2/s, erfc is the complementary error function, and t is the time. For r≥d a concentration gradient is shown where C(r)/C$_{IMP}$<1 while r<d C(r)/C$_{IMP}$ is assumed to be 1. The concentration gradient is shown for two times (3 hours and 24 hours) in Figure 5. 13 in the case of quiescent solution. Hydrogen bubbles would create additional transport by convection. The radial distance outward was normalized (r/d). Therefore, the concentration gradients overlay one another. The concentration gradient approaches 0 at r/d=10 showing that AlO$_2^-$ transport from IMPs can easily be transport over an area approximately 10 times the IMP diameter. This is a concern for small particles at a high density were the chemical concentration profiles may overlap.

5.3.6 Effect of Particle Composition on the Corrosion of AZ31B

Galvanic corrosion is influenced by large potential differences between the anode and cathode, as well a large area ratio of anode to cathode where this may be driven by the composition of the IMP. This is particularly an issue for Mg-alloys which have negative electrochemical potentials[71]. In the Mg-Al alloy system, the α-Mg acts as the anode while the IMP acts as the cathode. Thermodynamic predictions indicate a wide variety of Al-Mn and Al-Mn-Fe IMPs which form in AZ31, depending on processing temperature, such as the Al$_4$Mn which is no longer present above 300 °C while Al$_8$Mn$_5$ forms above 375 °C [55]. It was observed that the 450 °C anneal had the highest cathodic kinetics for each particle size and particle spacing

161

(Figures 5. 10-5. 11). This may be due to variations in the phase transformations and IMP formation during heat treatment [55,72,73]. The Al_8Mn_5 (-1.25 V_{SCE}) is a slightly stronger cathode than the Al_4Mn (-1.45 V_{SCE}) which may lead to the increase in the cathodic kinetics observed in the samples heat treated at 450 °C (Table 5. 1, Figure 5. 10-5. 11).

Variation in the composition of these particles also leads to differences in the kinetics at the interface between these particles and the α-Mg matrix as determined from the IMP OCP (Table 5. 1). The amount of attack from the particles is dependent not only on the composition of the particle but also on the effect of the alloying element in solid solution with the α-Mg matrix. For example, Mg-Zr alloys have been shown to have an increased corrosion rate when processed with smaller particles because, with smaller particles, more Zr is contained in the α-Mg solid solution which is shown to increase the generalized corrosion attack of the matrix [74].

However, in this study the Al content is likely similar to solid solution to both the potential field from the galvanic couple and the enrichment or Al/AlO_2^- redeposition from these particles to the sample surface [17,70]. This region around the particle will also exert some spatial current and potential distribution over some radial distance [75] where the OCP (dependent on composition) determines the potential distribution. This corrosion zone would spread radially outwards from the particle. Most cathodic particles remain on the sample surface, even after corrosion, but the corrosion attack initiates at the edge of these particles and into the surrounding α-Mg matrix [13,57]. The corrosion depth, as calculated from Equation 5.5, suggests that the corrosion depth is less than the particle diameter (Table 5. 3) and therefore can be modeled as a one-dimensional system, ignoring the complications of particles under the sample surface, which become exposed as the corrosion propagates.

The variation in the degree of localized anodic induced galvanic corrosion can be described in terms of the potential distribution around the cathodic particle using an analytical solution of the Laplace equation[76,77]. If the radius of this particle or cluster of particles is d, the polarization resistance for the alloy is R_p (as determined through EIS measurements [45]), E_c is the OCP for the particle, E_m is the OCP of the material matrix, ρ is the solution resistivity and r is the radial distance from the edge of the particle. Therefore, the potential can be described as a function of this potential using Equation 5.9 for the one-dimensional estimation of the potential distribution, assuming r>>d [78].

$$E(r) = E_m - (E_m - E_c) \exp\left[-\left(\frac{3\rho}{4R_p d}\right)^{\frac{1}{2}} r\right]$$

Equation 5.9

The variation in this potential distribution is shown in Figure 5. 14(a) for both an Al-Mn particle (OCP= -1.25 V_{SCE}), an Al-Mn-Fe particle (OCP= -1.05 V_{SCE}) and an Al-Fe particle (OCP= -0.75 V_{SCE}) assuming the same size particle. The OCPs used in this calculation were determined as the approximate average of the typical isolated OCPs for these types of particles (Table 5. 1) [13,79]. In terms of particle spacing, particles which have a higher population density can interact with one another or have overlapping, elevated potentials over the entire Mg solid solution and increase the corrosion rate [78]. From the calculation of this potential distribution, there is a certain spacing in which these zones will interact (~25 µm) for a 1 µm particle (Figure 5. 14(a)). If the particles are spaced wider than this potential zone's width, the zones will not overlap and the corrosion rate will not be negatively affected by distant potential fields from cathodic particles. Longer heat treatments can reduce overlapping zones or make them less likely due to increased spacing (Figure 5. 4(b,d)).

Some particles have a more positive initial OCP and the potential distribution around them is approximately larger (100 µm versus 25 µm) due to variations in the particle composition and size (Figure 5. 14(a)). In order for these particles to not be as detrimental on the corrosion rate, they would have to have a larger spacing than the Al-Mn or there would need to be fewer of these particles (i.e. fewer sites for cathodic activation). This is true for the particle spacing seen in AZ31B where the Al-Mn IMPS have an E(r) and particle spacing of 25 µm while the Al-Mn-Fe IMPS have a E(r) and particle spacing of 100 µm (Figure 5. 4).

5.3.7 Effect of Particle Size on the Corrosion of AZ31B

Particles function as fast sites for H_2 evolution [80]. With more particles, despite their smaller size, there are more sites for active hydrogen evolution. This typically corresponds to a faster corrosion rate in Mg alloys [63,67]. The potential distribution around IMPs with various sizes can be calculated using Equation 5.9 for both Al-Mn and Al-Mn-Fe particles as observed in the alloy (Figure 5. 14(b-c)). It is shown that this region of elevated potential slightly increases with increasing particle size for the same IMP area fraction. However, the size of this zone must be discussed in the context of the particle sizes seen during heat treatment as well as the particle spacing. For a certain particle size and spacing, if the corrosion interaction field operates over a

longer length than the particle spacing, these electrochemical and possibly chemical fields may interact and increase the corrosion rate. A more devastating effect on the corrosion rate would occur for particles which have a higher OCP than Al-Mn or Al-Mn-Fe particles, such as Al-Fe particles which would have a larger potential distribution radius.

To assess the independent effects of size and spacing, one would have to conduct another study in which the area fraction was changed. This is illustrated in Figure 5. 15 which illustrates the region around a cathodic electrode in Mg as the size and spacing of the particles is decreased and the area fraction is kept the same. The geometry of the schematic has been simplified with equal spacing between all particles (Figure 5. 15). This has been undertaken in a separate study using model alloys.

The radial potential distribution around the particle, E(r), may undergo anodically induced cathodic activation, as is seen in many Mg alloys [57,58,62] where the corrosion initiates as these particles. The potential distribution can be related to this amount of anodically induced cathodic activation by determining the full area of anodically induced zone (A^{AIZ}) around the particle through the relationship of E(r), which is approximately equivalent to the radius of the corrosion affected area, r_{zone}, and the number of particles, N. This can be denoted as the grey dotted regions around the particles in Figure 5. 15.

$$A^{AIZ} = \pi (r_{zone})^2 (N) \hspace{4cm} \text{Equation 5.10}$$

The number of particles is determined from the particle spacing and the area fraction for the 1 cm^2 electrochemical testing area. With the same area fraction, as the IMP size increases there is a slight decrease in the area of this anodically induced zone within the electrochemical testing area (Figure 5. 16(a)). This same trend is also seen with an increase in the IMP spacing (Figure 5. 16(b)). The Al-Mn particles are much smaller; however, there are more of these IMPs throughout the material. Meanwhile, there are fewer of the Al-Mn-Fe particles, though they are much larger in size. Therefore, while the Al-Mn-Fe particles in isolation would be expected to have more galvanic interaction with the α-Mg matrix, there is a lower density of particles throughout the material, resulting in a smaller cathodically activated region. Similarly, because there are more Al-Mn particles, there are more cathodically active regions around these particles [17,21].

5.3.8 Variation in the Cathodic Kinetics with Immersion Environment

It was observed that the TRIS environment had less of a decrease in the cathodic kinetics with particle spacing compared to 0.6 M NaCl (Figure 5. 11). It has been previously observed that anodically induced cathodic activation occurs less readily in the TRIS environment [66]. As the pH remains 8, Al replating, which occurs in the chloride-containing, alkaline environment is not able to occur (Equation 5.7 does not occur). Therefore, the anodically induced cathodic activation does not occur [68]. Moreover, in chloride environments, the air-formed MgO oxide hydrolyzes after contact with H_2O, leading to the precipitation of $Mg(OH)_2$ on the sample surface [57,59,69]. However, in TRIS only a small amount of $Mg(OH)_2$ is precipitated [68] as the buffer dissolves the initial air-formed oxide and prohibits additional oxide growth. Hence, the TRIS solution eliminates the zone around the particles and provides a useful diagnostic to confirm the impact of particles and their activated zones on the corrosion of Mg.

5.3.9 Variation in the Corrosion Rate with Particle Distribution: Reflection on Weld Corrosion

As discussed previously in Chapter 2, the particle size (as well as grain size as a consequence of high temperature processing) increases. There were 0.74 ±0.12 μm diameter particles in the FZ, 1.22 ±0.80 μm in HAZ1 and 1.52 ± 0.41 μm in HAZ2 and 0.28 ± 0.18 μm in the wrought base. Approximately the same area fractions of these particles were observed the base material and HAZ while there was a smaller area fraction of these particles in the FZ. From the results determined on the corrosion of AZ31 via heat treatments, there is a decrease in the corrosion rate with large particles (and subsequent increased particle spacing with the same area fraction) due to fewer sites for cathodic activation to occur. From this trend, there would be a decrease in the corrosion rate in HAZ1 and HAZ2 over the wrought base plate. This is the trend that is observed.

Due to the variation in grain size, it merits comment as a consequence of the recrystallization and grain growth observed in the FZ, HAZ1 and HAZ2. While grain size did not have as large of a relationship with the corrosion rate as IMP size/spacing, there was an overall decrease in the corrosion rate with increasing grain size. The FZ had the largest grain size (28.4 ± 5.0 μm), although HAZ1 also had large grains 19.3 ± 2.8 μm and HAZ2 grains were approximately 15.4 ± 1.4 μm. The wrought base had the smallest grains (6 ± 2.0 μm). With an increase in the grain size, there was a decrease in the corrosion rate, with the FZ and HAZs

expecting to have a lower corrosion rates than the wrought base from this perspective based on the microstructure.

5.5 <u>Conclusions</u>

1. Heat treatment induced changes in the IMP (i.e. Al-Mn, Al-Mn-Fe and Al-Fe) size and spacing are shown to have a significant impact on the intrinsic corrosion of wrought AZ31 in NaCl as well as hydrogen evolution reaction rate.

2. The electrochemically assessed corrosion rate and the cathodic reaction rate are inversely proportional to IMP size and spacing at a fixed area fraction of IMPs of the same type in unbuffered NaCl solution.

3. Al-Mn particles raise the potential less than Al-Mn-Fe particles and affect a smaller radial zone in their vicinity. However, Al-Mn-Fe particles have a larger spacing after processing.

4. IMPs create a zone of galvanic interaction with the α-Mg matrix and a zone of chemical AlO_2^- deposition. The zones extend 25 μm for Al-Mn IMPs and 100 μm for Al-Mn-Fe IMPs and overlap for small closely spaced particles. The IMP and zone both contribute to the enhanced corrosion rate and anodically induced cathodic activation.

5. A variation in the cathodic kinetics occurs with exposure environment. The chloride containing environment leads to large variations in the corrosion kinetics with particle size and spacing due to Al dissolution and replating on the sample surface due to the alkalization of the sample surface as well as anodic activation of anodic zones in the α-Mg proximate to the particles. However, in the pH neutral buffer environment, TRIS, there is no variation in the cathodic kinetics as the pH suppresses the Al release and replating.

6. In terms of weld corrosion, the larder particle spacing in the HAZ is beneficial to the lower corrosion rate observed in this zone (Chapter 2) in comparison to the corrosion rate of the HAZ versus the FZ which has smaller, more closely spaced particles.

References

1. M. Kulekci, "Magnesium and its alloys applications in automotive industry," Int J Adv Manuf Technol 39, 9-10 (2008): p. 851-865.
2. M.M. Avedesian and H. Baker, "Magnesium and Magnesium Alloys," ASM International (1999).
3. T.B. Abbott, "Magnesium: Industrial and Research Developments Over the Last 15 Years," Corrosion 71, 2 (2015): p. 120-127.
4. E. Ghali, W. Dietzel, and K.U. Kainer, "General and localized corrosion of magnesium alloys: A critical review," J. of Materi Eng and Perform 13, 1 (2004): p. 7-23.
5. G.L. Makar and J. Kruger, "Corrosion Studies of Rapidly Solidified Magnesium Alloys," Journal of the Electrochemical Society 137, 2 (1990): p. 414-421.
6. I.J. Polmear, "Light Alloys: From Traditional Alloys to Nanocrystals 4th Edition," Elsevier (2006).
7. P. Hoyer, G.L. Angrisani, C. Klose, F.W. Bach, and T. Hassel, "Influence of aluminium on the corrosion behaviour of binary magnesium–aluminium alloys in saline solutions," Materials and Corrosion 65, 1 (2014): p. 23-30.
8. M.A. Jakab, F. Presuel-Moreno, and J.R. Scully, "Effect of Molybdate, Cerium, and Cobalt Ions on the Oxygen Reduction Reaction on AA2024-T3 and Selected Intermetallics Experimental and Modeling Studies," Journal of the Electrochemical Society 153, 7 (2006): p. B244-B252.
9. F.P.-M. M. A. Jakab, J. R. Scully, "Critical Concentrations Associated with Cobalt, Cerium, and Molybdenum Inhibition of AA2024-T3 Corrosion: Delivery from Al-Co-Ce(-Mo) Alloys," Corrosion Journal 61, 3 (2005): p. 246-263.
10. J.J. Bhattacharyya, S.R. Agnew, and G. Muralidharan, "Texture enhancement during grain growth of magnesium alloy AZ31B," Acta Materialia 86, 0 (2015): p. 80-94.
11. I.J. Polmear, Light Alloys Metallurgy of the Light Metals. Third ed, ed. P.P.H. Prof Sir Robert Honeycombe: Arnold, 1995). p. 362.
12. D.A. Porter and K.E. Easterling, Phase Transformations in Metals in Alloys. 2nd ed, 1992.
13. A.D. Südholz, N.T. Kirkland, R.G. Buchheit, and N. Birbilis, "Electrochemical Properties of Intermetallic Phases and Common Impurity Elements in Magnesium Alloys," Electrochemical and Solid-State Letters 14, 2 (2011): p. C5-C7.
14. O. Lunder, J.E. Lein, T.K. Aune, and K. Nisancioglu, "The Role of Mg17Al12 Phase in the Corrosion of Mg Alloy AZ91," Corros Sci 45, 9 (1989).
15. M. Jönsson, D. Thierry, and N. LeBozec, "The influence of microstructure on the corrosion behaviour of AZ91D studied by scanning Kelvin probe force microscopy and scanning Kelvin probe," Corros Sci 48, 5 (2006): p. 1193-1208.
16. M. Pourbaix, Atlas of electrochemical equilibria in aqueous solutions (Huston, TX: National Association of Corrosion Engineers, 1974.
17. M. Danaie, R.M. Asmussen, P. Jakupi, D.W. Shoesmith, and G.A. Botton, "The cathodic behaviour of Al–Mn precipitates during atmospheric and saline aqueous corrosion of a sand-cast AM50 alloy," Corros Sci 83, (2014): p. 299-309.
18. A.A. Nayeb-Hashemi and J.B. Clark, Phase diagrams of binary magnesium alloys (Materials Park, OH: ASM International, 1988.

19. H. Okamoto, Phase diagrams for binary alloys (Materials Park, OH: ASM International, 2000.

20. K. Gusieva, C.H.J. Davies, J.R. Scully, and N. Birbilis, "Corrosion of magnesium alloys: the role of alloying," International Materials Reviews (2014): p. 169-194.

21. M. Zamin, "The Role of Mn in the Corrosion Behavior of Al-Mn Alloys," Corrosion 37, 11 (1981): p. 627-632.

22. R.W. Revie and H.H. Uhlig, Corrosion and Corrosion Control: An Introduction to Corrosion Science and Engineering (Hoboken, New Jersey: Wiley-interscience, 2008.

23. M. Ferhat, A. Benchettara, S.E. Amara, and D. Najjar, "Corrosion behavior of Fe-C alloys in a Sulfuric Medium," Journal of Materials and Environmental Science 5, 4 (2014): p. 1059-1068.

24. Z.Y. Chen, *The role of particles on the initial atmospheric corrosion of copper and zinc: laterial distribution, secondary spreading and CO^{2-}/So^{2-} influence*, in *Doctoral thesis, school of industrial engineering and management*. 2005, Royal Institute of Technology (KTH): Stockholm, Sweden.

25. S. Feliu Jr, A. Samaniego, V. Barranco, A.A. El-Hadad, I. Llorente, and P. Adeva, "The effect of low temperature heat treatment on surface chemistry and corrosion resistance of commercial magnesium alloys AZ31 and AZ61 in 0.6 M NaCl solution," Corros Sci 80, (2014): p. 461-472.

26. M.C. Zhao, M. Liu, G.-L. Song, and A. Atrens, "influence of the beta-phase morphology on the corrosion of the Mg alloy AZ91," Corros Sci 50, (2008): p. 1939-1953.

27. C. Liu, Y. Xin, G. Tang, and P.K. Chu, "Influence of heat treatment on degradation behavior of bio-degradable die-cast AZ63 magnesium alloy in simulated body fluid," Materials Science and Engineering: A 456, 1–2 (2007): p. 350-357.

28. J.D. Majumdar, U. Bhattacharyya, A. Biswas, and I. Manna, "Studies on thermal oxidation of Mg-alloy (AZ91) for improving corrosion and wear resistance," Surface and Coatings Technology 202, 15 (2008): p. 3638-3642.

29. M.A. Melia, P. Steiner, N. Birbilis, J.M. Fitz-Gerald, and J.R. Scully, "Excimer Laser Surface Modification of AZ31B-H24 for Improved Corrosion Resistance " Corrosion Journal 72, 1 (2016): p. 95-109.

30. N.N. Aung and W. Zhou, "Effect of grain size and twins on corrosion behaviour of AZ31B magnesium alloy," Corros Sci 52, 2 (2010): p. 589-594.

31. N. Birbilis, K.D. Ralston, S. Virtanen, H.L. Fraser, and C.H.J. Davies, "Grain character influences on corrosion of ECAPed pure magnesium," Corrosion Engineering, Science & Technology 45, 3 (2010): p. 224-230.

32. J.R. Kish, G. Williams, J.R. McDermid, J.M. Thuss, and C.F. Glover, "Effect of Grain Size on the Corrosion Resistance of Friction Stir Welded Mg Alloy AZ31B Joints," Journal of the Electrochemical Society 161, 9 (2014): p. C405-C411.

33. C. op't Hoog, N. Birbilis, and Y. Estrin, "Corrosion of Pure Mg as a Function of Grain Size and Processing Route," Advanced Engineering Materials 10, 6 (2008): p. 579-582.

34. K.D. Ralston and N. Birbilis, "Effect of Grain Size on Corrosion: A Review," Corros Sci 66, 7 (2010).

35. K.D. Ralston, N. Birbilis, and C.H.J. Davies, "Revealing the relationship between grain size and corrosion rate of metals," Scripta Materialia 63, 12 (2010): p. 1201-1204.

36. K.D. Ralston, G. Williams, and N. Birbilis, "Effect of pH on the Grain Size Dependence of Magnesium Corrosion," Corrosion 68, 6 (2012): p. 507-517.

37. P. Schmutz, V. Guillaumin, R.S. Lillard, J.A. Lillard, and G.S. Frankel, "Influence of Dichromate Ions on Corrosion Processes on Pure Magnesium," Journal of the Electrochemical Society 150, 4 (2003): p. B99-B110.

38. G. Muralidharan, T.R. Muth, W.H. Peter, T.R. Watkins, Y. Wang, D. Randman, B. Davis, M. Alderman, C. Romanoski, and F. Hunter, *Shear rolling of magnesium sheet for automotive, defense, and energy applications*. 2013, Oak Ridge National Laboratory.

39. G. Muralidharan, T.R. Muth, W.H. Peter, T.R. Watkins, D. Randman, D.B. Davis, D.M. Alderman, and C. Romanoski, *Shear Rolling of Magnesium Sheet for Automotive, Defense, and Energy Applications*. 2013. p. Medium: ED.

40. M.A. Steiner, J.J. Bhattacharyya, and S.R. Agnew, "The origin and enhancement of texture during heat treatment of rolled AZ31B magnesium alloys," Acta Materialia 95, (2015): p. 443-455.

41. ASTM-E112, "Standard Test Methods for Determining Average Grain Size," ASTM International (2013).

42. C.A. Schneider, W.S. Rasband, and K.W. Eliceiri, "NIH Image to ImageJ: 25 years of image analysis," Nature Methods 9, (2012): p. 671-675.

43. ASTM-G1, "Standard Practice for Preparing, Cleaning, and Evaluating Corrosion Test Specimens," ASTM International G1, (2011).

44. S. Associates, *ZView*.

45. L.G. Bland, A.D. King, N. Birbilis, and J.R. Scully, "Assessing the Corrosion of Commercially Pure Magnesium and Commercial AZ31B by Electrochemical Impedance, Mass-loss, Hydrogen Collection and ICP-OES Solution Analysis," Corrosion Journal 71, 2 [Special Issue] (2015): p. 128-145.

46. A.D. King, N. Birbilis, and J.R. Scully, "Accurate Electrochemical Measurement of Magnesium Corrosion Rates; a Combined Impedance, Mass-Loss and Hydrogen Collection Study," Electrochimica Acta 121, 1 (2014): p. 394-406.

47. J.R. Scully, Corrosion Journal 56, (2000): p. 199-218.

48. M. Stern and A.I. Geary, Journal of the Electrochemical Society 104: p. 56-63.

49. Z. Shi, F. Cao, G.L. Song, M. Liu, and A. Atrens, "Corrosion behaviour in salt spray and in 3.5% NaCl solution saturated with Mg(OH)2 of as-cast and solution heat-treated binary Mg–RE alloys: RE=Ce, La, Nd, Y, Gd," Corros Sci 76, 0 (2013): p. 98-118.

50. F. Cao, Z. Shi, J. Hofstetter, P.J. Uggowitzer, G. Song, M. Liu, and A. Atrens, "Corrosion of ultra-high-purity Mg in 3.5% NaCl solution saturated with Mg(OH)2," Corros Sci 75, (2013): p. 78-99.

51. D.A. Jones, "Principles and Prevention of Corrosion," Prentice Hall Upper Saddle River. NJ. 2nd Ed (1996).

52. ASTM-G106, "Standard Practice for Verification of Algorithm and Equipment for Electrochemical Impedance Measurements," ASTM International (2010).

53. L. Commin, M. Dumont, R. Rotinat, F. Pierron, J.E. Masse, and L. Barrallier, "Texture evolution in Nd:YAG-laser welds of AZ31 magnesium alloy hot rolled sheets and its influence on mechanical properties," Mat Sci Eng a-Struct 528, 4-5 (2011): p. 2049-2055.

54. R.M. Asmussen, W.J. Binns, R. Partovi-Nia, P. Jakupi, and D.W. Shoesmith, "The stability of aluminum-manganese intermetallic phases under the microgalvanic coupling conditions anticipated in magnesium alloys," Materials and Corrosion 67, 1 (2016): p. 39-50.

55. D.A. Nicole Stanford, "The Effect of Mn-rich Precipitates on the Strength of AZ31 Extrudates," Metallurgical and Materials Transactions A 44, 10 (2013): p. 4830-4843.

56. G.B. Hamu, D. Eliezer, and L. Wagner, "The relation between severe plastic deformation microstructure and corrosion behavior of AZ31 magnesium alloy," Journal of Alloys and Compounds 468, (2009): p. 222-229.

57. Z.P. Cano, M. Danaie, J.R. Kish, J.R. McDermid, G.A. Botton, and G. Williams, "Physical Characterization of Cathodically-Activated Corrosion Filaments on Magnesium Alloy AZ31B," Corrosion 71, 2 (2015): p. 146-159.

58. Z.P. Cano, J.R. McDermid, and J.R. Kish, "Cathodic Activity of Corrosion Filaments Formed on Mg Alloy AM30," Journal of the Electrochemical Society 162, 14 (2015): p. C732-C740.

59. M. Taheri, R.C. Phillips, J.R. Kish, and G.A. Botton, "Analysis of the surface film formed on Mg by exposure to water using a FIB cross-section and STEM–EDS," Corros Sci 59, 0 (2012): p. 222-228.

60. P. Dauphin-Ducharme, R.M. Asmussen, U.M. Tefashe, M. Danaie, W.J. Binns, P. Jakupi, G.A. Botton, D.W. Shoesmith, and J. Mauzeroll, "Local Hydrogen Fluxes Correlated to Microstructural Features of a Corroding Sand Cast AM50 Magnesium Alloy," Journal of the Electrochemical Society 161, 12 (2014).

61. U.M. Tefashe, M.E. Snowden, P.D. Ducharme, M. Danaie, G.A. Botton, and J. Mauzeroll, "Local flux of hydrogen from magnesium alloy corrosion investigated by scanning electrochemical microscopy," Journal of Electroanalytical Chemistry 720–721, (2014): p. 121-127.

62. M. Taheri, J.R. Kish, N. Birbilis, M. Danaie, E.A. McNally, and J.R. McDermid, "Towards a Physical Description for the Origin of Enhanced Catalytic Activity of Corroding Magnesium Surfaces," Electrochimica Acta 116, (2014): p. 396-403.

63. G. Williams, N. Birbilis, and H.N. McMurray, "The source of hydrogen evolved from a magnesium anode," Electrochemistry Communications 36, 0 (2013): p. 1-5.

64. M. Taheri and J.R. Kish, "Nature of Surface Film Formed on Mg Exposed to 1 M NaOH," Journal of the Electrochemical Society 160, 1 (2013): p. C36-C41.

65. T. Cain, S.B. Madden, N. Birbilis, and J.R. Scully, "Evidence of the Enrichment of Transition Metal Elements on Corroding Magnesium Surfaces Using Rutherford Backscattering Spectrometry," Journal of the Electrochemical Society 162, 6 (2015): p. C228-C237.

66. L.G. Bland, J.M. Fitz-Gerald, and J.R. Scully, "Metallurgical and Electrochemical Characterization of the Corrosion of AZ31B-H24 Tungsten Inert Gas Weld: Isolated Weld Zones," Corrosion Journal 72, 9 (2016): p. 1116-1132.

67. M. Curioni, F. Scenini, T. Monetta, and F. Bellucci, "Correlation between electrochemical impedance measurements and corrosion rate of magnesium investigated by real-time hydrogen measurement and optical imaging," Electrochimica Acta 166, (2015): p. 372-384.

68. L.G. Bland, B.C.R. Troconis, R.J.S. Jr., J.M. Fitz-Gerald, and J.R. Scully, "Metallurgical and Electrochemical Characterization of the Corrosion of Mg-Al-Zn Alloy AZ31B-H24 Tungsten Inert Gas Weld: Galvanic Corrosion Between Weld Zones " Corrosion Journal in press (DOI: 10.5006/2078), (2016).

69. R.C. Phillips and J.R. Kish, "Nature of Surface Film on Matrix Phase of Mg Alloy AZ80 Formed in Water," Corrosion 69, 8 (2013): p. 813-820.

70. R.M.A. Mohsen Danaie, Pellumb Jakupi, David W. Shoesmith, and G.A. Botton, "The role of aluminum distribution on the local corrosion resistance of the microstructure in a sand-cast AM50 alloy," Corros Sci 77, (2013).

71. T. Cain, L. Bland, N. Birbilis, and J. Scully, "A compilation of corrosion potentials for magnesium alloys," Corrosion 70, 10 (2014): p. 1043-1051.

72. A.D.P. Adarsh Shukla, "Thermodynamic Assessment of the Al-Mn and Mg-Al-Mn Systems," Journal of Phase Equilibria and Diffusion 30, 1 (2009): p. 28-39.

73. M. Asgar-Khan and M. Medraj, "Thermodynamic Description of the Mg-Mn, Al-Mn and Mg-Al-Mn Systems Using the Modified Quasichemical Model for the Liquid Phases," Materials Transactions 50, 5 (2009): p. 1113-1122.

74. D.S. Gandel, M.A. Eastona, M.A. Gibsona, T. Abbott, and N. Birbilis, *The Influence of Mg-Zr Master Alloy Microstructure on the Corrosion of Mg*, in *Magnesium Technology 2013*. 2013, John Wiley & Sons, Inc. p. 157-162.

75. A.D. King, J.S. Lee, and J.R. Scully, "Galvanic Couple Current and Potential Distribution between a Mg Electrode and 2024-T351 under Droplets Analyzed by Microelectrode Arrays," Journal of the Electrochemical Society 162, 1 (2015).

76. J.R. Scully and D.E. Peebles, "Metastable pitting corrosion of aluminum, Al-Cu, and Al-Si thin films in dilute HF solutions and its relevancy to the processing of integrated circuit interconnections," MRS Online Proceeding Library (1990).

77. R.G. Buchheit, *Local corrosion of Al-Li-Cu alloys*, in *Materials Science and Engineering*. 1991, University of Virginia: Charlotteville, VA.

78. S. Jain, J.L. Hudson, and J.R. Scully, "Effects of constituent particles and sensitization on surface spreading of intergranular corrosion on a sensitized AA5083 alloy," Electrochimica Acta 108, (2013): p. 253-264.

79. G.L. Song and A. Atrens, "Understanding Magnesium Corrosion. A Framework for Improved Performance " Advanced Engineering Materials 5, 12 (2003).

80. N. Birbilis, A.D. King, S. Thomas, G.S. Frankel, and J.R. Scully, "Evidence for enhanced catalytic activity of magnesium arising from anodic dissolution," Electrochimica Acta 132, 0 (2014): p. 277-283.

Table 5. 1. Open circuit potential for various IMPs [4, 13, 74]

IMP	Solution	Open Circuit Potential (V_{SCE})
Pure Mg	0.6 M NaCl	-1.65
AZ31B	0.6 M NaCl	-1.57
Al_6Mn	0.85 M NaCl + $Mg(OH)_2$	-1.52
Al_4Mn	0.85 M NaCl + $Mg(OH)_2$	-1.45
Al_8Mn_5	0.85 M NaCl + $Mg(OH)_2$	-1.25
$Mg_{17}Al_{12}$	0.85 M NaCl + $Mg(OH)_2$	-1.2
$Mg_{17}Al_{12}$	0.1 M NaCl	-1.2
Al_8Mn_5Fe	0.85 M NaCl + $Mg(OH)_2$	-1.2
Mg_2Al_3	0.85 M NaCl + $Mg(OH)_2$	-1.18
$Al_6Mn(Fe)$	0.85 M NaCl + $Mg(OH)_2$	-1.1
$Al_6(MnFe)$	0.85 M NaCl + $Mg(OH)_2$	-1.0
$Al_3Fe(Mn)$	0.85 M NaCl + $Mg(OH)_2$	-0.95
Al_3Fe	0.85 M NaCl + $Mg(OH)_2$	-0.74

Table 5. 2. Anodic charge associated with corrosion rate of Mg as calculated by integration of i_{corr} derived from EIS-estimated R_P where B_{King}=36.0 mV, B_{Shi}=36.8 mV[49], and B_{Cao}=31.1 mV[54] in 0.6 M NaCl were used[45, 46] after exposure in 0.6 M NaCl at open circuit for 24 hours as per the equivalent circuit.

				B_{king}	for B_{shi}	for B_{Cao}
Temp (°C)	Time (min)	$\Sigma Q_{\Delta m}(C/cm^2)$	Depth (μm)	$\Sigma Q_{EIS}^{SG}(C/cm^2)$	$\Sigma Q_{EIS}^{SG}(C/cm^2)$	$\Sigma Q_{EIS}^{SG}(C/cm^2)$
As received	--	10.9 ± 1.1	7.9 ± 1.0	10.8 ± 1.3	9.0 ± 1.3	7.6 ± 1.1
300	4	5.8 ± 0.4	2.4 ± 0.4	3.2 ± 0.5	2.7 ± 0.5	2.3 ± 0.4
300	300	4.1 ± 0.4	2.0 ± 0.3	2.8 ± 0.4	2.3 ± 0.4	2.0 ± 0.3
300	10080	2.3 ± 0.3	2.0 ± 0.3	2.7 ± 0.4	2.2 ± 0.4	1.9 ± 0.3
400	4	5.1 ± 0.6	3.2 ± 0.6	4.4 ± 0.8	3.7 ± 0.8	3.1 ± 0.6
400	1080	1.8 ± 0.5	1.4 ± 0.2	1.9 ±0.3	1.6 ± 0.3	1.3 ± 0.2
400	10080	1.9 ± 0.7	1.6 ± 0.4	2.2 ± 0.6	1.9 ± 0.6	1.6 ± 0.5
450	4	1.4 ± 0.8	1.1 ± 0.6	1.5 ± 0.8	1.2 ± 0.8	1.1 ± 0.7
450	1320	1.6 ± 0.7	0.8 ± 0.7	1.1 ± 0.9	0.9 ± 0.9	0.8 ± 0.7
450	10080	0.5 ± 0.3	0.5 ± 0.2	0.7 ± 0.3	0.6 ± 0.3	0.5 ± 0.2

a)
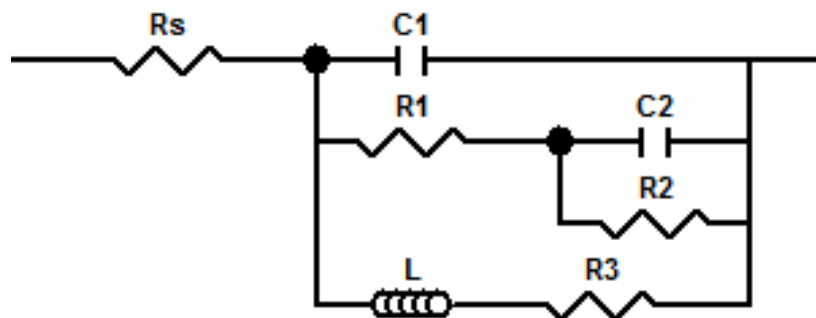
b)
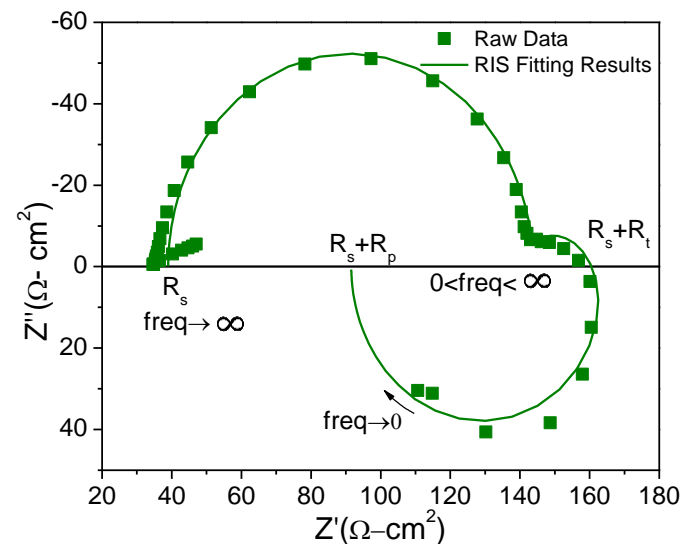
Figure 5. 1. a) Equivalent circuit diagram used to model pseudo-inductive electrochemical impedance response on corroding Mg in 0.6 M NaCl solution and b) EIS measurement (scatter plot) and model fit (solid lines) of high purity Mg after 24 hours of immersion at open circuit in quiescent 0.1 M NaCl displaying low frequency inductance. R_t defined as the value corresponding to Z' when $-Z''= 0$, while R_P is defined as the zero frequency impedance at $-Z''= 0$.

174
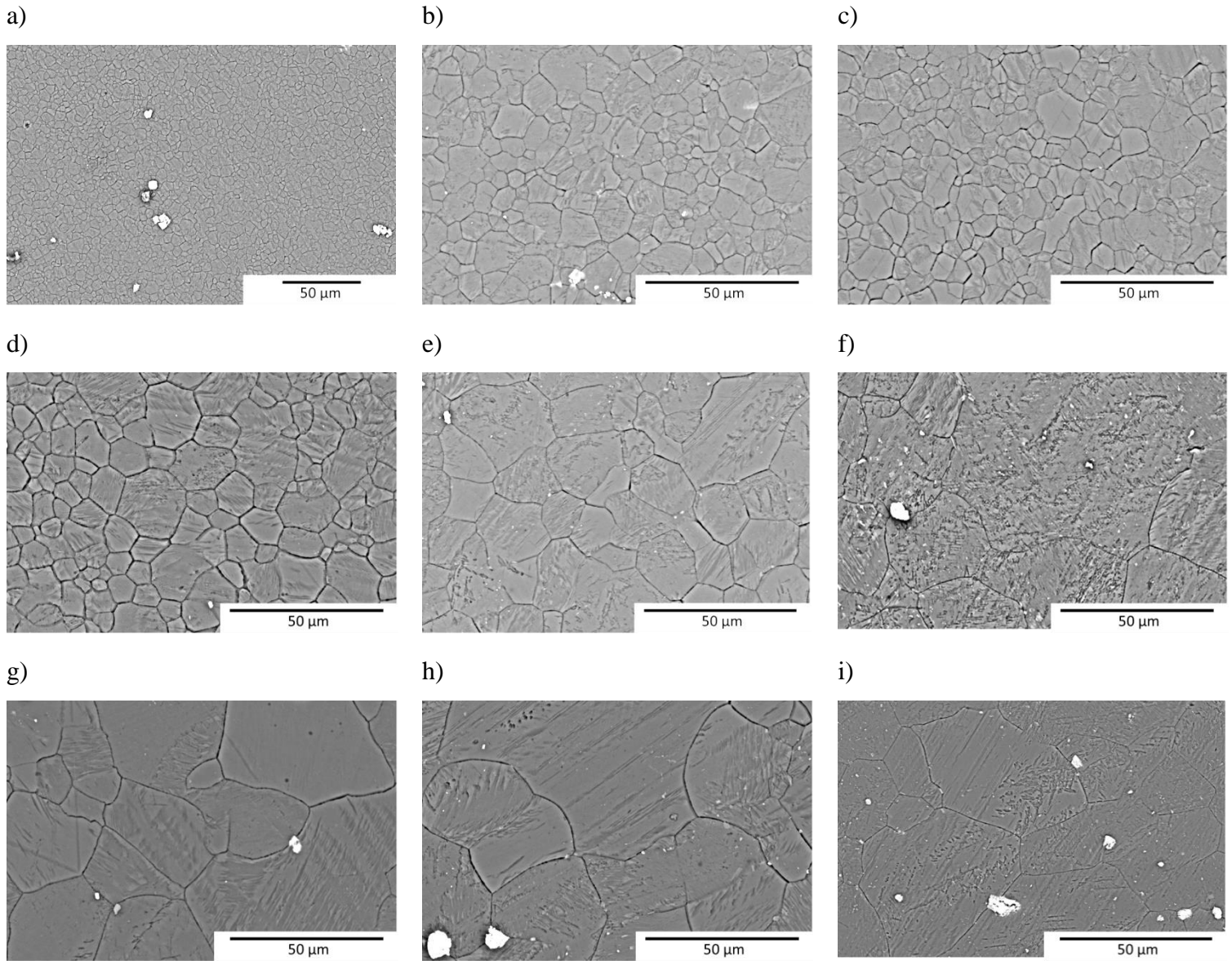
Figure 5. 2. Backscatter electron micrograph of various grain sizes and particle distributions achieved through different heat treatments. a) As-received, b) 300 °C for 4 min, c) 300 °C for 7 days, d) 400 °C for 4 min, e) 400°C for 10 min, f) 400°C for 7days, g) 450 °C for 4 min h) 450 °C for 10 min and i) 450 °C for 7 days

a) b)

c) d)
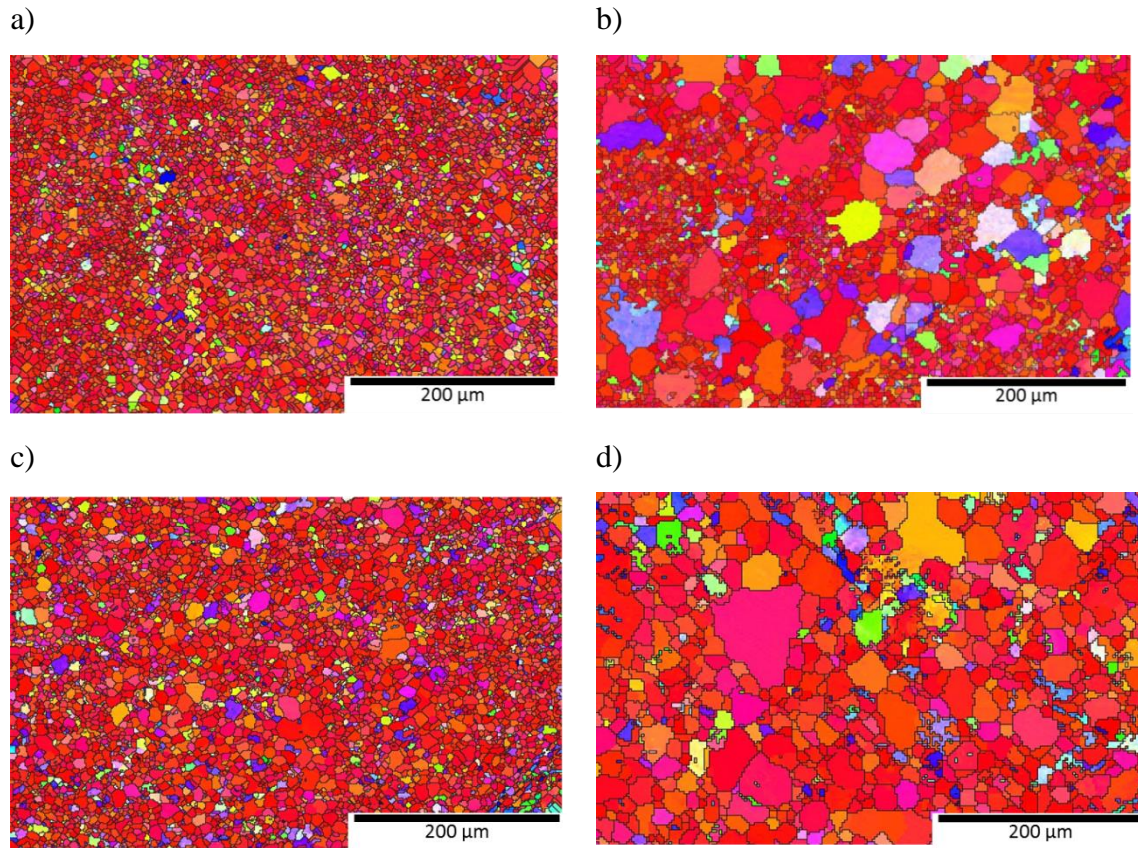
Figure 5. 3. Backscatter electron micrograph of various grain sizes and particle distributions achieved through different heat treatments. a) 300 ℃ for 4 min, b) 300 ℃ for 300 min, c) 400 ℃ for 4 min, d) 400 ℃ for 1000 min. Some abnormal grain growth characteristics are shown in b) and d).

176
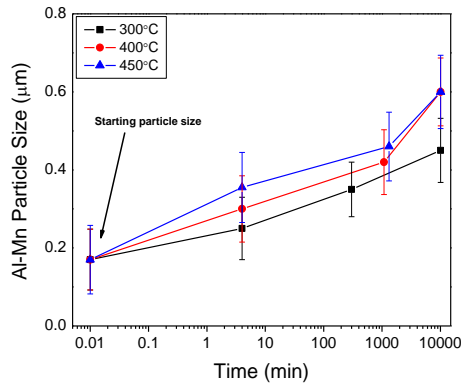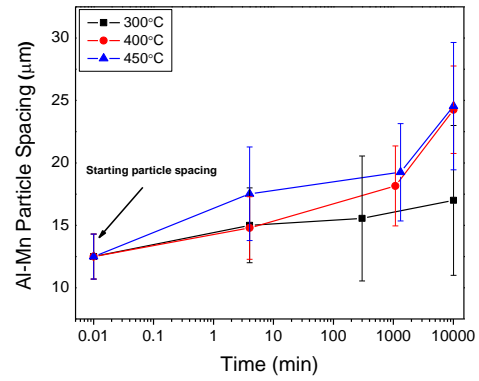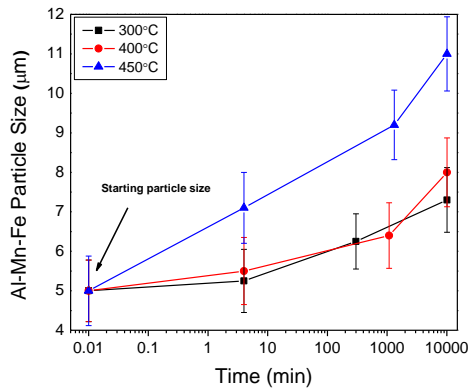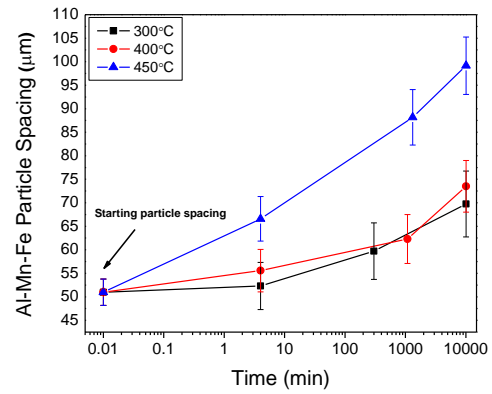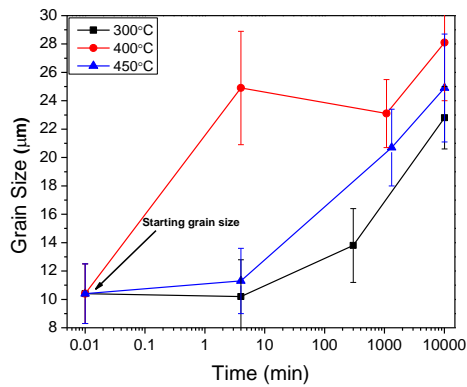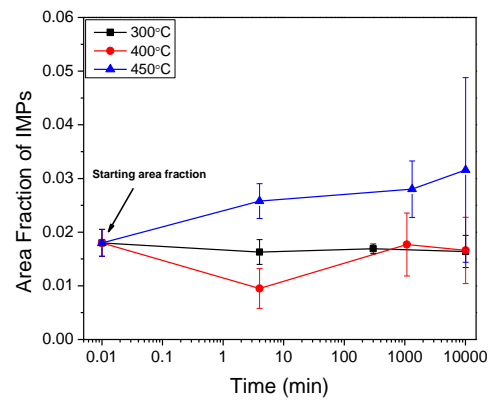
Figure 5. 4. Summary of a) Al-Mn particle size, b) Al-Mn particle spacing, c) Al-Mn-Fe particle size, d) Al-Mn-Fe particle spacing, e) grain size and f) area fraction of IMPs for AZ31 heat treated samples. Standard deviation is shown.
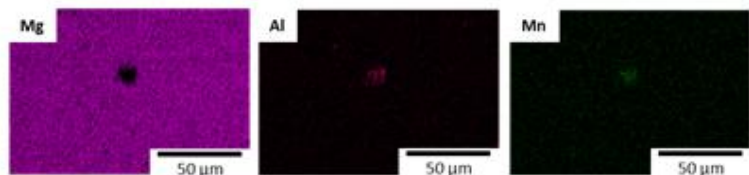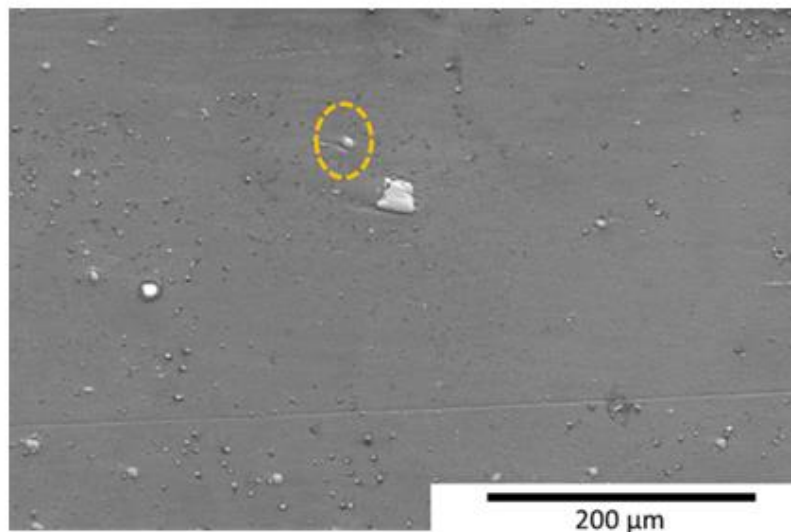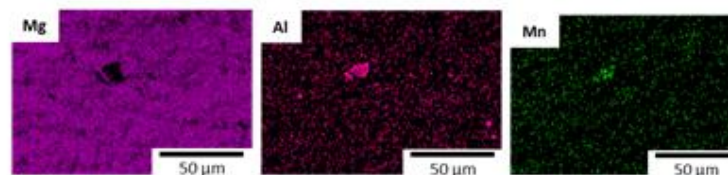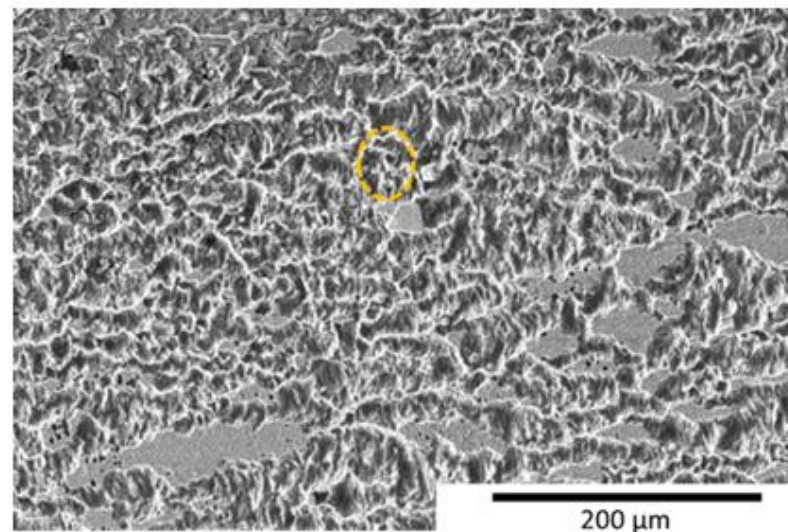
Figure 5. 5. Secondary electron micrographs of (a) AZ31B HT sample before exposure and EDS of element distributions in AZ31B HT sample before exposure, (b) AZ31B HT specimen after exposure and cleaned with CrO_3 to remove any oxides, (d) EDS of element distributions in AZ31B HT sample after exposure after 3 hr immersion at OCP in 0.6 M NaCl. Sample was heat treated at 300 °C for 4 min.
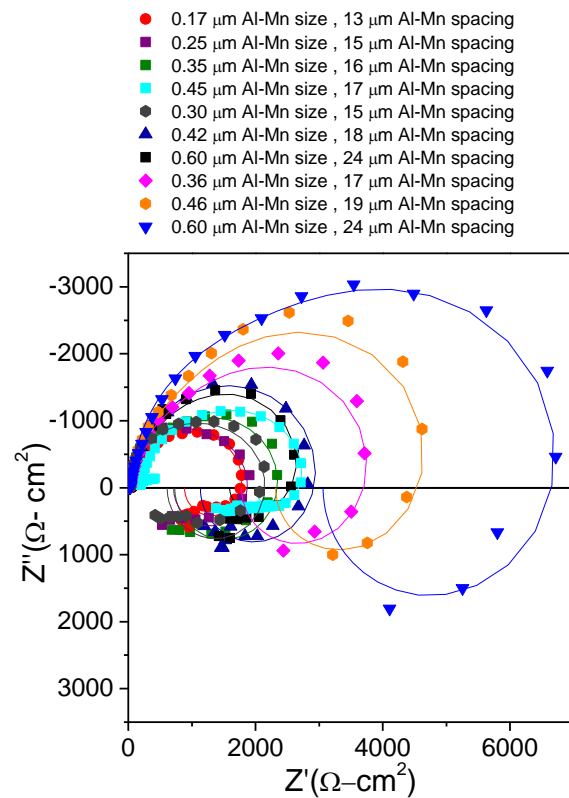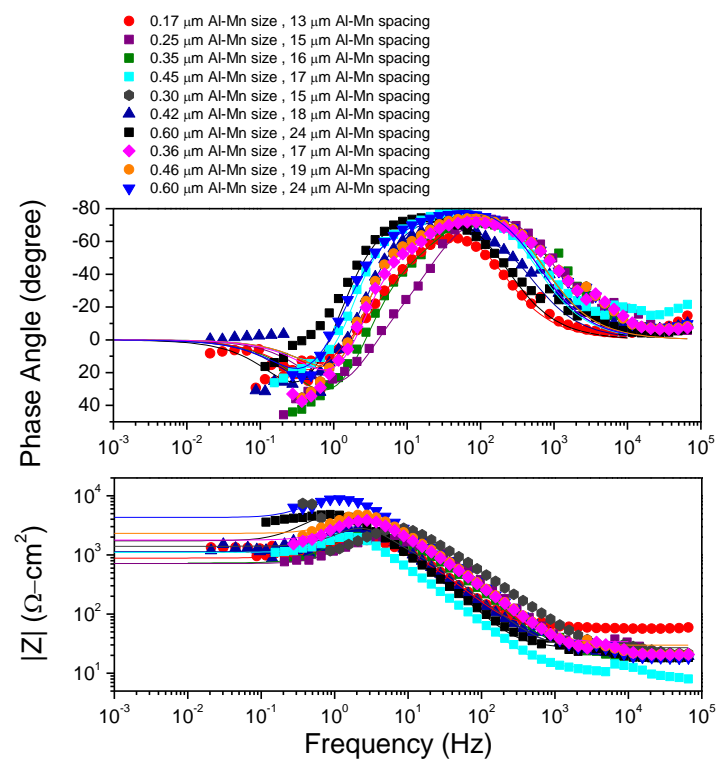
Figure 5. 6. (left) Nyquist plots and (right) Bode magnitude and phase plot for AZ31B heat treated samples with variation in the particle size and spacing. Data shown along with respective fits following 24 hours immersion in 0.6 M NaCl at open circuit. Particles have been labeled only by Al-Mn particle size and spacing for simplification.
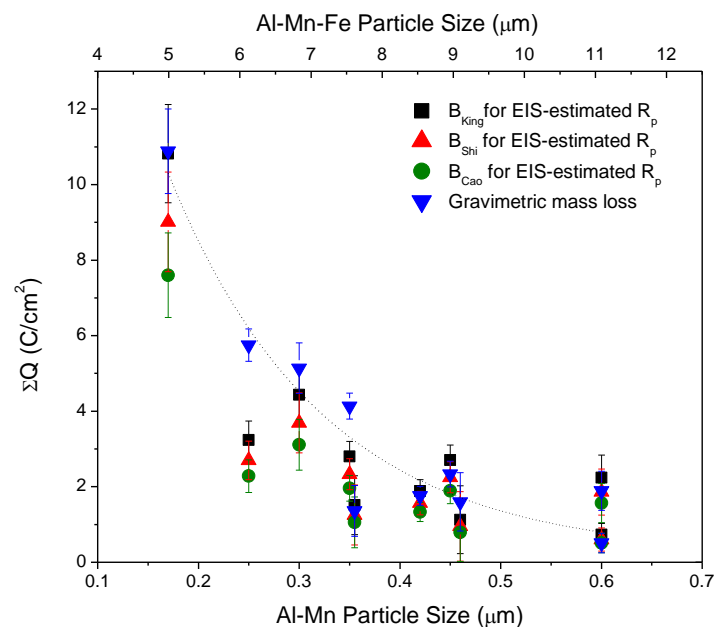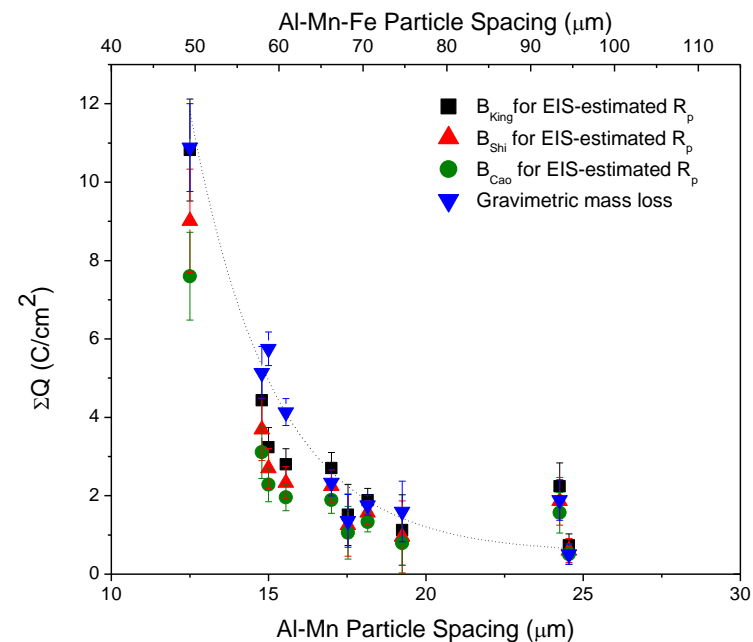
Figure 5. 7. Variation in the electrochemical impedance spectroscopy derived anodic charge, Q_a^{EIS} and $Q_a^{\Delta m}$, corrosion rate as determined at OCP in 0.6 M NaCl over 24 hours as a function of a) Al-Mn and Al-Mn-Fe particle size and b) Al-Mn and Al-Mn-Fe particle spacing. The standard error of three replicates is shown.

a)
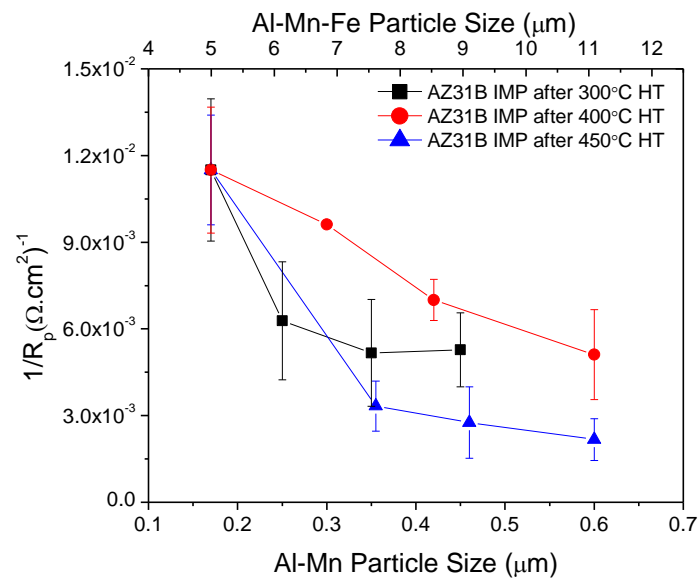
b)
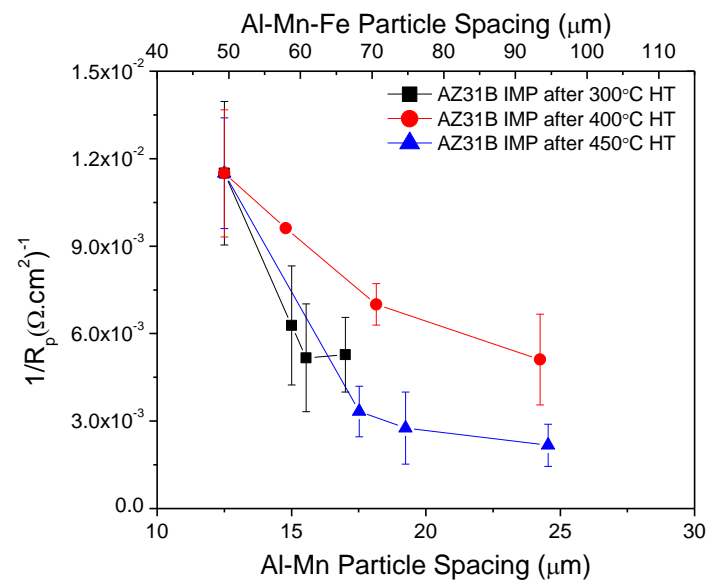
Figure 5. 8. Effect of Al-Mn and Al-Mn-Fe particle a) size and b) spacing on the corrosion rate of AZ31B after 24 hours in 0.6 M NaCl. The standard error of three replicates is shown.
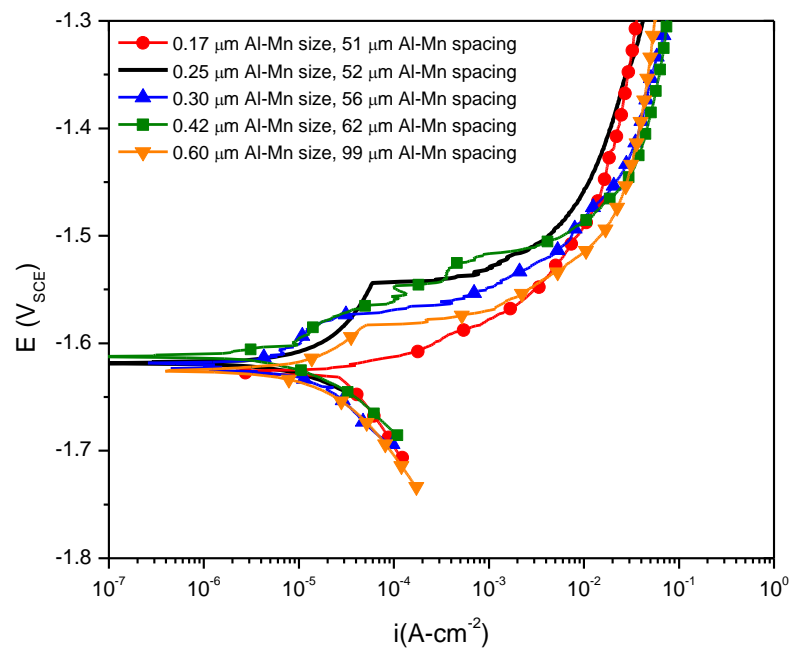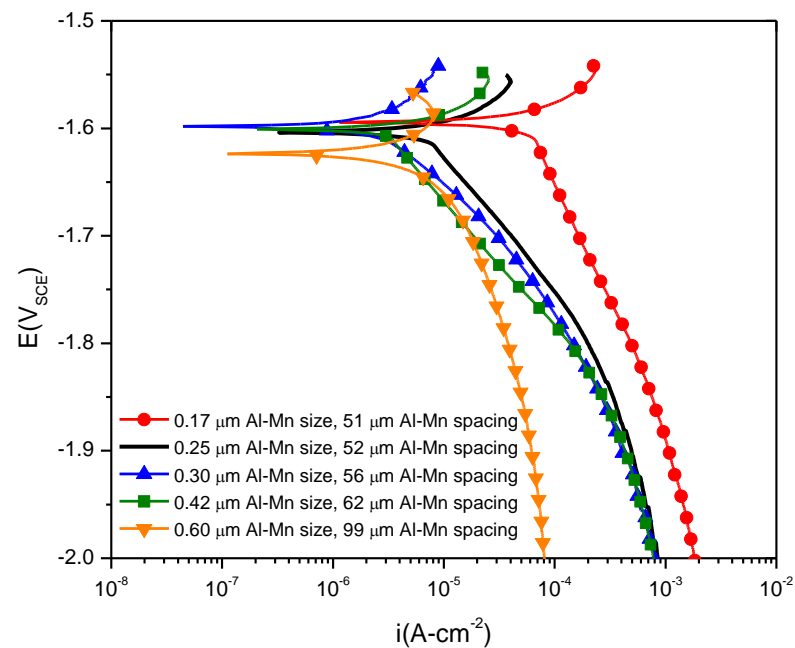
Figure 5. 9. a) Variation in the E-log(i) anodic kinetics and b) variation in the E-log(i) cathodic kinetics with heat treatment for various samples with different particle sizes and spacings. Representative curves are shown and taken after 24 hours at OCP in 0.6 M NaCl. Particles have been labeled only by Al-Mn particle size and spacing for simplification.
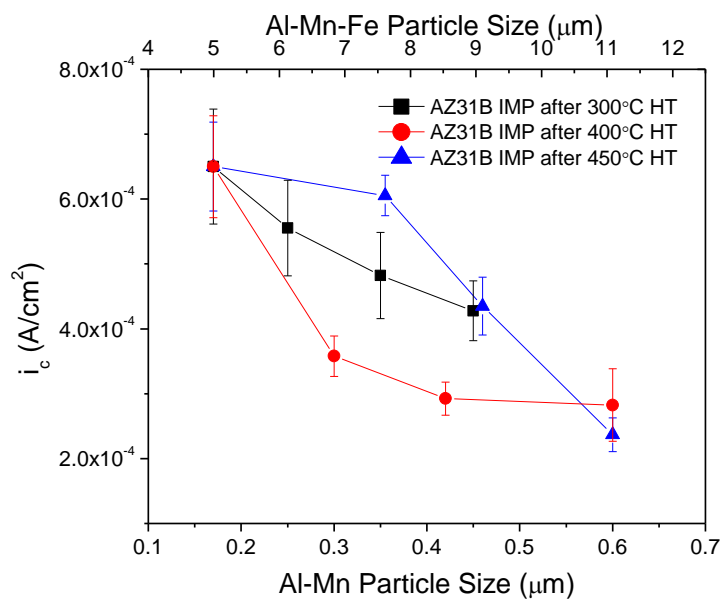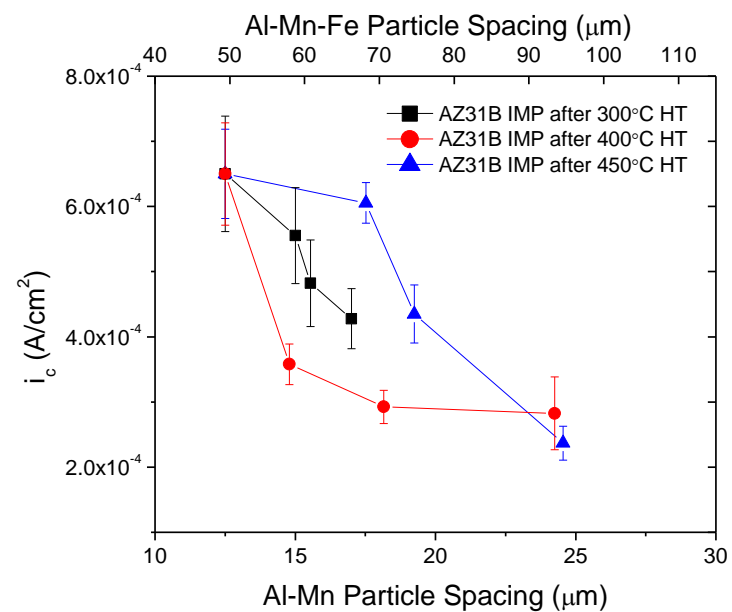
Figure 5. 10. Effect of Al-Mn and Al-Mn-Fe particle a) size and b) spacing on the cathodic reaction rate of AZ31B after 24 hours in 0.6 M NaCl. The standard error of three replicates is shown.
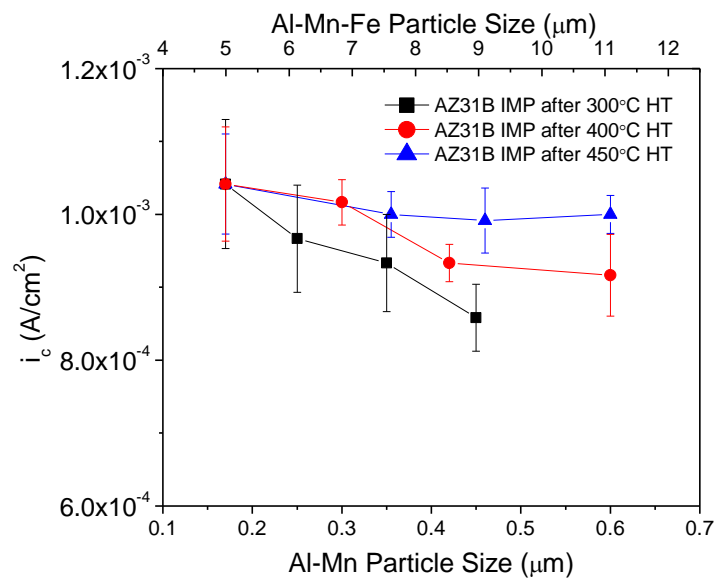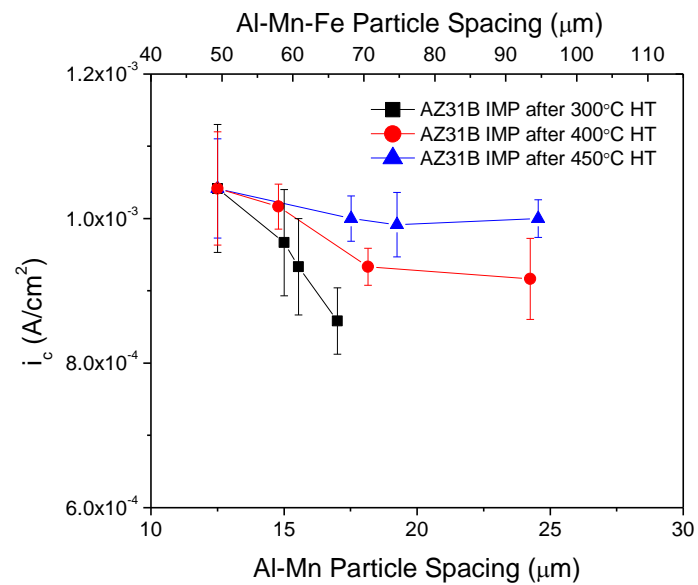
Figure 5. 11. Effect of Al-Mn and Al-Mn-Fe particle a) size and b) spacing on the cathodic reaction rate of AZ31B after 24 hours in 0.1 M TRIS. The standard error of three replicates is shown.
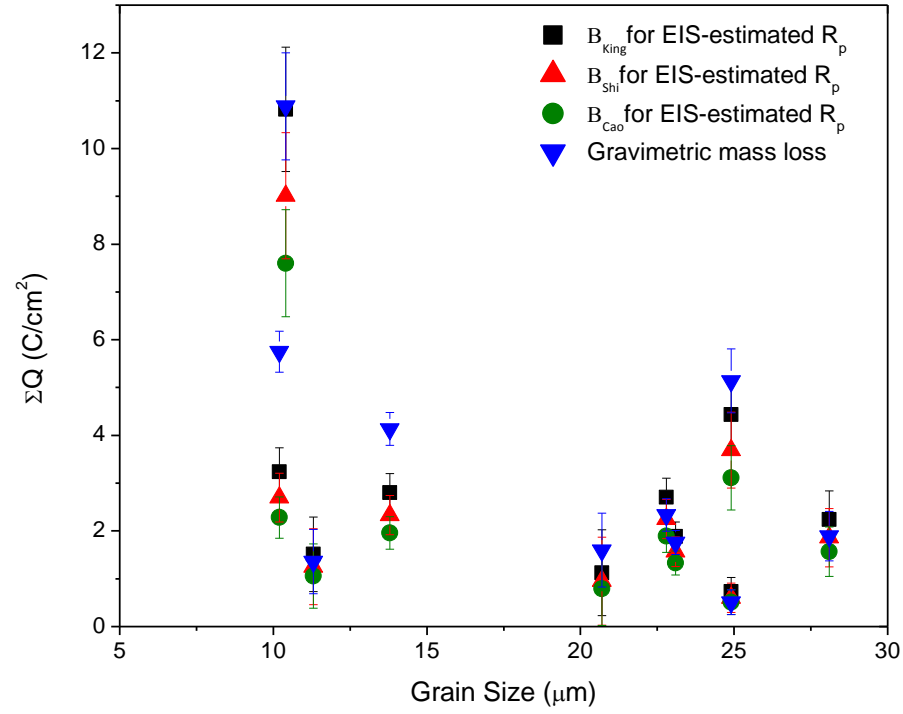
Figure 5. 12. Variation in the electrochemical impedance spectroscopy derived anodic charge, $\mathbf{Q_a^{EIS}}$ and $\mathbf{Q_a^{\Delta m}}$, corrosion rate as determined at OCP in 0.6 M NaCl over 24 hours as a function of grain size. The standard error of three replicates is shown.
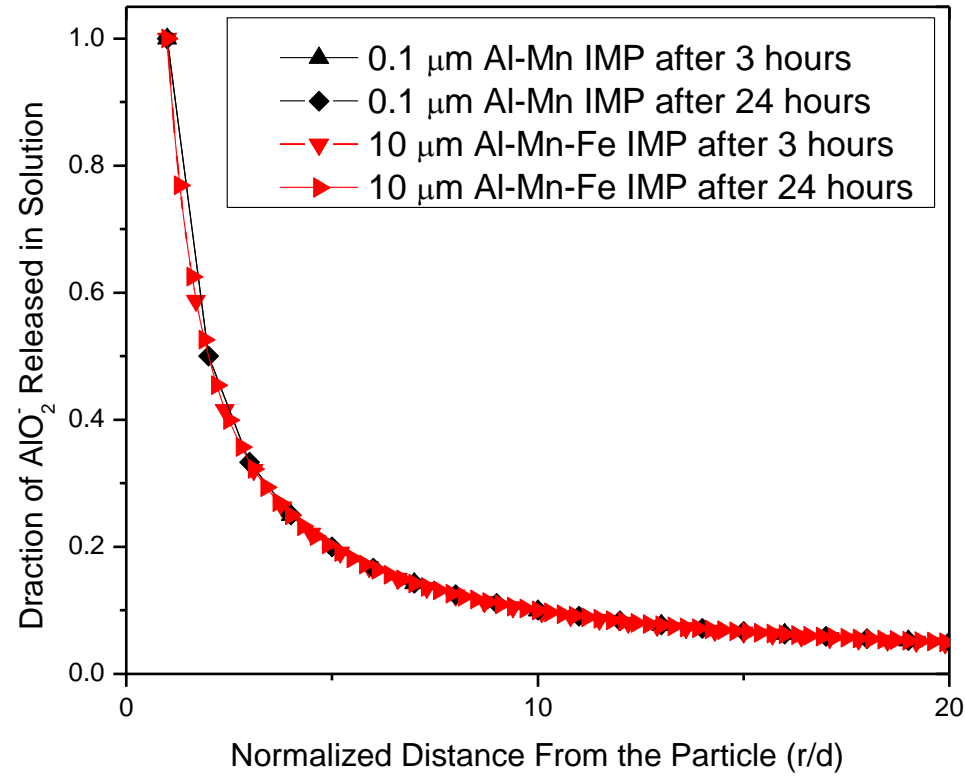
Figure 5. 13. The one-dimensional steady state concentration gradient of AlO_2^- away from the Al-rich IMP interface assuming spherical transport for both 0.1 μm (Al-Mn) and 10 μm (Al-Mn-Fe) intermetallic phase embedded in Mg.
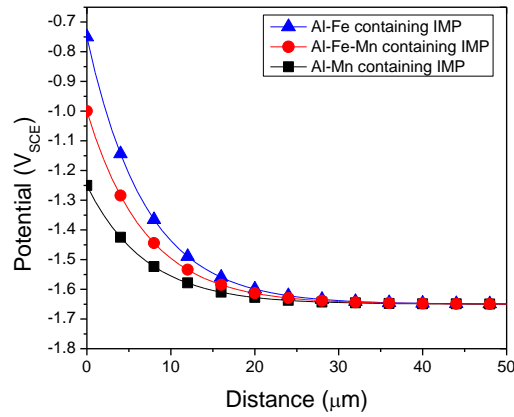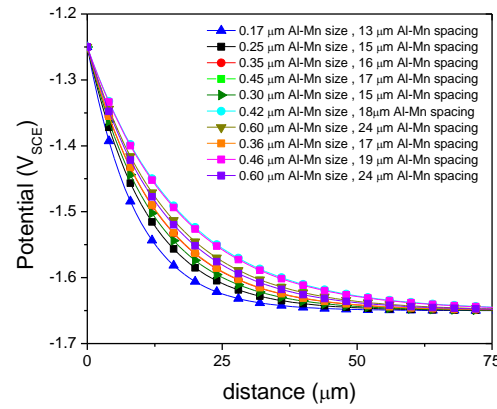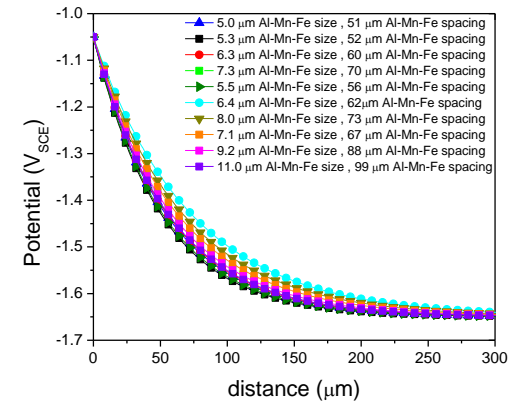
Figure 5. 14. a) Effect of IMP composition on potential distribution. d=0.1 μm. Effect of IMP size on potential distribution ,E(r). As the particle size increases, the zone of galvanic interaction increases for b) Al-Mn particles and c) Al-Mn-Fe particles. R_p =90.8 Ω-cm^2,[45], p=25 Ω^{-1}cm^{-1}.
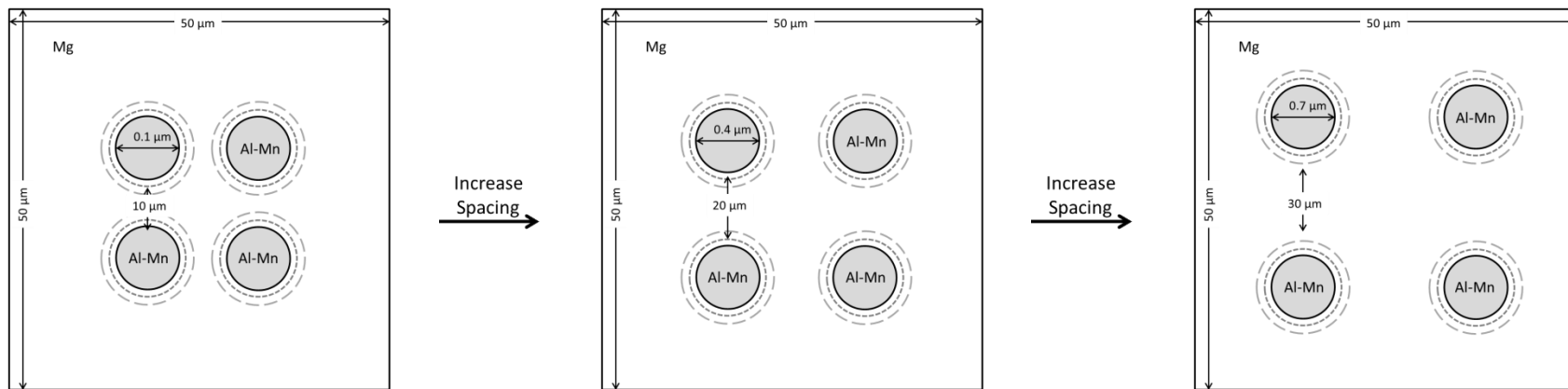
Figure 5. 15. Schematic of the corrosion zone around a particle for the example case of an Al-Mn IMP (a similar situation would occur for an Al-Mn-Fe IMP) with varied spacing and constant size. Schematic not to scale.
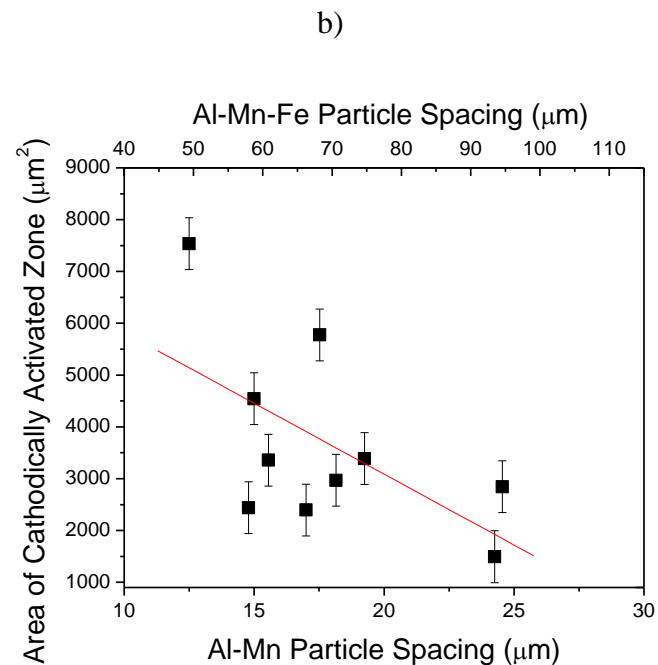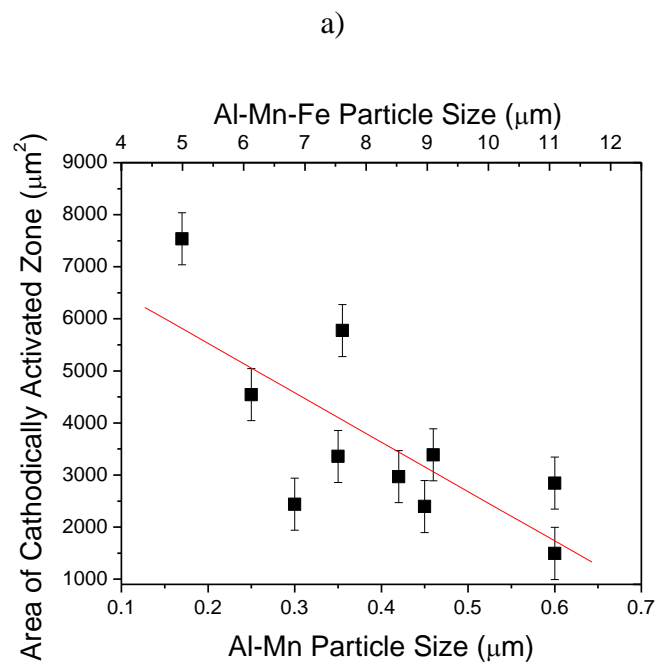
Figure 5. 16. Cathodically Activated Regions around IMPs for samples with approximately the same IMP area fraction as determined through ImageJ[TM] as a function of a) IMP size and b) IMP spacing. A liner fit of the data is shown. Error bars reported as standard error for three replicate measurements.

6 Exploring the Effects of Intermetallic Particle Size and Spacing on the Corrosion of Mg-Al Alloys Using Model Electrodes

The effect of the area fraction, size and distribution of model cathodic, intermetallic particles (IMPs) in an anodic Mg matrix on corrosion was investigated. Model samples were developed to study IMP effects in isolation from other metallurgical effects, with particles simulated by Al electrodes embedded in a Mg matrix. Arrays of model Mg-Al electrodes were constructed using high purity Al as a surrogate for Al-rich IMPs and flush mounted in commercial purity Mg. The area fraction, size and spacing of these electrodes each altered the corrosion rate and cathodic reaction kinetics over a 24 and 48 hour immersion period at the open circuit potential. Corrosion rate increased with increasing area fraction of the Al electrodes but decreased with increasing electrode spacing. The effected zone around electrodes and at the Al/Mg interface was explored in detail to ascertain its impact on the resultant global corrosion rate and kinetics. The effect of local pH at the Al electrode on the prospects for Al^{3+} corrosion and redeposition was also explored.

A manuscript based on this chapter has been submitted to the Journal of the Electrochemical Society as a Full Research Paper, "Exploring the Effects of Intermetallic Particle Size and Spacing on the Corrosion of Mg-Al Alloys Using Model Electrodes."

Representative author contributions:

L.G. Bland: experiments, metallurgical and electrochemical characterization
N. Birbilis: supplied IMP curves, analysis and interpretation
J.R. Scully: adviser, analysis and interpretation

6.1 Introduction

Magnesium (Mg) alloys continue to be of growing interest due to their good balance of specific properties (i.e. properties relative to weight) [1-3]. However, due to the inherently negative electrochemical potential of Mg and its alloys [4,5], Mg-alloys are highly reactive compared to other engineering metals. Mg-alloys are susceptible to several forms of localized corrosion, whilst also highly prone to macro- as well as micro-galvanic corrosion. Due to the low solid solubility of most alloying elements in Mg [6] and particularly low solubility limits for most transition elements; secondary phases readily form during most types of material processing, including casting [7,8] and welding [9-15], which can adversely alter the corrosion performance.

There are many secondary phases, or intermetallic particles (IMPs), which are particularly common in Mg alloys. Each IMP [16] has its own unique dissolution or reduction kinetics, dependent on its composition, size and dispersion within the material. For example, in the Mg-Al alloys which contain Mn (such as AZ31, AZ91 and AM50), Al-Mn IMPs that are rich in Al such as Al_4Mn, Al_6Mn, display relatively low rates of cathodic kinetics in comparison to other IMPs that are rich in Mn such as Al_8Mn_5; the latter displaying relatively rapid cathodic kinetics [1,7,17]. Similarly, the so called Al-Mn-Fe IMPs, such as $Al_8(Mn,Fe)_5$ function as highly potent cathodic sites in Mg, although the Mn has been shown to prevent some of the detrimental galvanic effects of Fe impurities by incorporating the Fe into the Al-Mn IMPs [1,6,16]. Furthermore, Mg-Zn IMPs have approximately the same open circuit potential (OCP) as many Mg alloys, however the cathodic kinetics of this IMP are more rapid than Mg [16], attributed to the presence of Zn. Mg-Zn IMPs are cathodic to the α-Mg and, therefore, tend to localize corrosion micro-galvanic coupling which is often manifest at the Mg matrix/IMP interface. Some of these trends are outlined in Table 6. 1. However, the effects of so-called 'cathodic' IMPs with regard to the dissolution they cause upon the α-Mg matrix require further attention, particularly regarding of how the size and location/spacing of IMPs alter the overall corrosion rate.

Of relevance to the corrosion of Mg and its alloys, it has been suggested [18-21] that the exchange current density for the hydrogen evolution reaction (HER) increases with the rate of Mg dissolution. Meanwhile, other workers have used spatial and temporal methods to determine that Mg dissolution is accompanied by enhanced cathodic activity on the Mg surface [19,22-26]. Cathodically active sites have been examined through the use of scanning vibrating electrode technique (SVET) on 99.9% [25] and 99.99% [23] pure Mg, Mg-Nd binary alloys [24] and AZ31 [22,27].

To date, mechanisms have been proposed, which explain this behavior, including: (i) transition metal enrichment [28,29], (ii) particle enrichment to the oxide layer [26,30,31] and (iii) Al replating [30].

Evidence of cathodic activation has been noted to also be influenced by cathodic sites upon the Mg sample surface, namely intermetallic particles (IMPs) and impurities [19,26,32]. However, it has also been demonstrated that most of the hydrogen evolution reaction (HER) upon corroding Mg-alloys occurs at the anodic front (i.e. the sites of active dissolution) [21]. The dissolution of Mg at these sites has been observed to develop as dark regions which propagate through the a mechanism with filiform-like morphology typically cited on many Mg alloys, including AZ31 and AM30 [32,33]. The Mg-alloy corrosion rate was also found to correlate with the percent area of these dark, corroded regions in chloride environments [9,34]. Rapid HER on Mg-alloys was also correlated with increased corrosion or cathodic activity at these dark sites [20,21]. Furthermore, this enhanced cathodic activity on the surface can occur due to Al alkaline corrosion and subsequent replating. Al can be dissolved due to cathodic or alkaline dissolution of Al-rich IMPs due to a local pH increase during galvanically induced corrosion, enabling the Al $\rightarrow$ AlO$_2^-$ and/or Al $\rightarrow$ Al$_2$O$_3$ reaction when thermodynamically possible at IMPs [30,35]. As these Al-rich particles corrode, they can be enriched within the metal oxide layer [26,30,32,36]. Such selective dissolution of Al would constitute dealloying, and during this dealloying process, the Al-Mn particle (Al$_8$Mn$_5$ in most cases) is able to transform to Mn-O oxide (such as Mn$_3$O$_4$) [30]. This transformation or dealloying process has been noted and empirically shown elsewhere [30,37]. Following selective dissolution, Al can then replate upon the Mg-alloy surface. The replated alloying elements can function as cathodes and enhance the rates of HER [30].

The objective of the present work was to analyze how the size, area fraction and distribution of Al-rich IMPs impact the corrosion rate of Mg-Al alloys. In a previous study exploiting the heat treatment of AZ31B (3 wt% Al, 2 wt% Zn, 1 wt% Mn, bal. Mg) to vary particle size and spacing, it was found that small reactive particles were more detrimental to the corrosion rate than larger particles [38]. In this study, the Al-Mn particles were 0.1-0.8 μm in diameter and spaced 10-30 μm while the Al-Mn-Fe particles were 5-10 μm and spaced at greater distances (50 μm-100 μm) from center-to-center, depending on heat treatment [38]. However, heat treatment could change other factors such as grain size, IMP composition and even the α-Mg matrix composition. It was noted that the area and volume fraction of these IMPs remained approximately the same for each heat treatment time and temperature [38]. To better understand the

effect of IMP size and distribution, without influence from other metallurgical characteristics, model Mg-Al arrays were developed. These model samples were developed considering these particles as arrays of high cathodic, Al electrodes embedded in the anodic Mg matrix. The model alloys were constructed using high purity Al electrodes as a surrogate for Al-rich IMPs. It is also important to emphasize that the model alloys herein are simplified so that the spacing and area fraction of Al can be altered, without the simultaneous alteration of matrix Al-content or the IMPs. This is an important distinction, as the present study aims to focus upon the corrosion kinetic factors as a function of cathode size and geometry. This is different to studying the role of Al-content, which has been summarized recently elsewhere [39].

In terms of weld corrosion, the particle distribution in an AZ31 tungsten inert has (TIG) weld varied by weld zone. In particular, the high temperatures seen during welding cause Ostwald ripening which increase the particle size as well as the particle spacing. Studying the effect of particle distribution by Mg-Al electrode arrays will allow for better systematic understanding on how this distribution alters the corrosion rate within the weld zone without having to account for metallurgical factors (such as grain size and processing) which can influence the corrosion rate.

6.2 Experimental Procedures

6.2.1 Materials

Extruded commercially pure Mg rod (99.9%) was supplied by Alfa Aesar as well as 99.999% Al and 99.99% Fe electrodes (varying in diameter from 1 mm to 0.25 mm). Only the Al electrode arrays were analyzed within the full analysis, however a brief comparison of the corrosion morphology due to electrode composition is discussed. The composition of the commercially pure Mg is reported in wt. %, as provided by QUANT (Quality Analysis and Testing Corporation) (0.01% Al, 0.01% Mn, 0.01% Zn, 0.021% Si, 0.005% Cu, 0.001% Ni, 0.006% Fe and Mg Bal). The bare electrodes were prepared by successive grinding with silicon-carbide paper and rinsing with ethanol to a final grit of 1200 prior to testing. Compositional analysis did not detect any Al redistribution during sample preparation (before electrochemical testing).

6.2.2 Model Samples for Intermetallic Particle Size and Distribution

Model Mg-Al arrays were developed with flush mounted pure Al electrodes embedded in commercial purity Mg (Figure 6. 1) with variations in the area fraction of Al electrodes as well as variations in the electrode size and spacing to test these characteristics in isolation, without concern of influence from outside metallurgical characteristics (i.e. grain size, IMP phase transformations, material residual stresses) which may affect the intrinsic corrosion rate.

A typical range of dissolution of reduction kinetics for various Al-containing IMPs seen in Mg alloys [16]. High purity Al has been chosen as a surrogate because it has a measured OCP (-0.9 V_{SCE}) within the range of electrochemical potentials for the Al-containing IMPs in Mg, in comparison to the commercial purity Mg matrix (-1.65 V_{SCE}) (Figure 6. 2, Table 6. 1). For the purposes of this analysis, it is assumed that the pure Al electrode will behave similar to Al_xMn_y IMPs [16,40,41].

To test differences in the corrosion kinetics with area fraction, 1 mm diameter Al electrodes were embedded in the Mg with different area fractions of high purity Al, brought about by increasing the number of Al electrodes (of equivalent diameter) in the Mg. The corrosion kinetics of the entire array were compared to the as-received Mg corrosion rate, as previously reported for 0.6 M NaCl at OCP [42]. The variation in the electrode area fraction, diameter and spacing are reported in Table 6. 2. The variation in the corrosion kinetics with electrode size were tested using Al electrodes with varying diameters (1 mm, 0.5 mm and 0.25 mm) while retaining the same area fraction of Al (Table 6. 2). This required using a different number of electrodes, embedded in the Mg, depending on the electrode diameter. The spacing of these electrodes was varied from 3 mm to 7 mm to test how the electrode spacing altered the corrosion kinetics. The Al electrodes were shorted to the Mg such that the sample was one planar electrode.

Model samples were analyzed with scanning electron microscopy (SEM) using a FEI Quanta 650 microscope to determine the composition of any Al-containing oxides at the electrode edge. Compositional analysis was performed using energy dispersive spectroscopy (EDS) methods [43] on the as-corroded specimens with full consideration of the ZAF corrections (Z is the atomic number correction, A is the absorption correction and F is the fluorescence correction) on the Aztec software tool [43]. Images were recorded at a working distance of 10 mm while operating at an accelerating voltage of 5 kV. The extent of corrosion damage was

194

determined using the ImageJ^{TM} software package [44]. 3D images were also obtained using a Hirox optical microscope to determine the depth of corrosion where the ASTM G1-03 standard chromic acid solution (200 g/L CrO_3) was used to remove any corrosion product [45]. The 3D profile of the corrosion damage was profiled using the MountainMaps software package [46].

6.2.3 Corrosion Rate Determination

Array electrodes were exposed at OCP in 0.6 M NaCl in ambient conditions for 24 hours with intermittent electrochemical impedance spectroscopy (EIS) measurements taken at frequencies from 10 kHz-10 mHz. The pH of this solution was initially ~5.3 and was measured to be ~11 after 24 hours. EIS scans were analyzed and fit using the software program ZView to an equivalent circuit, seen in Figure 6. 3. The relative corrosion rate was determined using the polarization resistance, R_p, where the corrosion rate, $i_{corr} \propto 1/R_p$ [42,47]:

$$\frac{1}{R_p} = \frac{1}{R_1 + R_2} + \frac{1}{R_3} \qquad \qquad \text{Equation 6.1}$$

The experimental setup consisted of a three-electrode electrochemical flat cell with a 1 cm^2 sample window. For simplification, only EIS determined R_p was determined as it has been shown previously to yield similar corrosion rates as determined from hydrogen evolution, inductively coupled optical emission spectroscopy solution analysis and gravimetric mass loss [9,42,47]. A Pt mesh was used as a counter electrode and a saturated calomel electrode (SCE) was used as the reference electrode. The Bode magnitude and phase plots are typical fits, determined through at least three replicates.

Cathodic kinetics were determined in unbuffered 0.6 M NaCl and buffered tris(hydroxymethyl)aminomethane (TRIS) for 3, 24 and 48 hours at OCP, followed by a cathodic potentiodynamic polarization scan ranging from 0.5 V_{SCE} above OCP to -2.3 V_{SCE} below OCP in a downward sweep at a rate of 1 mV/second. At least three cathodic polarization curve replicates were run with the average cathodic current density, i_c, (as determined at -1.8 V_{SCE}) reported.

The galvanic current between Mg and Al were determined using a zero resistance ammeter (ZRA) in a flat cell [48,49]. The samples were coupled with the Mg as the working electrode (WE) and Al as the counter electrode (CE). The cathode to anode ratio was varied from 2:1, 1:1 and 1:2. The Mg anode size remained the same while the Al cathode was increased to examine how the cathode area affected the corrosion current density. The effect of the anodic polarization induced by galvanic coupling of the Mg in close contact with Al-rich phases was

determined through potentiostatic polarization at the Mg-Al galvanic couple potential (-1.63 V_{SCE}) for 24 hours in 0.6 M NaCl.

Variation in the pH of the solution was examined using a universal pH solution on a Mg-Al array embedded with one 1 mm Al electrode. A thin layer of the 0.6 M NaCl solution (initial pH ~5.3) and 0.1 M TRIS (pH ~7) was deposited on top of the sample and left for approximately 10 minutes. Local pH was established quickly. An approximate value for the local pH levels on the surface was determined from a universal pH standard.

6.3 <u>Results</u>

6.3.1 Imaging of the Effect of Intermetallic Particle Material on Galvanic Corrosion

Samples with the same area fraction of electrodes (each spaced 5 mm from center-to-center) were immersed at OCP in 0.6 M NaCl for 3 hours to examine the corrosion morphology. Samples with the same area fraction and electrodes measuring 0.25 mm and 0.5 mm showed slightly more localized corrosion at the electrode and somewhat non-uniform corrosion across the electrode surface (Figure 6. 4 (a-b)). However, samples with one 1 mm electrode had more localized corrosion at the Al-Mg interface with less corrosion further away from the electrode (Figure 6. 4 (c)). Concerning Fe model electrodes in comparison to Al, the area around the Al electrode affected by corrosion was approximately 750 μm while the corrosion area around the Fe electrode was approximately 1500 μm (Figure 6. 4 (c-d)). The depth of the corrosion attack was similar at 600 μm ± 300 μm in most cases.

As the the area of the Al increased, in an Al:Mg galvanic couple, the galvanic couple current density and galvanic couple potential increased (Figure 6. 5(a-b)). Typical potentiostatic data of Mg over a 24 hour period, taken by applying the galvanic couple potential (-1.43 V_{SCE}) indicated a net anodic charge with time (Figure 6. 5(c)). The net current decreased around approximately 100 to 1000 seconds during polarization to -1.43 V_{SCE} which implies an inhibition in the anodic dissolution reaction rate or an increase in the cathodic reaction rate. This is trend correlates with data shown for similar anodic potentials on commercial purity Mg undergoing anodically induced cathodic activation [28].

6.3.2 EIS of Mg-Al Electrode Arrays

Effect of Electrode Area Fraction for a Fixed Diameter and Spacing on the Corrosion Rate

196

Figure 6. 6(a) contains the Bode magnitude and phase plots for the commercial purity Mg, embedded with increasing area fractions of high purity Al electrodes, as described in Table 6. 2 for samples in 0.6 M NaCl. The Al electrodes in each case had a diameter of 1 mm and were spaced 5 mm apart from center-to-center. The capacitive elements were adequately represented by conventional capacitors, as opposed to constant phase elements, and experimental data and had a good fit where the error % was estimated at less than 20% for each run. The as-received commercial purity Mg had the highest measured frequency dependent impedance and $1/R_p$ [42]. The relative corrosion rate was determined for each area fraction over the full 24 hour immersion as $1/R_p$ (Figure 6. 6(b)) where $1/R_p$ increased with the area fraction of Al.

It is similarly shown that the cathodic kinetics of the system increase with Al area fraction (Figure 6. 7(a-b)) in 0.6 M NaCl. However, even though $1/R_p$ increased by an order of 4, the increase in the cathodic kinetics, assessed at -1.8 V_{SCE}, was by several orders of magnitude. The cathodic kinetics for samples immersed in 0.1 M TRIS displayed very little variation in the cathodic kinetics with increasing Al area fraction, with only a slight increase brought about by the addition of Al to the electrode (Figure 6. 8(a-b)). This is characteristic of this electrolyte, which displays little to no cathodic activation [10].

Effect of Electrode Diameter on the Corrosion Rate

The effect of electrode diameter and spacing, with constant Al area fraction, on $1/R_p$ is shown in Figure 6. 9-6. 11 for 0.6 M NaCl for two electrode spacings and three electrode diameters. The spacing of the electrodes were examined at 3 mm and 7 mm with a diameter of 0.25 mm, 0.5 mm and 1 mm to yield a constant area fraction (Table 6. 1). EIS spectra were taken for each type of Mg-Al array (Figure 6. 9(a-b)) in 0.6 M NaCl. The Mg-Al array with 16 Al electrodes, each with a 0.25 mm diameter, had the lowest measured R_p and therefore the highest relative corrosion rate ($1/R_p$). The Mg-Al array with 1 Al electrode, measuring 1 mm in diameter, had the lowest overall $1/R_p$ (Figure 6. 10). The cathodic kinetics, as determined at -1.8 V_{SCE}, increased with decreasing Al electrode size (Figure 6. 11) in 0.6 M NaCl, given the same area ratio. However, the cathodic kinetics in 0.1 M TRIS were approximately the same for all samples (Figure 6. 12). In summary, closely spaced, small electrodes had the highest reaction rate in chloride-containing environments, given the same area fraction of Al (as larger electrodes), but little variation was detected in the non-chloride containing environment.

Effect of Electrode Spacing on the Corrosion Rate

The variation in the electrode spacing, with constant Al diameter and area fraction, on corrosion rate and cathodic kinetics are in Figure 6. 13-6. 15 for 0.6 M NaCl. EIS was obtained for each array (Figure 6. 13(a-b)). Plotted as a function of $1/R_p$ (Figure 6. 14), the relative corrosion rate increased with decreasing electrode spacing for a fixed Al electrode diameter and area fraction. The variation in electrode spacing is shown for both Mg-Al arrays with 0.25 mm Al electrodes (Figure 6. 14(a)) and 0.5 mm Al electrodes (Figure 6. 14(b)) in 0.6 M NaCl. There was approximately the same variation in the $1/R_p$ with electrode spacing for both the 0.25 mm electrodes and the 0.5 mm diameter electrodes. Typical cathodic polarization curves for Mg electrodes embedded with 0.5 mm and 0.25 mm electrodes with different electrode spacings are shown in Figure 6. 15(a-b) in 0.6 M NaCl. The cathodic kinetics in 0.6 M NaCl, as determined at -1.8 V_{SCE} (Figure 6. 15(c-d) revealed that, as the electrode spacing increased (for a fixed Al electrode area fraction), the rate of the HER decreased for both 0.5 mm and 0.25 mm electrodes. Typical cathodic polarization curves for Mg electrodes embedded with 0.5 mm and 0.25 mm electrodes with different electrode spacings are shown in Figure 6. 16(a-b) in 0.1 M TRIS. The cathodic kinetics in 0.1 M TRIS, as determined at -1.8 V_{SCE} (Figure 6. 16(c-d)) were approximately the same for all electrode spacings.

6.3.3 Variation in pH with Surface Location

The variation pH with surface location was measured in a thin film environment for both 0.6 M NaCl and 0.1 M TRIS (Figure 6. 17(a-c)). A key for the pH measurement, as determined by a universal pH indicator, is contained in Figure 6. 17(a). The region directly above and adjacent to the Al electrode became highly alkaline (pH ~11), according to the universal pH indicator, in the 0.6 M NaCl (Figure 6. 17 (b)). Spreading of pH away from the Al electrode was observed immediately after the universal pH solution was added (Figure 6. 17(c)). However, in the buffered, 0.1 M TRIS environment, there was much less variation in the pH, indicating that the TRIS buffer efficiently allows a retention of pH ~7-8, even in the rapidly dissolving Mg-Al environment (Figure 6. 17(d)). From SEM and EDS analysis of the Al electrode and the corroded interface in 0.6 M NaCl, the largest amount of dissolution occurred at this interface (Figure 6. 18(a)). The oxide formed during dissolution contains Al (Figure 6. 18(b)).

6.4 Discussion

6.4.1 Effect of a Potential Distribution Field at the Electrode Interface on Corrosion Rate

The resultant, accelerated corrosion from an array of cathodic phases embedded in Mg was assessed. The extent of corrosion attack was dependent on the electrode material embedded in α-Mg matrix, where Fe was much more active than Al (Figure 6. 4) [16]. The relative corrosion rate, assessed by $1/R_p$, along with the corresponding cathodic kinetics, were evaluated (Figure 6. 6-6. 16). When Al was embedded in Mg, the potential was likely elevated in a zone around the Al electrode. This potential elevation, due to each electrode in the array, will increase the corrosion rate of Mg. The variation in the extent of corrosion can be understood by considering the potential distribution around a single cathodic electrode using an analytical solution of the Laplace equation [50,51]. Consider the case where the radius of an electrode or cluster of electrodes is d, the polarization resistance of the alloy is R_p (as determined from EIS measurements [42]), E_c is the OCP for the electrode, E_m is the OCP of the matrix, ρ is the solution resistivity, d is the electrode diameter and r is the radial distance from the edge of the electrode. In this case, the elevated potential distribution with radial distance ($E(r)$) can be described using Equation 6.2 [52].

$$E(r) = E_c - (E_m - E_c)\exp\left[-\left(\frac{3\rho}{4R_p d}\right)^{\frac{1}{2}} r\right]$$

Equation 6.2

The diameter estimated for this radial distance is plotted in Figure 6. 19 for both an Al and a Fe electrode. It is clear that $E(r)$ is elevated for a radial distance of ~2000/4000 μm. The potential distribution around the electrode, $E(r)$, may trigger (anodic dissolution induced) cathodic activation of the nearby Mg-matrix in this zone, as is seen in many Mg-alloys [26,32,33] - with corrosion initiation and propagation proximate to cathodic electrodes. For electrodes with different compositions but the same area fraction and electrode size, as presented for both Al and Fe electrodes in Mg (Figure 6. 4), it was observed that the affected radial zone around the Fe electrode was larger than that around the Al electrode because the Fe electrode is a 'stronger cathode', whereby it has more rapid HER kinetics for a given cathodic potential. Equation 6.2, also showed that $E(r)$ around a Fe electrode was larger than around an Al electrode - with $E(r)$ increasing with increasing electrode diameter for both electrode compositions (Figure 6. 19(a-b)).

199

However, when the number of electrodes was varied but the area fraction and composition of these electrodes remained constant, the analysis can become more complicated as a multitude of electrodes must be accounted for. Under the premise that the amount of anodically induced cathodic activation can be determined through considering the sum of all anodically induced zones (A^{AIZ}) around the electrode by relating it to the number of electrodes, N, the extent of anodically induced cathodic activation across an entire sample surface with multiple electrodes can be approximated by:

$$A^{AIZ} = \pi(r_{zone})^2(N)$$ Equation 6.3

Where N is the number of electrodes or, in the case of the Mg-Al arrays, the number of Al electrodes embedded in Mg and $r_{zone} \sim E(r)$ where potential is elevated. With the same area fraction, as the electrode size decreases there is a decrease in the area of this anodically induced zone on the sample surface for a given r as determined for 0.25 mm, 0.5 mm and 1 mm diameter electrodes (Figure 6. 20). From the 3D corrosion morphology of at the Mg/Al electrode interface (Figure 6. 4), a localized corrosion morphology was seen for the 1 mm electrode case, while a non-localized, more spread out corrosion morphology was seen for the 0.25 and 0.5 mm electrode cases.

The effect of the electrode area fraction on the EIS determined corrosion rate and the cathodic kinetics determined from polarization testing was also observed in 0.6 M NaCl (Figure 6. 6-6. 7). As the area fraction of electrodes increased, the corrosion rate similarly increased in 0.6 M NaCl As more cathodic Al electrodes were embedded into the Mg, there were more cathodically activated regions (leading to a larger overall A^{AIZ}), as seen in Figure 6. 20. As the area of the Al increased and the area of the Mg decreased which lead to more galvanic attack since the Al electrodes function as active sites for the HER. This trend has been previously noted for Mg-Fe galvanic couples where the corrosion rate dramatically increases with an increasing Fe:Mg ratio [53]. The galvanic couple current density and potential are seen to increase with cathode:anode ratio (Figure 6. 5(a-b)). The galvanic potential between Mg and Al is more positive in comparison to the OCP of Mg, therefore polarizing the Mg sample anodically. Such a scenario is similarly the case when the Mg sample is held at -1.43 V_{SCE} for 24 hrs (Figure 6. 5(c)). Enhanced catalytic activity on the sample surface would be expected [28].

As the electrode size increased, with the same area fraction, there are fewer electrodes for cathodic activation (Figure 6. 9-6. 11). But the radius of the potential distribution around the

electrode E(r) extends to larger r (Figure 6. 19). However, E(r) fields do not overlap as the spacing between electrodes becomes larger than r_{zone}. This is corroborated through Figure 6. 13-6. 15, where the corrosion rate and cathodic kinetics decreased within increasing electrode spacing. Typically during processing, as the electrode size increases, the spacing also increases [38].

6.4.2 Effect of AlO_2^- Dissolution and Replating on Corrosion Rate

The dramatic increase in the measured cathodic current density with increasing area fraction is larger than a linear multiplication factor with respect to the Al area (Figure 6. 6-6. 7). It is proposed that the increase in the Al electrode area enhances cathodic activity due to both transition metal enrichment [28] as well as Al cathodic corrosion and replating on the sample surface. At intermediate pH, the dominant reaction is the formation of Al oxide in the solid state [54]:

$$Al + 3H_2O \rightarrow Al_2O_3(s) + 6H^+ + 6e^- \hspace{3cm} \text{Equation 6.4}$$

However, local alkalization of the surface occurs at the Mg/Al interface to pH~11 (as shown in Figure 6. 17(b-c)), resulting in:

$$Al + 2H_2O \rightarrow AlO_2^- + 4H^+ + 3e^- \hspace{3cm} \text{Equation 6.5}$$

The Nernst potentials for each of these reactions at pH=11 are -2.50 V_{SCE} and -2.44 V_{SCE} (assuming an AlO_2^- concentration of 10^{-6} M) which is much lower than the OCP of pure Mg (-1.63 V_{SCE}). According to the Al Pourbaix diagram [54] and knowledge of the thermodynamics of the system that Equation 6.4 is the dominant reaction when in near neutral solutions while Equation 6.5 is dominant in strongly alkaline (pH≥11) solutions. The redistribution of the Al to the surrounding oxide is seen through EDS (Figure 6. 18). The movement of the AlO_2^- away from the electrode creates a composition gradient which will increase the corrosion rate as the AlO_2^- spreads.

The concentration gradient, C(r), of the AlO_2^- by diffusion and convection released in solution from the IMP can be plotted assuming a one-dimensional radial diffusion from a spherical electrode according to:

$$\frac{C(r)}{C_{IMP}} = \frac{d}{r}\left[erfc\left(\frac{r-d}{2\sqrt{Dt}}\right)\right] \hspace{3cm} \text{Equation 6.6}$$

201

Where C_{IMP} is the concentration of dissolved AlO_2^- at the electrode (assumed to be 1 M), d is the diameter of the electrode, r is the radial distance away from the electrode, D is the diffusion coefficient of AlO_2^- in H_2O $1.0x10^{-9}$ m^2/s, erfc is the complementary error function and t is the time. For r≥d a concentration gradient is shown for the assumptions that $C(r)/C_{IMP}$<1 and for r<d $C(r)/C_{IMP}$=1. The concentration gradient, in the case of quiescent solution, after 3 and 24 hours in shown in Figure 6. 21. Additional AlO_2^- transport by convection due to H_2 gas evolution at the Al/Mg interface has been excluded for this analysis. The radial distance outward was normalized (r/d); therefore, the concentration gradients overlay one another. The concentration gradient approaches 0 at r/d=10, therefore the electrodes can transport AlO_2^- over a radial distance approximately 10 times as large as their diameter.

This zone functions as locations for cathodic activation in Mg alloys and corrosion initiation. In a chloride environment, the alkaline shift at these electrodes can lead to higher rates of AlO_2^- dissolution and possible Al deposition away from the electrode. The effect of pH in the chloride-containing environment was measured using a universal pH indicator (Figure 6. 17) in 0.6 M NaCl, where a large alkaline shift at the Al electrode was observed, which could lead to AlO_2^- release according to the ½ cell reaction in Equation 6.5. Spreading of this pH indicator, likely due to stirring from the HER, can encourage redistribution of the Al along the surface.

However, in the chloride-free buffered environment, 0.1 M TRIS, little variation in the cathodic kinetics were seen for variations in the electrode area fraction, size or spacing (Figure 6. 8, 6. 12 and 6. 16). It has been previously illustrated that little to no cathodic activation upon anodic polarization occurs in this environment [10]. At a buffered pH of ~7-8 in this solution there is a lack of $Al \rightarrow AlO_2^-$, as the dominant half-cell reaction produces Al_2O_3. A secondary effect is the lack of an $Mg(OH)_2$ film in TRIS which leads to a faster corrosion rate and little to no metal enrichment to this hydroxide film can occur [10]. This could also lead to less cathodic activation with time [26,28,32].

6.4.3 Variation in the Corrosion Rate with Electrode Distribution: Reflection on Weld Corrosion

As discussed in Chapter 2 and 4, an increase in the particle spacing with the same area fraction decreased the global corrosion rate as was observed in the AZ31B TIG weld. Also, a decrease in the number of particles (via larger particles to account for the same area fraction) decreased the global corrosion rate. This was confirmed, independent of metallurgical factors

such as grain size, with Al electrodes embedded in Mg. The 0.5 mm diameter electrodes required 4 electrodes to have the same area fraction as the 0.25 mm electrodes. However, the higher number of electrodes increased the corrosion rate due to the increase in sites for cathodic activation as well as Al enrichment away from the electrode. In the weld, high temperature fusion welding causes Ostwald ripening which can decrease the number of particles as they coalesce. Despite the larger size of the particles, there are fewer of them within the weld which will decrease the global corrosion rate.

6.5 <u>Conclusions</u>

1. For the Mg-Al model alloys studied, the cathodic kinetics and open circuit corrosion rate were shown to increase with increasing area fraction of Al electrodes; as determined from EIS as well as DC cathodic polarization curves. The increase in cathodic kinetics provides a rationalization as to the mechanistic origin of increased corrosion rate; however it merits comment that the increase in the corrosion rate determined through the EIS method, was smaller.

2. For a fixed area fraction of Al electrodes embedded in Mg, the cathodic kinetics and corrosion rate decrease with larger electrodes and increasing electrode spacing - due to less overlap of both galvanic potential zones and the zone affected by AlO_2^- chemical concentration fields in 0.6 M NaCl.

3. In the case of decreasing the Al electrode size, whilst maintaining the same total area fraction of Al, it was found that overall cathodic kinetics and corrosion rate increased with significant increases in i_c (-1.8 V_{SCE}) as well as $1/R_p$. This was an important finding, as it can be rationalized that with smaller electrode sizes yet the same area fraction, more fast cathodic sites exist in the array and therefore more sites for cathodic activation develop at the electrode/Mg interface and zones around Al-rich IMPs. This accounts for enhance corrosion kinetics and cathodic HER kinetics in the case of small, closely spaced Al electrodes in a Mg matrix. This conclusion is supported by a study involving Al-rich IMPs whose size was varied by heat treatment [38].

References

1. E. Ghali, magnesium and magnesium alloy, in Uhlig's corrosion handbook. 200, John Wiley & Sons: new york. p. 793-830.
2. T.B. Abbott, "Magnesium: Industrial and Research Developments Over the Last 15 Years," Corrosion 71, 2 (2015): p. 120-127.
3. S.R. Agnew and J.F. Nie, "Preface to the viewpoint set on: The current state of magnesium alloy science and technology," Scripta Mater 63, 7 (2010): p. 671-673.
4. T. Cain, L. Bland, N. Birbilis, and J. Scully, "A compilation of corrosion potentials for magnesium alloys," Corrosion 70, 10 (2014): p. 1043-1051.
5. D.A. Jones, "Principles and Prevention of Corrosion," Prentice Hall Upper Saddle River. NJ. 2nd Ed (1996).
6. K. Gusieva, C.H.J. Davies, J.R. Scully, and N. Birbilis, "Corrosion of magnesium alloys: the role of alloying," International Materials Reviews (2014): p. 169-194.
7. S. Lun Sin, D. Dubé, and R. Tremblay, "Characterization of Al–Mn particles in AZ91D investment castings," Materials Characterization 58, 10 (2007): p. 989-996.
8. O. Lunder, J.H. Nordlien, and K. Nisangliou, "Corrosion resistance of cast Mg-Al alloys," Corrosion Reviews 15, 3-4 (1997): p. 439-469.
9. L.G. Bland, J.M. Fitz-Gerald, and J.R. Scully, "Metallurgical and Electrochemical Characterization of the Corrosion of AZ31B-H24 Tungsten Inert Gas Weld: Isolated Weld Zones," Corrosion Journal In Press, (2016).
10. L.G. Bland, B.C.R. Troconis, R.J. Santucci, J.M. Fitz-Gerald, and J.R. Scully, "Metallurgical and Electrochemical Characterization of the Corrosion of Mg-Al-Zn Alloy AZ31B-H24 Tungsten Inert Gas Weld: Galvanic Corrosion Between Weld Zones " Corrosion Journal in press, (2016).
11. J.R. Kish, G. Williams, J.R. McDermid, J.M. Thuss, and C.F. Glover, "Effect of Grain Size on the Corrosion Resistance of Friction Stir Welded Mg Alloy AZ31B Joints," Journal of the Electrochemical Society 161, 9 (2014): p. C405-C411.
12. G.L. Makar and J. Kruger, "Corrosion Studies of Rapidly Solidified Magnesium Alloys," Journal of the Electrochemical Society 137, 2 (1990): p. 414-421.
13. G. Song, L.M. Liu, M.S. Chi, and J.F. Wang, "Investigations on laser-TIG hybrid welding of magnesium alloys," Mater Sci Forum 488-489, (2005): p. 371-375.
14. R.C. Zeng, J. Chen, W. Dietzel, R. Zettler, J.F. dos Santos, M.L. Nascimento, and K.U. Kainer, "Corrosion of friction stir welded magnesium alloy AM50," Corros Sci 51, 8 (2009): p. 1738-1746.
15. T. Zhu, Z.W. Chen, and W. Gao, "Microstructure formation in partially melted zone during gas tungsten arc welding of AZ91 Mg cast alloy," Materials Characterization 59, 11 (2008): p. 1550-1558.
16. A.D. Südholz, N.T. Kirkland, R.G. Buchheit, and N. Birbilis, "Electrochemical Properties of Intermetallic Phases and Common Impurity Elements in Magnesium Alloys," Electrochemical and Solid-State Letters 14, 2 (2011): p. C5-C7.
17. A.A. G. Song, "Understanding magnesium corrosion. A framework for improved alloy performance," Advanced Engineering Materials 5, (2003): p. 837-858.
18. G.S. Frankel, A. Samaniego, and N. Birbilis, "Evolution of hydrogen at dissolving magnesium surfaces," Corros Sci 70, 0 (2013): p. 104-111.

19. N. Birbilis, A.D. King, S. Thomas, G.S. Frankel, and J.R. Scully, "Evidence for enhanced catalytic activity of magnesium arising from anodic dissolution," Electrochimica Acta 132, 0 (2014): p. 277-283.

20. G.S. Frankel, A. Samaniego, and N. Birbilis, "Evolution of hydrogen at dissolving magnesium surfaces," Corros Sci 70, (2013): p. 104-111.

21. G.S. Frankel, S. Fajardo, and B.M. Lyncha, "Introductory lecture on corrosion chemistry: a focus on anodic hydrogen evolution on Al and Mg," faraday discussions 180, (2015): p. 11-33.

22. G. Williams, H. ap Llwyd Dafydd, and R. Grace, "The localised corrosion of Mg alloy AZ31 in chloride containing electrolyte studied by a scanning vibrating electrode technique," Electrochimica Acta 109, 0 (2013): p. 489-501.

23. G. Williams, N. Birbilis, and H.N. McMurray, "The source of hydrogen evolved from a magnesium anode," Electrochemistry Communications 36, 0 (2013): p. 1-5.

24. G. Williams, K. Gusieva, and N. Birbilis, "Localized Corrosion of Binary Mg-Nd Alloys in Chloride-Containing Electrolyte Using a Scanning Vibrating Electrode Technique," Corrosion 68, 6 (2012): p. 489-498.

25. G. Williams and H.N. McMurray, "Localized Corrosion of Magnesium in Chloride-Containing Electrolyte Studied by a Scanning Vibrating ElectrodeTechnique," Journal of the Electrochemical Society 155, 7 (2008): p. C340-C349.

26. M. Taheri, J.R. Kish, N. Birbilis, M. Danaie, E.A. McNally, and J.R. McDermid, "Towards a Physical Description for the Origin of Enhanced Catalytic Activity of Corroding Magnesium Surfaces," Electrochimica Acta 116, (2014): p. 396-403.

27. J. Swiatowska, P. Volovitch, and K. Ogle, "The anodic dissolution of Mg in NaCl and Na2SO4 electrolytes by atomic emission spectroelectrochemistry," Corros Sci 52, 7 (2010): p. 2372-2378.

28. T. Cain, S.B. Madden, N. Birbilis, and J.R. Scully, "Evidence of the Enrichment of Transition Metal Elements on Corroding Magnesium Surfaces Using Rutherford Backscattering Spectrometry," Journal of the Electrochemical Society 162, 6 (2015): p. C228-C237.

29. S. Fajardo and G.S. Frankel, "Effect of impurities on the enhanced catalytic activity for hydrogen evolution in high purity magnesium," Electrochimica Acta 165, (2015): p. 255-267.

30. M. Danaie, R.M. Asmussen, P. Jakupi, D.W. Shoesmith, and G.A. Botton, "The cathodic behaviour of Al–Mn precipitates during atmospheric and saline aqueous corrosion of a sand-cast AM50 alloy," Corros Sci 83, (2014): p. 299-309.

31. M.P. Brady, G. Rother, L.M. Anovitz, K.C. Littrell, K.A. Unocic, H.H. Elsentriecy, G.-L. Song, J.K. Thomson, N.C. Gallego, and B. Davis, "Film Breakdown and Nano-Porous Mg(OH)2 Formation from Corrosion of Magnesium Alloys in Salt Solutions," Journal of the Electrochemical Society 162, 4 (2015): p. C140-C149.

32. Z.P. Cano, M. Danaie, J.R. Kish, J.R. McDermid, G.A. Botton, and G. Williams, "Physical Characterization of Cathodically-Activated Corrosion Filaments on Magnesium Alloy AZ31B," Corrosion 71, 2 (2015): p. 146-159.

33. Z.P. Cano, J.R. McDermid, and J.R. Kish, "Cathodic Activity of Corrosion Filaments Formed on Mg Alloy AM30," Journal of the Electrochemical Society 162, 14 (2015): p. C732-C740.

34. M. Curioni, F. Scenini, T. Monetta, and F. Bellucci, "Correlation between electrochemical impedance measurements and corrosion rate of magnesium investigated by real-time hydrogen measurement and optical imaging," Electrochimica Acta 166, (2015): p. 372-384.

35. M. Mokaddem, P. Volovitch, F. Rechou, R. Oltra, and K. Ogle, "The anodic and cathodic dissolution of Al and Al-Cu-Mg alloy," Electochimica Acta 55, (2010): p. 3779-3786.

36. R.C. Phillips and J.R. Kish, "Nature of Surface Film on Matrix Phase of Mg Alloy AZ80 Formed in Water," Corrosion 69, 8 (2013): p. 813-820.

37. C. Xu, R. Wang, Y. Zhang, and Y. Ding, "A general corrosion route to nanostructured metal oxides," Nanoscale 2, 6 (2010): p. 906-909.

38. L.G. Bland, J.J. Bhattacharyya, S.R. Agnew, J.M. Fitz-Gerald, and J.R. Scully, "Effect of Al-Mn and Al-Mn-Fe Intermetallic Particle Size and Distribution on the Corrosion of Mg-3Al-1Zn alloy: AZ31," Acta Materialia In Review, (2016).

39. M. Esmaily, D.B. Blücher, J.E. Svensson, M. Halvarsson, and L.G. Johansson, "New insights into the corrosion of magnesium alloys — The role of aluminum," Scripta Mater 115, (2016): p. 91-95.

40. M.K. Cavanaugh, N. Birbilis, R.G. Buchheit, and F. Bovard, "Investigating localized corrosion susceptibility arising from Sc containing intermetallic Al3Sc in high strength Al-alloys," Scripta Mater 56, 11 (2007): p. 995-998.

41. G. Song and A. Atrens, "Understanding Magnesium Corrosion—A Framework for Improved Alloy Performance," Adv Eng Mater 5, 12 (2003): p. 837-858.

42. L.G. Bland, A.D. King, N. Birbilis, and J.R. Scully, "Assessing the Corrosion of Commercially Pure Magnesium and Commercial AZ31B by Electrochemical Impedance, Mass-loss, Hydrogen Collection and ICP-OES Solution Analysis," Corrosion Journal 71, 2 [Special Issue] (2015): p. 128-145.

43. "AZtecEnergy: EDS Software," Oxford Instruments (2015).

44. C.A. Schneider, W.S. Rasband, and K.W. Eliceiri, "NIH Image to ImageJ: 25 years of image analysis," Nature Methods 9, (2012): p. 671-675.

45. ASTM-G1, "Standard Practice for Preparing, Cleaning, and Evaluating Corrosion Test Specimens," ASTM International G1, (2011).

46. D. Surf, Mountains Surface Imaging and Metrology Software.

47. A.D. King, N. Birbilis, and J.R. Scully, "Accurate Electrochemical Measurement of Magnesium Corrosion Rates; a Combined Impedance, Mass-Loss and Hydrogen Collection Study," Electrochimica Acta 121, 1 (2014): p. 394-406.

48. R. Baboian, "Electrochemical Techniques for Predicting Galvanic Corrosion," ASTM STP 576 (1976): p. 5-19.

49. ASTM-81, "Standard Guide for Conducting and Evaluating Galvanic Corrosion Tests in Electrolytes," ASTM International G71, (2014).

50. J.R. Scully and D.E. Peebles, "Metastable pitting corrosion of aluminum, Al-Cu, and Al-Si thin films in dilute HF solutions and its relevancy to the processing of integrated circuit interconnections," MRS Online Proceeding Library (1990).

51. R.G. Buchheit, Local corrosion of Al-Li-Cu alloys, in Materials Science and Engineering. 1991, University of Virginia: Charlotteville, VA.

52. S. Jain, J.L. Hudson, and J.R. Scully, "Effects of constituent particles and sensitization on surface spreading of intergranular corrosion on a sensitized AA5083 alloy," Electrochimica Acta 108, (2013): p. 253-264.

53. D.R. Banjade, S.D. Porter, B.M. McMullan, and J.N. Harb, "Hydrogen Evolution during the Corrosion of Galvanically Coupled Magnesium," Journal of the Electrochemical Society 163, 3 (2016): p. C116-C123.

54. M. Pourbaix, Atlas of electrochemical equilibria in aqueous solutions (Huston, TX: National Association of Corrosion Engineers, 1974.

Table 6. 1. Open circuit potential for various Al containing IMPs [1,16,41,42]

IMP	Solution	Open Circuit Potential (V_{SCE})
Commercial purity Mg	0.1 M NaCl	-1.55
Commercial purity Mg	0.6 M NaCl	-1.65
Commercial purity Mg	5 M NaCl	-1.67
Al_6Mn	0.85 M NaCl + $Mg(OH)_2$	-1.52
Al_4Mn	0.85 M NaCl + $Mg(OH)_2$	-1.45
Al_8Mn_5	0.85 M NaCl + $Mg(OH)_2$	-1.25
$Mg_{17}Al_{12}$	0.85 M NaCl + $Mg(OH)_2$	-1.2
$Mg_{17}Al_{12}$	0.1 M NaCl	-1.2
Al_8Mn_5Fe	0.85 M NaCl + $Mg(OH)_2$	-1.2
Al_4Mn	0.85 M NaCl + $Mg(OH)_2$	-1.15
$Al_6Mn(Fe)$	0.85 M NaCl + $Mg(OH)_2$	-1.1
High purity Al	0.6 M NaCl	-1.0
$Al_6(MnFe)$	0.85 M NaCl + $Mg(OH)_2$	-1.0
$Al_3Fe(Mn)$	0.85 M NaCl + $Mg(OH)_2$	-0.95
Al_3Fe	0.85 M NaCl + $Mg(OH)_2$	-0.74
Mg_2Al_3	0.85 M NaCl + $Mg(OH)_2$	-1.18

Table 6. 2. Design of model Mg-Al alloys with variations in the area fraction of Al electrodes embedded in Mg. Variations in the electrode size and spacing. Aluminum is 99.999% pure metal.

Number of electrodes	Al Electrode Diameter (mm)	Al Electrode Spacing (mm)	Area of Mg (mm^2)	Area of Al (mm^2)	Al Area Fraction	
--	--	--	791.7	--	--	--
1	1[i]	--	790.9	0.785	0.001	Vary Al Area
2	1[a]	5	790.1	1.590	0.002	
3	1[a]	5	789.3	2.390	0.003	
4	1[a]	5	788.5	3.190	0.004	
4	0.5[j,k]	3	790.9	0.785	0.001	Vary Spacing
4	0.5[c]	4	790.9	0.785	0.001	
4	0.5[c]	5	790.9	0.785	0.001	
4	0.5[c]	6	790.9	0.785	0.001	
4	0.5[b,c]	7	790.9	0.785	0.001	
16	0.25[b,c]	3	790.9	0.785	0.001	Vary Spacing
16	0.25[c]	4	790.9	0.785	0.001	
16	0.25[c]	5	790.9	0.785	0.001	
16	0.25[c]	6	790.9	0.785	0.001	
16	0.25[b,c]	7	790.9	0.785	0.001	

[i] Discussed in Figures 6.6-6.8
[j] Discussed in Figures 6.9-6.12
[k] Discussed in Figures 6.13-6.16
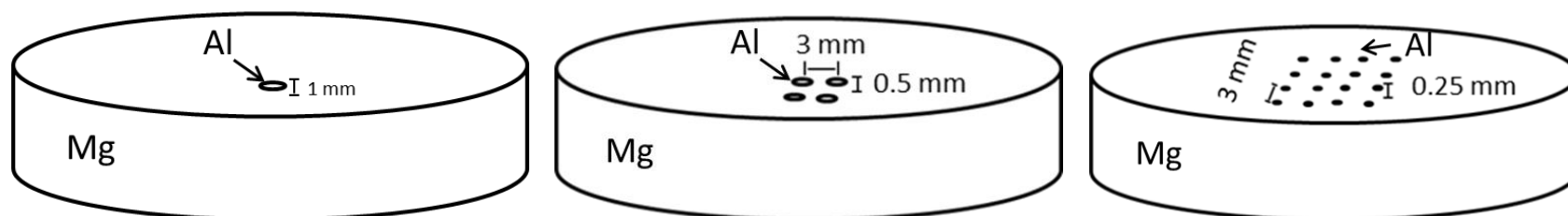
Figure 6. 1. Model sample designs indicate varying the Al-electrode diameter while retaining the same total Al area fraction. Samples were also created with variations in the area fraction by adding more electrodes at the same diameter and spacing. The electrode spacing was varied from 3 to 7 mm. Al used was 99.999% pure metal basis, whilst Mg matrix was commercially pure.
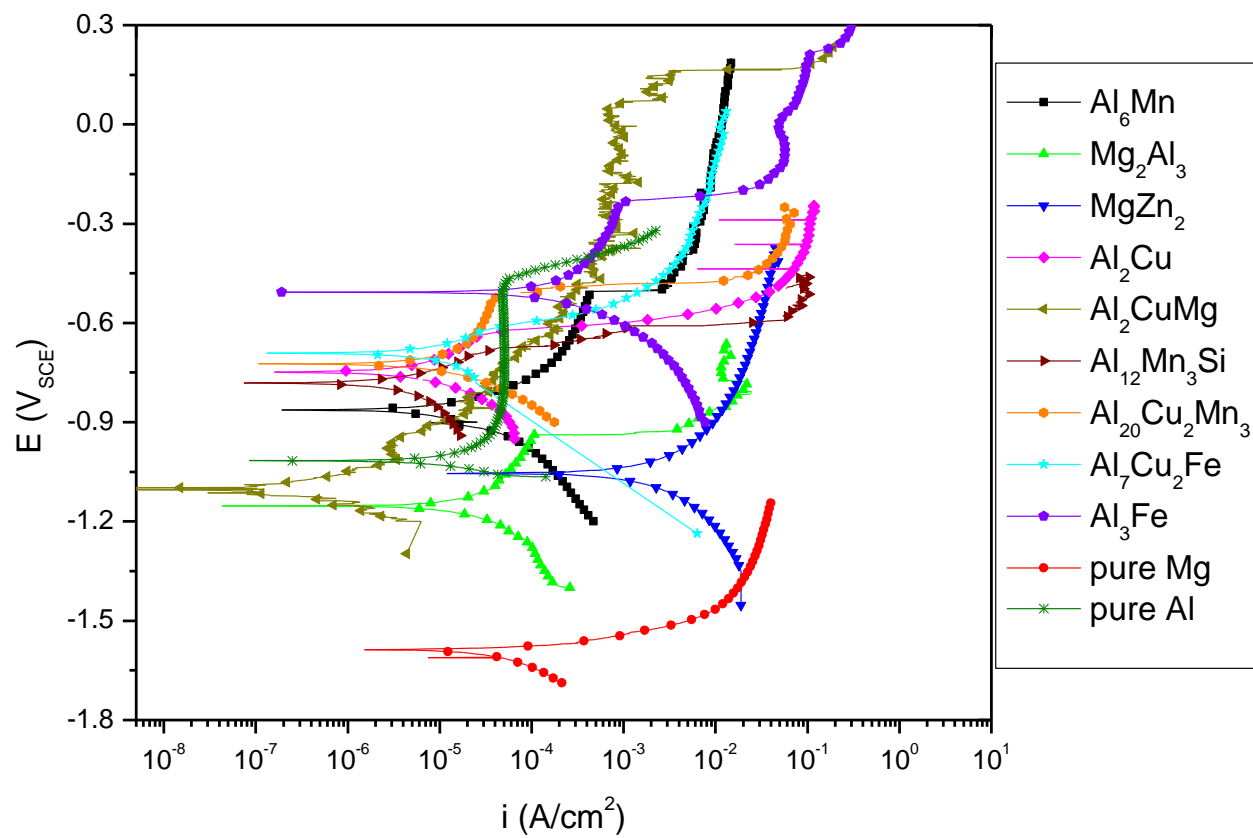
Figure 6. 2. Anodic polarization curves of pure Mg, Pure Al, and various Al containing intermetallic particles in 0.6 M NaCl.
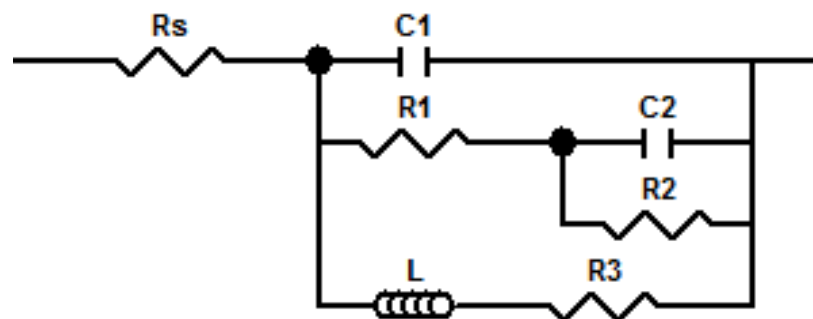
Figure 6. 3. Equivalent circuit used to model pseudo-inductive electrochemical impedance response on corroding Mg in 0.6 M NaCl.
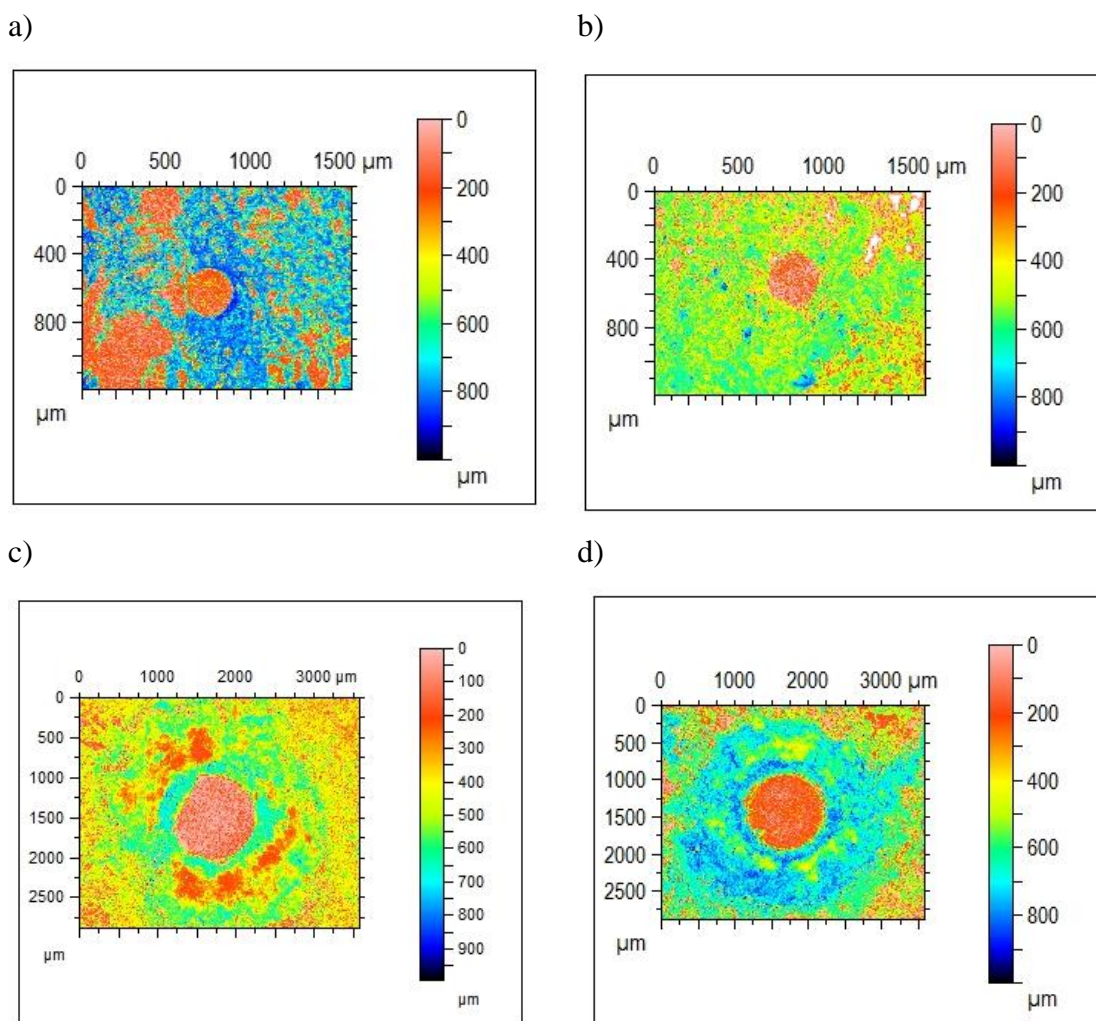
Figure 6. 4. Variation in the 3D corrosion morphology for Mg electrode arrays with various electrode diameters and array electrode materials. Samples were immersed in 0.6 M NaCl for 3 hrs at OCP and cleaned with chromic acid (CrO_3) to remove any oxide product. a) 0.25 mm Al electrode, b) 0.5 mm Al electrode, c) 1 mm Al electrode and d) 1 mm Fe electrode. All samples retained the same area fraction of electrodes, although only one electrode is shown.

a)

b)

c)
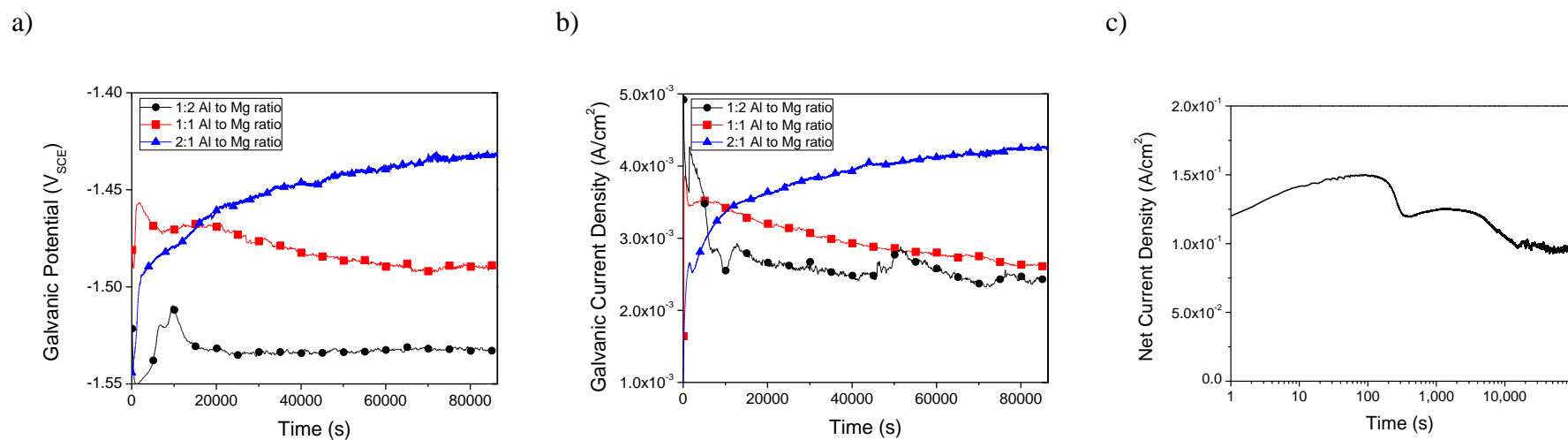
Figure 6. 5. a) Galvanic potential and b) galvanic current density of Mg-Al couple in 0.6 M NaCl with a 2:1, 1:1 and 2:1 Cathode:Anode ratio. c) potentiostatic polarization of 99.9% commercial purity Mg over 24 hrs in 0.6 M NaCl taken at the galvanic couple potential of Mg to Al (-1.43 V_{SCE}).

214
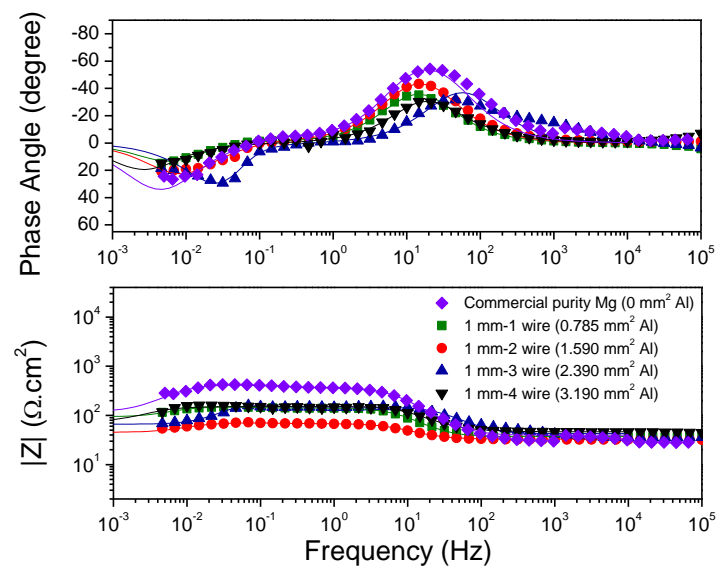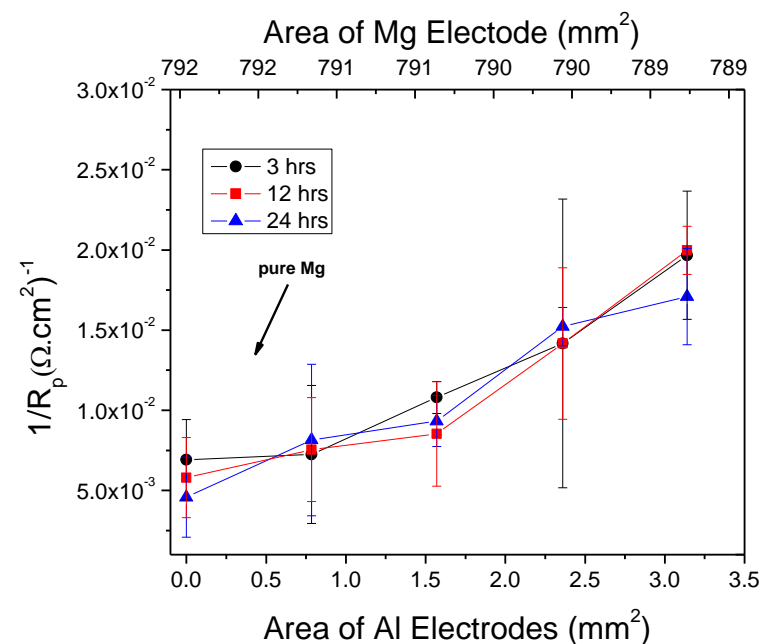
Figure 6. 6. a) Bode phase and magnitude plot and b) EIS determined polarization resistance with a variation in the area fraction of commercial purity Mg embedded with increasing area fraction of 1 mm diameter high purity Al electrodes, each spaced 5 mm apart. Data shown along with respective fits following a 24 hour immersion in 0.6 M NaCl at OCP.

a)
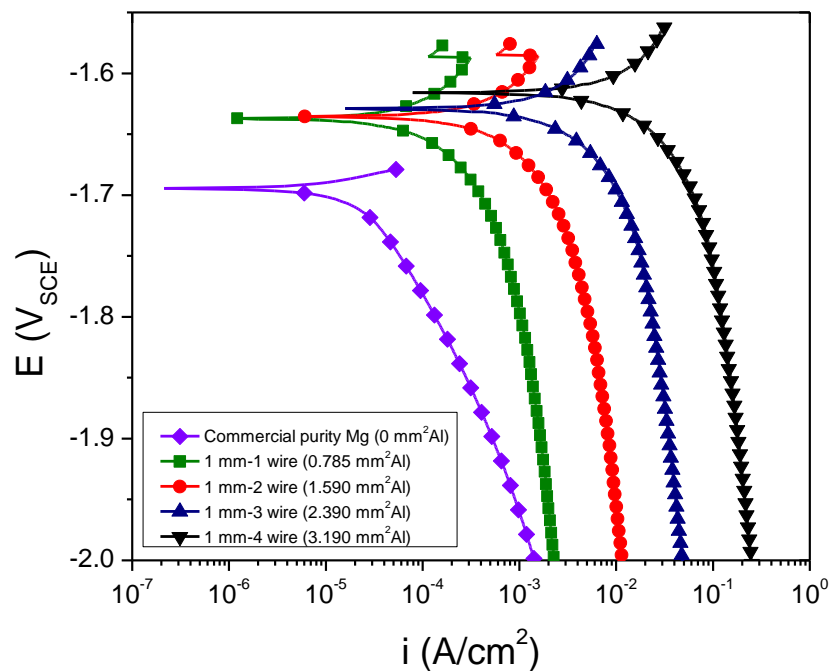
b)
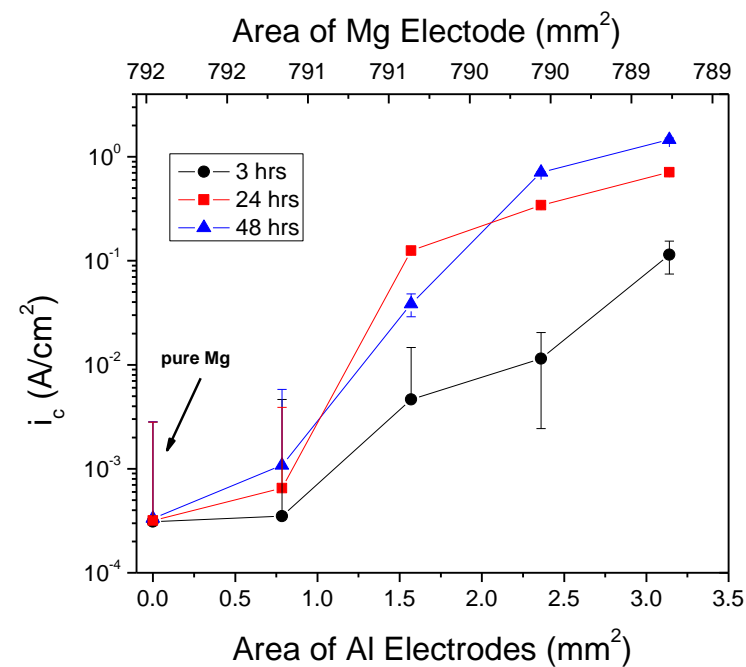
Figure 6. 7. a) typical cathodic polarization curves and b) variation in cathodic kinetics of the HER represented by i_c with a variation in the area of high purity Al electrodes embedded in Mg with increasing area of 1 mm diameter high purity Al electrode(s), each spaced 5 mm apart. Al electrodes with different area fraction from 1 Al electrode to 4 Al electrodes embedded in Mg. Cathodic kinetics determined from cathodic polarization at -1.8 V_{SCE} after 3, 24 and 48 hour holds at OCP.

a)
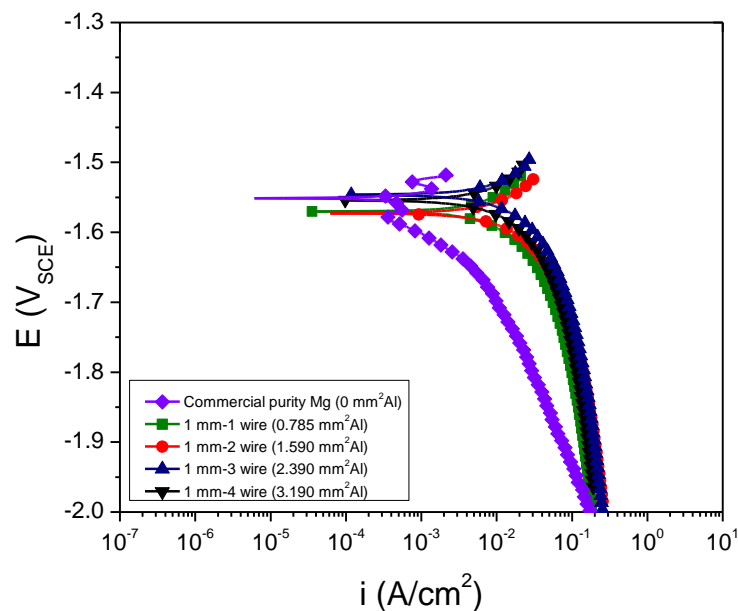
b)
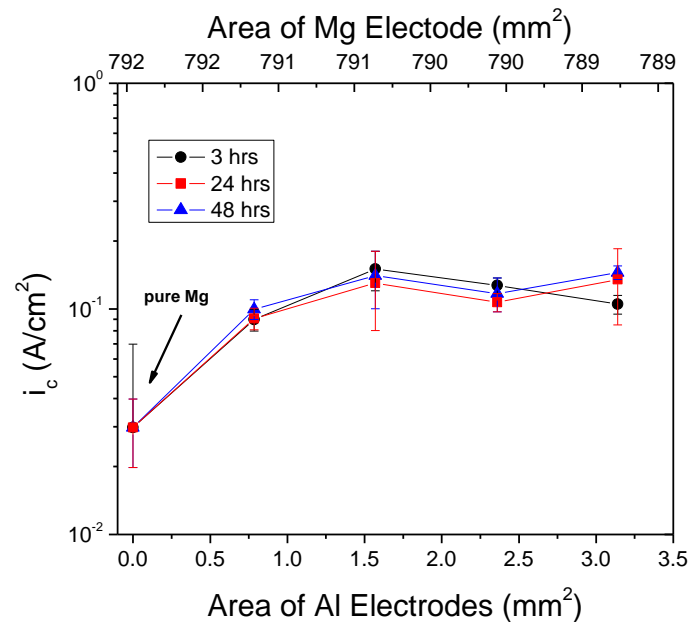
Figure 6. 8. a) typical cathodic polarization curves and b)variation in cathodic kinetics with a variation in the area of high purity Al electrodes for commercial purity Mg embedded with increasing area of 1 mm high purity Al electrode, each spaced 5 mm apart. Al electrodes with different area fraction from 1 Al electrode to 4 Al electrodes embedded in Mg. Cathodic kinetics determined from cathodic polarization curves taken at -1.8 V_{SCE} after 3, 24 and 48 hour holds at OCP in 0.1 M TRIS.
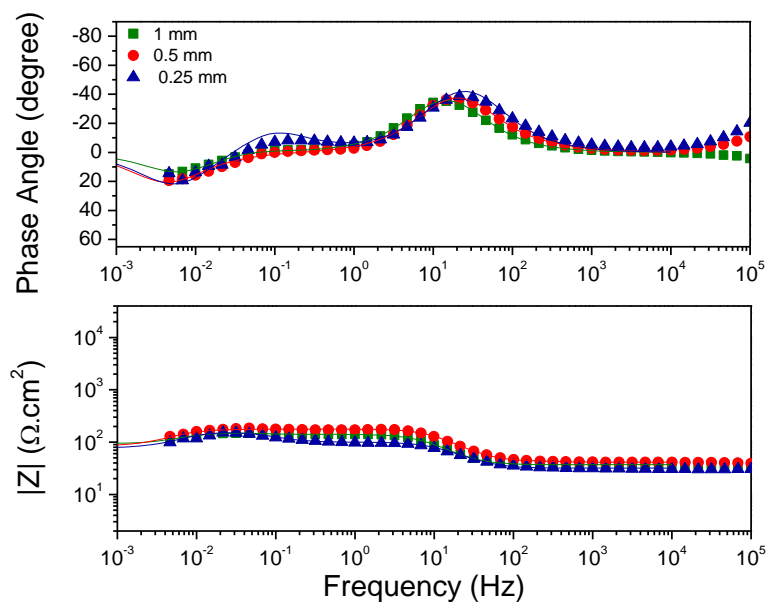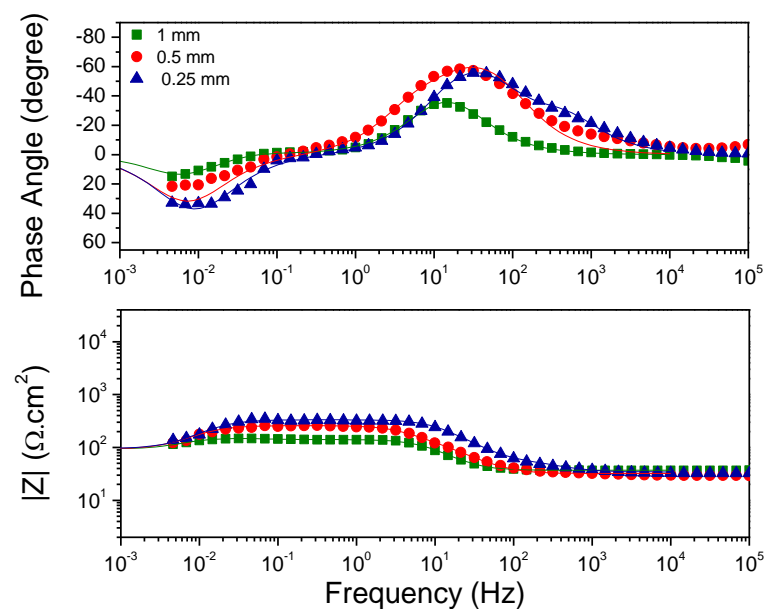
Figure 6. 9. Bode magnitude and phase plot for commercial purity Mg embedded with high purity Al electrodes of different electrode diameters from 1 mm to 0.25 mm. The spacing of these electrodes was kept the same at either a) 3 mm or b) 7 mm. The area fraction of high purity Al electrodes was kept constant at 0.001by retaining an area of 790.9 mm^2 of commercial purity Mg and 0.785 mm^2 of high purity Al in each case as shown in Table 6. 2. Data shown along with respective fits following 24 hrs immersion in 0.6 M NaCl at open circuit.

a)
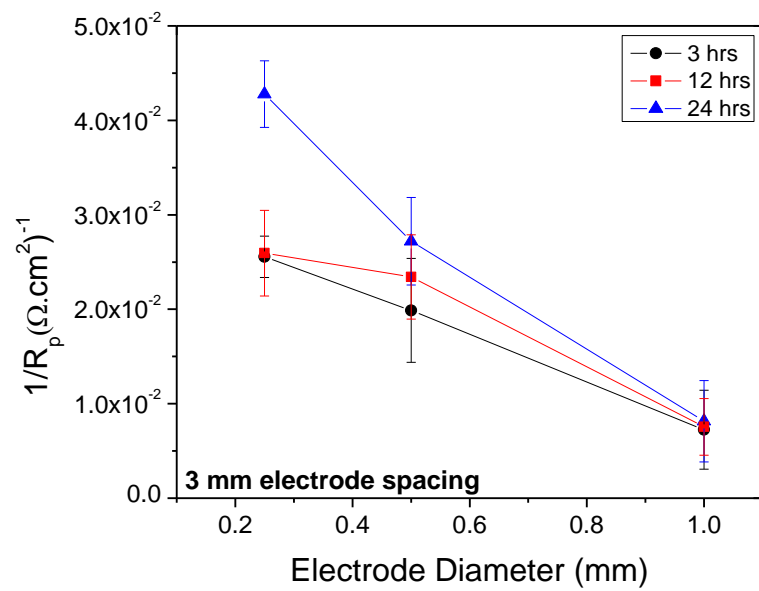
b)
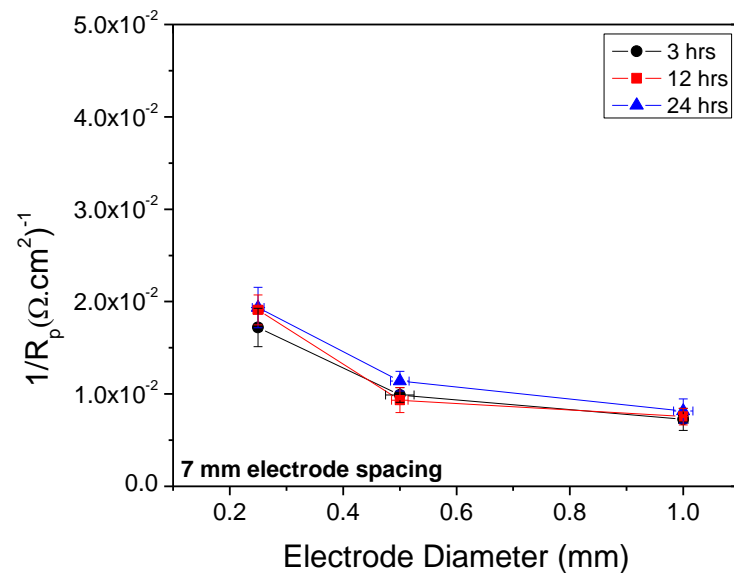
Figure 6. 10. Variation in the polarization resistance with a variation in the electrode diameter over 24 hours at OCP. Commercial purity Mg embedded with high purity Al electrodes of different diameters from 1 mm to 0.25 mm. The area fraction of high purity Al electrodes was kept constant at 0.001by retaining an area of 790.9 mm^2 of commercial purity Mg and 0.785 mm^2 of high purity Al. The spacing of these electrodes were a) 3 mm and b) 7mm.

a)
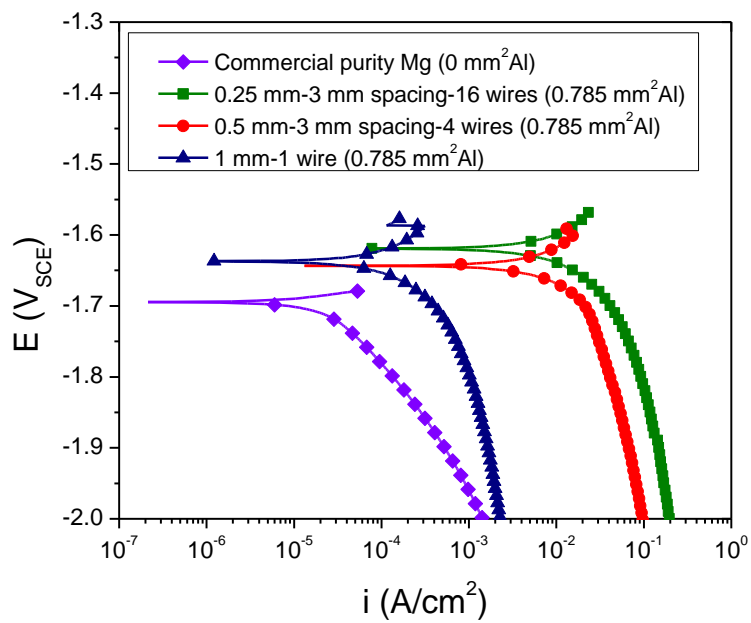
b)
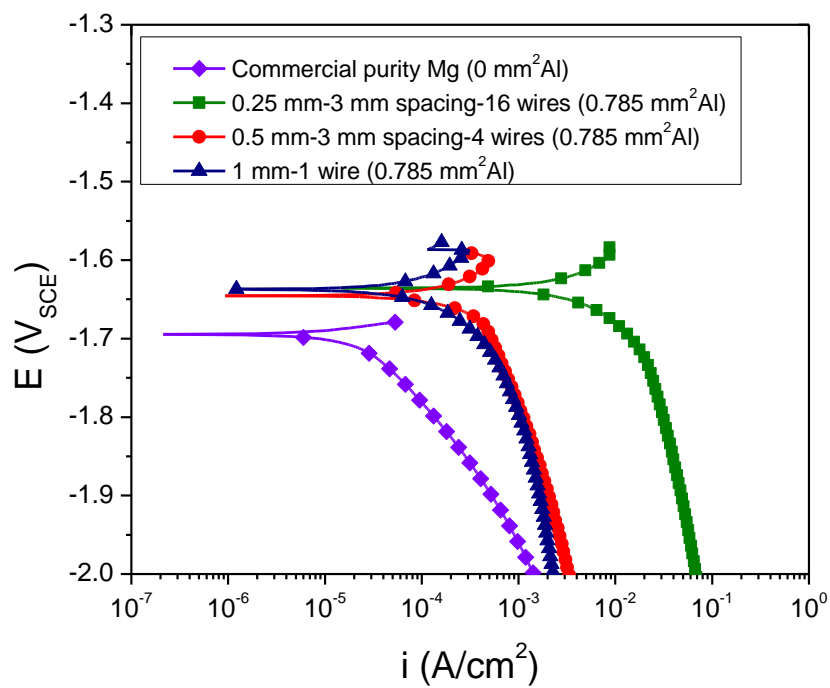
c)

d)
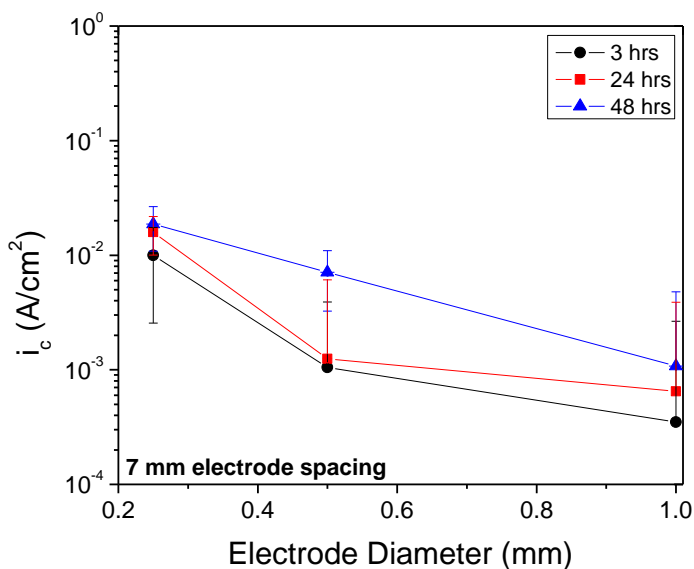
Figure 6. 11. Variation in cathodic kinetics with a variation in the electrode diameter. Commercial purity Mg embedded with high purity Al electrodes of different diameters from 1 mm to 0.25 mm. The area fraction of high purity Al electrodes was kept constant at 0.001by retaining an area of 790.9 mm^2 of commercial purity Mg and 0.785 mm^2 of high purity Al. Typical cathodic polarization curves for a) 3 mm and b) 7mm diameter electrodes. Cathodic kinetics determined from cathodic polarization curves taken at -1.8 V$_{SCE}$ after 3, 24 and 48 hour holds at OCP in 0.6 M NaCl for a) 3 mm and b) 7mm diameter electrodes.

221

a)
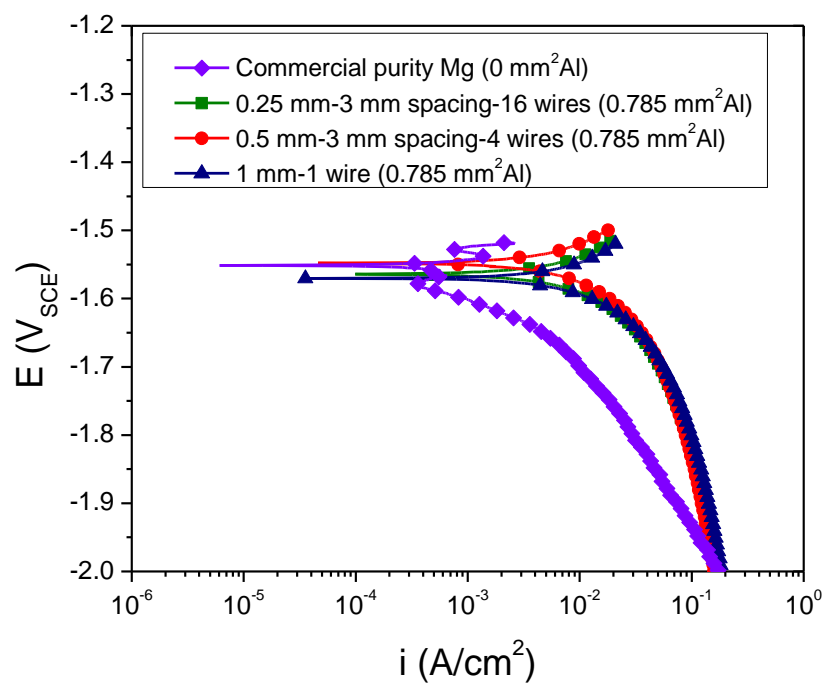
b)
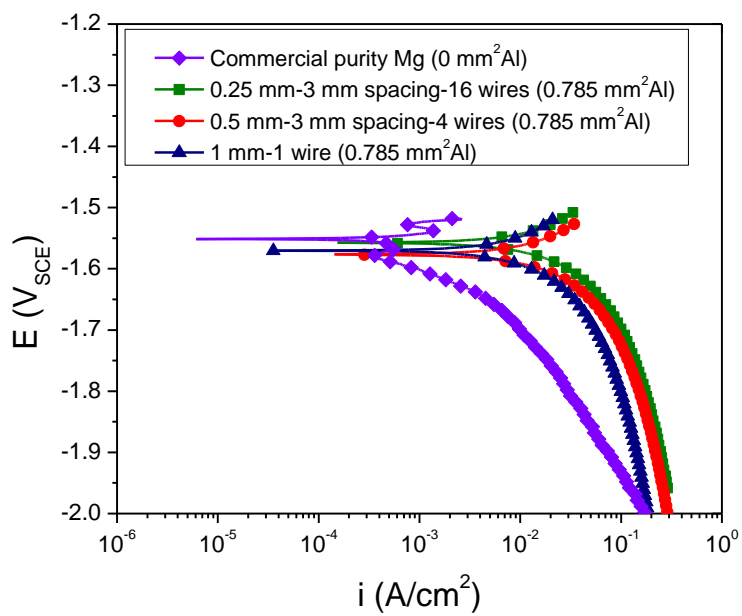
c)
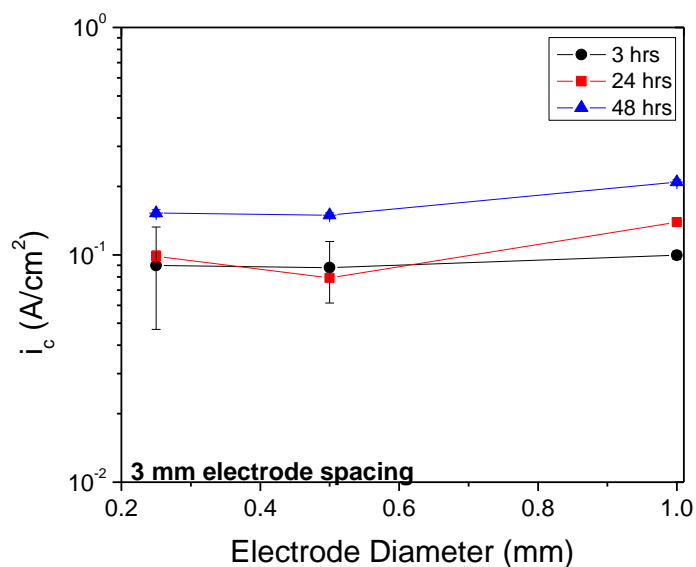
d)
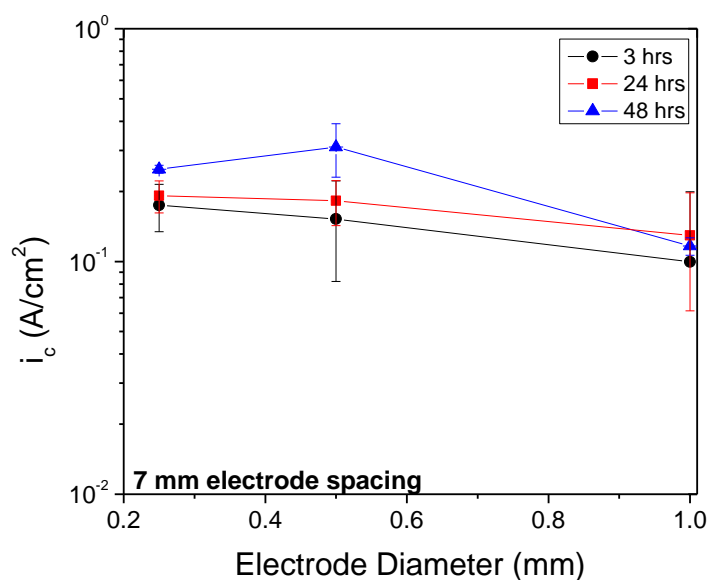
Figure 6. 12. Variation in cathodic kinetics with a variation in the electrode diameter. Commercial purity Mg embedded with high purity Al electrodes of different diameters from 1 mm to 0.25 mm. The area fraction of high purity Al electrodes was kept constant at 0.001by retaining an area of 790.9 mm^2 of commercial purity Mg and 0.785 mm^2 of high purity Al. Typical cathodic polarization curves for a) 3 mm and b) 7mm diameter electrodes. Cathodic kinetics determined from cathodic polarization curves taken at -1.8 V$_{SCE}$ after 3, 24 and 48 hour holds at OCP in 0.1 M TRIS for a) 3 mm and b) 7mm diameter electrodes.
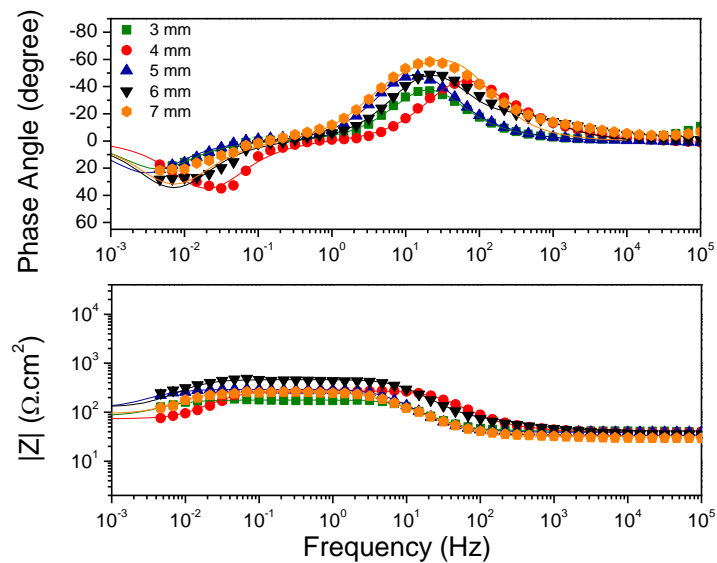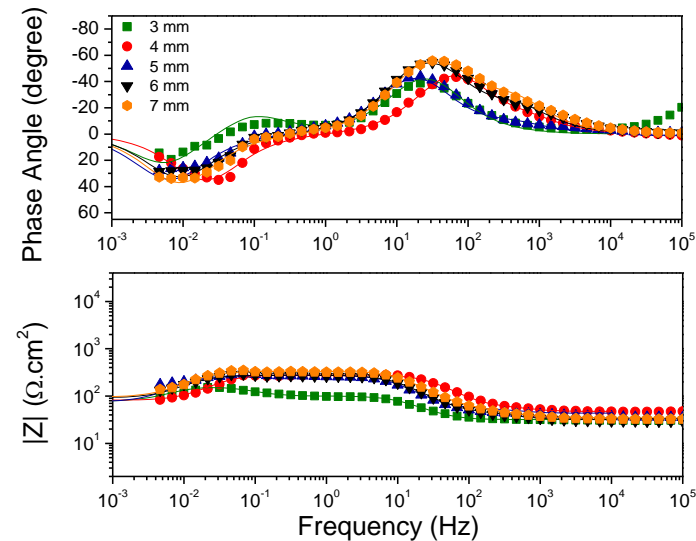
Figure 6. 13. Bode magnitude and phase plot for commercial purity Mg embedded with high purity Al electrodes with different electrode diameter from 0.5 mm to 0.25 mm diameter. The spacing of these electrodes was varied from 3 to 7 mm. The area fraction of Al electrodes was kept constant at 0.001 by retaining an area of 790.9 mm^2 of Mg and 0.785 mm^2 of Al. Data shown along with respective fits following 24 hrs immersion in 0.6 M NaCl at open circuit.

a)
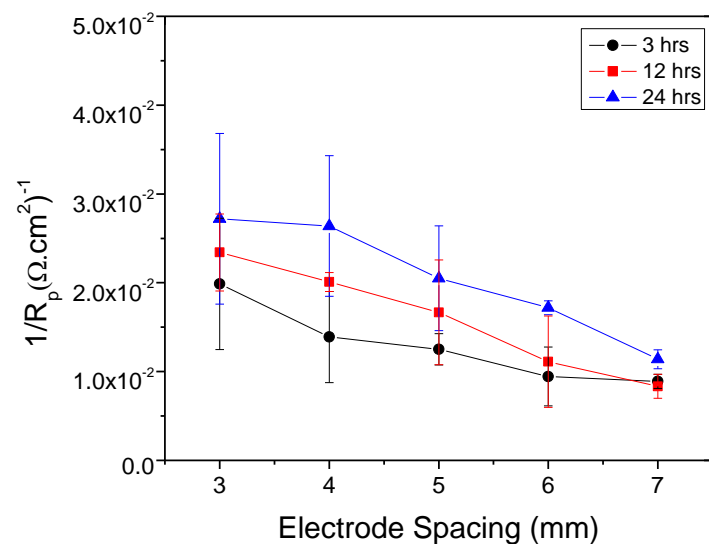
b)
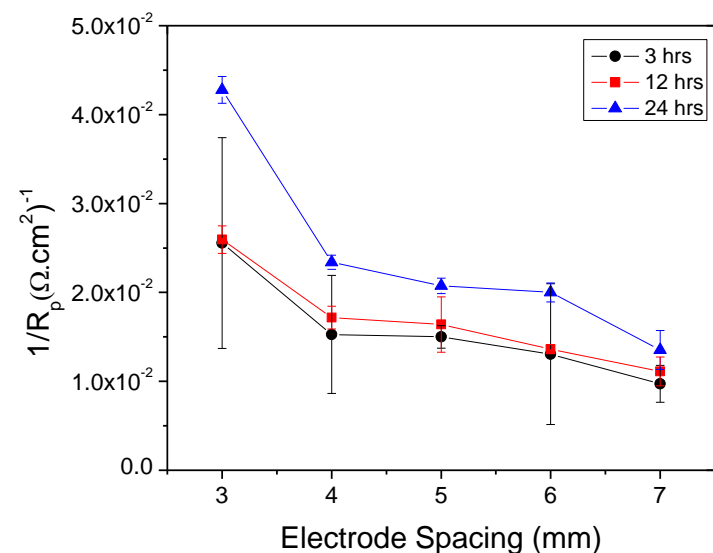
Figure 6. 14. Variation in polarization resistance with electrode spacing for a) 0.50 mm diameter and b) 0.25 mm diameter high purity Al electrodes embedded in commercial purity Mg. The area fraction of high purity Al electrodes was kept constant at 0.001 by retaining an area of 790.9 mm^2 of commercial purity Mg and 0.785 mm^2 of high purity Al.

a)
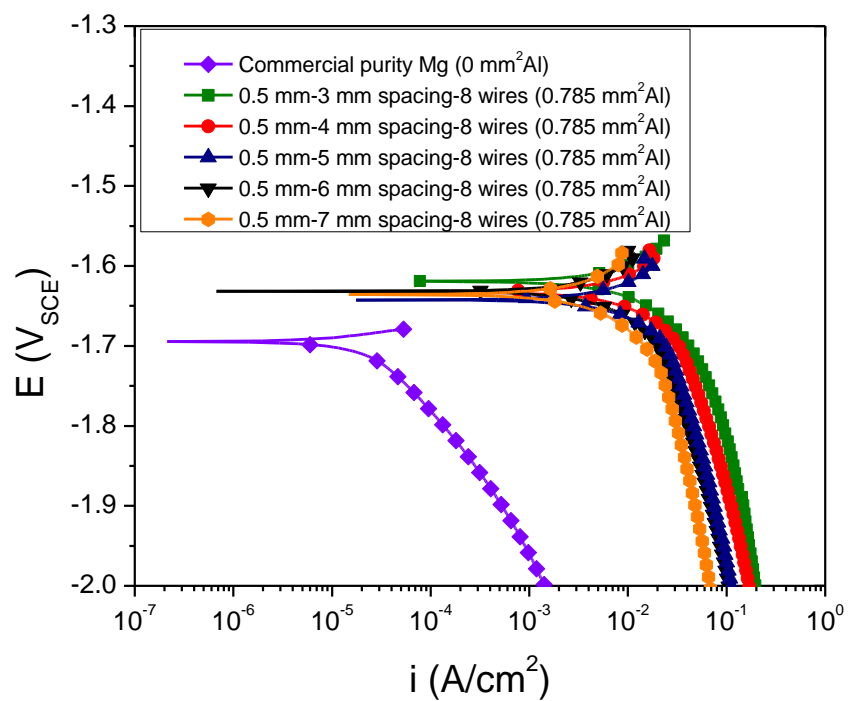
b)
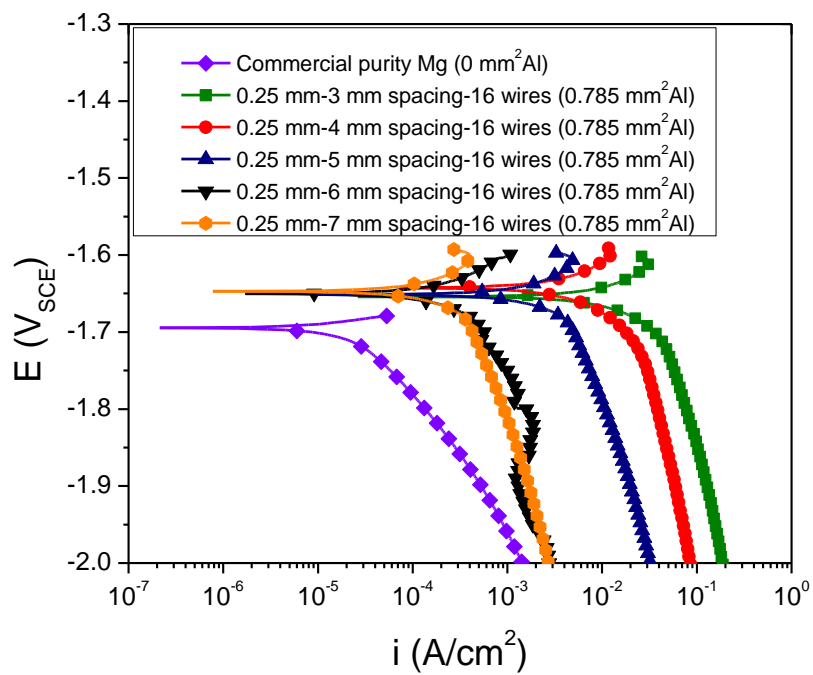
c)
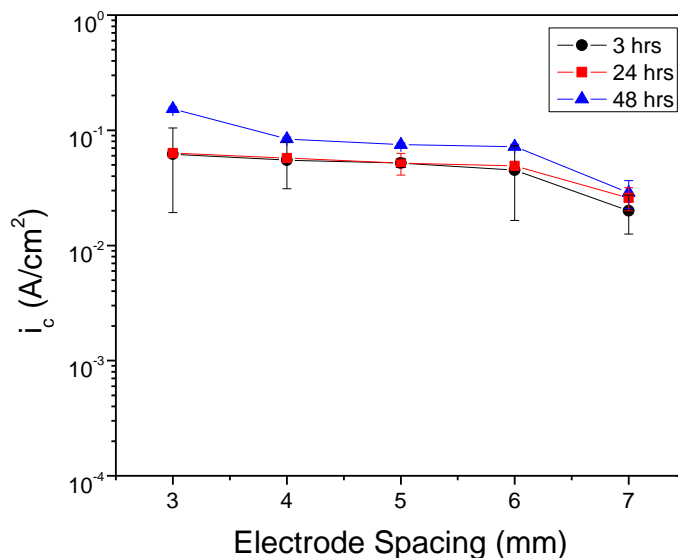
d)
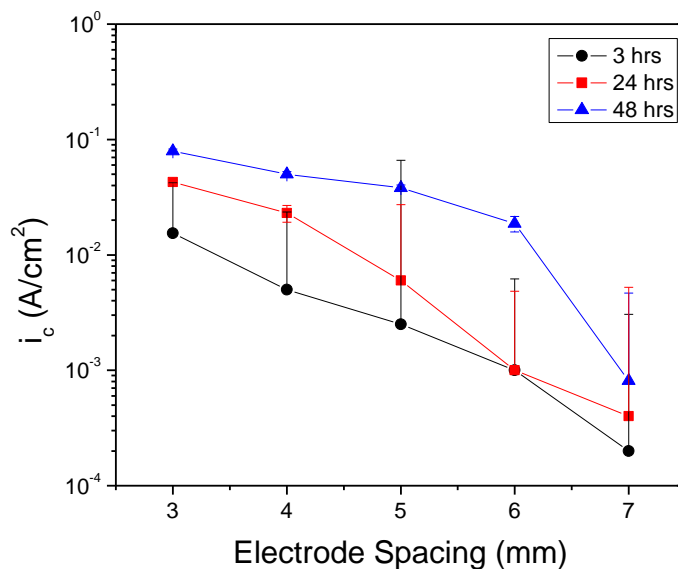
Figure 6. 15. Variation in cathodic kinetics with a variation in the electrode spacing. Commercial purity Mg embedded with high purity Al electrodes of different diameters from 1 mm to 0.25 mm. The area fraction of high purity Al electrodes was kept constant at 0.001by retaining an area of 790.9 mm^2 of commercial purity Mg and 0.785 mm^2 of high purity Al. Typical cathodic polarization curves for a) 3 mm and b) 7mm diameter electrodes. Cathodic kinetics determined from cathodic polarization curves taken at -1.8 V$_{SCE}$ after 3, 24 and 48 hour holds at OCP in 0.6 M NaCl for a) 3 mm and b) 7mm diameter electrodes.

a)
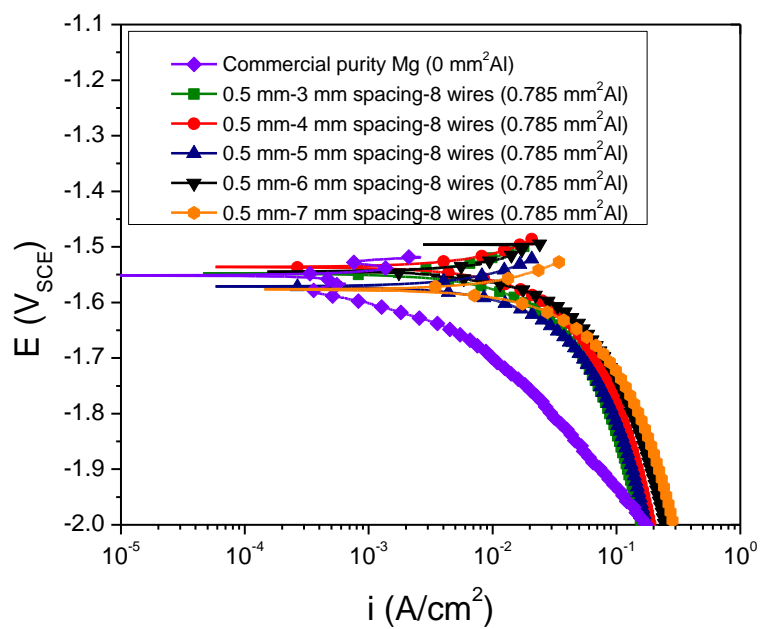
b)
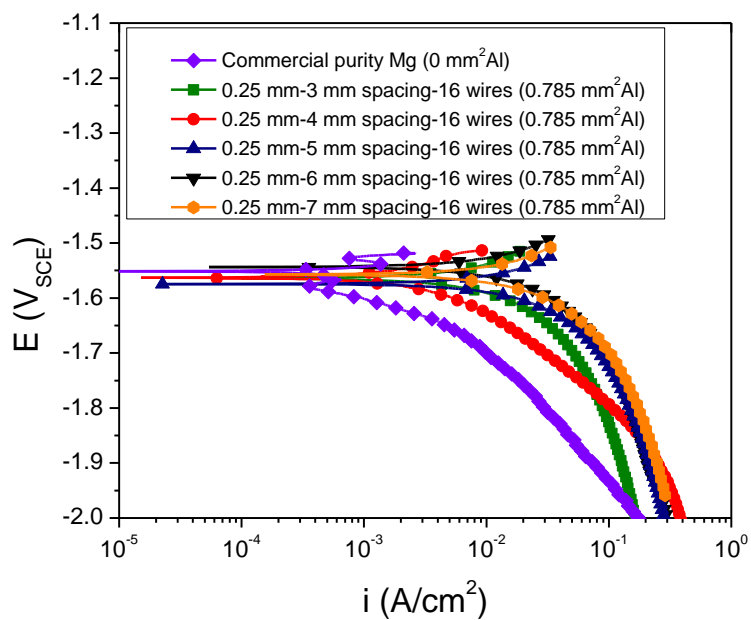
c)
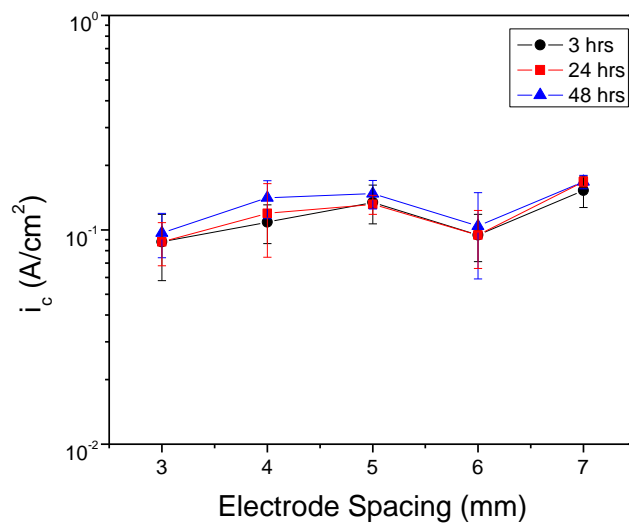
d)
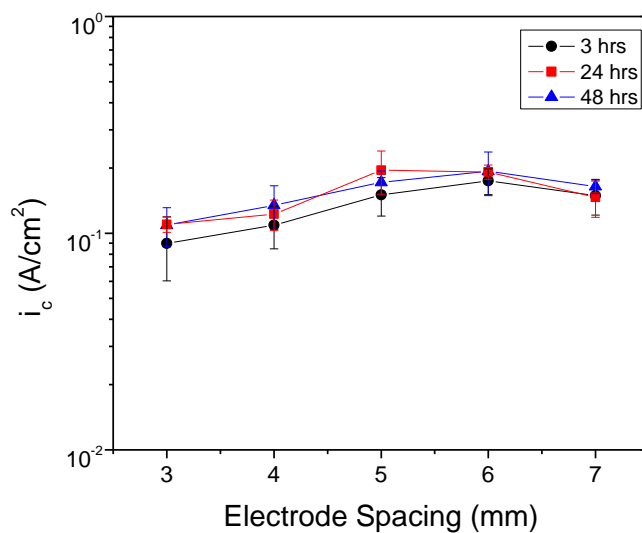
Figure 6. 16. Variation in cathodic kinetics with a variation in the electrode spacing. Commercial purity Mg embedded with high purity Al electrodes of different diameters from 1 mm to 0.25 mm. The area fraction of high purity Al electrodes was kept constant at 0.001by retaining an area of 790.9 mm^2 of commercial purity Mg and 0.785 mm^2 of high purity Al. Typical cathodic polarization curves for a) 3 mm and b) 7mm diameter electrodes. Cathodic kinetics determined from cathodic polarization curves taken at -1.8 V$_{SCE}$ after 3, 24 and 48 hour holds at OCP in 0.1 M TRIS for a) 3 mm and b) 7mm diameter electrodes.
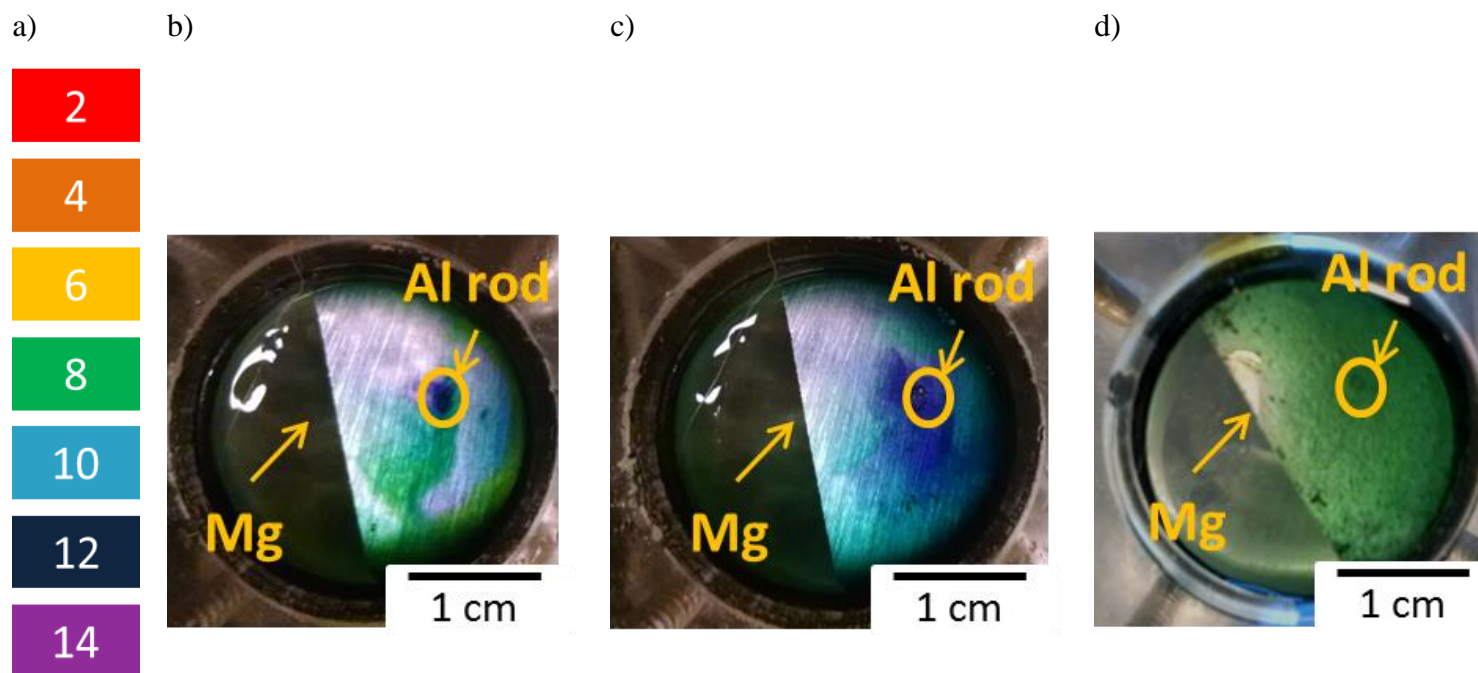
Figure 6. 17. a) Key for pH colors as detected by universal pH indicator. Variation in the pH distribution with exposure environment for b) 0.6 M NaCl (starting pH~5.3) immediately after adding the pH indicator, c) 5 minutes after adding the pH indicator and d) pH distribution in 0.1 M TRIS (starting pH~7).
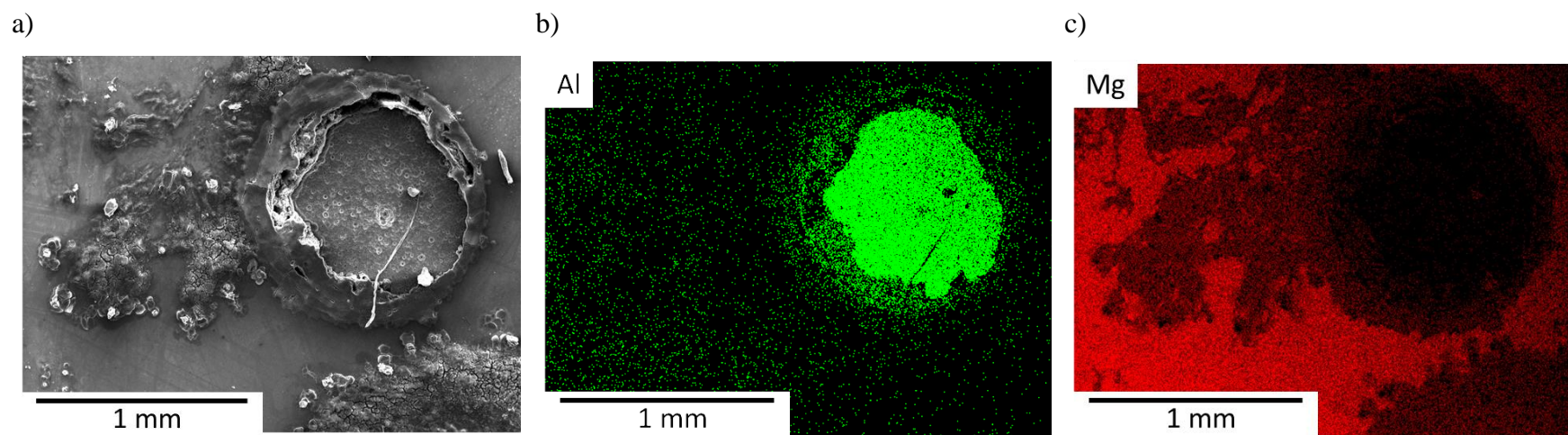
Figure 6. 18. a) corrosion product around Al electrode embedded in Mg, b) Al distribution after corrosion and c) Mg EDS after corrosion in 0.6 M NaCl.

a)
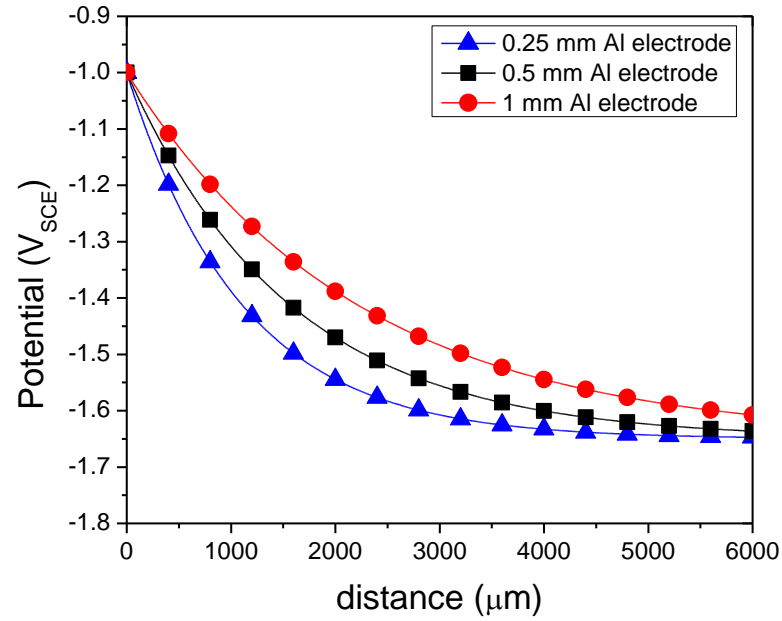
b)
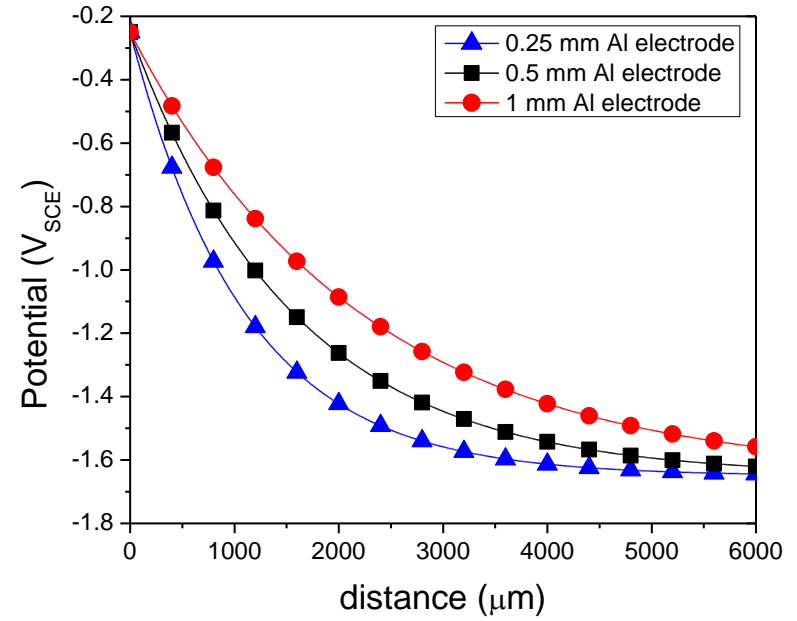
Figure 6. 19. Effect of electrode size on potential distribution E(r) where d=0.25 mm to d=1 mm. As the electrode size increases, the throwing power increases for b) Al electrodes and b) Fe electrodes. R_p =90.8 Ω-cm^2,[45], p=25 Ω^{-1}cm^{-1}.
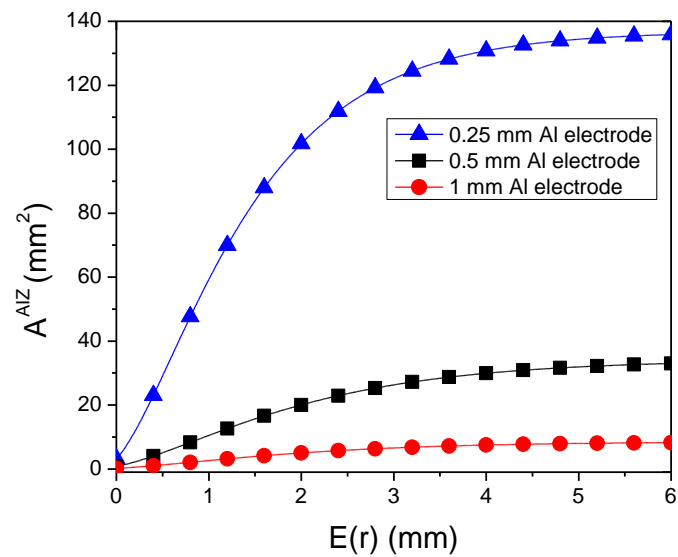
Figure 6. 20. Area of anodically induced zone (A^{AIZ}) for a given potential distribution E(r) for different electrode sizes.
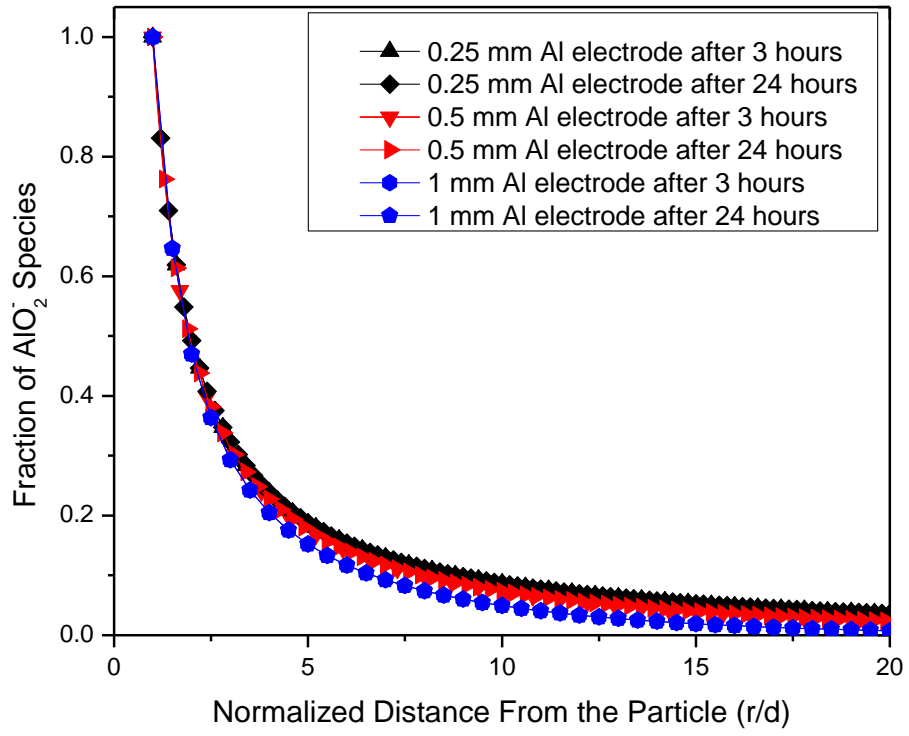
Figure 6. 21. Variation in the one-dimensional concentration gradient of Al^{3+} away from the Al-rich IMP interface assuming a spherical particle for both Al-Mn and Al-Mn-Fe IMPS.

7 Revisiting the Effect of Crystallographic Orientation on the Corrosion of Commercially Pure Mg

The electrochemical dissolution of Mg indicates a strong crystallographic dependence in chloride-containing, alkaline environments. There is a different crystallographic orientation dependence initially during corrosion in non-chloride containing, near neutral pH buffered environments which dissolve air-formed MgO oxides, such as Tris(hydroxymethyl)aminomethane (TRIS) and Ethylenediaminetetraacetic (EDTA). The origins of the differences in corrosion rate trend were investigated utilizing electrochemical impedance spectroscopy (EIS). High frequency constant phase elements were exploited to determine oxide thicknesses as a function of crystal orientation. In unbuffered NaCl, corrosion kinetics was faster on basal planes and a slow corrosion rate on low index, prismatic and pyramidal planes. This variation in the corrosion kinetics with crystallographic orientation in 0.6 M NaCl was interpreted to depend on the MgO and $Mg(OH)_2$ film thickness as a function of orientation. In particular, the variation in the MgO thickness and epitaxy for faces with various crystallographic orientations may strongly alter the corrosion kinetics. The crystallographic orientation dependence seen in the buffered neutral pH environments was initially related to surface energy trends but this dependency was lost when $Mg(OH)_2$ films form once the buffer is overcome.

A manuscript based on this chapter has been submitted to the Journal of the Electrochemical Society as a Full Research Paper, "Revisiting the Effect of Crystallographic Orientation on the Corrosion of Commercially Pure Mg."

Representative author contributions:

L.G. Bland: experiments, metallurgical and electrochemical characterization
K. Gusieva: metallurgical and electrochemical characterization
J.R. Scully: advisor, analysis and interpretation

7.1 <u>Introduction</u>

7.1.1 Corrosion Dependence on Crystallographic Orientation for Various Metal Systems

For many metals and alloys, corrosion rate has been found to exhibit strong dependence on crystallographic orientation [1-5]. Assessing anisotropic corrosion properties by using single crystal samples limits the number of facets tested [3,4,6,7]. While such studies give an indication of the corrosion properties of specific orientations, they are limited to a few crystal planes [3,4,6,7]. This paucity of grain orientations at closely spaced h, k, l Miller-Bravais indices values falls short of yielding an overarching understanding of the corrosion rate as a function of crystal orientation because corrosion properties can vary significantly over only a few degrees difference in crystallographic orientation[1]. Integration of a large number of grains on polycrystalline samples on a grain by grain basis over small differences in h, k, l values provides the opportunity to uncover the true orientation dependence of the corrosion rate as a function of surface plane.

Moreover, significant differences on this corrosion response are reported between studies [1-13]. For body-centered cubic (bcc) stainless steel in 0.6 M NaCl, the highest percentage of pitting events is observed on planes oriented ~25° away from {001} [8] while the {100} orientation is also reported to have the highest dissolution rate in H_2SO_4 [2] and NO_3^- [9]. For face-centered cubic (fcc) Al in NaOH, orientations near {111} show the most dissolution[10-12]. To fully understand the effect of crystallographic orientation on corrosion rates, the effects of crystal structure on atomistic bonding, the number of dangling bonds, surface energy, film thickness, film/substrate epitaxy [1,2,6,13] as well as the reaction thermodynamics and kinetics at the metal-oxide-solution interface during both passive and active corrosion [3,7] should be considered. Unfortunately, many studies have not made a careful distinction between filmed and bare actively dissolving conditions.

7.1.2 Crystallographic Orientation Dependence on Corrosion for Mg and Mg Alloys

A systematic sampling of orientations in Mg alloys has been complicated due to highly crystallographically textured Mg alloy sheet or plate often formed upon mechanical processing [14-17]. For these reasons, as well as the inability to accurately assess corrosion rates in Mg system by electrochemical methods [18-20], conflicting results have been reported regarding the orientation dependence of Mg corrosion [21,22]. For instance, corrosion was only observed on planes that were oriented near the <0001> direction with respect to the sample surface in NaCl environments with

added dichromate ions [23]. Also, the Mg (0001) surface exhibited pitting corrosion susceptibility at the open circuit potential (OCP) while the (10$\bar{1}$0), and (11$\bar{2}$0) surfaces were passive at open circuit and pitting only initiated at potentials slightly anodic to their open circuit potentials in a similar environment [24]. However, Mg-Al alloys (such as AZ31) corroded at a lower rate on the closely packed basal plane [25], although this was complicated by the presence of secondary phases.

Electron Backscatter Diffraction (EBSD) correlated with surface topography measurements, such as profilometry techniques now enables understanding of the dissolution behavior of a large number of crystal planes [1]. In this study, these prior difficulties have been overcome by EBSD analysis of many grains. Profilometry and electrochemical impedance spectroscopy (EIS) were then both conducted on individual, isolated grains to reveal the orientation dependence of corrosion under open circuit conditions.

7.1.3 Effect of Surface Energy on Crystallographic Dissolution

Existing literature on Mg often suggests that surface energy varies with crystal orientation. The surface energy for Mg {0001}, {10$\bar{1}$0} and {10$\bar{1}$2} surfaces are 0.9, 1.2 and 1.4 J/m^2, respectively, as calculated with empirical electron theory [6,26]. This implies that exposed faces close to the {0001} plane should have a lower thermodynamic driving force and might corrode slower than those planes which are oriented slightly off from the {0001} plane from a surface energy minimization perspective [23]. Previous work on fcc Fe-Pd shows that the highest dissolution occurred at planes oriented approximately 45° away from the {100} orientation which correlated to the highest determined surface energy [1]. However, Mg is a system which corrodes in [Cl$^-$] solutions far away from equilibrium [1].

7.1.4 Nature and Crystallographic Aspects of the Native Oxide Film on Mg

For Mg, the oxide film is affected by factors such as solution pH, where a more protective film is typically formed in alkaline solutions [27-30]. Several techniques have been used to analyze the nature of this film. The surface film formed on Mg is duplex in nature, consisting of a thin, nano-crystalline MgO inner layer and a Mg(OH)$_2$ platelet layer [31-33]. X-ray photoelectron spectroscopy (XPS) [34-36] and focused ion beam (FIB) [27,33,37] studies on the surface of Mg have shown that the surface film consists of both MgO and Mg(OH)$_2$ [38]. The initial, crystalline MgO layer is formed during exposure to air. Hydration of the bulk inner MgO layer occurs and the layer thickens to form the outer Mg(OH)$_2$ layer [27,33]. The thickness of the oxide

layer on Mg has been calculated through XPS and FIB cross-section [27,33,37]. While this thickness is extremely dependent on exposure time and environment, the outer, $Mg(OH)_2$ layer is typically on the order of ~500 nm in thickness and flake-like while the inner MgO layer is only on the order of 50-90 nm thick [27,33,37]. MgO films on the basal {0001} surface are thinner than those on either {01$\bar{1}$0} and {11$\bar{2}$0} in dilute sodium sulphate solutions [39]. This relationship has been similarly reported for polycrystalline Ti using EBSD measurements [40]. While the {0001} and {01$\bar{1}$0} planes consist of equiaxed crystals of MgO, the {11$\bar{2}$0} surface forms MgO with oriented flakes perpendicular to the metal/oxide interface [27,33].

7.1.5 Opportunity to Ascertain Crystallographic Dependence of Simultaneous Corrosion and Oxide Formation with Impedance Spectroscopy

The use of electrochemical impedance spectroscopy (EIS) has been determined to give a reliable and repeatable estimation of the instantaneous corrosion rate on Mg and its alloys [18-20]. The components of the equivalent circuit have been shown to correspond to the Mg sample surface and described in terms of their physical meaning [41]. Therefore oxide film thickness may be determined under in-situ conditions. The goal of this research was to utilize EIS to understand the effects of crystallography on oxide thickness and the corrosion rate for oxide free and oxide covered crystal surfaces.

The EIS determined oxide thickness has been achieved for other material systems, such as Ni-Cr-Mo [42], Al [43,44] and the HCP Zr [5] but further analysis in the Mg system is needed. The circuit diagram for accurate EIS determination in Mg has been suggested in other work respective to the oxide growth (Figure 7. 1) [41]. The use of two capacitive circuit elements is necessary in order to model the full frequency response of the Mg to the electrolyte [18,41]. The high frequency capacitor, C_1 represents the passive oxide and films while the low frequency capacitor, C_2 represents the double-layer capacitance. These two capacitances can be simultaneously determined in the case where the capacitances differ in magnitude [41]. Good correlation has been shown between the percent area of corroded surface and the capacitive elements [41,45], showing that the thickness of this oxide with time can be determined by these capacitive values.

7.1.6 Objective

The objective of this study is to understand origins of the crystallographic dependence of corrosion rate in a polycrystalline Mg sample under film and film-free conditions. The work

herein is the first of its kind to perform EIS on single grains in a polycrystalline material system (as compared to single crystals) in order to assess both oxide thickness and to determine the corrosion rate as a function of orientation. The conflicting information on the crystallographically dependent corrosion rates in Mg is comprehensively investigated here by examining corrosion rate as a function of the air formed and electrochemical oxide growth as well as under slightly buffered acidic circumstance where films are minimized. This enables testing of the effects of surface energy on corrosion rate of Mg.

In terms of weld corrosion, melting of the weld FZ creates a randomized texture which is dramatically different than the basal {0 0 0 1} texture observed in the HAZs or wrought base plate. This crystallographic study enabled a systematic study of the effect of crystallographic orientation on the corrosion rate of Mg in order to determine if the basal orientation in the HAZs and wrought base plate or the randomized texture in the FZ were worse for corrosion. Using commercially pure Mg allowed for evaluation of these crystallographic orientations without the influence of composition, solidification boundaries or intermetallic particles.

7.2 <u>Experimental Procedures</u>

7.2.1 Materials

Extruded commercially pure Mg rod was provided by Alfa Aesar. The sample was re-melted and resolidified in order to minimize the as-received extruded texture. All compositions are reported in wt. %, with the actual compositions provided by QUANT (Quality Analysis and Testing Corporation) via Inductively Coupled Plasma optical Emission Spectroscopy (ICP-OES) analysis as (0.01 wt% Al, 0.01 wt% Mn, 0.01 wt% Zn, 0.021 wt% Si, 0.005 wt% Cu, 0.001 wt% Ni, 0.006 25% Fe and Mg Balance).

7.2.2 Metallurgical Sample Characterization

Sample Heat Treatment for Large Grain Growth

All polycrystalline samples have been heat treated to alleviate any deformation twins formed during previous processing. Commercially pure Mg samples were heat treated at 575°C for 5 h to achieve a grain size of approximately 1.5 mm in diameter. This enabled grains to be easily found by low magnification SEM, EIS electrochemical testing and optical microscopy before and after corrosion while still achieving a large sample size in each EBSD image.

Electron Backscatter Diffraction

Samples were analyzed with optical microscopy as well as scanning electron microscopy (SEM) using a Hirox optical microscope and FEI Quanta 650 microscope, respectfully. Samples were polished through colloidal silica, ion flat milled and etched with a Picric acid etch (3g picric acid, 30 mL acetic acid, 100 mL ethanol and 15 mL distilled water) immediately before being placed in the SEM. Etching removed the MgO oxide which may have formed, even after ion polishing, to enable improved EBSD imaging. Samples were polished on 1200 grit SiC after EBSD to remove any carbon contamination from the SEM before being exposed for corrosion analysis. Samples were rapidly polished (<< 1 μm) to maintain some of the etched microstructure for grain identification. EBSD was performed at low magnification to image a large number of grains at once using the Aztec software package [46]. Approximately 200 grains were analyzed over multiple EBSD micrographs.

Corrosion Morphology and Oxide Thickness in Various Electrolyte Environments

The corrosion morphology was assessed to determine how the corrosion initiated and progressed. Secondary Electron SEM micrographs were taken of each sample before and after immersion in unbuffered 0.6 M NaCl, 0.1 M *Tris*(hydroxymethyl)aminomethane (TRIS) and 0.1 M Ethylenediaminetetraacetic acid (EDTA) for 12 h at OCP. The starting pH for each of these environments was 5.1, 7 and 8, respectfully. TRIS and EDTA are both chelating buffer agents, which chemically dissolve oxide films and therefore enable Mg corrosion studies without a thick MgO or $Mg(OH)_2$ oxide layer [47]. All samples were subsequently cleaned with CrO_3 to remove any corrosion products and examine the corrosion morphology. 3D images were also obtained using a Hirox optical microscope to determine the depth of corrosion. The area-fraction of the sample surface which was corroded in the form of dark areas, if observed, was determined using the software package, ImageJ[TM] [48]. The corroded area-fraction of the sample surface was determined using the software package Mountains[® 49].

Surface and Corrosion Film Characterization

Raman spectroscopy was performed utilizing a Renishaw InVia Raman Microscope for commercially pure Mg after exposure to 0.6 M NaCl, 0.1 M TRIS and 0.1 M EDTA after immersion in these various environments for 24 h at OCP. All samples were analyzed utilizing a 514 nm laser at 50 % power under at 50x objective lens with 3000 l/mm grating. Raman analysis

was performed on approximately three spots on the sample surface and a typical Raman spectrum is reported.

Texture and Orientation Determination of Each Grain

The Euler angle Φ from the Bunge convention, synonymous with the angle termed $\beta_{\{0001\}}$, was used to report the {hkil} pole normal to the orientation of a crystal facet in a grain [50]. The Euler angles of each plane normal, with respect to the {0 0 0 1} plane, were reported, as exported from the Aztec [46] software, and the {hkil} were determined from Equation 7.1 [51].

$$\begin{bmatrix} h \\ k \\ i \\ l \end{bmatrix} = \begin{bmatrix} \frac{\sqrt{3}}{2} & -\frac{1}{2} & 0 \\ 0 & 1 & 0 \\ -\frac{\sqrt{3}}{2} & -\frac{1}{2} & 0 \\ 0 & 0 & \frac{c}{a} \end{bmatrix} \begin{bmatrix} \sin \phi_2 \sin \phi \\ \cos \phi_2 \sin \phi \\ \cos \phi \end{bmatrix} \qquad \text{Equation 7.1}$$

Where h, k, i and l are the Miller-Bravais indices and c/a is approximately 1.624 for Mg, where c = 5.21 Å and a = 3.21 Å.

To describe the Miller-Bravais index of each plane on an exposed grain facet, {hkil}, variables, described in Figure 7. 2(a), were used to describe a given {hkil} on an inverse pole figure (IPF). The {hkil} is defined in terms of the interplanar angles, β_i, the angle measured from a primary low index hexagonal plane normal to the {hkil} of interest and the α_i, the angle between β_i and either to great circles from the {0 0 0 1} to $\{0\,1\,\bar{1}\,0\}$ or from {0 0 0 1} to $\{\bar{1}\,2\,\bar{1}\,0\}$. The interplanar angles between any two planes $\{h_1\,k_1\,i_1\,l_1\}$ and $\{h_2\,k_2\,i_2\,l_2\}$ in the hexagonal system were determined from Equation 7.2 [52].

$$\cos\emptyset = \frac{h_1 h_2 + k_1 k_2 + \frac{1}{2}(h_1 k_2 + h_2 k_1) + \frac{3a^2}{4c^2} l_1 l_2}{\sqrt{\left(h_1^2 + k_1^2 + h_1 k_1 + \frac{3a^2}{4c^2} l_1^2\right)\left(h_2^2 + k_2^2 + h_2 k_2 + \frac{3a^2}{4c^2} l_2^2\right)}} \qquad \text{Equation 7.2}$$

Corrosion Rate Determination by EIS

The corrosion behavior of single grain facets of commercially pure Mg was monitored with EIS over a 24 h immersion period in 0.6 M NaCl, 0.1 M TRIS and 0.1 M EDTA at OCP. The corrosion rate of the isolated grains was accomplished using electroplaters tape with a 1.23 mm^2 area hole to expose each grain. EIS scans were acquired from 100 kHz to 0.001 Hz with 6 points per decade and an AC amplitude of ±20 mV. EIS scans were analyzed and fit using the

software program ZView [53] to an equivalent circuit, seen in Figure 7. 1, and were fit to a low frequency limit of at least 0.01 Hz for 0.1 M TRIS and 0.1 M EDTA and to 0.001 Hz in 0.6 M NaCl. The inclusion of the full inductive frequency response of Mg enables for a more accurate determination of the corrosion rate of Mg alloys by the inclusion of the full polarization resistance, R_p, established at low frequencies [18,19]. The determination of R_P was calculated using the following equation as reported elsewhere [18,19,41] for Figure 7. 1(a) and 1(b) respectfully.

$$\frac{1}{R_p} = \frac{1}{R_1 + R_2} + \frac{1}{R_3}$$
Equation 7.3

$$R_p = R_1 + R_2$$
Equation 7.4

The corrosion rate and anodic charge was determined through integration of $1/R_p(t)$ with respect to time using the Stern-Geary equation[39] as detailed in Equation 7.5.

$$Q_a^{EIS} = \int i_{corr(\theta)}dt = \int \frac{\beta_a \beta_c}{2.303 R_P(t)(\beta_a + \beta_c)}dt$$
Equation 7.5

It has been shown previously, that the Mg interface as interrogated by AC methods in chloride-containing environment can be considered reasonably stationary through the direct integration of the Kramers-Kronig (K-K) transformations of the real and imaginary components [54,55]. There is good correlation and low residual noise (<<1% of calculated) through 0.001 Hz for 0.6 M NaCl (Figure 7. 3(a)). Recall that the inductive loop, which is typically observed on Mg in the chloride-containing environments at low frequencies is observed in 0.6 M NaCl [19]. However, in the TRIS and EDTA environments, good correlation could only be achieved up to 0.01 Hz (Figure 7. 3(b-c)) as determined through the Gamry Echem Analyst software. This agrees with previous work which has found that this solution lacked a well-defined inductive loop as is typically seen in the [Cl⁻] environments[19]. Moreover, this was verified herein using K-K transforms. This is in agreement with previous work which shows than an inductive loop and the propagation of cathodically activated dark regions[41] are not seen in these buffered, chelating environments[19,47].

The corrosion penetration depth was calculated from Faraday's law:

$$x = \frac{Q(E.W.)}{F\rho}$$
Equation 7.6

Where E.W. is the equivalent weight of commercially pure Mg, taken as 12.16 g/eq, F is Faraday's constant (96,485 C/eq), and ρ is the density of Mg. This corrosion depth is important for single grain EIS analysis, particularly for highly reactive Mg samples. If the material corrodes deeper than the depth of a grain (relative to x=0 μm at the sample surface) then the crystallographic dependence determined through single grain EIS is lost. Therefore, an absolute upper bound in corrosion was taken as the grain size/2. However, it is recognized that corrosion beyond the first 100 atom layers may result in a corroded surface different from the crystallographic orientation of the face of the grain first exposed [1].

Film Thickness Determination by EIS

The film thickness on individual grains was determined after the same EIS test program, over a 24 h immersion period in 0.6 M NaCl, 0.1 M TRIS and 0.1 M EDTA using the software program ZView [53] to fit experimental data to the equivalent circuit Figure 7. 1(a) for 0.6 M NaCl or Figure 7. 1(b) for 0.1 M TRIS and EDTA[12] solutions due to the variation in physical presence or absence of films. The equivalent circuits were comprised of constant phase elements (CPEs). A CPE impedance, Z_{CPE}, can be expressed in terms of the model parameters α (a time-constant) and Y_o (CPE parameter) as shown in Equation 7.7 [56] were the CPE parameter was used for C_1 and C_2 for determining the oxide thickness.

$$Z_{CPE} = \frac{1}{(j\omega)^{\alpha}Y_o} \qquad \text{Equation 7.7}$$

Where j is an imaginary number and ω is the AC frequency response. The oxide film can be modeled as a capacitor [41]. For Figure 7. 1(a,b), it was assumed that $\alpha=1$ for an ideal capacitor where $Y_o = C$, however, this term varied in Figure 7. 1(b,d) with time. In the case of an ideal capacitor, the effective dielectric capacitance, C_{eff}^{id}, of the film can be expressed by Equation 7.8.

$$C_{eff}^{id} = \frac{\varepsilon\varepsilon_o A}{l_{ox}} \qquad \text{Equation 7.8}$$

Where the ε is the dielectric constant for MgO (9.8), ε_o is the permittivity of vacuum (8.84×10^{-14} F/cm)[57], A is the sample exposure area and l_{ox} is the oxide thickness. In the case of a non-ideal capacitor, the effective capacitance, C_{eff}^{non-id} can be obtained from a constant phase element [58].

---

[12] Data below the K-K transform limit did not prove to be valid.

$$C_{eff}^{non-id} = Y_o(2\pi\omega'')^{\alpha-1} \qquad\qquad \text{Equation 7.9}$$

Where ω'' is the frequency where Z_{CPE} reaches a maximum [58]. From this calculation, Equation 7.7 can be used to determine the oxide thickness. For this analysis, Y_o and α were both determined via fitting of the equivalent circuits (Figure 7. 1).

7.3 <u>Results</u>

7.3.1 Materials Characterization

After heat treatment, grains were determined to be approximately 1.5 mm in diameter by the line intercept method and equiaxed with a heterogeneous distribution of grain sizes. The texture of the samples were determined from EBSD, reported in an inverse pole figure (IPF), to be approximately random which gave a good population of grains with various crystallographic orientations to ascertain the crystallographic orientation dependence of corrosion. Few deformation twins were seen during metallurgical characterization.

7.3.2 Electrochemical Impedance Behavior in Film and Non-Film Forming Environments

Corrosion dependence on the crystallographic orientations was influenced by the exposure environment. Specifically, film-forming versus non-film forming environments dramatically affected the resultant intrinsic corrosion rate and morphology in Mg. Examining the EIS frequency response in 0.6 M NaCl versus 0.1 M TRIS and 0.1 M EDTA (Figure 7. 4), it was observed that, after 24 h, TRIS and EDTA had the highest corrosion rates. This may be indicative of the absence of a thick, partially protective surface film, consisting of $MgO/Mg(OH)_2$ as has been reported in literature [33,37,59,60]. Films as well as absorbed intermediates were also observed (indicated by the presence of a low frequency inductive loop) in NaCl. This inductive loop was absent in TRIS and EDTA, as confirmed by the K-K transform where low-frequency data points scattered in the first and fourth imaginary-real quadrants were invalid (Figure 7. 3). Similarly, higher corrosion rates may be indicative of the lack of changes in the local surface environment in these buffered solutions, specifically usual elevation of pH towards the $Mg^{+2}/Mg(OH)_2$ equilibrium [61]. The pH for the chloride containing environments before exposure was typically around 5.3 before becoming more alkaline with the generation of OH^-, ~10, immediately after corrosion of Mg in the unbuffered solution. At pH~10, MgO and $Mg(OH)_2$ are stable, thermodynamically [61]. However, the pH of the buffer solutions remains 7 and 8 which does not thermodynamically support the formation of MgO or $Mg(OH)_2$. Mg

244

exposed to 0.1 M TRIS and 0.1 M EDTA showed no obvious crystallographic orientation dependence with max $1/R_p$ or i_{corr} at intermediate β-angles (Figure 7. 5(a-f)). However, samples exposed to 0.6 M NaCl (Figure 7. 6) showed various morphologies related to crystallographic orientation. The low index {0 1 $\bar{1}$ 0} showed a wide "filiform-like" corrosion morphology while other, higher index grains, showed more corrosion propagation.

The molecular identity of the oxide films, formed in the 0.6 M NaCl, 0.1 M TRIS and 0.1 M EDTA exposure environments, were confirmed through the use of Raman spectroscopy (Figure 7. 7). Fitting of the Raman shift to the characteristic $Mg(OH)_2$ peaks indicate a strong presence of the $Mg(OH)_2$ film in the chloride containing 0.6 M NaCl solution. However, these peaks had less intensity in the EDTA and TRIS solution which suggests that only a small amount of $Mg(OH)_2$ was detected which was likely a remnant of the air formed film or metastable film formation. This issue will be discussed below. MgO (or the MgO stretch) was not detected through Raman Spectroscopy, even after thermal oxidation of the material suggesting significant hydroxylation of oxides.

7.3.3 Crystallographic Dependent Dissolution in Polycrystalline Mg

Polycrystalline samples were exposed to 0.6 M NaCl after EBSD characterization. The orientation of each grain was determined as shown in Figure 7. 8(a) and 7. 9(a). After a 12 h immersion at open circuit in 0.6 M NaCl, the corrosion morphology revealed that some grains preferentially corroded and developed characteristic dark areas [20,41,47] while other grains remained intact. In Figure 7. 8(b), grain 18 was substantially corroded by the filiform morphology [62-65]. This grain had an orientation approximately 20° from the {0 0 0 1} basal plane. However, grains 21 and 19, near {$\bar{1}$ 2 $\bar{1}$ 0} orientations, had not corroded. Figure 7. 9 displays a grain with a strong basal orientation (red grain 1). The near basal plane (labeled as 1) corroded preferentially to those of a non-basal orientation. The corrosion depth (Equation 7.6) in 0.6 M NaCl is approximately 50 μm on the basal plane after 24 hours while this depth is 225 μm and 450 μm for 0.1 M TRIS and 0.1 M EDTA respectively (Figure 7. 10(b-d)). The relationship between the corrosion depth is roughly linear with time for each specified [h k i l] indicating an approximately constant corrosion rate. Also, the trend approximately shows a decrease in the corrosion propagation depth at a given time with increasing $β_{\{0001\}}$ away from the basal plane at

all exposure times. Therefore, the effect of the original crystallographic orientation is maintained through the full exposure time for each environment.

The volume of corrosion propagation was also plotted as a function of orientation on an inverse pole figure for 0.6 M NaCl (the environment which showed anisotropic crystallographic orientation morphology). The depth, as a fraction of the dark, corroded regions [60,66] was also plotted as a function of orientation. It has been observed previously, that as the material corrodes, the sample surface becomes dark [66] and this dark region typically contains enriched transition elements [67,68] and possible Al redeposition [45,69,70]. It has similarly been shown that the exchange current density for the hydrogen evolution reaction (HER), the dominant cathodic reaction on Mg, increases with time due to this enhanced cathodic activity on the sample surface [59,71,72]. Figure 7. 11(a) shows the percent "dark" surface area for different orientations after immersion in 0.6 M NaCl for 24 h at OCP. This surface area has been corrected for the percent of the whole grain corroded. The corrosion rate can also be plotted as a function of the volume of material dissolved (Figure 7. 11(b)) as determined with a Hirox optical microscope, similar to that shown in Figure 7. 9(c). In both cases, corrosion is highest on $\{0\,0\,0\,1\}$ planes or those exposed grain facets. Grains oriented within ~30° of the basal plane while those oriented near the $\{0\,1\,\bar{1}\,0\}$ and $\{\bar{1}\,2\,\bar{1}\,0\}$ planes had the least.

7.3.4 Crystallographic Dependence on the Instantaneous Corrosion Rate on Isolated Mg Grains

For commercially pure Mg, the EIS spectra at OCP in 0.6 M NaCl had two capacitive loops and an inductive loop [35,73-80]. Using the equivalent circuit shown in Figure 7. 1(a), a reasonable fit was achieved with $\alpha=0.95$ for the CPE. This $\alpha<1$ is typical for the case of surface heterogeneity [81] and would be particularly true for the highly reactive Mg system. From the frequency response, the two capacitive loops and an inductive loop were seen for all crystallographic orientations (Figure 7. 12). Concerning R_p as a function of $\beta_{\{0001\}}$ angle, inFigure 7. 12, R_p increases with increasing $\beta_{\{0001\}}$ meaning that the i_{corr} decreased with increasing $\beta_{\{0001\}}$ (away from the basal crystal surface) which is quite consistent with the corrosion morphology observed in Figure 7. 8-7. 9. It was shown that the basal plane had the highest corrosion rate while the low index planes had the lowest corrosion rates in the NaCl solution. This is consistent with % dark area and volume lost (Figure 7. 11) in the NaCl solution.

EIS spectrum for non-chloride containing TRIS and EDTA was also determined for grain orientations localized at various $\beta_{\{0001\}}$ angles. This solution lacked a well-defined inductive loop as is typically seen in the [Cl⁻] environments and therefore $1/R_p$ was fit to the equivalent circuit Figure 7. 1(b). The absence of the inductive loop was confirmed previously from the K-K transform where data below 0.01 Hz was invalid (Figure 7. 3). There is a slight variation in these environments with this trend with time. In TRIS, at 0 h there is a slight increase in the corrosion rate at $\beta_{\{0001\}}=20°-60°$ (potentially due to a surface energy effect) (Figure 7. 13). However, this trend disappears after 3 h, with the $1/R_p$ increasing with increasing $\beta_{\{0001\}}$. This same trend was also determined in the non-chloride containing EDTA solution (Figure 7. 14).

For each of these environments, the integration of the corrosion current density over the full 24 h immersion, using Equation 7.5 was determined for each of these specified crystallographic orientations (Figure 7. 15). It is shown that, in the 0.6 M NaCl environment the corrosion rate and corrosion depth (as determined via Equation 7.6) increases with increasing $\beta_{\{0001\}}$ angle. However, in the TRIS and EDTA environments, there is also a slight increase in the corrosion rate and depth around $\beta_{\{0001\}}=60°$. This correlates to the plane with the highest surface energy.

7.3.5 Effect of Oxide Thickness on the Crystallographic Orientation Dependent Dissolution of Mg

The model-determined oxide thickness (determined through Equation 7.6) was highly dependent on the capacitive response in the Mg system [41]. C_1 typically has a value of 10^{-6} F/cm² while C_2 has a value of approximately 10^{-5} F/cm² [41]. From a sensitivity study using circuit model Figure 7. 1(a), replacing CPE with a capacitor, C_1 can be distinguished from C_2 when $C_2 \neq C_1$. However, when $C_1=C_2$ one 1st quadrant loop appears as the time constants for R_1C_1 and R_2C_2 are too similar (Figure 7. 16). EIS fitting in 0.6 M NaCl (Figure 7. 12), C_1 and C_2 are similar while, in Figure 7. 13-14 (i.e. in TRIS and EDTA) the values differ. The oxide thickness was determined using Figure 7. 1(a), at first fit assuming CPE. The Y_o was determined to perform close to an ideal capacitor, with $\alpha \sim 0.95$ for most fits (Equation 7.7-7.9). In summary, l_{ox}, as determined through Equation 7.8, was determined from the value for C_1 (as replaced by a CPE).

The EIS determined oxide thickness is plotted in Figure 7. 17 for 0.6 M NaCl. The change in this thickness was plotted as a function of the $\beta_{\{0001\}}$ value or the distance away from the basal plane Figure 7. 17(a). It was observed that the planes furthest from the basal plane had

247

the thickest determined oxide (~50 nm) while those planes close to the basal plane had a thinner oxide thickness (~5 nm) which is similar to the values reported elsewhere [27,33,35-37]. The corrosion rate was inversely proportional to this thickness (Figure 7. 15).

The oxide thickness as a function of β angle was also determined for the non-chloride containing TRIS and EDTA environments (Figure 7. 17(b-c)). The oxide thickness can be determined using the equivalent circuit in Figure 7. 1(b) down to 0.01 Hz according to the K-K transform (Figure 7. 3). The oxide thickness was extremely small on the basal planes (almost 0 nm) and slightly higher on the pyramidal and prismatic planes (~1 nm). Moreover, the EIS calculated oxide thickness was much smaller than in the 0.6 M NaCl environment. This agreed with the Raman determined oxide response which indicates that the high dissolution rate of Mg eventually saturates the buffer capacity (Figure 7. 7). The determination of the i_{corr} was observed to increase with decreasing oxide thickness. However, the variation in the i_{corr} and oxide thickness was much smaller for all crystallographic orientations in the EDTA and TRIS environments.

7.4 <u>Discussion</u>

7.4.1 Variation in the Oxide Dissolution and Precipitation with Exposure Environment

Figure 7. 18(a) shows a schematic of the oxide growth on Mg in 0.6 M NaCl [37], consisting of a duplex $MgO/Mg(OH)_2$ oxide. The thick, plate-like $Mg(OH)_2$ layer (approximately 500 nm) and is formed after exposure to H_2O [27,33] due to the hydration of the inner MgO layer and formation of $Mg(OH)_2$ onto the sample surface [33,37,64]. The initial MgO layer nucleates on the Mg surface and is measured to be on the order or 50 nm [27,33]. The most densely packed crystal planes for both α-Mg and MgO, {0001}Mg and {111}MgO, are almost parallel to each other, with a couple of degrees deviation [82]. These lattice mismatches mean that the $MgO/\alpha - Mg_{\{0001\}}$ interface is therefore epitaxial [82]. However, the non-basal planes have a slightly higher mismatch and are either semi-coherent or non-coherent [82].

The phenomenon is slightly different in the buffered 0.1 M TRIS and 0.1 M EDTA solutions (Figure 7. 18(b)). Once the sample is exposed to this solution, the air-formed MgO oxide is dissolved by the TRIS/EDTA solution. The remaining air-formed MgO is converted to $Mg(OH)_2$ at the sample surface and buffer capacity is exceeded, therefore there is a small $Mg(OH)_2$ signal which was detected during Raman Spectroscopy (Figure 7. 7). The presence of

$Mg(OH)_2$ was confirmed in all environments, but it was shown that much more $Mg(OH)_2$ formed in 0.6 M NaCl. In this chloride environments, the typical pH after exposure is on the order of ~10 due to the alkalization of the bulk NaCl solution to pH values in the stable region for $Mg(OH)_2$ according to analysis of the Mg Pourbaix diagram [83]. However, both TRIS and EDTA are buffer solutions with stable pH values of 7 and 8, respectfully, which would lead to less oxide formation according to the Mg Pourbaix diagram even after loss of Mg [83].

There was a notable difference in the thickness of this hydroxide with crystallographic orientation with the thinnest oxide on the basal plane and the thickest oxide on the low index orientations for each environment (Figure 7. 17(a-c)). The thickness of this oxide is inversely proportional to the i_{corr}. From the EIS determined i_{corr}, the oxide thickness was on the order of 5 nm to 50 nm in 0.6 M NaCl and <<1 nm to 1 nm in 0.1 M TRIS and 0.1 M EDTA. The oxide thickness on a different HCP material, Zr, was determined through EIS [5,84]. The basal plane had a slower oxidation rate compared to the prismatic planes [5,84]. This variation in oxide growth kinetics was argued to be due to the variation in the oxygen diffusion kinetics through the high packed basal plane and the lower packed prismatic plane [5,84].

7.4.2 Corrosion Rates on Oxide Covered Mg Surfaces

In the chloride, film-forming environment, there was a large variation in the corrosion morphology with crystallographic orientation that is inversely proportional to oxide thickness (Figure 7. 6). Similarly, the i_{corr} increases with decreasing oxide thickness in 0.6 M NaCl (Figure 7. 17(a), 7. 19(b)). The trend reported here agrees with other literature [24] which has reported that the (0001) surface exhibited more corrosion susceptibility at the OCP while the ($10\bar{1}0$), and ($11\bar{2}0$) surfaces are typically passive at open circuit and pitting is only initiated at potentials anodic to their OCPs [24] or that more corrosion occurs more readily on planes near the basal orientation [23]. This inverse proportionality can be explained if oxidation of Mg^{2+} is dependent on oxide film thickness. Thicker hydroxides may limit water penetration and cation transport.

7.4.3 Surface Energy

The effect of surface energy on corrosion is a factor in the corrosion of bare Mg, such as in TRIS or EDTA. Referring to Figure 7. 17(b-c) and Figure 7. 19(b), it can be seen that i_{corr} roughly matches with surface energy trends (for short immersion times) estimated for Mg from embedded atom method and empirical electron theory [26,85]. These calculation techniques show that, in vacuum, the surface energy (γ) varies from 0.9 to 1.4 J/m^2 and even as high as 1.65 J/m^2

[26,85]. Of course this is in vacuum and the actual value of γ in TRIS and EDTA is unknown. The standard free energy of the following reaction applies to the case of Mg corroding in an acid where, in such a half-cell reaction, the number of nearest neighbors is not considered:

$$Mg \rightarrow Mg^{2+} + 2e^- \quad (E^{0,Mg}) \hspace{5cm} \text{Equation 7.10}$$

$$2H^+ + 2e^- + H_2 \quad (E^{0,SHE}) \hspace{5cm} \text{Equation 7.11}$$

Or the overall reaction is:

$$Mg + 2H^+ \rightarrow Mg^{2+} + H_2 \hspace{5cm} \text{Equation 7.12}$$

This reaction will occur spontaneously in water. Consider the free energy of the reaction in Equation 7.12 under standard conditions, at room temperature, where Mg corrodes in acidified water at unity activity of the dissolved species.

$$\Delta_r G^0 = -nF\Delta E^0 = -nF(E^{0,SHE} - E^{0,Mg}) \hspace{3cm} \text{Equation 7.13}$$

In the case where $E^{0,SHE} = 0$ V and $E^{0,Mg} = -2.36$ V. Therefore, $\Delta_r G^0 = 456$ kJmol^{-1} for n = 2 and F = 96485 C/eq. The free energy of the overall reaction is quite negative. However, this energy is lowered by irrational planes which contain kinks, ledges and terraces with fewer bonds than the {0 0 0 1} plane:

$$k\Delta\gamma = \left(\frac{1.4J}{m^2} - \frac{0.9J}{m^2}\right)\left(\frac{m^2}{1x10^{19}atoms}\right)\left(\frac{6.023x10^{23}atoms}{mol}\right) = 30.1 \text{ kJmol}^{-1} \hspace{0.5cm} \text{Equation 7.14}$$

for the case of high energy surface sites with 1.4 J/m^2 compared to 0.9 J/m^2 for the close packed plane [26,85] (as determined from $\beta_{\{0001\}}$=60° along α=0°) where γ is the surface energy term and k is a correction factor as shown in Figure 7. 19(a). Here, the reaction from Equation 14 is more favorable by 30.1 kJ/mol.

This is equivalent to a lowered standard half-cell potential, $E^{0,Mg}_{\{hkil\}}$, now written to describe a {h k i l} plane:

$$E^{0,Mg}_{\{hkil\}} = \frac{\sum \nu\mu_{ox} - \sum \nu\mu_{red} - \sum \nu k\Delta\gamma_{\{hkil\}}}{nF} \hspace{3cm} \text{Equation 7.15}$$

When n=2 and ν is the stoichiometric coefficient. Under these conditions, the standard half-cell potential, $E^{0,Mg}_{\{hkil\}}$, is lowered from -2.36 V to -2.52 V for $\beta_{\{0001\}}$=60° along α=0° and the additional thermodynamic driving force is 160 mV.

However, this indicates that the reaction occurs more readily. This driving force is not great (~7 % change) for Mg because the oxidation reaction occurs at OCP (such as -1.74 V_{SCE}) far from equilibrium. Thus, the effect of surface energy is rationalized to produce some effect on bare electrodes but it is easily overcome by other factors, such as the role of the oxide.

7.4.4 Corrosion Rates on Mg Bare surfaces

Slight crystallographic orientation dissolution was observed (Figure 7. 5) in exposure environments where the MgO film is dissolved and little of the $Mg(OH)_2$ film is precipitated (Figure 7. 18). The variation in the corrosion rate which crystallographic orientation was different in the buffered, non-chloride environments (Figure 7. 15) with a slight increase in the corrosion rate at $\beta_{\{0001\}}=60°$. This is approximate to what would be expected according to the trend with surface energy (Figure 7. 19(a)). The TRIS and EDTA remove most of the oxide film formed during active corrosion. This would lead to the expected trend of corrosion rate as a function of surface energy with a slight increase in the corrosion rate around $\beta_{\{0001\}}=60°$. It can be assumed that, by completely removing this oxide film, the corrosion rate would better correlate with surface energy. This trend of corrosion rate with surface energy is briefly seen during the initial stages of immersion, particularly in Figure 7. 17(b) after 0 hours where the surface energy dominates more than oxide kinetics due to the bare Mg surface in 0.1 M TRIS. Similarly, comparing surface energy to the i_{corr} after ~0 hours of immersion, the corrosion rate trends slightly with surface energy (Figure 7. 19(c)). However, after longer immersion times, the surface energy characteristics no longer dominate, potentially because the rapid corrosion rates of Mg oversaturate the buffer solution.

7.4.5 Variation in the Corrosion Rate with Crystallographic Orientation: Reflection on Weld Corrosion

It was observed that, in a chloride environment, the basal orientation was most likely to suffer from corrosion attack and propagation. In terms of AZ31B weld corrosion this is particularly important because the wrought base plate and HAZs have a dominant basal {0 0 0 1} texture on the LT surface[20]. From Chapter 2, it was observed that the FZ had a slightly lower corrosion rate than either of the HAZs. Some of this effect may be due to the variation in texture. Less basal orientations in the FZ would mean less corrosion propagation on these non-basal orientations.

7.4 Conclusions

1. EIS derived i_{corr} for isolated grains with specific crystallographic orientations can be acquired by EBSD and masking methods. Due to accurate use of corrosion rate derived from R_p, the corrosion rate can accurately be determined for each of these specified crystallographic orientations to show that the resultant intrinsic corrosion properties are highly anisotropic.

2. Corrosion rate is highly anisotropic for the Mg material system in chloride containing environments. The fastest corrosion rate occurs on the basal plane in NaCl.

3. The film formation is highly dependent on the exposure environment and orientation. A thick precipitated $Mg(OH)_2$ film forms in the alkaline, chloride environments. Meanwhile, this film does not occur as readily in the near neutral pH, non-chloride TRIS and EDTA environments, leading to weak crystallographic orientation dependence.

4. Oxide thickness is strongly dependent on crystallographic orientation in the chloride containing environment, 0.6 M NaCl with the thickest oxide growth on the $(10\bar{1}0)$, and $(11\bar{2}0)$ planes and the thinnest oxide on the (0001) plane.

5. In the non-chloride TRIS and EDTA environments, a slight increase in the corrosion rate was seen at $\beta_{\{0001\}}=60°$ which may more closely correlate with the irrational plate of greatest surface energy. The crystallographic orientation dependence on the corrosion is relatable to the surface energy, but far from equilibrium. However, it does not correlate exactly with surface energy because some $Mg(OH)_2$ film is still formed, according to Raman Spectroscopy.

References

1.   D. Horton, A. Zhu, J. Scully, and M. Neurock, "Crystallographic controlled dissolution and surface faceting in disordered face-centered cubic FePd," MRS Communications 4, 03 (2014): p. 113-119.

2.   K. Fushimi, K. Miyamoto, and H. Konno, "Anisotropic corrosion of iron in pH 1 sulphuric acid," Electrochim Acta 55, 24 (2010): p. 7322-7327.

3.   B.W. Davis, P.J. Moran, and P.M. Natishan, "Metastable pitting behavior of aluminum single crystals," Corros Sci 42, 12 (2000): p. 2187-2192.

4.   M. Yasuda, F. Weinberg, and D. Tromans, "Pitting Corrosion of Al and Al-Cu Single-Crystals," J Electrochem Soc 137, 12 (1990): p. 3708-3715.

5.   H.G. Kim, T.H. Kim, and Y.H. Jeong, "Oxidation characteristics of basal (0 0 0 2) plane and prism (1 1 $\bar{2}$ 0) plane in HCP Zr," Journal of Nuclear Materials 306, 1 (2002): p. 44-53.

6.   R.S. Lillard, G.F. Wang, and M.I. Baskes, "The role of metallic bonding in the crystallographic pitting of magnesium," Journal of the Electrochemical Society 153, 9 (2006): p. B358-B364.

7.   G.M. Treacy and C.B. Breslin, "Electrochemical studies on single-crystal aluminium surfaces," Electrochim Acta 43, 12-13 (1998): p. 1715-1720.

8.   J.A.S. A. Shahryari, and S. Orrianovic, "The influence of crystallographic orientation distribution on 316LVM stainless steel pitting behavior," Corros Sci 51, 677 (2009).

9.   A.S. M.M. Lohrengel, and C. Rosenkranz, "Grain-dependent anodic dissolution of iron," Electochimica Acta 52, 7738 (2007).

10.   N.L. B. Holme, A. Bakken, O. Lunder, J.E. Lein, L. Vines, T. Hauge, and a.K.N. O. Bauger, "Preferential grain etching of AlMgSi(Zn) model alloys," J Electrochem Soc 157, (2010): p. C424.

11.   G.E.T. E.V. Koroleva, P. Skeldon, and B. Noble, "Crystallographic dissolution of high purity aluminium," proceedings of the royal society of london A 463, (2007): p. 1729.

12.   E.V.K. M. Gentile, P. Skeldon, G.E. Thompson, P. Bailey, and T.C. and Q. Noakes, "Influence of grain orientation on zinc enrichment and surface morphology of an Al-Zn alloy," Surf Interface Anal 42, 287 (2010).

13.   B. Holme, N. Ljones, A. Bakken, O. Lunder, J.E. Lein, L. Vines, T. Hauge, O. Bauger, and K. Nisancioglu, "Preferential Grain Etching of AlMgSi(Zn) Model Alloys," J Electrochem Soc 157, 12 (2010): p. C424-C427.

14.   U. Konig and B. Davepon, "Microstructure of polycrystalline Ti and its microelectrochemical properties by means of electron-backscattering diffraction (EBSD)," Electrochimica Acta 47, 1-2 (2001): p. 149-160.

15.   E.V. Koroleva, G.E. Thompson, P. Skeldon, and B. Noble, "Crystallographic dissolution of high purity aluminium," P Roy Soc a-Math Phy 463, 2083 (2007): p. 1729-1748.

16.   A. Schreiber, J.W. Schultze, M.M. Lohrengel, F. Karman, and E. Kalman, "Grain dependent electrochemical investigations on pure iron in acetate buffer pH 6.0," Electrochim Acta 51, 13 (2006): p. 2625-2630.

17.   A. Shahryari, J.A. Szpunar, and S. Orrianovic, "The influence of crystallographic orientation distribution on 316LVM stainless steel pitting behavior," Corros Sci 51, 3 (2009): p. 677-682.

18.   A.D. King, N. Birbilis, and J.R. Scully, "Accurate Electrochemical Measurement of Magnesium Corrosion Rates; a Combined Impedance, Mass-Loss and Hydrogen Collection Study," Electrochim Acta 121, 1 (2014): p. 394-406.

19.   L.G. Bland, A.D. King, N. Birbilis, and J.R. Scully, "Assessing the Corrosion of Commercially Pure Magnesium and Commercial AZ31B by Electrochemical Impedance, Mass-loss, Hydrogen Collection and ICP-OES Solution Analysis," Corrosion Journal 71, 2 [Special Issue] (2015): p. 128-145.

20.   L.G. Bland, J.M. Fitz-Gerald, and J.R. Scully, "Metallurgical and Electrochemical Characterization of the Corrosion of AZ31B-H24 Tungsten Inert Gas Weld: Isolated Weld Zones," Corrosion Journal 72, 9 (2016): p. 1116-1132.

21.   G.-L. Song and Z. Xu, "Crystal orientation and electrochemical corrosion of polycrystalline Mg," Corros Sci 63, (2012): p. 100-112.

22.   M. Liu, D. Qiu, M.-C. Zhao, G. Song, and A. Atrens, "The effect of crystallographic orientation on the active corrosion of pure magnesium," Scripta Mater 58, 5 (2008): p. 421-424.

23.   P. Schmutz, V. Guillaumin, R.S. Lillard, J.A. Lillard, and G.S. Frankel, "Influence of Dichromate Ions on Corrosion Processes on Pure Magnesium," J Electrochem Soc 150, 4 (2003): p. B99-B110.

24.   M.A.H. C.R. McCall, R.S. Lillard, "Crystallographic pitting in magnesium single crystals," Corros Eng Sci Techn 40, 4 (2005): p. 337-343.

25.   G.L. Song and Z. Xu, "Effect of microstructure evolution on corrosion of different crystal surfaces of AZ31 Mg alloy in a chloride containing solution," Corros Sci 54, 0 (2012): p. 97-105.

26.   B.Q. Fu, W. Liu, and Z.L. Li, "Calculation of the surface energy of hcp-metals with the empirical electron theory," Appl Surf Sci 255, 23 (2009): p. 9348-9357.

27.   M. Taheri and J.R. Kish, "Nature of Surface Film Formed on Mg Exposed to 1 M NaOH," J Electrochem Soc 160, 1 (2013): p. C36-C41.

28.   D.A. Vermilyea and C.F. Kirk, "Studies of Inhibition of Magnesium Corrosion," J Electrochem Soc 116, 11 (1969): p. 1487-1492.

29.   E. Gulbrandsen, J. Taftø, and A. Olsen, "The passive behaviour of Mg in alkaline fluoride solutions. Electrochemical and electron microscopical investigations," Corros Sci 34, 9 (1993): p. 1423-1440.

30.   W.A. Badawy, N.H. Hilal, M. El-Rabiee, and H. Nady, "Electrochemical behavior of Mg and some Mg alloys in aqueous solutions of different pH," Electrochim Acta 55, 6 (2010): p. 1880-1887.

31.   J.H. Nordlien, S. Ono, and N. Masuko, "Morphology and Structure of Oxide Films Formed on Magnesium by Exposure to Air and Water," J Electrochem Soc 142, 10 (1995): p. 3320-3322.

32.   Y. Zhu, G. Wu, Y.H. Zhang, and Q. Zhao, "Growth and characterization of Mg(OH)2 film on magnesium alloy AZ31," Appl Surf Sci 257, 14 (2011): p. 6129-6137.

33.   M. Taheri, R.C. Phillips, J.R. Kish, and G.A. Botton, "Analysis of the surface film formed on Mg by exposure to water using a FIB cross-section and STEM–EDS," Corros Sci 59, 0 (2012): p. 222-228.

34.   H.B. Yao, Y. Li, and A.T.S. Wee, "An XPS investigation of the oxidation/corrosion of melt-spun Mg," Appl Surf Sci 158, 1–2 (2000): p. 112-119.

35.   S. Feliu, C. Maffiotte, A. Samaniego, J.C. Galvan, and V. Barranco, "Effect of the chemistry and structure of the native oxide surface film on the corrosion properties of commercial AZ31 and AZ61 alloys," Appl Surf Sci 257, 20 (2011): p. 8558-8568.

36.   S. Feliu, J.C. Galván, A. Pardo, M.C. Merino, and R. Arrabal, "Native Air-Formed Oxide Film and its Effect on Magnesium Alloys Corrosion," Corrosion Journal 3, 80-91 (2010).

37.   R.C. Phillips and J.R. Kish, "Nature of Surface Film on Matrix Phase of Mg Alloy AZ80 Formed in Water," Corrosion 69, 8 (2013): p. 813-820.

38.   K. Nisancioglu, "Morphology and Structure of Oxide Films Form on Magnesium by Exposure to Air and Water," J Electrochem Soc 142, 10 (1995).

39.   B. McNally. Crystallographic Orientation Dependence of Film Formation on Corrosion Magnesium. in Corrosion. 2014. San Antonio, TX.

40.   U. König and B. Davepon, "Microstructure of polycrystalline Ti and its microelectrochemical properties by means of electron-backscattering diffraction (EBSD)," Electrochimica Acta 47, 1–2 (2001): p. 149-160.

41.   M. Curioni, F. Scenini, T. Monetta, and F. Bellucci, "Correlation between electrochemical impedance measurements and corrosion rate of magnesium investigated by real-time hydrogen measurement and optical imaging," Electrochim Acta 166, (2015): p. 372-384.

42.   P. Jakupi, D. Zagidulin, J.J. Noël, and D.W. Shoesmith, "The impedance properties of the oxide film on the Ni–Cr–Mo Alloy-22 in neutral concentrated sodium chloride solution," Electrochim Acta 56, 17 (2011): p. 6251-6259.

43.   J. Bessone, C. Mayer, K. Jüttner, and W.J. Lorenz, "AC-impedance measurements on aluminium barrier type oxide films," Electrochim Acta 28, 2 (1983): p. 171-175.

44.   J.B. Bessone, D.R. Salinas, C.E. Mayer, M. Ebert, and W.J. Lorenz, "An EIS study of aluminium barrier-type oxide films formed in different media," Electrochim Acta 37, 12 (1992): p. 2283-2290.

45.   M. Danaie, R.M. Asmussen, P. Jakupi, D.W. Shoesmith, and G.A. Botton, "The cathodic behaviour of Al–Mn precipitates during atmospheric and saline aqueous corrosion of a sand-cast AM50 alloy," Corros Sci 83, (2014): p. 299-309.

46.   "AZtecEnergy: EDS Software," Oxford Instruments (2015).

47.   L.G. Bland, B.C.R. Troconis, R.J.S. Jr., J.M. Fitz-Gerald, and J.R. Scully, "Metallurgical and Electrochemical Characterization of the Corrosion of Mg-Al-Zn Alloy AZ31B-H24 Tungsten Inert Gas Weld: Galvanic Corrosion Between Weld Zones " Corrosion Journal in press (DOI: 10.5006/2078), (2016).

48.   C.A. Schneider, W.S. Rasband, and K.W. Eliceiri, "NIH Image to ImageJ: 25 years of image analysis," Nature Methods 9, (2012): p. 671-675.

49.   D. Surf, *MountianMaps*. 2016.

50.   H.J. Bunge, Texture analysis in materials science : mathematical methods. 1982.

51.   J.C.Haung, Y.N. Wang, "texture analysis in hexagonal materials," Mater Chem Phys 81, (2003): p. 11-26.

52.   D.W. Hogan and D.J. Dyson, "Angles between planes in the hexagonal and tetragonal crystal systems," Micron (1969) 2, 1 (1970): p. 59-61.

53.   S. Associates, *ZView*.

54.   A.H. Carl H. Hamann, Wolf Vielstich, Electrochemistry, 2nd, Completely Revised and Updated Edition. 2nd ed, 2007.

55.   F. Mansfeld, "Electrochemical impedance spectroscopy (EIS) as a new tool for investigating methods of corrosion protection," Electrochim Acta 35, 10 (1990): p. 1533-1544.

56.   B. Hirschorn, M.E. Orazem, B. Tribollet, V. Vivier, I. Frateur, and M. Musiani, "Constant-Phase-Element Behavior Caused by Resistivity Distributions in Films II. Aplications," J Electrochem Soc 157, 12 (2010): p. C458-C463.

57.	B. Hirschorn, M.E. Orazem, B. Tribollet, V. Vivier, I. Frateur, and M. Musiani, "Constant-Phase-Element Behavior Caused by Resistivity Distributions in Films I. Theory," J Electrochem Soc 157, 12 (2010): p. C452-C457.

58.	C.H. Hsu and F. Manfeld, "Technical Note: Concerning the Conversion of the Constant Phase Element Parameter Y_0 into a Capacitance," Corrosion 57, 9 (2001).

59.	G. Williams, H. ap Llwyd Dafydd, and R. Grace, "The localised corrosion of Mg alloy AZ31 in chloride containing electrolyte studied by a scanning vibrating electrode technique," Electrochim Acta 109, 0 (2013): p. 489-501.

60.	G. Williams, N. Birbilis, and H.N. McMurray, "The source of hydrogen evolved from a magnesium anode," Electrochemistry Communications 36, 0 (2013): p. 1-5.

61.	M. Pourbaix, Atlas of electrochemical equilibria in aqueous solutions (Huston, TX: National Association of Corrosion Engineers, 1974.

62.	A. Samaniego, I. Llorente, and S. Feliu Jr, "Combined effect of composition and surface condition on corrosion behaviour of magnesium alloys AZ31 and AZ61," Corros Sci 68, (2013): p. 66-71.

63.	G. Williams and R. Grace, "Chloride-induced filiform corrosion of organic-coated magnesium," Electrochim Acta 56, 4 (2011): p. 1894-1903.

64.	Z.P. Cano, M. Danaie, J.R. Kish, J.R. McDermid, G.A. Botton, and G. Williams, "Physical Characterization of Cathodically-Activated Corrosion Filaments on Magnesium Alloy AZ31B," Corrosion 71, 2 (2015): p. 146-159.

65.	Z.P. Cano, J.R. McDermid, and J.R. Kish, "Cathodic Activity of Corrosion Filaments Formed on Mg Alloy AM30," J Electrochem Soc 162, 14 (2015): p. C732-C740.

66.	G. Williams and H.N. McMurray, "Localized Corrosion of Magnesium in Chloride-Containing Electrolyte Studied by a Scanning Vibrating ElectrodeTechnique," J Electrochem Soc 155, 7 (2008): p. C340-C349.

67.	N. Birbilis, T. Cain, J.S. Laird, X. Xia, J.R. Scully, and A.E. Hughes, "Nuclear Microprobe Analysis for Determination of Element Enrichment Following Magnesium Dissolution," J Electrochem Soc 4, 10 (2015): p. C34-C37.

68.	T. Cain, S.B. Madden, N. Birbilis, and J.R. Scully, "Evidence of the Enrichment of Transition Metal Elements on Corroding Magnesium Surfaces Using Rutherford Backscattering Spectrometry," J Electrochem Soc 162, 6 (2015): p. C228-C237.

69.	L.G. Bland, J.J. Bhattacharyya, S.R. Agnew, J.M. Fitz-Gerald, and J.R. Scully, "Effect of Al-Mn and Al-Mn-Fe Intermetallic Particle Size and Distribution on the Corrosion of Mg-3Al-1Zn alloy: AZ31," Acta Mater In Review, (2016).

70.	L.G. Bland, N. Birbilis, and J.R. Scully, "Exploring the Effects of Intermetallic Particle Size and Spacing on the Corrosion of Mg-Al Alloys Using Model Electrodes," J Electrochem Soc In Review, (2016).

71.	G.S. Frankel, A. Samaniego, and N. Birbilis, "Evolution of hydrogen at dissolving magnesium surfaces," Corros Sci 70, (2013): p. 104-111.

72.	N. Birbilis, A.D. King, S. Thomas, G.S. Frankel, and J.R. Scully, "Evidence for enhanced catalytic activity of magnesium arising from anodic dissolution," Electrochim Acta 132, 0 (2014): p. 277-283.

73.	G. Song, A. Atrens, D. St John, X. Wu, and J. Nairn, "The anodic dissolution of magnesium in chloride and sulphate solutions," Corros Sci 39, 10-11 (1997): p. 1981-2004.

74.   G. Baril, C. Blanc, M. Keddam, and N. Pebere, "Local electrochemical impedance spectroscopy applied to the corrosion behavior of an AZ91 magnesium alloy," J Electrochem Soc 150, 10 (2003): p. B488-B493.

75.   G. Baril, C. Blanc, and N. Pebere, "AC impedance spectroscopy in characterizing time-dependent corrosion of AZ91 and AM50 magnesium alloys - Characterization with respect to their microstructures," J Electrochem Soc 148, 12 (2001): p. B489-B496.

76.   G. Baril, G. Galicia, C. Deslouis, N. Pebere, B. Tribollet, and V. Vivier, "An impedance investigation of the mechanism of pure magnesium corrosion in sodium sulfate solutions," J Electrochem Soc 154, 2 (2007): p. C108-C113.

77.   G. Baril and N. Pebere, "The corrosion of pure magnesium in aerated and deaerated sodium sulphate solutions," Corros Sci 43, 3 (2001): p. 471-484.

78.   I. Nakatsugawa, R. Martin, and E.J. Knystautas, "Improving Corrosion Resistance of AZ91D Magnesium Alloy by Nitrogen Ion Implantation," Corrosion 52, 12 (1996): p. 921-926.

79.   Y.C. Xin, C.L. Liu, W.J. Zhang, J. Jiang, T.Y. Guoyi, X.B. Tian, and P.K. Chua, "Electrochemical behavior Al2O3/Al coated surgical AZ91 magnesium alloy in simulated body fluids," J Electrochem Soc 155, 5 (2008): p. C178-C182.

80.   A.M. Fekry and M.A. Ameer, "Electrochemistry and impedance studies on titanium and magnesium alloys in Ringer's solution," International Journal of Electrochemical Science 6, 5 (2011): p. 1342-1354.

81.   B. Hirschorn, M.E. Orazem, B. Tribollet, V. Vivier, I. Frateur, and M. Musiani, "Determination of effective capacitance and film thickness from constant-phase-element parameters," Electrochim Acta 55, 21 (2010): p. 6218-6227.

82.   F. Czerwinski, "Oxidation Characteristics of Magnesium Alloys," Jom-Us 64, 12 (2012): p. 1477-1483.

83.   M.M. Avedesian and H. Baker, "Magnesium and Magnesium Alloys," ASM International (1999).

84.   J.P. Pemsler, "Diffusion of Oxygen in Zirconium and Its Relation to Oxidation and Corrosion," J Electrochem Soc 105, 6 (1958): p. 315-322.

85.   J.M. Zhang, D.D. Want, and K.W. Xu, "Calculation of the surface energy of hcp metals by using the modified embedded atom method," Appl Surf Sci 253, (2006): p. 2018-2024.

86.   F. Cao, Z. Shi, J. Hofstetter, P.J. Uggowitzer, G. Song, M. Liu, and A. Atrens, "Corrosion of ultra-high-purity Mg in 3.5% NaCl solution saturated with Mg(OH)2," Corros Sci 75, (2013): p. 78-99.

87.   Z. Shi, F. Cao, G.L. Song, M. Liu, and A. Atrens, "Corrosion behaviour in salt spray and in 3.5% NaCl solution saturated with Mg(OH)2 of as-cast and solution heat-treated binary Mg–RE alloys: RE=Ce, La, Nd, Y, Gd," Corros Sci 76, 0 (2013): p. 98-118.
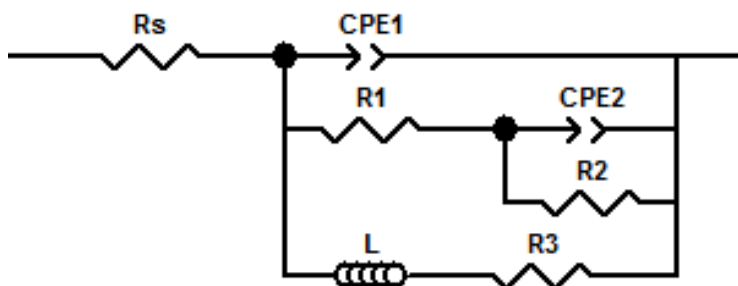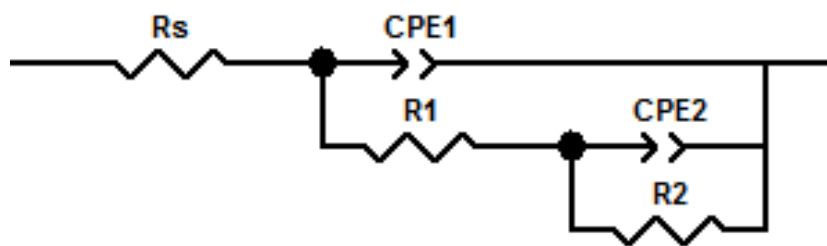
Figure 7. 1. (a) Electrical equivalent circuit diagram used to model pseudo-inductive electrochemical impedance response on corroding Mg in 0.6 M NaCl solution and (b) the equivalent circuit diagram used to determine the oxide thickness in 0.1 M TRIS and EDTA. Constant phase elements were modeled using ideal capacitors when α was within 10% of 1.

a)
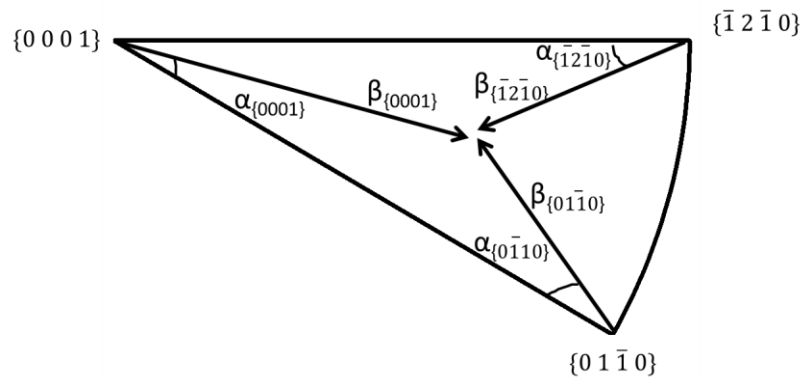
b)
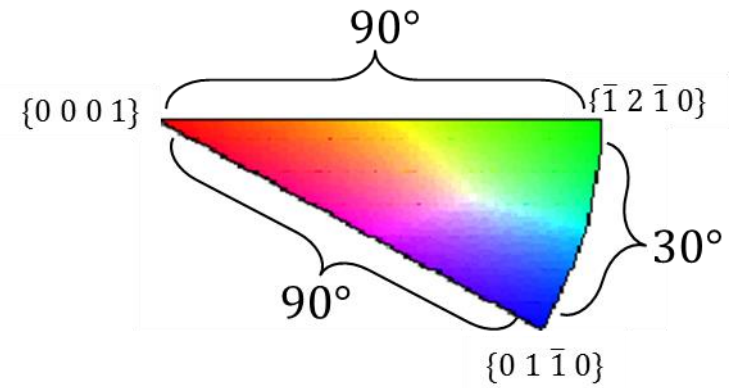
Figure 7. 2. Schematic representation of {hkil} positions defined by the angular distance, β_i, from the 3 common low index hexagonal planes: {**0001**}, {**01$\bar{1}$0**} and {**$\bar{1}$2$\bar{1}$0**}. α_i represents the angle between β_i and the edge of the stereographic triangle is defined by the {**0001**} and {**01$\bar{1}$0**} poles for $\alpha_{\{0001\}}$ and $\alpha_{\{01\bar{1}0\}}$ and between the {**0001**} and {**$\bar{1}$2$\bar{1}$0**} poles for $\alpha_{\{0001\}}$ and $\alpha_{\{\bar{1}2\bar{1}0\}}$.

a)
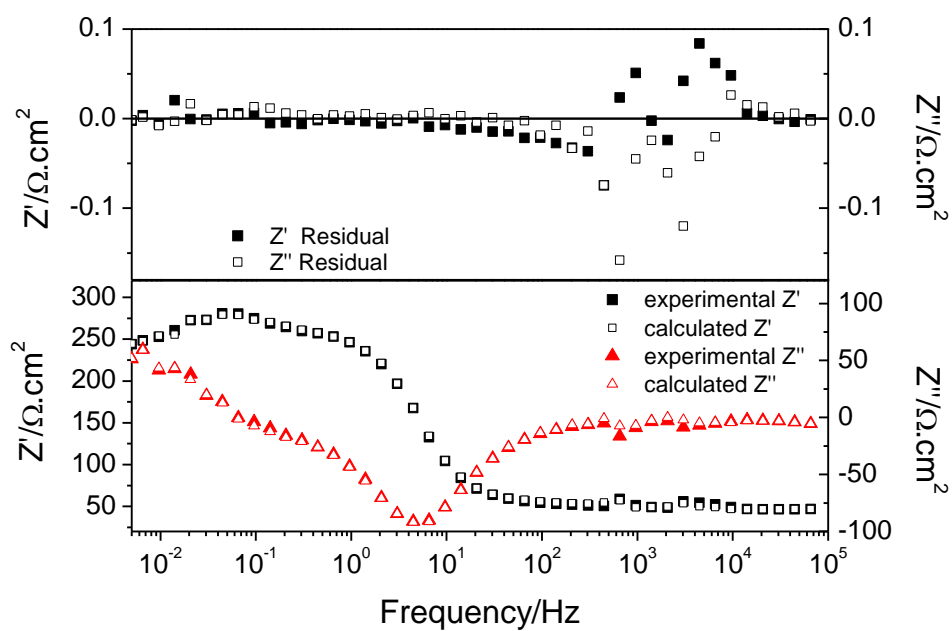
b)
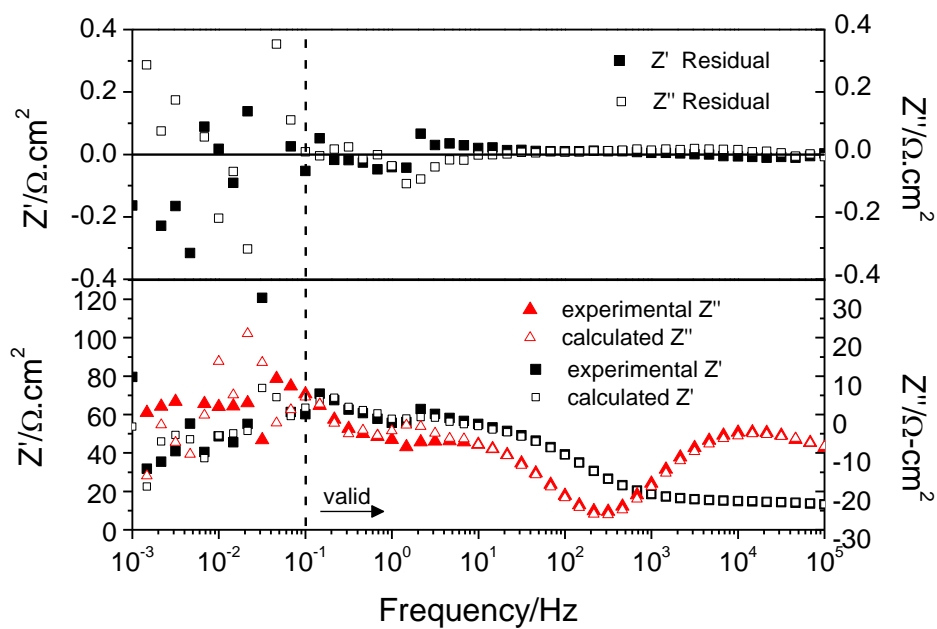
c)
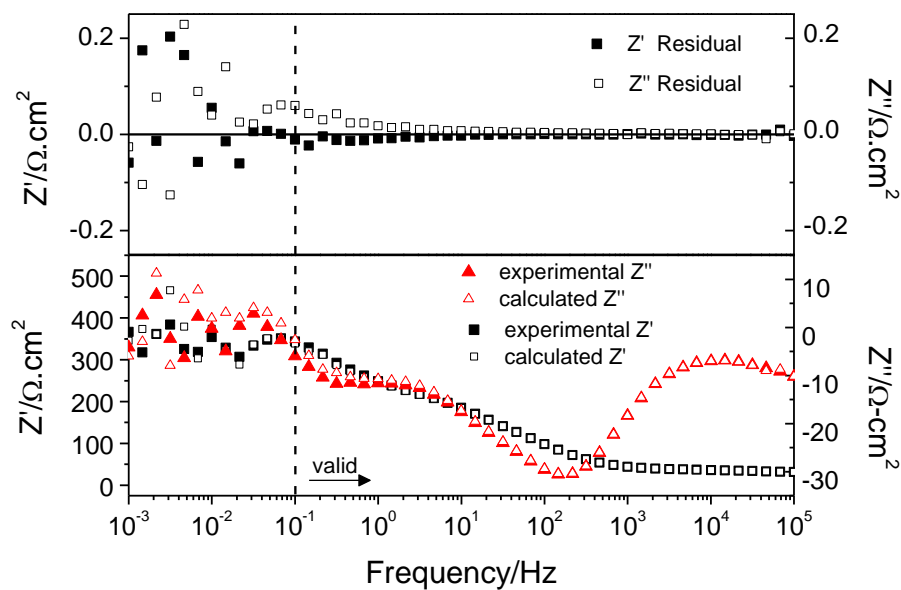
Figure 7. 3. Typical Kramers-Kronig transforms of the real and imaginary components of the impedance of high purity Mg after 24 h immersion in (a) 0.6 M NaCl, (b) 0.1 M EDTA and (c) 0.1 M TRIS.
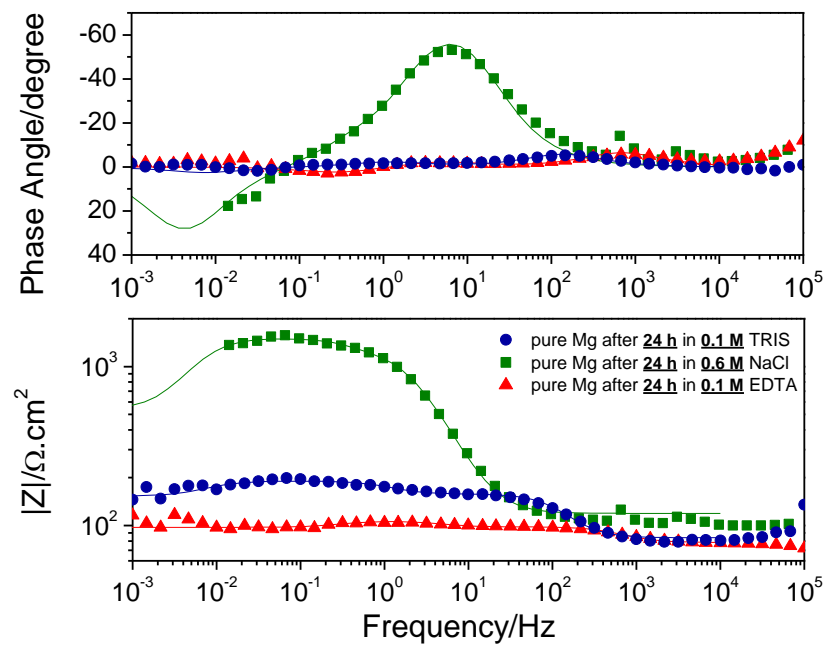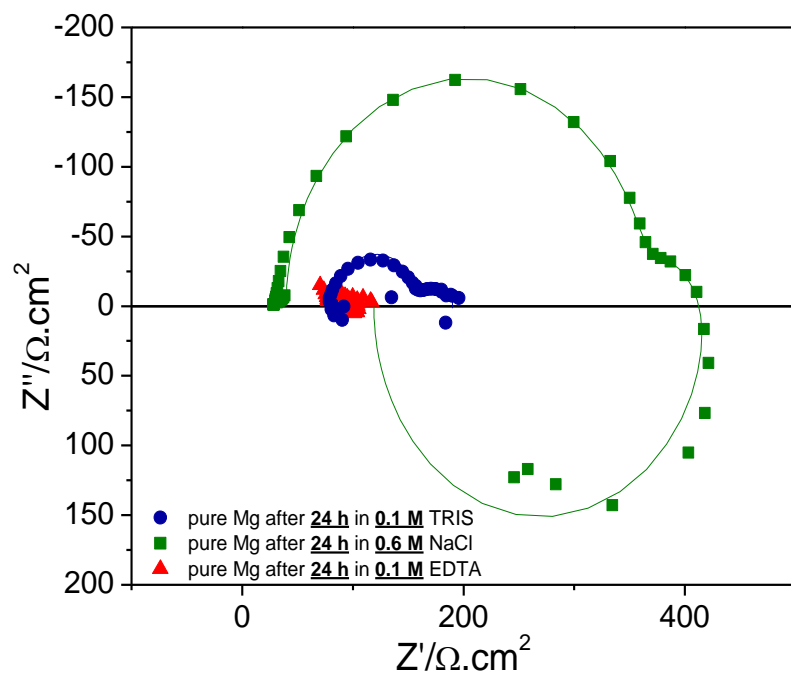
Figure 7. 4. (left) Nyquist plots and (right) Bode magnitude and phase plot for pure polycrystalline Mg. Data shown along with respective fits following 24 h immersion in 0.6 M NaCl, 0.1 M TRIS and 0.1 M EDTA at open circuit.
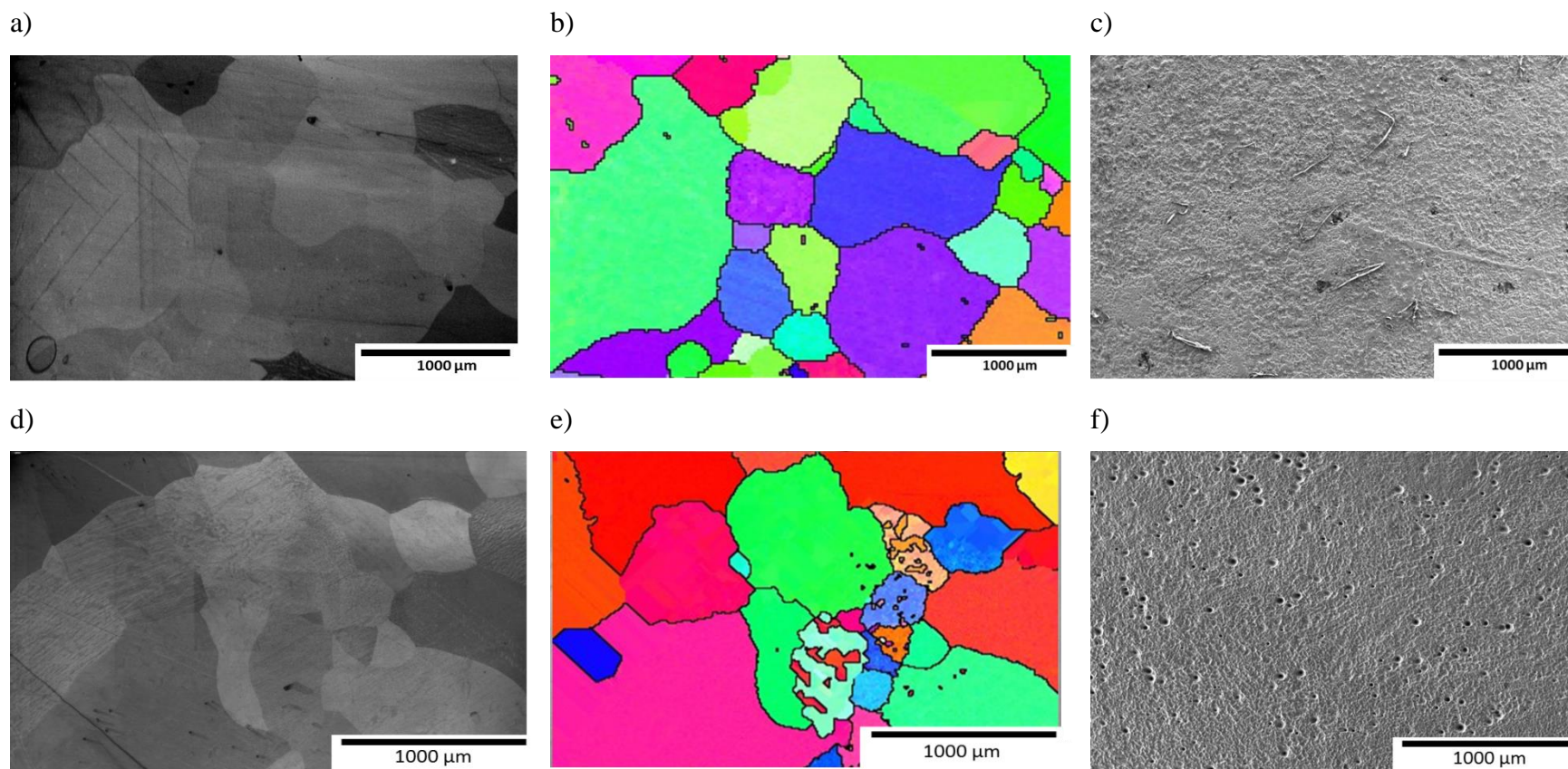
Figure 7. 5. Secondary electron micrographs of (a) commercially pure Mg before exposure, (b) commercially pure Mg EBSD before exposure , (c) commercially pure Mg after exposure in 0.1 M TRIS, (d) pure Mg before exposure, (e) commercially pure Mg EBSD before exposure , (f) commercially pure Mg after exposure in 0.1 M EDTA.
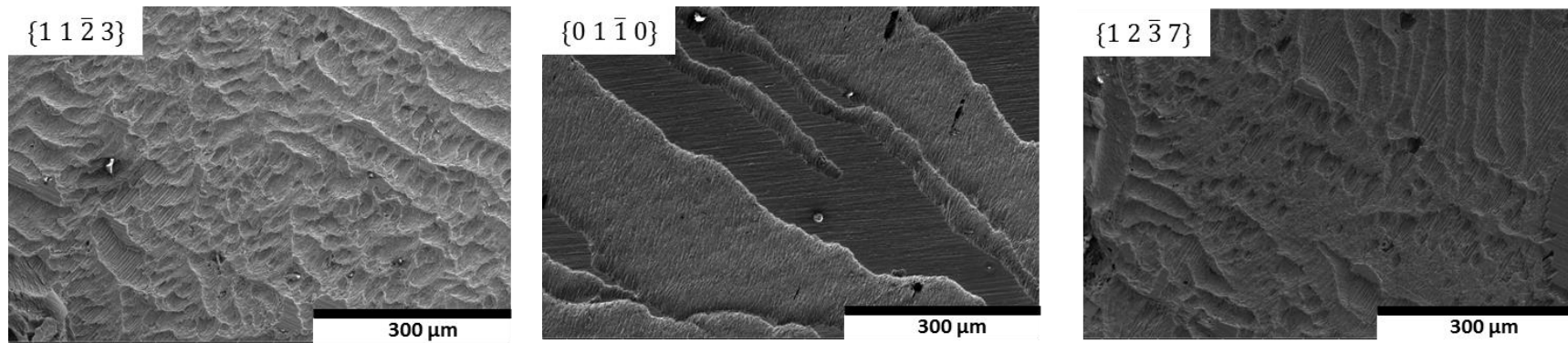
Figure 7. 6. Various grain facets with the indicated crystallographic orientations showing various corrosion morphologies after 12 hours of immersion in 0.6 M NaCl. Samples were cleaned of oxides with CrO$_3$ before imaging.

a)
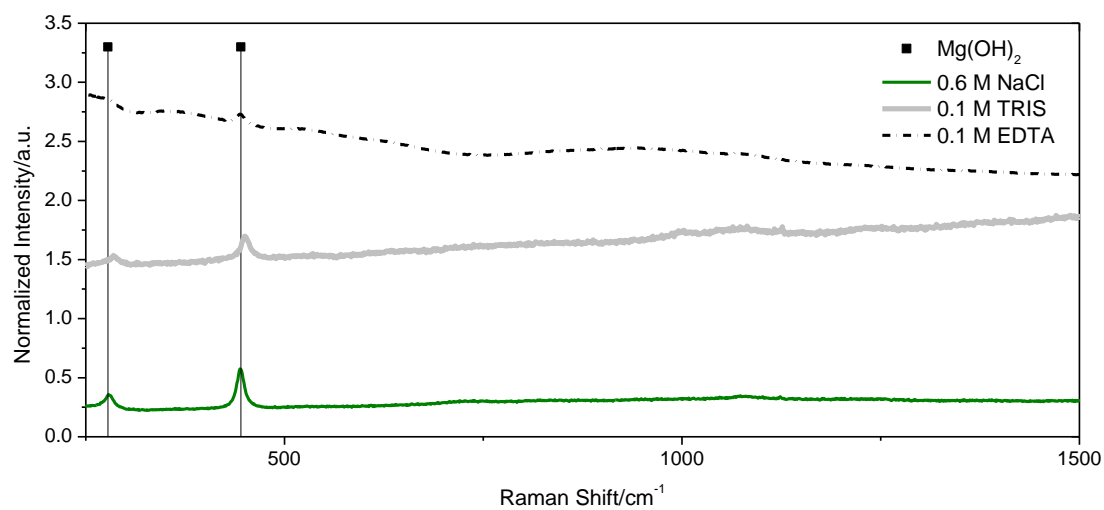
Figure 7. 7. Raman spectrum of oxide growth on commercially pure Mg after 24 h at OCP in 0.6 M NaCl, 0.1 M TRIS and 0.1 M EDTA. Characteristic Raman spectrum lines for $Mg(OH)_2$ oxide formation are shown according to Raman Standard RRUFF ID: R040077.
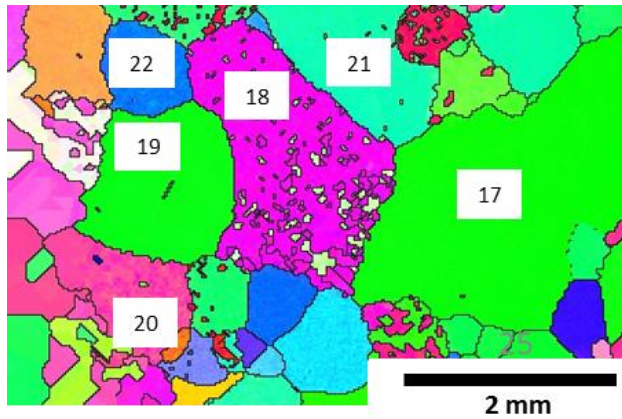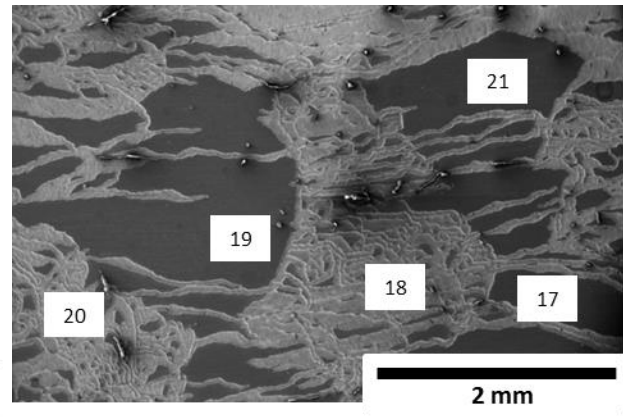
Figure 7. 8. (a) EBSD map of polycrystalline commercially pure Mg and (b) corresponding secondary SEM micrograph showing the marked, specified grains after exposure after 3 h immersion at OCP in 0.6 M NaCl and cleaned with CrO_3 to remove any oxides. The color refers to the IPF in Figure 7.1.
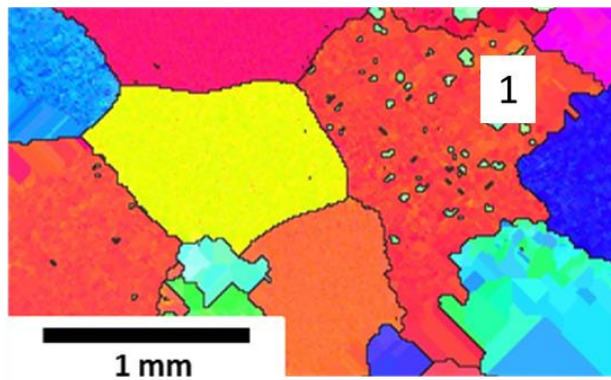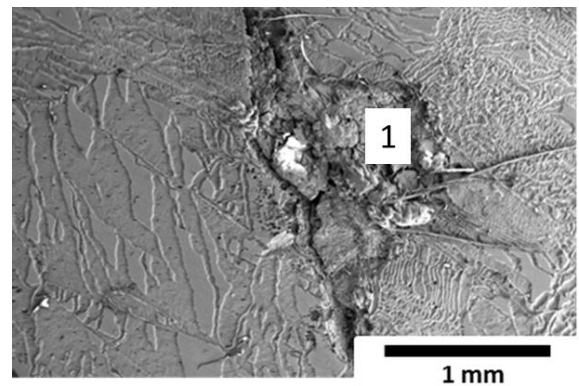
Figure 7. 9. (a) EBSD map showing strongly oriented basal grain and (b) secondary SEM micrograph showing preferential dissolution of the basal oriented grain after exposure after 3 h immersion at OCP in 0.6 M NaCl and cleaned with CrO_3 to remove any oxides. The color refers to the IPF in Figure 7.1.
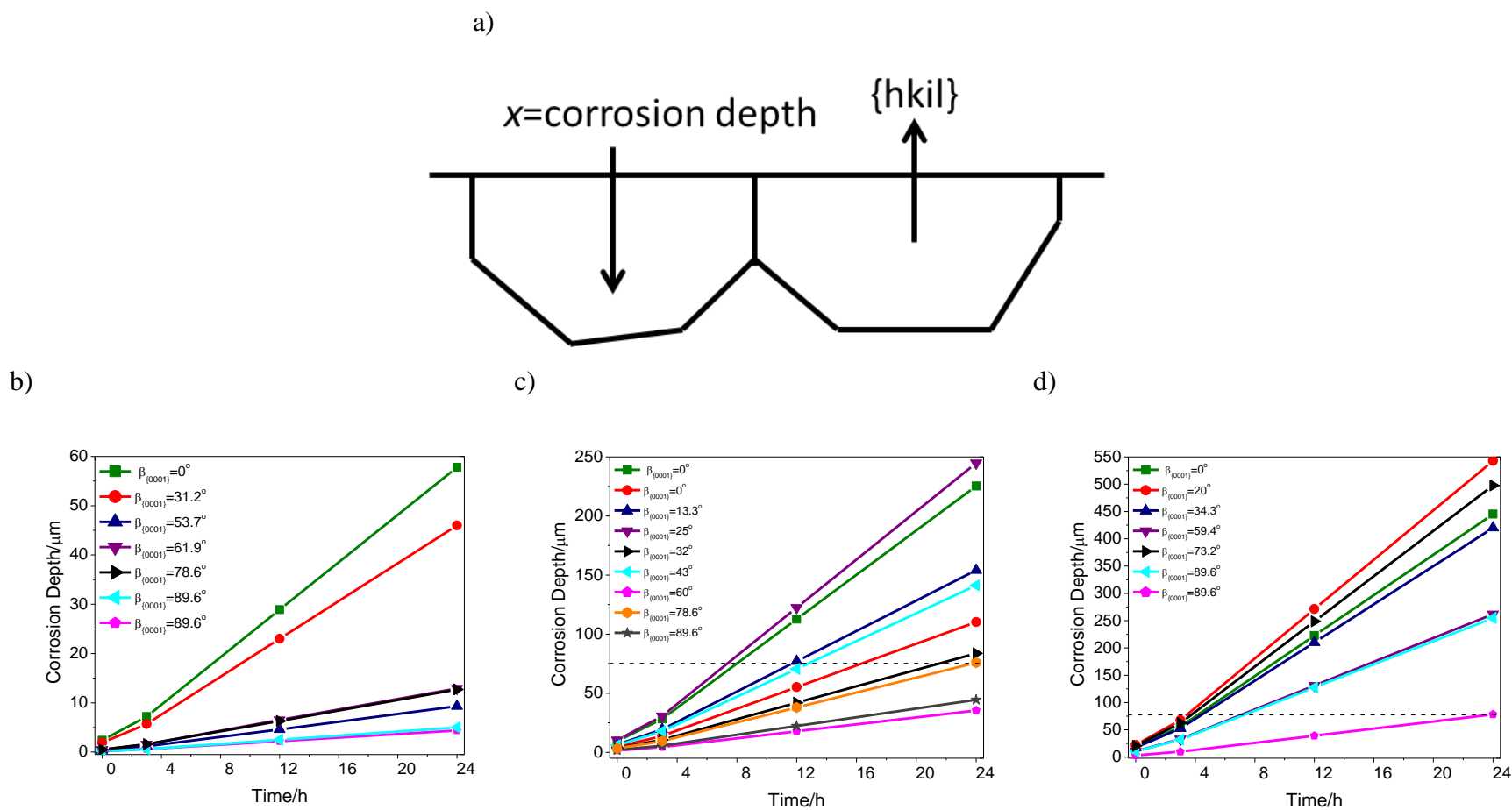
Figure 7. 10. (a) Schematic of corrosion penetration depth assuming uniform corrosion for isolated grains as calculated from EIS determined i_{corr} as a function of the $\beta_{\{0001\}}$ angle in (b) 0.6 M NaCl, (c) 0.1 M TRIS and (d) 0.1 M EDTA at OCP over a 24 h immersion. The dashed line indicates the half grain diameter.

267
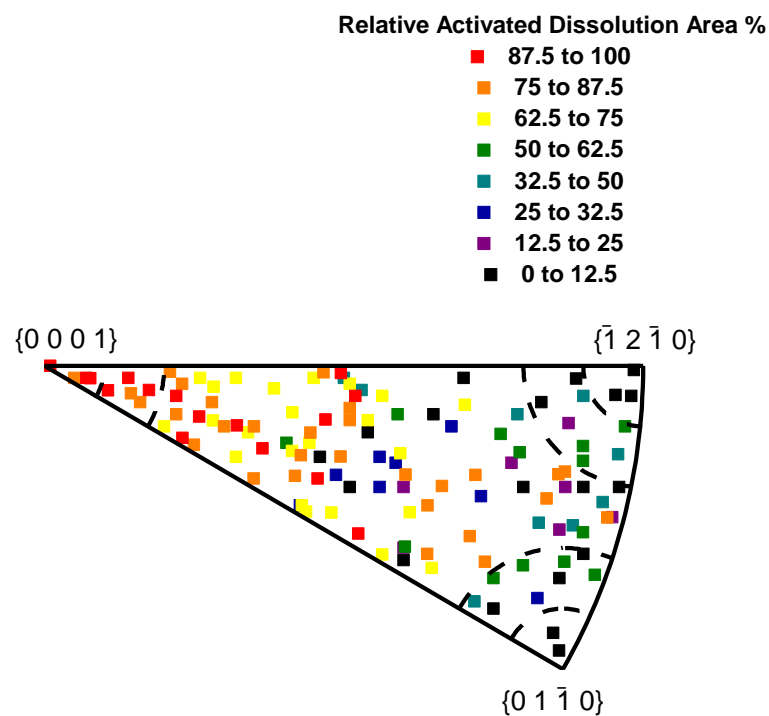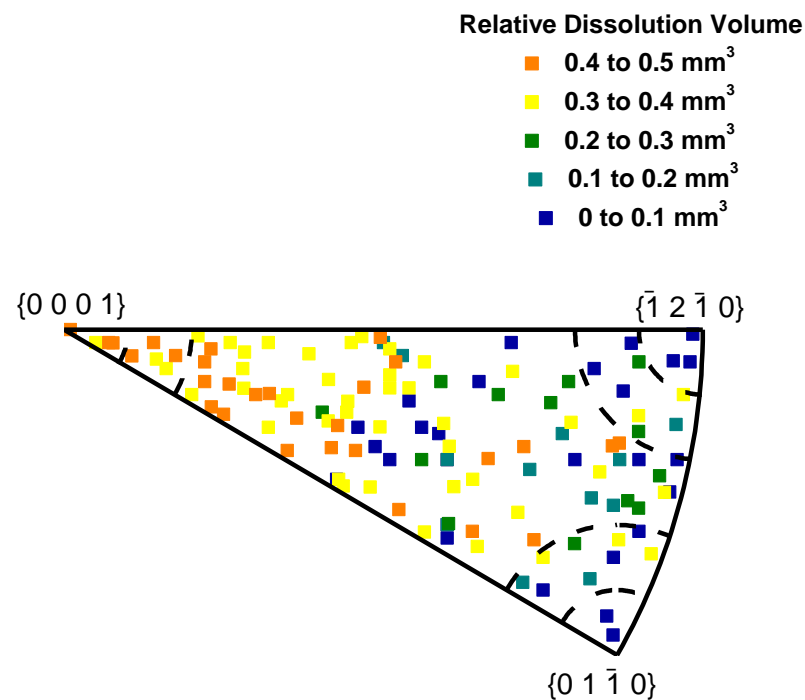
Figure 7. 11. (a) Percent of cathodically activated black dissolution area within individual corroded for grains with the indicated orientation after 24 h at OCP for individual grains in 0.6 M NaCl as determined through ImageJ[TM]. (b) Relative dissolution volume corroded after 24 h at OCP for individual grains in 0.6 M NaCl as determined through Hirox optical microscopy.
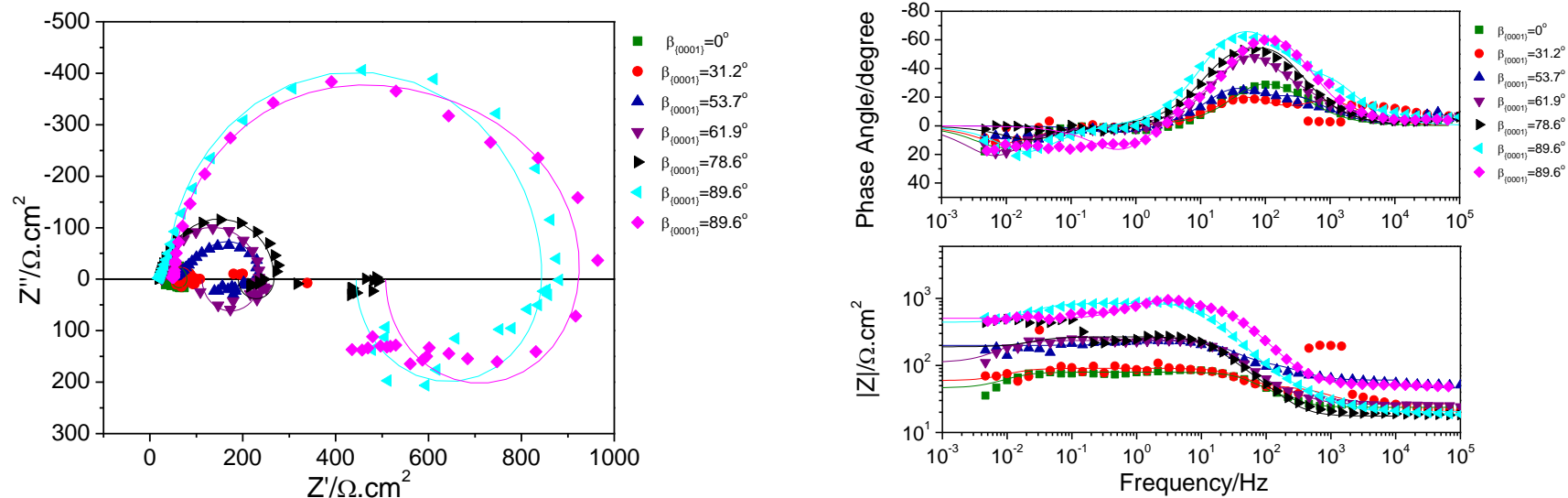
Figure 7. 12. (left) Nyquist plots and (right) Bode magnitude and phase plot for isolated grains with different crystallographic orientations. Data shown along with respective fits following 24 h immersion in 0.6 M NaCl at open circuit.
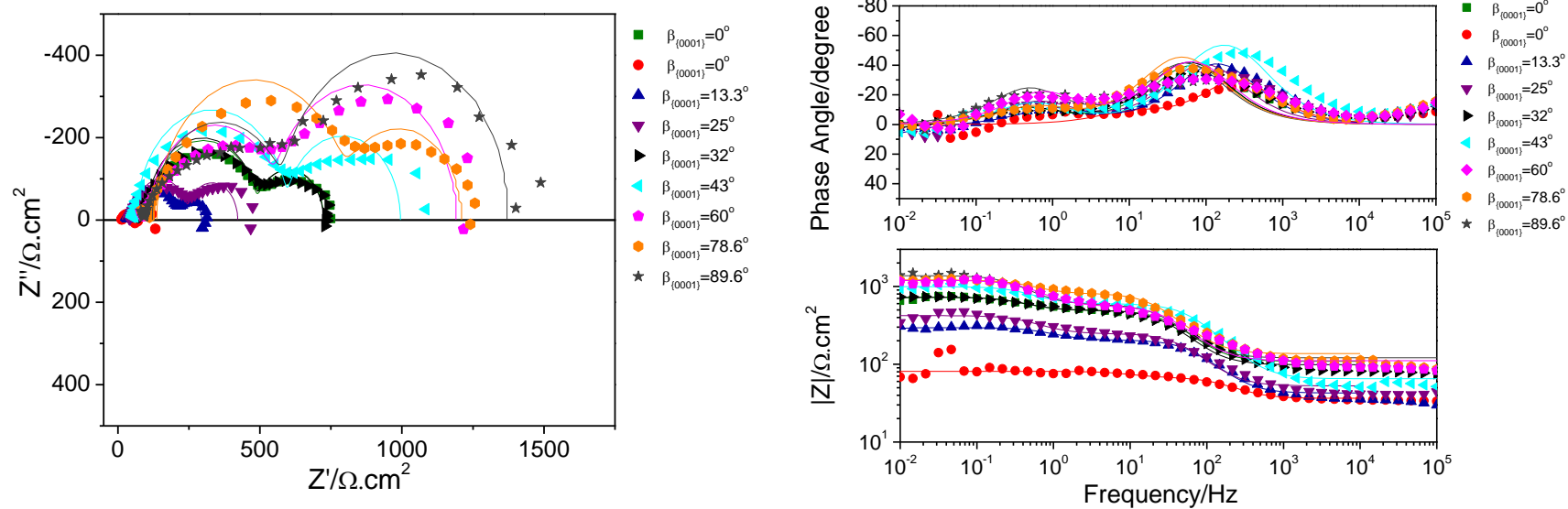
Figure 7. 13. (left) Nyquist plots and (right) Bode magnitude and phase plot for isolated grains with different crystallographic orientations. Data shown along with respective fits following 24 h immersion in 0.1 M TRIS at open circuit. Invalid data points are taken out.
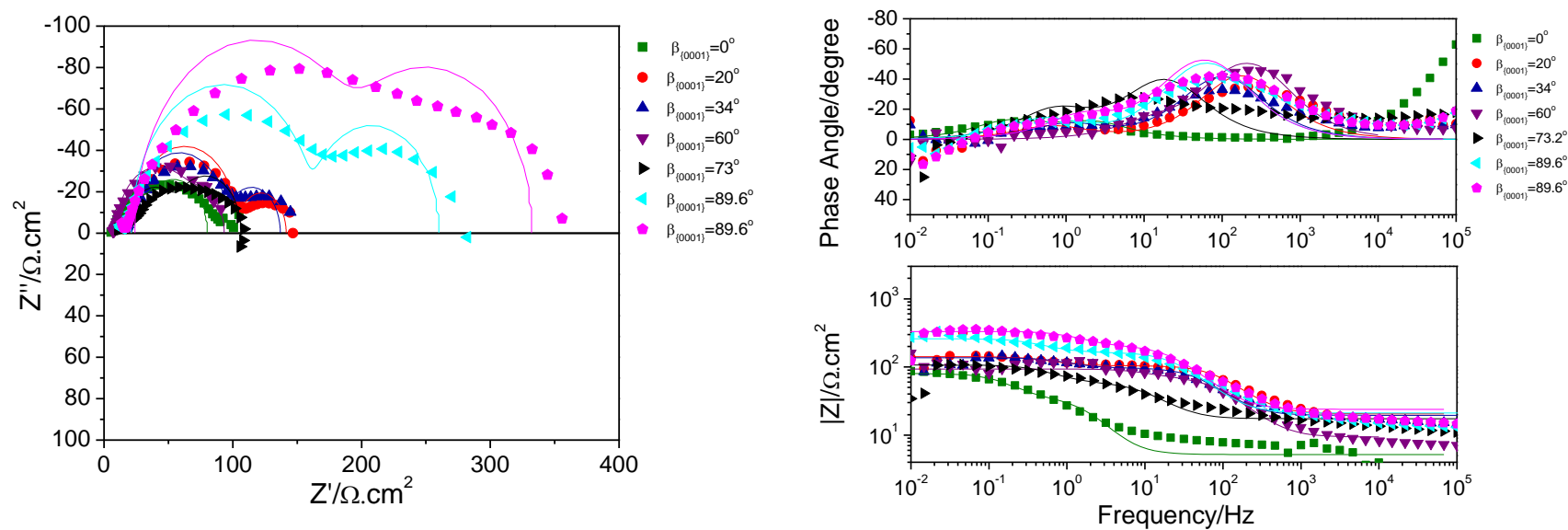
Figure 7. 14. (left) Nyquist plots and (right) Bode magnitude and phase plot for isolated grains with different crystallographic orientations. Data shown along with respective fits following 24 h immersion in 0.1 M EDTA at open circuit. Invalid data points are taken out.
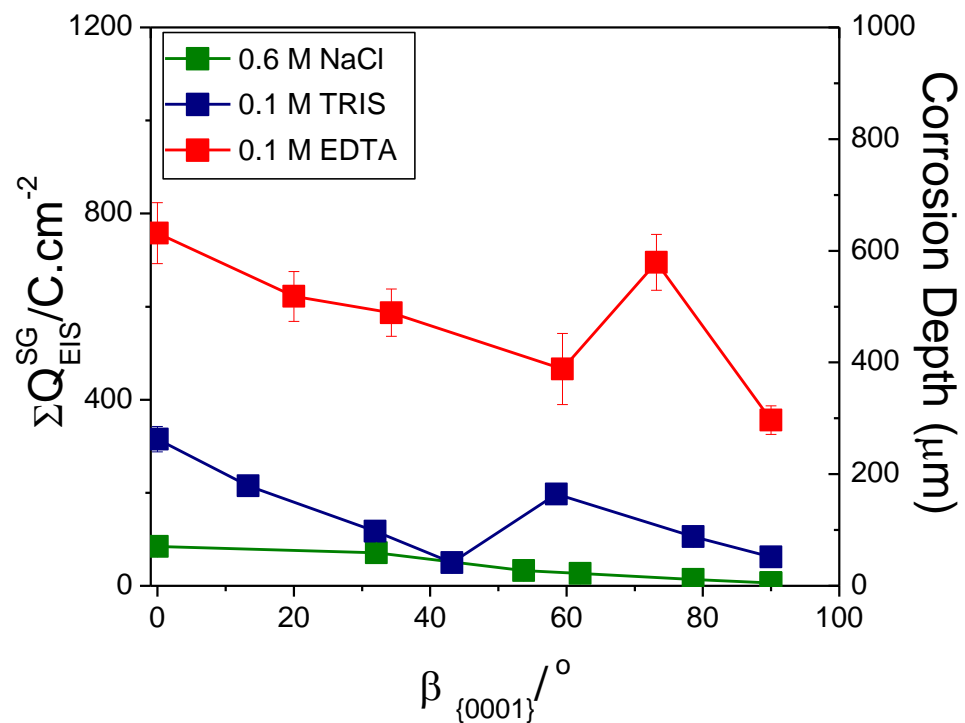
Figure 7. 15. Variation in the electrochemical impedance spectroscopy derived corrosion rate as determined at OCP in 0.6 M NaCl, 0.1 M TRIS and 0.1 M EDTA over 24 hours as a function of $\beta_{\{0001\}}$. Error bars show the deiation between the EIS determined corrosion rate with various Tafel assumptions [18,19,86,87].
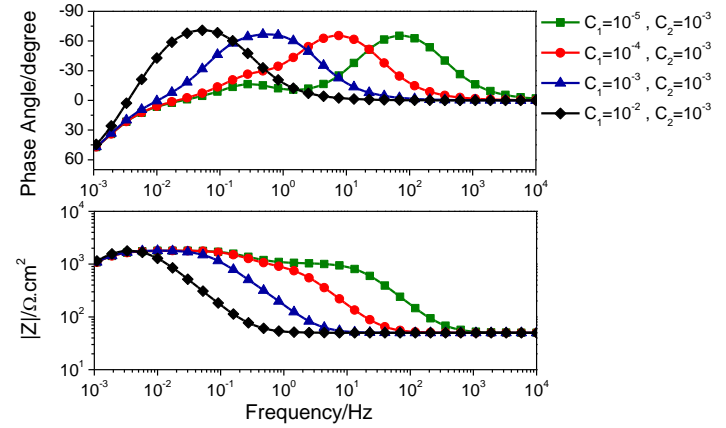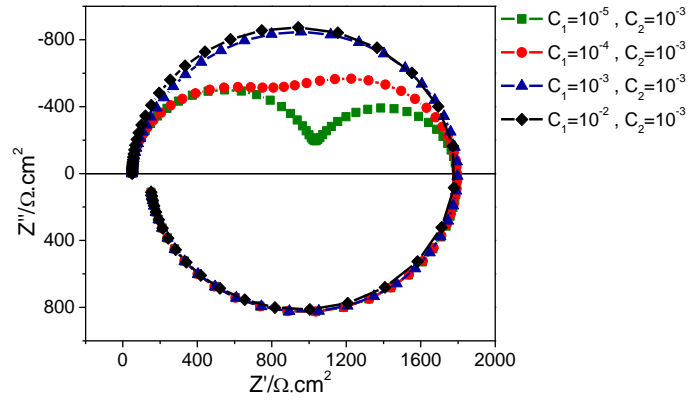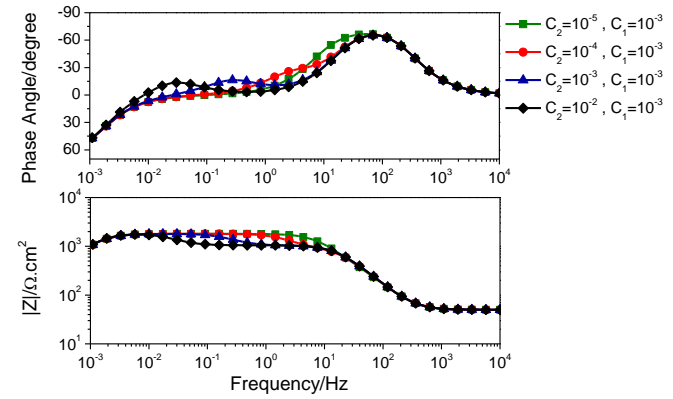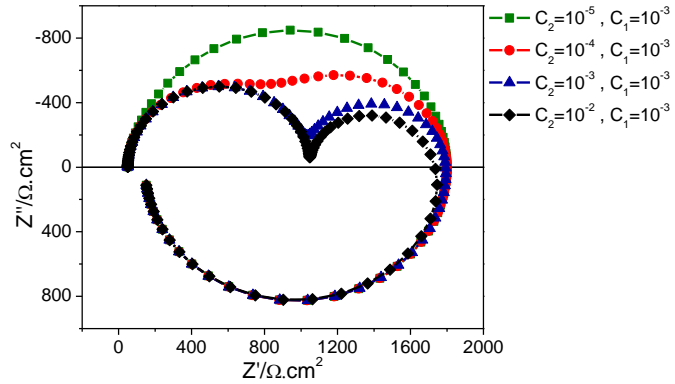
Figure 7. 16. (a) (left) Nyquist plots and (right) Bode magnitude and phase plot with a variation in C_1 and C_2 kept constant. (b) (left) Nyquist plots and (right) Bode magnitude and phase plot with a variation in C_2 and C_1 kept constant. $R_1=R_2=800$ Ω. $R_3=50$ Ω. $L=1 \times 10^6$ L.

a)

b)

274
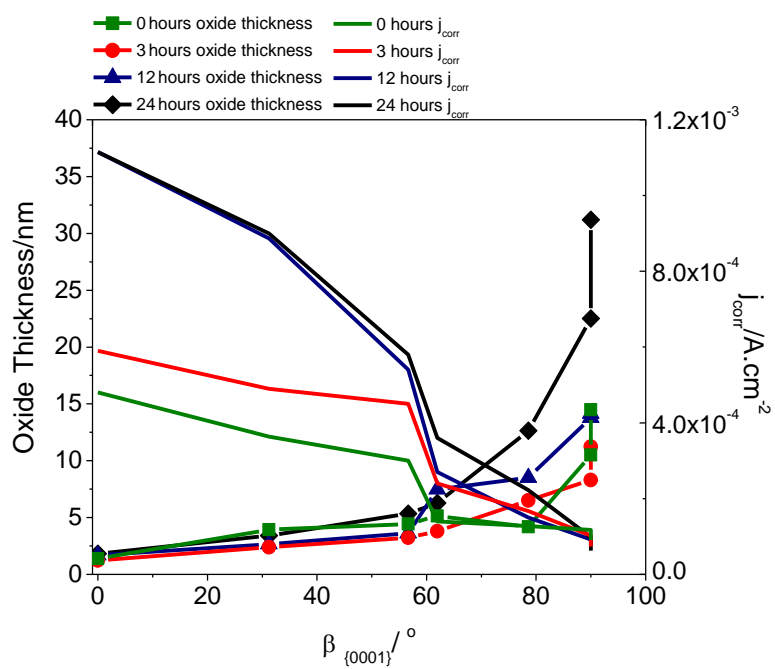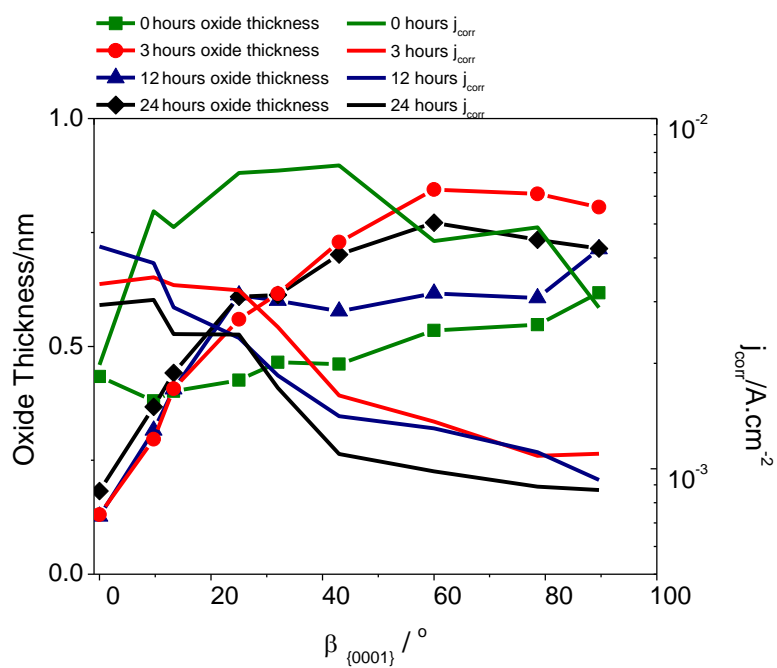
c)
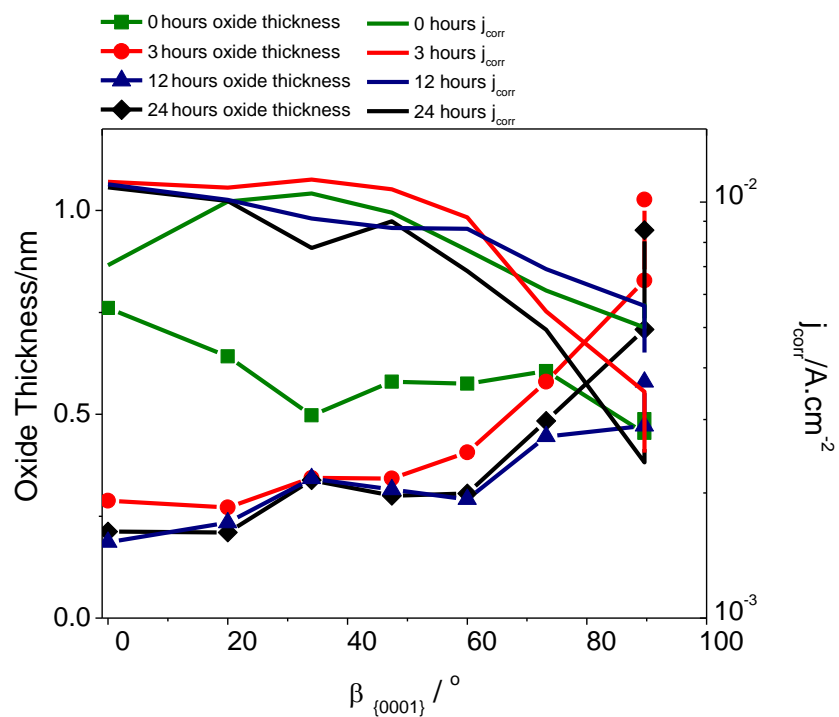
Figure 7. 17. Oxide and EIS determined i_{corr} thickness with β angle in (a) 0.6 M NaCl, (b) 0.1 M TRIS and (c) 0.1 M EDTA at OCP over a 24 h immersion as determined through an equivalent circuit compromising of CPEs.
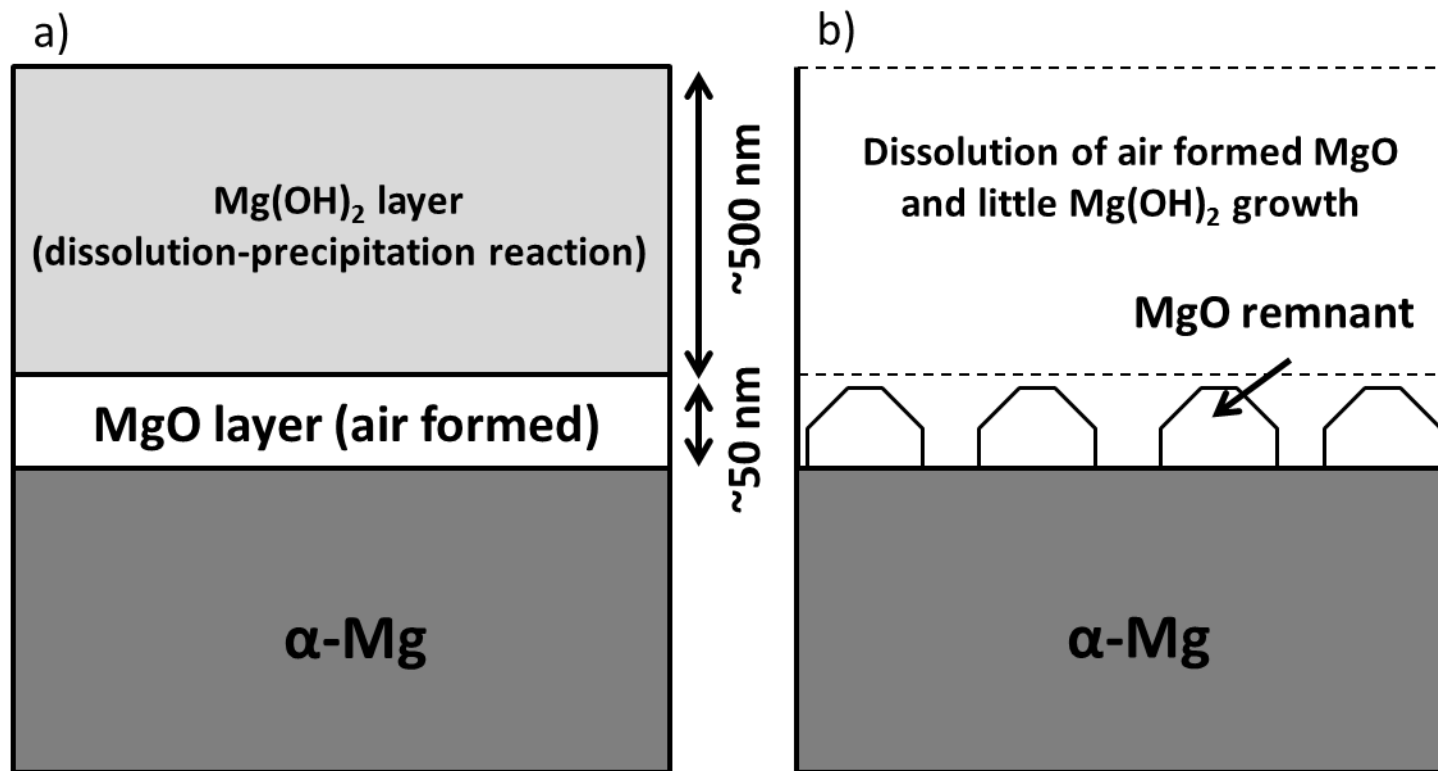
Figure 7. 18. Schematic of Oxide Growth on Mg alloys in (a) 0.6 M NaCl and (b) 0.1 M TRIS and 0.1 M EDTA. Adapted from [37].

a)
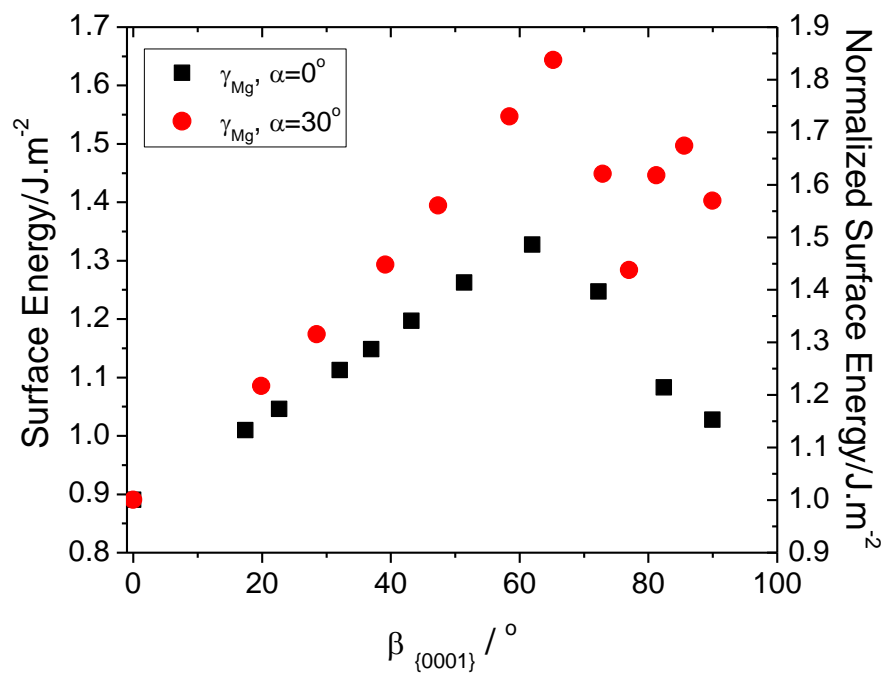
b)
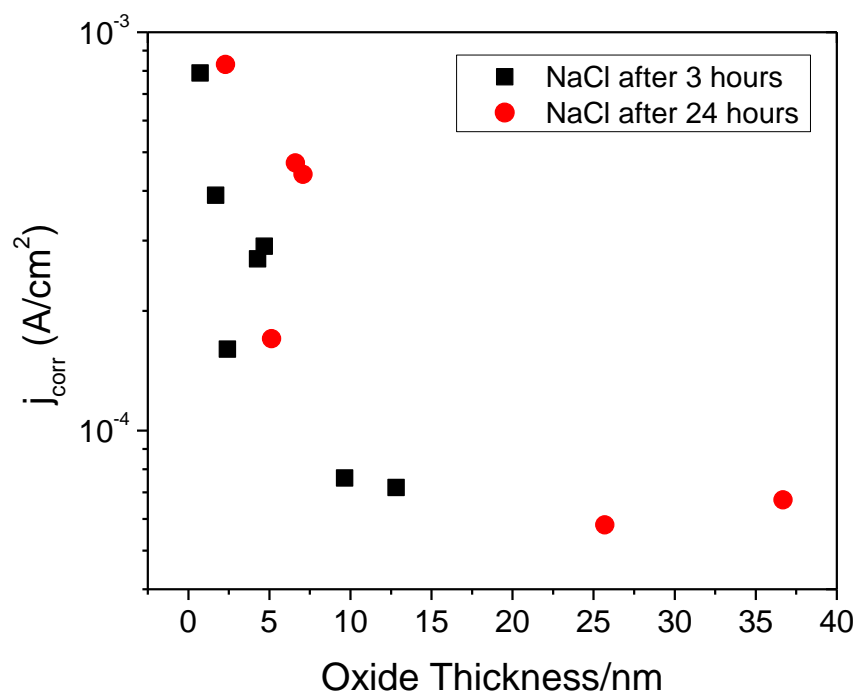
c)
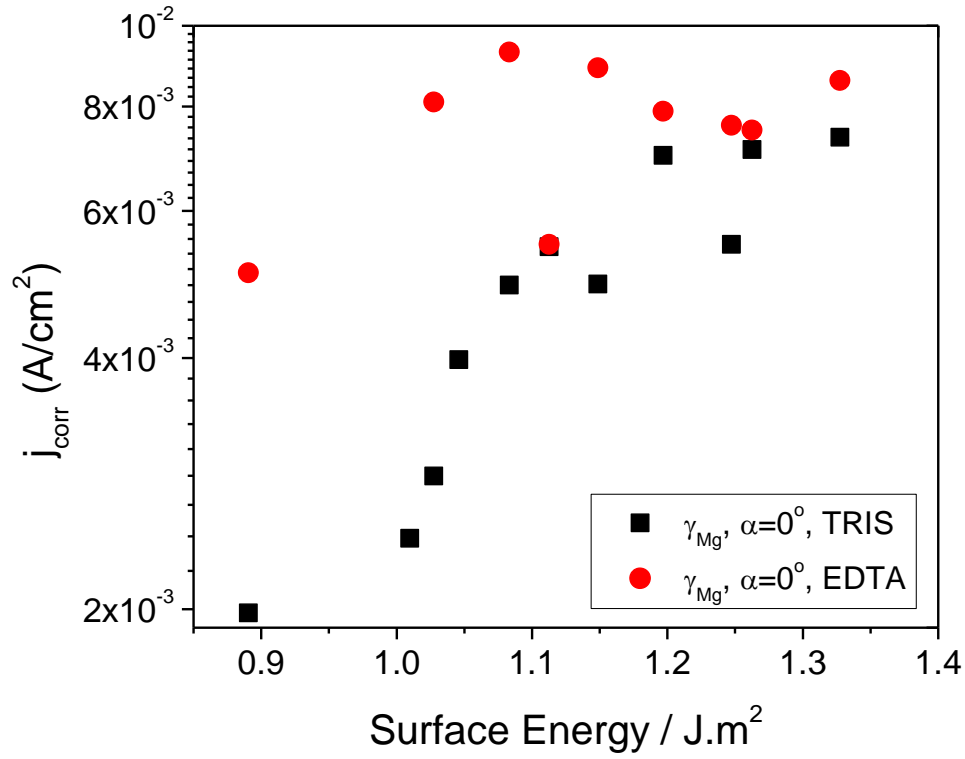
Figure 7. 19. (a) Calculated surface energy, γ, as a function of $\beta_{\{0001\}}$ at $\alpha = 0$ and $30°$ [85]. The highest surface energy occurs at orientations around $\beta_{\{0001\}} = 60°$. (b) Variation in the i_{corr} with oxide thickness for oxide covered surfaces. (c) Variation in the i_{corr} with surface energy for bare surfaces

8 Assessing the Corrosion of High Al Composition and Multi-phase Mg-Al Alloys by Electrochemical Impedance, Mass-Loss, Hydrogen Collection, and ICP-OES Solution Analysis

The corrosion behavior for several die-cast Mg-Al alloys (AM50, AM50 and AZ91) were examined and compared to commercial purity Mg and AZ31B utilizing simultaneous measurement of electrochemical impedance (EIS), hydrogen gas collection over a 24 hour immersion period, gravimetric mass loss, and Inductively Coupled Plasma Optical Emission Spectrometry (ICP-OES) solution analysis of the total Mg concentration released. Tests were conducted in three electrolytes, unbuffered 0.6 M NaCl, 0.1 M tris(hydroxymethyl)aminomethane (TRIS), and 0.6 M NaCl buffered with TRIS to a pH of 7. Integration of R_P over time was perform, as evaluated from EIS at frequencies as low as 0.001 Hz, considering full inclusion of the pseudo-inductive impedance behavior of Mg. This provided good agreement with the cumulative mass loss, ICP-OES solution analysis and volume of hydrogen collected for AM50, AM50 and AZ91. The variation in the cathodic kinetics for the die-cast alloys were determined over 3, 24 and 48 hour immersion periods and compared to commercial purity Mg and AZ31B-H24. The global corrosion rate decreased with increasing Al content, even though Al wt% above the solubility limit (2 wt% at room temperature), resulted in increasing volume fractions of the $Al_8Mn_5(Fe)$, Al_2Mn_3 and Al_3Fe intermetallic particles (IMPs). Each of the alloys contained varying amounts of primary α, eutectic α+β, and the β-phase. Al in the solid solution α-Mg phase decreased its overall anodic reaction rate while the $Mg_{17}Al_{12}$ phase was speculated to not function as a strong cathode as deduced from cathodic E-log(i) studies. Also, decreasing amounts of cathodic activation with increasing Al content was a factor in determining overall corrosion rate. However, the localization factor of corrosion increased with Al content.

A manuscript based on this chapter has been submitted as a Full Research Paper to Corrosion Journal, "Assessing the Corrosion of High Al Composition and Multi-phase Mg-Al Alloys by Electrochemical Impedance, Mass-Loss, Hydrogen Collection, and ICP-OES Solution Analysis"

Representative author contributions:
L. G. Bland: metallurgical characterization, analysis and interpretation
L.C. Scully: electrochemical experiments
J.R. Scully: adviser, analysis and interpretation

8.1 Introduction

8.1.1 Die Cast Alloys and Metallurgy

Die-cast Mg-Al alloys are typically used as automotive parts such as seat frames, steering wheels and safety parts due to their light weight, good castability and good mechanical properties at room temperature[1]. Therefore, casting is a predominant processing route for Mg components[2] due to their good fluidity and low susceptibility to hydrogen porosity[3]. During die-casting, the material is melted and resolidified which leads to large variations in the distribution of solute elements, the formation of intermetallic particles (IMPs) and a randomized crystallographic texture[4]. During resolidification, the solute elements are more soluble in the liquid state than the solid state; therefore, regions that solidify last are enriched in solute. These solidification boundaries and IMPs, which form during processing[5-9], have their own electrochemical characteristics and can function as active cathodes during corrosion[6,10,11].

The resultant microstructure of Mg-Al, die-cast alloys is well known[12-20]. The microstructure of these alloys, containing above 3 wt% Al, contain some amount of the β-phase ($Mg_{17}Al_{12}$) as well as other Al-Mn and Al-Mn-Fe IMPs[12]. According to the lever rule on an equilibrium Mg-Al phase diagram, AZ31 would consist of 97 wt% α-Mg and 3 wt% β-phase, AM50 would consist of 93 wt% α-Mg and 7 wt% β-phase, AM60 would consist of 90 wt% α-Mg and 10 wt% β-phase while AZ91 would consist of 83 wt% α-Mg and 17 wt% β-phase. However, this estimation is not accurate for die-casting. During non-equilibrium casting, varying amounts of this phase are formed, with increasing amounts of the β-phase formed with increasing Al concentration (i.e. 5 wt% in AM50 < 6 wt% in AM60 < 9 wt% in AZ91)[12]. However, much less β-phase is produced that predicted by the lever rule under equilibrium assumptions[12]. The amount and distribution of these phases is highly dependent on the composition of the Mg-Al alloy as well as the processing parameters[7,18-27].

Despite the additional added Al to the alloy, the Al in solution in the α-Mg is similar for AZ31B, AM50, AM60 and AZ91D. The Al content is determined by the solvus line between Mg solid solution and $Mg_{17}Al_{12}$ for temperatures close to room temp defining the highest equilibrium concentration of Al in solid solution without precipitating additional $Mg_{17}Al_{12}$ within the α-Mg as a secondary phase[28]. These alloys have Mn additions which are designed to getter Fe. However, the Mn also partitions some of the Al into Al-Mn and Al-Mn Fe IMPs. For the low Al

content alloys such as AZ31 (i.e. ≤3 wt% Al), the remainder of the Al remains in solid solution. However, in AM50, AM60 and AZ91, the additional Al not sequestered by Mn would be portioned to the β-phase. The Zn, present in AZ91, is retained in both the α-matrix as well as in the β-phase as it is soluble in both[28].

8.1.2 Corrosion of Al-containing alloys

The corrosion rate of Mg-Al alloys, with varying Al content, has been studied in many contexts[1,7,13,15-18,20,29-32]. In particular, the corrosion rate of Mg-Al alloys in relationship to the amount of β-phase present in the alloy has been considered [7,18,20]. Similarly, a large amount of literature details the atmospheric corrosion of these high Al-content Mg alloys [1,13,15-17,29-32].

While Mg-Al alloys are known for their low-weight, this family of alloys are highly reactive due to their low electrochemical potential in the galvanic series[33,34]. These alloys are particularly susceptible to micro-galvanic corrosion due to cathodic secondary phases present in the material[6,10]. The effect of the β-phase has two, opposing effects on the corrosion behavior (1) the β-phase can act as a galvanic alloy, coupled locally as a cathode during corrosion initiation due to its more positive open circuit potential (OCP) (~1.3 V_{SCE}) and, therefore, increase the corrosion rate of Mg-Al alloys and (2) the β-phase can function as a lateral corrosion barrier [19,35]. β-phase can form stable oxide films due to the presence of Al, stable as $Al(OH)_3$, (at low to near neutral pH) or Mg at a high pH, stable as $Mg(OH)_2$ (according to their respective Pourbaix diagrams[36]). Micro-galvanic coupling between the α-Mg and β-phase can still occur but the oxides might regulate cathodic reaction rates. The variation in this corrosion response is also highly dependent on the amount and distribution of this phase within the alloy where the fraction of this phase can be altered through different processing techniques as well as other alloying elements[7,18-27]. However, little supporting evidence has been provided on the conditions in which the β-phase functions as a cathode or as a barrier. Better understanding on which effect of the β-phase is most important, and under what conditions is important to understand the overall corrosion of the alloy class.

Variations in experimental design such as to electrolyte chemistry, solution pH, and immersion time can significantly alter corrosion rates[37]. Also, differences in the corrosion rates occur based on short-term versus long-term estimation methods[38,39]. The instantaneous corrosion rate has been called into question, especially when determined by Tafel extrapolation from polarization curves, H_2 evolution rate, electrochemical impedance spectroscopy (EIS) derived

polarization resistance, R_P[40] and spectrochemical approaches conducted over the short term[41,42]. However, long-term cumulative corrosion damage can be assessed by mass loss, measurement of the H_2 evolved over the full immersion time, solution analysis for Mg^{2+} cations and integration of i_{corr} vs. time data determined by the evolution of R_P over time[37]. Even comparing 3 hour to 24 hour immersion results for the same environment and alloy can lead to large variations in the resultant estimated overall corrosion rate due to variations in the galvanic couple behavior, electrolyte pH and $Mg(OH)_2$ formation over these time periods because of changes with time[39,43] and where different microstructural features dominating the corrosion rate at different immersion times. The work herein gives the first estimate of corrosion rate for a broad range of Mg-Al alloys using a rigorous analysis based on four of these approaches over a 24 hours time period to provide a better understanding of the electrochemical behavior of Mg-Al alloys with various Al content. In order to facilitate comparisons, commercial purity (CP) Mg and AZ31B-H24 were tested to examine a broader range of Al contents[37,38,44].

8.1.3 Objective

The objective of this study is to evaluate the corrosion of Mg-Al alloys containing solidification structures formed during a resolidification process. For the overall objective (i.e. Mg-Al welds), the microstructure and composition of these alloys have been used as a model alloy as a surrogate for the microstructure seen in the AZ31B-H24 tungsten inert gas (TIG) weld to enable an evaluation of the effect of composition and microstructure on the corrosion of Mg-Al alloys over the range from 0 to 9 wt% Al with and without Zn.

8.2 <u>Experimental Procedures</u>

8.2.1 Materials

Three as-die-cast Mg-Al alloys, supplied by US Magnesium LLC, AM50A [M10501], AM60B [M10601] and AZ91D [M11916] were characterized for the variation in their corrosion rates with increasing Al content (compositions are listed in Table 8. 1). The corrosion rates were compared to commercially pure (CP) Mg and AZ31B-H24[37,38,44]. The wrought surface was prepared by grinding in ethanol with silicon-carbide paper to a final grit of 1200.

8.2.2 Metallurgical Characterization

Samples were analyzed scanning electron microscopy (SEM) on a FEI Quanta 650 microscope. Images were taken at a working distance of 10 mm and an accelerating voltage of 5

kV. Electron backscatter diffraction (EBSD) was obtained for each alloy at a working distance of 15 mm and an accelerating voltage of 20 kV. Compositional analysis was performed using energy dispersive spectroscopy (EDS) methods with ZAF[13] corrections on the Aztec^{TM} software tool[45]. Images were recorded at a working distance of 10 mm while operating at an accelerating voltage of 5 kV. The grain size was determined using the linear intercept method at both 5x and 20x magnification via ASTM Standard E113-96 [46]. The corrosion morphology was examined for each alloy to determine how the corrosion initiated and progressed over 24 hours. The sample was marked using a Vickers hardness tester to enable examination of the corrosion morphology, before and after exposure, at the same location. Secondary Electron SEM micrographs were taken before immersion in 0.6 M NaCl and after immersion in 0.6 M NaCl for 24 hours at OCP. All samples were cleaned with CrO_3 to remove any corrosion products and examine the corrosion morphology according to ASTM-G1[47].

8.2.3 Characterization of the Corrosion Behavior of Mg-Al Alloys

Anodic charge consumed (over 24 hours) was determined under full immersion conditions with four parallel and simultaneous techniques: (1) electrochemical impedance spectroscopy (EIS), (2) gravimetric mass loss, (3) H_2 gas collection and (4) inductively coupled plasma optical emission spectroscopy (ICP-OES) solution analysis. A vertical electrochemical test cell with a Pt counter electrode and a saturated calomel electrode (SCE) was used which allowed for collection of H_2 into a vertical funnel and burette[37,38,48]. All EIS scans were acquired from 100 kHz to 0.001 Hz with 6 points per decade and an AC amplitude of $\pm$20 mV. EIS spectra were fit using ZView to an equivalent circuit previously established and shown in Figure 8. 1[37,38,49]. Before electrochemical testing, the electrolyte was pre-saturated with H_2 as it has been shown that H_2 gas is extremely soluble and aqueous environments[50]. Tests were performed in unbuffered 0.6 M NaCl (stating pH~5.3) at OCP. The pH was monitored and typically rose to ~10 in 24 hours. Following testing, samples were cleaned according to ASTM-G1 using 200 g/L CrO_3 and left to dry in a dry box for 24 hours[47].

Corrosion rate was estimated using the Stearn-Geary relationship[40,51]:

$$i_{corr} = \frac{B}{R_P} = \frac{\beta_a\beta_c}{2.303R_P(\beta_a + \beta_c)}$$

Equation 8.1

---

[13]Z= atomic number correction, A=absorption correction, F=fluorescence correction

where β_a and β_c are the anodic and cathodic Tafel slopes, respectively, and $B = (1/2.303) \times (\beta_a.\beta_c/(\beta_a + \beta_c))$. Three different Tafel assumptions were used which are consistent with literature[37,52,53]. Corrosion rate (i_{corr}) was converted to the anodic charge consumed (where $i_a=i_c$ at open circuit) over the full 24 hour immersion test by integrating the EIS-estimated corrosion rate:

$$Q_a^{EIS} = \int \frac{\beta_a\beta_c}{2.303R_P(t)(\beta_a + \beta_c)} dt \qquad \text{Equation 8.2}$$

The mass loss of Mg (Δm) waas measured gravimetrically to ± 0.1 mg resolution and converted to the anodic charge (Q_a) via Faraday's law[33]:

$$Q_a^{\Delta m} = znF = \frac{z\Delta mF}{a} \qquad \text{Equation 8.3}$$

Where z is equivalent electrons per mole of Mg^{2+} oxidized, n is the number of moles of Mg, F is Faraday's constant (95,498 C/eq) and a is the molar mass of Mg. For each of the Mg-Al alloys, their equivalent weight was used to account for each of the given major alloying elements and their respective concentrations[33] as specified by ASTM G106[54]. This was determined as the sum the fractional number of equivalents of all alloying elements to determine the total number of equivalents in the alloy, N_{eq}:

$$N_{eq} = \sum \left(\frac{f_i}{a_i/z_i}\right) = \sum \left(\frac{f_i z_i}{a_i}\right) \qquad \text{Equation 8.4}$$

Where f_i, a_i and z_i are mass fraction, atomic weight and electrons exchanged. The equivalent weight (grams/equivalent) is then the reciprocal of the total number of equivalents ($EW = N_{eq}^{-1}$). The equivalent weight for AM50A, AM60B and AZ91D were 11.99, 11.95 and 12.11 g/eq, respectively. This was determined assuming congruent Mg^{2+}, Al^{3+}, Mn^{2+} and Zn^{2+} oxidation[14] which are justified given the thermodynamic properties of each element and the assumption of high pH.

The volume of H_2 gas evolved was converted to a corresponding cathodic charge (Q_c) where $Q_a=Q_c$ at OCP[33] via Faradays Law and the Ideal Gas Law. Thus:

$$Q_c^{H2} = Q_a^{H2} = znF = \frac{zPVF}{RT} \qquad \text{Equation 8.5}$$

---

[14] At a pH of ~11, Al dissolution occurs to $Al(OH)_3$ or AlO_2^- and Zn dissolution to ZnO or ZnO_2^{-2} are thermodynamically possible at the typical OCP and anodic polarization range of this study.

P is the pressure inside the burette (assumed to be approximately 1 atm at sea level), V is the volume of H_2 gas collected, R is the ideal gas constant and T is the temperature.

All solutions were analyzed using a Thermo Scientific[TM] iCAP 7200 ICP-OES. Samples were prepared by mixing 1 M HCl into the solution after electrochemical testing and sonicated to ensure that no corrosion product was left on the bottom of the container. The following wavelengths were used and recorded for the calculation of the charge consumed for solution analysis: Mg (279.553 nm), Mg (280.270 nm), Al (226.910 nm), Al (308.215 nm), Al (396.152 nm), Fe (238.204 nm), Fe (239.562 nm), Mn (257.610 nm), Mn (259.373 nm), Zn (206.200 nm), and Zn (213.856 nm) following from previous work[41,55] where the detection limits for each of these elements have been reported elsewhere[56]. The ICP reports the concentration of elements in the collected solution (ppm) which can be similarly converted to anodic charge (Q_a^{ICP}) using Faraday's law (Equation 8.3).

The average corrosion penetration depth ($x_{average}$) was calculated from Faraday's law:

$$x_{average} = \frac{Q(E.W.)}{F\rho} \qquad \text{Equation 8.6}$$

Where E.W. is the equivalent weight of commercially pure Mg, taken as 12.16 g/eq, F is Faraday's constant (96,485 C/eq), and ρ is the density of Mg. From this, the degree of localized corrosion was determined from a localization factor (LF):

$$LF = \frac{x_{max}}{x_{average}} \qquad \text{Equation 8.7}$$

The x_{max} was determined from 3D imaging using an Optical Hirox microscope. These numbers have been reported as the average for ~5 measurements. These numbers have been reported as the average for ~5 measurements. The relative area fraction of primary α-Mg corroded was determined through ImageJ.

Cathodic kinetics were determined in unbuffered 0.6 M NaCl (pH ~5.3), 0.1 M buffered tris(hydroxymethyl)aminomethane (TRIS) (pH ~7), and 0.6 M NaCl buffered to a pH ~7 with TRIS. Samples were held at OCP for 3, 24 and 48 hours, respectively, followed by a cathodic potentiodynamic polarization scan ranging from 50 mV above OCP to -2.3 V below OCP in a downward sweep at a rate of 1 mV/second were also performed to analyze the cathodic kinetics. The cathodic current density, i_c, was determined at -1.8 V_{SCE} with the standard error reported.

285

8.3 <u>Results</u>

8.3.1 Cast Mg Alloy Metallurgical Characterization

Examining at the composition of the primary α-Mg matrix for the die-cast alloys, the Al composition of this phase (i.e. the amount of Al in solid solution) for each alloy is approximately the same (~2 wt%), as determined through quantitative EDS methods[12]. Instead, the additional Al content leads to the formation of several Al-containing intermetallic particles (IMPs)[6,19,44]. EDS of each of the die-cast Mg-Al alloys shows several secondary phases. An Al-Mn phase, Al_8Mn_5 was seen all three of the die-cast alloys (Figure 8. 2), along the Mg-Al phase, $Mg_{17}(Al,Zn)_{12}$ (Figure 8. 3). The Al_8Mn_5 appears as either cube-like or rod-like particles heterogeneously throughout the material. Similarly, two distinct morphologies were observed for the β-phase: (1) eutectic α+β and (2) a eutectic, laminar β-phase[6,19,44] (Figure 8. 3). This laminar structure is present to varying degrees in all three of these alloys. The example shown here was taken from the AZ91 sample to show the additional distribution of Zn in the β-phase. However, the morphology of this phase is the same for AM50 and AM60 (albeit without the additional Zn content).

The size and distribution of these phases was highly dependent on the specific alloy with the β-phase appearing as $Mg_{17}Al_{12}$ in AM50 and AM50 and $Mg_{17}(Al,Zn)_{12}$ in AZ91. Also, the morphology of this phase varied with Al content. In the AM50 alloy, these β-phase and α+β eutectic structures were spaced approximately 50 μm apart with the Al-Mn and/or Al-Mn-Fe IMPs heterogeneously throughout the material (Figure 8. 4(a)). Also, the EBSD of the AM50 revealed a randomized texture with relatively large grains (~500 μm) (Figure 8. 4(b)). As determined through EBSD phase identification, only a small phase fraction of the microstructure was the β-phase while the Mn_5Al_8 phase was prevalent (Table 8. 2). The β-phase for this alloy was mainly contained in an α+β eutectic (Figure 8. 5). This corresponded with image analysis of the area fraction of this eutectic phase which showed that, relative to the primary α-Mg, there was only a small area fraction of this eutectic phase Table 8. 3.

In the AM60 alloy, these β-phase and α+β eutectic structures were spaced ~25 μm with various Al-Mn and Al-Mn-Fe IMPs (Figure 8. 6(a)). EBSD showed no preferential texture (Figure 8. 6(b)) and a grain size of ~500 μm. The β-phase was heterogeneously distributed throughout the material as well as several other IMPs, as determined through EBSD (Table 8. 2).

286

The β-phase consisted of both the β-phase as well as eutectic α+β (Figure 8. 7, Table 8. 3). However, it is noted that the β-phase contained outside of the eutectic is relatively small (in size) in comparison to AZ91.

Last, the microstructure of the AZ91 alloy was observed to α+β eutectic as well as β-phase (rich in Al-Zn due to the addition of Zn (Figure 8. 3, Figure 8. 8(a)). This alloy has the most closely spaced solificiation structures (~15μm) with Al-Mn-Fe IMPs still distributed throughout the material (Figure 8. 8(a)). EBSD of the material also had no distinct texture (Figure 8. 8(b)). the AZ91 alloy had the largest fraction of the β-phase but contained approximately the same phase fraction of other IMPs (Table 8. 2). The AZ91 alloy had the highest amount of β-phase which was contained in the alloy as both an independent β-phase and as eutectic α+β (Figure 8. 9, Table 8. 3). Most of the β-phase present in this alloy was as the lamellar microstructure (Table 8. 3).

In contrast, wrought AZ31B and CP Mg were used as a comparison. AZ31B wrought sheet is known to have a strong basal {0 0 0 1} texture and contain $Al_8(Mn,Fe)_5$ but no β-phase while extruded rod CP Mg is be equiaxed with few impurities. The metallurgy of these materials is discussed elsewhere [10,57].

8.3.2 Resultant Corrosion Morphology of Al Containing Cast Mg Alloy

Samples were immersed for 24 hours at OCP in 0.6 M NaCl to observe the variation in the corrosion morphology with Al additions and phases formed. Comparative results in Mg and AZ31B under similar conditions are discussed elsewhere[57]. Samples were marked with a fiducial mark and imaged before corrosion. Corrosion was not seen to initiate until approximately 3-4 hours of immersion according to time-lapse videos (not shown for brevity). Compositional contrast on AM50 shows primary α, α+β eutectic and the Al_8Mn_5 phase throughout the material, as confirmed through EDS analysis (Figure 8. 10(a)). Corrosion initiated in the primary α-Mg region (Figure 8. 10(b)). In AM60, the α+β eutectic as well as additional β-phase IMPs were observed throughout the material as well the Al_8Mn_5 phase (Figure 8. 11(a)). A large amount of the lamellar, β-phase is intact both before and after corrosion (Figure 8. 11(a-b)). However, corrosion initiated in the primary α-Mg (Figure 8. 11(b)). In AZ91, the lamellar β-phase was observed throughout the sample (Figure 8. 12(a)) and little corrosion occurred, even after 24 hours of immersion at OCP (Figure 8. 12(b)). Upon closer inspection, as shown in Figure 8. 12(c), the β-phase is intact while the primary α-Mg matrix has corroded.

From image analysis of the relative amount of primary α-Mg corroded for each alloy, it was observed that only a small area fraction of primary α-Mg was corroded on the sample surface (Table 8. 3). Therefore, the corrosion was only in localized places on the sample surface. A LF was determined for each of the die-cast alloys and is discussed later to determine the variation in the corrosion on a local scale versus the global corrosion rate.

8.3.3 Corrosion Electrochemistry of Al Containing Cast Mg Alloys in Comparison to AZ31B and CP Mg

Open Circuit Potential with Time

The OCP was recorded as a function of time in 0.6 M NaCl for each Mg-Al alloy and compared to CP Mg and AZ31, as previously reported[38,57], after the samples were held at OCP for 3, 24 and 48 hours at OCP. The measured OCP for each alloy increased with time. The starting OCP for each alloy was approximately -1.59 V_{SCE} which was slightly more positive than the OCP determined for AZ31, -1.6 V_{SCE}, and CP Mg had the most negative reported OCP (-1.63 V_{SCE}). Over the 24 hour immersion period, the OCP increased for all alloys in the first initial 3 hours. During this time period, the pH of the solution had risen from ~5.3 to 7. However, from 3 hours to 24 hours of immersion time, it is noted that the AZ31 OCP slightly increases while the higher Al content alloys (AM50, AM60 and AZ91), all retain approximately the same OCP measurements. After 3 hours of immersion, the pH of the solution continued to increase to ~11.

The OCP was also measured in two buffered neutral pH environments, 0.1 M TRIS and 0.6 M NaCl TRIS buffered with TRIS. The pH for these environments remained ~7 for the full exposure. In the 0.1 M TRIS environment, the measured OCP for each alloy was approximately -1.5 $V_{SCE.}$ There was little variation with the OCP with alloy content. In 0.6 M NaCl buffered with TRIS. There was a slight increase in the OCP from -1.51 V_{SCE} to -1.52 V_{SCE}. However, the increase in this pH was much smaller than in just 0.6 M NaCl. There was a slight increase in the OCP with added Al content.

Corroborating EIS, mass loss, H_2 collection and ICP-OES of high Al containing alloys after 24 hour corrosion at OCP

The characteristic EIS response of Mg-Al alloys in chloride-containing environments shows the presence of two capacitive loops and an inductive loop which is similarly reported in CP Mg and AZ31B[14,58-65]. The use of a low-frequency inductor was required, as well as fitting to a significantly low enough frequency (~1 mHz) to acquire an accurate representation of

corrosion rate (Figure 8. 1). The EIS response from each of the Al-containing Mg-Al alloys is shown in Figure 8. 14 after 24 hours of immersion in 0.6 M NaCl. A reasonably good fit was achieved for each of the die-cast alloys using the equivalent circuit (<15% error). Each of the fitting results is shown in Table 8. 4. The R_p for each of the die-cast alloys was determined according to the respective equivalent circuit.

$$\frac{1}{R_p} = \frac{1}{R_1 + R_2} + \frac{1}{R_3}$$ Equation 8.9

From the EIS determined R_p and i_{corr}, a notable increase in the R_p (a decrease in the i_{corr}) was observed. This particularly occurs in the first 3 hours after immersion in 0.6 M NaCl. The decrease in the corrosion rate with time is typically rationalized to occur due to the rapid alkalization of the Mg surface (as confirmed by the increase in the pH from ~5.3 to ~11 during the exposure time). The variation in the corrosion rate with time has been noted for other Mg alloys[38,43] and is a reason why comparing different immersion times and tests for Mg alloys can lead to large variations in the resultant corrosion rate.

Integration of the corrosion current density over the 24 hour immersion time using Equation 1, conversion of the mass loss using Faraday's Law Equation 2, calculation of the H_2 collected over 24 hours using the ideal gas law and Faraday's Law, and measurement of the magnesium dissolved in solution using ICP-OES and Faraday's Law resulted in anodic charge estimations that were consistent with each other for a given alloy (Table 8. 5-5, Figure 8. 16). Corrosion anodic charge varied with Al content. Several Tafel slope assumptions were utilized[37,53,54] and it was shown that little variation in the EIS determined corrosion rate was obtained, even with large variations in the Tafel assumptions. This is because Equation 1 is much more dependent on the EIS-determined R_P then reasonable variations in the Tafel slopes which produce small changes in B[38]. Further commentary is given below regarding normalization by area.

Kinetics with Time

The anodic E-log(i) polarization kinetics for CP Mg, AZ31, AM50, AM60 and AZ91 were observed after 24 hours at OCP (Figure 8. 17(a)) for 0.6 M NaCl, 0.6 M NaCl buffered with TRIS and 0.1 M TRIS and typical anodic polarization curves are shown. It was observed that there was little perceptible variation with respect to the anodic kinetics for AM50, AM60 and AZ91 in each of these environments (Figure 8. 17). This agreed with previous work which

showed that the kinetics of anodically driven Mg-Al alloys, where corrosion is forced to occur primarily in the primary α-Mg matrix, did not vary given the same Al composition in the primary α-Mg matrix[44]. However, the die-cast alloys (which have a slightly higher Al content) exhibited reduced anodic kinetics in the charge transfer control region in comparison to CP Mg and AZ31B (Figure 8. 17).

IR correction of i-E data was performed via the linear E-log(i) fit method in 0.6 M NaCl. R_Ω was determined to be ~10 Ω (1 cm^2 test area), as obtained from EIS (Table 8. 4). From the iR corrected anodic potentiodynamic scans for the die-cast alloys, there is a low apparent anodic Tafel slope of about 25-30 mV/dec that is representative of a non-polarizable charge transfer controlled Mg oxidation process on all alloys (Figure 8. 17(b))[37,38]. While these rapidly acquired anodic characteristics make it difficult to calculate accurate long-term corrosion rates using either Tafel extrapolation or linear polarization resistance based techniques, the iR corrected data can be used to make an assessment of the anodic kinetics of the favorable primary α-Mg corrosion phase at a given time. The D.A. Jones approach was utilized to obtain the anodic rate, independent of i_c ($|i_a|=|i_{app}|+|i_c|$)[33]. In Figure 8. 17(b) it is shown that the anodic dissolution kinetics decrease due to the addition of Al to the alloy. That is, higher Al content in AM alloys and AZ91 exhibit lower anodic reaction rates.

Typical cathodic polarization curves for CP Mg, AZ31, AM50, AM60 and AZ91 after 24 hours at OCP are shown in Figure 8. 18 for 0.6 M NaCl, 0.6 M NaCl buffered with TRIS and 0.1 M TRIS are excluded for brevity but showed no trends. In the 0.6 M NaCl environment, only a slight difference in the cathodic kinetics was shown with varied alloying content (Figure 8. 18). After 3 hours (Figure 18(a)) the cathodic kinetics did not vary with each alloy. However, after 24 hours at OCP the cathodic reaction rate increased with increasing Al content. In contrast, little variation in the cathodic kinetics was shown for either the 0.6 M NaCl environment buffered with TRIS or 0.1 M TRIS and were excluded for brevity.

8.4 <u>Discussion</u>

8.4.1 Resultant Corrosion Morphology in High Al Containing Cast Mg Alloys

      From the resultant morphology (Figure 8. 10-9), much less surface corrosion propagation of dark attack areas occurs in the die-cast Mg-Al alloys than in the previously studied, AZ31[57]. However, between the three alloys, some trends in the initiation and propagation are seen. Corrosion typically initiated in the primary α-Mg matrix (Figure 8. 10-11). It is unclear whether the corrosion was deeper with increasing Al content, or simply more localized.

      The β-phase ($Mg_{17}Al_{12}$) has two potential roles in corrosion. This phase has been proposed to function as an active cathode (therefore increasing the micro-galvanic coupling seen within the alloy between this phase and the α-Matrix) and act as a barrier against lateral corrosion propagation from one primary α-Mg grain to another[7,20,21]. In terms of galvanic corrosion between the primary α-Mg and the β-phase, since there is approximately the same amount of Al in solid solution for AM50, AM50 and AZ91, there would be approximately the same galvanic potential driving force between the α and β-phases in each case. It should be noted that the volume fraction differs in these alloys, as seen in Table 2. However, Figure 8. 19 indicates that the precise chemical composition of the Al phase matters toward HER reactivity[6,66,67]. In any case, it merits comment that the OCP of the primary α-Mg would be less-noble than that of the Al-rich IMPs and solidification boundaries (formed during casting) and cause galvanic corrosion to occur. Due to this difference in the electrochemical potential between the primary α-Mg and the solidification boundaries, as well as IMPs, micro-galvanic coupling between these phases would lead to the corrosion damage morphologies seen in Mg alloys (Figure 8. 10-10). However, the β-phase is not nearly as strong of a cathode as other IMPs such as Al_3Fe or Al_6Mn.

      Corrosion typically initiated in the primary α-Mg in close proximity to the β-phase as well as near Al-Mn-Fe containing IMPs for AM50, AM60 and AZ91 (Figure 7-9) where these secondary phases functioned as active cathodes. However, the global corrosion rate in these high Al-content alloys is much lower than seen previously for AZ31[57] (Figure 8. 16). During propagation, the corrosion remained in specific, isolated primary α-Mg grains (which is typically surrounded by β-phase and/or eutectic α+β) and did not propagate beyond the surrounding β-phase and/or eutectic α+β. This is shown in Figure 8. 12(c) in particular. Therefore, the β-phase provides a galvanic driving force for corrosion initiation in the primary α-Mg phase, but limit

propagation in the alloy because of the lateral barrier to filiform type attack morphology and notable slow HER on β-phase (Figure 8. 19).

The degree of localized corrosion (at the primary α-Mg/β-phase interface) versus uniform corrosion was compared for CP Mg, AZ31, AM50, AM60 and AZ91 using the LF (Equation 7). The LF is the ratio of the maximum penetration depth to the average depth (Equation 6). Therefore, the higher the LF the higher the estimation of localized corrosion damage. From this assessment, CP Mg has a lower LF than any of the die-cast alloys while AM60 and AZ91 have the highest LF (Table 8. 8). Therefore, while AM60 and AZ91 have lower overall (assumed uniform) corrosion rates, they have extensive localized corrosion, such as the localized micro-galvanic corrosion between the primary α-Mg matrix and IMPs. Speculatively, primary α-Mg with a basal orientation is preferentially attached next to the α+β eutectic or β-phase which can cause a variation in the corrosion at this interface. However, this is not discussed further and could be proposed as a future avenue for research.

8.4.2 Comparison of Corrosion rate of AM50, AM60 and AZ91

To date, it has been generally accepted that the addition of Al within Mg alloys increases the corrosion resistance when alloying remains in solid solution [25,68-70]. However, there is some debate on whether or not the addition of Al, above 4 wt% will increase the corrosion rate [44]. Some studies have shown that Al additions up to 5-9 wt% increase the corrosion resistance [71-73]. However, other studies shown that high Al-content alloys, such as AZ91 have a decreased corrosion resistance [74]. One potential error in determining the corrosion rate is due to the fact that, during dissolution, the near surface pH can rise to alkaline levels (pH >10) for Mg, and the surface of Mg also displays enhanced catalytic HER activity (i.e. ability to support the cathodic HER reaction) as shown by independent works [75,76]. Therefore comparing a short-term test to a long-term test is problematic as the electrolyte and relative rates of reaction become altered with time. In a direct comparison of the die-cast alloys, using four parallel techniques it is shown that an increase in the Al content increases the global corrosion resistance for die-cast alloys (Figure 8. 16, Table 8. 5-6), confirmed or independently corroborated for the four methods used here. The four, parallel methods, were able to yield repeatable values of the corrosion rate, showing that, for full immersion tests, at OCP in chloride-containing environments the accumulated charge per unit area decreases with increasing Al content.

This variation in the corrosion rate with alloying content has to be considered in terms of the amount of Al in solid solution versus the Al partitioned to IMPs. For AM50, AM60 and AZ91, the Al in solid solution is approximately the same (~2 wt%). However, there is also a variation in the volume fraction of second phases and the composition of these secondary phases specific to each alloy (Table 8. 2). In particular, the β-phase is not present in AZ31B but is present in AM50, AM60 and AZ91 (Table 8. 2) along with a higher phase fraction of Al_2Mn_3, Al_3Fe and $Al_8Mn_5(Fe)$. More specifically, the β-phase and eutectic α+β appears in AM50, AM60 and AZ91. From recent literature, the cathodic reaction rates of these IMPs are on the order of 10^{-3} A/cm^2 to as low as 10^{-5} A/cm^2 while the OCP is anywhere from -1.6 V_{SCE} to -0.5 V_{SCE} depending on composition[6,10,11,77] (Table 8. 7). It is noted that, examining the cathodic polarization curves of solid solution alloys with increasing amounts of Al[67], the cathodic reaction rates generally decrease with increasing Al content, especially when Fe is not present (Figure 8. 19)[67] despite the variation in the OCPs for various Al-containing IMPs. Therefore, both the effect of Al in solid solution on the anodic kinetics of Mg dissolution in the primary α-Mg solid solution and the effect of Al-rich cathodes are both factors in determining the corrosion rate of Mg-Al alloys.

8.4.3 Variation in Kinetics on Mg-Al alloys with Al content

From examining the iR corrected data, there is a decrease in the anodic reaction rate with increasing Al content (Figure 8. 17(a)) which agrees with literature[44]. An additional benefit is the random texture in die-cast alloys versus wrought alloys with a basal texture[78]. There is little variation in the cathodic kinetics (in the initial 3 hours) when Al is added to Mg (Figure 8. 18(a)), particularly since little to no corrosion initiation was observed in the first 3-4 hours. However, at 24 hours, cathodic HER kinetics are enhanced, as shown in Figure 8. 18(b). There was no variation in the cathodic kinetics for all times and alloys in 0.6 M NaCl buffered with TRIS to pH~7 as well as 0.1 M TRIS, possibly due to buffering as discussed below.

Variation in the cathodic kinetics with time, environment and alloying content is likely due to the variation in the oxide identity based on the environment and material. It has been shown previously that the precipitation of $Mg(OH)_2$ in chloride environments can strongly affect the corrosion morphology, corrosion rate and cathodic activation[10,11,43,57,78]. Therefore, the overall more rapid corrosion rates on CP Mg and AZ31 will lead to higher dissolution and therefore a thicker hydroxyl film during corrosion. This film will locally render the sample

surface more alkaline and lead to large variations in the cathodic kinetics with time. This is particularly observed in Figure 8. 18(a-b) where the cathodic kinetics after 3 hours do not vary increasing Al content but after 24 hours the cathodic kinetics increase with increasing Al content.

8.4.4 Variation in Al composition and Effect of Al replating on the Anodically Inducted Cathodic Activation of Mg Alloys

A recently cited phenomenon in Mg corrosion is the anodically induced cathodic activation [79-83]. The corrosion rate of the Mg increases over time due to changes in the cathodic kinetics at the sample surface[82,83]. Cathodic activation can first be considered as a function of exposure environment. The starting pH of 0.6 M NaCl was measured to be approximately 5.3 with the pH changing to approximately 11. This increased alkalinity of the exposure environment, particularly at the sample surface, can lead to the dissolution Al on the sample surface as well as the redeposition of Al as $Al(OH)_3$ away from the IMP interface[29,84] where the pH may differ. A potential explanation for the variation in cathodic kinetics with time is enrichment of both Al and/or transition elements to the sample surface[85,86] as well as AlO_2^- dissolution as a consequence of the alkalization of the sample surface to pH>11[29,80,86,87]. Additionally, the Al content in the alloy can lead to AlO_2^- redeposition. The strong effect of pH on cathodic activation is confirmed via tests in 0.1 M TRIS and 0.6 M NaCl buffered with TRIS environments where cathodic activation does not occur[10,11,43]. Both of these environments start with a pH of ~7 and, even after a 24 hour immersion, maintain a pH of ~7. At this near neutral pH, the dissolution and redeposition of alloying elements onto the sample surface is not thermodynamically possible [36] and therefore less cathodic activation occurs. This was observed in 0.1 M TRIS which shows little to no cathodic activation[10,11,43].

Cathodic activation can also be considered as a function of alloy composition. Examining the composition of the alloys in this study (Table 8. 1), it is shown that the CP Mg rod contained the highest Fe content which has been previously detected to enrich to the metal/oxide interface[80]. This may lead to differences in the cathodic activation process over time due to enrichment of this transition element to the sample surface[86]. Considering variation in the cathodic kinetics and OCP with time for the die-cast alloys, as well as the previously studied commercially pure Mg and AZ31 in 0.6 M NaCl[10,11,43,57], an assessment can be made on the amount of cathodic activation seen for each of these systems and how it relates to the alloying content. The greatest amount of cathodic activation (the largest variation in the cathodic kinetics

and OCP) was observed for the CP Mg material as well as AZ31B-H24 (Figure 8. 13, Figure 8. 18). There was a slight increase in the cathodic kinetics and OCP for the AM50, AM60 over the 48 hours in 0.6 M NaCl and a negligible amount of cathodic activation for AZ91 over the 48 hours; this was much less than determined previously for lower Al-content alloys (Figure 8. 13, Figure 8. 18). The variation in the cathodic kinetics and OCP can also be rationalized through considering the variation in $Mg(OH)_2$ formation. The CP Mg and AZ31 samples have the highest overall corrosion rates and therefore will produce more $Mg(OH)_2$ which may retain dissolved alloying elements and transition elements which can increase the cathodic kinetics and OCP more rapidly with time[29,87]. From the EIS determined anodic charge produced in 0.6 M NaCl (Figure 8. 16), the intrinsic corrosion rate for AM50A, AM60B and AZ91D were much lower than AZ31B and CP Mg. The lower corrosion rate may lead to less dissolution of the Mg and Al and therefore less enrichment of alloying elements to the sample surface[80,86,88,89].

8.4.5 Variation in the Corrosion Rate Due to Composition: Reflection on Weld Corrosion

It was observed, through studying the corrosion rate of several die-cast Mg-Al alloys with varying Al composition that the global corrosion rate decreased with increasing Al content. However, it was also observed, through utilization of a localization factor (LF), that these die-cast alloys were more prone to localized corrosion attack than either AZ31B or commercial purity Mg. As observed in the AZ31 TIG FZ, there are Al-Zn solidification boundaries (similar to the Al and Al-Zn solidification boundaries in the die-cast alloys) which affect the corrosion rate. The overall corrosion rate in the FZ is lower than the HAZs or wrought base plate. This may be due to the Al enrichment in the FZ (caused by Mg evaporation during processing). However, from examining the corrosion morphology, the FZ does suffer from localized corrosion damage at the interface of these solidification boundaries, similar to the die-cast alloys.

8.5 Conclusions

1. An accurate and repeatable method to determine the intrinsic corrosion rate of a variety of die-cast Mg-Al alloys has been employed herein. Each of the four methods provided (EIS analysis, mass loss, H_2 gas collection, and ICP-OES solution analysis) gives a straightforward and similar calculation of the corrosion rate, under OCP conditions for high ($\geq$3 wt%) Mg-Al alloys.

2. In order to accurately determine the corrosion rate for Mg alloys in chloride-containing environments there is little variation in the Stern-Geary determined corrosion rate for an

assortment of Tafel slope assumptions. Through this type of calculation, the EIS determined R_p dominates the given corrosion rate determination. For this reason, appropriate use of the low-frequency inductive loop must be undertaken as this inductive loop is repeatedly seen in many Mg alloys in unbuffered 0.6 M NaCl, as reported to date, in chloride-containing environments. The use of the full inductor loop gives a repeatable measurement of the EIS determined corrosion rate.

3. The corrosion rate for commercially pure Mg, AZ31, AM50, AM60 and AZ91 have been compared and, it is seen that the corrosion rate decreases globally with increasing Al content. However the localization factor increases with Al content. Deeper corrosion occurs in the die-cast alloys with ≥3 wt% Al content.

4. In terms of microstructure, the corrosion is seen to initiate in the α-Mg, frequently proximate to the Al-rich β-phase or Al-Mn IMPs in the die-cast alloys with ≥3 wt% Al content.

5. The corrosion behavior of the β-phase is seen to be complex. While it can act as a cathode during micro-galvanic corrosion of the α and β-phases as seen in the initiation of the corrosion process, it can also act as a lateral barrier to the propagation of corrosion damage from one damage site, as seen in how the corrosion propagation remains localized to single α-Mg grains. The variation in this behavior has to do with the variation in the initiation and propagation behavior of the corrosion within the Mg-Al alloys.

6. Variations in the cathodic kinetics and amounts of cathodic activation were observed with exposure environment as well as alloying content. Higher amounts of cathodic activation were observed in the alkaline environments, potentially due to the corrosion and redeposition of alloying elements (such as Al) onto the sample surface. There was less cathodic activation in the higher Al content alloys, both due to the lower corrosion rates of the die-cast alloys and modest HER reactions on the β-phase.

Table 8. 1. Compositions of 99.9% Mg Rod (Alfa Aesar) and, AZ31B-H24 ([UNS M11311] Magnesium Elektron). All compositions reported in wt. %, with the actual compositions provided by QUANT (Quality Analysis and Testing Corporation).

	UNS #	Al	Mn	Zn	Si	Cu	Ni	Fe	Mg
Mg Rod	--	0.01	0.01	0.01	0.021	0.005	0.001	0.006	Bal.
AZ31B-H24	M11311	3.02	0.33	0.99	0.025	0.005	0.002	0.005	Bal.
AM50A	M10501	5.0	0.5	0.22	<0.10	0.01	0.002	0.004	Bal.
AM60B	M10601	6.0	0.5	0.22	<0.10	0.01	0.002	0.005	Bal
AZ91D	M11916	9.3	0.15	0.99	<0.30	0.01	0.002	0.005	Bal.

Table 8. 2. Phase Fraction of Various Al-Mn IMPs in Mg-Al alloys, as determined through EBSD and image analysis.

	Phase Fraction of $Mg_{17}Al_{12}$	Phase Fraction of Al_3Mn_2	Phase Fraction of $AlFe_3$	Phase Fraction of Al_8Mn_5
Mg Rod	--	--	--	--
AZ31B-H24	--	0.1	--	0.15
AM50A	0.1	0.12	0.01	0.16
AM60B	0.5	0.42	0.02	0.23
AZ91D	0.9	0.05	0.03	0.14

Table 8. 3. Area fraction of β-phase and eutectic α+β relative to primary α-Mg as determined through ImageJ[48] image analysis.

	Area Fraction of β -$Mg_{17}Al_{12}$	Area Fraction of eutectic α+β	Area Fraction of primary α
AM50A	1	9	90
AM60B	10	10	80
AZ91D	20	5	75

Table 8. 4. Typical fitting results of electrochemical impedance measurements made on CP Mg, AZ31B AM50A, AM60B and AZ91D in 0.6 M NaCl at open circuit after 3, 12, and 24 hours of immersion, as per the equivalent circuits seen in Figure 8. 1. All runs were performed with a vertical flat cell with a 1 cm^2 sample window.

	CP Mg			AZ31B			AM50			AM60			AZ91		
	3 hrs	12 hrs	24 hrs	3 hrs	12 hrs	24 hrs	3 hrs	12 hrs	24 hrs	3 hrs	12 hrs	24 hrs	3 hrs	12 hrs	24 hrs
R_s (Ω)	81	93	100	32	31	31	19	27	26	30	33	41	23	43	41
C_1 (μF)	160	110	90	19	21	24	7	6	7	8	8	8	5	6	6
R_1 (Ω)	140	390	820	690	440	600	1870	2550	1092	1130	1460	1390	2220	4670	4630
C_2 (μF)	3600	9500	4700	40	70	48	2	12	31	69	44	45	20	30	18
R_2 (Ω)	22	77	160	310	180	300	2360	3880	1050	792	1490	1190	1670	7000	6500
L (L)	3610	9870	26200	310	230	300	3730	16900	6120	3930	3040	2360	1490	1790	650
R_3 (Ω)	100	100	100	1160	680	1150	7880	18100	3830	5740	6030	5040	5380	8130	4890
R_p (Ω)	62	83	91	470	170	320	2750	4740	1370	1440	1980	1710	2260	4790	3400

Table 8. 5. Anodic charge produced by oxidation of CP Mg, AZ31B AM50A, AM60B and AZ91D as calculated by integration of i_{corr} derived from EIS-estimated polarization resistance for three different Tafel approximations after exposure in 0.6 M NaCl at open circuit for 24 hrs.

		Tafel Assumptions				
		CP Mg	AZ31B	AM50	AM60	AZ91
B$_{king}$[37]	β_c (mV/dec)	315.0	315.0	315.0	315.0	315.0
	β_a (mV/dec)	112.5	112.5	112.5	112.5	112.5
	B (mV/dec)	36.0	36.0	36.0	36.0	36.0
	ΣQ_{EIS} (C/cm^2)	97.5 ± 18.3	15.9 ± 5.3	5.9 ± 1.0	3.1 ± 0.5	2.5 ± 0.2
B$_{Shi}$	β_c (mV/dec)	160.0	160.0	160.0	160.0	160.0
	β_a (mV/dec)	180.0	180.0	180.0	180.0	180.0
	B (mV/dec)	36.8	36.8	36.8	36.8	36.8
	ΣQ_{EIS} (C/cm^2)	99.6 ± 17.6	13.1 ± 4.5	6.0 ± 1.0	3.2 ± 0.5	2.6 ± 0.2
B$_{Cao}$	B (mV/dec)	31.1	31.1	31.1	31.1	31.1
	ΣQ_{EIS} (C/cm^2)	84.1 ± 12.2	11.1 ± 3.2	5.1 ± 0.9	2.7 ± 0.4	2.2 ± 0.2

Table 8. 6. Anodic charge consumed by CP Mg, AZ31B AM50A, AM60B and AZ91D as calculated by mass loss, hydrogen accumulation, and ICP-OES after exposure in 0.6 M NaCl at open circuit for 24 hrs.

	CP Mg	AZ31B	AM50	AM60	AZ91
Δm (mg)	6.7 ± 1.0	1.1 ± 0.4	0.3 ± 0.4	0.2 ± 0.4	0.2 ± 0.4
$\Sigma Q_{\Delta m}$ (C/cm^2)	104.9 ± 20.6	16.9 ± 5.7	7.98 ± 0.2	6.86 ± 3.9	5.78 ± 2.1
ΔV_{H2} (cm^3)	5.71 ± 1.4	1.0 ± 0.3	0.65 ± 0.4	0.3 ± 0.3	0.45 ± 0.2
ΣQ_{H2} (C/cm^2)	97.93 ± 23.6	16.6 ± 4.6	7.51 ± 1.2	2.44 ± 1.5	3.2 ± 1.8
ΣQ_{ICP} (C/cm^2)	71.55 ± 14.3	21.2 ± 8.0	6.52 ± 3.2	5.67 ± 1.6	2.54 ± 1.3

Table 8. 7. OCP and i_c for various Al containing IMPs [6,38,88,89] and Mg-Al solid solution alloys [75,90]

IMP	Solution	Immersion time	pH	i_c (A/cm^2) determined 100 mV below E_{corr}	OCP (V_{SCE})	ref
Al_6Mn	0.6 M NaCl	--	6	1×10^{-3}	-1.52	[11,74]
$AlZn_2$	0.6 M NaCl	--	6	1×10^{-2}	-1.45	[11,74]
$Mg_{17}Al_{12}$	0.1 M NaCl	--	6	1×10^{-5}	-1.2	[6]
Al_3Fe	0.6 M NaCl	--	6	1×10^{-2}	-0.74	[11,74]
Mg_2Al_3	0.6 M NaCl	--	6	2×10^{-4}	-1.18	[11,74]
2 wt% Al[15]	0.85 M NaCl + $Mg(OH)_2$	immediately	11	6×10^{-2}	-1.51	[75]
3.89 wt% Al[3]	0.85 M NaCl + $Mg(OH)_2$	immediately	11	6×10^{-2}	-1.51	[75]
5.78 wt% Al[3]	0.85 M NaCl + $Mg(OH)_2$	immediately	11	3×10^{-2}	-1.50	[75]
8.95 wt% Al[3]	0.85 M NaCl + $Mg(OH)_2$	immediately	11	9×10^{-3}	-1.49	[75]
3.43 wt% Al[3]	ASTM D1384 water [9116]	3 hours	--	5×10^{-5}	-1.49	[90]
5.74 wt% Al[3]	ASTM D1384 water [91]	3 hours	--	5×10^{-5}	-1.45	[90]
9.42 wt% Al[3]	ASTM D1384 water [91]	3 hours	--	5×10^{-5}	-1.40	[90]
5.74 wt% Al-1.19 wt% Zn[3]	ASTM D1384 water [91]	3 hours	--	1×10^{-4}	-1.43	[90]
$Mg_{17}Al_{12}$	ASTM D1384 water [91]	3 hours	--	1×10^{-3}	-1.31	[90]
$Mg_{17}(Al, Zn)_{12}$	ASTM D1384 water [91]	3 hours	--	5×10^{-4}	-1.24	[90]
Mg-6Zn[3]	ASTM-G31 [92]	--	--	5×10^{-4}	-1.56	[93]
$Mg_{17}(Al, Zn)_{12}$	0.1 M $NaClO_4$	--	--	1×10^{-3}	-1.71	[94]
Al-5.5Mn	0.138 M $MgCl_2$	12 hours	6	5×10^{-6}	-0.85	[85]
Al-5.5Mn	0.275 M NaCl	12 hours	6	5×10^{-6}	-0.75	[85]
Al-13.5 Mn	0.138 M $MgCl_2$	12 hours	6	3×10^{-6}	-0.95	[85]
Al-13.5 Mn	0.275 M NaCl	12 hours	6	3×10^{-6}	-0.95	[85]

---

[15] Single phase alloy

[16] The specified corrosive water can be prepared by dissolving 148 mg sodium sulfate, 165 mg sodium chloride and 139 mg sodium bicarbonate in 1L of distilled or deionized water.

Table 8. 8. Localization Factor for CP Mg and Mg-Al Alloys as determined through Equation 6-7

	Average Penetration Depth (μm)	Maximum Penetration Depth (μm)	Localization Factor (LF)
Mg Rod	70	300	4.3
AZ31B-H24	22	100	4.5
AM50A	10	100	10
AM60B	8	200	25
AZ91D	5	300	60
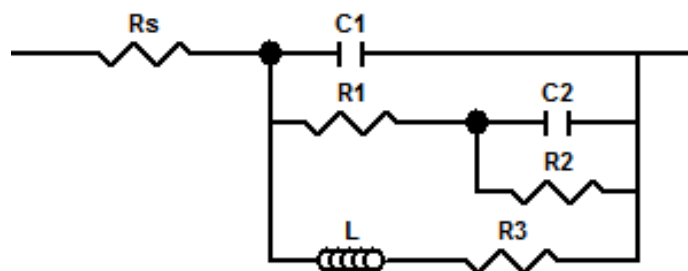
Figure 8. 1. Equivalent circuit diagram used to model pseudo-inductive electrochemical impedance response on corroding Mg in 0.6 M NaCl.
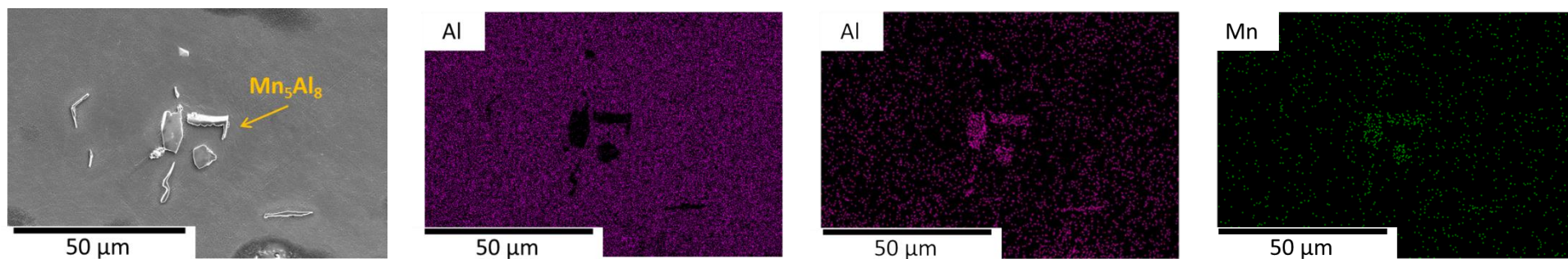
Figure 8. 2. Typical secondary phase, Mn_5Al_8 seen in the Mg-Al alloy system as shown in AM50.
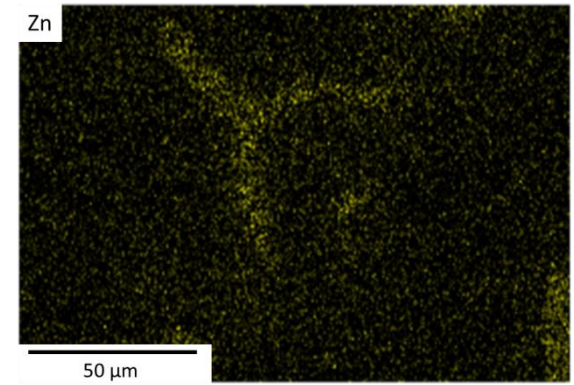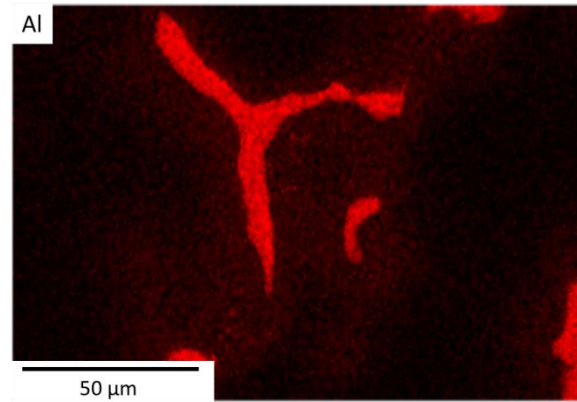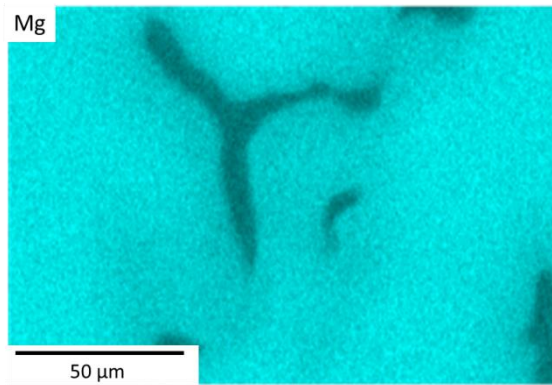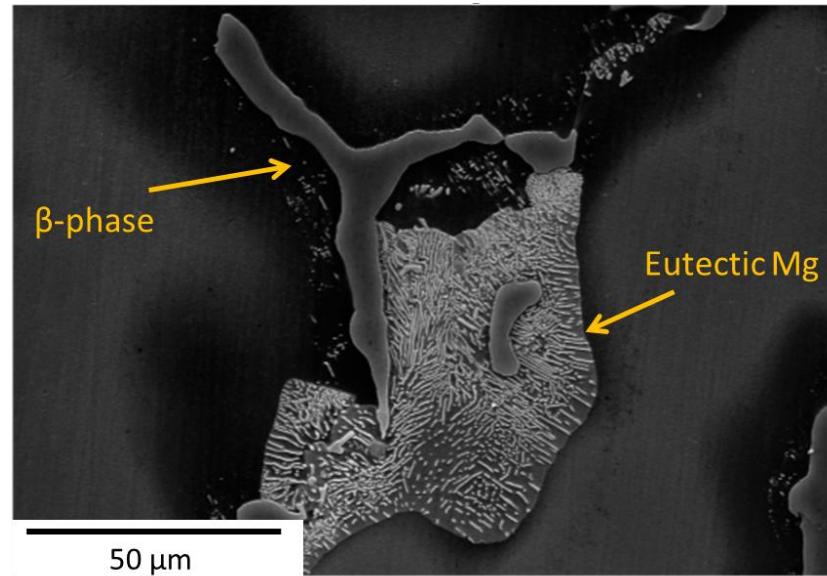
Figure 8. 3. Typical secondary β-phase, $Mg_{17}(Al,Zn)_{12}$ and the eutectic secondary phase, seen in the Mg-Al alloy system as shown from AZ91.
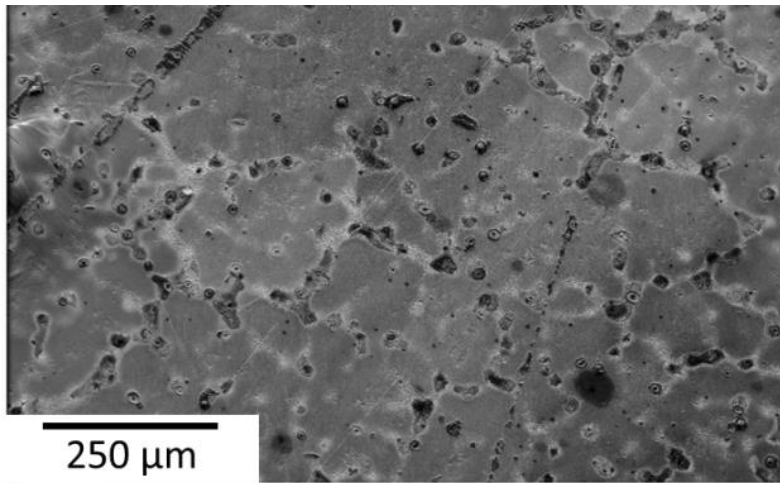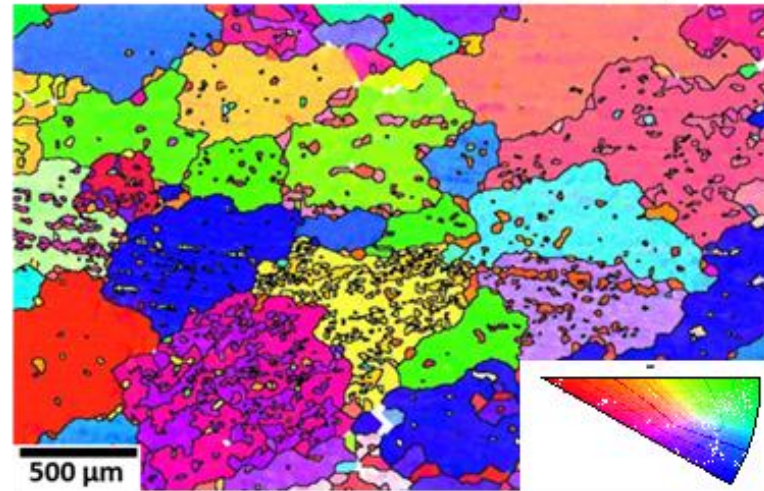
Figure 8. 4. (a) Secondary SEM image of AM50 cast alloy with (b) EBSD
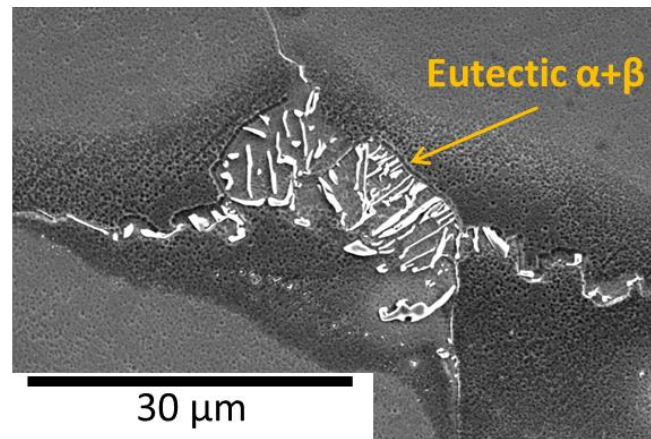
Figure 8. 5.Typical secondary β-phase, $Mg_{17}Al_{12}$ contained in a eutectic (α+β), seen in the Mg-Al alloy system as shown from AM50.
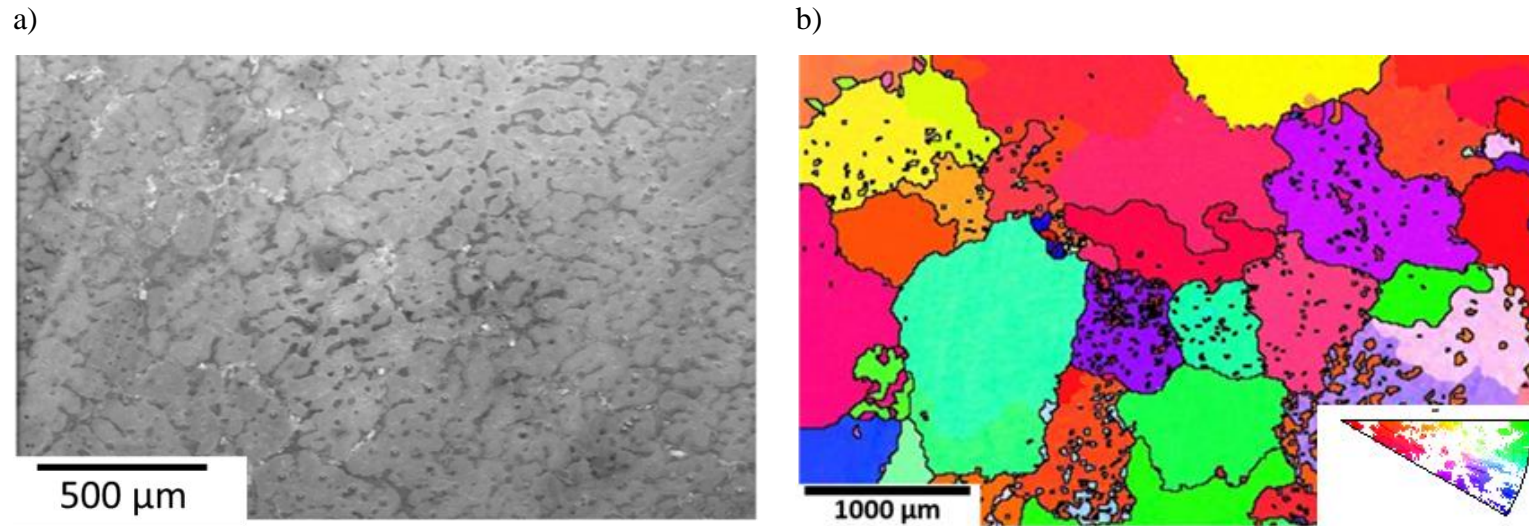
Figure 8. 6. (a) Secondary SEM image of AM60 cast alloy with (b)EBSD.
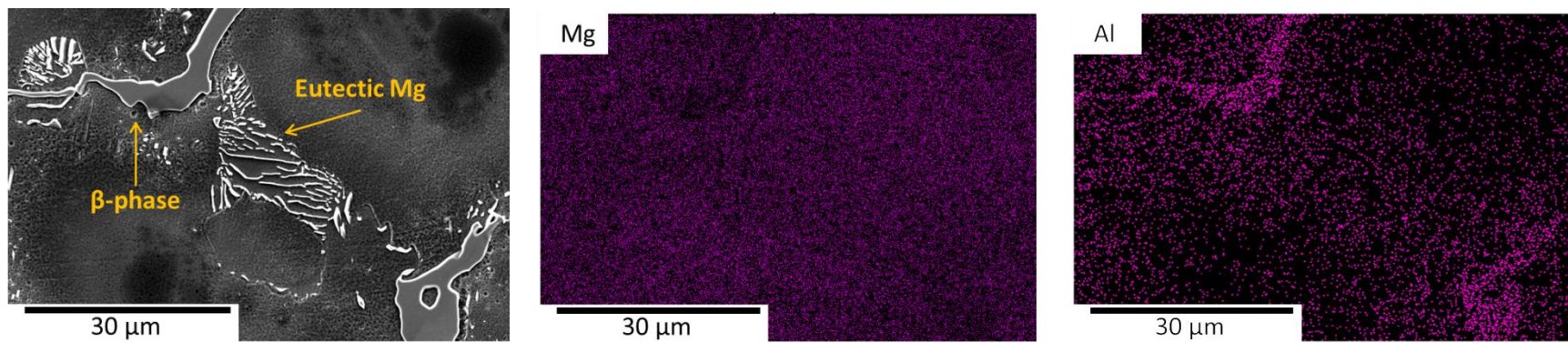
Figure 8. 7. Typical secondary β-phase, $Mg_{17}Al_{12}$ and the eutectic secondary phase, seen in the Mg-Al alloy system as shown from AM60.
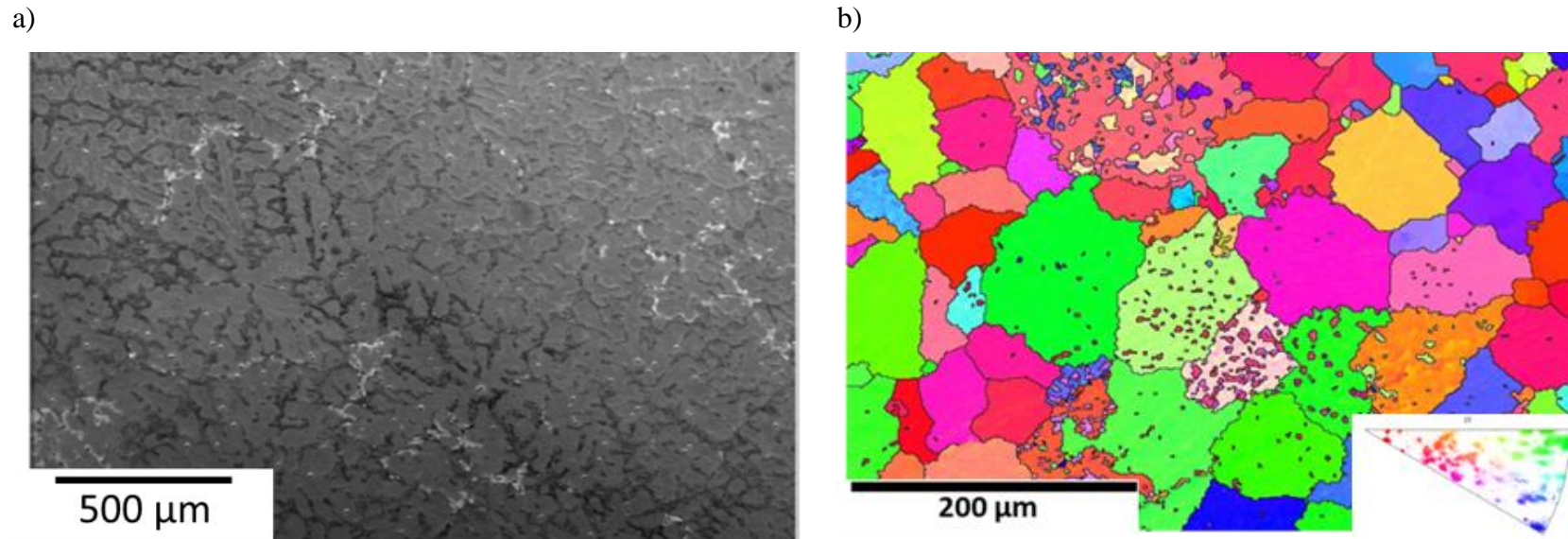
Figure 8. 8. (a) Secondary SEM image of AZ91 cast alloy with (b) EBSD.
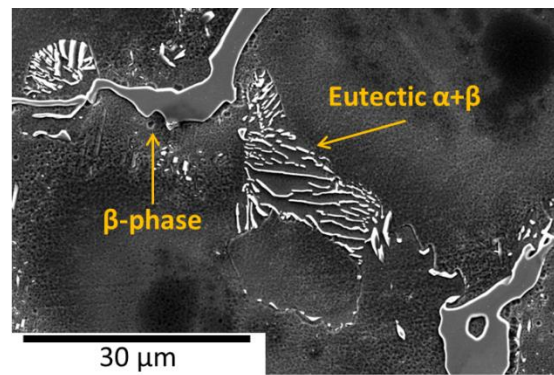
Figure 8. 9. Typical secondary β-phase, $Mg_{17}Al_{12}$ contained in a eutectic (α+β) as well as isolated β-phase, seen in the Mg-Al alloy system as shown from AZ91.

307
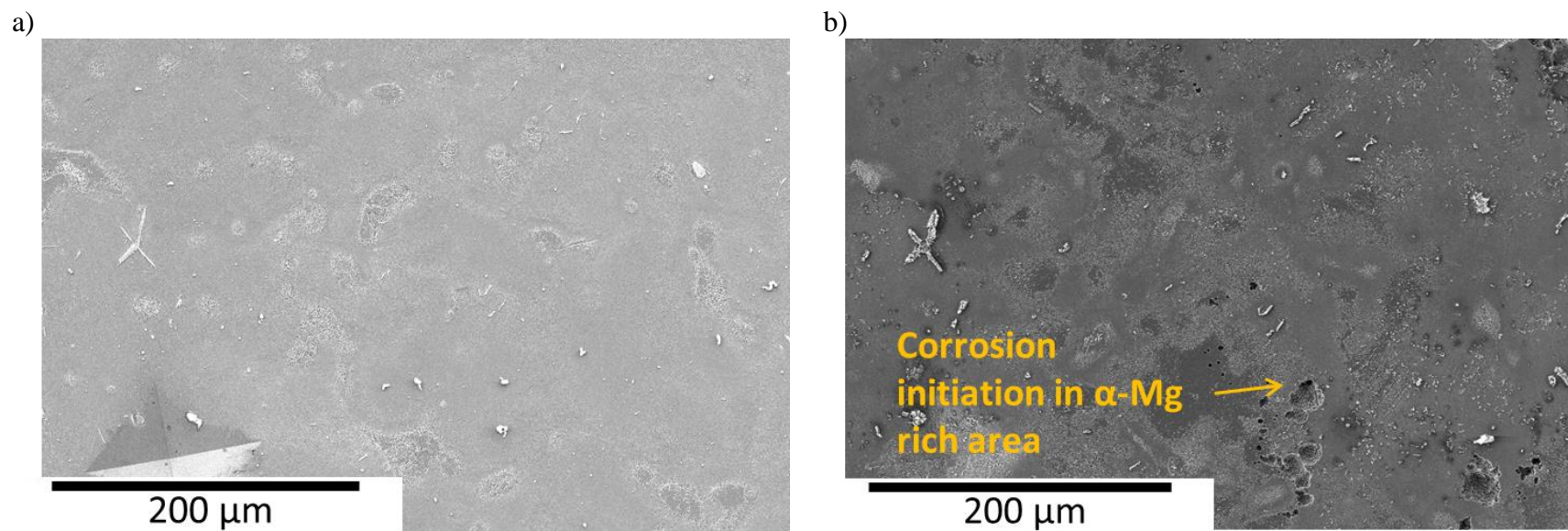
Figure 8. 10. Secondary electron micrographs of (a) AM50 sample before exposure, (b) AM50 specimen after exposure and cleaned with CrO_3 to remove any oxides after 24 hour immersion at OCP in 0.6 M NaCl.

a)

c)

Corrosion initiation in α-Mg rich area

200 μm

200 μm
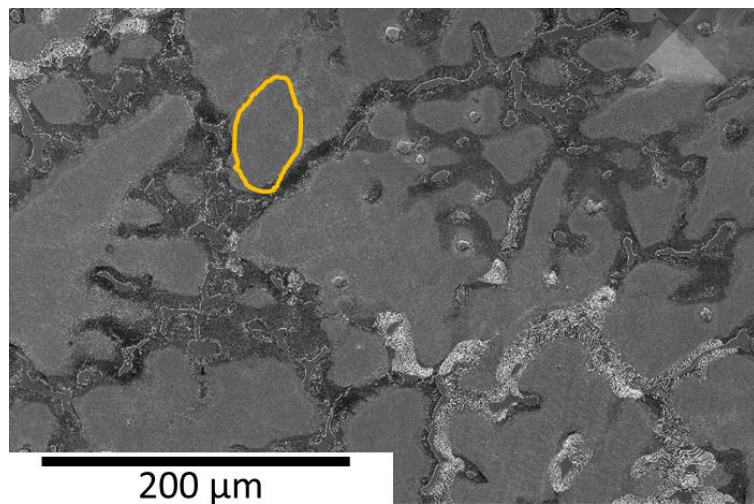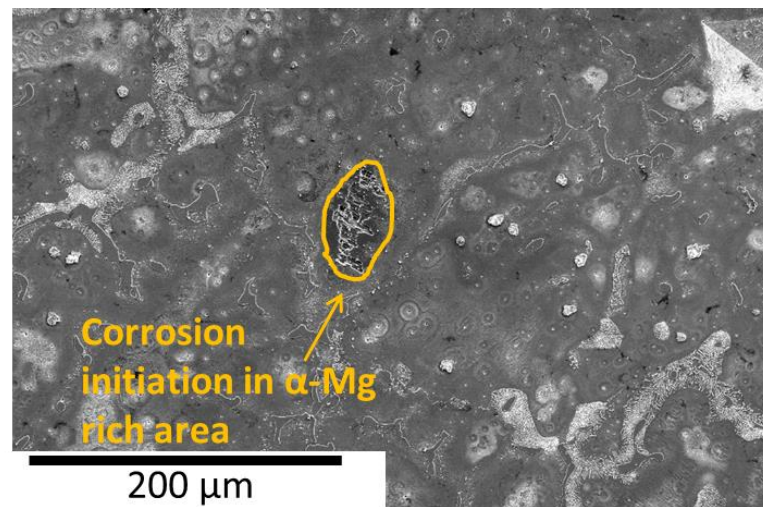
Figure 8. 11. Secondary electron micrographs of (a) AM60 sample before exposure, (b) AM60 specimen after exposure and cleaned with CrO_3 to remove any oxides after 24 hour immersion at OCP in 0.6 M NaCl.
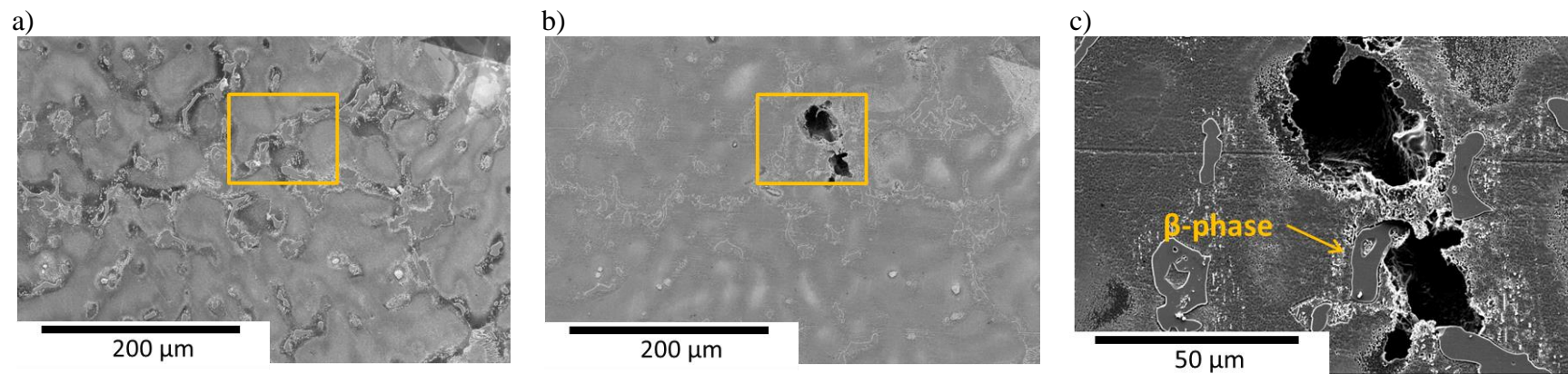
Figure 8. 12. Secondary electron micrographs of (a) AZ91 sample before exposure, (b) AZ91 specimen after exposure and (c) high magnification micrograph of corrosion damage to the α-Mg matrix. The sample was cleaned with CrO_3 to remove any oxides after 24 hour immersion at OCP in 0.6 M NaCl.

a)
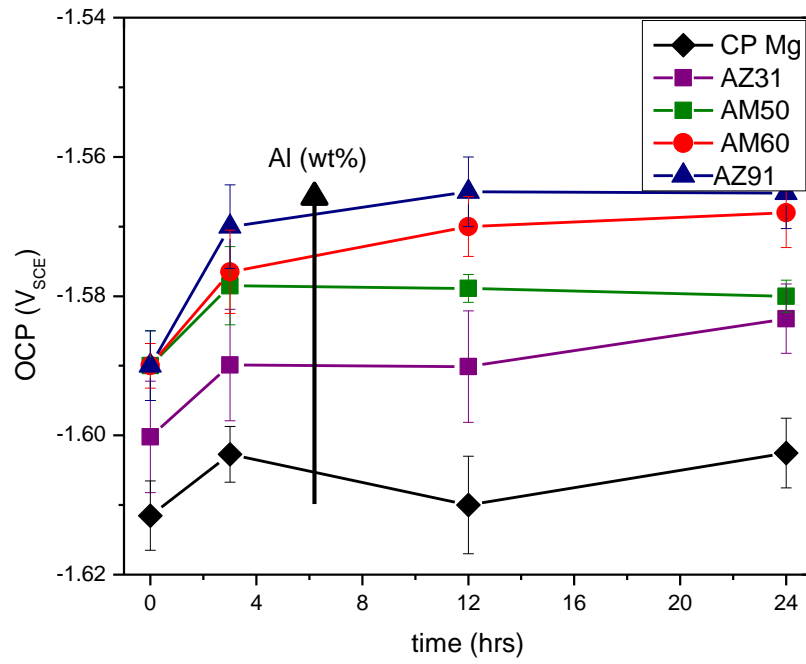
b)
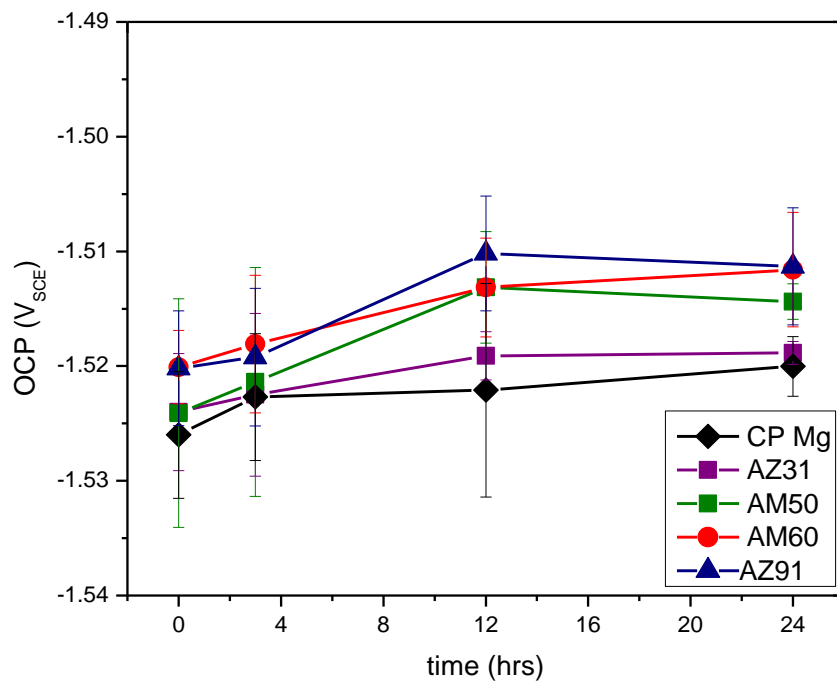
c)
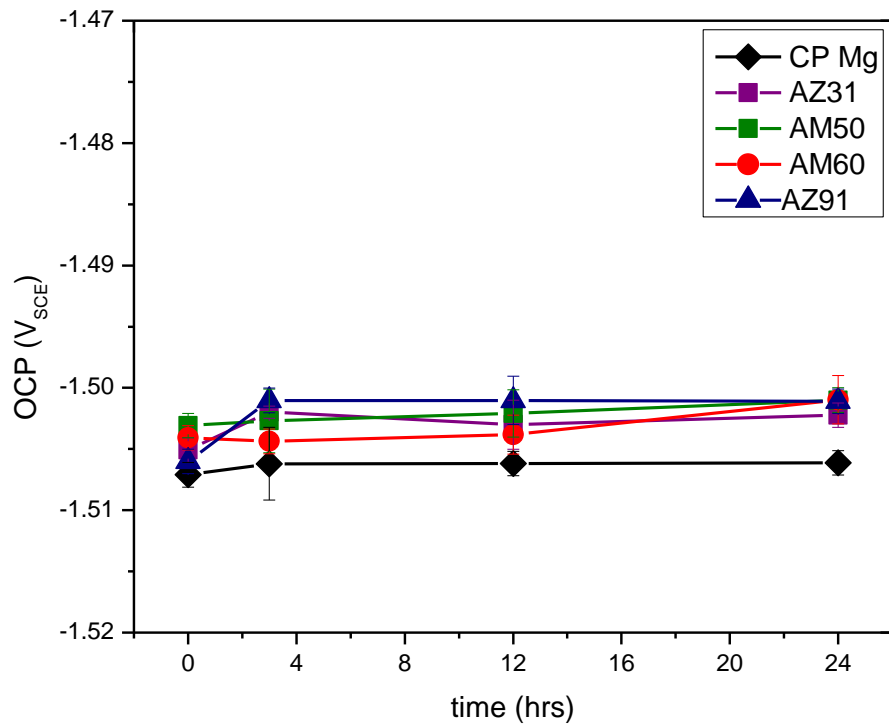
Figure 8. 13. Measured OCP for CP Mg, AZ31, AM50, AM60 and AZ91 measured at 0, 3, 12 and 24 hours in (a) 0.6 M NaCl, (b) 0.6 M NaCl buffered with TRIS to pH=7 and (c) 0.1 M TRIS.
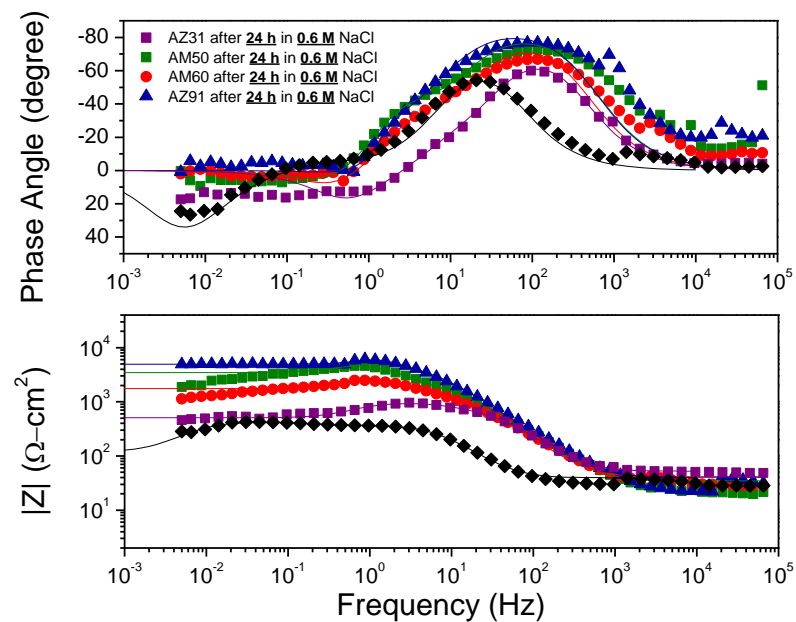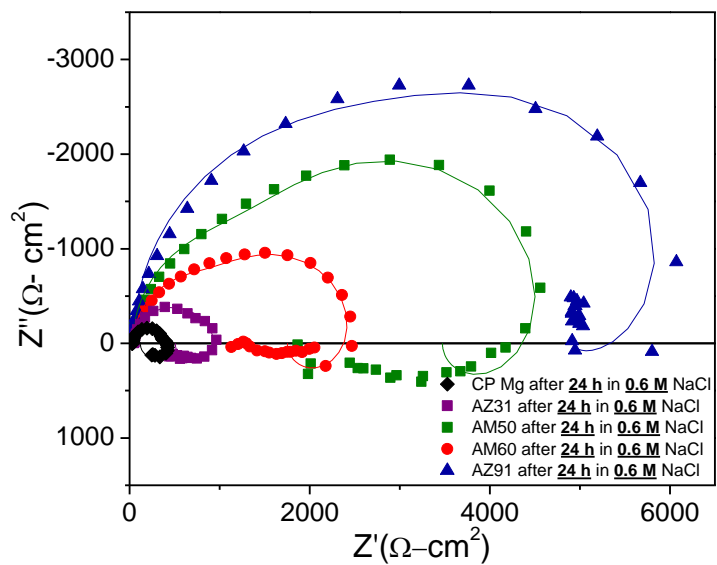
Figure 8. 14. (left) Nyquist plots and (right) Bode magnitude and phase plot for CP Mg, AZ31B, AM50, AM60 and AZ91. Data shown along with respective fits following 24 hours in 0.6 M NaCl at open circuit.
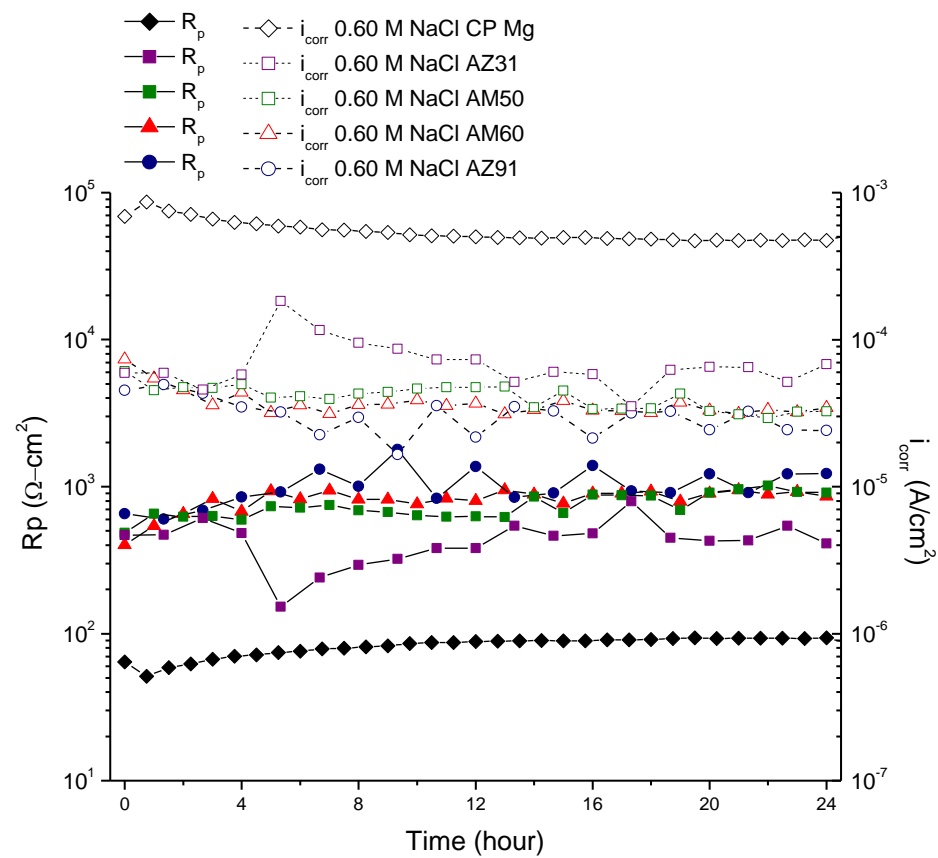
 Figure 8. 15. Typical EIS-estimated polarization resistance and corresponding corrosion current density vs. time of exposure in 0.6 M NaCl on CP Mg, AZ31B, AM50, AM60 and AZ91.
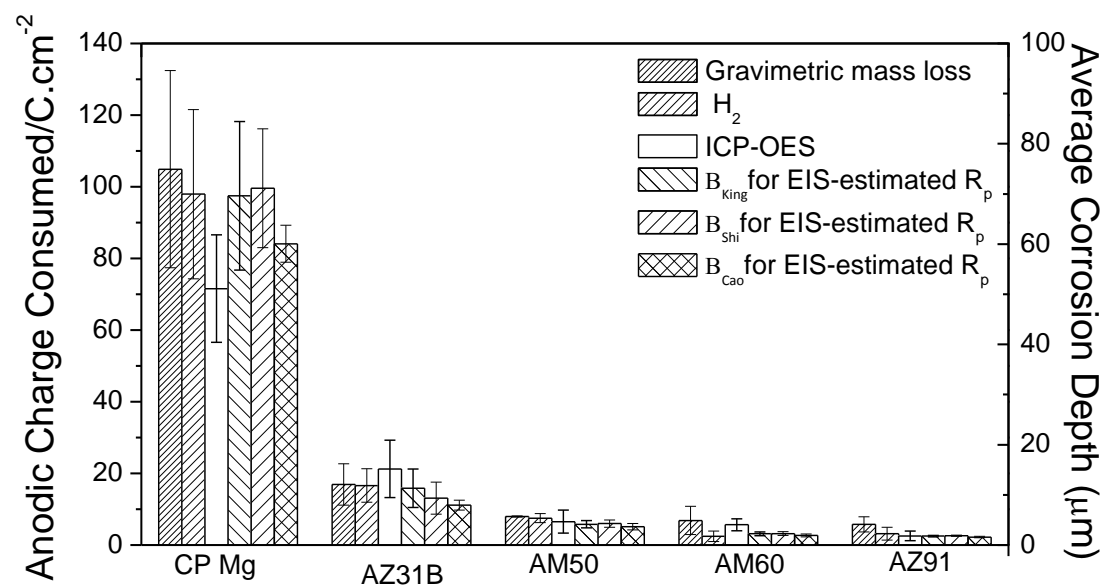
Figure 8. 16. Anodic charge consumed by wrought plate AZ31B-H24 and isolated weld zones in 0.6 M NaCl at open circuit after 24 hours immersion as estimated by gravimetric mass loss, H_2 collection, ICP-OES, and EIS-estimated R_P where B_{King}=36.0 mV, B_{Shi}=36.8 mV[53], and B_{Cao}=31.1 in 0.6 M NaCl was used[37,38].

a)
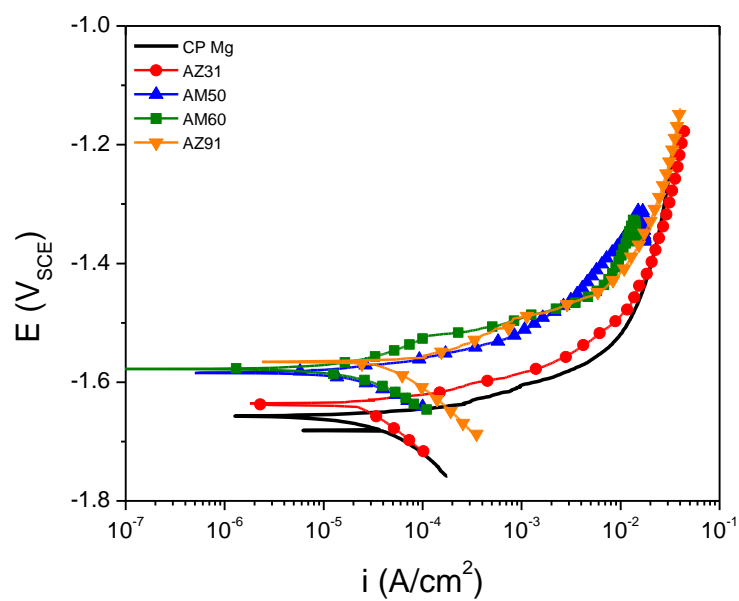
b)
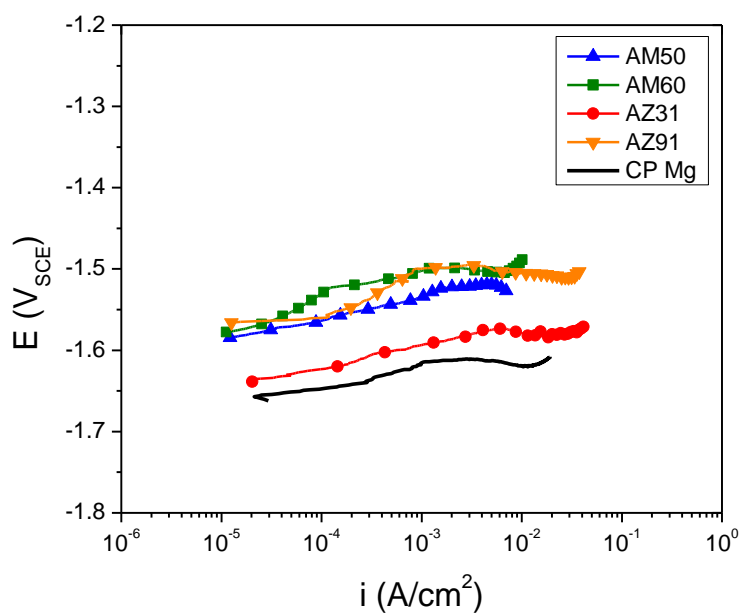
Figure 8. 17. a) Typical anodic polarization curves for 0.6 M NaCl after 24 hours at OCP and b) IR-corrected polarization plot.

a)

b)
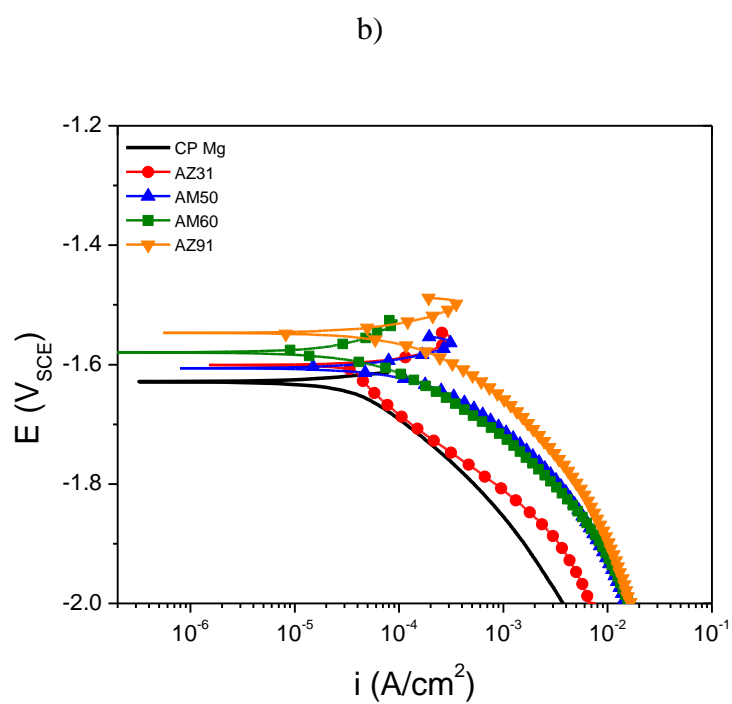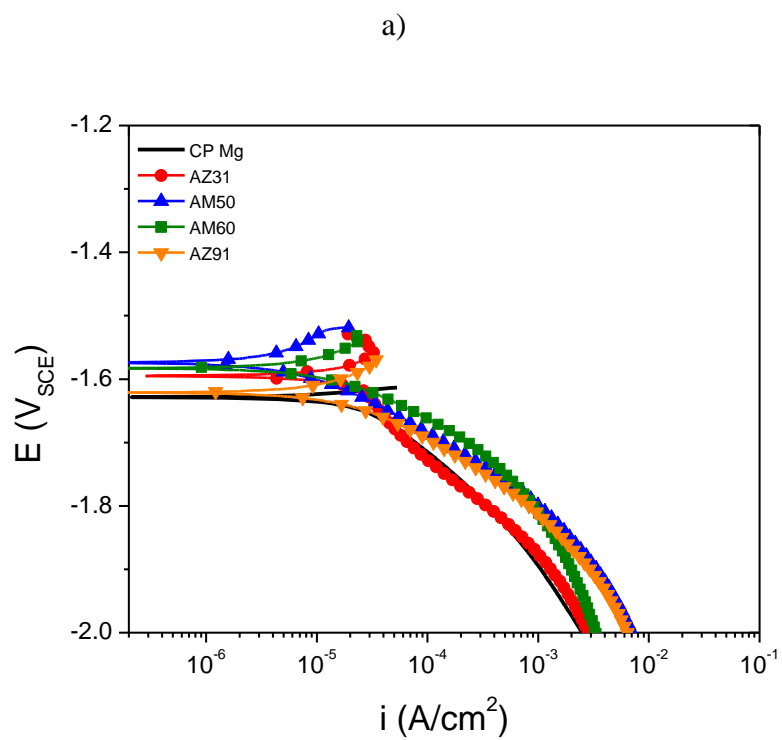
Figure 8. 18. Typical cathodic polarization curves for 0.6 M NaCl after a) 3 hours at OCP and b) 24 hours at OCP.
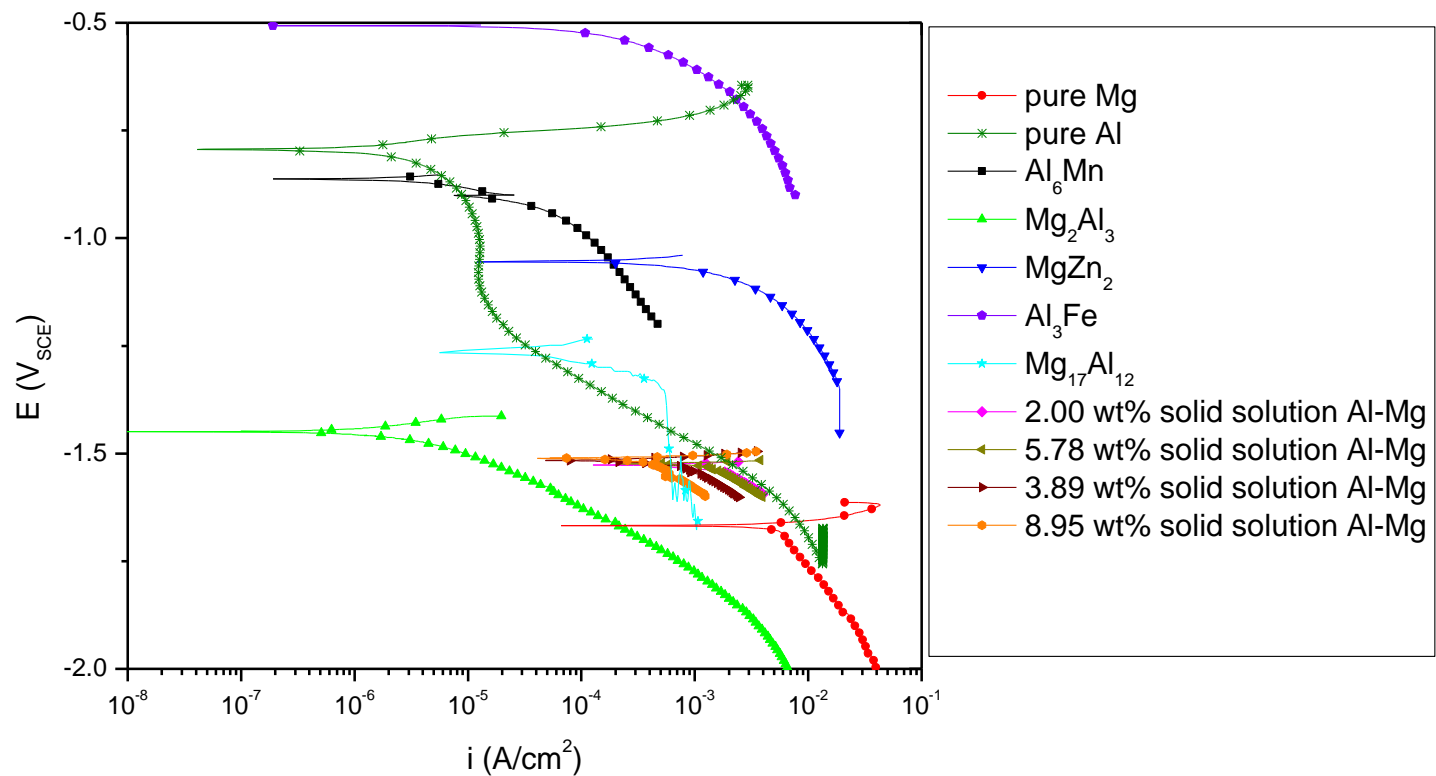
Figure 8. 19. Various cathodic polarization curves taken for Al-containing IMPs in [Cl⁻] containing environments. Curves replotted from [6,11,74,75] as well as experimental. Information on the cathodic kinetics for these curves contained in Table 8. 6.

9 Spatial Mapping of the Localized Corrosion Behavior of Magnesium Alloy AZ31 Tungsten Inert Gas Welds

Scanning Electrochemical Microscopy (SECM) and Scanning Kelvin Probe Force Microscopy (SKPFM), have been utilized to investigate the real-time corrosion of AZ31B tungsten inert gas (TIG) fusion welds, correlated with microstructure. In-situ SECM mapping was successfully performed in a partially non-aqueous electrolyte consisting of H_2O + methanol. The nature of the galvanic couples within the material (between weld zones and at localized intermetallic particle (IMP) sites) was investigated using SECM and SKPFM to map the potential differences due to various microstructural features across the weld. Variations in the activity on the solidification boundaries in the FZ as well as the IMPs in the HAZ were mapped using these in-situ techniques to better define how the microstructure alters the corrosion rate for a heterogeneous metal system. The galvanic coupling and evolution of the intrinsic corrosion behavior between the weld zones was explained using a combination of in-situ time lapse videos, SEM surface analysis, SECM, SKPFM and mixed potential theory. The effect of topology is also discussed. Micro-galvanic couples between microstructural features such as IMPs and solidification boundaries transition over time to broad areas within the material. These IMPs act as strong cathodes and dominate the corrosion processes in Mg.

A manuscript based on this chapter has been prepared to submit as a Full Research Paper, "Spatial Mapping of the Localized Corrosion Behavior of Magnesium Alloy AZ31 Tungsten Inert Gas Welds."

Representative author contributions:

L.G. Bland: scanning electrochemical experiments, electrochemical experiments, interpretation and analysis
R.F. Schaller: scanning electrochemical microscopy interpretation and analysis
S. Johns: Scanning Kelvin Probe Microscopy Experiments
M.F. Hurley: Scanning Kelvin Probe Microscopy Analysis
J.M. Fitz-Gerald: Metallurgical characterization and analysis
J.R. Scully: Adviser, interpretation and analysis

9.1 <u>Introduction</u>

Autogenous welding of magnesium (Mg) is typically performed by three main techniques which broadly includes tungsten inert gas (TIG), laser, and friction stir processes [1-9]. Regardless of the joining technique, the corrosion rate varies with alloy composition and microstructure, weld zone geometry, thickness, weld parameters, corrosion solution immersion time, and local environment [9-13]. For a specific weld system, the changes in the corrosion rate can be attributed to compositional and microstructural variations which are formed during processing and subsequent changes in surface morphology and composition during corrosion [2,3]. Specifically, there are two main zones to consider, the first is the fusion zone (FZ), in this zone, the region completely melts and solidifies during processing, characterized by variations in the crystallographic texture, grain recrystallization/growth and secondary phases formed during processing (i.e., element-rich solidification boundaries and intermetallic particles (IMPs)) [2,3,14,15]. The second series are the heat affected zones (HAZs). These zones are typically delineated within a weld zone, each having a similar composition and texture to the wrought-base but are characterized by variations in the grain growth characteristics as well as IMP coalescing through Oswald ripening [16]. The IMPs function as local cathodes and sites for fast hydrogen evolution [15,17,18]. Mapping of this reaction on the sample surface will be discussed here.

To date, weld corrosion of an AZ31 TIG weld has been studied for both the isolated weld zones [2] and galvanically connected weld zones [3]. It was shown that the corrosion behavior of the weld varied with time as well as exposure environment where polarity reversal was observed between weld zones due to variations in the cathodic kinetics with time. In particular, the variations in these galvanically connected weld zones were mapped on the millimeter scale utilizing multichannel multielectrode arrays (MMAs) in conjunction with in-situ time lapse video [3]. However, the use of mapping techniques such as SECM and SKPFM allow for smaller spatial mapping in order to better correlate microstructural features (such as IMPs and solidification boundaries) to active corrosion sites.

Localized corrosion mapping techniques, such as scanning electrochemical microscopy (SECM) [19-24], scanning kelvin probe force microscopy (SKPFM) [25-27], scanning vibrating electrode technique (SVET) [28-32] and local electrochemical impedance spectroscopy (LEIS) [33] have been utilized to probe the surface reactions on Mg alloys. Metals, which are particularly susceptible to localized corrosion processes (galvanic, micro-galvanic, or pitting), can be mapped

320

through SECM [34-37]. Moreover, SECM has been used to observe the localized corrosion events in various welds, including aluminum-alloy, stainless steel, and nickel joints [34-37]. For example, the variation in the corrosion activity in weld joints made of different metals can be mapped using SECM to determine where the weld will be most reactive [36,38]. This includes the micro-galvanic coupling between electrochemically connected weld zones caused by slight variations in each zone's electrochemical potential after processing [2,3] due to different area fractions of IMPs, solidification boundaries, and varying compositions of the α-Mg matrix.

SECM enables the mapping of both individual weld zones and complete weld regions with micrometer length scale resolution. The micrometer length scale resolution provided by the SECM is dependent on the size of the micro-electrode tip and it typically 10 to 25 μm in diameter. The SECM enables in-situ measurements of the weld zones rather than the previously applied techniques of masking or sectioning combined with MMAs for localized detection [3]. This may help to enhance the understanding of localized corrosion events in weld corrosion for future mitigation schemes.

SECM is of particular interest due to the ability to probe the anodic and cathodic reactions on the sample surface in-situ with a micro-electrode tip [23,24,39]. The various local reactions on the sample surface are specific to the anodic and cathodic reactions within the material system and require accurate use of SECM techniques, including various SECM modes, redox-mediators, step size, scanning speed and tip size [39,40]. These reactions are summarized as follows:

$$2H_2O + 2e^- \rightarrow H_2 + 2OH^-$$
Equation 9.1

$$Mg \rightarrow Mg^{2+} + 2e^-$$
Equation 9.2

Since Mg oxidation occurs with an $E_{OCP} \sim -1.63$ V_{SCE} it is easy to find mediators that have an $E_r > E_{OCP,Mg}$. The SECM can be applied in sample generation-tip collection (SG-TC) mode to probe the hydrogen evolution reaction (HER) with or without the use of a mediator [23]. Selection of an appropriate mediator for Mg is particularly difficult due to the negative reduction potential for Mg which prevents metal ions from dissolving during corrosion processes to be electrochemically converted at the microelectrode (ME) tip [39]. However, some mediators have been shown to have success in the Mg system. One such mediator is Ferrocene methanol (FcMeOH), in the feedback mode. In the latter approach, the oxidation of FcMeOH $\rightarrow$ $FcMeOH^+ + e^-$ occurs at the tip and $FcMeOH^+$ diffuses to the surface where it reduces back to FcMeOH [19]. Similarly, success has been achieved in mapping the active corrosion locations

using hexaammineruthenium(III) $Ru(NH_3)_6Cl_3$ as a mediator [20]. Here, the reduction of $Ru(NH_3)_6^{3+}$ occurs at actively corroding sites following the half-cell reaction $Ru(NH_3)_6^{3+} \rightarrow e^- + Ru(NH_3)_6^{2+}$ along with the oxidation of $Ru(NH_3)_6^{2+}$ at the tip.

The spatial resolution offered by SECM over an MMA is advantageous for mapping the development of the intrinsic weld zone corrosion rates with time, as reported elsewhere[3]. However, the fast kinetics of Mg corrosion [41,42] and the large amount of hydrogen gas evolved creates convective flow in the electrolyte around the electrode tip, thus interfering with the detection of the mediator at the tip, making optimization of SECM on Mg difficult [39]. However, the choice of an appropriate mediator and a less corrosive, non-aqueous electrolyte can alleviate some of these issues [19]. Some success has been found for mapping Mg using a methanol electrolyte[43]. A non-aqueous electrolyte, such as ethelyne glycol or methanol mixed with a NaCl solution was found to slow the kinetics of Mg corrosion, while still enabling mapping of the active corroding sites on the Mg surface [19]. Similarly, the galvanic relationships in the SECM electrolyte must be considered as they can alter the cathodic and anodic characteristics of the material observed in chloride. This is particularly important for Mg, which is susceptible to micro-galvanic corrosion due to small differences in the electrochemical potential between the α-Mg matrix and second phase particles, as well as solidification boundaries formed during fusion processing. These galvanic current differences will be important to spatially resolve the corrosion rate across the weld surface, particularly since polarity reversal has been shown, in this work, to occur between AZ31 TIG weld zones in chloride environments [3].

Another scanning technique, SKPFM, can be used to characterize the localized variations in surface potential or work function along a sample surface arising from surface heterogeneities, such as IMPs [25,44]. The observed composition dependent surface potential differences can then be used to predict and interpret corrosion behavior. SKPFM can be used to measure the work function (Volta potential) of various phases formed in the weld during processing [1] with sub-mircron resolution. The range of Volta potentials for Mg-Al alloys as well as many Al-Mn phases within these materials has been established previously[25]. The variation in these Volta potentials can give an indication of the probability of the development and direction of galvanic couples during active corrosion conditions [45,46]. This technique is important to characterize the variation in IMP density and resultant corrosion properties due to the individual, intrinsic

properties of various cathodic IMPs in the α-Mg matrix at a much finer resolution than offered by SECM.

In this research, the ability to spatially map the actively corroding regions within an AZ31 TIG weld was explored using the in-situ SECM technique and SKPFM. The SECM and SKPFM maps across AZ31 weld zones were correlated with active corroding sites, taking into account characteristics of Mg welds such as microstructure, polarity reversal, and anodically induced cathodic activation [28,32,47,48].

9.2 <u>Experimental Approach</u>

9.2.1 Materials

Commercially pure magnesium rod (99.9%) supplied by Alfa Aesar was used in this study along with AZ31B-H24 sheet supplied by Magnesium Elektron. Commercially pure Mg rod (99.8%) and Al (99.9%) was used to test the viability of methanol as an electrolyte while AZ31B was used for experimental mapping. All compositions are reported in wt. %, provided by QUANT (Quality Analysis and Testing Corporation) via Inductively Coupled Plasma optical Emission Spectroscopy (ICP-OES) analysis as given in Table 9.1.

9.2.2 Weld Metallurgical Characterization

All samples were fabricated by TIG welding a sandwich structure geometry as shown in (Figure 9. 1). The top plate was drilled and countersunk at 45° to approximately 0.635 cm in diameter and welded to the bottom plate along the periphery of the countersunk hole. A Miller Syncrowave 200 TIG was operated at 125 amps under Ar at 48.3 kPa with a flow rate of 18.5 L/min, and air cooled without a copper chill plate. This process created large metallurgical weld zones (7 mm, 2 mm, 9 mm for the FZ, HAZ1 and HAZ2 radius respectfully), amenable to this study. All samples were prepared on material freshly ground to 240 grit to remove any oxides formed prior to processing. All samples were examined along the SL surface, polished with colloidal silica and etched with a picric acid etch (3g picric acid, 30 mL acetic acid, 100 mL ethanol and 15 mL distilled water) to determine the weld microstructure.

Samples were analyzed with optical microscopy using a Hirox optical microscope as well as scanning electron microscopy (SEM) using a FEI Quanta 650. Semi-quantitative compositional analysis was performed using energy dispersive x-ray spectroscopy (EDS) methods with ZAF corrections (where Z is the atomic number correction, A is the absorption

correction and F is the fluorescence correction) on the Aztec software tool [49]. Micrographs were recorded at a working distance of 10 mm while operating at an accelerating voltage of 5 kV. Electron Backscatter Diffraction (EBSD) was performed while operating at an accelerating voltage of 20 kV and a working distance of 15 mm.

9.2.3 Galvanic Corrosion Determination of Metals in Non-aqueous Electrolye

The galvanic currents of coupled commercial purity Mg and high purity Al planar electrodes spaced approximately 15 cm apart were determined using a zero resistance ammeter (ZRA) in a flat cell in 0.1 M NaCl solution combined with increasing amounts of methanol, from 0 to 100% methanol [50,51]. This test ensured that the galvanic polarity between Mg and Al remained the same in methanol. Mg was designated as the working electrode (WE) while 99.9 % pure Al was designated as the counter electrode (CE). The cathode to anode ratio was kept at 1:1 in a flat cell with a 1 cm^2 exposure area. All galvanic couples were tested at least three times and characteristic runs are reported herein.

Increasing amounts of methanol, from 10 wt% to 100 wt% were substituted as the electrolyte to determine how the cathodic kinetics varied with these non-aqueous additions. The cathodic kinetics were determined after 3 hours at OCP in 0.1 M NaCl followed by a cathodic potentiodynamic polarization scan ranging from 0.5 mV above OCP to -2.3 V below OCP in a downward sweep at a rate of 1 mV/second. The corrosion rate in these same electrolytes is discussed elsewhere[43].

9.2.4 Scanning Electrochemical Microscopy

Scanning Electrochemical Microscopy (SECM) was performed with a VersaSCAN motion controller and VersaSTAT 3 potentiostat. A 25 μm Pt ME and Ag/AgCl reference electrode were used for data measurement. Before testing, the ME tip was polished using 0.25 μm polishing paste and rinsed with ethanol to ensure a clean probe tip surface. Samples were polished in ethanol through 1 μm. Tests were initially conducted with various amounts of non-aqueous methanol added to solution to slow the cathodic kinetics of the Mg system. This is particularly important as the HER creates stirring of the solution at the UME tip which is known to make spatial mapping of Mg with the SECM difficult. A solution of 50 wt% H$_2$O, 50 wt% methanol in 0.1 M NaCl was selected (as determined from corrosion studies[43]). Based on the ability to spatially map the HER while maintaining a steady tip current throughout the duration of the scan, Ru(NH$_3$)Cl$_6$ was selected as the mediator. The Ru system had the highest longevity

324

and greatest ability to map areas of Mg^{2+} dissolution on the weld surface. The reduction of $Ru(NH_3)_6^{3+}$ occurs at actively corroding sites following the half-cell reaction $Ru(NH_3)_6^{3+} + e^- \rightarrow Ru(NH_3)_6^{2+}$ along with the subsequent oxidation of $Ru(NH_3)_6^{2+}$ at the tip (Figure 9. 2). For all scans, the Pt ME tip was positioned 30 µm away from the sample surface and polarized at -100 mV. Slow area scans were run at 100 µm/s with a step size of 10 µm while fast scans were was run at 200 µm/s with a step size of 50 µm.

The cyclic voltammogram (CV) of the solution (taken far from the sample surface) shown in Figure 9. 3(a) was recorded at 100 mV/s using a 25 µm diameter Pt ME in a solution of 50 wt% H_2O, 50 wt% methanol with 0.1 M NaCl + 1 mM$Ru(NH_3)_6^{3+}$. A steady-state signal of 2000 pA was determined during the anodic sweep for E > -250 mV (vs. Ag/AgCl). A set polarization voltage for the ME of -100 mV (vs. Ag/AgCl) was selected for all SECM measurements. The Pt ME was positioned 30 µm above the Mg sample surface using an approach curve, conducted at 100 µm/s (Figure 9. 3(b)). The ME tip approached the surface until a maximum current (approximately 80% of the steady-state signal as determined from the anodic sweep) was measured and then the tip was set at 30 µm above this location.

9.2.5 Scanning Kelvin Probe Force Microscopy

AZ31B TIG-weld sample surface preparation

Prior to SKPFM imaging, the TIG welded AZ31B sample surface was initially mechanically polished at 350 rpm with successively finer grit SiC abrasive paper (LECO wet/dry 600, 800, 1200 grit) using water lubrication. To prevent corrosion during polishing, final polishing was conducted without water in a 1:3 mixture of glycerol (Fisher Chemical, Certified ACS, ≥99.5 %) to denatured ethanol (UltraPure, ACS/USP grade, 190 proof). Alumina powders (Electron Microscopy Sciences 3.0 µm Al_2O_3, 1.0 µm Type DX α-Al_2O_3, and 0.05 µm Type DX γ-Al_2O_3) were mixed with the glycerol/ethanol lubricant to make slurries. Residual polishing compound was removed using a clean polishing pad saturated in ethanol prior to ultrasonication in ethanol for 30 seconds, and blown dry with clean, compressed air. To aid in co-localization of SKPFM and SEM/EDS, cross-shaped fiducial markers were inscribed on the sample surface in each of the regions of interest (FZ, HAZ1, and HAZ2) using a Cascade Microtech MH2-B high resolution manual micropositioner tip.

Corrosion

For post-corrosion imaging, corrosion of the sample was conducted by immersing the sample in 0.6 M NaCl solution for 1 minute. The sample was then rinsed with deionized water for 5 seconds, followed by a 5 second rinse with acetone, sonication for 30s in ethanol, air dried with compressed air. The amount of corrosion damage was relatively less than seen in the SECM experiments due to the sensitivity limitations of tracking surface topography with the AFM.

Scanning Kelvin Probe Force Microscopy

SKPFM was performed on a Bruker Dimension Icon atomic force microscope (AFM) operating in PeakForce frequency modulation mode (PF FM-KPFM). The procedure employed has been described in detail elsewhere[25,45,52]. Briefly, after a first pass to acquire the sample topography using PeakForce tapping mode (rapid force curve acquisition), the AFM probe retraced the sample topography at a constant lift (offset) height of 100-150 nm. During this interleaved lift mode pass, the probe was oscillated at its natural resonance frequency, f_0, by a dither piezo while a 5 V AC bias was simultaneously applied at a frequency of $f_{AC} = 2$ kHz. The difference in potential between the KPFM probe (Bruker PFQNE-AL, $k = 0.8$ N/m, $f_0 = 300$ kHz, $r_c = 5$ nm) and the sample surface was then nulled by applying a variable DC bias to the sample, as evidenced by the disappearance of the probe oscillation sidebands at $f_0 \pm f_{AC}$. This variable DC bias provided a direct measure of the difference in surface potential between the KPFM probe and the sample as the probe rastered above the surface, resulting in a surface potential map of the sample. To enable quantitative surface potential measurements and comparison with data from other samples, a KPFM standard consisting of aluminum (Al) islands surrounded by gold (Au) patterned on a silicon (Si) wafer was imaged before and after the TIG welded AZ31B sample. This allowed referencing of all measured surface potentials relative to gold (as opposed to the probe), which was chosen as a standard due to its inertness/nobility[25]. All image processing and analysis were carried out using NanoScope Analysis version 1.50 (64 bit).

Scanning Electron Microscopy (SEM)

SEM corresponding to the SKPFM (performed at Boise State) was carried out on a Hitachi S-4300N equipped with a tungsten filament electron source and an Oxford Instruments Energy EDS detector. To minimize carbon deposition and resultant impact on the sample (including its corrosion behavior), secondary electron (SE) imaging was performed using an acceleration voltage of 5 keV. EDS was conducted at 20 keV to construct elemental maps for identification of the phase(s) present in each region of the sample. Using the fiducial markers

326

and unique surface features present, SE images and EDS maps were overlaid on previously acquired SKPFM images of the same region to correlate elemental composition of observed microstructural phases with measured differences in nanoscale surface potential. Pre- and post-corrosion SEM imaging were carried out after the corresponding SKPFM imaging due to carbon deposition by the electron beam, which could affect the surface potentials measured via SKPFM[25,45,53]. Likewise, post-corrosion imaging was conducted in a region near, but not overlapping, pre-corrosion imaging to ensure SEM-induced carbon deposition did not affect the measured SKPFM surface potentials or observed corrosion behavior.

9.3 Results

9.3.1 AZ31 alloy Microstructure

The microstructures of the starting AZ31 wrought base plate along with the FZ and HAZs of a TIG weld samples are shown in Figure 9. 4(a-c). The base material is characterized as heavily twinned with Al-Mn and Al-Mn-Fe IMPs distributed randomly throughout the α-Mg matrix (Figure 9. 4(a)) as determined through EDS (Table 9. 1). The composition of these IMPs, as determined by EDS, was consistent with $(Fe,Mn)Al_6$ and Al_4Mn, two common IMPs cited for Al-Mn containing Mg alloys [15,54,55]. The FZ shows a high density of the Al-Mn and Al-Mn-Fe IMPs throughout, as well as solidification structures which have been shown previously to be rich in Al and Zn (Table 9. 1) [2]. Two HAZs have been identified in an AZ31 TIG weld, both of which consist of a similar composition to the AZ31 wrought base plate with slightly larger Al-Mn and Al-Mn-Fe particles throughout. Due to the high temperatures imposed during welding, this region has undergone a large amount of grain growth, leading to twin-free grains on the order of 20 μm. This microstructure has been described in more detail elsewhere [2,3].

The corrosion morphology in 0.6 M NaCl made of a 100% aqueous solution, after 3 hours at OCP, was observed by electron microscopy. The resultant morphology in the AZ31 base material (Figure 9. 4 (a)) has corroded by the filiform mechanism [56]. This morphology is similar to what is seen in the HAZ (Figure 9. 4 (c)). However, a different morphology is observed in the FZ, as the corrosion propagates along the Al-Zn solidification boundaries, most likely due to the galvanic coupling between the α-Mg matrix and the Al-Zn boundaries. An analysis of this corrosion morphology and the resultant corrosion properties of both the isolated and galvanically connected weld zones is not the main topic of this paper and is described elsewhere [2,3].

Corrosion morphology was also observed in a 0.1 M NaCl solution made of 50 wt% H_2O + 50 wt% methanol to determine the effect of methanol on the resultant corrosion morphology (Figure 9. 5). In each of the weld zones, approximately the same corrosion morphology was observed as in NaCl without methanol[3,57]. In the wrought base as well as the HAZ, filiform corrosion was seen to be the dominant corrosion mechanism. An IMP (previously identified as Al-Mn) is circled in both images, showing that many of the IMPs remain after corrosion. In the FZ, a greater amount of the surface remained uncorroded, but the corrosion had propagated in a similar manner, along the Al-Zn solidification boundaries [2,3].

9.3.2 Corrosion Electrochemistry of Commercially Pure Mg in Varying Amounts of Non-Aqueous Methanol

Galvanic Corrosion Between Mg and Al

The galvanic corrosion potential between commercially pure Mg and 99.9% pure Al in varying wt% of methanol was measured over a 24 hour period in 0.1 M NaCl in a zero resistance ammeter (ZRA) configuration (Figure 9. 6(a)). The galvanic potential between the two metals decreased with increasing amounts of methanol. The galvanic current density was measured for these same environments (Figure 9. 6(b)). The galvanic current also decreased with increasing amounts of methanol.

Open Circuit Potential and Cathodic Kinetics

The variation in the OCP for commercially pure Mg with increasing amounts of methanol is shown in Figure 9. 7, taken in 0.1 M NaCl after 24 hours at OCP. It was generally observed that the OCP increased with the addition of methanol to the solution. Also, the cathodic kinetics were observed to decrease with an increase in the methanol content. In pure H_2O, the measured OCP was -1.57 V_{SCE} while the cathodic kinetics (determined at -1.8 V_{SCE}) were 1.3×10^{-3} A/cm^2. Alternatively, the measured OCP for the 100 wt% methanol solution was -1.52 V_{SCE} with cathodic kinetics of 1.3×10^{-4} A/cm^2 showing that the addition of methanol can decrease the cathodic kinetics by a full order of magnitude. Even replacing small amounts of the solution with methanol can dramatically decrease the overall corrosion kinetics on commercially pure Mg. For proper analysis of the in-situ spatial mapping on Mg alloys, a balance has to be met for an environment with slow kinetics while also still being able to map active corrosion as it would in an aqueous solution. From this analysis, 0.1 M NaCl with 50 wt% H_2O + 50 wt% methanol was selected. Corrosion rates in various amounts of methanol using EIS and mass loss are reported

elsewhere[43] and the corrosion rate of commercial purity Mg decreases with increasing methanol content.

9.3.3 Scanning Electrochemical Microscopy

SECM on AZ31B Wrought Base

SECM was performed on an AZ31B wrought-base plate with a corresponding SEM micrograph (Figure 9. 8). On the SEM micrograph (Figure 9. 8(a)) several IMPs (previously shown to be Al-Mn [2,15]) are heterogeneously spaced on the sample surface. The sample was immersed in an environment of 0.1 M NaCl containing of 50 wt% H_2O + 50 wt% methanol and 1 mM $Ru(NH_3)Cl_6$ and exposed for approximately 30 minutes. This provided sufficient time for active corrosion to initiate in the H_2O/methanol mixture. After approximately 1 hour, the IMP clusters (labeled as 1 and 2 in the SEM and the resulting SECM scans of current and identified as $Al_8Mn(Fe)_5$ via EDS[15,57]) indicated a higher SECM current than observed in the area surrounding this high SECM current, correlated with active corrosion (Figure 9. 8(b)). After the scan was completed, the SECM ME was removed from solution, cleaned, and repositioned 30 μm above the sample surface (via an approach curve) to account for any change in the sample height from corrosion as well as to clean the probe tip surface. After approximately 3 hours of immersion, the region around the Al-Mn IMP still exhibited a high current, indicative of a highly active corrosion area. However, the measured current was not localized to the IMP/α-Mg but had begun to expand over the sample surface (Figure 9. 8(c)). This current expansion or spreading was subsequently seen during the following in-situ scan (Figure 9. 8(d)).

SECM was replicated with a corresponding SEM micrograph (Figure 9. 9). Two groups of IMPs (labeled as 1 and 2) were identified on the AZ31 SEM micrograph and shown to correlate with the SECM scan area with high activity (Figure 9. 9). After the first scan (taken immediately after immersion), Group 1 showed a higher measured current and active corrosion while Group 2 was not active (Figure 9. 9(b)). However, after 3 hours, Group 2 appeared active while Group 1 was not (Figure 9. 9(c)).

SECM on AZ31B TIG Weld

An optical micrograph of an AZ31 TIG weld is overlaid on the same scale as the SECM scan to better understand the sections of a weld in cross-section along with the SECM scans of current (Figure 9. 10(a)). SECM scans on this specimen, performed immediately after immersion shows that some areas of the weld have locally high currents and are actively corroding. These

regions are heterogeneously located along the sample surface (Figure 9. 10(b)). A second scan, taken after 3 hours of immersion, show that these active regions have expanded and additional regions became active, as determined via the reduction of $Ru(NH_3)_6^{3+}$ (Figure 9. 10(c)). A final SECM scan, after 6 hours of immersion, demonstrated that the sample surface is uniformly active and fully corroding (Figure 9. 10(d)).

SECM was performed on an AZ31B TIG weld with a fast line scan rate (200 µm/s) and large step size (50 µm). Due to the large size of the weld, a fast scan rate provided the best conditions to acquire an overall image of the actively corroding zones of a weld without the Pt ME degrading its ability to support fast electron transfer (ETR). An optical micrograph of an AZ31 TIG weld is overlaid the same scale as the SECM current scan to better understand the sections of a weld in cross-section along with the SECM scans of current (Figure 9. 11). The FZ is along the bottom of the optical micrograph as well as on the SECM images (Figure 9. 11(a-b)) while the HAZs are along the top of the images (Figure 9. 11(a,c)). The SECM scan was started each time in the FZ and ended in the HAZ. Therefore, it can be concluded that the lower current in the SECM is not simply an artifact of the ME tip degrading with time. The same trend was shown for scans that started in the FZ and ended in the HAZ (excluded for brevity). It was observed during the first SECM scan that the FZ had the lowest current while the HAZ had the highest measured current (Figure 9. 11(b)). This corresponds to the FZ not corroding while the HAZ actively corroded[18]. In the second SECM scan, it was observed that the FZ had the highest measured current while the HAZ had a lower current (Figure 9. 11(c)) which corresponded to the FZ being the actively corroding weld region. This variation in the galvanic polarity reversal as a function of weld zone with time is indicative of the polarity reversal previously noted in AZ31 TIG welds [3].

SECM was performed on an AZ31 TIG weld, left to corrode in the 50 wt% H_2O + 50 wt% methanol and 1 mM $Ru(NH_3)Cl_6$ environment for 12 hours. The sample was fully corroded and a typical corrosion morphology had developed across the full sample [2]. The corrosion morphology observed in the SECM exposure environment was similar to features previously observed in 0.6 M NaCl (Figure 9. 12(a)) [2,3,15]. A specified location, labeled 1 on the optical micrograph, correlates to a corroded region of filiform corrosion. In the SECM scan of current, location 1 is also identified as it correlates to the optical micrograph (Figure 9. 12(b)). This region appeared as a low measured current on the sample surface but topographical changes

occurred. Therefore, after the long exposure time, the probe tip current measured at the SECM tip was dominated by morphological features rather than by enhanced current due to active corrosion.

9.3.4 Scanning Kelvin Probe Force Microscopy

SKPFM of AZ31B Weld FZ

SKPFM was conducted to further investigate the weld microstructure influence on corrosion evolution. The high spatial resolution of SKPFM Volta potential measurements provided greater detail on expected micro-galvanic activity originating between microstructural features. The FZ of an AZ31 TIG weld typically had a relatively higher density of Al-Mn type particles (Figure 9. 13) than the base metal or HAZ zones. A representative area of the FZ is seen in Figure 9. 13 along with the co-located SKPFM Volta potential map. In Figure 9. 13(b) the brightest spots had the highest Volta potential corresponding with Al-Mn type IMPs exposed on the surface. The Al-Zn solidification network structure was also observed, seen as less-bright, more diffuse regions indicating a relative Volta potential greater than the surrounding matrix. The Al-Mn particles also appeared to typically reside within or near to the Al-Zn network. Volta potential line measurements of the FZ were performed to determine the expected micro-galvanic coupling behavior. Representative analysis regions containing both Al-Mn particles and the Al-Zn solidification structure compared to the Mg matrix phase are seen in Figure 9. 14. The Volta potential difference for the Al-Mn particles was ~300 mV vs. matrix, in agreement with published data and indicative of strong local cathodes[25]. The Al-Zn solidification network also had a higher relative Volta potential than the matrix, ~80 mV, indicating these regions are cathodic to the Mg matrix in solution immersion conditions, but the galvanic couple driving force is significantly weaker than for the IMPs.

The FZ of AZ31 TIG welds were also characterized with SKPFM following corrosion attack. FZ samples were immersed in 0.6 M NaCl for 1 minute to initiate and briefly propagate early stages of corrosion damage. The short immersion duration was used to minimize the depth of corrosion damage. For the AFM to maintain accurate tracking on the surface, steep topography changes of less than a few hundred nanometers in the Z direction are needed. The FZ surface post-corrosion and corresponding AFM topography map with Volta potential overlay are shown in Figure 9. 15. The more noble Al-Mn IMP are seen as bright white spots in the SEM image (Figure 9. 15(a)) and typically protrude from the surface (Figure 9. 15(b)), and operate as

local cathodes. A few areas of trenching are also seen with particle remnants in the center or the absence of a particle due to complete dislodging. Moreover, the Al-Zn solidification network was observed as more diffuse regions with higher elevation and Volta potential than the surrounding Mg matrix. The more diffuse Al-Zn network was cathodic to the Mg matrix and also typically entrained many of the strongly cathodic IMPs present on the surface following corrosion.

SKPFM of AZ31B Weld HAZ

The HAZ of TIG welded AZ31B samples were also characterized with SKPFM pre- and post-corrosion. In Figure 9. 16(a-e), SEM/EDS and SKPFM Volta potential maps of a typical HAZ region before and after exposure to 0.6 M NaCl solution at OCP are shown. Figure 9. 16(f) is an AFM topography map since the topography of the corrosion damaged surface degraded the ability of the AFM in SKPFM mode to accurately track surface potential during the second pass scan (see experimental section measurement details). The white arrow in Figure 9. 16 identifies a typical, prominent Al-Mn particle that was tracked during testing. The particle had a Volta potential approximately ~300 mV more positive that the surrounding Mg matrix, typical of the Al-Mn type particles present in both the FZ and HAZ though the density of particles was much lower in the HAZ. Volta potentials of these particles were also in agreement with previously reported SKPFM determined Volta potentials for Al-Mn particles in Mg alloys[25]. Following corrosion damage, the particle and adjacent region tracked in Figure 9. 16 were seemingly unaffected and did not to influence nearby corrosion filament propagation.

9.4 <u>Discussion</u>

9.4.1 Methanol as a potential solvent for in-situ mapping of Mg alloys

Several SECM mediators have been shown to be capable of spatially mapping the corrosion of Mg [19,20]. Also, work has shown that non-aqueous solutions can better control the cathodic kinetics in order to map these active cathodic sites [19]. However, a better understanding of how non-aqueous solutions affected the galvanic currents and refinement concerning the fraction of non-aqueous solution substituted in the electrolyte for H_2O was explored in order to better resolve the galvanic corrosion over time using spatial mapping techniques.

In previous work, ethylene glycol was successfully proposed as a non-aqueous electrolyte which has the capability of slowing the cathodic kinetics on a Mg surface in order to make

accurate in-situ measurements using spatial mapping techniques, such as SECM [19]. The work herein proposes a second non-aqueous electrolyte which may also be used to slow the cathodic kinetics on Mg for SECM imaging, methanol. The cathodic kinetics were determined through cathodic polarization curves, at -1.8 V_{SCE} (Figure 9. 7). The addition of increasing amounts of methanol to the electrolyte, decreased the overall cathodic kinetics.

However, in-situ mapping methods are helpful for determining the active corrosion reactions on a sample surface. This means that decreasing the corrosion rate too much (through the use of a completely non-aqueous environment) would not be a viable depiction of the localized corrosion behavior. In order to get the best SECM scans on a AZ31B weld, a tradeoff was required. With increasing methanol content, the corrosion rate decreased as well as the galvanic potential difference measured between Mg and Al. Moreover, the mediator [Ru(NH$_3$)$_6$]Cl$_3$ was not completely soluble in methanol. The solution of 50% methanol and 50% H$_2$O was found to achieve sufficient corrosion across the sample with significant current at the ME tip.

9.4.2 Corroborating Microstructural Features with Scanning Electrochemical Microscope

To determine the actively corroding regions on both an AZ31B wrought-sample and AZ31B TIG weld, the SECM scans can be compared and correlated with optical and SEM micrographs. From the micrographs, locations with a high measured net current correlate to IMPs with the sample. Previous work on SECM of Mg alloys has shown that these IMPs correlate to regions of large H$_2$ flux [20]. The corrosion reactions on Mg are extremely heterogeneous, with different areas of the material corroding at different time scales. This has to be taken into account for in-situ mapping of SECM. The IMPs act as active cathodes, sites for rapid HER. From the SECM micrographs, these features reflect sites of large measured current. Correspondingly, high SECM currents can be correlated to an active HER as well as to the location of IMPs according to SEM micrographs of the same location. This is particularly important in terms of Mg corrosion as this increase in the cathodic reaction at the IMPs increases with time due to the phenomenon of anodically induced cathodic activation [28,47,58,59]. As more of these IMPs activate, the cathodic reactions on the sample surface will increase, therefore leading to increased cathodic kinetics with time, even at OCP.

9.4.3 Variation in Corrosion Current Sites with Time

The cathodic sites on the sample surface do not activate simultaneously (Figure 9. 9(b-c)). Therefore, to understand the real-time corrosion of a Mg alloy, several scans have to be taken at various immersion times where we observe the activation of various IMPs throughout the scan sequences.

The spread of current with time is shown here as well as in other works (Figure 9. 8) [19,20,23]. As these cathodic regions grow with time, the anodic region coverage across the electrode changes [28]. This change in anodic and cathodic activity on the electrode surface has been previously visualized and analyzed [58,60-63]. The proposed mechanisms for spreading are (i) Al-enrichment at the sample surface resulting in a cathodic region [15,18,64], (ii) exposure of cathodic features laying immediately below the polished surface, (iii) radial diffusion of dissolved hydrogen at the IMP [20]. These sites can act as locations for cathodic activation in Mg alloys and corrosion initiation [15,18]. In a Cl^- environment, the alkaline shift at these particles can lead to higher rates of Al^{3+} dissolution leading to incongruent dissolution and Al replating elsewhere [18,64] and lead to increased cathodic reaction rates with time. This is similar to the increase in the measured current across the sample surface with time [28,30-32]. SVET techniques have also shown this increase in the cathodic activity in Mg alloys [30,32] and AZ31 weld zones [4]. The increase in the cathodic activity on the sample surface in Mg alloys has been called anodically induced cathodic activation. The increase in the measured current in SECM images may correlate to this phenomenon.

9.4.4 Effect of Polarity Reversal on the Spatial Mapping of Mg Alloys

In AZ31B TIG welds, polarity reversal has been seen to occur between galvanically connected weld zones [3]. Electrochemically connected weld zones interact with one another when immersed in the same solution for an extended period of time [3]. The rapid corrosion rates on the sample surface, including dissolution of IMPs in the FZ and HAZs as well as dissolution of the solidification boundaries in the FZ, can lead to variations in the cathodic kinetics and OCP with time, enabling the zones to alter between the active anode and the active cathode. Over time, this polarity reversal can dominate the galvanic behavior instead of the initial microstructure. This phenomenon was previously captured using ZRA and MMA for electrochemically connected weld zones [3] has also been captured using SECM with a rapid scan rate and large step size. Due to the large size of the weld, a fast scan rate (200 μm/s) was best suited to acquire an overall

image of the actively corroding zones of a weld without the Pt degrading. However, a fast scan rate decreases the resolution of the in-situ image and limits the ability to observe specific microstructural features such as IMPs and solidification boundaries because these microstructural features are smaller than the designated step size (50 μm) [2].

9.4.5 Effect of Topology on the Spatial Mapping of Mg Alloys

SECM

The tip-to-substrate distance changes with topology. This is particularly important in the highly reactive Mg system which can have rapid changes in topology with time due to the its fast corrosion rate. When a tip scans over a surface of constant reactivity, the tip current is a measure of the tip to substrate distance and therefore purely delivers topographical information [40]. However, for Mg, which is shown to have heterogeneous reaction rates across the surface, this is more complex. For a sample that is pre-corroded or corroded for a long exposure time, shown in Figure 9. 12, the measured current is dominated by the topographical information. This is observed in the SECM scans, which correlate closely to the optical micrograph of a CrO_3 cleaned sample (Figure 9. 12(a)). However, for an actively corroding surface, this topographical and actively corroding information is mixed and cannot be considered in isolation without the use of optical and SEM micrographs.

SKPFM

SKPFM was effective for mapping the Volta potential variations in the AZ31B weld microstructure to determine expected local cathode sites on uncorroded samples. To investigate the dry sample surface following corrosion, the utility of SKPFM was limited to only the early stages of corrosion filament formation. AFM tracking on high-aspect-ratio topography, such as pits or corrosion filament networks, is dependent on the scan parameters and AFM tip geometry. For the Mg alloys studied corrosion damage more than a few hundred nanometers deep typically exceeded the threshold for accurate tracking of the sample surface. SKPFM characterization of AZ31B weld zones after exposure to 0.6M NaCl for 1 minute confirmed differences in local cathodes within the FZ and HAZ weld microstructures. The extensive Al-Zn solidification network in the FZ had a more noble Volta potential than the surrounding Mg matrix. A post-corrosion Volta potential map (Figure 9. 15) confirmed the Al-Zn network regions as preferred cathodic sites supporting dissolution of adjacent, anodic Mg matrix phase regions. Moreover, cathodic activity was likely enhanced by the clustering of strongly cathodic Al-Mn type IMPs

within the Al-Zn network. In the HAZ, the Al-Zn network was absent and the only areas of expected significant micro-galvanic coupling observed were limited to IMPs (Figure 9. 16). SKPFM characterization following early stage corrosion of the HAZ regions further confirmed the irregular activation behavior of IMPs. Most particles and the less-noble surrounding Mg matrix phase in the HAZ regions observed did not activate or appear to participate in corrosion filament propagation.

9.5 <u>Conclusions</u>

1. The use of methanol as a non-aqueous exposure environment provides a method to sufficiently reduce HER rates to spatially map regions of high reactivity (SECM) and Volta potential differences on a Mg sample.

2. The regions of high HER are shown to correlate with the positions of IMPs present on the sample surface, as detected through SEM imaging correlated with regions of SECM scans exhibiting high ME current.

3. The use of a semi-non-aqueous environment can be helpful for more realistic in-situ maps of the corrosion of Mg. The addition of water to the system allows for measurement of the same actively corroding sites as in 100 % H_2O.

4. The current on the sample surface, as measured through SECM, is shown to spread across the sample surface with time. This may correlate to anodically induced cathodic activation caused by α-Mg corrosion as well as replating of Al along the sample surface.

5. The Al-Zn solidification network present in the FZ of TIG welded samples had a more noble Volta potential than the surrounding Mg matrix and was a preferred cathodic site to support dissolution of the surrounding Mg matrix phase.

6. IMPs in the FZ and HAZ had similar Volta potentials and were the highest Volta potentials observed in the weld microstructure. Within the FZ extensive Al-Mn type IMP clustering in the Al-Zn phase likely further enhanced local cathodic activity and galvanically coupled dissolution of the Mg matrix phase. In the HAZ the IMPs were expected to be strong local cathodes but did not activate corrosion uniformly or directly control corrosion filament propagation.

336

References

1. G. Ben-Hamu, D. Eliezer, C.E. Cross, and T. Böllinghaus, "The relation between microstructure and corrosion behavior of GTA welded AZ31B magnesium sheet," Materials Science and Engineering: A 452–453, (2007): p. 210-218.
2. L.G. Bland, J.M. Fitz-Gerald, and J.R. Scully, "Metallurgical and Electrochemical Characterization of the Corrosion of AZ31B-H24 Tungsten Inert Gas Weld: Isolated Weld Zones," Corrosion Journal 72, 9 (2016): p. 1116-1132.
3. L.G. Bland, B.C.R. Troconis, R.J.S. Jr., J.M. Fitz-Gerald, and J.R. Scully, "Metallurgical and Electrochemical Characterization of the Corrosion of Mg-Al-Zn Alloy AZ31B-H24 Tungsten Inert Gas Weld: Galvanic Corrosion Between Weld Zones " Corrosion Journal in press (DOI: 10.5006/2078), (2016).
4. J.R. Kish, G. Williams, J.R. McDermid, J.M. Thuss, and C.F. Glover, "Effect of Grain Size on the Corrosion Resistance of Friction Stir Welded Mg Alloy AZ31B Joints," Journal of the Electrochemical Society 161, 9 (2014): p. C405-C411.
5. K. Abderrazak, W. Ben Salem, H. Mhiri, P. Bournot, and M. Autric, "Nd:YAG Laser Welding of AZ91 Magnesium Alloy for Aerospace Industries," Metall Mater Trans B 40, 1 (2009): p. 54-61.
6. A. Belhadj, J.E. Masse, L. Barrallier, M. Bouhafs, and J. Bessrour, "CO2 laser beam welding of AM60 magnesium-based alloy," J Laser Appl 22, 2 (2010): p. 56-61.
7. X. Cao, M. Jahazi, J.P. Immarigeon, and W. Wallace, "A review of laser welding techniques for magnesium alloys," J Mater Process Tech 171, 2 (2006): p. 188-204.
8. L. Commin, M. Dumont, R. Rotinat, F. Pierron, J.E. Masse, and L. Barrallier, "Texture evolution in Nd:YAG-laser welds of AZ31 magnesium alloy hot rolled sheets and its influence on mechanical properties," Mat Sci Eng a-Struct 528, 4-5 (2011): p. 2049-2055.
9. L. Commin, M. Dumont, J.E. Masse, and L. Barrallier, "Friction stir welding of AZ31 magnesium alloy rolled sheets: Influence of processing parameters," Acta Materialia 57, 2 (2009): p. 326-334.
10. X. Cao, M. Xiao, M. Jahazi, J. Fournier, and M. Alain, "Optimization of processing parameters during laser cladding of ZE41A-T5 magnesium alloy castings using Taguchi method," Mater Manuf Process 23, 3-4 (2008): p. 413-418.
11. B. Majumdar, R. Galun, B.L. Mordike, and A. Weisheit, "Influence of processing parameters on morphology and structure of single spot excimer laser melted Mg alloy surfaces," Laser Eng 13, 2 (2003): p. 75-89.
12. G. Padmanaban and V. Balasubramanian, "Optimization of laser beam welding process parameters to attain maximum tensile strength in AZ31B magnesium alloy," Optics & Laser Technology 42, 8 (2010): p. 1253-1260.
13. G. Padmanaban and V. Balasubramanian, "Effects of laser beam welding parameters on mechanical properties and microstructure of AZ31B magnesium alloy," Transactions of Nonferrous Metals Society of China 21, 9 (2011): p. 1917-1924.
14. R.S. Coelho, A. Kostka, H. Pinto, S. Riekehr, M. Koçak, and A.R. Pyzalla, "Microstructure and mechanical properties of magnesium alloy AZ31B laser beam welds," Materials Science and Engineering: A 485, 1–2 (2008): p. 20-30.

15. L.G. Bland, J.J. Bhattacharyya, S.R. Agnew, J.M. Fitz-Gerald, and J.R. Scully, "Effect of Al-Mn and Al-Mn-Fe Intermetallic Particle Size and Distribution on the Corrosion of Mg-3Al-1Zn alloy: AZ31," Acta Materialia In Review, (2016).

16. D.A. Porter and K.E. Easterling, Phase Transformations in Metals in Alloys. 2nd ed, 1992.

17. A.D. Südholz, N.T. Kirkland, R.G. Buchheit, and N. Birbilis, "Electrochemical Properties of Intermetallic Phases and Common Impurity Elements in Magnesium Alloys," Electrochemical and Solid-State Letters 14, 2 (2011): p. C5-C7.

18. L.G. Bland, N. Birbilis, and J.R. Scully, "Exploring the Effects of Intermetallic Particle Size and Spacing on the Corrosion of Mg-Al Alloys Using Model Electrodes," Journal of the Electrochemical Society In Review, (2016).

19. R.M. Asmussen, W.J. Binns, P. Jakupi, P. Dauphin-Ducharme, U.M. Tefashe, J. Mauzeroll, and D. Shoesmith, "Reducing the corrosion rate of magnesium alloys using ethylene glycol for advanced electrochemical imaging," Corros Sci 93, (2015): p. 70-79.

20. P. Dauphin-Ducharme, R.M. Asmussen, U.M. Tefashe, M. Danaie, W.J. Binns, P. Jakupi, G.A. Botton, D.W. Shoesmith, and J. Mauzeroll, "Local Hydrogen Fluxes Correlated to Microstructural Features of a Corroding Sand Cast AM50 Magnesium Alloy," Journal of the Electrochemical Society 161, 12 (2014).

21. P. Dauphin-Ducharme, C. Kuss, D. Rossouw, N.A. Payne, L. Danis, G.A. Botton, and J. Mauzeroll, "Corrosion Product Formation Monitored Using the Feedback Mode of Scanning Electrochemical Microscopy with Carbon Microelectrodes," Journal of the Electrochemical Society 162, 12 (2015): p. C677-C683.

22. S.S. Jamali, S.E. Moulton, D.E. Tallman, M. Forsyth, J. Weber, and G.G. Wallace, "Applications of scanning electrochemical microscopy (SECM) for local characterization of AZ31 surface during corrosion in a buffered media," Corros Sci 86, (2014): p. 93-100.

23. U.M. Tefashe, P. Dauphin-Ducharme, M. Danaie, Z.P. Cano, J.R. Kish, G.A. Botton, and J. Mauzeroll, "Localized Corrosion Behavior of AZ31B Magnesium Alloy with an Electrodeposited Poly(3,4-Ethylenedioxythiophene) Coating," Journal of the Electrochemical Society 162, 10 (2015).

24. U.M. Tefashe, M.E. Snowden, P.D. Ducharme, M. Danaie, G.A. Botton, and J. Mauzeroll, "Local flux of hydrogen from magnesium alloy corrosion investigated by scanning electrochemical microscopy," Journal of Electroanalytical Chemistry 720–721, (2014): p. 121-127.

25. M.F. Hurley, C.M. Efaw, P.H. Davis, J.R. Croteau, E. Graugnard, and N. Birbilis, "Volta Potentials Measured by Scanning Kelvin Probe Force Microscopy as Relevant to Corrosion of Magnesium Alloys," Corrosion 71, 2 (2015): p. 160-170.

26. M. Jönsson, D. Thierry, and N. LeBozec, "The influence of microstructure on the corrosion behaviour of AZ91D studied by scanning Kelvin probe force microscopy and scanning Kelvin probe," Corros Sci 48, 5 (2006): p. 1193-1208.

27. A. Pardo, M.C. Merino, A.E. Coy, F. Viejo, R. Arrabal, and S. Feliú Jr, "Influence of microstructure and composition on the corrosion behaviour of Mg/Al alloys in chloride media," Electrochimica Acta 53, 27 (2008): p. 7890-7902.

28. G. Williams, N. Birbilis, and H.N. McMurray, "The source of hydrogen evolved from a magnesium anode," Electrochemistry Communications 36, 0 (2013): p. 1-5.

29. S.V. Lamaka, O.V. Karavai, A.C. Bastos, M.L. Zheludkevich, and M.G.S. Ferreira, "Monitoring local spatial distribution of Mg2+, pH and ionic currents," Electrochemistry Communications 10, 2 (2008): p. 259-262.

30. G. Williams and H.N. McMurray, "Localized Corrosion of Magnesium in Chloride-Containing Electrolyte Studied by a Scanning Vibrating ElectrodeTechnique," Journal of the Electrochemical Society 155, 7 (2008): p. C340-C349.

31. G. Williams, K. Gusieva, and N. Birbilis, "Localized Corrosion of Binary Mg-Nd Alloys in Chloride-Containing Electrolyte Using a Scanning Vibrating Electrode Technique," Corrosion 68, 6 (2012): p. 489-498.

32. G. Williams, H. ap Llwyd Dafydd, and R. Grace, "The localised corrosion of Mg alloy AZ31 in chloride containing electrolyte studied by a scanning vibrating electrode technique," Electrochimica Acta 109, 0 (2013): p. 489-501.

33. G. Baril, C. Blanc, M. Keddam, and N. Pebere, "Local Electrochemical Impedance Spectroscopy Applied to the Corrosion Behavior of an AZ91 Magnesium Alloy," Journal of the Electrochemical Society 150, 2003 (2010): p. B488-B493.

34. K.S. de Assis, F.V.V. de Sousa, M. Miranda, I.C.P. Margarit-Mattos, V. Vivier, and O.R. Mattos, "Assessment of electrochemical methods used on corrosion of superduplex stainless steel," Corros Sci 59, (2012): p. 71-80.

35. J. Izquierdo, M.B. González-Marrero, M. Bozorg, B.M. Fernández-Pérez, H.C. Vasconcelos, J.J. Santana, and R.M. Souto, "Multiscale electrochemical analysis of the corrosion of titanium and nitinol for implant applications," Electrochimica Acta 203, (2016): p. 366-378.

36. A. Davoodi, Z. Esfahani, and M. Sarvghad, "Microstructure and corrosion characterization of the interfacial region in dissimilar friction stir welded AA5083 to AA7023," Corros Sci 107, (2016): p. 133-144.

37. R. Sánchez-Tovar, M.T. Montañés, and J. García-Antón, "Effects of microplasma arc AISI 316L welds on the corrosion behaviour of pipelines in LiBr cooling systems," Corros Sci 73, (2013): p. 365-374.

38. D. Trinh, P. Dauphin Ducharme, U. Mengesha Tefashe, J.R. Kish, and J. Mauzeroll, "Influence of Edge Effects on Local Corrosion Rate of Magnesium Alloy/Mild Steel Galvanic Couple," Analytical Chemistry 84, 22 (2012): p. 9899-9906.

39. S. Thomas, J. Izquierdo, N. Birbilis, and R.M. Souto, "Possibilities and Limitations of Scanning Electrochemical Microscopy of Mg and Mg Alloys," Corrosion 71, 2 (2015): p. 171-183.

40. A.J. Bard and M.V. Mirkin, Scanning Electrochemical Microscopy. second ed (Boca Raton, FL: Taylor & Francis Group, LLC, 2012.

41. L.G. Bland, A.D. King, N. Birbilis, and J.R. Scully, "Assessing the Corrosion of Commercially Pure Magnesium and Commercial AZ31B by Electrochemical Impedance, Mass-loss, Hydrogen Collection and ICP-OES Solution Analysis," Corrosion Journal 71, 2 [Special Issue] (2015): p. 128-145.

42. A.D. King, N. Birbilis, and J.R. Scully, "Accurate Electrochemical Measurement of Magnesium Corrosion Rates; a Combined Impedance, Mass-Loss and Hydrogen Collection Study," Electrochimica Acta 121, 1 (2014): p. 394-406.

43. L.G. Bland, R.F. Schaller, and J.R. Scully. *Utilization of a Partially Non-aqueous Electrlyte for the Spatial Mapping of Mg Corrosion using a model Mg-Al electrode*. in *The Metals Society*. 2016. San Diego, CA.

44. V. Guillaumin, P. Schmutz, and G.S. Frankel, "Characterization of Corrosion Interfaces by the Scanning Kelvin Probe Force Microscopy Technique," Journal of the Electrochemical Society 148, 5 (2001): p. B163-B173.

45. A. Kvryan, K. Livingston, C.M. Efaw, K. Knori, B.J. Jaques, P.H. Davis, D.P. Butt, and M.F. Hurley, "Microgalvanic Corrosion Behavior of Cu-Ag Active Braze Alloys Investigated with SKPFM," metals 6, 91 (2016).

46. P. Schmutz and G.S. Frankel, "Corrosion Study of AA2024-T3 by Scanning Kelvin Probe Force Microscopy and In Situ Atomic Force Microscopy Scratching," Journal of the Electrochemical Society 145, 7 (1998): p. 2295-2306.

47. N. Birbilis, A.D. King, S. Thomas, G.S. Frankel, and J.R. Scully, "Evidence for enhanced catalytic activity of magnesium arising from anodic dissolution," Electrochimica Acta 132, 0 (2014): p. 277-283.

48. M. Taheri, J.R. Kish, N. Birbilis, M. Danaie, E.A. McNally, and J.R. McDermid, "Towards a Physical Description for the Origin of Enhanced Catalytic Activity of Corroding Magnesium Surfaces," Electrochimica Acta 116, (2014): p. 396-403.

49. "AZtecEnergy: EDS Software," Oxford Instruments (2015).

50. R. Baboian, "Electrochemical Techniques for Predicting Galvanic Corrosion," ASTM STP 576 (1976): p. 5-19.

51. ASTM-81, "Standard Guide for Conducting and Evaluating Galvanic Corrosion Tests in Electrolytes," ASTM International G71, (2014).

52. R.L. Liu, M.F. Hurley, A. Kvryan, G. Williams, J.R. Scully, and N. Birbilis, "Controlling the corrosion and cathodic activation of magnesium via microalloying additions of Ge," Scientific Reports 6, (2016): p. 28747.

53. C.F. Mallinson and J.F. Watts, "Communication—The Effect of Hydrocarbon Contamination on the Volta Potential of Second Phase Particles in Beryllium," Journal of The Electrochemical Society 163, (2016): p. C420-C422.

54. M. Zamin, "The Role of Mn in the Corrosion Behavior of Al-Mn Alloys," Corrosion 37, 11 (1981): p. 627-632.

55. R.M. Asmussen, W.J. Binns, R. Partovi-Nia, P. Jakupi, and D.W. Shoesmith, "The stability of aluminum-manganese intermetallic phases under the microgalvanic coupling conditions anticipated in magnesium alloys," Materials and Corrosion 67, 1 (2016): p. 39-50.

56. A. Samaniego, I. Llorente, and S. Feliu Jr, "Combined effect of composition and surface condition on corrosion behaviour of magnesium alloys AZ31 and AZ61," Corros Sci 68, (2013): p. 66-71.

57. L.G. Bland, J.M. Fitz-Gerald, and J.R. Scully, "Metallurgical and Electrochemical Characterization of the Corrosion of AZ31B-H24 Tungsten Inert Gas Weld: Isolated Weld Zones," Corrosion Journal In Press, (2016).

58. G.S. Frankel, A. Samaniego, and N. Birbilis, "Evolution of hydrogen at dissolving magnesium surfaces," Corros Sci 70, (2013): p. 104-111.

59. G.S. Frankel, S. Fajardo, and B.M. Lyncha, "Introductory lecture on corrosion chemistry: a focus on anodic hydrogen evolution on Al and Mg," faraday discussions 180, (2015): p. 11-33.

60. S. Lebouil, A. Duboin, F. Monti, P. Tabeling, P. Volovitch, and K. Ogle, "A novel approach to on-line measurement of gas evolution kinetics: Application to the negative difference effect of Mg in chloride solution," Electrochimica Acta 124 (2013).

61. R.M. Souto, A. Kiss, J. Izquierdo, L. Nagy, I. Bitter, and G. Nagy, "Spatially-resolved imaging of concentration distributions on corroding magnesium-based materials exposed to aqueous environments by SECM," Electrochemistry Communications 26, (2013): p. 25-28.

62. T.R. Thomaz, C.R. Weber, T. Pelegrini Jr, L.F.P. Dick, and G. Knörnschild, "The negative difference effect of magnesium and of the AZ91 alloy in chloride and stannate-containing solutions," Corros Sci 52, 7 (2010): p. 2235-2243.

63. G. Song, A. Atrens, D. St John, X. Wu, and J. Nairn, "The anodic dissolution of magnesium in chloride and sulphate solutions," Corros Sci 39, 10-11 (1997): p. 1981-2004.

64. M. Danaie, R.M. Asmussen, P. Jakupi, D.W. Shoesmith, and G.A. Botton, "The cathodic behaviour of Al–Mn precipitates during atmospheric and saline aqueous corrosion of a sand-cast AM50 alloy," Corros Sci 83, (2014): p. 299-309.

Table 9. 1**.** AZ31B-H24 ([UNS M11311] Magnesium Elektron). All compositions reported in wt. %, with the actual compositions provided by QUANT (Quality Analysis and Testing Corporation). Compositions of α-matrix for isolated weld zones, IMPs and solidification boundaries due to welding found by SEM EDS analysis.

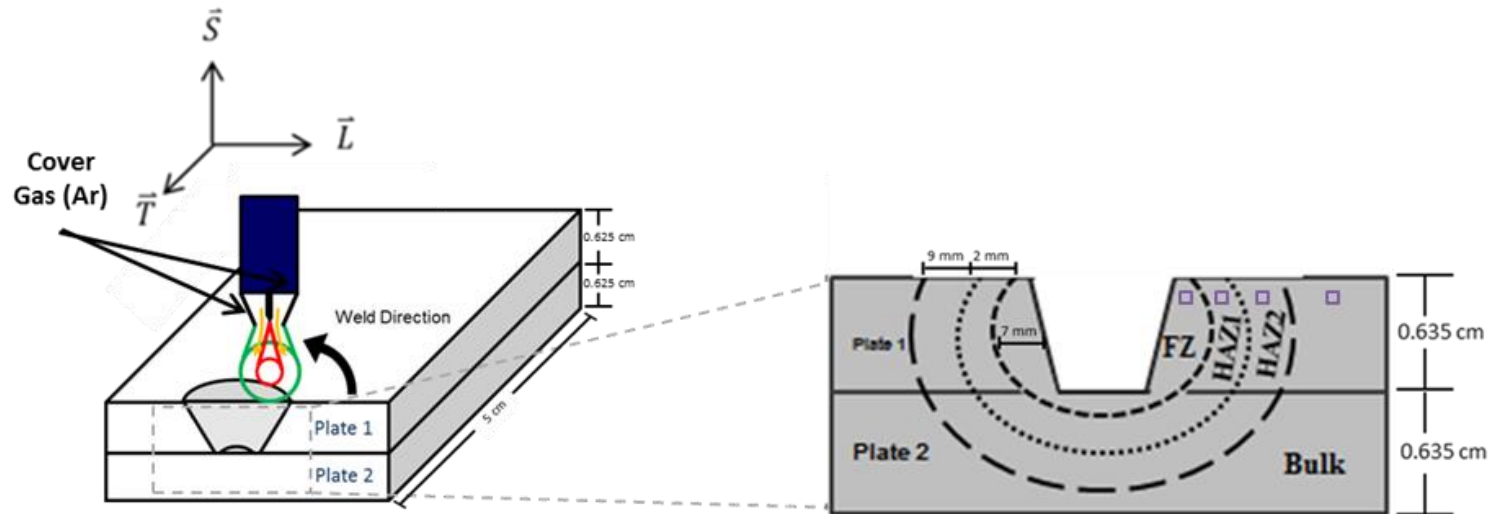|	UNS #	Al	Mn	Zn	Si	Cu	Ni	Fe	Mg
Commercially Pure Mg Rod	--	0.01	0.01	0.01	0.021	0.005	0.001	0.006	Bal.
AZ31B-H24	M11311	3.02	0.330	0.990	0.025	0.005	0.002	0.005	Bal.
HAZ2 α-matrix	---	2.6	0.330	0.990	---	---	---	---	Bal.
HAZ1 α-matrix	---	2.2	0.330	0.8	---	---	---	---	Bal.
FZ α-matrix	---	1.8	0.5	0.5	---	---	---	---	Bal.
Al-Mn-Fe particles	---	75.1	12.4	---	---	---	---	12.5	---
Al-Mn particles	---	67	33	---	---	---	---	---	---
Al-Zn Solidification Boundaries	---	52.1	--	47.9	---	---	---	--	---

Figure 9. 1. Schematic of TIG welding process and a schematic of weld zones, specifying the FZ and HAZs. Far enough away from the weld zone, the sample will become unaffected base material. All samples were welded through a 45° countersunk hole in order to have full penetration through both plates. The area of the isolated weld zone test locations is marked.
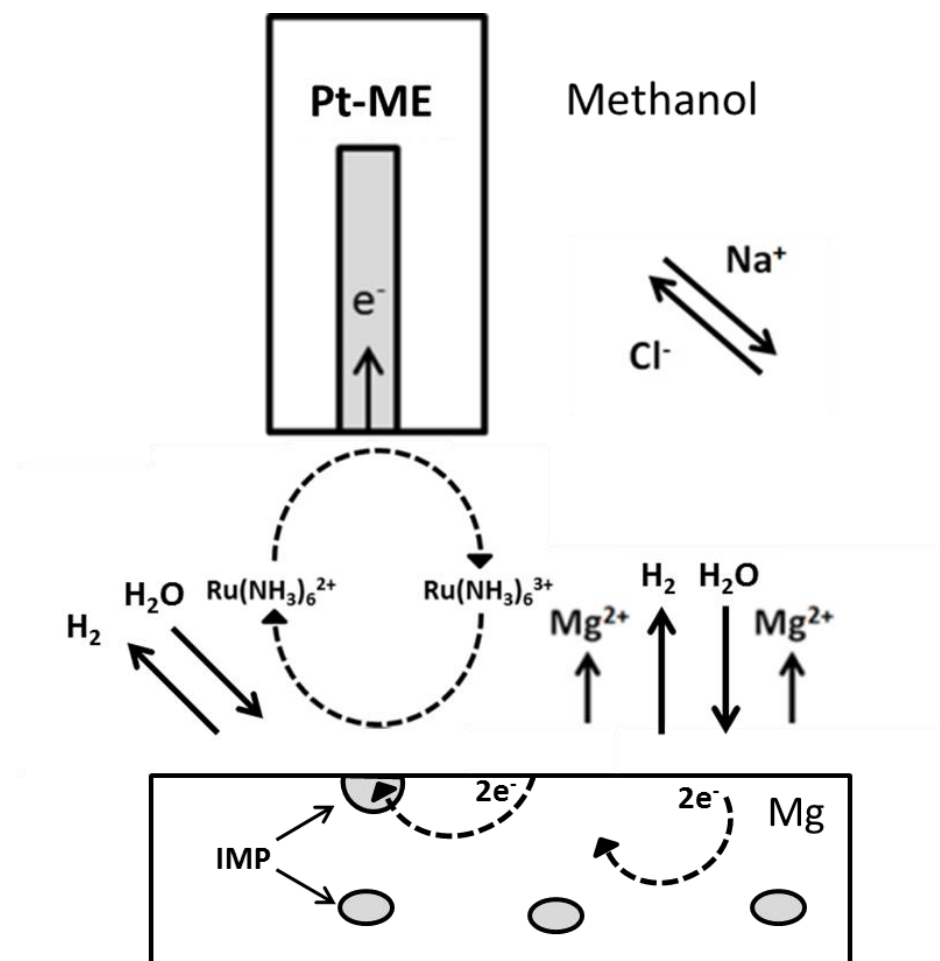
Figure 9. 2. Schematic of scanning electrochemical microscope applied in generation-tip collection (SG-TC) mode with $Ru(NH_3)_6Cl_3$ as a mediator. During Mg corrosion without a mediator, the anode half-cell reaction is Mg $\rightarrow$ Mg^{2+} + 2e$^-$ and water reduction by $2H_2O$ + 2e$^-$ = 2OH$^-$ +H_2.
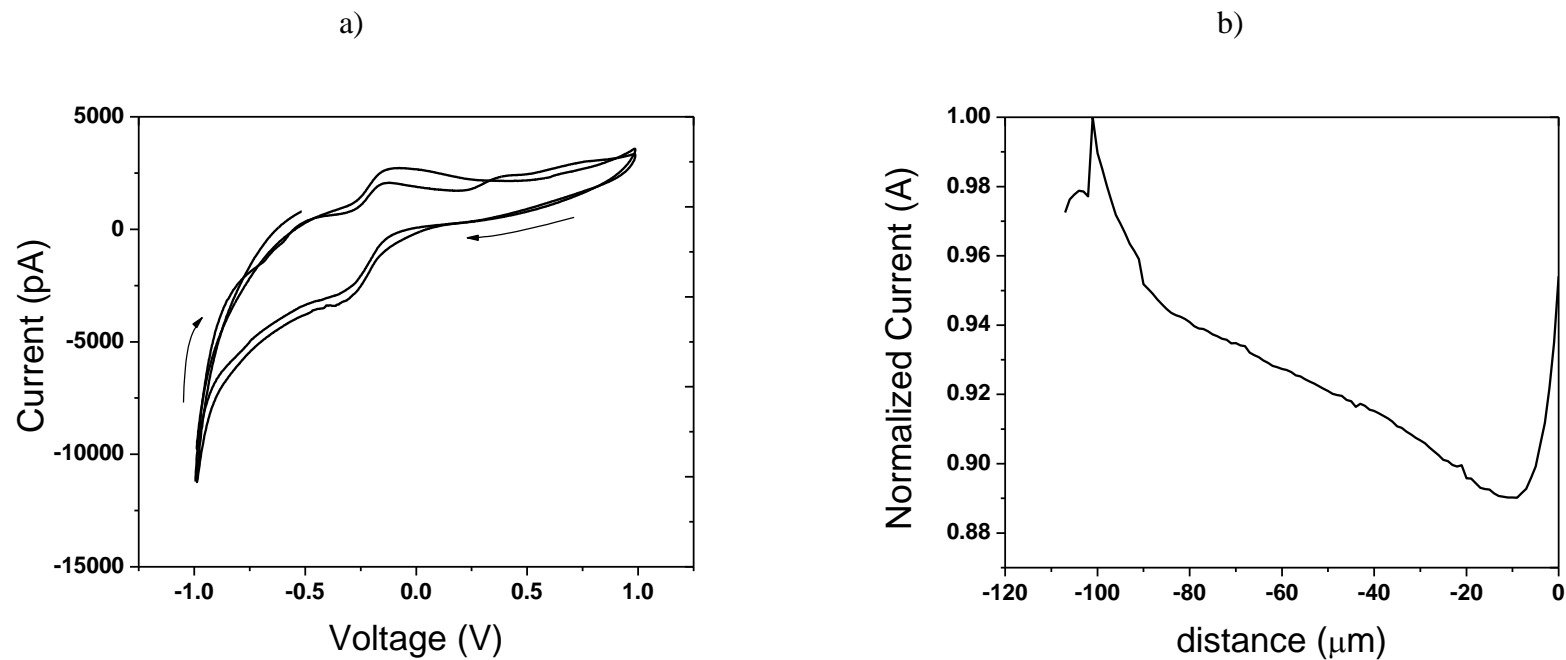
a)

b)

Figure 9. 3. a) CV of 0.1 M NaCl with $[Ru(NH_3)_6]Cl_3$ as the mediator in 50 wt% methanol + 50 wt% H_2O. Scan was taken for 3 cycles well away from the sample surface at 100 mV/s. b) Approach curve over an AZ31B sample. The tip approached the surface at 100 μm/s with the tip polarized at -0.1 V and normalized to the current at -0.1 V on the CV.

Figure 9. 4. Before corrosion secondary electron image of the (a) AZ31B wrought base, (b) AZ31B FZ, (c) AZ31B HAZ, resultant corrosion morphology of (d) AZ31B wrought base, (e) AZ31B FZ, (f) AZ31B HAZ after corrosion and cleaned with CrO_3 to remove any oxides after 3 hour immersion at OCP in 0.6 M NaCl. All images taken along the SL surface.
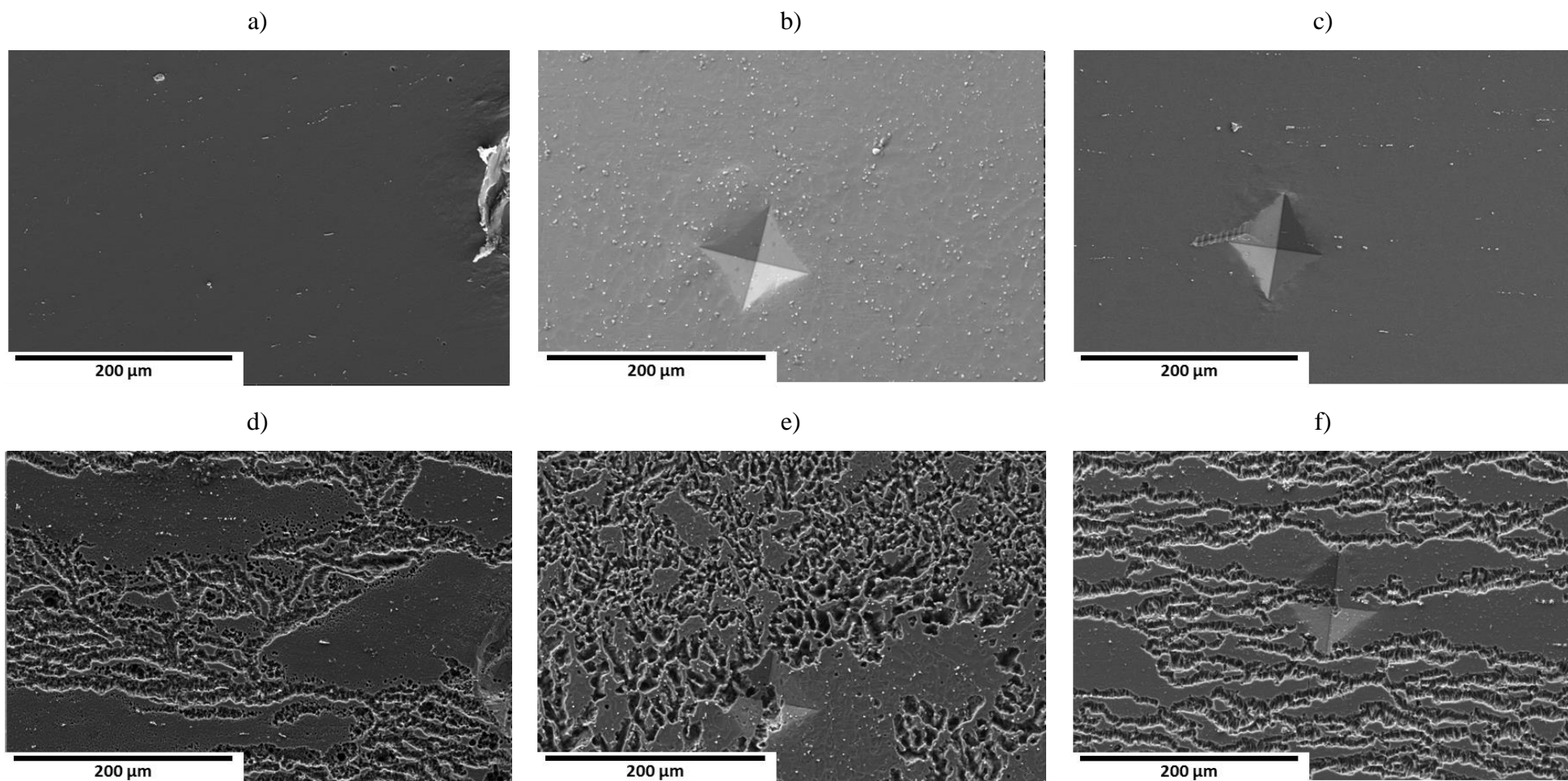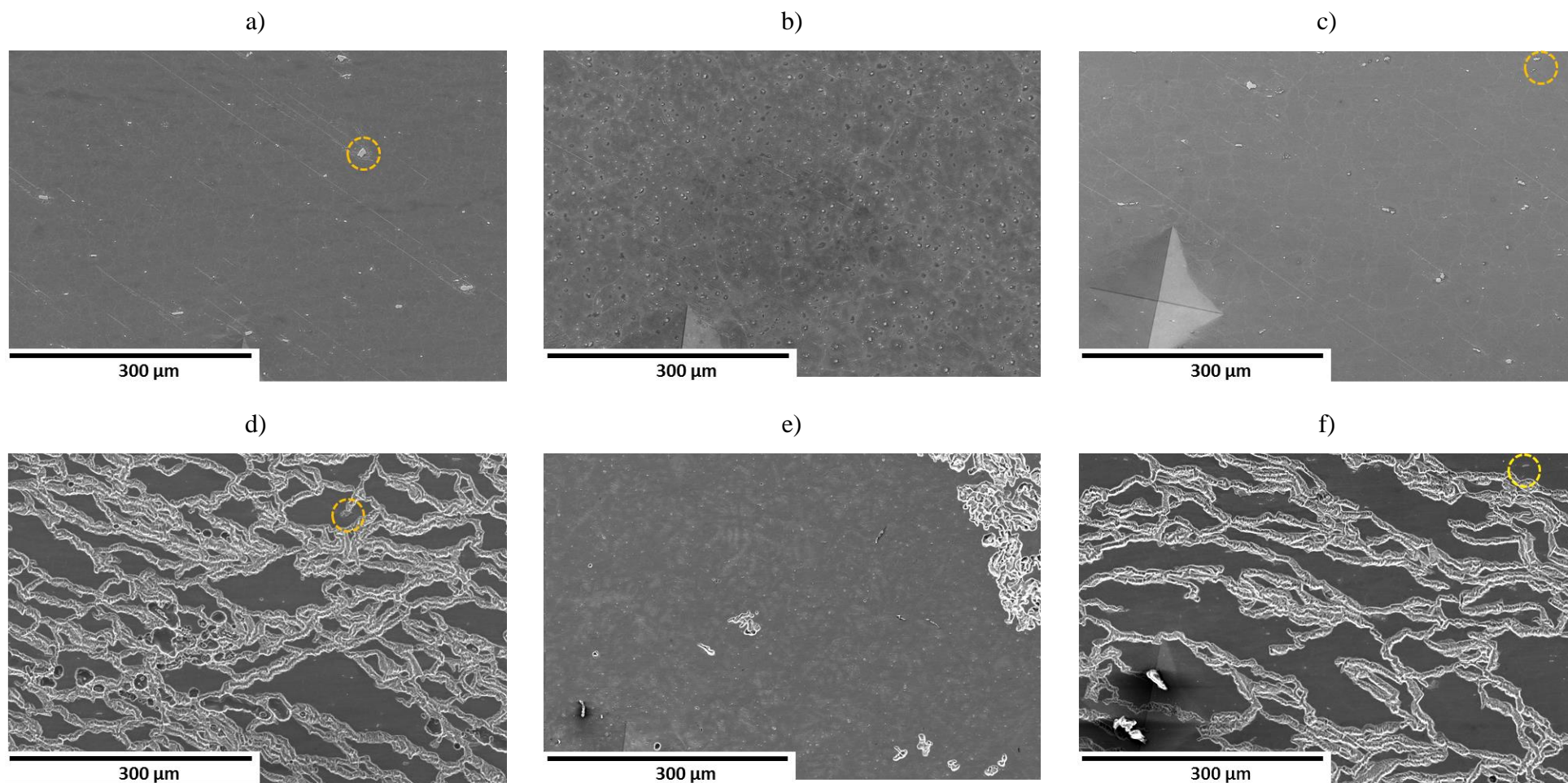
Figure 9. 5. Before corrosion secondary electron image of the (a) AZ31B wrought base, (b) AZ31B FZ, (c) AZ31B HAZ, resultant corrosion morphology of (d) AZ31B wrought base, (e) AZ31B FZ, (f) AZ31B HAZ after corrosion and cleaned with CrO_3 to remove any oxides after 3 hoyr immersion at OCP in 0.1 M NaCl made of 50 wt% H_2O + 50 wt% methanol. All images taken along the SL surface.
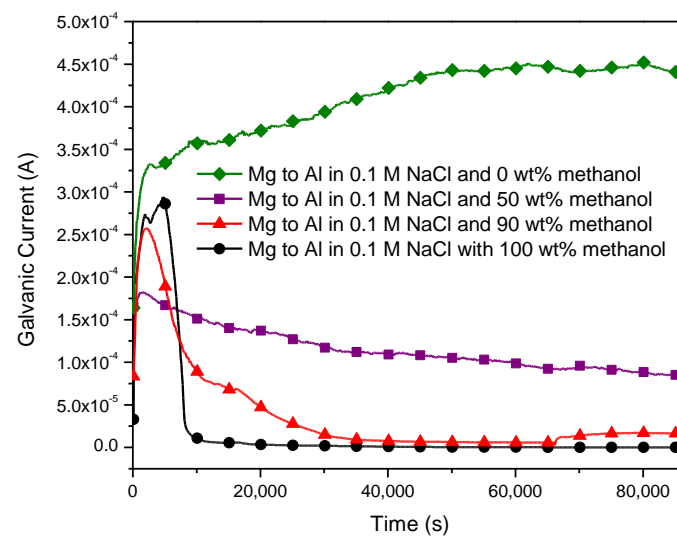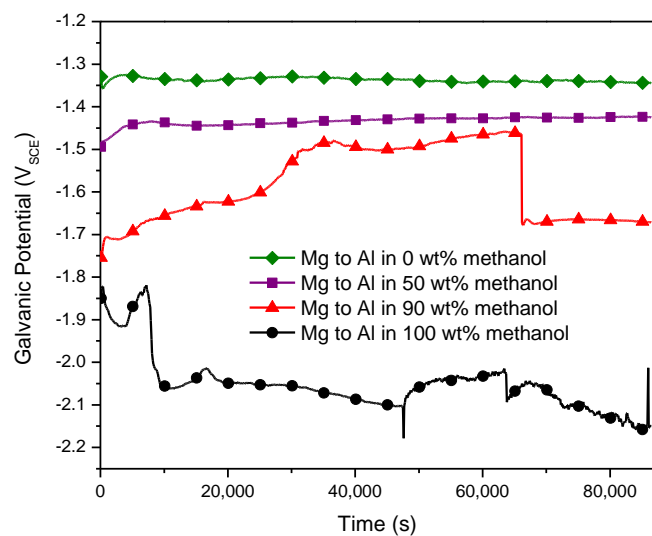
Figure 9. 6. (a) Galvanic potential and (b) galvanic current between commercial purity Mg and Al over 24 hours in 0.1 M NaCl with various amounts of methanol (0 wt% to 100 15%) where the Mg is the anode and the Al is the cathode. Each electrode had an exposed area of 0.8 cm^2.
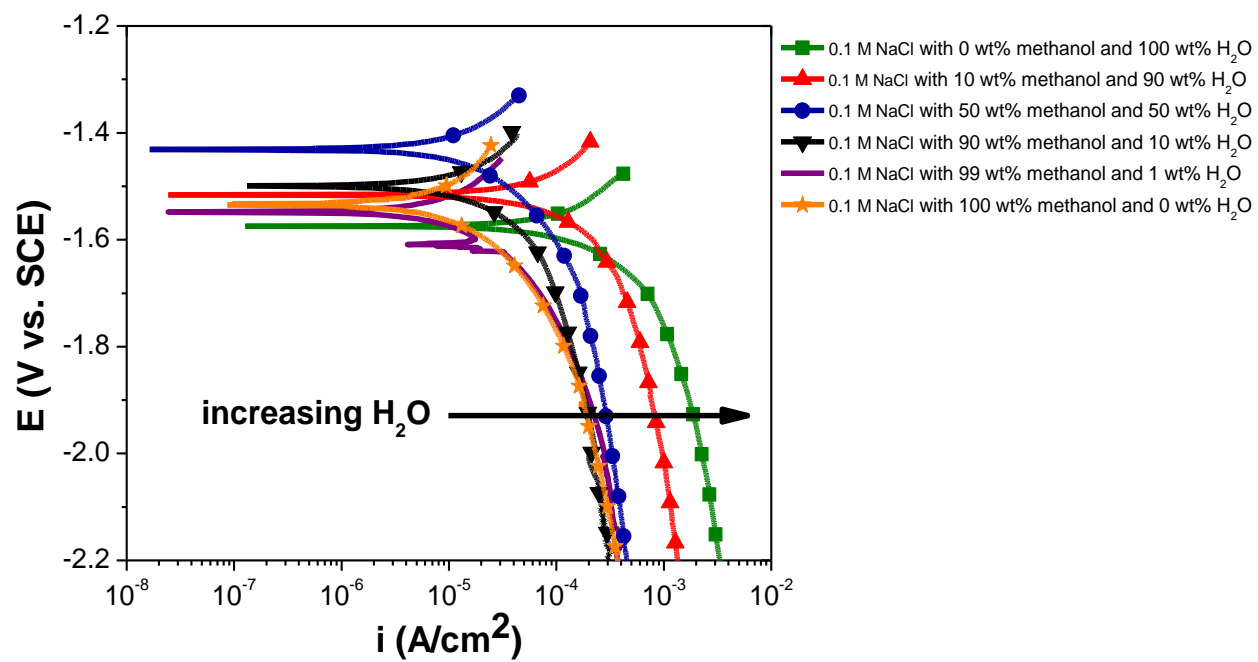
Figure 9. 7. Cathodic polarization of partially non-aqueous electrolytes taken in 0.1 M NaCl on commercially pure Mg to determine the effect of methanol on the corrosion kinetics.

Figure 9. 8. Scanning Electrochemical Microscope scan of current on an AZ31B sample. Scan was taken in 0.1 M NaCl with [Ru(NH$_3$)$_6$]Cl$_3$ as the mediator in 50 wt% methanol + 50 wt% H$_2$O. Scan was run at 100 μm/s with a step size of 10 μm. The tip was positioned 30 μm away from the sample surface and polarized at -100 mV.

Figure 9. 9. a) SEM SE micrograph of AZ31B as-received surface showing various IMPs, b) Scanning Electrochemical Microscope scan of current on an AZ31B sample taken immediately af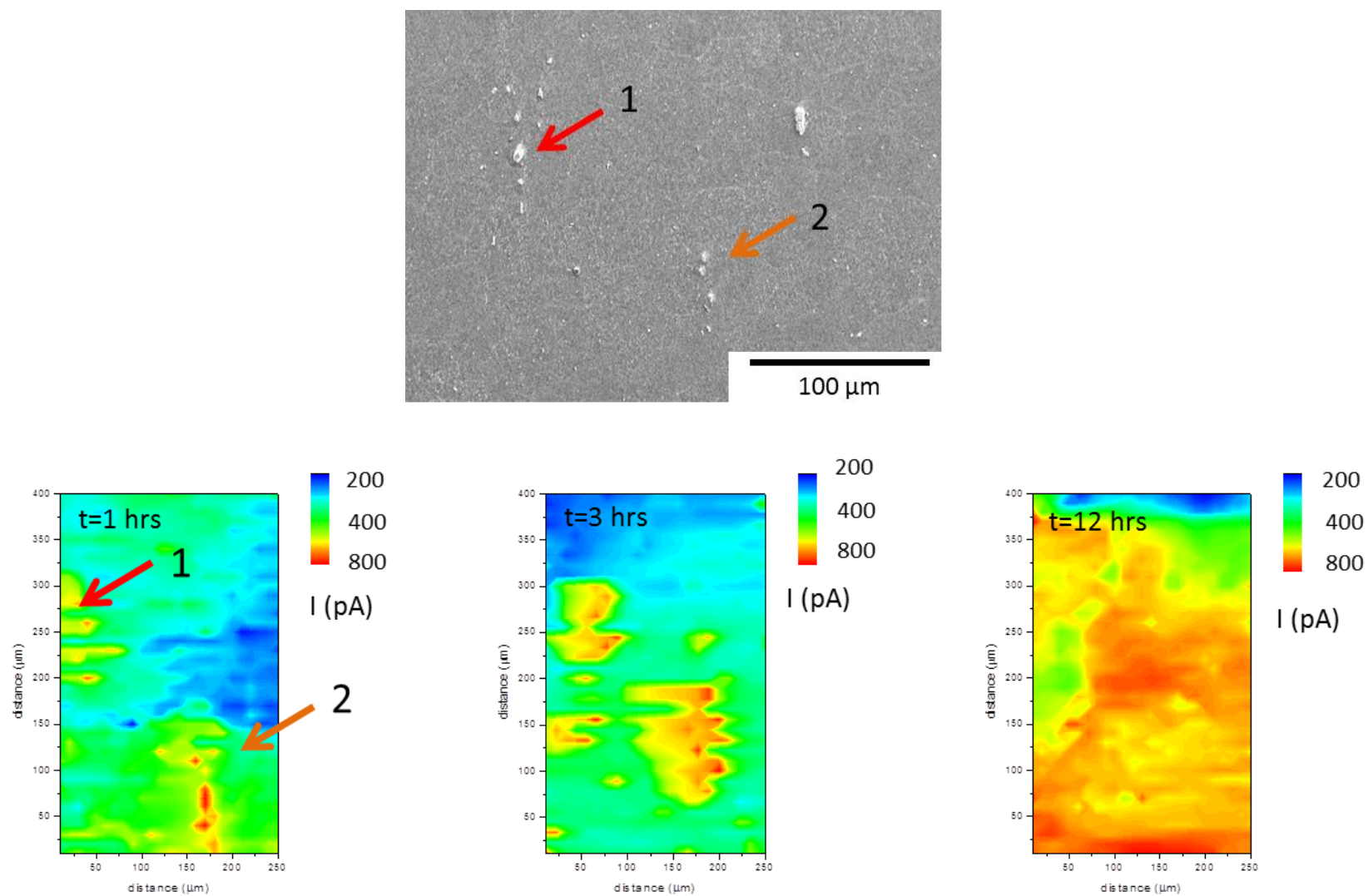ter immersion, c) Scanning Electrochemical Microscope image of an AZ31B sample taken after 3 hours of immersion. Scan were taken in 0.1 M NaCl with $[Ru(NH_3)_6]Cl_3$ as the mediator in 50 wt% methanol + 50 wt% H_2O. Scan was run at 100 μm/s with a step size of 10 μm. The tip was positioned 30 μm away from the sample surface and polarized at -100 mV.
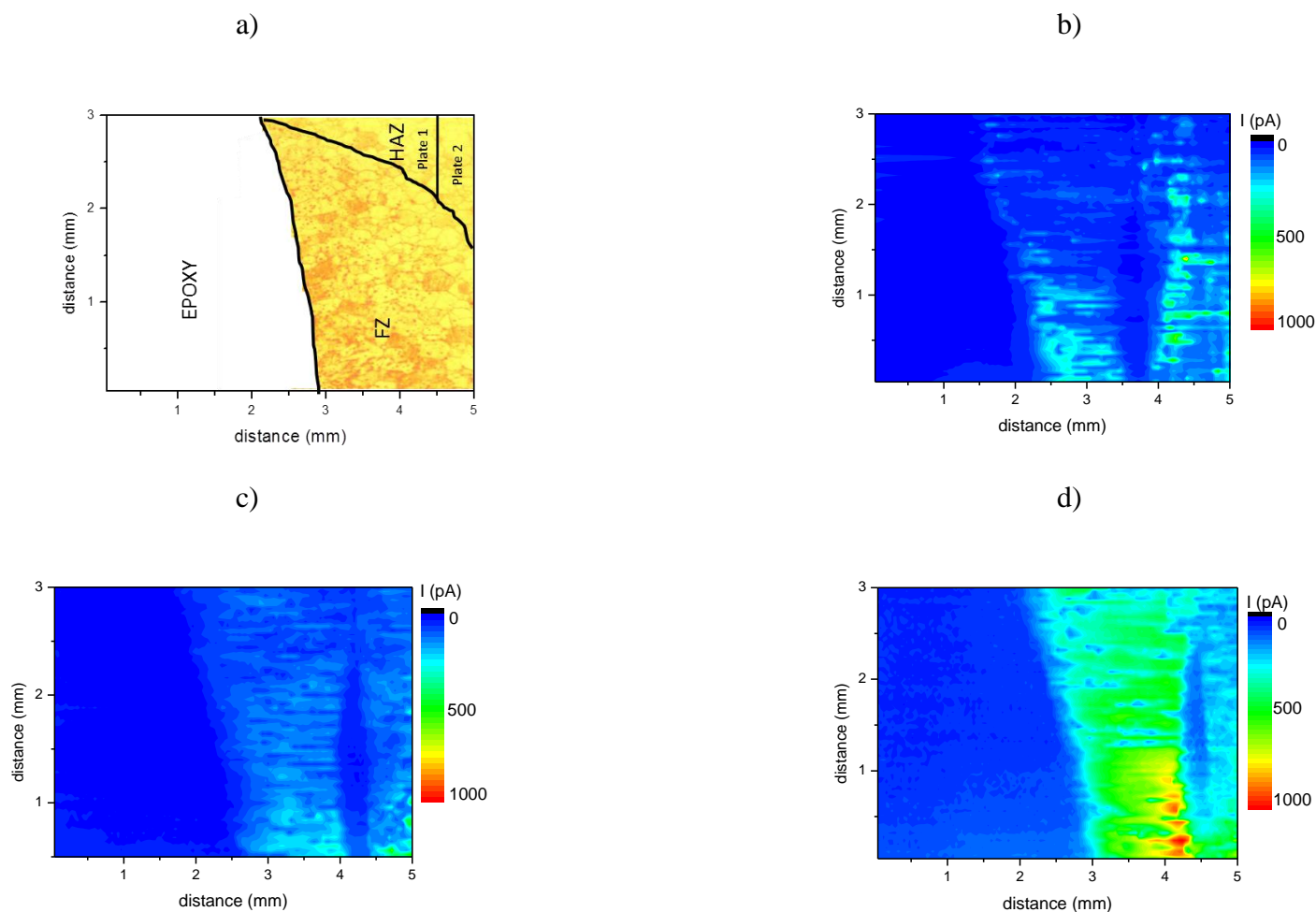
Figure 9. 10. a) Optical micrograph of AZ31B TIG weld showing a FZ and HAZ as a schematic for the location of the weld zones in the SECM image, b) Scanning Electrochemical Microscope scan of current on an AZ31B TIG weld sample taken immediately after immersion, c) after 3 hours of immersion and d) after 6 hours of immersion. Scan were taken in 0.1 M NaCl with $[Ru(NH_3)_6]Cl_3$ as the mediator in 50 wt% methanol + 50 wt% H_2O. Scan was run at 100 μm/s with a step size of 10 μm. The tip was positioned 30 μm away from the sample surface and polarized at -100 mV.
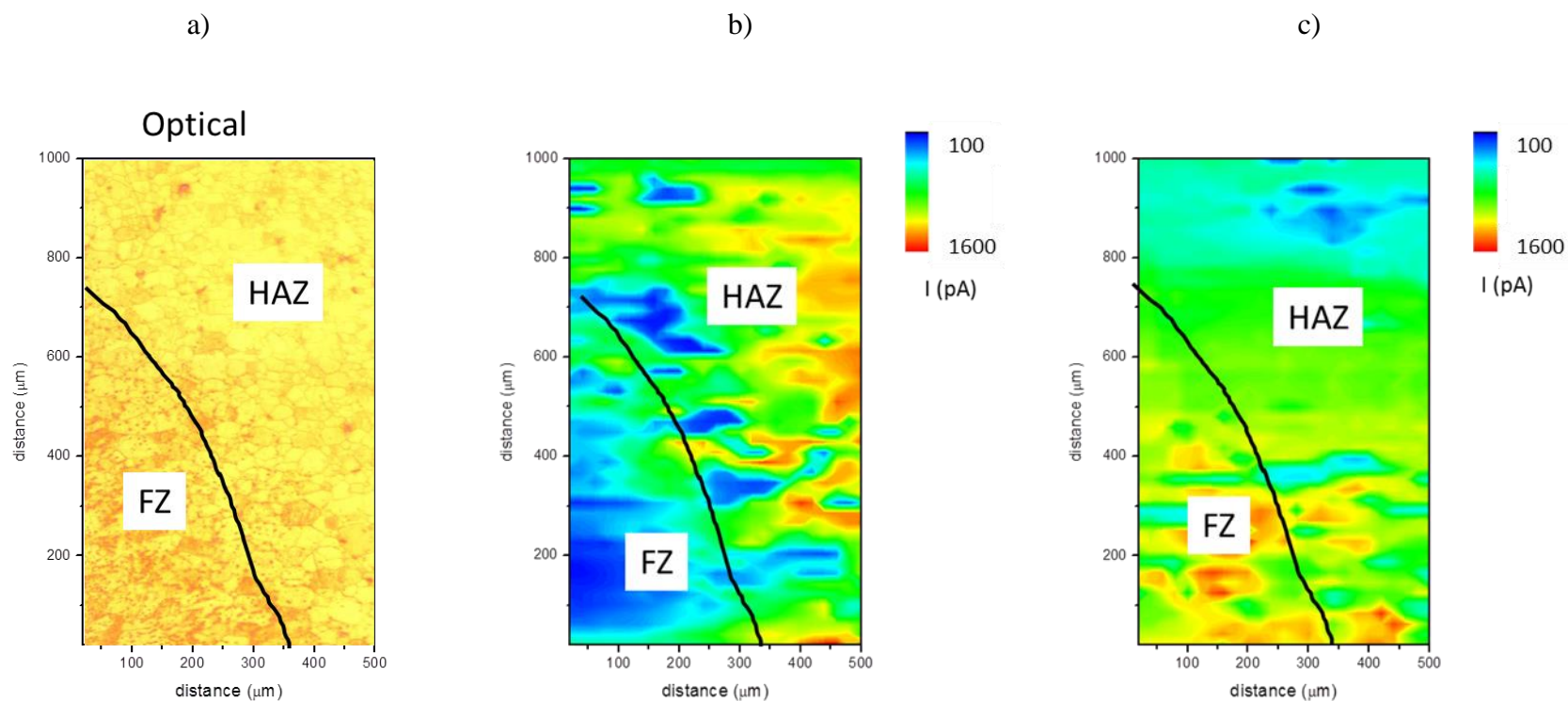
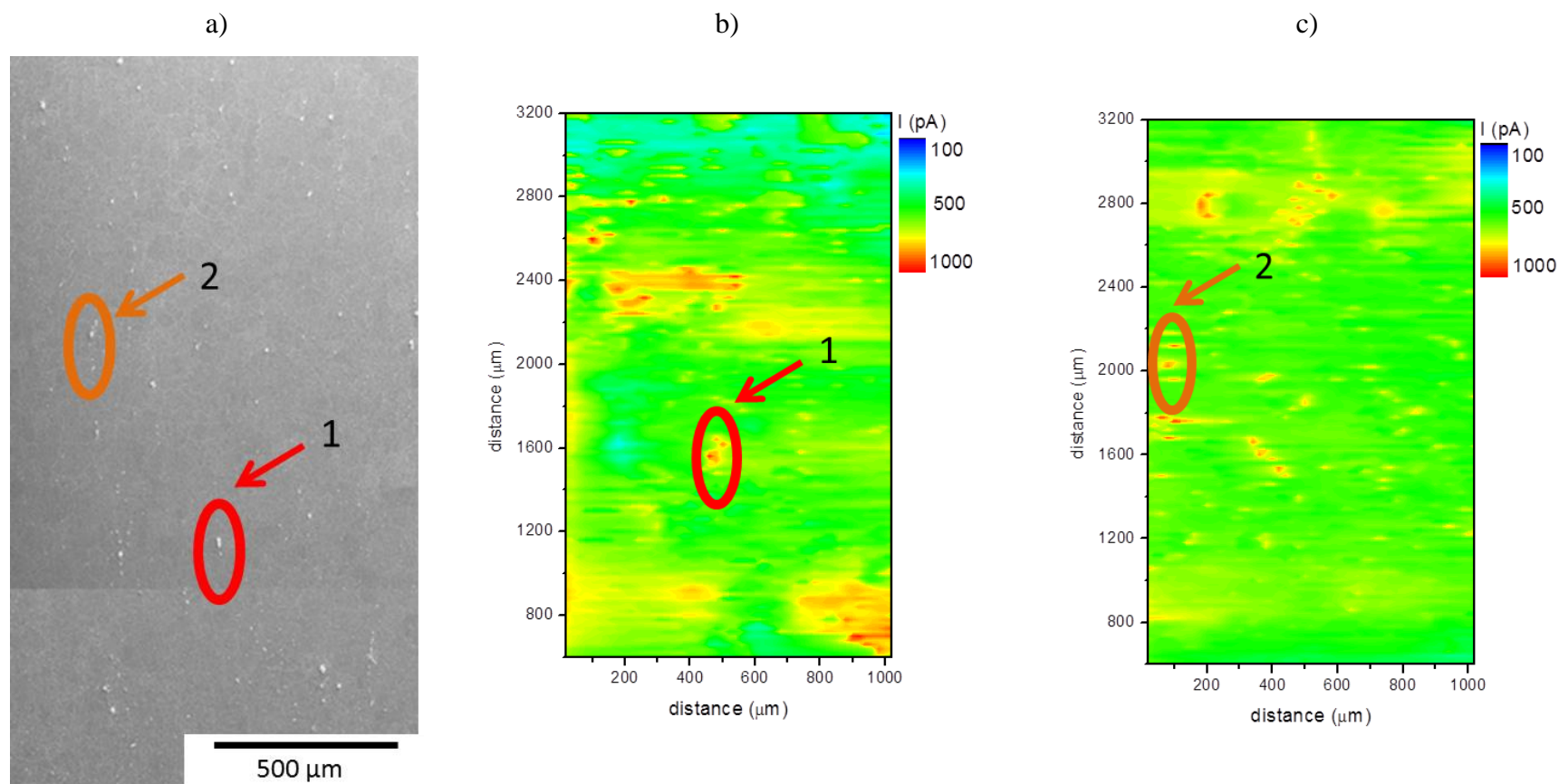Figure 9. 11. a) optical micrograph of AZ31B TIG weld, b) Scanning Electrochemical Microscope scan of current on an AZ31B sample after 0 hours. Scan was taken in 0.1 M NaCl with $[Ru(NH_3)_6]Cl_3$ as the mediator in 50 wt% methanol + 50 wt% H_2O. Scan was run at 200 μm/s with a step size of 50 μm. The tip was positioned 30 μm away from the sample surface and polarized at -100 mV.
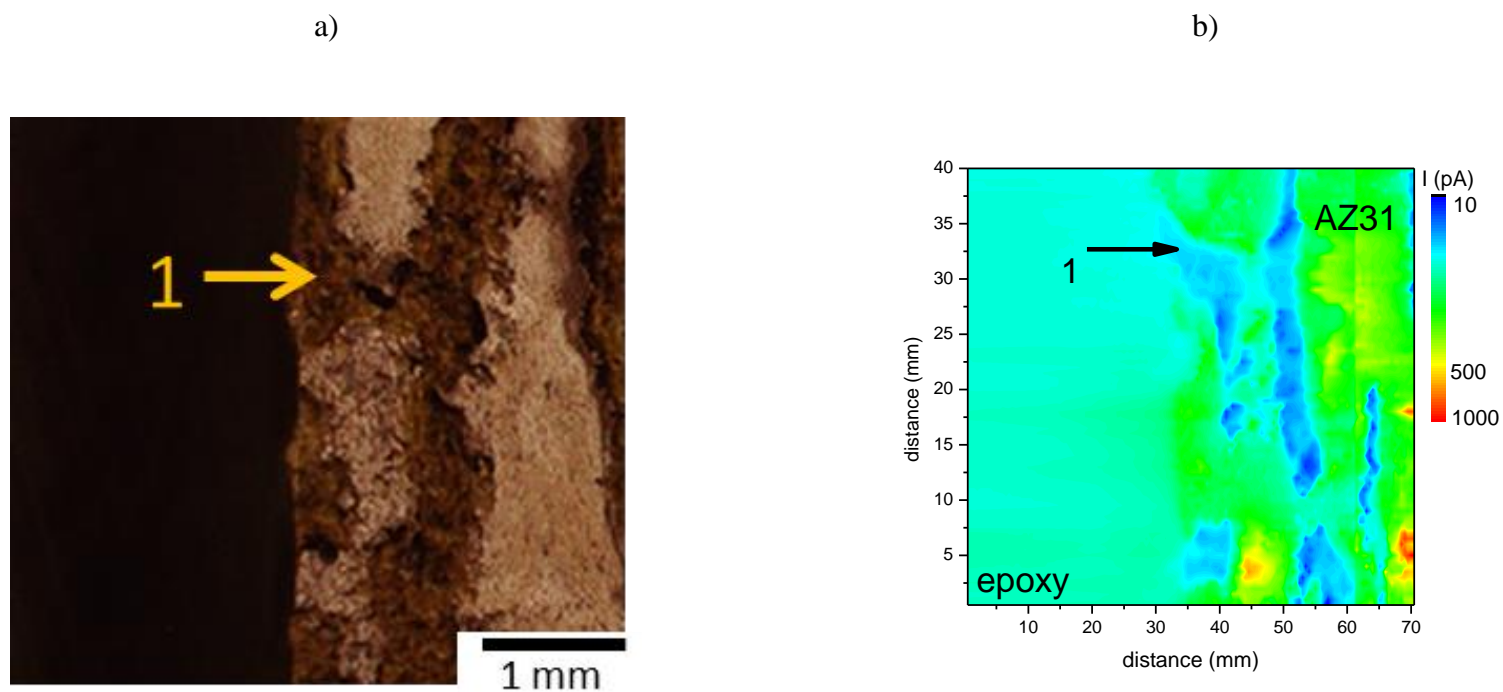
Figure 9. 12. a) Topographical, corrosion morphology. B) Scanning electrochemical Microscope scan of current on an AZ31B TIG weld sample. Scan was taken in 0.1 M NaCl with $[Ru(NH_3)_6]Cl_3$ as the mediator in 50 wt% methanol + 50 wt% H_2O. Scan was run at 100 μm/s with a step size of 10 μm. The tip was positioned 30 μm away from the sample surface and polarized at -100 mV.
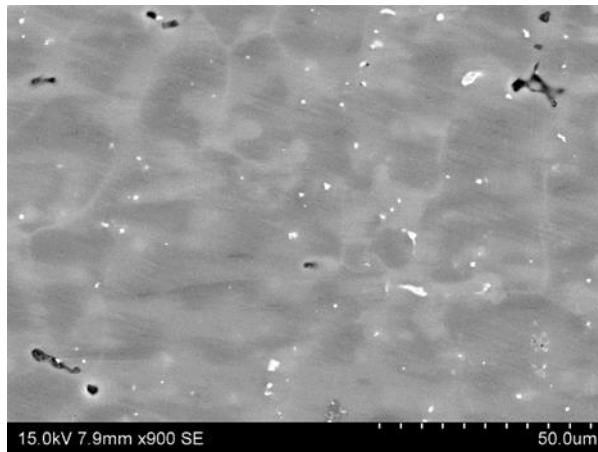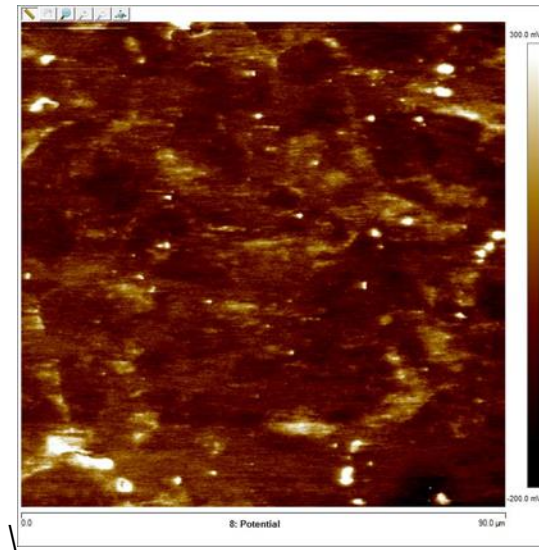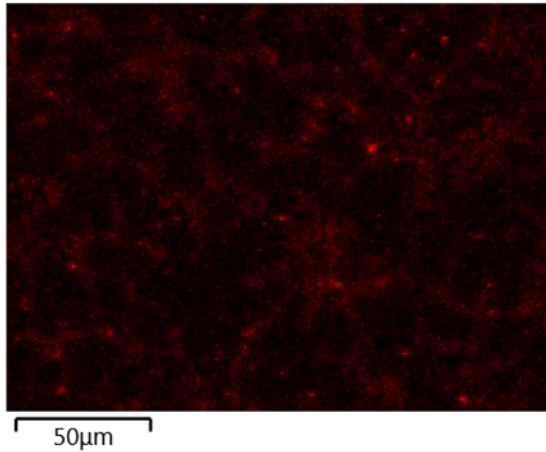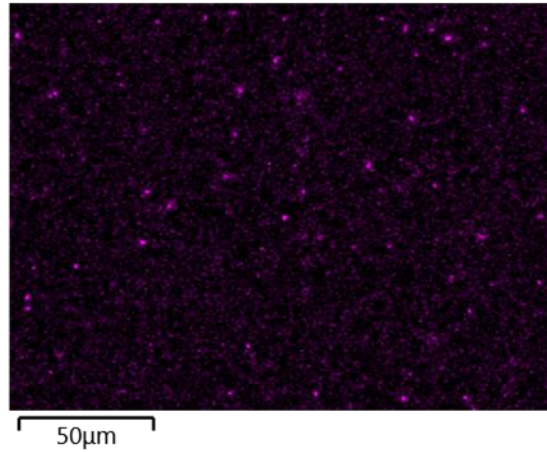
Figure 9. 13. SEM micrograph showing typical FZ microstructure (a) and accompanying, co-located SKPFM Volta potential map (b) with Al (c) and Mn (d) EDS maps for the same. In (b) bright spots are Al-Mn type precipitates and the less bright regions are Al-Zn rich solidification network.
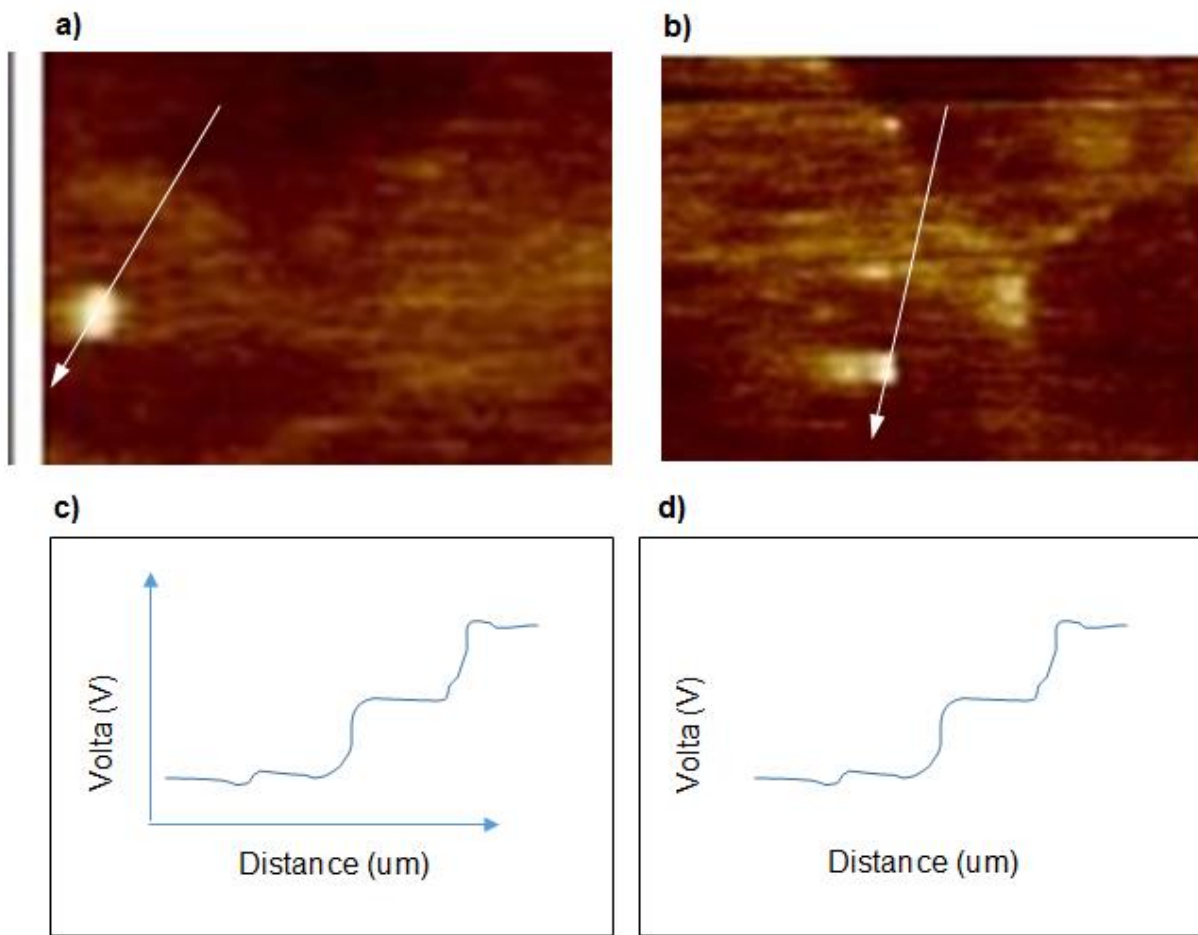
Figure 9. 14. SKPFM maps (a,b) of regions in the FZ, see Figure X. White arrows indicate measurement of Volta potential with distance (c,d).

5.00kV 6.9mm x1.20k SE   40.0um

20.0 μm
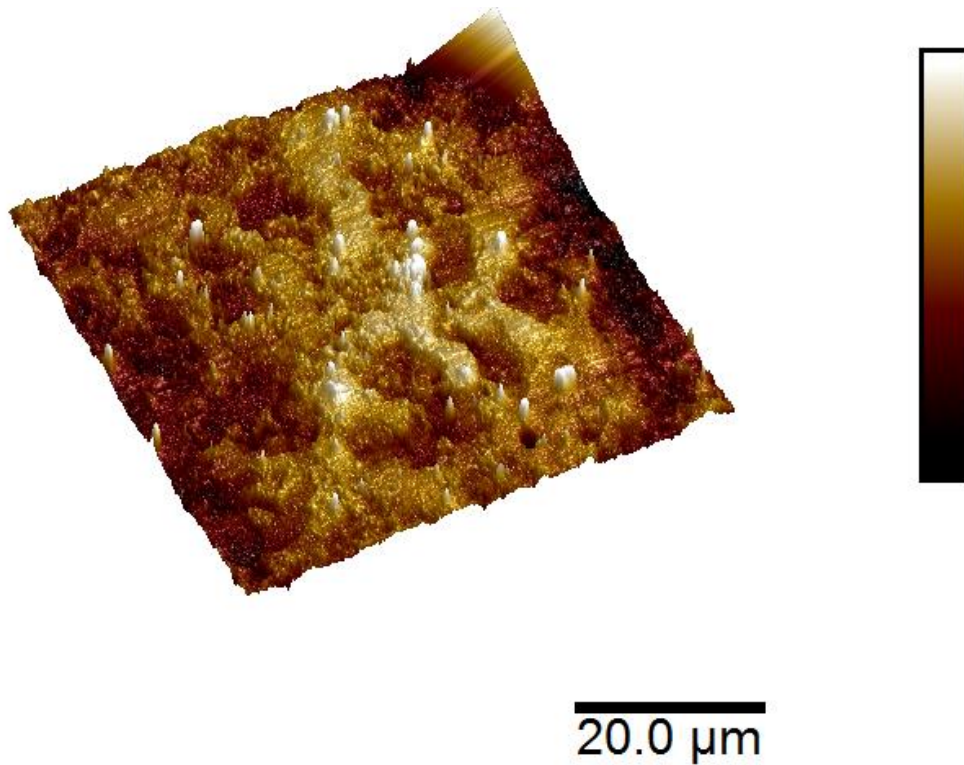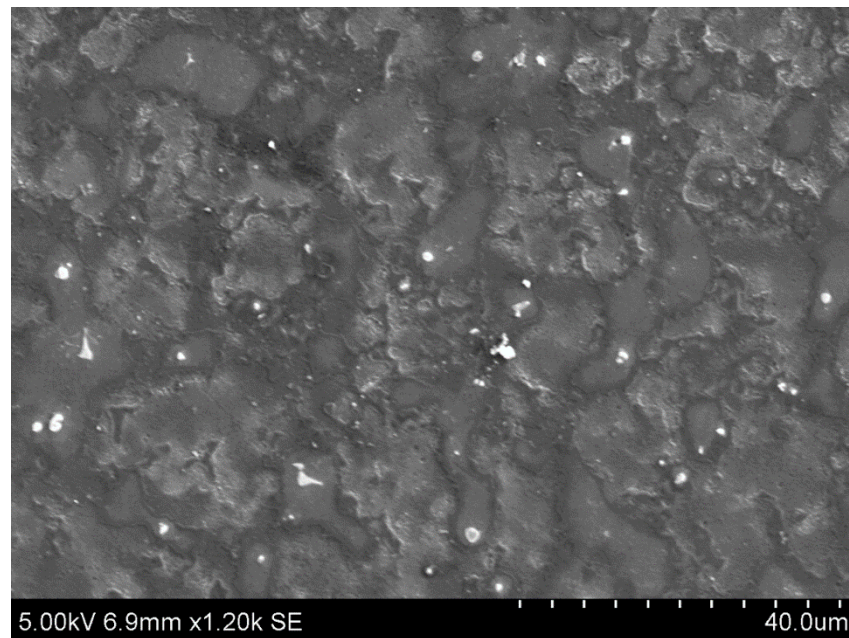
Figure 9. 15. SEM image of the FZ (top) following exposure to 0.6 M NaCl for 1 min to initiate corrosion attack. The bottom image shows the 3D AFM topography with SKPFM Volta potential skin overlaid.

357
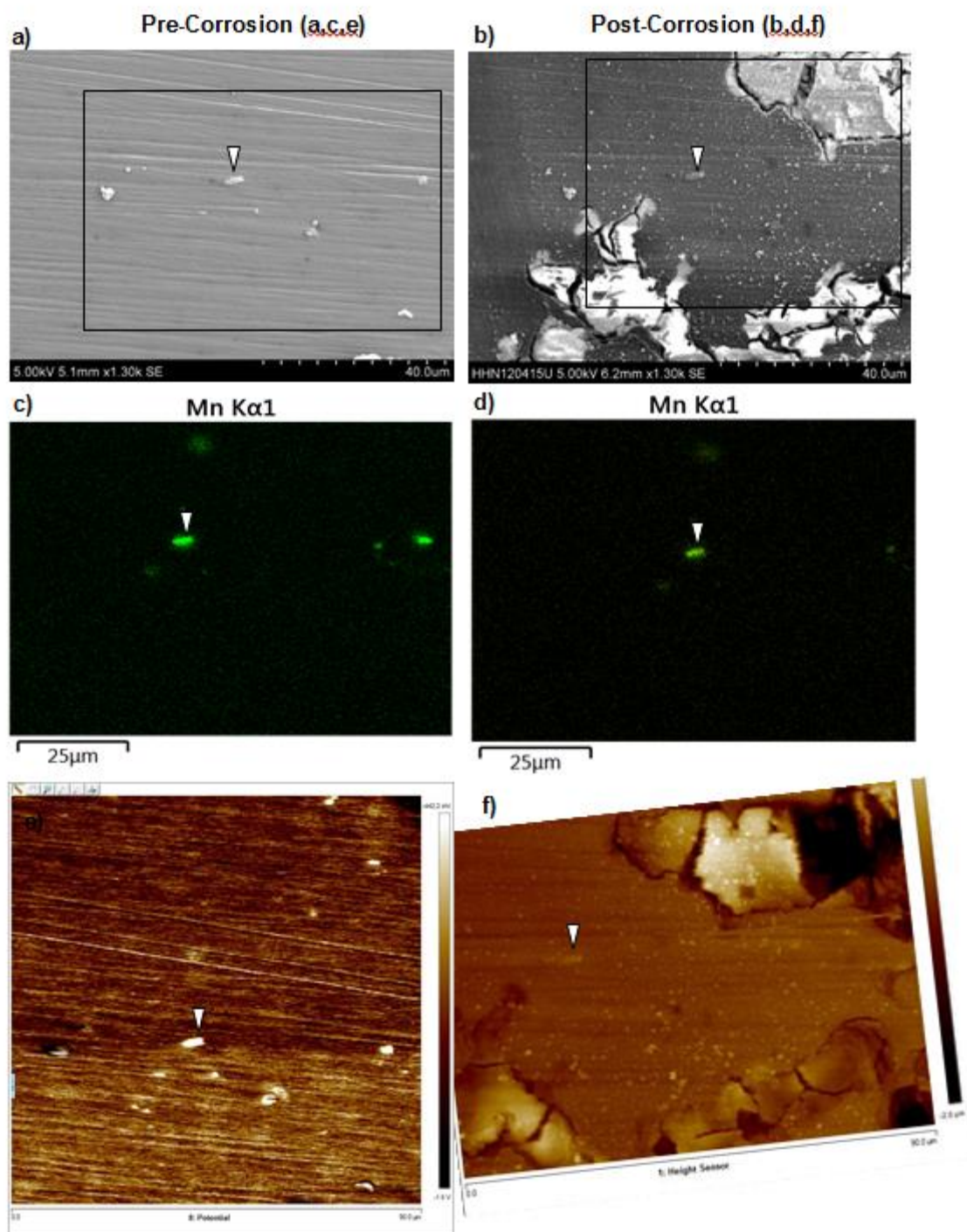
Figure 9. 16. AZ31B surface in the HAZ showing the a prominent Al-Mn IMP (white arrow) that has not participated in corrosion damage on the surface following exposure to 0.6 M NaCl for 1 min. SEM images and corresponding Mn EDS maps of the sample surface pre- (a,c) and post-corrosion (b,d). An SKPFM Volta potential map of the pre-corrosion surface (e) and AFM topography image (f) of the post-corrosion surface are also shown. The black boxes in (a) and (b) indicate the regions of SKPFM and AFM scans.

358

10 Conclusions, Mitigation Strategy and Future Work

10.1 <u>Conclusions</u>

This dissertation has studied the role of various metallurgical characteristics (i.e. intermetallic particle size/spacing, grain size, crystallographic orientation and solidification boundaries) on the corrosion properties of an AZ31B-H24 tungsten inert gas (TIG) weld. The investigation proposed a method of four parallel techniques (1) electrochemical impedance spectroscopy (EIS), (2) gravimetric mass loss, (3) hydrogen gas collection and (4) inductively coupled optical emission spectroscopy (ICP-OES) solution analysis which have been able to be utilized in multiple studies to reliably estimate the corrosion rate of a broad range of Mg-Al alloys in various environments.

It is recognized that the corrosion rate of the weld zone is a function of each of the metallurgical characteristics of that zone, however, studying these characteristics in isolated, model systems, allowed for better understanding of the effect of each of these characteristics in isolation. The metallurgical characteristics which dominate each zone are summarized in Figure 10. 1. It is argued that each of the metallurgical characteristics have some effect on corrosion. However, some of these characteristics have a larger impact than others. It was observed that crystallographic orientation may be important toward weld corrosion (Chapter 7) and developing a method to decrease the strong basal texture in AZ31B may increase the corrosion resistance. Also, solidification boundaries were shown to alter the corrosion resistance. However, the Al-Zn solidification boundaries observed in the FZ were shown to not be as strong of a cathode (and not as detrimental to the corrosion resistance) in comparison to Al-Mn and Al-Mn-Fe IMPs. Furthermore, IMPs and second phases dominate the corrosion of Mg-Al alloys while grain size (per se with other factors equal) does not have a significant impact on the corrosion rate (Chapter 5-6). Understanding of the particle size and distribution on the corrosion rate has been observed and processing methods which can increase the particle size and spacing may increase the corrosion resistance in Mg-Al alloys. Also, decreasing the area fraction or number of these particles can also decrease the corrosion rate for the same area fraction smaller more closely spaced particles increased the corrosion rate. For this reason, a method to homogenize the sample surface has been proposed as a potential mitigation method. Future work could include better

understanding and developing methods to homogenize the various weld zones to further increase the corrosion resistance.

In terms of the significance of these metallurgical characteristics on weld corrosion, the effect of grain size, IMP size, spacing and area fraction, crystallographic orientation and solidification boundaries can be ranked. From the work herein, particularly from Chapter 6, it was determined that area fraction of the IMPs has the largest impact on corrosion rate. In 0.6 M NaCl, the an increase in the area fraction (by 4 times the area) lead to an increase in the corrosion rate by 2 orders of magnitude (with an increase in the cathodic reaction rate by 4 orders of magnitude). It is reasoned that enhanced catalytic activity on the sample surface would be expected (28). However, the area for the anodically induced zone (A^{AIZ}) is about ten times larger, the increase in the cathodic kinetics per unit area is on the order of 1000 times larger as descried in Equation 6.3. Therefore, the effect of the Al redistribution as well as the enhanced cathodic activity (due to metal enrichment both increase the overall cathodic reaction rate dramatically as seen in Figure 6.7(b)[47].

The second most important metallurgical factor is the IMP size and spacing. In the 0.6 M NaCl solution, this was shown to affect the corrosion rate over an order of magnitude for both size and spacing. This is particularly important because there is an increase in the particle size and spacing in the weld HAZ which can then be correlated to the respective decrease in the corrosion rate observed in this weld zone.

The third most important metallurgical factor was crystallographic orientation. In the 0.6 M NaCl solution (described in Chapter 7) the variation in the corrosion rate on the basal orientation versus the prismatic or pyramidal orientations was about an order of magnitude. This is particularly important because the HAZs and the wrought base plate have a strong basal texture whereas the FZ has a more randomized texture. The decrease in the basal orientation in the FZ may explain the lower corrosion rate in the FZ.

Also, the solidification boundaries in the FZ have to be considered. It was shown in Chapter 8 that the solidification boundaries do not impact the corrosion rate as much as the IMPs. However, they can lead to higher amounts of localized corrosion. This is particularly important in the FZ as this zone suffers from localized corrosion rate in the α-Mg adjacent to the solidification boundaries.

The variation in grain size was observed to have little to no impact on the corrosion rate in the weld zone as well as in the Chapter 5 when corrosion rate was determined for various heat treatments on AZ31. This agrees with previous work[48].

10.2 <u>Suggested Mitigation Strategy</u>

The main suggested mitigation strategy is laser surface modification (LSM). Some initial work, similar to Chapter 3 for the AZ31 TIG weld isolated weld zones, has been performed on an LSM AZ31 TIG weld. However, this study (contained herein) simply sets the ground work for future, proposed work.

Surface modification is frequently used to increase the wear resistance of an alloy, particularly to enhance the tribological and mechanical properties of the material surface [1,2]. Laser surface modification has been proposed as one of those techniques. Several laser surface modification methods (diode laser surface melting[1,3], CO_2 and Nd:YAG laser surface modification [4]) have been successfully applied to Mg in the past which have been shown to mitigate micro-galvanic corrosion of Mg from cathodic second phases typically present in the as-received α-Mg matrix [5,6]. This process has been shown to homogenize these secondary phases in the material and decrease the corrosion rate with time [5,6].

Homogenization of Mg alloys is particularly important because it can decrease the amount of micro-galvanic corrosion to the α-Mg matrix in response to cathodically active intermetallic particles (IMPs) [7-9]. It has been shown previously that the spacing, size and area fraction of these IMPs can influence the corrosion rate of Mg alloys [7,8]. Homogenization of these particles can reintroduce these solute elements back into the α-Mg matrix which, depending on the electrochemical impact of the solute element on the corrosion properties of Mg may increase the corrosion resistance of the alloy [10]. For example, Al, Li, Mn and In added above their solubility limit will enhance the cathodic kinetics while Ca (above the solubility limit) will increase the anodic kinetics [10]. This is particularly a concern because most solute elements have substantially low solubility in Mg (12 wt % of Al, 2 wt% of Mn, 6 wt% of Zn and <0.01 wt% of many transition elements) which leads to the formation of IMPs as well as solidification boundaries (i.e. regions rich in solute which form during non-equilibrium solidification as are typically seen in a welded or cast microstructure) [10-12].

Decreasing the amount of cathodic sites (i.e. IMPs and solidification boundaries) in a Mg alloy may be particularly important as it may decrease the amount of cathodically induced

activation which occurs in the material [13-15]. Increased cathodic activity on the sample surface causes the hydrogen evolution reaction (HER) (as well as the HER exchange current density) to increase [13,15-19]. Rapid HER on the material can be correlated with increased corrosion or cathodic activity at these sites [20,21]. Therefore, processing methods which can decrease the number of these sites, such as LSM, may decrease the cathodic activation within the material and therefore decrease the corrosion rate.

10.3 <u>Experimental Procedures</u>

10.3.1 Material

The wrought AZ31B-H24 sheet was provided by Magnesium Elektron. The composition of the material is reported in wt. %, as provided by Quality Analysis and Testing Corporation (QUANT) as 3.02% Al, 0.3% Mn, 0.99% Zn, 0.025% Si, 0.005% Cu, 0.002% Ni, 0.005% Fe and Mg Bal.

10.3.2 Metallurgical Characterization of Laser Surface Modified Welds

All samples were fabricated by TIG welding as a butt weld [11,12]. This geometry allowed for a flat surface to do LSM across the surface. The Miller Syncrowave 200 TIG welder was operated at 125 amps under argon gas at 48.3 kPa with a flow rate of 18.5 L/min, and air cooled. All samples were prepared on material freshly ground through 240 grit to remove any oxides formed before processing. Welds were then processed using LSM within 30 minutes of the final polishing procedure. Samples were irradiated using a Lambda Physik pulsed excimer laser (λ= 248 nm, 25 ns full width at half maximum). The samples were rastered using a Newport linear actuator for a total irradiation of 200 laser pulses per area and a 50 % overlap with an oval shaped spot size of 30 mm X 1 mm described elsewhere [6]. Samples were processed in a pressurized chamber, fixed at 2 psi (14 kPa) above atmosphere, with a continual flow Ar (99.9%) processing gas at a rate of 20 L/min. A schematic of this process is contained in Figure 10. 2.

LSMed samples were analyzed with optical microscopy as well as scanning electron microscopy (SEM) using a FEI Quanta 650 microscope. Compositional analysis was performed using energy dispersive spectroscopy (EDS) methods [22]. Images were recorded at a working distance of 10 mm while operating at an accelerating voltage of 5 kV.

362

10.3.3 Corrosion Characterization

Electrochemical impedance spectroscopy (EIS), along with mass loss and hydrogen gas collection were measured simultaneously to characterize the corrosion behavior of an AZ31 TIG weld after LSM and compared to the corrosion rate, determined previously, for the wrought base plate and an AZ31 TIG weld [11,23]. The corrosion rate of the isolated LSMed weld zones was accomplished using electroplaters tape with a 1.23 mm^2 area hole to expose each zone. EIS scans were analyzed and fit using the software program ZView [24] to an equivalent circuit, seen in Figure 10. 3 [23,25,26] and were fit to a low frequency limit of at least 1 mHz. All values reported here are averages of at least three runs and based on the values obtained from EIS analysis performed at the open circuit potential (OCP).

The corrosion rate of a freely corroding metal was determined through an evaluation of R_P using the well-known Stern-Geary relationship [27,28]:

$$i_{corr} = \frac{B}{R_P} = \frac{\beta_a \beta_c}{2.303 R_P (\beta_a + \beta_c)} \qquad \text{Equation 10.1}$$

where β_a and β_c are the anodic and cathodic Tafel slopes, respectively, and $B = (1/2.303) \times (\beta_a \cdot \beta_c / (\beta_a + \beta_c))$. Several different Tafel assumptions were used, as found in literature [25,29,30]. The anodic charge density can then be estimated by integrating the EIS-estimated corrosion rate over the time of exposure, with knowledge of appropriate Tafel slopes estimated from literature [25,29,30]:

$$Q_a^{EIS} = \int i_{corr(\theta)} dt = \int \frac{\beta_a \beta_c}{2.303 R_P(t)(\beta_a + \beta_c)} dt \qquad \text{Equation 10.2}$$

Prior to testing, the electrolyte was pre-saturated with H_2 to reduce error in measuring the volume of the H_2 generated on the sample surface since H_2 gas was extremely soluble in most aqueous environments [31]. Following testing, samples were cleaned with ASTM G1-03 standard chromic acid solution (200 g/L CrO_3) and dried in a dry box for a least 24 hrs [32].

Faraday's law was used to convert mass loss, H_2 gas evolved and solute dissolved into anodic charge consumed with time. This was compared with the R_p estimated corrosion rate calculated by the EIS equivalent circuit. In order to calculate the mass loss of Mg (Δm), as measured gravimetrically with ± 0.1 mg resolution, the consumed anodic charge density (Q_a) was calculated using Equation 3:

$$Q_a^{\Delta m} = \frac{znF}{A} = \frac{z\Delta mF}{A(E.W.)}$$ Equation 10.3

Where z was equivalent electrons per mole of Mg oxidized, +2, n was the number of moles of Mg, F was Faraday's constant and a was the molar mass of Mg and A was the area of the exposed electrode. The equivalent weight (E.W.) of AZ31, N_{eq}, was determined using the procedure recommended in ASTM G106.[33] The EW was determined as the weighted average of a/z for the major alloying elements in a given alloy.[34] This is given by the following expression:

$$N_{eq} = \sum \left(\frac{f_i}{a_i/z_i}\right) = \sum \left(\frac{f_i z_i}{a_i}\right)$$ Equation 10.4

The E.W. (grams/equivalent) was then the reciprocal of the total number of equivalents (E.W.= N_{eq}^{-1}). The EW for AZ31B was determined to be 12.13 g/eq and was determined assuming congruent oxidation of Mg^{2+}, Al^{3+}, Mn^{2+} and Zn^{2+} where z=2+, z=3+, z=2+ and z=2+, respectively. When the NaCl solution became alkaline (approximately pH 10-11), Al^{3+} dissolution may become thermodynamically favored.

The volume of H_2 gas evolved can be converted to a corresponding cathodic charge (Q_c) via a combination of the Ideal Gas Law and Faraday's Law, which, during OCP corrosion, equals the anodic charge density (Q_a) per unit area of Mg corroding.[34] Thus:

$$Q_c^{H2} = Q_a^{H2} = \frac{znF}{A} = \frac{zPVF}{ART}$$ Equation 10.5

where P was the pressure inside the burette (assumed to be approximately 1 atm at sea level), V was the volume of H_2 gas collected, R was the ideal gas constant, T was the temperature and z as well as n are defined above.

Furthermore, to determine the corrosion rate with time, all samples were exposed for different immersion times to evaluate the effect of immersion time on the measured corrosion rate. Samples were immersed for 3, 24, or 48 hours at OCP in 0.6 M NaCl followed by a cathodic potentiodynamic polarization scan ranging from 0.5 mV above OCP to -2.3 V below OCP in a downward sweep at a rate of 1 mV/second.

The corrosion morphology was determined for each isolated weld zone to determine how the corrosion initiated and progressed over 24 hrs. Secondary Electron SEM micrographs were taken of each of the weld regions before immersion in 0.6 M NaCl and after immersion in 0.6 M NaCl for 24 hrs at OCP. All samples were cleaned with CrO_3 to remove any corrosion products and examine the corrosion morphology. Before the initial corrosion, the sample was marked

using a Vickers hardness tester to enable examination of the corrosion morphology at each stage in precise locations.

10.4 <u>Results</u>

10.4.1 Metallurgical Characterization of AZ31B TIG Weld After LSM

The microstructure and composition of an AZ31B TIG Weld after LSM was examined. This can be compared to the microstructure of the weld before LSM as described previously [12,23] as well as the LSM of the wrought base [6]. The material appeared as a homogeneous surface with no grain boundaries, however, as observed through EBSD, the bulk texture did not differ from the as-welded material (Figure 10. 4). The FZ was observed to have few IMPs throughout as well as a highly randomized texture via EBSD (Figure 10. 4). Compositional contrast and EDS of the FZ (Figure 10. 5) verify that very few IMPs were present in this weld zone and no Al-Zn rich solidification boundaries (previously observed to occur in the melted and resolidified FZ after TIG welding due to solute redistribution during solidification [11,12]) were formed during processing. The HAZ was shown to retain the dominant basal orientation, observed in both the wrought plate and the TIG weld (Figure 10. 4). Compositional analysis of the HAZ after LSM shows that there are several IMPs throughout this zone which are Al-rich (Figure 10. 6). These IMPs show "tails" which have resulted from partial melting or resolidification during processing (Figure 10. 6) as has been seen previously on wrought plate AZ31B processed by LSM [6]. These tails were oriented perpendicular to the orientation of the cylindrical laser spot and the areas sounding the particles were shown to be rich in Al, according to EDS analysis (Figure 10. 6(c)) [6].

10.4.2 Corrosion Morphology AZ31B TIG Weld After LSM

The corrosion morphology was observed on an AZ31 TIG Weld after LSM. In the FZ, little to no compositional contrast was observed in the BSE electron micrograph (Figure 10. 7(a)). After a 24 hour immersion at the open circuit potential in 0.6 M NaCl, corrosion has been shown to initiate and propagate along the sample surface, appearing as cracks in the LSM surface layer (Figure 10. 7((c-d)). In the HAZ, several IMPs were observed both before and after processing which had the representative "tail" as observed due to the partial homogenization of this secondary phase from LSM (Figure 10. 8(b,d)). The corrosion morphology in the HAZ had propagated further than in the FZ. The cracks, observed from the onset of corrosion were present along with a filiform-like morphology (Figure 10. 8(c-d)) which has been shown as the main

morphology seen in AZ31 material [14,35,36] and other Mg alloys [37-41]. The LSM layer appears semi-protective up to 24 hours although corrosion does initiate and propagate due to further immersion times, particularly in the HAZ where secondary phases may accelerate micro-galvanic corrosion and initiation [7,8].

10.4.3 Corrosion Characteristics of AZ31B TIG Weld after LSM

Kinetics of Isolated Weld Zones after LSM

The anodic and cathodic kinetics for the AZ31B TIG weld after LSM were observed in 0.6 M NaCl and compared to an AZ31B TIG weld before LSM. The anodic kinetics (taken after 3 hours at OCP in 0.6 M NaCl) a negligible variation in anodic kinetics was observed for all materials (Figure 10. 9). However, there was a strong variation in the cathodic kinetics for each of the samples (Figure 10. 10) after 3 hours and 24 hours at OCP in 0.6 M NaCl. For each immersion time, the wrought base plate had the highest cathodic kinetics while TIG welding resulting in a lower cathodic reaction rate for both the as-welded material and the weld after LSM. The LSMed weld had the slowest cathodic kinetics after both 3 and 24 hours of immersion (Figure 10. 10).

The cathodic kinetics were plotted as a function of time for the wrought plate, AZ31 TIG weld and the AZ31 TIG weld after LSM. The cathodic kinetics were observed to increase with time for each sample (Figure 10. 11) which has been shown to be indicative of cathodic activation, a phenomenon typically cited to occur in Mg alloys [13,15,16,20,21].

Corrosion Rate of Isolated Weld Zones after LSM

The Nyquist and Bode plots for an AZ31B wrought base, AZ31 TIG weld and an AZ31 TIG weld after LSM are shown in Figure 10. 12. For each sample, the equivalent circuit shown in Figure 10. 12 was able to make a reasonable fit with <15% error on each circuit element. The EIS spectra revealed two capacitive loops and an inductive loop for each sample, as has been previously described for Mg alloys in chloride environments [8,11,23,25,26]. From the EIS determined R_p the LSMed weld had the highest R_p (which correlates to the lowest corrosion rate).

Using the Stean-Geary relationship along with Faraday's law, the corrosion rates for the AZ31B TIG weld after LSM were calculated and compared to the corrosion rate for the wrought base plate and the AZ31B TIG weld (Figure 10. 13). It was observed that LSM decreased the cathodic charge consumed over a 24 hour immersion period in 0.6 M NaCl. These numbers correlate well to previous work on AZ31B wrought plate after LSM [6].

10.5 <u>Discussion</u>

10.5.1 Resultant Corrosion morphology in Isolated FZ and HAZ after Laser Surface Modification

After the sample was immersed in 0.6 M NaCl for 24 hours, it appeared as though the LSM layer had begun to crack in both the LSMed FZ and the LSMed HAZ (Figure 10. 7-10.8). This cracking appeared to have propagated further in the LSMed HAZ than in the LSMed FZ which correlates to the higher corrosion rates seen in the LSMed HAZ over the LSMed FZ. However, this corrosion had propagated much less, even after 24 hours, than the corrosion propagation on the wrought base and as-welded speciments, as shown elsewhere [11,12]. However, the initiation of cracks along the LSMed surface revealed that, while LSM is a solution to temporarily decrease the corrosion rate of a sample, it is not a long-term solution.

10.5.2 Corrosion Rates and Cathodic Kinetics of Isolated Laser Surface Modified Weld Regions

The corrosion rates of an AZ31 TIG weld after LSM were characterized. The FZ had the lowest corrosion rate while the HAZ had a slightly higher corrosion rate (Figure 10. 13). There is a distinct ranking of the corrosion rate for the wrought base, AZ31 TIG weld and AZ31 TIG weld after LSM as follows $i_{corr(LSM\_FZ)} < i_{corr(LSM\_HAZ)} < i_{corr(HAZ)} < i_{corr(FZ)} < i_{corr(base)}$. The use of three different Tafel slope assumptions revealed little variation in the corrosion rate or ranking.

Looking at the cathodic kinetics for the wrought plate, AZ31 TIG weld and AZ31 TIG weld after LSM the cathodic kinetics decreased after welding (Figure 10. 10-10. 11). However, a much more substantial decrease in the cathodic kinetics occurred to the weld after LSM which correlates to the higher corrosion resistance caused by LSM. However, it is noted that the cathodic kinetics increase (for each sample type) with time (Figure 10. 11). This is typically indicative of the cathodic activation and has been seen in AZ31 previously [7,8,11,12,23].

10.5.3 Variation in Cathodic Activation Due to Laser Surface Modification

There was a smaller increase in the cathodic kinetics for the LSMed weld zones than either the unprocessed weld zones or the wrought base material (Figure 10. 11). This may be indicative of less cathodic activation occurring in the LSMed weld [7,8,11,12]. Due to the partial homogenization of the IMPs and the solidification boundaries, there are less sites for cathodic activation at IMPs. Therefore the cathodic kinetics do not increase as dramatically with time.

At the cathodic IMPs in the α-Mg matrix, there is typically a localized pH increase to ~11. The increased alkalinity within this region leads to dissolution Al on the sample surface as well as the redeposition of Al away from the IMP interface [42,43] as AlO_2^- according to [44]:

$$Al + 2H_2O \rightarrow AlO_2^- + 4H^+ + 3e^- \tag{6}$$

However, without these pH cells there is less thermodynamic probability for the Al to redistribute along the sample surface as AlO_2^- [7,8]. This agrees with the trend seen in the cathodic kinetics with time (Figure 10. 10-10. 11) for the wrought base, AZ31 TIG weld and the AZ31 TIG weld after LSM.

10.5.4 Corrosion of AZ31B Weld Versus AZ31B Weld after Laser Surface Modification

The corrosion rate of the AZ31B wrought plate material as well as the isolated weld zones were studied and compared. It was shown that, after welding, the corrosion rate for each of the isolated weld zones was lower than the wrought plate material. This agreed with the previous work which shows that wrought plate has a higher corrosion rate the weld region [45,46].

10.6 <u>Conclusions and Future Work</u>

1. Laser surface modification of an AZ31 TIG weld is presented as a viable method to decrease the intrinsic corrosion rate of a weld in marine environments.
2. Homogenization of the sample surface leads to a decrease in the number of sites for cathodic activation and therefore less of an increase in the cathodic kinetics with time.
3. Future work would be to improve the lifespan of this surface layer.
4. Future work would be to test the LSM layer in the TRIS and EDTA environments.

References

1. G. Abbas, L. Li, U. Ghazanfar, and Z. Liu, "Effect of high power diode laser surface melting on wear resistance of magnesium alloys," Wear 260, 1–2 (2006): p. 175-180.
2. J. Yang, F.-z. Cui, I.S. Lee, and X. Wang, "Plasma surface modification of magnesium alloy for biomedical application," Surface and Coatings Technology 205, Supplement 1, (2010): p. S182-S187.
3. A.S. K. Murayama, T. Takagi, S. Kamado, Y. Kojima, H. Hiraga, "Surface Modification of Magnesium Alloys by Laser Alloying Using Si Powder," materials science forum 419-422, (2003): p. 969-974.
4. T.M. Yue, A.H. Wang, and H.C. Man, "Improvement in the corrosion resistance of magnesium ZK60SiC composite by excimer laser surface treatment," Scripta Mater 38, 2 (1997): p. 191-198.
5. R.K.S. Raman, S. Murray, and M. Brandt, "Laser assisted modification of surface microstructure for localised corrosion resistance of magnesium alloys," Surf Eng 23, 2 (2007): p. 107-111.
6. M.A. Melia, P. Steiner, N. Birbilis, J.M. Fitz-Gerald, and J.R. Scully, "Excimer Laser Surface Modification of AZ31B-H24 for Improved Corrosion Resistance " Corrosion Journal 72, 1 (2016): p. 95-109.
7. L.G. Bland, J.J. Bhattacharyya, S.R. Agnew, J.M. Fitz-Gerald, and J.R. Scully, "Effect of Al-Mn and Al-Mn-Fe Intermetallic Particle Size and Distribution on the Corrosion of Mg-3Al-1Zn alloy: AZ31," Acta Mater In Review, (2016).
8. L.G. Bland, N. Birbilis, and J.R. Scully, "Exploring the Effects of Intermetallic Particle Size and Spacing on the Corrosion of Mg-Al Alloys Using Model Electrodes," J Electrochem Soc In Review, (2016).
9. A.D. Südholz, N.T. Kirkland, R.G. Buchheit, and N. Birbilis, "Electrochemical Properties of Intermetallic Phases and Common Impurity Elements in Magnesium Alloys," Electrochemical and Solid-State Letters 14, 2 (2011): p. C5.
10. K. Gusieva, C.H.J. Davies, J.R. Scully, and N. Birbilis, "Corrosion of magnesium alloys: the role of alloying," Int Mater Rev (2014): p. 169-194.
11. L.G. Bland, J.M. Fitz-Gerald, and J.R. Scully, "Metallurgical and Electrochemical Characterization of the Corrosion of AZ31B-H24 Tungsten Inert Gas Weld: Isolated Weld Zones," Corrosion Journal 72, 9 (2016): p. 1116-1132.
12. L.G. Bland, B.C.R. Troconis, R.J.S. Jr., J.M. Fitz-Gerald, and J.R. Scully, "Metallurgical and Electrochemical Characterization of the Corrosion of Mg-Al-Zn Alloy AZ31B-H24 Tungsten Inert Gas Weld: Galvanic Corrosion Between Weld Zones " Corrosion Journal in press (DOI: 10.5006/2078), (2016).
13. M. Taheri, J.R. Kish, N. Birbilis, M. Danaie, E.A. McNally, and J.R. McDermid, "Towards a Physical Description for the Origin of Enhanced Catalytic Activity of Corroding Magnesium Surfaces," Electrochim Acta 116, (2014): p. 396-403.
14. Z.P. Cano, M. Danaie, J.R. Kish, J.R. McDermid, G.A. Botton, and G. Williams, "Physical Characterization of Cathodically-Activated Corrosion Filaments on Magnesium Alloy AZ31B," Corrosion 71, 2 (2015): p. 146-159.

15. N. Birbilis, A.D. King, S. Thomas, G.S. Frankel, and J.R. Scully, "Evidence for enhanced catalytic activity of magnesium arising from anodic dissolution," Electrochim Acta 132, 0 (2014): p. 277-283.
16. G. Williams, H. ap Llwyd Dafydd, and R. Grace, "The localised corrosion of Mg alloy AZ31 in chloride containing electrolyte studied by a scanning vibrating electrode technique," Electrochim Acta 109, 0 (2013): p. 489-501.
17. G. Williams, N. Birbilis, and H.N. McMurray, "The source of hydrogen evolved from a magnesium anode," Electrochemistry Communications 36, 0 (2013): p. 1-5.
18. G. Williams, K. Gusieva, and N. Birbilis, "Localized Corrosion of Binary Mg-Nd Alloys in Chloride-Containing Electrolyte Using a Scanning Vibrating Electrode Technique," Corrosion 68, 6 (2012): p. 489-498.
19. G. Williams and H.N. McMurray, "Localized Corrosion of Magnesium in Chloride-Containing Electrolyte Studied by a Scanning Vibrating ElectrodeTechnique," J Electrochem Soc 155, 7 (2008): p. C340-C349.
20. G.S. Frankel, A. Samaniego, and N. Birbilis, "Evolution of hydrogen at dissolving magnesium surfaces," Corros Sci 70, (2013): p. 104-111.
21. G.S. Frankel, S. Fajardo, and B.M. Lyncha, "Introductory lecture on corrosion chemistry: a focus on anodic hydrogen evolution on Al and Mg," faraday discussions 180, (2015): p. 11-33.
22. "AZtecEnergy: EDS Software," Oxford Instruments (2015).
23. L.G. Bland, A.D. King, N. Birbilis, and J.R. Scully, "Assessing the Corrosion of Commercially Pure Magnesium and Commercial AZ31B by Electrochemical Impedance, Mass-loss, Hydrogen Collection and ICP-OES Solution Analysis," Corrosion Journal 71, 2 [Special Issue] (2015): p. 128-145.
24. S. Associates, *ZView*.
25. A.D. King, N. Birbilis, and J.R. Scully, "Accurate Electrochemical Measurement of Magnesium Corrosion Rates; a Combined Impedance, Mass-Loss and Hydrogen Collection Study," Electrochim Acta 121, 1 (2014): p. 394-406.
26. M. Curioni, F. Scenini, T. Monetta, and F. Bellucci, "Correlation between electrochemical impedance measurements and corrosion rate of magnesium investigated by real-time hydrogen measurement and optical imaging," Electrochim Acta 166, (2015): p. 372-384.
27. J.R. Scully, Corrosion Journal 56, (2000): p. 199-218.
28. M. Stern and A.I. Geary, J Electrochem Soc 104: p. 56-63.
29. F. Cao, Z. Shi, J. Hofstetter, P.J. Uggowitzer, G. Song, M. Liu, and A. Atrens, "Corrosion of ultra-high-purity Mg in 3.5% NaCl solution saturated with Mg(OH)2," Corros Sci 75, (2013): p. 78-99.
30. Z. Shi, F. Cao, G.L. Song, M. Liu, and A. Atrens, "Corrosion behaviour in salt spray and in 3.5% NaCl solution saturated with Mg(OH)2 of as-cast and solution heat-treated binary Mg–RE alloys: RE=Ce, La, Nd, Y, Gd," Corros Sci 76, 0 (2013): p. 98-118.
31. J.L. Bullister, N.L. Guinasso, and D.R. Schink, "Dissolved hydrogen, carbon monoxide, and methane at the CEPEX site," Journal of Geophysical Research: Oceans 87, C3 (1982): p. 2022-2034.
32. ASTM-G1, "Standard Practice for Preparing, Cleaning, and Evaluating Corrosion Test Specimens," ASTM International G1, (2011).

33. ASTM-G106, "Standard Practice for Verification of Algorithm and Equipment for Electrochemical Impedance Measurements," ASTM International (2010).

34. D.A. Jones, "Principles and Prevention of Corrosion," Prentice Hall Upper Saddle River. NJ. 2nd Ed (1996).

35. A. Samaniego, I. Llorente, and S. Feliu Jr, "Combined effect of composition and surface condition on corrosion behaviour of magnesium alloys AZ31 and AZ61," Corros Sci 68, (2013): p. 66-71.

36. L. Wang, T. Shinohara, and B.-P. Zhang, "Influence of chloride, sulfate and bicarbonate anions on the corrosion behavior of AZ31 magnesium alloy," J Alloy Compd 496, 1–2 (2010): p. 500-507.

37. O. Lunder, J.E. Lein, S.M. Hesjevik, T.K. Aune, and K. Nişancioğlu, "Corrosion morphologies on magnesium alloy AZ 91," Materials and Corrosion 45, 6 (1994): p. 331-340.

38. M.P. Brady, G. Rother, L.M. Anovitz, K.C. Littrell, K.A. Unocic, H.H. Elsentriecy, G.-L. Song, J.K. Thomson, N.C. Gallego, and B. Davis, "Film Breakdown and Nano-Porous Mg(OH)2 Formation from Corrosion of Magnesium Alloys in Salt Solutions," J Electrochem Soc 162, 4 (2015): p. C140-C149.

39. R.C. Zeng, J. Zhang, W.J. Huang, W. Dietzel, K.U. Kainer, C. Blawert, and W. Ke, "Review of studies on corrosion of magnesium alloys," T Nonferr Metal Soc 16, (2006): p. s763-s771.

40. E. Ghali, W. Dietzel, and K.U. Kainer, "General and localized corrosion of magnesium alloys: A critical review," J Mater Eng Perform 13, 1 (2004): p. 7-23.

41. Z.P. Cano, J.R. McDermid, and J.R. Kish, "Cathodic Activity of Corrosion Filaments Formed on Mg Alloy AM30," J Electrochem Soc 162, 14 (2015): p. C732-C740.

42. M. Danaie, R.M. Asmussen, P. Jakupi, D.W. Shoesmith, and G.A. Botton, "The cathodic behaviour of Al–Mn precipitates during atmospheric and saline aqueous corrosion of a sand-cast AM50 alloy," Corros Sci 83, (2014): p. 299-309.

43. R.M.A. Mohsen Danaie, Pellumb Jakupi, David W. Shoesmith, and G.A. Botton, "The role of aluminum distribution on the local corrosion resistance of the microstructure in a sand-cast AM50 alloy," Corros Sci 77, (2013).

44. M. Pourbaix, Atlas of electrochemical equilibria in aqueous solutions (Huston, TX: National Association of Corrosion Engineers, 1974.

45. G. Ben-Hamu, D. Eliezer, C.E. Cross, and T. Böllinghaus, "The relation between microstructure and corrosion behavior of GTA welded AZ31B magnesium sheet," Materials Science and Engineering: A 452–453, 0 (2007): p. 210-218.

46. L. Liu and R. Xu, "Investigation of the corrosion behaviour of laser-TIG hybrid welded Mg alloys," Corros Sci 52, 9 (2010): p. 3078-3085.

47. T. Cain, S.B. Madden, N. Birbilis, and J.R. Scully, "Evidence of the Enrichment of Transition Metal Elements on Corroding Magnesium Surfaces Using Rutherford Backscattering Spectrometry," J Electrochem Soc 162, 6 (2015): p. C228-C237.

48. J.R. Kish, G. Williams, J.R. McDermid, J.M. Thuss, and C.F. Glover, "Effect of Grain Size on the Corrosion Resistance of Friction Stir Welded Mg Alloy AZ31B Joints," J Electrochem Soc 161, 9 (2014): p. C405-C411.
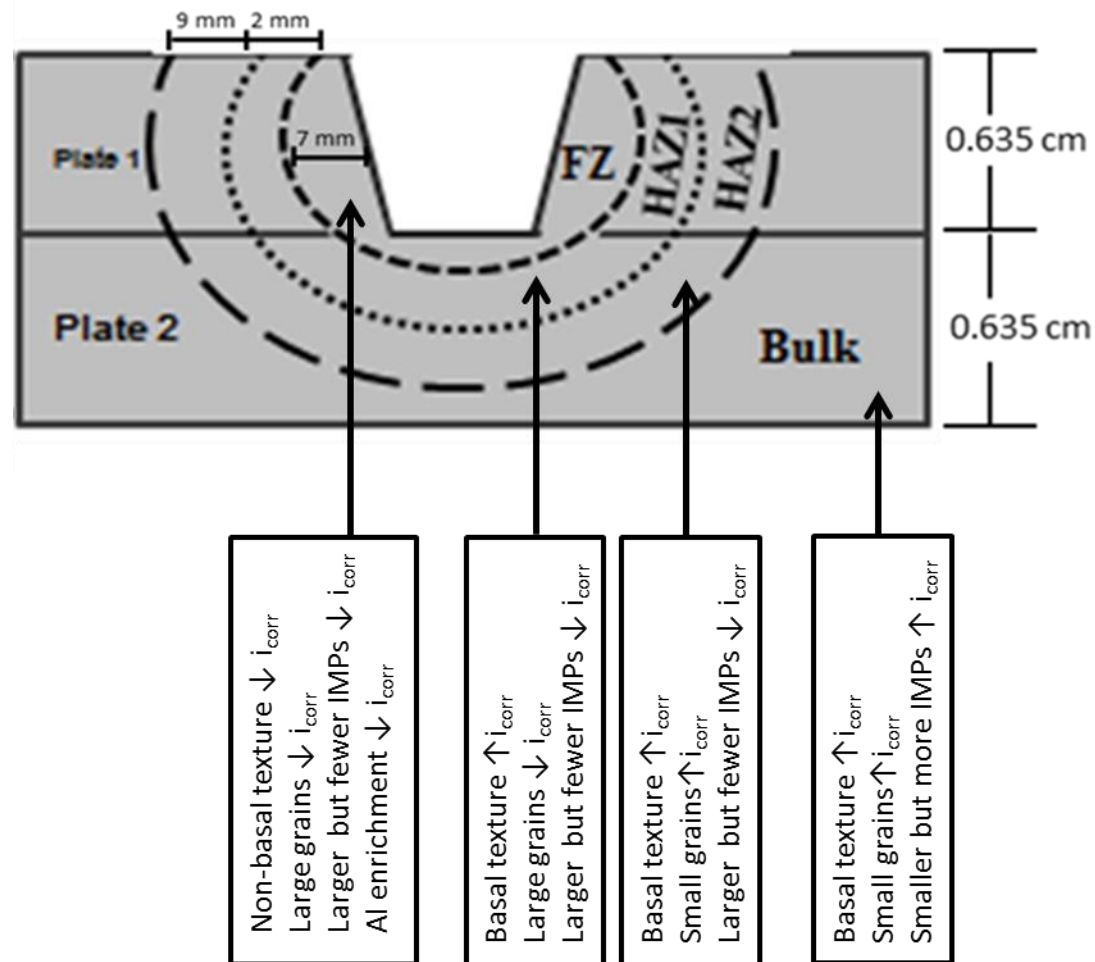
Figure 10. 1. Summary of the metallurgical characteristics, by weld zone, which affect the overall corrosion rate in Mg-Al alloys
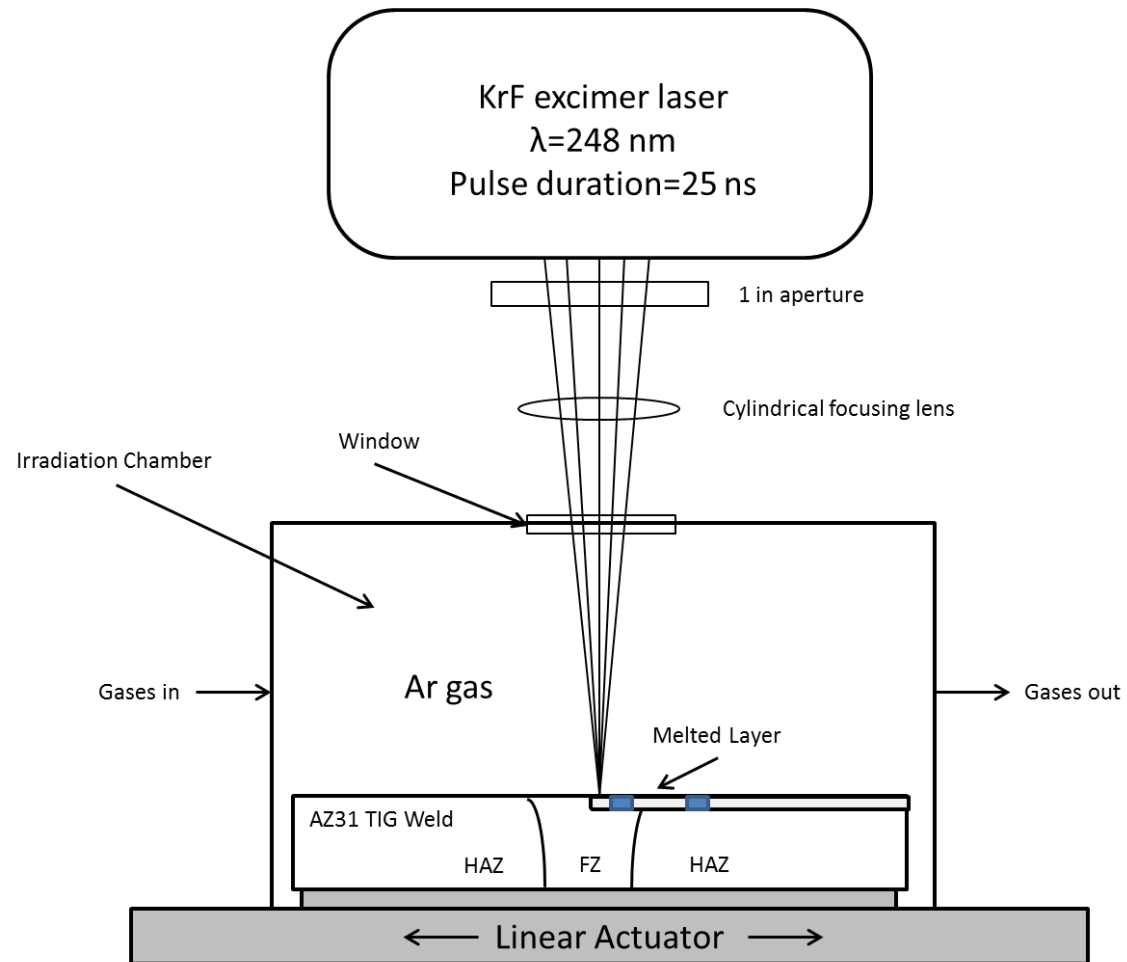
Figure 10. 2. Schematic of LSM process on an AZ31 TIG weld. LSM was performed on a sample of two butt joined AZ31B plates. The blue squares (color version) refer to where isolated LSMed weld zone corrosion tests were performed.
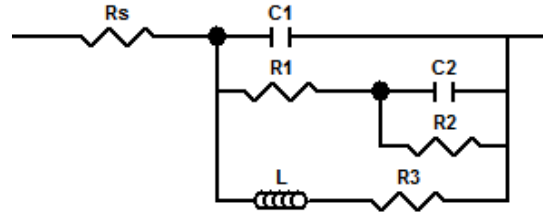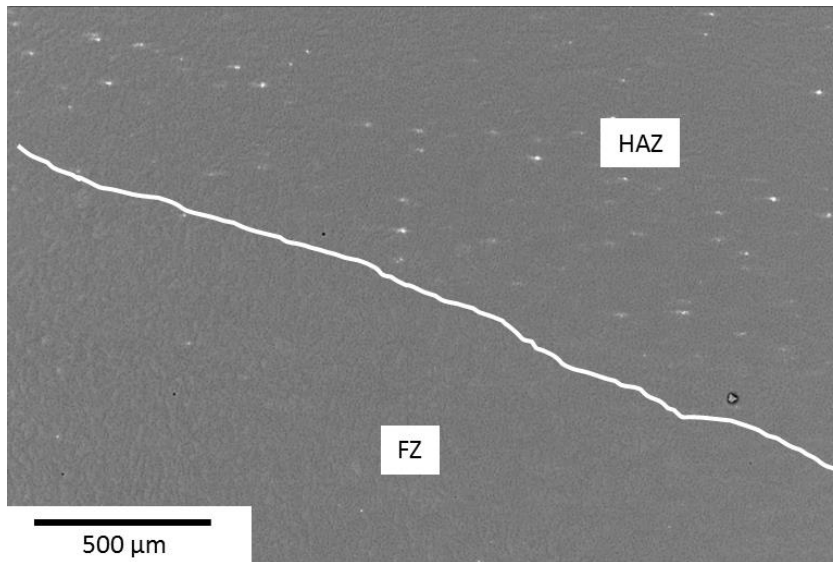
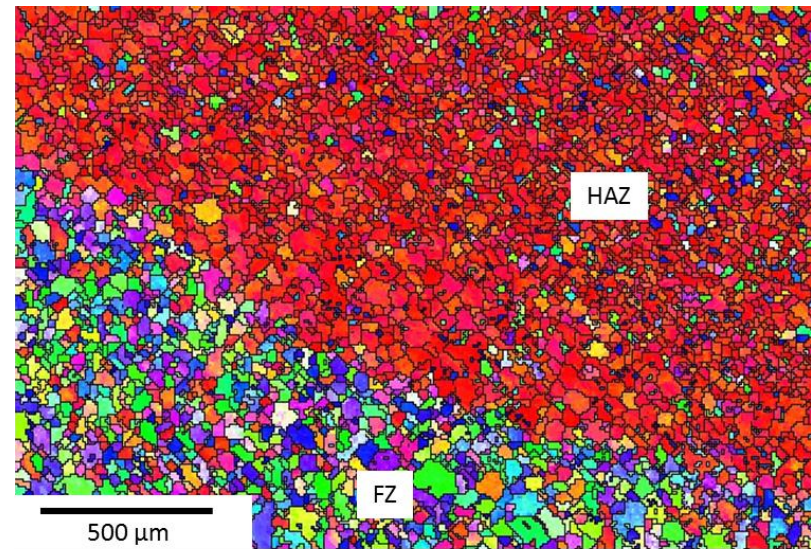Figure 10. 3: Equivalent circuit diagram used to model pseudo-inductive electrochemical impedance response on corroding Mg in 0.6 M NaCl solution.

a)

b)

Figure 10. 4. a) Secondary electron micrograph of AZ31B-H24 LSM TIG weld along the edge of the FZ and HAZ with b) EBSD map, showing the variation in crystallographic orientation along the weld regions.
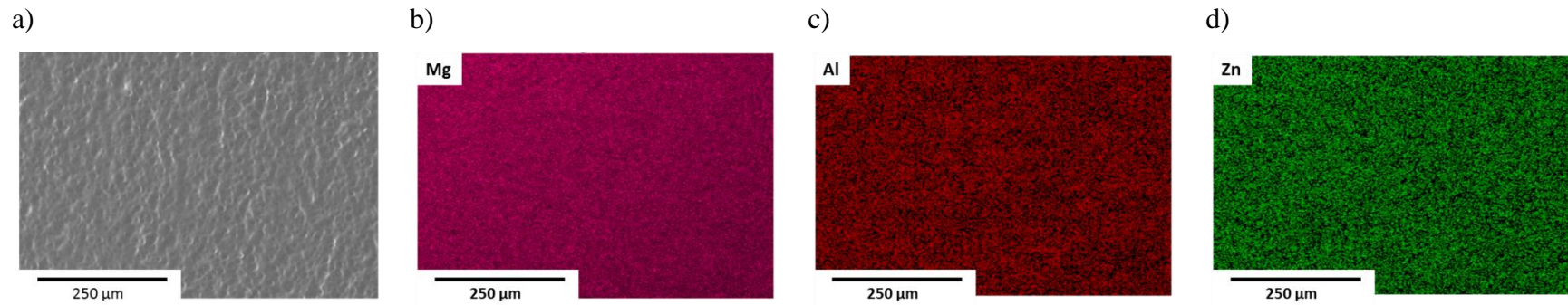
Figure 10. 5. a) Electron micrograph of AZ31B TIG weld FZ after LSM b) Mg, c) Al and d) Zn EDS maps showing a homogenous surface.
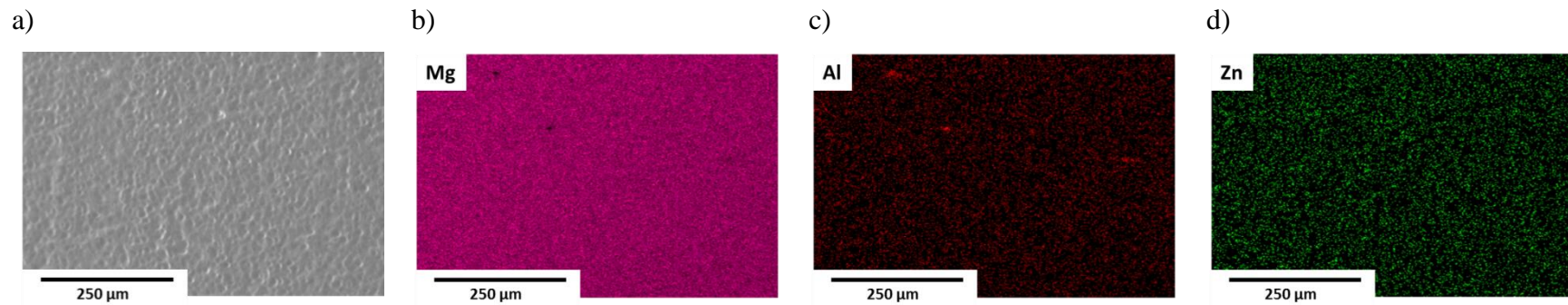
Figure 10. 6. a) Electron micrograph of AZ31B TIG weld HAZ after LSM b) Mg, c) Al and d) Zn EDS maps showing compositional variations at Al-rich IMPs.
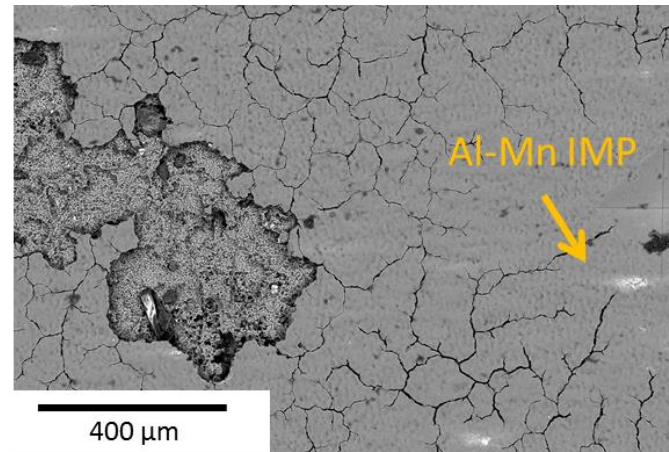
a)

b)

400 μm

400 μm

c)

d)

400 μm

400 μm
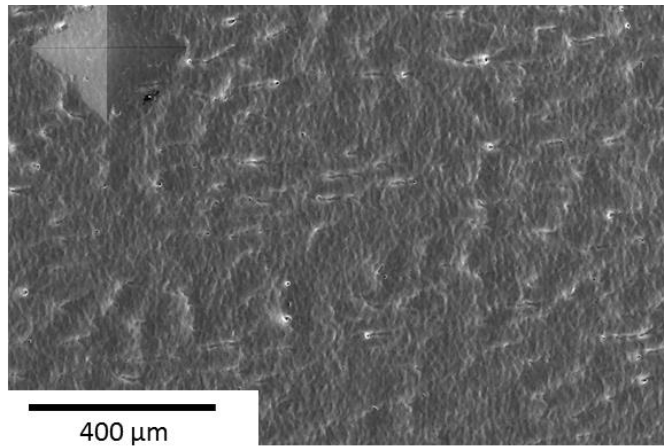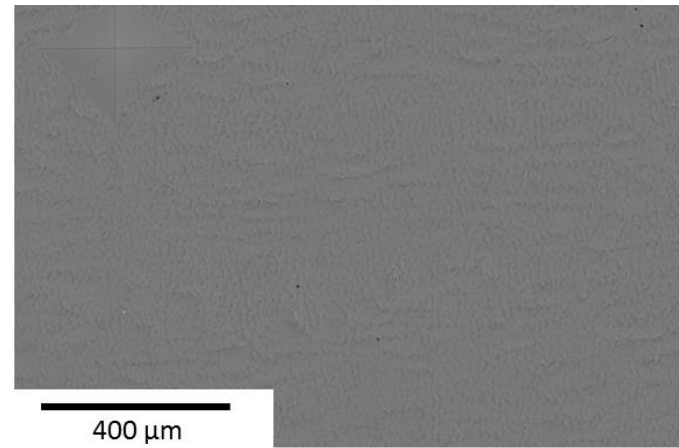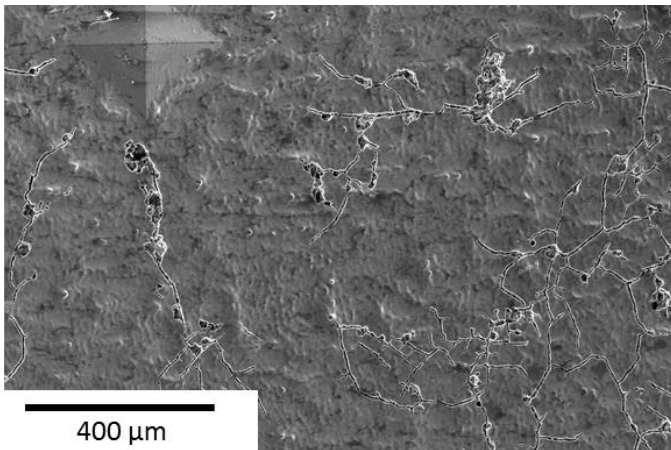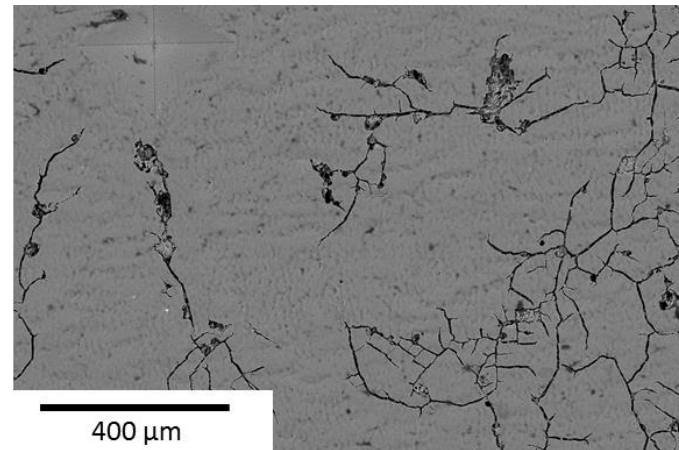
Figure 10. 7. a) Secondary micrograph and b) backscatter micrograph of AZ31B TIG weld FZ after LSM before exposure. c) Secondary micrograph and d) backscatter micrograph of AZ31B TIG weld FZ after LSM after exposure in 0.6 M NaCl for 24 hours and cleaned with CrO_3 to remove any oxides.
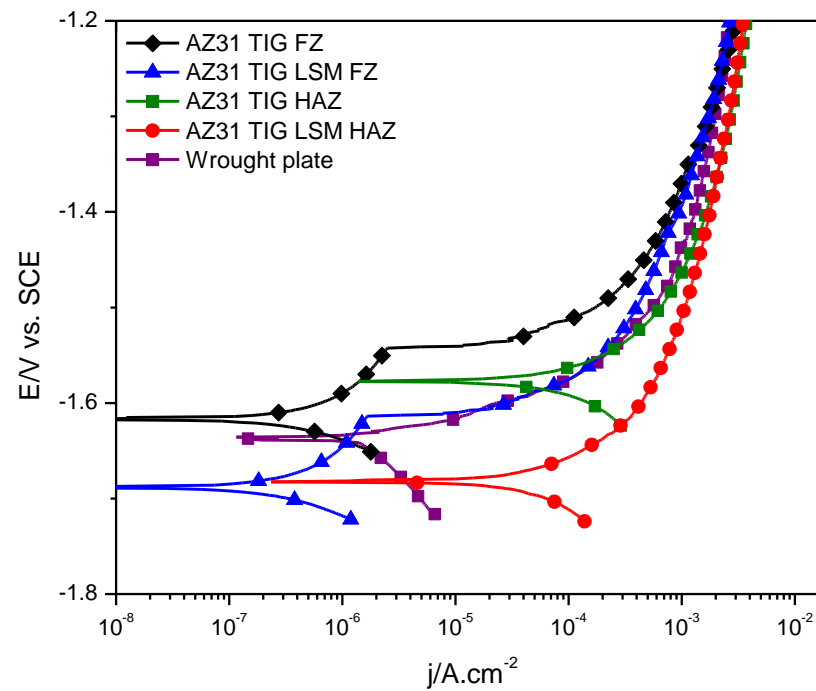
376

a)

b)

Al-Mn IMP

400 μm

400 μm

c)

d)

Al-Mn IMP

400 μm

400 μm
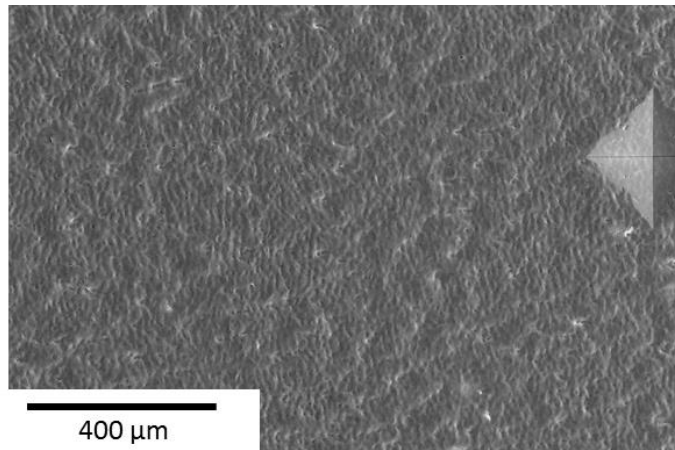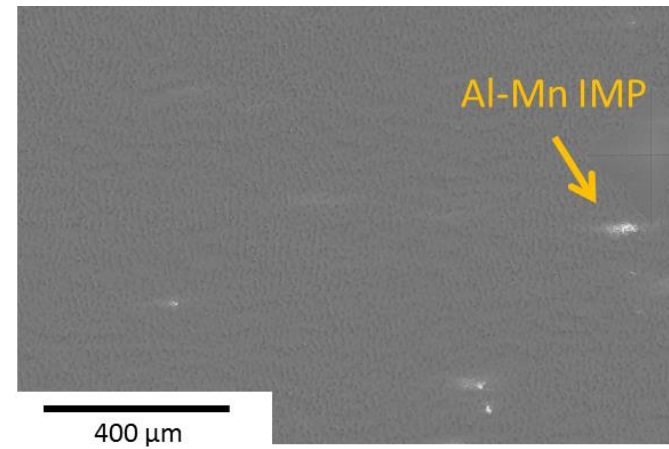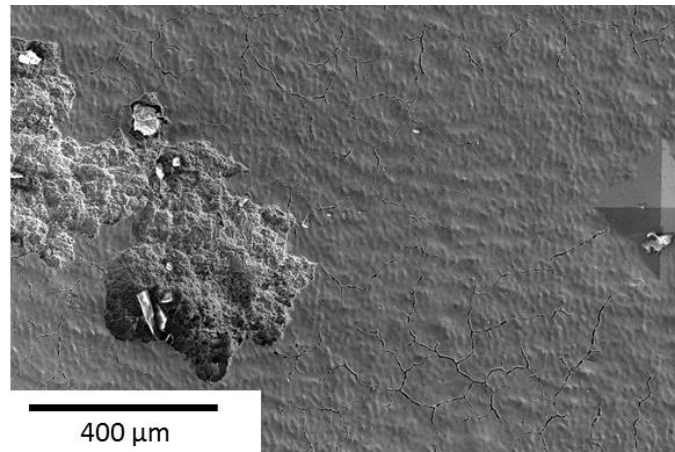
Figure 10. 8. a) Secondary micrograph and b) backscatter micrograph of AZ31B TIG weld HAZ after LSM before exposure. c) Secondary micrograph and d) backscatter micrograph of AZ31B TIG weld HAZ after LSM after exposure in 0.6 M NaCl for 24 hours and cleaned with CrO_3 to remove any oxides.

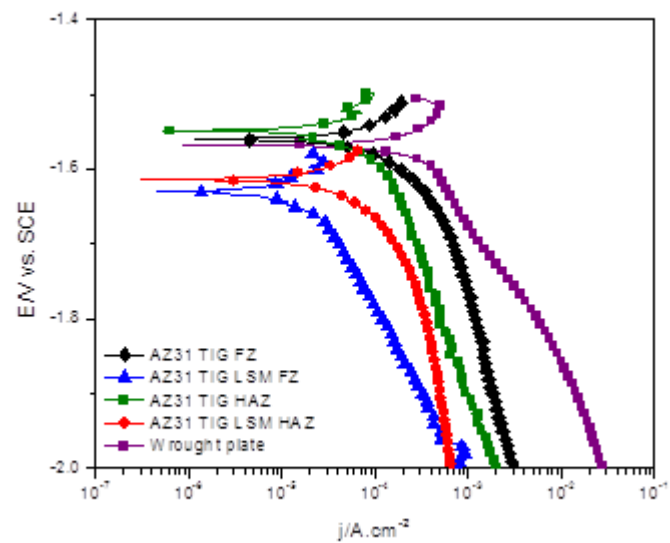Figure 10. 9. Variation in the anodic kinetics of an AZ31B TIG isolated weld zones after LSM in 0.6 M NaCl after 3 hours at OCP.

a)
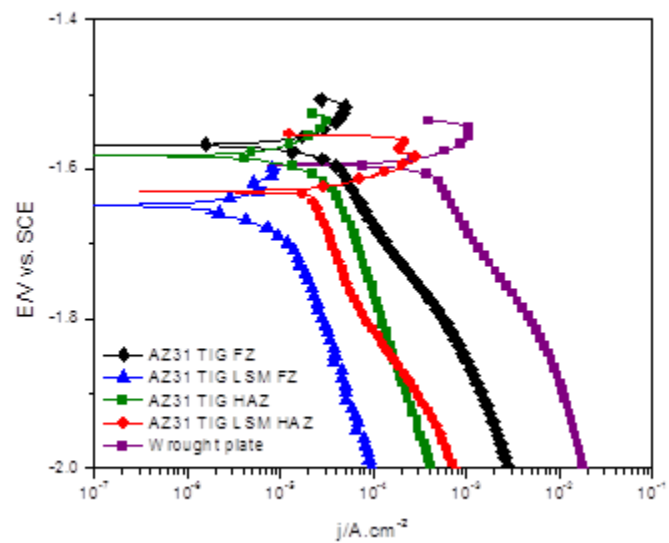
b)

Figure 10. 10. Variation in the cathodic kinetics of an AZ31B TIG isolated weld zones after LSM in 0.6 M NaCl after a)3 hours and b) 24 hours at OCP.
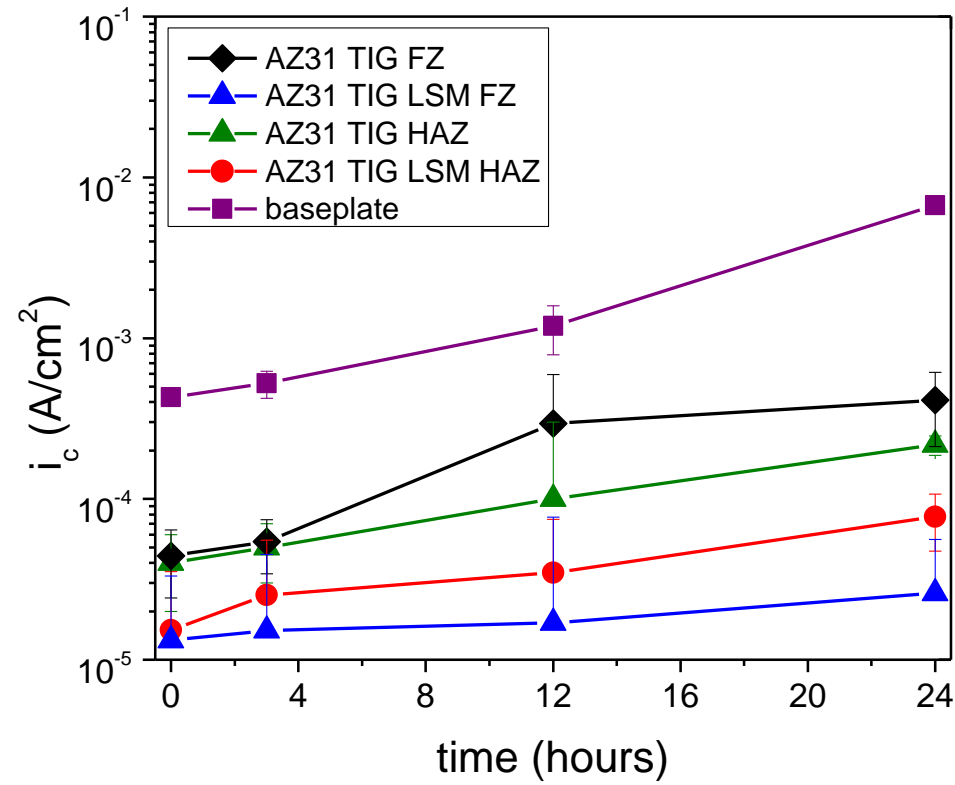
Figure 10. 11. Variation in the cathodic kinetics for wrought plate AZ31B-H24, AZ31 TIG weld isolated weld zones and AZ31 TIG weld isolated weld zones after LSM in 0.6 M NaCl measured at 0, 3, 12 and 24 hrs.
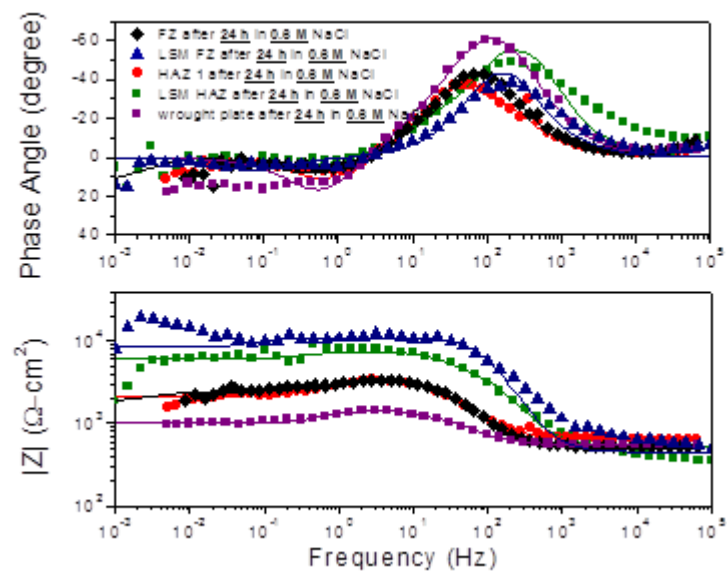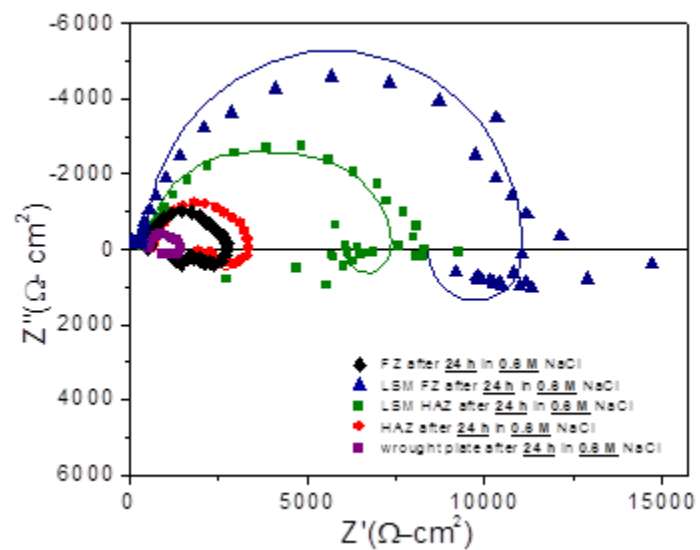
Figure 10. 12. (left) Nyquist plots and (right) Bode magnitude and phase plot for AZ31B TIG weld isolated weld zones after LSM. Data shown along with respective fits following 24 hours immersion in 0.6 M NaCl at open circuit.
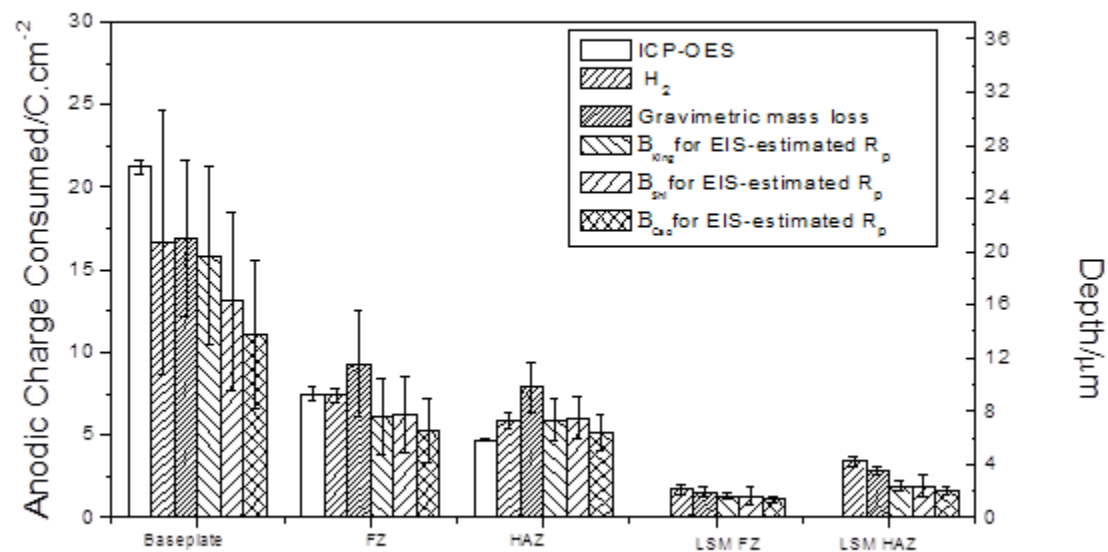
Figure 10. 13. Anodic charge consumed by wrought plate AZ31B, isolated TIG weld zones and isolated TIG weld zones after LSM in 0.6 M NaCl at open circuit after 24 hrs immersion as estimated by gravimetric mass loss, H_2 collection, ICP-OES, and EIS-estimated R_P where B_{King}=36.0 mV, B_{Shi}=36.8 mV[30], and B_{Cao}=31.1 in 0.6 M NaCl was used[23,25].